Doctoral thesis ETH No. 16512

Non-linearity and small strain behaviour in lacustrine clay

A dissertation submitted to

ETH ZURICH

for the degree of

DOCTOR OF SCIENCE OF ETH ZURICH

presented by

SOPHIE MESSERKLINGER

Dipl.-Ing. TU Graz

born 23.09.1977

citizen of Austria

accepted on the recommendation of

Prof. Dr. Sarah Marcella Springman, examiner

Prof. Dr. Helmut Schweiger, co-examiner

2006

Content

Abstract

The pre-failure stress-strain behaviour of post-glacial lacustrine soils was investigated through an extensive triaxial testing programme conducted on natural block samples of Kloten clay. A detailed study of the role of stress path history and anisotropy on the non-linear elasto-plastic stiffness behaviour was performed.

Distinct horizontal stratification of clay and silt layers, due to the annual fluctuation in the deposition mode in lakes, is typical for lacustrine deposits. This inherent anisotropy of the subsoil influences its mechanical behaviour significantly. Consequently, natural block samples were taken using a newly developed tube with a design based on extensive literature studies and testing programmes.

Pre-failure stress-strain behaviour was investigated in the triaxial apparatus with a novel measurement system, specifically designed to perform direct measurements of axial and radial displacements. Two miniature submersible LVDT's are fixed directly onto the soil specimen with a pair of mountings for the axial displacement measurement. This device is capable of recording displacements accurate to within 5 microns, corresponding to 0.01 % axial strain, over a range of 14 %. The radial displacement measurement is accomplished by a newly designed laser scanning device consisting of three lasers mounted inside the triaxial cell around the test specimen. This device is moved in the axial direction over the entire specimen height and provides the absolute and relative radial sample dimension during the test performance, determined without contact, with an accuracy of 10 microns, which corresponds to 0.04 % radial strains over a range of 20 %. A circular slice approach is proposed for the calculation of the specimen volume from the laser scan data.

A multi-stage stress path test programme was conducted in which each specimen was one-dimensionally reconsolidated beyond the in-situ pre-consolidation stress

state and permitted to swell back along this stress path to an over-consolidation ratio of two before the drained probing stress path, with a stress ratio varying according to the specimen, was applied. Therewith, the non-linear elasto-plastic stiffness behaviour, within the entire triaxial stress space, was observed and analysed by means of kinematic hardening theory, establishing the existence, shape and extent of kinematic yield surfaces and the bounding surface from examination of the shear and volumetric stress-strain curves.

The analyses of the experimental test results from the probing stress path showed non-congruent elliptical shapes for the history and the yield surface, with a proportion of around 6 on the longitudinal axis. With the application of an anisotropic elastic stiffness matrix, modified for use in the triaxial stress space, the ratio of the axial to the radial stiffness was determined as 1.7. Bender element measurements provided the reference values for the small strain elastic shear stiffness. Plastic strain vectors were evaluated and indicated that associated flow rules are mostly valid for the history and yield surfaces.

The evaluation of the laser scan data highlighted the different behaviour of silt and clay layers in the natural lacustrine clay specimens. Investigation of the development of necking in extensional shear tests showed that necking develops after the peak failure stress was reached and confirmed the applicability of a cylindrical specimen shape up to failure for data evaluation.

The introduction of these findings into geotechnical design, especially for serviceability limit state (SLS), is performed by Finite Element simulations applying the following constitutive models: Modified Cam Clay, 3-SKH, S_CLAY1 and Soft Soil. Comparison of the simulations to the test results showed that each model has preferential stress ratios where they perform best but none of the models is capable of simulating the deformation response of the entire stress space. The location of the yield state influences the quality of the deformation predictions significantly next to the definition of the plastic potential. However, further investigations are necessary in order to formulate the stress-strain response observed for lacustrine clays into a constitutive model that will be universally applicable for the simulation of boundary value problems in the everyday design of Swiss engineers.

Zusammenfassung

In diesem Forschungsprojekt wurde das Verformungsverhalten von nacheiszeitlichen feinkörnigen Gletscherablagerungen untersucht. Dabei wurde vor allem auf den Einfluss der Spannungsgeschichte und der natürlichen Anisotropie auf das nichtlineare elasto-plastische Steifigkeitsverhalten eingegangen. Dafür wurden drainierte triaxiale Spannungspfadversuche an Seebodenlehmproben von Kloten durchgeführt. Seebodenlehm ist aufgrund seiner Entstehungsgeschichte aus wechselnden Lagen von dünnen Silt- und Tonschichten aufgebaut. Deshalb wurden für diese Untersuchungen natürliche Blockproben verwendet, die mit einem speziell dafür entwickelten Probenrohr entnommen wurden.

Für die experimentellen Untersuchungen wurde ein triaxialer Versuchsapparat entwickelt, mit dem die axialen und radialen Verformungen direkt an der Bodenprobe gemessen werden können. Die axiale Dehnungsmessung erfolgte mit einem Wegaufnehmer (LVDT), der mit zwei Halterungen an der Probe fixiert war und eine Messgenauigkeit von 5 Mikrometer erreichte, was einer axialen Dehnungsgenauigkeit von 0.01 % entspricht. Für die radiale Verformungsmessung wurden drei wasser- und druckdicht verpackte Laser in der Versuchszelle an einer gemeinsamen Platte montiert, die in vertikaler Richtung bewegt werden kann und die Oberfläche der Probe mit einer Genauigkeit von 10 Mikrometer, oder 0.04 % radialer Dehnung, berührungsfrei über die gesamte Probenhöhe scannt. Für die Bestimmung des Probenvolumens aus den Laserscanndaten wurde ein Kreisscheiben-Ansatz verwendet.

Mit diesem Apparat wurden drainierte Spannungspfadversuche durchgeführt. Dabei wurden die Proben bis zu einem Spannungszustand über den In-situ-Spannungen eindimensional konsolidiert und anschliessend entlang desselben eindimensionalen Spannungspfads drainiert entlastet, bevor der drainierte

Versuchsspannungspfad auf die Probe aufgebracht wurde. Mit diesem Versuchsprogramm war es möglich, das nicht-linear elasto-plastische Steifigkeitsverhalten im gesamten triaxialen Spannungsraum zu untersuchen. Die Auswertung wurde unter Anwendung der kinematischen Verfestigungstheorie durchgeführt, wobei die Lage, Grösse und Form der kinematischen Flächen und der Fliessfläche durch Evaluierung der deviatorischen und volumetrischen Spannungs-Dehnungskurven ermittelt wurde.

Die Auswertung ergab eine nicht-kongruente, elliptische Form der Fliessfläche und der kinematischen Fläche, die aus dem Einfluss der Spannungsgeschichte resultiert, mit einem Grössenverhältnis von circa 6. Mit der Einführung einer modifizierten anisotropen Steifigkeitsmatrix wurde das Verhältnis von axialer zu radialer Steifigkeit mit 1.7 ermittelt. Die elastische Schersteifigkeit wurde mit Benderelementen gemessen. Die Evaluation der plastischen Dehnungsvektoren zeigte, dass eine assoziierte Fliessregel sowohl das Dehnungsverhalten an der Fliessfläche als auch an der Fläche der Spannungsgeschichte gut repräsentiert.

Die Auswertung der radialen Probenverformung aus den Lasermessungen hob das unterschiedliche Verformungsverhalten der einzelnen Ton- und Siltschichten hervor. Die Untersuchung der Entwicklung des Einschnürungsbereiches von Proben, die in Extension abgeschert wurden, zeigte, dass sich die Einschnürung erst nach dem maximalen Versagens-Spannungszustand ausbildet und somit die Datenauswertung unter Annahme einer zylindrischen Probenform anwendbar ist.

Die Überführung dieser Erkenntnisse in die geotechnische Bemessung der Gebrauchstauglichkeit wurde mit der Finite-Element-Methode erreicht, wobei Simulationen mit folgenden Stoffgesetzen durchgeführt wurden: Modified Cam Clay, 3-SKH, S_CLAY1 und Soft Soil. Der Vergleich der Simulationsergebnisse mit den Versuchsresultaten zeigte, dass es für jedes Modell Spannungsbereiche gibt, in denen das Verformungsverhalten gut simuliert wird, aber kein Modell in der Lage ist, das Verformungsverhalten im gesamten Spannungsraum mit akzeptabler Genauigkeit zu simulieren. Für die Einbindung des ermittelten Verformungs-verhaltens in ein Stoffgesetz mit dem Ziel, alltägliche geotechnische Gebrauchs-tauglichkeitsbemessungen in Seebodenlehm durchzuführen, ist noch einiges an Forschungsarbeit notwendig.

Acknowledgements

List of Symbols

A	cross sectional area, e.g. of the triaxial sample
A_c	current cross sectional area of a test sample
D	sample diameter
E	Young's modulus
E^*	Young's modulus in the anisotropic stiffness analysis
G'	shear modulus
G'_{max}	maximum shear modulus
G'_{bender}	shear modulus determined with the bender element method
H	sample height
H_1, H_2	hardening modulus in the $3-SKH$ model
K'	bulk modulus
K_0	coefficient of earth pressure at rest
M	coefficient for consolidation analysis
M	Parameter in the SS model
R	equivalent sample radius determined from all three laser scan data with the circular cross section approach.
R_{L1}, R_{L2}, R_{L3}	sample radius measured by laser 1, 2 or 3, respectively
R_{0L1}, R_{0L2}, R_{0L3}	initial sample radius measured by laser 1, 2 or 3, respectively
$R_{act\,L1}$, $R_{act\,L2}$, $R_{act\,L3}$	current sample radius measured by laser 1, 2 or 3, respectively
S, T	scaling factors of the yield surfaces in the $3-SKH$ model
T_v	time factor in the consolidation analysis
U_m	degree of consolidation
V	sample volume

b	variable of the anisotropic stiffness analysis; $b = \dfrac{1}{E_r}\left(1 - v_{rr}\right)$
b_1, b_2	variable in the hardening modulus of the $3-SKH$ model
c'	cohesion
c_v	consolidation coefficient
d	consolidation path
dH	change of sample height during test performance
dV	volume change during test performance
e	current void ratio
e_0	initial void ratio
e_η	void ratio at $p' = 1\,kPa$ for the stress path with the ratio η
e_λ	void ratio at $p' = 1\,kPa$ for the ICL
h, h_1	hardening modulus in the $3-SKH$ model
l	travel distance in the bender element analysis
m_f	sample weight
m_1, m_2, m_3	radial distance measured by laser 1, 2 or 3, respectively
p'	mean effective stress, defined as: $p' = \dfrac{\sigma_a' - 2\sigma_r'}{3}$
p_0', p_p', p_m', p_c'	mean effective pre-consolidation stress
p_a'	mean effective stress at the centre of the history surface in the $3-SKH$ model
p_b'	mean effective stress at the centre of the yield surface in the $3-SKH$ model
q	deviator stress, defined as: $q = \sigma_a' - \sigma_r'$
q_a	deviator stress at the centre of the history surface in the $3-SKH$ model
q_b	deviator stress at the centre of the yield surface in the $3-SKH$ model
t	travel time in the bender element analysis
t	time period in the consolidation analysis
u	pore water pressure

v_s	shear wave velocity
v	pore volume
v_η	pore volume at $p' = 1\,kPa$ for the stress path with the ratio η
v_κ	pore volume at $p' = 1\,kPa$ of the elastic plane for a defined pre-consolidation stress
v_λ	pore volume at $p' = 1\,kPa$ for the *ICL*
w	water content
x_0	centre coordinate sample in the laser scan cross section
x_1, x_2, x_3	sample surface coordinate in the laser scan cross section
y_0	centre coordinate sample in the laser scan cross section
y_1, y_2, y_3	sample surface coordinate in the laser scan cross section
z	length of the consolidation path
α	anisotropy factor
	anisotropy parameter in the S_CLAY1 model
β	hardening parameter in the S_CLAY1 model
χ_d, χ_v	variable in the S_CLAY1 model
∂	differential
δ	increment
ε	strain
γ	unit soil weight
η	stress ratio in the q - p' stress space; $\eta = \dfrac{q}{p'}$
η_{Ko}	stress ratio for one-dimensional conditions
φ	friction angle
κ	swelling index defined in the e - $\ln p'$ or v - $\ln p'$ space
κ^*	swelling index defined in the $\ln v$ - $\ln p'$ space
$\kappa^\otimes$	swelling index defined in the $\varepsilon_v - \ln p'$ space
λ	compression index defined in the e - $\ln p'$ or v - $\ln p'$ space
λ^*	compression index defined in the $\ln v$ - $\ln p'$ space
$\lambda^\otimes$	compression index defined in the $\varepsilon_v - \ln p'$ space

μ	hardening parameter in the S_CLAY1 model
v'	Poisson's ratio
v'_{ar}	anisotropic Poisson's ratio between axial and radial direction equal to v_{vh}
v'_{rr}	anisotropic Poisson's ratio the two radial directions equal to v'_{hh}
v^*	Poisson's ratio in the anisotropic stiffness analysis
ρ	current sample density
ρ_s	specific density of soil
ρ_w	specific density of water
σ'	effective stress
ψ	parameter "exponent in the hardening function" of the $3-SKH$ model
Δ	increment
Γ	pore volume at $p'=1\,kPa$ for the CSL
M	critical state value
M_{comp}	gradient of the critical state line in the q – p' space in compression
M_{ext}	gradient of the critical state line in the q – p' space in extension

subscripts:

act	current, actual
a	axial
f	failure
h	horizontal
i	$i=1,2,3,...n$
iso	isotropic
K_0	one-dimensional
Li	laser *i*
r	radial
s	shear

v	volumetric
v	vertical
0	initial
1, 2, 3	principal directions

superscripts:

p	plastic
e	elastic
0	initial

Abbreviations:

CSL	critical state line
FE , *FEM*	finite element, finite element method
ICL	isotropic consolidation line
LVDT	linear variable differential transducer
MCC	Modified Cam Clay model
NCL	normal consolidation line
OCR	overconsolidation ratio
POP	pre-overburden pressure
PWP	pore water pressure
PIV	particle image velocimetry
*S _ CLAY*1	constitutive model for soft soils
SKH	surface kinematic hardening
SLS	serviceability limit state
SS	soft soil model
ULS	ultimate limit state
Y	yield surface
3 − *SKH*	three surface kinematic hardening model

1 Introduction

Intensive development of structures and the necessary supporting infrastructure is ongoing in and around large cities. Although these urban areas are already densely settled with buildings above and below the ground, there is still a pressing need to build new structures between or beneath the existing ones.

1.1 Design in geotechnical engineering

Designing such a major structure requires fulfilment of the design conditions at ultimate limit state (ULS) as well as at serviceability limit state (SLS). The ULS is dependent upon the strength properties of the construction material, while the deformations needed for the SLS are primarily determined from the stiffness properties[‡]. Consequently, both material properties, the strength and the stiffness respectively, of all the relevant construction materials have to be established within the appropriate boundary conditions. While the properties of manufactured materials, such as steel or concrete, are well known and do not change very much from their specification, the strength and stiffness properties of geo-materials including soils or rocks are different for each construction site, and vary significantly as a function of stress history and stress state, amongst other influencing factors. As a result, they have to be investigated for each major structure or for those associated with high risks.

One of the major challenges in designing and building in urban areas, apart from designing the new infrastructure, is the protection of the existing surroundings.

[‡] Unless otherwise defined as shear or bulk modulus for the shear stiffness and compressibility respectively, stiffness will be referred to more generally as any combination of the two components.

Magnitudes of deformation, which are within the SLS of the new construction, can still exceed the serviceability limit of buildings and infrastructure nearby. Common examples are cracks in underground piped services or differential settlements of neighbouring buildings (e.g. Burland & Hancock, 1977; Burland et al., 1979; Addenbrooke & Potts, 1996; Dimmock et al., 2002). In this respect, proof of the serviceability limit state becomes a most challenging part in the design of infrastructure in urban areas.

1.2 Stiffness of geomaterials

The serviceability of the interaction between soil and structure is, as mentioned above, primarily described by the stiffness properties of the materials. For geo-materials, the stiffness behaviour is highly nonlinear (Fig. 1.1).
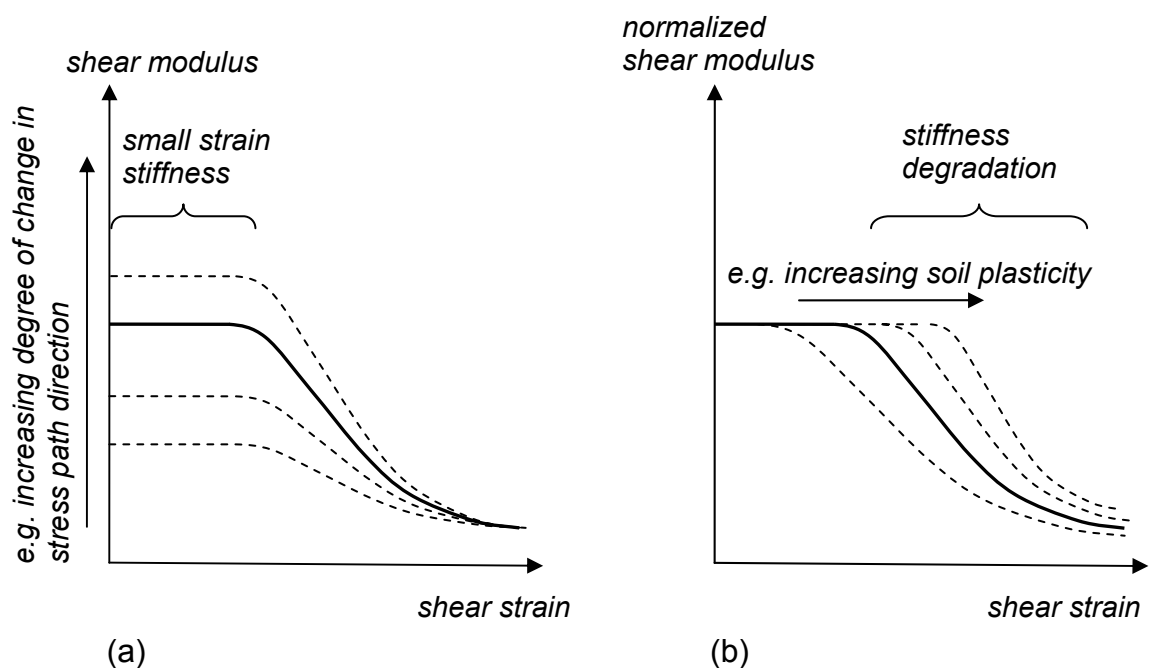
Fig. 1.1: Typical shear stiffness behaviour of soils at stress path reversal: a) variation of the initial shear stiffness, depending on the degree of stress path reversal; b) variation of the shear stiffness degradation, depending on the soil plasticity.

It is dependent on the soil type, and is highly influenced by current soil conditions such as the stress state, stress history, degree of overconsolidation or the magnitude of applied strains, to point out only a few (Richardson, 1988; Burland,

1989; Simpson, 1992; Atkinson, 2000). The stiffness is high when the load path reverses or changes direction significantly. This value is called *"small strain stiffness"* (Fig. 1.1).

The magnitude of stiffness at small strains depends on the soil type in particular, as well as on the stress state and on the degree of change in the load path direction (Richardson, 1988) among other variables. With ongoing straining along a stress path constant gradient, the initial small strain stiffness decreases continuously to values an order of magnitude smaller. The rapidity in stiffness decrease depends, for example, on the plasticity of the soil. For low plasticity soils, the shear stiffness decrease starts at a shear strain level of 10^{-3} %. With increasing plasticity, the shear stiffness starts to decrease at increasing shear strains of up to 10^{-2} %, (Vucetic & Dobry, 1991). An intensive investigation on factors affecting the initial stiffness and stiffness degradation is given in Santagata (1999).

1.3   Modelling of small strain deformation behaviour

The importance of considering such behaviour in the design of urban areas was put forward e.g. by Cole & Burland (1972), Burland & Hancock (1977), Simpson et al. (1979), Burland & Karla (1986), Burland (1989) and was a key topic at the European Conference on Soil Mechanics and Foundation Engineering in Florence, Italy (1990) as well as in the Symposiums on "Pre-Failure Deformation Characteristics of Geomaterials" in Torino, Italy (1999) and in Lyon, France (2003). Consequently, a series of constitutive models has been developed that incorporate one or several of the discussed features of nonlinear soil stiffness behaviour: e.g. the multi surface models proposed by Mröz (1967) and Prévost (1977 & 1978), the kinematic hardening models by Dafalias & Popov (1975 & 1976) and Mröz et al. (1978 & 1979), the brick model of Simpson et al. (1979), the logarithmic nonlinear elastic model of Jardine et al. (1986), the two surface bubble model by Al-Tabbaa (1987) and Al-Tabbaa & Wood (1989), the three surface kinematic hardening model by Stallebrass (1990), or the MIT-E3 model of Whittle & Kavvadas (1994). These models apply different, more or less empirical and curve fitting, methods in order to simulate the soil stiffness response more realistically.

On the basis of laboratory investigations of high quality samples (e.g. Jardine, 1985) and with the analysis of soil investigations presented in the literature (e.g. Hardin & Drnevich, 1972; Smith et al., 1992), Jardine (1992) proposed a framework (Fig. 1.2) for the description of the non-linear elastic soil stiffness behaviour based on physical observations.
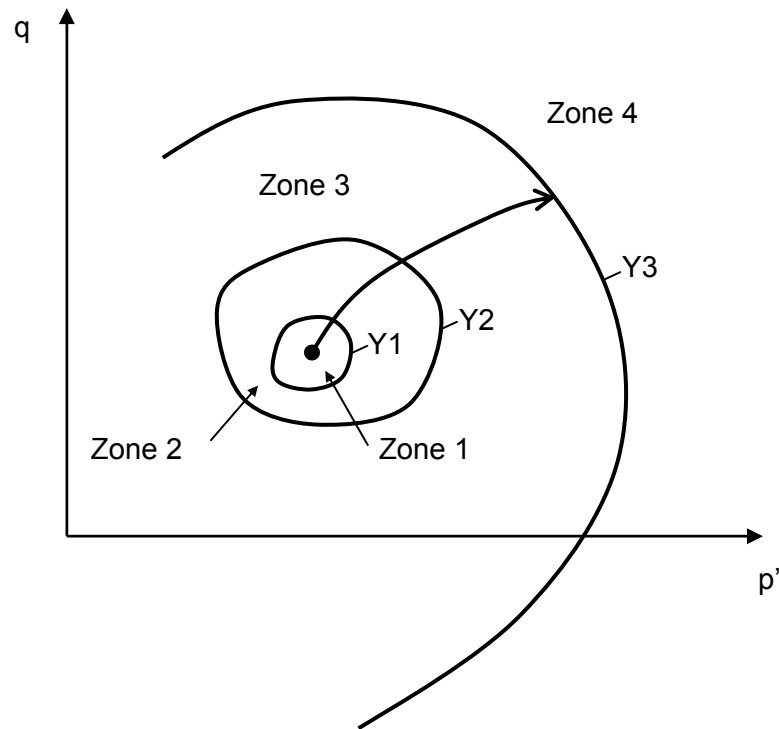
Fig. 1.2:   Definition of yield surfaces (after Jardine, 1992).

He establishes that when a soil sample is loaded from an overconsolidated stress state, the stress path moves through three stiffness zones before reaching the bounding surface. The first zone is the linear elastic region, the second zone is the non-linear elastic region and the third zone is the region inside the bounding surface where non-recoverable "plastic" strains develop already. These three zones were defined by three yield surfaces (Fig. 1.2) and the zones 1 and 2 represent the recoverable elastic region, as discussed above. Therefore, the strains are fully recoverable in both zones but the behaviour does not have to be isotropic. These two zones move together with the current stress state when a stress path is applied. Irrecoverable strains develop in zone 3 and these increase in magnitude as the stress state approaches the bounding surface, Y3, whereupon

the plastic strains dominate the deformation behaviour. The boundary of the zones is usually detectable in the stress-strain plots of a corresponding stress path test. Each intersection of the stress path with a yield surface is represented by a kink in the stress-strain curve. While the stress states of the yield surfaces 2 and 3 are generally clearly visible, the size of the Y1 yield surface is especially difficult to define for soft soils (Jardine, 1992).

Some parts of this framework have been observed previously and described in other ways, such as the Y2 surface, which was also named the history surface, and was investigated by Richardson (1988) and modelled e.g. by Stallebrass (1990). A bounding surface with inclined elliptical shape in the $q – p'$ stress invariant space was determined experimentally e.g. by Graham et al. (1983), Diaz-Rodriguez et al. (1992) and was applied to model anisotropy, e.g. by Whittle (1987), Dafalias (1987), Wheeler (1997). The achievement of this framework is that it delivers a comprehensive description of the elastic stress-strain behaviour.

1.4 Investigation of small strain stiffness response in geomaterials

To compile this description of stiffness behaviour for a particular soil type, laboratory investigations have to be performed first. The necessity of making accurate strain measurements up to a strain magnitude of 10^{-2} to 10^{-3} % has to be taken into account when choosing testing methods and setting them up. Correspondingly, accurate displacement measurement methods are necessary. The laboratory and field methods that are feasible for these investigations can be divided into two groups. Those that determine the stiffness exclusively at strain levels of 10^{-4} % and less, and those methods that are additionally able to measure the change in stiffness with increasing strain level. Methods included in the first group are bender elements e.g. as installed in the platens of triaxial test apparatus in the laboratory, or seismic measurements applied in field tests to measure the travel time of a seismic wave along a known distance to estimate the material stiffness with the aid of the material density. The measured strain level of this stiffness value corresponds to the strains applied by the seismic wave. This measured strain range is around 10^{-3} % and below (Atkinson & Sällfors, 1991;

Burghignoli et al., 1991; Lo Presti, 1991; Tatsuoka & Kohata, 1995). Methods represented by the second group include local displacement measurement devices or image-based systems. Local displacement measurement devices, for example included in triaxial test apparatuses, are mounted directly on the sample over the central two thirds (e.g. Jardine et al., 1984; Costa-Filho, 1985; Burland, 1989; Atkinson & Sällfors, 1991). This direct mounting improves the measurement accuracy by excluding errors due to bedding and compliances of the test apparatus, and the stiffness over a strain range of 10^{-3} % up to 1 % can be investigated. The image-based deformation measurement method observes the movement of single particles of the soil (e.g. particle image velocimetry (PIV), White et al., 2003) or the distortion of a grid e.g. drawn on the rubber membrane of a triaxial sample with video cameras (e.g. Sture et al. 1999). This method is especially suitable for granular soils but has also been applied successfully for clays (White et al., 2003). In field investigations, the self boring pressuremeter test is one of the methods adopted to investigate the stiffness over a wide strain range.

In addition to data provided by experimental investigations, it is possible to estimate soil stiffness by high quality back-calculation of deformation measurements, obtained from previous constructions (e.g. Cole & Burland, 1972; or Burland, 1989), which consider the entire system behaviour and the construction progress. Back-calculations are applied, in particular, in urban areas with fairly uniform and homogeneous soil conditions, where extensive development is going on.

However, determining the soil stiffness in the small strain range is still a challenge and requires sophisticated methods. So far, various specific aspects of small strain stiffness properties have been investigated on reconstituted samples for several regionally typical soil types or for natural marine clay samples, either by performing fundamental studies of the soil behaviour (e.g. Richardson 1988, Smith et al., 1992; Pennington et al., 1997; Callisto & Calabresi, 1998; Lings et al., 2000; Callisto & Rampello 2002) or to improve the constitutive models used in design (e.g. Stallebrass, 1990; Simpson, 1992; Whittle & Kavvadas 1994).

1.5   Lacustrine soils in Switzerland

In Switzerland, lacustrine clay represents one of the most challenging soils with respect to foundations and construction. The most significant difference of natural lacustrine clay compared to reconstituted samples is the distinct layered structure, which originates from seasonal variations in deposition mode. Postglacial lacustrine clays are mainly normally consolidated and hence very soft over depths of interest for construction, with significant potential for irreversible deformations. These lacustrine clays are located primarily around lakes, which are also the regions where cities and large communities have developed. Consequently, there was, and still is, a distinct need for the investigation of the failure and deformation behaviour of this soil. In 1975, Bucher investigated the peak and residual shear strength of various lacustrine clays. Heil (2006) discussed their strength and stiffness parameters determined mainly from triaxial and piezocone tests (Heil et al., 1997). Trausch Giudici (2004) investigated the initial stiffness of lacustrine clays in the laboratory with bender element tests and insitu geophysical field measurements (Maurer et al., 2000). Additionally, the plastic anisotropy of lacustrine clays was studied by Trausch Giudici (2004) based on triaxial stress path tests. Summarizing the investigations performed on Swiss lacustrine clays so far, it can be said that work has been carried out to investigate the failure, the yield and the initial stiffness characteristics. The aspect that is still missing is the stiffness degradation with shear strains. Neither the stress path dependent variation in the initial stiffness nor the shear stiffness decrease with ongoing straining has yet been investigated. But these are aspects of soil behaviour that should be known for geotechnical design in urban areas for accurate prediction of deformations, to confirm that these will be within the SLS.

1.6   Objectives of this thesis

Consequently, the aim of this research was to investigate the stiffness response and, in particular, the initial stiffness and shear stiffness decrease with increasing shear strain, of Swiss lacustrine clays. The investigation was performed in the laboratory with triaxial tests on natural clay samples, which were sampled as block samples using a 200 mm diameter thin walled sampler tube. A triaxial apparatus

was equipped with local strain measurement devices. Local LVDTs were used for axial deformation measurements and a laser scanning device was developed to measure the radial deformations over the entire sample height. Drained triaxial stress path tests were performed and all test samples were consolidated and unloaded along the same stress path. The reloading was done for each test along a different stress ratio. Therefore the variation of the initial stiffness due to the stress history as well as the stiffness degradation for stress path all over the elastic region was investigated. Two stiffness zones, based on the framework of Jardine (1992), could be established for soft Swiss lacustrine clay as well as the anisotropic characteristics of the small strain stiffness region.

Consequently, a further step has been made towards the successful modelling of the deformation behaviour of Swiss lacustrine clays. With the investigation of the elasto-plastic soil stiffness behaviour, more complex design methods together with better defined soil parameters can be used, which may lead to more accurate predictions of structural response and allow an optimization of design and construction costs.

1.7   Layout of this thesis

The *literature review* on the main research topics involved in this thesis is compiled in Chapter 2. A state-of-the-art report of research performed on Swiss lacustrine clays is given, followed by a summary of the challenges of taking high quality block samples. The most significant and recent improvements in sampling techniques are discussed. The key points in performing laboratory tests on clays are summarized together with recent developments in local strain measurement devices. Finally, common constitutive models and some of those that include aspects of the soil behaviour following stress reversal are discussed, and their parameter determination is described.

A detailed description of the soft *Swiss lacustrine clay* investigated in this thesis, is given in Chapter 3. The techniques of deriving natural block samples are described as well as the preparation procedures for the reconstituted test specimens. The results of the classification tests and mineralogical analyses are

presented and the general properties of Swiss lacustrine clay are summarized and discussed.

The laboratory testing equipment, which was developed within this thesis, is described in Chapter 4 on *triaxial test equipment*. The construction details of the test apparatuses and the measurement devices are illustrated. The monitoring system is shown and a detailed description of the calibration process and the accuracy is given.

The *triaxial testing programme* is presented in Chapter 5. The test setup procedure is illustrated and the evaluation procedure adopted for processing the results is discussed. Finally, the testing programme of the test series performed, and the test results of the particular test series, are presented.

The *analysis of the triaxial test results* is discussed in Chapter 6. From the first test series, the effect of varying the drained loading ratio is explored and the results are compared to theoretical solutions. Subsequently, the stiffness variation for each stress reversal load path is investigated. The stiffness at small strains is determined together with the strain range at which this high stiffness appears. The anisotropic effect of the natural clay samples on the stiffness parameter for the different load directions is also investigated. The failure behaviour is observed with the laser scanning device in the three test series and the effect of local necking on the stress distribution over the sample height at failure is explored.

The simulation results of the *numerical modelling* of the triaxial stress path tests are presented in Chapter 7. Firstly, the model parameter determination for a range of constitutive models is shown in detail, followed by an overview of the numerical codes applied. Then the results of the simulations of the triaxial tests of the test series are presented.

The 8th Chapter gives *remarks and conclusions* about the investigations. The sampling technique, typical properties of Swiss lacustrine clays, the new laser scanning device, triaxial testing of lacustrine clays and the constitutive models applied to Swiss lacustrine clays are discussed. This Chapter gives an overview of the investigations performed and points out the major findings of this research, with the aim to provide assistance for ongoing research.

2 Literature review

2.1 Swiss lacustrine clay

An overview of the formation of lacustrine clays in Switzerland and the resulting typical properties is given in this paragraph.

2.1.1 Geological formation

Switzerland was covered several times by glaciers during the last 1.5 million years. A detailed picture of the occurrence of ice ages and the extent of the alpine ice shield in Switzerland is given in Labhart (1995). However, the last ice age in which Switzerland was widely covered with glaciers was the Würm ice age (Penck, 1925), which ended at the end of the Pleistocene age, about 10,000 years ago.

During an ice age, glaciers continuously flow downwards from the Alps in valleys. The flowing occurs in several stratums as shown in Fig. 2.1 and ends at the tongue of the glacier where the ice melts. When the melting rate is lower than the flow rate, the glacier is expanding, and when the melting rate is higher than the flow rate, the glacier is retreating.

When the melting rate is in equilibrium with the ice movement rate, the tongue of the glacier remains stationary but the laminar flow in the glacier continues. If this is the case for a long enough period, the glacier scrapes out a basin of the bed rock, due to the enormous erosional power of a moving ice mass, up to 1,500 m thick, which is called an end-basin (Fig. 2.2a). At the end of the ice age, when the glacier retreats, the end-basin remains and becomes filled with water. Initially, the water source is the melting glacier and subsequently rivers are formed, which transport the melt water as well as rainwater from the Alps and enter the newly formed lake.
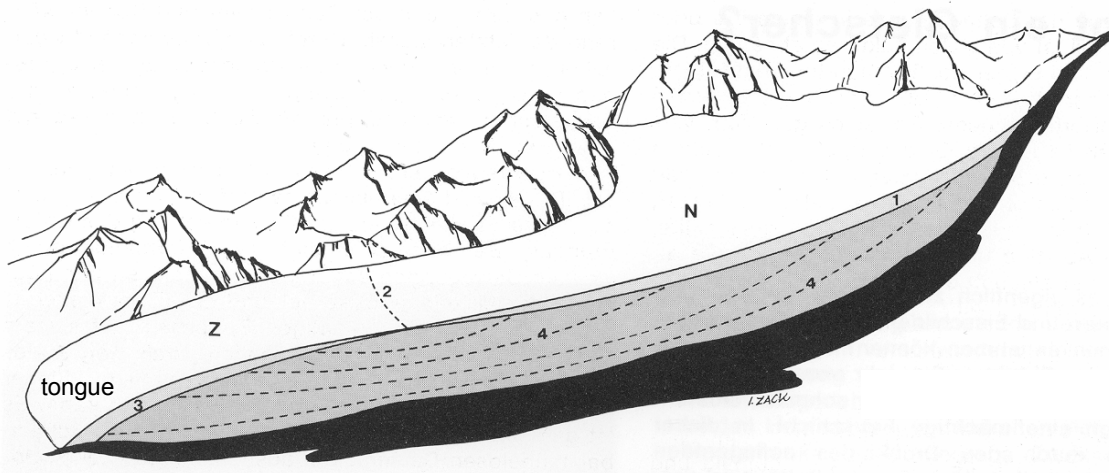
Fig. 2.1: Anatomy of a glacier: (N) Collecting basin: region were new ice mass (1) is built. (Z) Glacier wastage: region where ice is melting (melt-out) (3). (2) Boundary between region Z and N. (4) Laminar flow of the glacier. (van Husen, 1987).
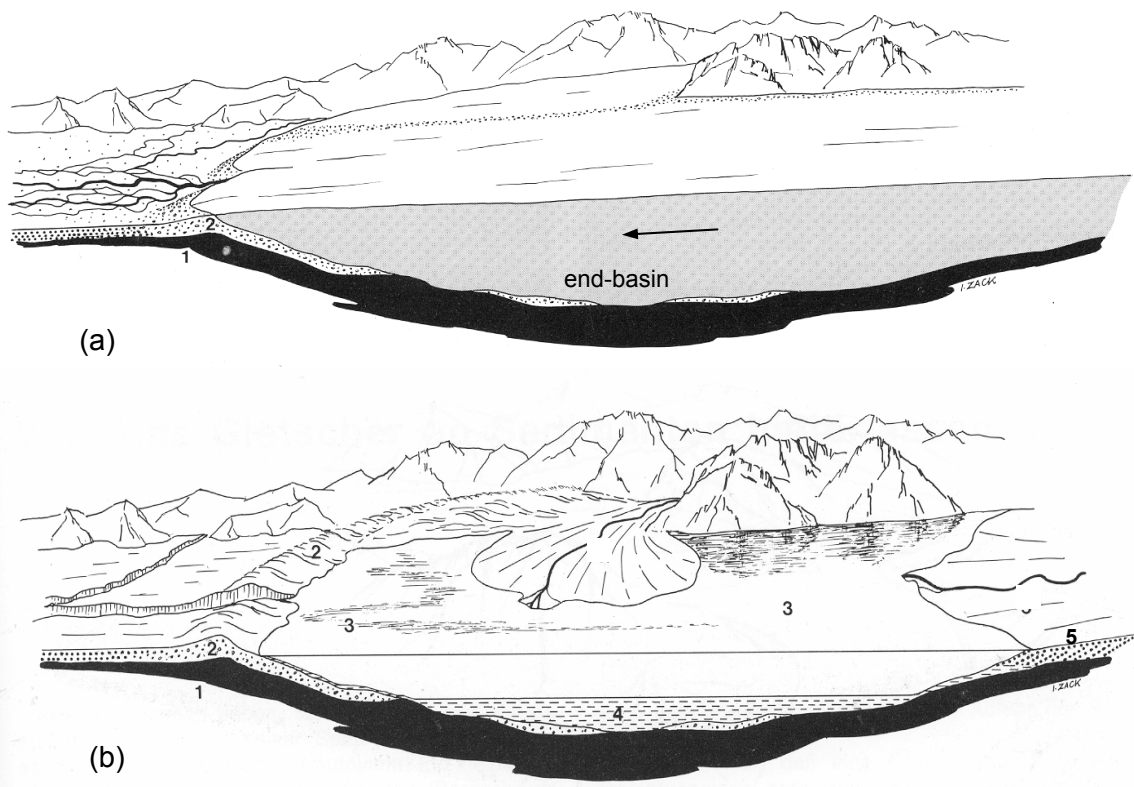
Fig. 2.2: (a) Formation of the end-basin and end moraine (2) behind a barrier of rock (1). (b) Glacial lake (3) in which lacustrine deposits sediment as foreset (5) and bottomset (4) (van Husen, 1987).

The last ice age in Switzerland was the Würm ice age (Penck, 1925), which shaped the earth′s surface to its recent morphology. Since then, rivers have transported enormous amounts of sediment and suspended sediment into lakes where they have been deposited (Fig. 2.2b). The sedimentation rate in the lake depends on the petrology of the drainage basin of the rivers. If the drainage basin was primarily built up by crystalline rocks, the corresponding end basins were often filled soon after their formation because of the great amount of suspended sediments available (van Husen 1987) compared to drainage basins built up by calcareous rocks. Due to this and also depending on the size of the end basin and the water supply, some lakes were filled in a relatively short time, whereas others are still remaining as lakes.

The remaining post-glacial lakes are still entered by rivers, which are formed of rain, melt water and suspended sediments. During spring and summer, when rivers display their maximum run-off, the greatest amount of till reaches the post-glacial lakes. For example, the river Rhine transports 3 to 6 million tonnes of suspended particles per year into Lake Constance (König, 1978). These tills can be split into gravels and sands, which are usually deposited in the delta to form a foreset[*] (Fig. 2.2), and the silts and clays which are spread over the entire lake area due to their low sinking velocity before they sediment out as lacustrine clays to form the bottomset[†] (Fig. 2.2). While the silts deposit during the summer period, the clay particles sediment out more slowly and deposit mainly in the winter period, after the silt fraction. The result is a distinct stratification (varving[‡]) of the sediment (Fig. 2.3), which is the most significant characteristic of lacustrine clays.

---

[*] Foreset bed: "Inclined layers of a cross-bedded unit, specifically on the frontal slope of a delta." (Bates & Jackson, 1984)

[†] Bottomset bed: "Horizontal or gently inclined layers of sediment deposited in front of the advancing foreset bed of a delta." (Bates & Jackson, 1984)

[‡] Varve: "A sedimentary lamina or sequence of laminate deposited in a body of still water within one year's time; specif. a pair of layers seasonally deposited in a glacial lake. A glacial varve normally includes a lower "summer" layer consisting of light-colored sand or silt, which grades upwards into a thinner "winter" layer, consisting of clayey, often organic, dark sediment." (Bates & Jackson, 1984).

The thickness of the annually sedimented layer depends on the amount of suspended material inflow and the area of distribution and is typically in the range of millimetres (König, 1978) in Switzerland. The overall thickness of these glacial and post-glacial deposits can nowadays reach up to 200 metres (e.g. Lake Constance: König, 1978).

Fig. 2.3:   Varved texture of natural lacustrine deposits shown on a sample from Wauwil. The sample is taken from a borehole at a depth of 27 m and broken into two halves to observe the stratification (ruler unit in centimetres).

Most of these deposits from the last ice age have not been loaded by ice or further sediments since then. They are only loaded by their self weight. A small degree of overconsolidation may result from the increase of the effective stresses due to subsequent changes in the water table and from secondary consolidation (creep) (Parry & Wroth, 1981). Consequently, these post-glacial deposits are called normally consolidated lacustrine clays or „soft Swiss lacustrine clays".

The formation of local lacustrine clay deposits in Switzerland and their properties are described in more detail e.g. by Rey (1994), who investigated the geology and formation of varved clays in Flurlingen-Schaffhausen and Dietlikon, which are two regions of the Swiss Mittelland or by Gyger et al. (1976), who gave a general overview of the sedimentation in the lake of Zürich since the last glaciation. An investigation of lacustrine clay from Lake Constance in terms of strength and stiffness properties was performed by Scherzinger (1991) and a state-of-the-art report on geology and engineering properties of lacustrine and varved clays was given at the Conference on "Characterisation and Engineering Properties of Natural Soils" in Singapore by DeGroot & Lutenegger (2003), Diaz-Rodriguez (2003), Long (2003) and Soccodato (2003).

2.1.2 Geographical location

The deposits of lacustrine clays in Switzerland are mainly concentrated in the Mittelland (Fig. 2.4), which is located between the Alps and the Jura mountains. This region is at the same time the most densely populated and fastest developing area in terms of infrastructure and construction. Therefore, understanding the geotechnical properties of Swiss lacustrine clays is of special interest (see also Chapter 1: Introduction).

2.1.3 Former research

Due to the pressing need to design structures in urban areas founded on lacustrine clay deposits, the investigation of soft lacustrine clay has a long tradition at ETH Zurich and especially at the Institute for Geotechnical Engineering, e.g. (Bucher, 1975; Amann et al., 1992; Heil et al., 1997; Springman et al., 1999). While investigations were mainly related to expertise work done by the Institute during the earlier stages, e.g. Lang (1976), the recent research projects focus more on the investigation of fundamental soil behaviour, e.g. Trausch Giudici (2004) or Heil (2006).

The main focus of these research projects on Swiss lacustrine clays was on the investigation of their failure properties. Determination of the undrained shear strength was investigated by insitu tests with a van der Berg piezocone (Cone Penetration Testing device with pore pressure measurement, CPTU; Amann et al.,

1992; Amann & Heil, 1995; Heil et al., 1997; Springman et al., 1999; Trausch Giudici 1999; Panduri, 2000). Laboratory studies were also performed by means of undrained triaxial shear tests (Heil, 2002 & 2006)
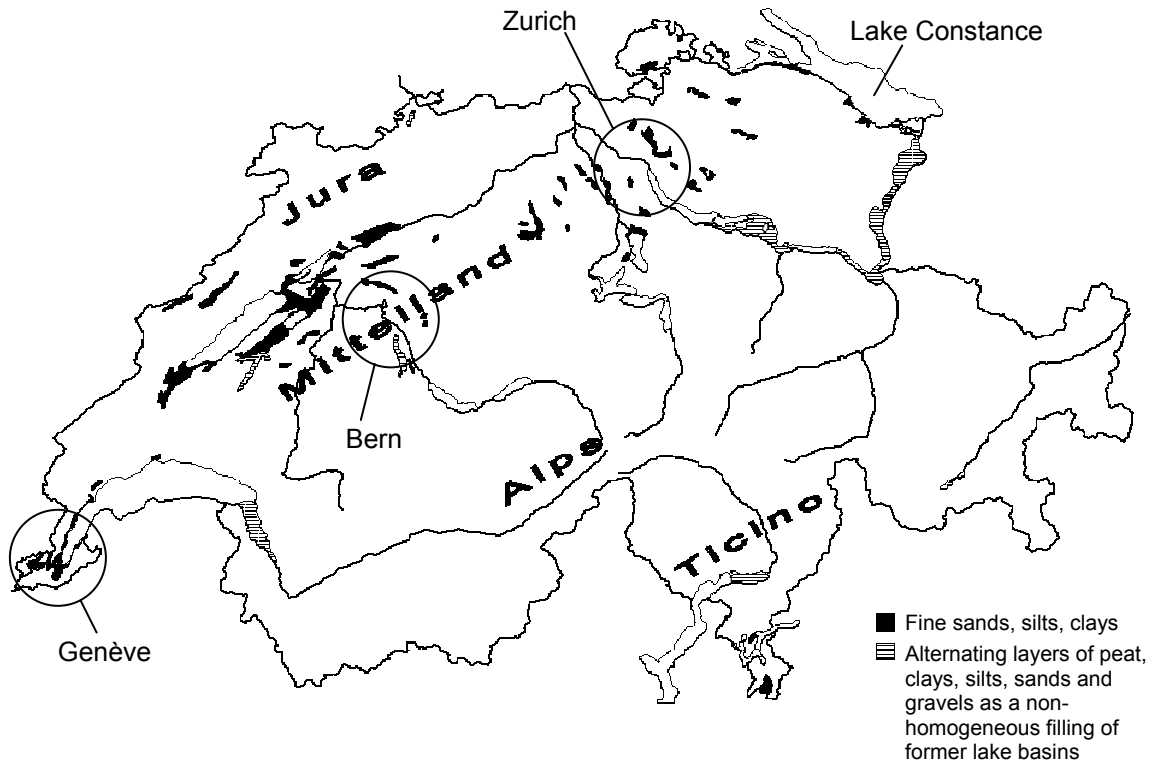
Fig. 2.4:   Occurrence of fine grained and soft clayey and peaty deposits in Switzerland (source: Hydrogeological map of Switzerland) after Amann & Heil (1995).

An additional emphasis was put on the investigation of the pre-failure behaviour by Trausch Giudici (2004). A geophysical investigation programme was initiated to investigate the elastic stiffness properties. The determination of the shear modulus at various stress and strain states of the soil was of particular interest (Maurer et al., 2000) and the elastic stiffness properties of Swiss lacustrine clays were investigated by bender elements in the laboratory with the triaxial test apparatus (Trausch Giudici, 2004). The elasto-plastic behaviour was also investigated with extensive triaxial stress path tests on natural samples (Trausch Giudici, 2002 & 2004).

Another research interest at the Institute is the influence of mineralogical composition on the mechanical properties of the clay. The peak as well as the

residual shear strength of different clay minerals (e.g. Kaolinite, Illite, Montmorillonite) was investigated, mainly with respect to the determination of slope stabilities (Müller-Vonmoos et al., 1985; Müller-Vonmoos & Loken, 1988).

2.2   Sampling of natural clays

A summary of the most important aspects of soft clay sampling is given, followed by a presentation of recently developed sampling techniques. The influence of the sampling technique on the material parameters derived in laboratory investigations is discussed, and finally recommendations for the block sampling of natural soft clays are outlined.

2.2.1 Introduction

One of the major impacts on the results of laboratory investigations is due to test specimen quality and the degree of disturbance. Natural samples taken from the field undergo a multitude of handling, packing and storage events, which influence the response of the sample in terms of the properties derived. These influences affect the sample either as stresses or as strains or both. The two main effects on a laboratory sample in comparison to the equivalent soil in-situ are stress release due to excavation, and the strains applied due to the sampling technique. A detailed list of sample disturbances that may be imposed on soil samples, from taking the sample in the field to setting up the sample in the test apparatus, is given in Jamiolkowski et al. (1985).

The sample quality of structured soils is governed by the magnitude of strains applied to the sample during sampling. If the applied strains are larger than the strains necessary to break up the structure, the derived samples become destructured (La Rochelle & Lefebvre, 1971). Most strain applied during sampling is caused by the sample device.

An analytical investigation of the sample disturbance due to tube sampling was performed by Baligh (1985). He studied the deformations that occur in soil samples due to undrained penetration of a rigid "object" in to saturated clays using the strain path method. This method assumes that the soil deformations are

independent of the shear resistance, which is applicable to deep penetration problems.

The strain history of a soil element at the centreline of a sampler during sampling was determined (Baligh, 1985). The tip of the sample tube applied in this calculation is rounded (Fig. 2.5c). The vertical strains (ε_z) that occur in the soil are given in Fig. 2.5a depending on the vertical location of a cylindrical sample orientated in the axial direction (Fig. 2.5b).
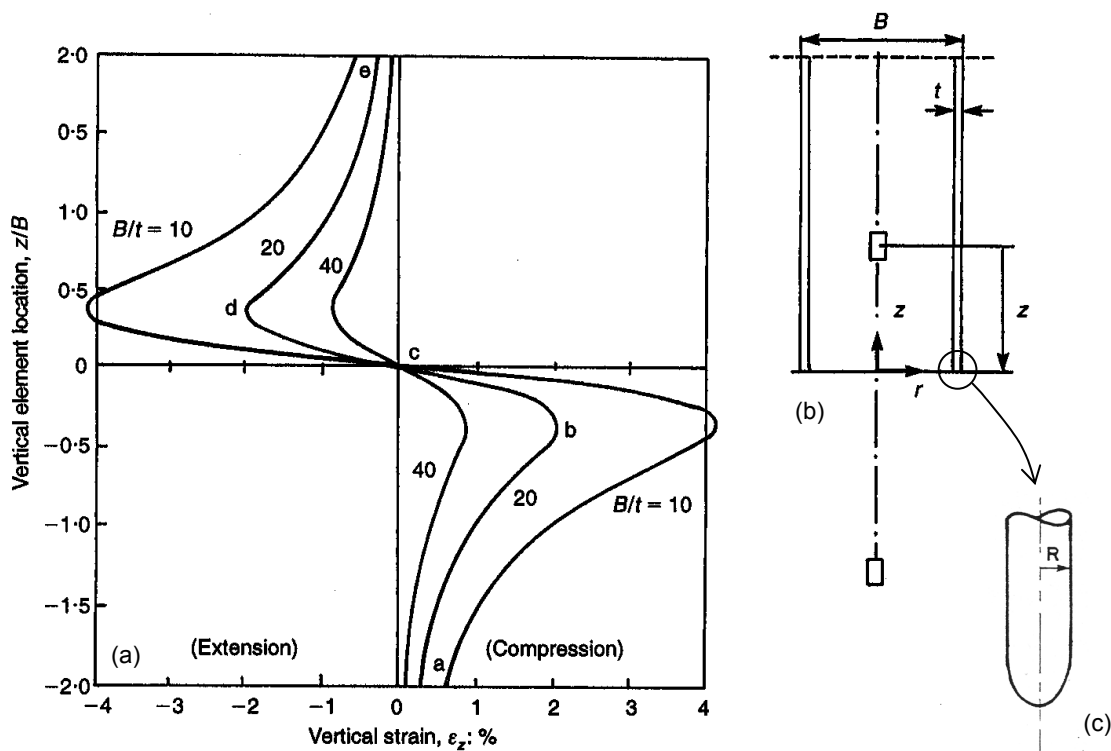
Fig. 2.5: Clay disturbance during sampling: (a) strain history of the sample at the centreline; (b) sample tube with the relative location of the soil specimen investigated; (c) close-up view of the tube tip applied in the simulations (Baligh, 1985).

Results for three different ratios of sample diameter (B) to sampler wall thickness (t) are presented and show that a significant amount of compressive strain is generated in the soil in front of the sample tube due to displacement occurring during insertion. This is followed by a similar amount of strain in extension after the soil sample enters the sampling tube. Although the magnitude of strains reduces

with the increase of the B/t ratio, the sample still undergoes a sequence of compressive and extensive strains of a magnitude of around 1 % or more.

A followup study was done by Baligh et al. (1987) in which the strain distribution of the whole sample cross section and the surrounding soil is determined by the strain path method (Fig. 2.6). The results show that a distinct smear zone in the soil sample is formed along the walls of the sample tube. Significant straining is developed in this zone mainly due to the friction between the wall of the sample tube and the adjacent soil, the stress concentration at the sample tube tip and the movement of the soil around the tip.
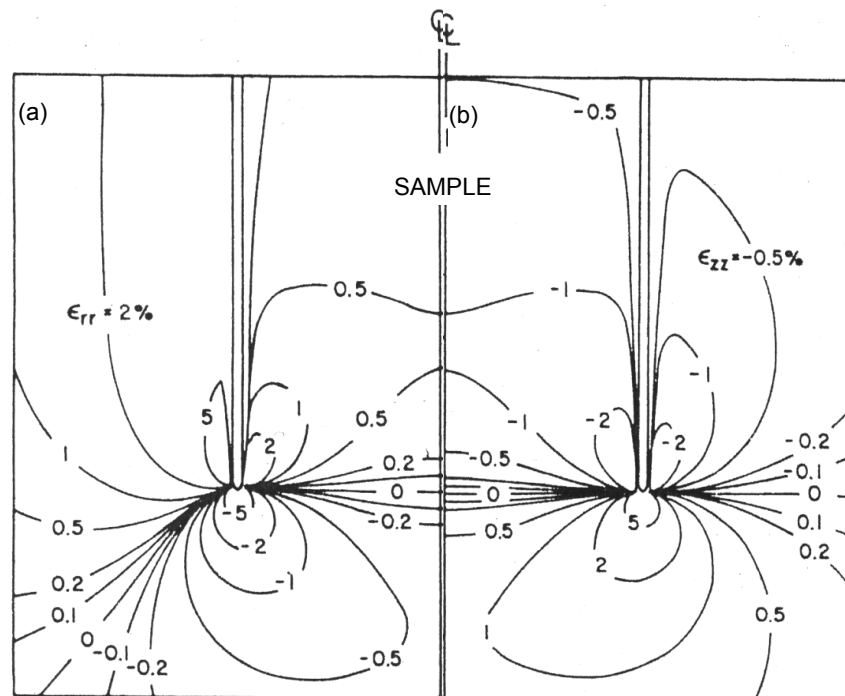
Fig. 2.6: Strain contour lines due to undrained penetration of a sample tube with B/t = 40 (Fig. 2.5): (a) radial strain; (b) vertical strain (Baligh et al., 1987).

But this smear zone occurs in the outer 20 % of the sample diameter (Fig. 2.6), and the applied strains reduce towards the centre. In the middle region, a more or less constant amount of strain is developed over the whole sample cross-section, which is mainly due to compression beneath the sample cross section. Consequently, a significant improvement in the quality of the test specimen can be achieved when the compressive stress induced as the sample tube penetrates is

minimized and when the sample diameter is large enough that the smear zone can be discarded during the test specimen preparation.

Subsequently, Clayton et al. (1998) used the strain path method to investigate the influences of area ratio, cutting-edge angles and inside clearance on the sample disturbance in more detail. A definition of the various ratios is given in Fig. 2.7.

Area ratio $AR = \dfrac{R^2 - R_1^2}{R_1^2}$

Inside clearance ratio $ICR = \dfrac{R_2 - R_1}{R_1}$

Inside cutting-edge angle $ICA = \alpha = \arctan\left(\dfrac{R_2 - R_1}{H_1}\right)$

Outside cutting-edge angle $OCA = \beta = \arctan\left(\dfrac{R - R_1}{H_2}\right)$
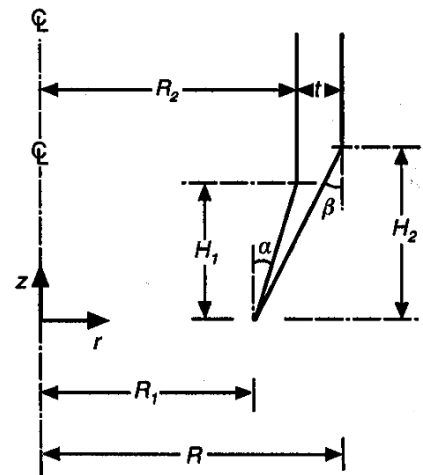
Fig. 2.7:   Definition of sampler parameters after Clayton et al. (1998).

The strain evaluations of Clayton et al. (1998) were done for a soil element along the centre line of the sample tube as well. The results are summarized in Fig. 2.8. The numerical study showed that the inside clearance has the most potential to generate axial strains and corresponding sample distortion. The inside clearance was originally introduced to reduce the shear stresses between the inside of the sample tube and the soil to prevent sample jamming. But La Rochelle et al. (1981) had already stated that sample disturbance due to friction between the soil and the inside of the sampler is comparably small and can be neglected. La Rochelle et al. (1981) further contended that inside clearance of a sample tube will subsequently permit lateral expansion of the sampled soil, which enlarges the area ratio effect and supports the statement of La Rochelle (1973) that sampling with sample tubes with inside clearance is like „squeezing" the soil into the tube. These suggestions and assumptions of La Rochelle have finally been supported by the numerical investigations of Clayton et al. (1998).

La Rochelle et al. (1981) comment that during the penetration of the tube, soil of the thickness of the tube wall has to be removed. If there is no cutting edge, the soil is squeezed similarly inside and outside of the tube. If the tube has cutting edges, the soil is squeezed towards the outside and this is increased as the cutting edge angle becomes smaller, so that the sample inside the tube will be less influenced by volume changes. La Rochelle et al. (1981) further stated that the effect of the area ratio can be minimized by small cutting edge angles.
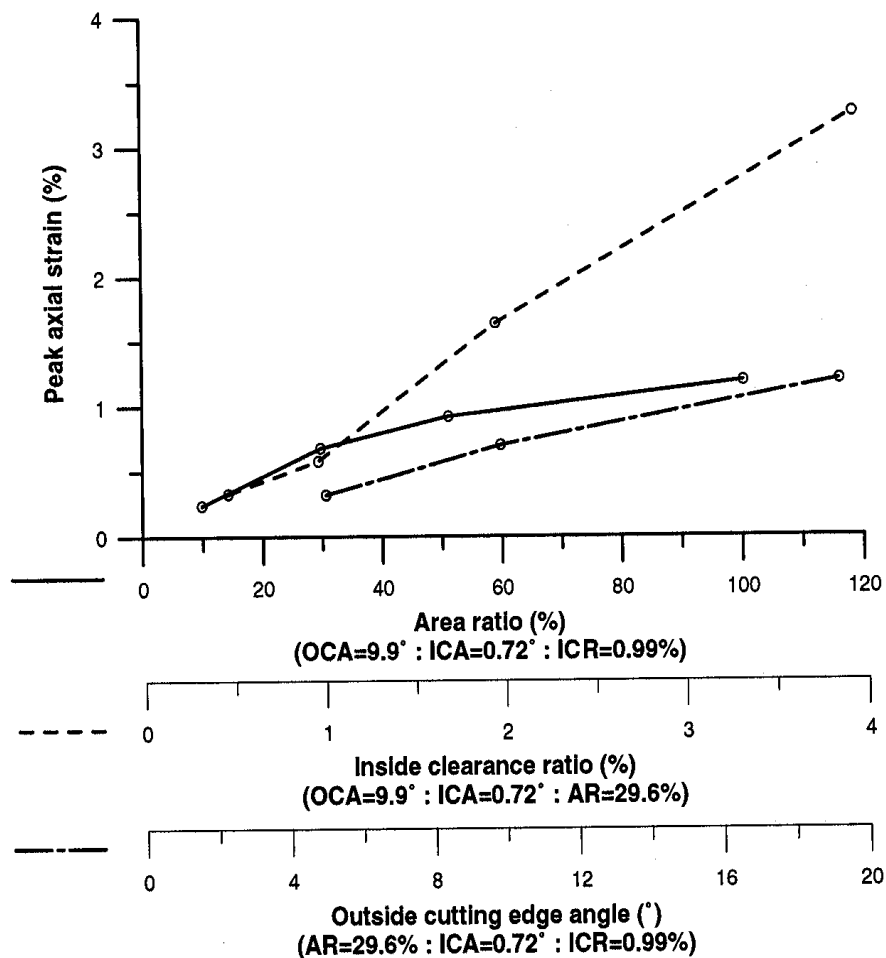
Fig. 2.8: Effect of tube geometry on peak axial strains in the centreline of a tube sample (Hight & Leroueil, 2003 after Clayton et al., 1998).

The results of the numerical study (Clayton et al., 1998) show that the area ratio of the sample tube and the outside cutting edge angle have a similar impact on sample disturbance with increasing values of the corresponding ratios. There was no indication that the effects exclude each other. Both, the area ratio and the

cutting edge angle have an influence on the sample quality, although the distortion that can occur from the area ratio and the outside cutting edge angle is small compared to the effect of increasing inside clearance.

These investigations show that the magnitude of axial strains caused by sample disturbance even for good quality tube samples still cannot be below about 0.5 %, and to achieve this requires a sample tube with an area ratio of below 20 % and an outside cutting edge angle of around 8° (Fig. 2.8).

2.2.2 Sampling techniques

The most common procedure to obtain natural samples from the field is to take tube samples from boreholes. This is done by pushing a tube into the ground and withdrawing the sample in its tube from the ground with assistance of a vacuum.

Lefebvre & Poulin (1979) found, by analysing laboratory test results of specimens obtained by different sampling techniques in the years between 1960 and 1970, that test results from specimens extracted from blocks show a significantly higher effect of structure than those obtained from tubes.

Another comparative study of soil parameters derived from block samples and 54 mm high quality tube samples was done by La Rochelle and Lefebvre (1971). This investigation showed that the undrained shear strength and the modulus of elasticity had values that were twice as high for tests on block samples compared with those on tube samples. The block samples were carved out of a shallow deposit, as shown in Fig. 2.9. This is a cheap and straightforward sampling method for stiff clays in trenches close to the surface. One of its major disadvantages is the sampling depth, which is limited by the trench depth as well as by bottom heave occurring in the trench. Therefore, the maximum depth of the sampling trenches is restricted to 3 to 4 metres.

To remedy this, Levebvre and Poulin developed a block sampling technique with which samples from greater depth could be taken. The new apparatus, which is shown in Fig. 2.10, was named the Sherbrooke sampler after the University of origin. The idea is to carve blocks out of the bottom of boreholes, as was done previously in trenches. A device (Fig. 2.10a) is lowered into the borehole to carve a cylinder with a diameter of 25 cm out of boreholes of diameter of 40 cm. The

borehole is supported by bentonite slurry. The carving device consists of three vertical steel rods, which are mounted together (Fig. 2.10a). On the bottom of each of the three rods, small vertical steel plates, called „cutting tools", are situated, which carve a cylinder of 25 cm diameter in the soil. Additional bentonite is pumped through the three rods to the cutting edges to help the excavation process. The sample height is expected to be about 35 cm.

Fig. 2.9:   Carving of block samples at the bottom of an opened trench (Lefebvre & Poulin, 1979).

Additionally, horizontal diaphragms are fixed on each cutting edge to separate the sample from the deposit. These can rotate towards the sample centre to close the bottom, as shown in Fig. 2.10b. The diaphragms are released with pins, operated from the surface, and powered by springs situated in the three vertical rods. These diaphragms also provide support under the sample whilst lifting it out of the borehole. Afterwards the samples are coated with paraffin and cotton strips and stored in containers for transport.

Any compression arising from pushing a device into the soil is avoided with this sampling technique. Due to the diaphragm, which cuts off the sample and creates

bottom support during removal from the borehole, no vacuum has to be applied to the sample and samples may be extracted from various depths. Therefore, many sampling influences due to taking the sample out of the in-situ deposit are reduced or completely avoided with this method. For layered soils, the only disadvantage is the unsupported cylindrical surface of the sample which leads to different drainage conditions between silt and clay layers, resulting in suction developing within the clay layers.
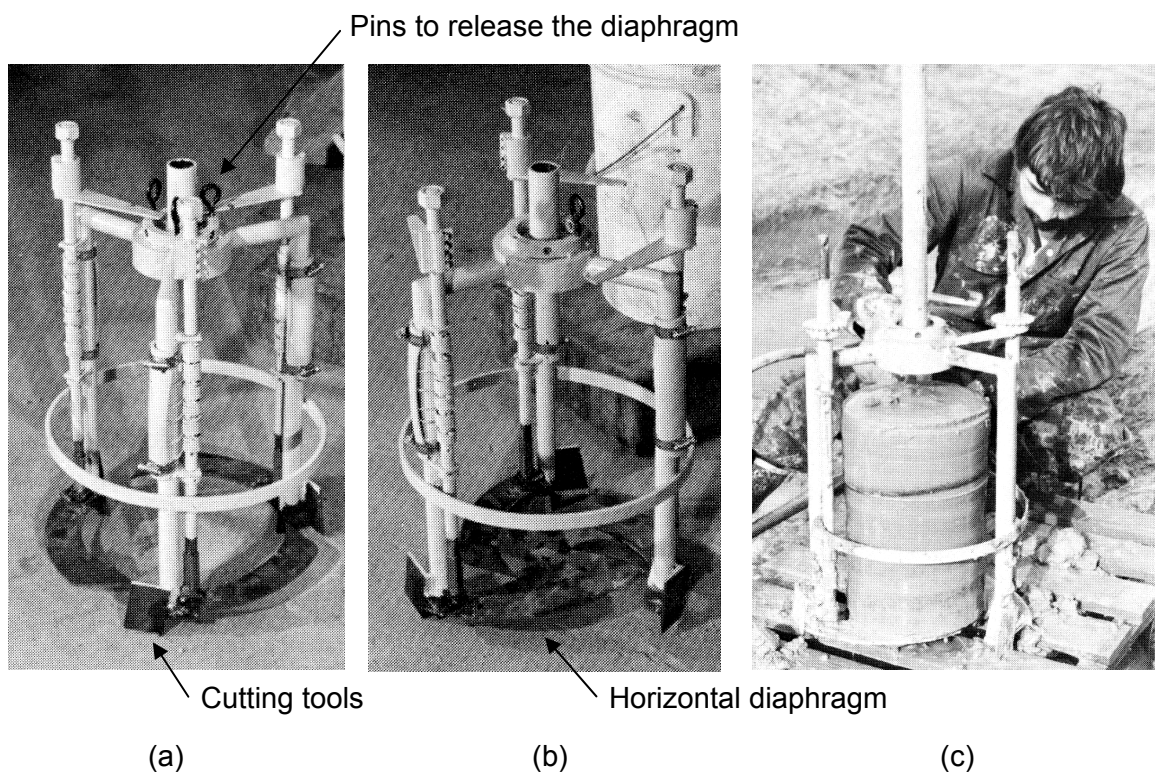
Fig. 2.10: Sherbrooke sampler (a) bottom diaphragm opened; (b) bottom diaphragm closed; (c) cylindrical sample extracted with the Sherbrooke sampler (Lefebvre & Poulin, 1979).

Simultaneously, another sampler has been developed at the University of Laval using a larger diameter tube, which is called the „Laval sampler" and was first presented by La Rochelle et al. (1981). This sampler consists of a tube of length of 66 cm, an inner diameter of 208 mm and a wall thickness of 5 mm. The accuracy of the sample tube dimensions (in terms of diameter and shape) is required to be ± 0.03 mm. The cutting edge angle is 5° therefore the effect of the tube thickness is assumed to be minimized (La Rochelle et al., 1981). This sample tube is fixed on

the sampler head and moves inside the coring tube, as shown in Fig. 2.11 b. The sampler is used in boreholes, usually supported by a bentonite slurry. The sampler is lowered in the borehole to the base of the existing borehole, where the sample tube is pressed into the soil and the bentonite slurry in the sample tube can flow out through the top of the sampling tube.
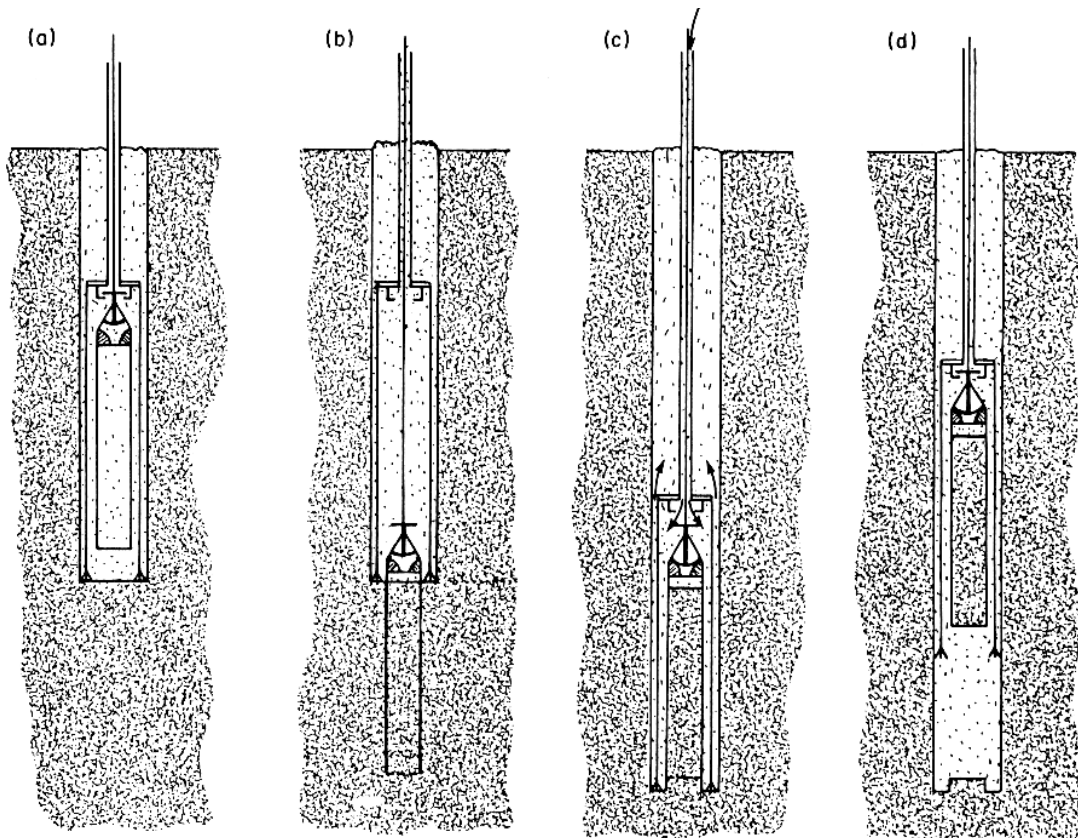
Fig. 2.11: Operation of the Laval sampler: (a) sampler is lowered into the borehole; (b) sample tube is pushed into the soil; (c) coring tube overcores the sample tube and injects bentonite slurry; (d) sampler with the soil sample is extracted from the borehole (La Rochelle et al., 1981).

Subsequently, the core tube cuts the sample tube out of the soil, by cutting a trench around the tube (Fig. 2.11 c). Two centimetres beyond the end of the sample tube the core tube is stopped, and valves at the top of the sampler are closed and sealed, so that no bentonite suspension can flow back to the sample tube during extraction of the sample. Bentonite suspension is pumped in between the core and the sample tube to clean the cutting devices and to separate the

sample from the deposit. By rotating the sample tube through 90° and lifting, the sample is separated from the parent soil and removed. Thereafter, the sample is extruded from the tube because it is assumed that samples stored in rigid steel tubes are more sensitive to vibrations or shocks imposed during transport than samples which are extracted from the tubes. Then the sample is cut into horizontal slices, and packed in layers separated by a Paraffin wax and Vaseline mixture, with Saran paper in between.

Although a tube is still pushed into the soil with the Laval sampler, the small angle of the cutting edges and a nearly perfectly circular shaped sample tubes mean that the volume change of the soil in the sample tube should be minimized. By over-coring the tube afterwards, and injecting bentonite slurry at the bottom, suction in the sample is reduced during extraction from the soil deposit.

2.2.3 Influence of sampling technique on the mechanical response of soil

Next to the fact that sampling changes the stress as well as the strain state, the most important question is how much this affects the shear and compression parameters of the soil that are subsequently determined by laboratory tests. Lacasse et al. (1985) describes an intensive study of the different behaviour of block samples derived by the Sherbrooke sampler and 95 mm tube samples. The aim of this study was to investigate whether the degree of sample disturbance depends on the clay type, and how the mechanical parameters determined by the different laboratory tests are affected. Two quick clays (Sensitivity: > 60, Plasticity index: 3 to 12, Grain content > 60 μm: 9 to 10 %, < 2 μm: 37 to 40 %) and one plastic clay (Sensitivity: 6 to 9, Plasticity index: 30 to 44, Grain content > 60 μm: 0 %, < 2 μm: 60 %) were investigated. Lacasse came to the conclusion that in tests where the samples are restrained on the radial boundaries, such as in oedometer tests, sample disturbance influences the results less compared to tests where the soil is partly or wholly unsupported, as for example in the unconfined compression test. The effect of sample disturbance on triaxial test results lies somewhere in between the rigidly supported and the free radial boundary case. It was clear that quick clays are more influenced by disturbance than the plastic clay.

This was explained by the sand and gravel contents, which are higher in quick clay than in plastic clay and which can generate horizontal movement of the sample tube, if it hits a sand or gravel grain during penetration into the deposit.

Another method of investigating the quality of a current sample is to determine the yield points from the stress-strain plots. If yield points are clearly visible, the sample is of high quality (Jamiolkowski, 2003).

Tanaka & Tanaka (1999) compared the results of unconfined compression tests on samples of Ariake clay, taken from a depth of 10 m. The samples were extracted using the following methods:

- Laval sampler, which has a 660 mm long sample tube with a diameter of 208 mm, no inside clearance, a cutting edge of 5° and 5 mm wall thickness (AR = 4.9 %; ICR = 0; ICA = 0°; OCA = 4.4°).
- Sherbrooke sampler, which carves a cylindrical samples of approximately 250 mm diameter and 350 mm height from a borehole.
- Japanese Standard Piston sampler, using a 1 m long tube with an internal diameter of 75 mm, with no inside clearance, a cutting edge of 6° and 1.5 mm wall thickness (AR = 4.3 %; ICR = 0; ICA = 0°; OCA = 5.3°).
- NGI 54 (Norwegian piston sampler), with a 768 mm long sample tube, which has an inner diameter of 54 mm and wall thickness up to 13 mm (AR = 53.9 %; ICR = 6 %)
- ELE100 piston sampler, with a 500 mm long tube having an internal diameter of 101 mm, no inside clearance, a cutting edge of 30° and 1.7 mm thick wall (AR = 3.4 %; ICR = 0; ICA = 0°; OCA = 28.7°).
- Shelby tube, which has an internal diameter of 72 mm, a wall thickness of 1.65 mm and is 610 mm long (AR = 4.6 %).

The results (Fig. 2.12) point out that the highest failure stress was achieved on Sherbrooke samples followed by those from the Japanese Standard Piston sampler and the Laval sampler. Comparing the 4 tube samplers with internal diameters of 100 mm and smaller, it can be seen that the diameter is not the only factor that influences the sample quality. The Japanese Standard sampler has an extremely low cutting edge angle of 6° and samples of high quality have been taken, although the diameter of 75 mm is similar to that of the Shelby tube. The

NGI54 sample tube has the smallest diameter of 54 mm but higher failure stresses could be achieved than for the samples from the ELE100 sampler with a sample tube diameter of 101 mm.

The stress-strain curves and accompanying parameter table:

	Laval	Sherbrooke	JSP	NGI5	ELE1	Shelby
AR [%]	4.9	-	4.3	54	3.4	4.6
ICR [%]	0	-	0	6	0	-
ICA [°]	0	-	0	-	0	-
OCA [°]	4.4	-	5.3	-	28.7	-
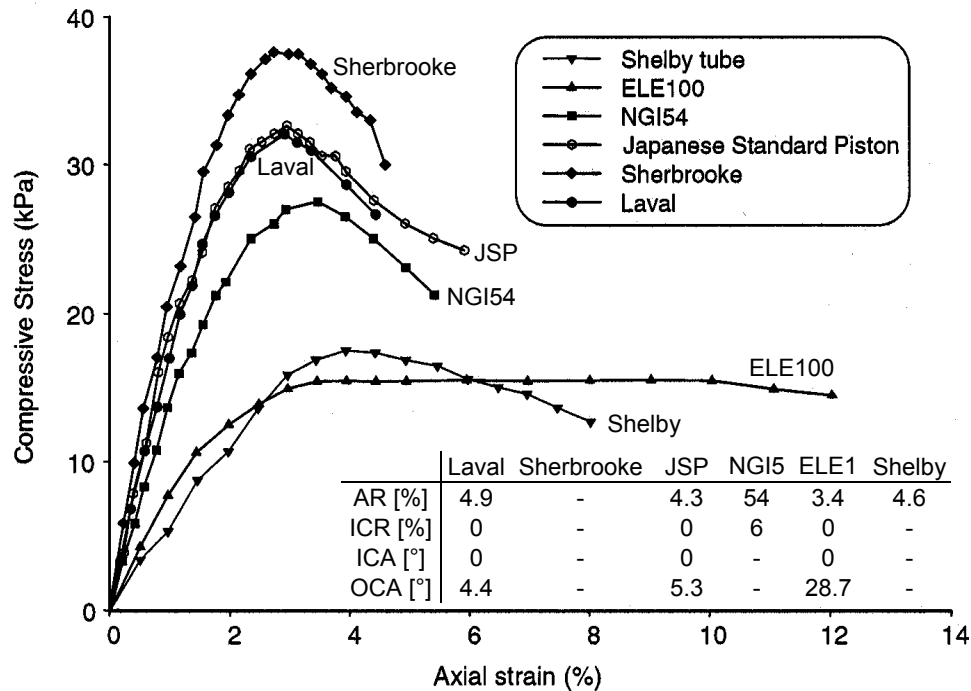
Fig. 2.12: Unconfined compression tests on samples of Ariake clay (Tanaka & Tanaka, 1999).

The sampler parameters (Fig. 2.5) are summarized in the table in Fig. 2.12. The comparison shows that when all parameters have a value close to zero for a specific sampler, high sample qualities are achievable. As soon as the value of one of the four parameters increases, the sample quality drops.

2.2.4 Discussion

Not only the quality, but also the designation of the sample, is determined based on the tube diameter. While samples with an internal tube diameter of 100 mm and below are called tube samples, those obtained from the Laval sampler (after La Rochelle et al., 1981) with a diameter of 200 mm or above are called block samples (even though they are cylindrical and not cubical), as are those extracted

by the Sherbrook sampler (Lefebvre & Poulin, 1979), where no tube is used for the sample extraction.

Relating the sample quality to the sampling apparatus, it is seen that the tube should have:

- no inside clearance (La Rochelle, 1973; La Rochelle et al., 1981; Clayton et al., 1998; Tanaka & Tanaka, 1999),
- a small area ratio (Clayton et al., 1998; Tanaka & Tanaka; 1999),
- a large sample diameter (Baligh et al., 1987),
- a small outside cutting-edge angle (La Rochelle et al., 1981; Clayton et al., 1998; Tanaka & Tanaka, 1999).

The sampled soil properties also have an influence on the subsequent sample quality. It is easier to obtain good quality samples if the soil is:

- plastic but not sensitive (Lacasse et al., 1985),
- without sand or gravel inclusions (Lacasse et al., 1985).

Subsequently, packing and storage processes should be reviewed to cause minimum disturbance. Leroueil (2003) suggested using cling wrap instead of cotton strips for the packing, to avoid air inclusions as much as possible. And he stated that, during storage, the temperature is more important than the humidity.

Sample preparation and test setup can cause various degrees of damage to the sample. Absorption of water and consequent swelling has to be considered because it can cause very large deformations (Lo Presti et al., 1999a). Berre (1982) suggested that the natural specimen should be set up in the triaxial apparatus without adding water (e.g. dry filter stones) to overcome this problem. Another possibility is to reconsolidate the sample to stress levels greater than 1.5 to 2 times the in-situ stress (Ladd & Foott, 1974). But the application of reconsolidation is limited for structured soils, as any stress increase results in volumetric straining and consequently in destructuration (Lo Presti et al., 1999b).

These are only a few points that can cause sample disturbance, but it shows already that all test specimens in laboratory investigations have a certain degree of disturbance. In the previous paragraphs, the influence of this disturbance on the soil parameters was shown by comparing the results of laboratory tests performed

on specimens sampled with different methods. Jamiolkowski (2003) presented the Messina Bridge project where samples from both abutments were investigated in the laboratory and comparable field tests were carried out. The results of the laboratory investigations and the cone penetration tests gave similar mechanical properties for both soils. Also the insitu CPTU tests gave the same response for both materials. Only the insitu geophysical investigations indicated a significantly stiffer response for the much older Messina gravel compared to the younger coastal deposit. This example highlights that any kind of physical changes in the soil cause disturbance and subsequently a change to the original properties.

2.3 Laboratory testing

This project will focus on the investigation of the small strain stiffness behaviour (e.g. Burland, 1989; Simpson, 1992; Atkinson, 2000). For this purpose, accurate methods of measuring displacement in the testing apparatuses are necessary, as discussed in the introduction.

The investigations are performed in triaxial testing apparatuses, therefore the most recent developments and the most significant error sources related to stress path testing are summarized. Finally, an overview of the developments in local strain measurement methods is given and the most appropriate methods for local displacement measurement in triaxial tests on soft clays are highlighted.

2.3.1 Triaxial testing

The popularity of performing triaxial tests to determine mainly the strength but also the stiffness properties of soils started in the 1950s following the establishment of the relevance of effective stresses in geotechnical design (Terzaghi, 1923). The triaxial test is a very convenient way to determine design parameters for effective stresses with the measurement and control of pore water pressures. Major steps in the development of triaxial testing techniques have been made at Imperial College (e.g. Bishop & Henkel, 1957; Bishop & Wesley, 1975; Jardine et al., 1984; Cuccovillo & Coop, 1997). With the requirements of increasing the accuracy of soil parameter determination in laboratory tests, e.g. Burland (1989) discussed

possible measurement errors that occur due to the triaxial test apparatus design, in addition to reviewing the effects of sampling technique and sample preparation.

2.3.2 Strain-measurement error sources

Intensive strain measurement accuracy investigations have been performed, e.g. by Germaine & Ladd (1988) or Baldi et al. (1988). The latter identified the sources of errors in the deformation measurement as seating, alignment, compliance and bedding errors, which are outlined as well in Fig. 2.13:

Seating errors caused by gaps closing between:
- ram or internal load cell and top platen,
- platens and porous stones.

Alignment errors resulting from equipment and specimen non-conformity, specifically:
- porous stones of non-uniform thickness,
- loading ram not vertical or centred,
- platen surface not horizontal,
- tilt of specimen.

Bedding errors are caused by surface irregularities and poor fit at the interfaces between the specimen and porous stone.

Compliance errors may occur because:
- the tie bars, which connect the bottom and the top plate of the triaxial cell, extend and cause relative displacement of the top of the cell with respect to the piston,
- the internal load cell deflects,
- the lubricant is compressed, in systems using lubricated ends,
- the porous paper is compressed.

This highlights that most errors in strain measurement occur around the edges of the sample in the device. Costa-Filho & Vaughan (1980) showed in an experimental laboratory study that a strain measurement made locally on the sample gives a much larger stiffness at small strains than a strain measurement across the end platens. The local strain measurement on the sample in this study

was done with LVDT's (Costa-Filho, 1985). As the LVDT's are cumbersome and difficult to use (Burland, 1989), a programme was initiated at that time to develop new simple and precise strain measurement devices for local use on the sample.
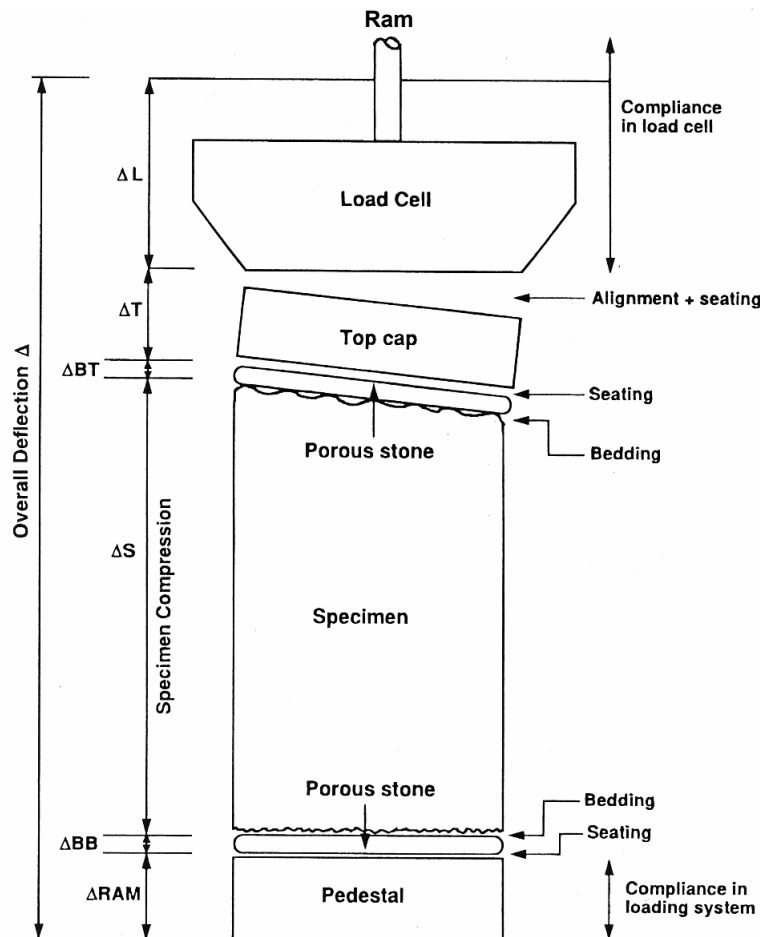
Fig. 2.13: Sources of errors in external axial deformation measurements (after Baldi et al. 1988).

2.3.3 Local strain measurement

A series of internal strain measurement devices were developed. Initially the displacements were measured with the inclinometer level proposed by Burland & Symes (1982), which was further modified to become the electro-level inclinometer (Jardine et al., 1984; 1985a; 1985b) and the pendulum inclinometer (Ackerly et al., 1987). The strain measurement principle of the electro-level inclinometer is the measurement of the rotation of the level due to the axial strains. This inclination is

measured by the change of impedance between electrodes in an electrolyte during change of inclination. The change in inclination in the pendulum inclinometer is measured by the pendulum, which is mounted on a strain-gauged spring. The advantage of the inclinometer levels is that they are inexpensive and that they are stable at large strains. Strain measurement accuracies of ± 0.0005 % for the pendulum inclinometer (Ackerly et al., 1987) and ± 0.001 % for the electro-level inclinometer (Jardine et al., 1984; 1986) can be achieved. A disadvantage is the complicated and time-consuming calibration procedure.

Another strain measurement device from this period is the Hall effect transducer (Clayton & Khatrush, 1986; Clayton et al., 1989). The strain measurement principle of the Hall effect transducer is to measure the flux density between a magnetic field and a semiconductor plate placed in the magnetic field. The flux density varies depending on the relative position of the semiconductor sensor in the magnetic field. This principle can be used for local axial as well as radial strain measurement, up to an accuracy of ± 0.002 %, but for radial strain measurements on soft clays, difficulties were experienced due to the need to mount the transducer on the sample (Clayton et al., 1989). One of the major disadvantages is the limited operation range of a few millimetres.

Tatsuoka (1988) and Goto et al. (1991) developed the local deformation transducer (LDT), which consists of two thin strips of bronze that are mounted on the sample. Two strain gauges are attached to each strip and connected up to measure the change in bending, and the axial strains are calculated. Although the device is inexpensive and simple to use, disadvantages are the axial operation range, which is limited to 1.5 mm, and mounting the strips on to the sample.

A measurement device used primarily for measuring local radial strains is the proximity transducer e.g. Cole (1978) and Hird & Yung (1989). The displacement measurement of the proximity transducer is based on the eddy current loss principle. A coil in the transducer, which is mounted at a certain distance from the sample, induces an eddy current to a conductive target, which can, for example, be an aluminium foil between the rubber membrane and the soil. As the distance between the transducer and the target changes, the magnitude of the induced

eddy current varies. As the impedance of the coil depends on the magnitude of the eddy current, the coil impedance is a function of the transducer – target distance.

An extensive comparison of the measurement accuracy, usability and further advantages and disadvantages of these transducers was made by Scholey et al. (1995) and showed that the LVDT's (Linear Variable Displacement Transducer) give high accuracies that they are stable in temperature and pressure and have a linear calibration range. The disadvantages are the size of the transducer, the necessity to fix the transducer on the sample and the possibility of damaging the transducer when the sample fails. Cuccovillo & Coop (1997) presented a design of a local LVDT transducer and a mounting which overcomes most of the disadvantages of LVDT's mentioned (Fig. 2.14).
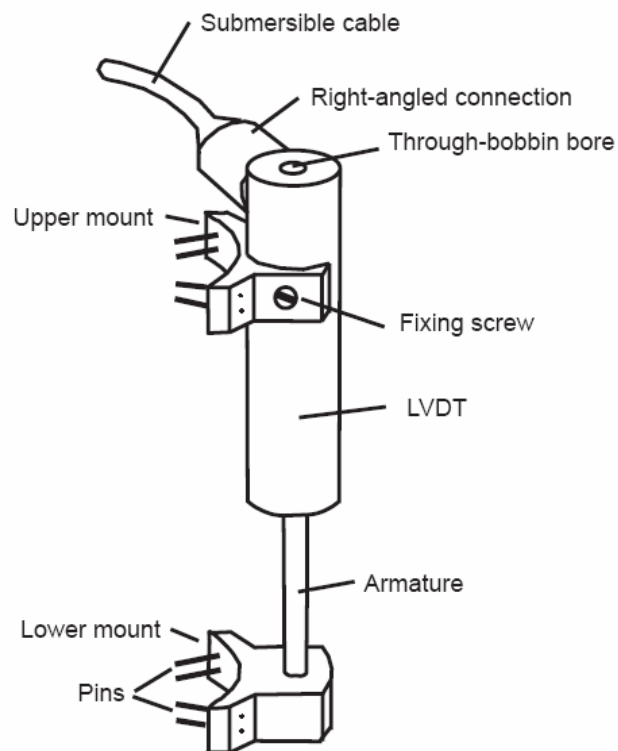
Fig. 2.14: Local LVDT transducer with mounting (Cuccovillo & Coop, 1997).

The LVDT is fixed to the sample with the upper and the lower mount, which are glued on the rubber membrane with flexible contact adhesive. In clays and uncemented soils, additionally four pins per mounting are pushed through the membrane into the soil and the holes caused by the pinhead are sealed with

vulcanizing solution. The LVDT has the cable connected to the side of the housing so that a through-bobbin bore is possible. This ensures that the transducer does not become jammed when the sample approaches failure at large axial strains.

Some additional uncertainties are generated by mounting with pins. The steel pins can reinforce the soil sample, and even more importantly, the hole in the rubber membrane is a potential leaking point. Gens (1982) investigated the possibility of slipping between the rubber membrane and the soil sample. He deduced that the rubber membrane does not slide on the sample surface, and so the displacement measurement is not improved by putting pins through the rubber membrane into the soil sample. Miller (1980), after Burland & Symes (1982), found that small relative displacements between the membrane and the soil occur only at strains close to, or beyond, failure. Since the small strain response is of most interest, the membrane slipping at large strains can usually be neglected and the pins omitted.

These developments concentrate mainly on the local axial strain measurement. To complete the observation of the deformation behaviour of a sample, the radial strains also need to be measured. This can be done with the Hall effect transducer (Clayton & Khatrush, 1986; Clayton et al., 1989) or even more conveniently with proximity transducers (e.g. Cole, 1978; Hird & Yung, 1989). Horizontally mounted LVDT's have also been used for local radial strain measurement, e.g. by Brown & Snaith (1974). Common disadvantages of these methods are the need to fix them on the sample by a mounting (less of an influence with the proximity transducer) and the fact that the transducer measures the radial strains at one particular point only, which is reasonable for remoulded samples but less applicable for natural, rather inhomogeneous, samples. Romero et al. (1997) constructed a triaxial device to test unsaturated soils under non-isothermal conditions. Amongst other features, they implemented a laser scanning system to measure the radial deformations over the entire specimen height. This strain measurement method overcomes the two main disadvantages of the previously mentioned measurement methods. The deformation can be measured without contact and over the whole sample height. Disadvantages can arise from the refraction of the laser beam on the Perspex wall of the triaxial cell. A sketch of the complete triaxial test apparatus designed by Romero et al. (1997) is given in Fig. 2.15.

1: Specimen;

2: LVDT (axial strain);

3: Laser displacement sensor (radial strain);

4: Load cell or alignment device (isotropic test);

5: Top thermocouple (external heater control);

6: Bottom thermocouple (gear pump control);

7: LVDT (vertical displacement of laser sliding subjection);

8: Confining pressure;

9: Load pressure chamber (vertical stress);

10: air pressure;

11: water pressure (volume change measuring system);

12: Water pressure (diffused air flushing system);

13: High air entry ceramic disc;

14: Coarse porous ring;

15: Confining fluid (air or silicone oil);

16: Silicon/latex membrane;

17: Perspex wall ;

18: Steel wall;

19: Vertical displacement electric motor;

20: Electrical connections to transducers and data acquisition system;

21: Connection to forced convection system (gear pump);

22: Connection from forced convection system (heater).

Fig. 2.15: Triaxial testing device for unsaturated soil samples (Romero et al., 1997).

The local radial displacement measurements are accomplished by two lasers (3), which are mounted outside the Perspex wall (17) of the triaxial cell. The lasers can be moved in an axial direction by a stepping motor and the vertical movement is registered by LVDT's (7). The lasers have a measurement range of ±10 mm, a stand-off distance of 45 mm and a resolution of 2 μm, which results in a measured radial strain resolution of $5 \cdot 10^{-5}$ for specimens 38 mm in diameter (Romero et al., 1997).

2.4 Constitutive modelling

2.4.1 Introduction

Since finite element analysis (Clough, 1960; Zienkiewicz, 1967) was introduced into the field of geomechanics, the formulation of suitable constitutive relationships for geomaterials has become a necessity in geotechnical research. One of the major steps in constitutive modelling was the development of the critical state concept (Roscoe et al., 1958; Roscoe & Schofield, 1963; Roscoe et al., 1963; Roscoe & Burland, 1968), which is based on previous fundamental investigations of the stress-strain relationship of soils (e.g. Hvorslev, 1937; Rendulic, 1937; Haefeli, 1951). Since then, numerous constitutive models have been developed to describe the behaviour of soils, with the aim of modelling typical phenomena such as small strain stiffness, stress path dependency or anisotropy.

Parallel to the critical state concept, other families of constitutive relationships have been introduced to geomechanical applications. Zienkiewicz & Pande (1977) formulated the first elasto-plastic constitutive model for rock in the Multilaminate framework based on the Multilaminate concept proposed by Taylor (1938) for metals. Kolymbas (1977) introduced the idea of describing the non-linear elastic mechanical properties of soils by unique functions over the whole stress-strain range, instead of introducing yield and potential functions that are necessary for elasto-plasticity. He called this concept hypoplasticity. The range of elastic, ideal-plastic models like the Mohr-Coulomb model were improved as well by incorporating e.g. non-linear elastic behaviour by adding the hyperbolic model of Duncan and Chang (1970) or by applying an anisotropic linear elastic stiffness

matrix. Next to these models that are based on continuum mechanics, discrete element models have been introduced into soil mechanics too (e.g. Cundall & Strack, 1979; Thornton, 2000). These models are more suitable for granular soils and will therefore not be discussed further herein.

A few of the relevant continuum models, which can be used to model either small strain stiffness, stress path dependency or anisotropy, are discussed in the following section specifically, their advantages and disadvantages for modelling soft soil behaviour in general, and non-linear elastic and anisotropic soil behaviour in particular. A detailed description of the model formulation is subsequently given in Chapter 7 for the selection of constitutive models that are used for numerical simulations of the lacustrine clay investigated.

2.4.2 Modified Cam Clay model

The elasto-plastic Modified Cam Clay model (MCC) was proposed by Roscoe & Burland (1968) as an improvement to the Original Cam Clay (OCC) model developed by Roscoe & Schofield (1963). Both models are derived from triaxial test results of "ideal" soil and are based on the critical state concept[‡] (e.g. Roscoe et al., 1958). The logarithmic yield surface of the OCC model, which has a discontinuity when it meets the isotropic stress path, is replaced in the MCC model by an elliptical yield surface. The other features of the OCC model such as isotropic hardening controlled by the plastic volumetric strains, the associated flow rule or the Drucker-Prager failure criterion are kept the same in the MCC model. A detailed presentation of the models formulation is presented in Chapter 7.

The OCC and the MCC models were the first two elasto-plastic models for fine-grained soils formulated within the critical state concept, and the MCC model has been widely used for practical applications and is the basis of many subsequent models. One of them is the 3_SKH model, which will be discussed next.

[‡] „The loading path after reaching the yield surface traverses this surface until the constant void ratio line is reached. The soil then continues to deform at constant stress and constant void ratio." (Roscoe et al., 1958; p. 43).

N.B.: The constant void ratio line was subsequently renamed as critical state line.

2.4.3 Three surface kinematic hardening model

The three surface kinematic hardening model (3–SKH) was developed (Stallebrass, 1990; Stallebrass & Taylor, 1997) specifically to predict the behaviour of overconsolidated soils starting from small strain or stress changes. The model is an extension of the two surface kinematic hardening model proposed by Al-Tabbaa (1987) and Al-Tabbaa & Wood (1989). A second kinematic surface is incorporated inside the yield surface in order to simulate the influence of recent stress history. A detailed description of the model formulation is outlined in Chapter 7. Due to the translation and hardening rules of the two kinematic surfaces, the model predicts a non-linear elastic stress – strain response, which is dependent on the angle of stress path rotation and the amount of stress change. Other features of the Al-Tabbaa model such as the elliptical state boundary surface, the same as in the Modified Cam Clay model (MCC) (Roscoe & Burland, 1968), the associated flow rule and the failure criterion were preserved.

Although the 3_SKH model can describe some aspects of the behaviour of fine grained soils generally well, several shortcomings of the bubble model were identified. Stallebrass (1990) observed that for stress states on the history surface, the model predicts a fairly rapid stiffness decrease as the history surface approaches the yield surface, which was not seen in the experimental data. This problem can be improved by modifying the hardening modulus. Additional disagreements between model and experimental results have been found for stress paths on the dry side of critical state. Concerning the stress domain, which is influenced by the recent stress path, the experimental data showed that the bulk stiffness decrease takes place within a smaller stress domain than the shear stiffness decrease. The two latter points are inherent characteristics of the 3 – SKH model. While these shortcomings are due to the incorporation of the second kinematic surface (the "history surface"), the following problems are due to incorporating the kinematic surfaces into the Modified Cam Clay model. The coefficient of earth pressure at rest during one-dimensional compression is over-predicted as the associated flow rule within the Modified Cam Clay model predicts extensive shear strains for yield at the K_0 stress ratio. This is especially significant for cyclic loading, where too much shear strain is accumulated based on the

model. For the generalization of the failure criterion to the full stress space, the shape of the yield and plastic potential surface and consequently the failure surface in the deviatoric plane are circular in the Modified Cam Clay model. This assumption implies that the angle of shearing resistance varies with Lode angle (Potts & Zdravkovic, 1999).

These latter problems were overcome e.g. by McDowell & Hau (2003), who incorporated a non-associated flow rule within the three surface kinematic hardening model. They scaled down the shear strains by a factor, retained associated flow under isotropic conditions and at critical state, and assumed a Lode angle dependent failure criterion. Another possibility was found by Masin (2003), who defined the 3–SKH model for anisotropic clays (AI3–SKH) with a plastic potential surface in triaxial compression, which has a more vertically elongated shape compared to the shape of the MCC yield surface. The shape of the plastic potential is directly derived from test results of anisotropically consolidated clays. In triaxial extension, the plastic potential surface is kept the same as in the MCC model (associated flow). The Matsuoka & Nakai (1974) failure criterion was used in the deviatoric plane.

Other aspects have not been included in the 3 – SKH model, such as time dependent aspects incorporating creep or secondary consolidation, or natural soil features such as anisotropy or structure.

2.4.4 Strain Dependent Modified Cam Clay model

The Strain Dependent Modified Cam Clay (SDMCC) model was proposed by Dasari (1996) and Bolton et al. (1994), to improve the numerical analyses of ground movements associated with the construction of diaphragm walls or tunnels. The aim was to simulate non-linear elasticity and stress history dependent stiffness. The elastic formulation of the model is incorporated into the Modified Cam Clay (Roscoe & Burland, 1968) yield surface. The non-linear elasticity was modelled by varying the shear and bulk moduli as a function of mean effective stress, overconsolidation ratio and the corresponding strain increment since the last reversal. The hysteretic stress-strain behaviour for unloading and reloading is modelled by the Masing rule (Masing, 1926). The stress history dependent

stiffness was formulated in the strain space. The direction of the vector for the previous and for the current strain increment is calculated and the angle between these vectors is determined. If the angle is larger than 90°, the model assumes that the stress path changed direction and simulates higher stiffness. The model was evaluated on laboratory tests on Gault clay and centrifuge tests on Speswhite kaolin and applied for numerical analyses of an excavation in Boston Blue Clay and a tunnel in London (Dasari, 1996). The comparison of the measurement data to the simulation results for the excavation showed that the settlements, and especially the settlement concentration behind the wall, could be predicted very well while the lateral wall movement is slightly overpredicted by this model.

2.4.5 BRICK model

The BRICK model (Simpson, 1992) was developed to model the deformation behaviour of retaining walls in stiff clays. Based on the shear stiffness analyses of the triaxial stress path tests on reconstituted London Clay by Richardson (1988) and on kaolin by Stallebrass (1990), Simpson introduced the physical analogue of "a man walking around a room and pulling behind him a series of bricks, each on a separate string" in his Rankine lecture (in 1992), to model the non-linear and strain history dependent elastic behaviour. This analogue was formulated in the strain space. The plastic strains are represented by the movement of the bricks and the elastic strains are the difference of the overall strains, given by the movement of the "men", which represents the current strain state, and the sum of the plastic strains. This model behaviour can be described as a kinematic hardening model with multiple yield surfaces, which model a stepwise stiffness reduction with increasing strains. These yield surfaces have no preferred direction therefore the model behaves isotropically. To complete the model for elasto-plastic soil behaviour, some assumptions from critical state soil mechanics (Schofield & Wroth, 1968) were also adopted.

The evaluation of the model response confirmed that the model simulated the stiffness decrease with straining, the stiffness increase for changes in the stress path direction, the failure stress states and strain ratio for one-dimensional consolidation paths well although neither the friction angle nor the K_0 value are

input parameters of the model. Puzrin & Houlsby (2001) proved that the BRICK model, as formulated by Simpson (1992) within conventional plasticity in the strain space, is consistent with the laws of thermodynamics.

The model has been applied successfully for several numerical analyses of deep excavations in overconsolidated clays. In the numerical case study of a multipropped deep excavation at Lion Yard in Cambridge, Ng et al. (1998) showed that the model is able to simulate the lateral wall movement as well as the settlements behind the excavation quantitatively. Qualitatively, the lateral wall movements were slightly overpredicted at the toe of the wall and the settlements behind the excavation were distributed more widely than observed.

2.4.6 MIT-E3 model

The MIT-E3 model was developed by Whittle (1987) to study the performance of offshore friction piles supporting tension leg platforms for normally to lightly overconsolidated recent marine sediments without structure, subjected to cyclic loading. Subsequently, the model was presented in Whittle (1993) and Whittle & Kavvadas (1994), where it was applied to overconsolidated clays.

The model uses an inclined ellipsoid as a bounding surface (Dafalias & Herrmann, 1982), which was originally introduced in the MIT-E1 model by Kavvadas (1982), to model anisotropic elasto-plastic behaviour. The yield surface is derived from the Modified Cam Clay yield ellipse (Roscoe & Burland, 1968) and the inclination as well as the ratio of the semi-axes of the ellipsoid are dependent on the applied stress path and can change during loading. A cone is defined in the three dimensional stress space with the apex at the origin and the orientation according to the defined anisotropic failure criteria of the soil. As these criteria are not determinable by triaxial tests, Whittle (1987) suggested keeping the orientation along the isotropic axis, which reduces the failure cone to an isotropic Drucker-Prager failure surface. The failure cone does not intersect at the apex of the yield ellipsoid, therefore the model needs a non-associated flow rule to fulfil the critical

state criterion. The non-associated flow rule is also necessary to fulfil the K_0 conditions[‡] for plastic strains.

The anisotropic elasto-plastic model introduces two hardening rules, which control the changes in the size and orientation of the yield surface, respectively. Both rules depend on the plastic volumetric strain increments.

The non-linear elastic behaviour inside the yield surface is described by a closed symmetric hysteretic loop based on the formulation of Hueckel & Nova (1979), which consists of a criterion for identifying the load reversal point and an expression for the decrease of the tangent bulk modulus, which is a function of the current stress state and the load reversal point. The shear stiffness is described by assuming a constant void ratio, which implies decoupled volumetric and shear behaviour. The stiffness values are dependent on the OCR but not on the stress direction, therefore the formulation is isotropic, non-linear elastic and does not include stress history dependency. Additionally, the concept of bounding surface plasticity (Dafalias, 1975; Krieg, 1975; Dafalias & Popov, 1976; Dafalias & Herrmann, 1982) is implied within the MIT-E3 model, to simulate the non-recoverable strains within the yield surface, which are important for cyclic loading. The bounding surface plasticity allows plastic straining for stress states within the bounding surface if loading occurs, for unloading it behaves elastically. The magnitude of these strains depends on the plastic behaviour defined at the image point on the bounding surface and the proximity of the current stress state to the image point on the bounding surface. This image point can be obtained by constructing a line through the current stress state and the origin. Where this line intersects the bounding surface defines the position of the image point. Therefore, the image point can change when the stress path within the bounding surface changes, which guarantees, together with the defined hardening modulus, a smooth transition from the elastic to the plastic behaviour when the stress state reaches the bounding surface. In the MIT-E3 model, the bounding surface is defined to be equal to the yield surface as well as the plastic potential.

[‡] The term K_0 condition is used for the one-dimensional stress ratio for which axial strains develop at zero radial strains.

The key features of the MIT-E3 model are an anisotropic yield surface, kinematic plasticity, strain softening under undrained conditions, small strain non-linear elasticity and bounding surface plasticity. Not included in the non-linear elastic formulation is the influence of the recent stress history and any anisotropic aspects. Additionally, natural soils often show distinct structural and creep effects and these are not modelled either.

Although the 15 material parameters that are required for the MIT-E3 model are challenging to determine, Whittle (1993) demonstrated the ability of the model to represent the behaviour of different laboratory tests and various stress paths for different types of clays. Investigations on several boundary value problem have been performed, mainly on excavations (e.g. Whittle et al., 1993) in which the deformation measurement data are compared to the corresponding analysis results obtained using the MIT-E3 model. Comparison of the lateral wall deflections showed that in the first stages, deflections are well simulated, while with ongoing excavation and support, the deflections are underpredicted. This is assumed to be due to the simulation of the struts by elastic springs, which do not represent any creep, shrinkage or temperature effects of these concrete struts. Comparison of the lateral movement of the soil behind the wall showed that the analysis underpredicts soil displacements close to the wall and overpredicts movements at locations further away. Comparison of the settlement profiles implied that the settlements close to the wall, as predicted in the analysis, are less concentrated and spread over a wider region.

With some modifications, as described in Ganendra & Potts (1995), the MIT-E3 model was implemented in the Imperial College finite element code (ICFEP) and used for the analysis of different boundary value problems (Potts & Zdravkovic, 2001). Susequently, Pestana & Whittle (1999) presented the MIT_S1 model, which is a generalised form of the MIT-E3 model applicable for clays as well as for sand. The MIT-S1 model uses a modified form for the bounding surface plasticity and the rotational hardening law is additionally dependent on the plastic shear strains. An isotropic cone after Matsuoka & Nakai (1974) is introduced as a failure criterion. The nonlinear elasticity formulated by a perfectly hysteretic loop and the bounding surface plasticity are the same as in the MIT-E3 model. The model

needs 13 parameters for simulating clays and 14 parameters for sands and was used for extensive comparison with measurement results of undrained triaxial, plane strain and direct simple shear tests on K_0 consolidated specimens (Pestana et al., 2002). It was shown that the model represents the non-linear elastic as well as the anisotropic plastic soil stiffness behaviour. It is able to simulate the response of highly overconsolidated soils as well as dilation for shearing in extension.

In summary, it can be said that the MIT-E3, and the ensuing MIT-S1, model can model many typical natural clay features. Unfortunately the model itself and the soil parameter determination are complex.

2.4.7 S_CLAY1 model

The anisotropic elasto-plastic S_CLAY1 model was proposed by Wheeler (1997) and subsequently slightly modified by Näätänen et al. (1999). The model was introduced to simulate the initial plastic anisotropy as well as the change in anisotropy during plastic straining for normally consolidated or lightly overconsolidated soft clays. An aim was to keep the model relatively simple, so that there would be a chance of widespread application in geotechnical design. The model is an extension of the Modified Cam Clay model (Roscoe & Burland, 1968), where the initial anisotropy of the plastic behaviour is represented by an inclined yield surface, similar to that proposed by Dafalias (1987). As the plastic straining conditions at critical state and at one-dimensional consolidation are fulfilled by the shape of the yield surface, the S_CLAY1 model uses an associated flow rule. The volumetric hardening rule and the failure criterion are the same as in the Modified Cam Clay model, but a rotational hardening law is introduced additionally to simulate the change in anisotropy during plastic straining. This rotational hardening law incorporates the effects of plastic volumetric strains as well as plastic shear strains. The model is described by the 5 conventional parameters from Modified Cam Clay and two additional parameters related to the rotational hardening. A detailed description of the model is given in Chapter 7.

The model was evaluated on triaxial test results of Finnish clays (e.g. Wheeler et al., 1999; Messerklinger, 2001; Koskinen, 2001) of Bothkennar clay (McGinty et

al., 2001) and of Kreuzlingen clay (Messerklinger & Springman, 2003). The results pointed out that for certain stress paths the plastic flow direction determined in the laboratory tests differ significantly from the predicted ones. The model was subsequently implemented into the Finite Element code CRISP (Britto & Gunn, 1987) and in a benchmark exercise, compared to the behaviour of other recently developed anisotropic elasto-plastic models (Wiltafsky et al., 2003). Recently, the influence of bonding and destructuration was incorporated (Koskinen et al., 2002) by introducing an intrinsic yield surface.

2.4.8 Multilaminate Model for Clay

The Multilaminate Model for Clay (MMC) was developed by Wiltafsky et al. (2002), Wiltafsky (2003a) and is based on the Multilaminate concept (Zienkiewicz & Pande, 1977). The MMC model is one of a series of Multilaminate models (Pande & Sharma, 1983; Krajewski, 1986; Sadrnejad & Pande, 1989; Karstunen, 1998; Schuller, 2000). The basic assumption of the Multilaminate concept is that a set of "integration planes" is defined in each integration point of the Finite Element (FE) analysis, on which the constitutive relationship (e.g. the MMC model) is described in terms of normal and shear stresses. During the FE analyses, the applied stresses of each integration point are transformed to the integration planes as well in terms of normal and shear stresses. Therefore the corresponding strains can be determined on each plane due to the constitutive relationship. To obtain the response at the integration point, the strain components are summarized over all integration planes by specific integration rules and weighting coefficients (e.g. after Bazant & Oh, 1986). Initial anisotropy, as well as a change in anisotropy during plastic straining, is simulated as the yield surfaces on the planes can develop independently of each other.

The MMC model described on the integration planes is an elasto-plastic model. The yield surface is composed of a yield cone and a yield cap. The yield cone allows deviatoric hardening with a non-associated flow rule, using a mobilized dilation angle according to the stress-dilatancy theory proposed by Rowe (1972), until the Mohr Coulomb failure criterion has been reached. The yield cap has an elliptical shape with the apex on the deviatoric stress axis. The yield cap allows

volumetric hardening described by an associated flow rule. Additionally, a tension cut-off criterion is incorporated. In the MMC model, only the plastic strains are derived from the contact planes, the elastic strain part is calculated globally by an isotropic, linear elastic stiffness matrix. Therefore the model just simulates plastic anisotropy. Due to the composition of the yield surface of two components with an intersection point, the plastic potential has a discontinuity at this point. An intensive evaluation of the MCC model on triaxial test results (e.g. Messerklinger, 2001; Wiltafsky et al., 2002; Neher et al., 2003) showed that the direction of the plastic, strain increments, simulated with the current definition of the plastic potentials corresponds well with the test data, although the amount of plastic strains tend to be underpredicted. The evaluation of the simulation of anisotropy due to one dimensional consolidation indicated that the MMC model simulates less distinct anisotropic behaviour compared, for example, to the S_CLAY1 model. Further investigations on the response envelopes of the model have been done by Scharinger (2004).

2.4.9 Discussion

These six advanced constitutive models for fine grained soils simulate one or more of the following soil behaviour properties: non-linear elasticity, stress path dependency, non-recoverable strains within the yield surface and plastic initial and induced anisotropy.

Different approaches have been proposed for modelling the non-linear elasticity. The 3-SKH model introduces one kinematic surface, while the BRICK model assumes a multitude of kinematic surfaces within the yield surface. The MIT-E3 as well as the SDMCC model applies a closed hysteretic loop for the simulation of the non-linear elastic behaviour by mapping the stress reversal points and defining a function for the stiffness decrease. The evaluation of the previously discussed models (in particular the 3-SKH model), showed that the definition of one kinematic surface can introduce shortcomings due to the introduced translation law for the surface, which may not represent the real soil behaviour for all stress paths. A more successful definition of these translation laws for non-linear elastic soil behaviour in the whole stress field was proposed by Puzrin & Burland (1996).

they suggested a logarithmic stress-strain function, either derived from small strain measurement data, or if these are not available, from data of standard tests. On the basis of that assumption, Puzrin & Burland (1998) proposed a model that incorporates non-linear stress strain behaviour, stress path dependency and cross-anisotropy in the small strain region.

Modelling of the non-linear elasticity by mapping stress states and assuming a stiffness degradation curve, as done in the SDMCC and MIT-E3 models, is a more empirical way of formulating the soil behaviour. This needs a certain amount of calibration and so it is less applicable to different soil types.

By defining a multitude of kinematic surfaces, as in the Brick model, the shortcomings due to formulating translation rules can be avoided and the soil behaviour is described more consistently. A multitude of isotropic and anisotropic kinematic hardening models have been successfully introduced already for the simulation of the deformation behaviour of different materials (e.g. Mroz, 1967; Prevost, 1977; Mroz et al., 1979). Prevost (1982) concluded in his comparison of the multi-surface models to the two surface models, that the multi-surface models suffer in storage capacity, while the two surface models may suffer in the selection of the translation rule of the kinematic surface.

The stress history dependency is either modelled with kinematic surfaces (3-SKH and BRICK model) or by the explicit calculation of the change of the stress or, as in the SDMCC model, the strain path.

The tendency for non-recoverable elastic strains to be generated for any unload and reload loop was only considered by the MIT-E3 model, as this model is especially made for cyclic loading. For applications to excavations for example, the successful simulation of the development of strains during one stress path is more important.

That the effect of anisotropy needs to become successfully incorporated in the constitutive model, especially for natural soils, was recognized a long time ago. The models presented simulate the plastic anisotropy either by using an inclined yield surface (MIT-E3 and S_CLAY1 models) or the Multilaminate framework (MMC model). The approach of introducing an inclined yield surface was derived

from the intensive evalution of test results on different natural soils (e.g. Tavernas & Leroueil, 1977; Diaz-Rodriguez et al., 1992). A series of models was developed subsequently that considered the initial anisotropy as a first step followed by the change in anisotropy during plastic straining (e.g. Dafalias, 1987; Yu & Axelsson, 1994; Banerjee & Yousif, 1986; Davies & Newson, 1993). Two of these models are the MIT-E3 and the S_CLAY1 model. The quality of the plastic strain prediction mainly depends on the definition of the plastic potential. While the MIT-E3 model, with a non-associated flow rule, simulated the amount and direction of plastic strains very well for all different stress paths (Whittle & Kavvadas, 1994), the S_CLAY1 model predicted the plastic strains less well for certain stress paths (Wheeler et al., 1999).

The Multilaminate concept was initially used for simulating joint sets in rock (Zienkiewicz & Pande, 1977), and was extended subsequently for use with soils. One of the major advantages of the Multilaminate model is that the anisotropic behaviour is implied within the concept therefore no additional material parameters are necessary.

Anisotropy of the elastic behaviour was not modelled by any of the six previously discussed models. Evaluation of the effect of anisotropic elastic soil behaviour in laboratory tests is now possible thanks to the introduction of the bender element method a few years ago. Basic laboratory investigations to determine the difference between horizontal and vertical shear stiffness using bender elements have been done by Jamiolkowski et al. (1995) with oedometer tests on six natural deposits. Pennington et al. (1997) performed triaxial stress path tests on reconstituted and natural clay samples to investigate the ratio of the initial horizontal and vertical shear stiffness and to compare the laboratory results to field measurement data.

The modelling of anisotropic elasticity is done by simulating cross-anisotropic (transverse isotropic) behaviour with an anisotropic stiffness matrix (e.g. Graham & Houlsby, 1983). They incorporated the anisotropy with the "anisotropic factor", which is the ratio of the horizontal to the vertical stiffness (Houlsby, 1981) to derive the parameters from standard triaxial stress path tests. Lings et al. (2000) performed sophisticated triaxial tests with bender element measurements, to

derive all five parameters necessary to describe anisotropic elastic material response. Puzrin & Burland (1998) also modelled the anisotropic behaviour within the small strain region by defining an anisotropic stiffness matrix.

The evaluation of the failure criteria for the 3-SKH model showed that a Lode angle dependent failure criterion is necessary to simulate the failure in three-dimensional stress space.

3 Swiss lacustrine clay

3.1 Investigated soils

The Swiss lacustrine clay investigated in the following study was taken from a highway building site in Opfikon, adjacent to Kloten. Kloten is an industrial suburb to the north-east of Zurich, next to the airport (Fig. 3.1 & Fig. 3.2). Due to the proximity of Kloten to Zurich airport, the properties of "Kloten clay" have been investigated over a long period, e.g. from Lang (1976) to Dr. von Moos AG (1995), and so this generic terminology will be used in this thesis.

The geological site investigations reported by Dr. von Moos AG (1995) showed that Kloten and the surrounding region is situated on post glacial lake deposits of the Rhine-Linth glacier in the Glatt valley. The lacustrine clay is found at the surface has a thickness of up to 20 m and is deposited on top of glacial moraines. This lacustrine clay in Kloten has a particle size content < 2 μm of about 20 % and plasticity investigations classified it as low plasticity clay. In all natural samples taken in Kloten, a significant and very regular stratification of clay and silt layers is visible.

The highway building site in Kloten from which the block samples were obtained was a tunnel project on the A1 highway. At present, this highway leads through the village of Kloten before arriving at Kloten airport. Due to the high noise pollution in the centre of the village, a project was initiated to bury the airport highway. This project consisted of a cut and cover tunnel on the southern approach of the highway (from Zürich). Block samples were extracted during the construction of the foundations of this tunnel. A detailed description of the sampling techniques is given in the following paragraphs.

Additionally, samples from Birmensdorf were taken with the aim of performing a comparative study on qualities of samples derived with different sample tubes. Birmensdorf is located to the south-west of Zurich (Fig. 3.1).
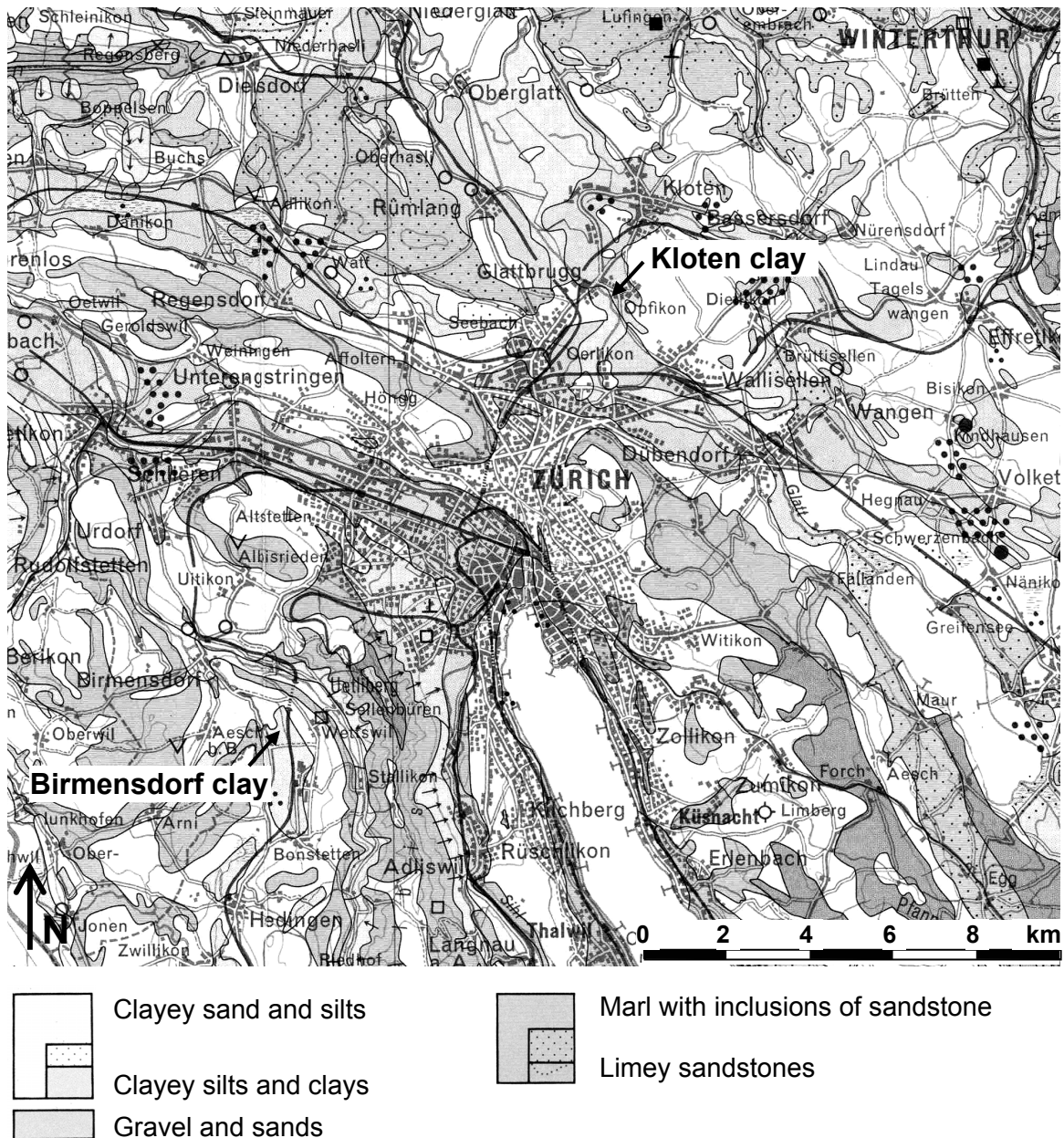
Fig. 3.1: Section of the geological map of Zurich and environs (Geologische Karte der Schweiz, 1980).

A detailed description of the project and the various aspects of construction is given in Franz & Göbbels (2000). The behaviour of Birmensdorf clay was investigated by Panduri (2000) and Trausch Giudici (2004). The soft post-glacial

clay deposit in Birmensdorf has a thickness of 30 m in the middle of the field, thinning to 5 m at the edge of the valley.
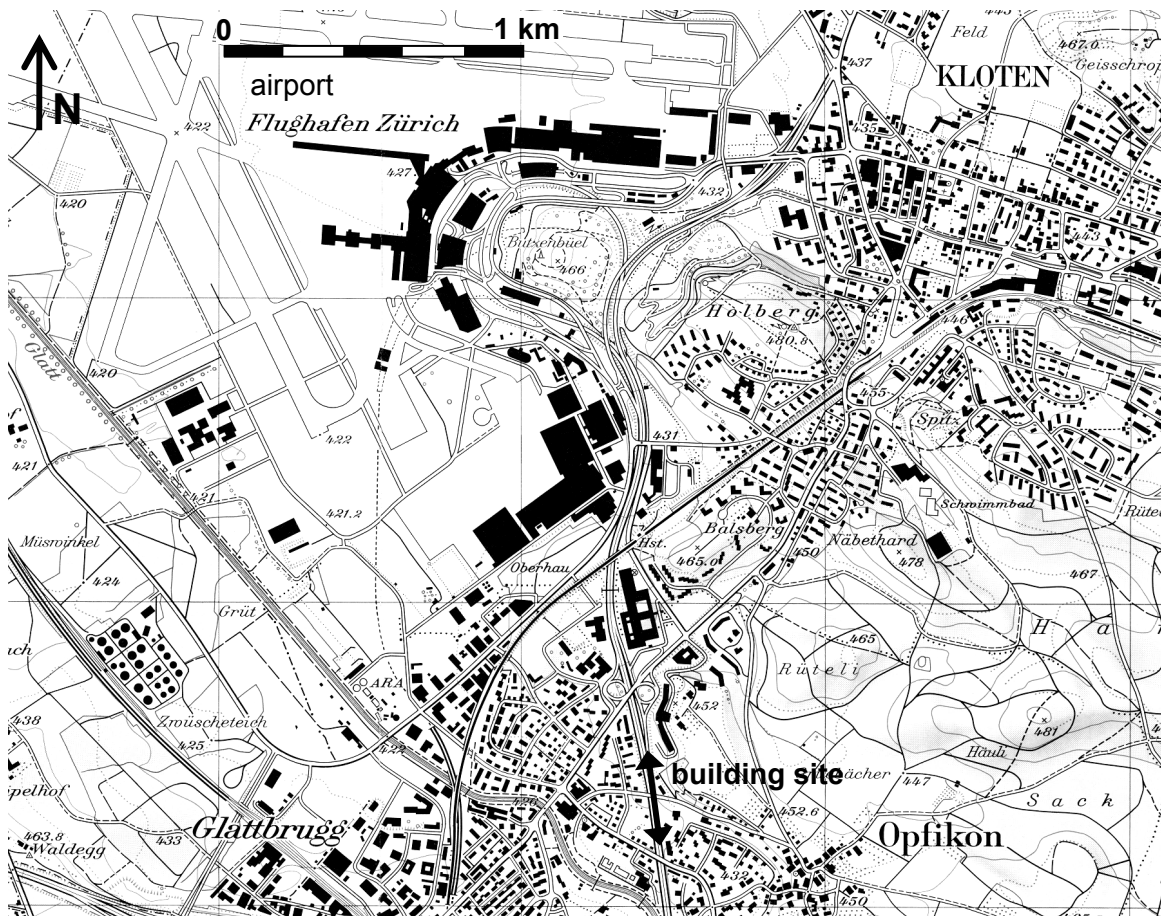
Fig. 3.2:   Location of the sampling site for natural Kloten clay (Landkarte der Schweiz, 1994).

3.2   Block sample extraction

The first attempt at sampling blocks in Swiss lacustrine clay following the methods of Lefebvre & Poulin (1979) was done in Kloten. A trench of about 1.5 m depth was excavated by machine at the bottom of the excavation pit and blocks of size 20 x 30 cm, with a height of 20 cm were carved out of the deposit. The base of the block was cut off with a steel plate with which the block was lifted out of the trench. The blocks were immediately packed in cling film wrap, waxed and placed in boxes that were filled with wet sawdust. These samples were given the internal laboratory number 46762.

Additionally, disturbed sample clay (46764) was taken by the excavator and stored in plastic boxes. This material was used for the preparation of reconstituted samples (46810). These sample numbers are also used in this thesis.

During sampling of the blocks of Kloten clay, several disadvantages of this sampling technique after Lefebvre & Poulin (1979) were recognized.

- During carving around the desired samples, the normally consolidated and hence very soft clay stuck to the tools. Even for this low plasticity Kloten clay, carving the samples out of the deposit was not straightforward and resulted in imperfectly geometric clay blocks, as shown in Fig. 3.3a. Consequently, these difficulties may have led to significant horizontal strains in the sample.
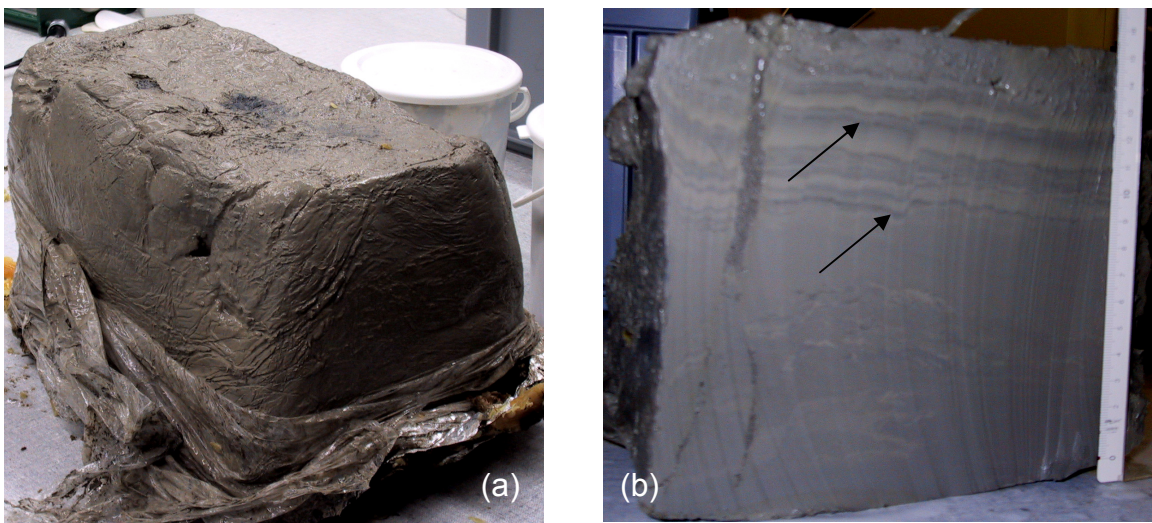
Fig. 3.3: Block samples from Kloten clay (46762) a) unpacked block b) cross section through the block sample (dimension unit in centimetre).

- No handling was necessary as the block was being carved out of the deposit or when the block was separated from the underlying soil with the steel plate. But to pack the sample into cling film wrap and wax it, the sample had to be turned around. The blocks with dimensions of about 20 x 20 x 30 cm had a self weight of more than 20 kg. Despite a careful approach in order to minimize disturbance, some deformations were applied to the block samples during turning and lifting. This observation was confirmed later in the laboratory, when one sample was unpacked and cut

(Fig. 3.3b). The horizontal layering is clearly visible in the cross section of the sample, especially on the top side of the sample. However, several vertical staggers along the horizontal layers are also recognizable. These vertical offsets have not been found in-situ, but must have been caused during sampling, packing and handling.

- Distinct varving of the deposit was visible, as already mentioned and alternating silt and clay layers, with a thickness of 2 – 4 mm, could easily be recognized. It took approximately 10 minutes to carve the blocks out of the deposit and pack them into cling film wrap. During this time, drainage along the silt layers to the side of the sample was possible.

All of these observations led to the conclusion that carving is not a suitable method for layered soft Swiss lacustrine clays. Of the two alternative block sampling methods discussed in Chapter 2, Sherbrooke, (Lefebvre & Poulin, 1979) and Laval (La Rochelle et al., 1981), the latter was the most promising for extracting varved clays from the base of a pit.

Therefore it was decided to design and construct a device, similar to the Laval sampler, to obtain block samples in soft Swiss lacustrine clays, with consideration of the most important aspects for obtaining good quality undisturbed samples, as discussed in Chapter 2. A sketch of the sampling tube is shown in Fig. 3.4a. A tube with an outer diameter of 200 mm was used. The wall thickness of the tube is 2 mm and the outside cutting edge angle is 11°. The tube has no inside clearance.

Additionally, a device to overcore the tube whilst pressing it into the soil was considered. Overcoring was suggested by La Rochelle et al. (1981) as well as by Leroueil (2003), with the aim of minimising the pressure beneath the tube and to make sure that the soil that becomes replaced by the sampling tube moves towards the outside of the sample tube. But after consideration of early sampling experience with this very sticky soil, it was decided that any kind of carving would not work and consequently the idea of an overcoring device was set aside. But to minimize the pressure in front of the tube, the length of the sample tubes was chosen to be shorter than would usually be expected for a 200 mm diameter tube. Short sample tubes have the additional advantage that the necessary external force to press them in is smaller.

Having several short samples next to each other also gives many test specimens with the same layering. Extraction of the sample tubes from the deposit is easier as well. In contrast to normal tube samples or Laval samples, these sample tubes were not pulled out of the soil by rotation and vacuum, but were separated from the deposit by digging the surrounding soil away until it was possible to cut the tube off from the underlying soil. Therefore no vacuum had to be applied to the sample. Another advantage of short sample tubes is that smaller portions of soil can be extruded in the laboratory. Contrary to the techniques adopted by La Rochelle et al. (1981) in respect of the Laval samples, it was decided to leave the soil samples in the steel tubes to overcome the distortions due to packing and to minimize any drainage.
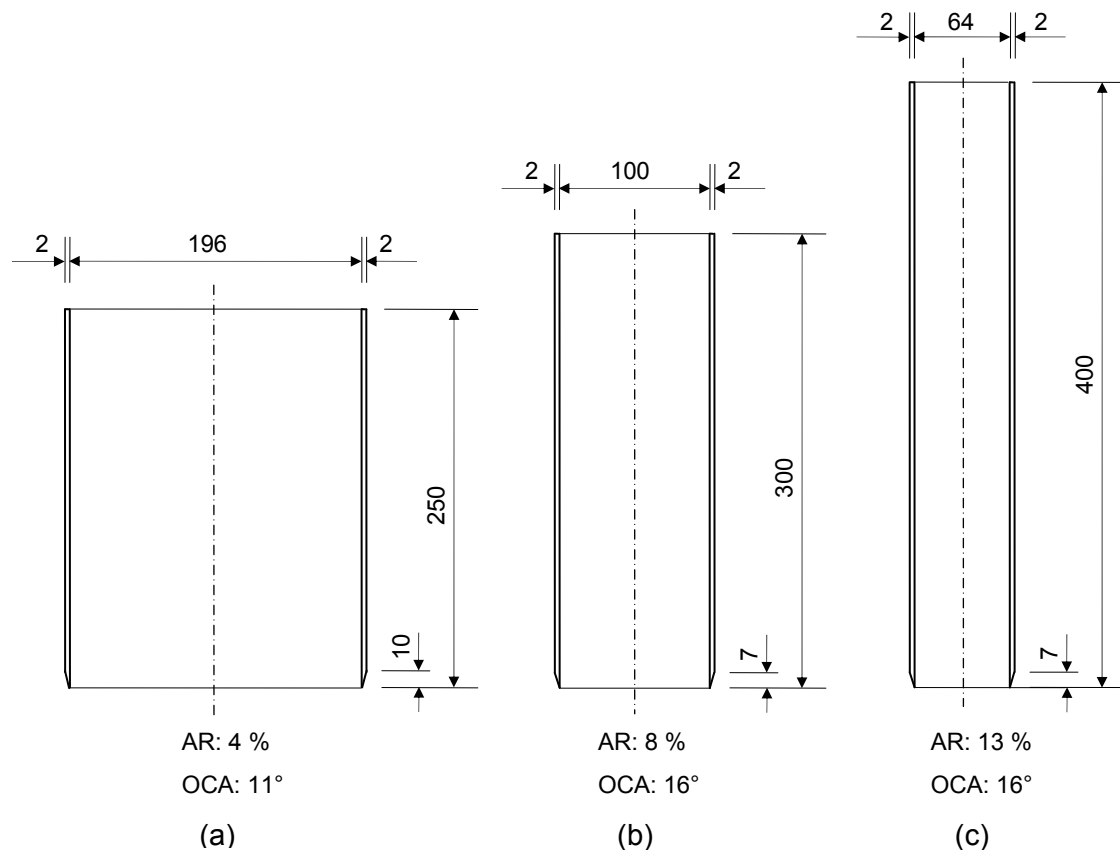
Fig. 3.4:   Sample tubes used for the comparative study on sample quality (dimensions in millimetres).

A device was constructed to extrude the soil from the tube (Fig. 3.5a&b), consisting of two parts, a circular steel plate, which a diameter of 195 mm, and a steel ring with an inner diameter of 196 mm (Fig. 3.5a). The plate is placed on the

bottom and the ring on the top side of the sample tube. The sample is then extruded from the tube in a press.

Top plate of the press

3 steel rods
fixed to the steel ring

diameter 10 mm
height 300 mm

2 mm   196 mm   2 mm

steel ring

Sample tube with the soil sample

250 mm

Push out direction
of the sample

10 mm

Circular steel plate
diameter 195 mm

5 mm

steel tube

wall thickness 10 mm
diameter 100 mm
height 280 mm

Bottom plate of the press

(a)

(b)
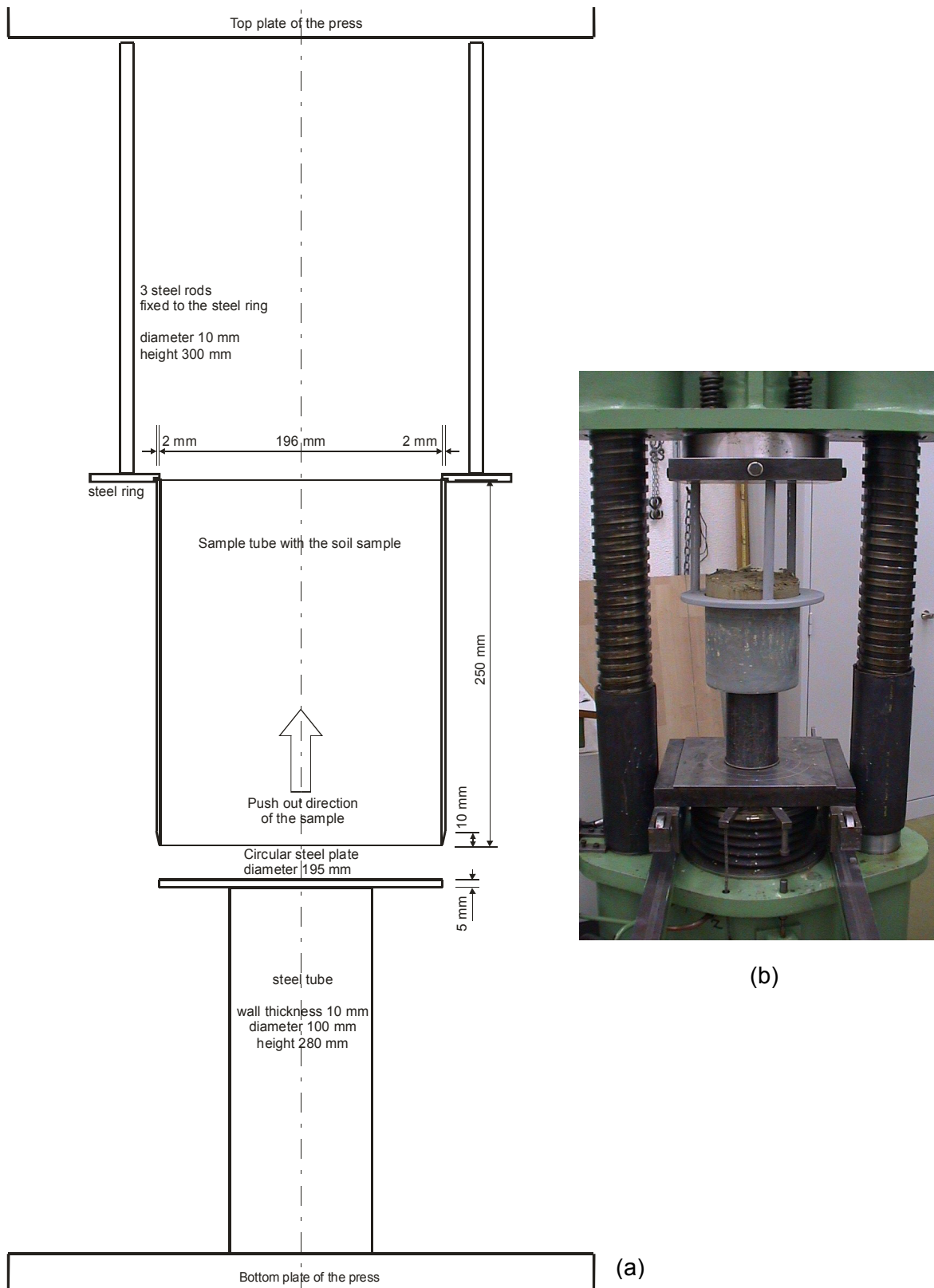
Fig. 3.5:   Extrusion device.

To get an indication of the relative sample quality achieved, samples were taken additionally with two standard sample tubes. A silty clay in Birmensdorf was selected where samples were taken already for a former project (Trausch Giudici, 2004). A trial pit was dug to a depth of 0.85 to 1.0 m and samples were taken.

It was decided to perform unconfined compression tests to evaluate the sample quality, as recommended by Lacasse et al. (1985). This type of test provides no radial support and consequently the soil reacts more sensitively to sample disturbance. The samples were extracted from the tubes with the aforementioned press. Immediately afterwards, test specimens with a diameter of 50 mm and a length of 80 mm were cut out, the dimensions of each sample were accurately measured and the weight was determined. Each sample was placed in the unconfined compression apparatus (Farnell, 1980), and loaded with a constant rate of strain (1.5 crank revolutions per second, as recommended in the instruction manual). The unconfined compression test apparatus spring was calibrated as 4.22 N/mm. The test results were evaluated after the recommendations of Jaecklin (1964), where it is assumed that the specimen volume remains constant during test performance until failure. Therefore the cross-sectional area of the specimen (A) can be calculated as:

$$A = A_0 \frac{h_0}{h_0 - \Delta h}$$

Eq. 3.1

where: A_0 is the initial sample cross sectional area determined from sample diameter in [mm^2],

h_0 is the initial sample height determined before the test in [mm],

Δh is the deformation of the sample in millimetres at peak stress, taken from the test data sheet in [mm].

Consequently, the deviator stress (q_f) is calculated from Eq. 3.2 where 4.22 is the spring resistance in N/mm.

$$q_f = \frac{4.22 \Delta h}{A}$$

Eq. 3.2

The results of the unconfined compression tests on the three different types of specimens are presented in Fig. 3.6. It can be seen that the samples from the larger tubes were able to mobilise greater peak deviator stresses in all cases than those from the 65 mm diameter ones. Although the unconfined compression test is not a highly sophisticated means of investigation and the effective stresses can not be determined, it is still visible that the shear resistance varies when the same soil is sampled with different sample tube diameters.
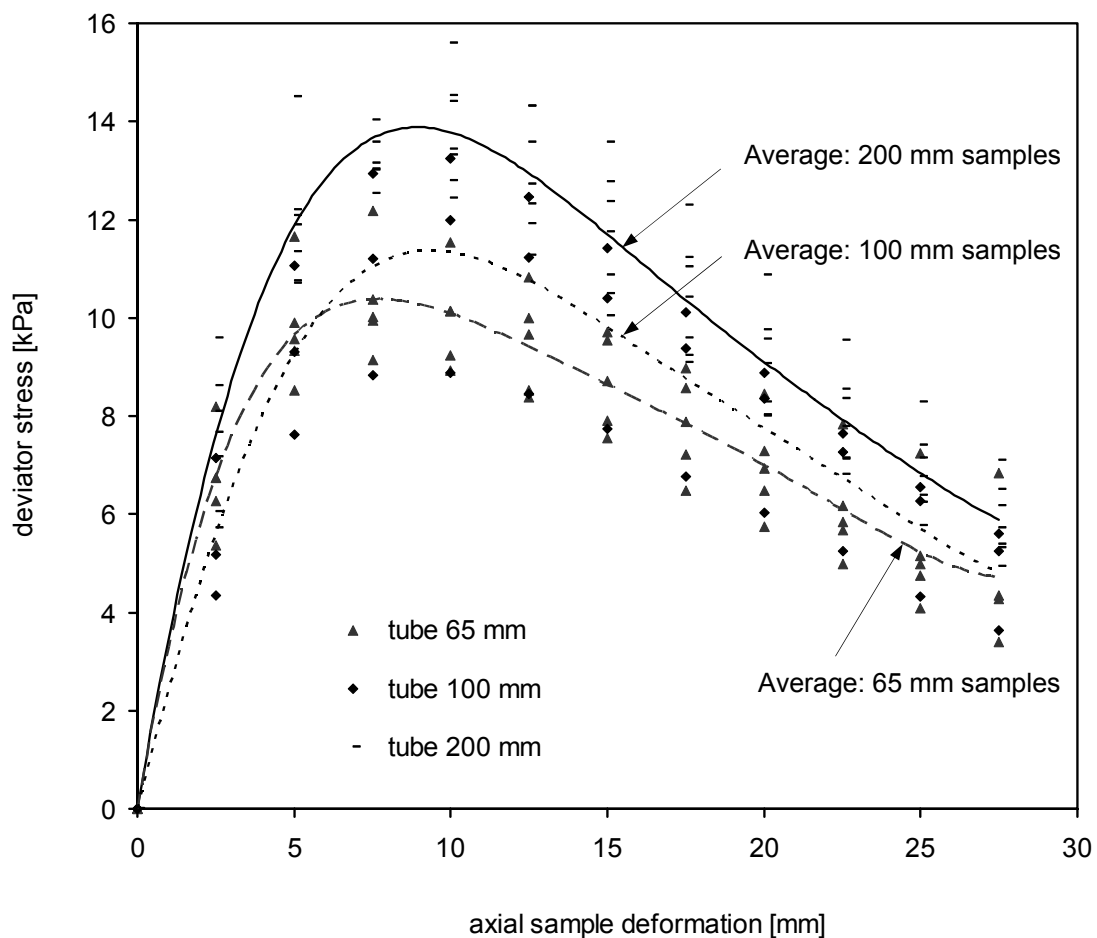
Fig. 3.6:   Results of the unconfined compression tests on natural Birmensdorf clay with specimens from three different sample tube diameters.

3.2.1 Natural block samples of Kloten clay

For further research on the non-linear elastic stiffness behaviour of Swiss lacustrine clays, block samples with the 200 mm sample tubes were taken at the construction site near Kloten (Fig. 3.2).

A trench of about 4 metres depth was excavated at the site and the samples (46862) were taken at the bottom of the trench (Fig. 3.7 a) in November 2003.

Top plate

Sample tubes

a)

b)
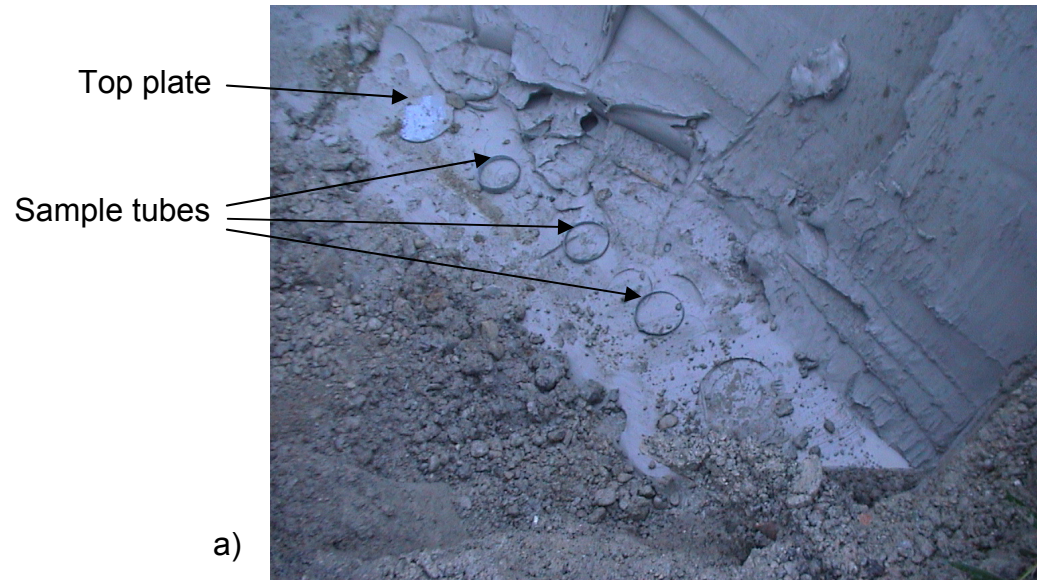
Fig. 3.7: a) Sample tubes pressed into the soil at the bottom of the trench; b) excavating the sample tubes in the trench.

Five tubes were statically pressed into the deposit by an excavator shovel. A steel plate was placed on top of the tube to protect the sample against disturbance from pieces of soil falling into the trench from the surrounding area and the excavator shovel. This plate assured that the force applied during pressing in was uniformly distributed over the cross section of the sample tube. The distance of the tubes

from each other was about twice their diameter. The sample tubes were excavated by hand with a shovel, as shown in Fig. 3.7b, to a depth of 5 – 10 centimetres below the tube. Afterwards the tube was separated easily from the deposit along one of the silt layers.

The samples were lifted out of the trench, cleaned, covered with plastic caps and placed in plastic boxes with wet sawdust. The top and the bottom of the tube was covered with layers of wax mixed with paraffin (1:1) and cling film wrap as soon as the samples were taken to the laboratory. The samples were stored in plastic boxes in the climate controlled room at a constant temperature of 10 °C.

3.3   Reconstituted sample preparation

Burland (1990) defined reconstituted clay in his Rankine lecture "as one that has been thoroughly mixed at a water content equal to or greater than the liquid limit." The major difference between reconstituted and remoulded clay is the mixing technique and the water content at mixing. While the reconstituted samples are mixed by a mechanical mixer at a water content of 1.1 – 1.5 of the liquid limit, the remoulded samples are homogenized by hand mixing at a water content of around the liquid limit. The type of mixing influences the mechanical properties of the sample.

Mitchell (1976) comments that the magnitude of this change of soil properties depends on the strength of the pre-existing fabric and the mixing effort. A comprehensive study of the influence of sample preparation on the mechanical properties of a clay was performed by Fearon & Coop (2000). They showed that the more energy applied to the specimen in terms of mixing effort, the higher its plasticity index, compressibility index and void ratio at the same consolidation stress. This highlights that the comparison of test results derived from natural and remoulded samples can lead to false interpretations. But also in the comparison of the behaviour of remoulded samples, the homogenisation effort applied to different reconstituted samples has to be taken into account.

Consequently, it was optimal to produce a large number of reconstituted samples within one mixing and reconsolidation process. The samples were prepared from clay that was extracted by an excavator and stored in plastic boxes until its use.

The plastic boxes were kept humid, so that the soil did not dry out. Significantly visible stones and organic constituents were separated before the sample preparation. Deionised water was added to the soil and it was mixed mechanically until the materials became a homogeneous suspension. This took from two hours to up to a half day. This suspension was put through a filter with a 1 mm mesh size to remove all remaining constituents, as shown in Fig. 3.8a. Afterwards, the suspension was put into a vacuum mixer, which continuously mixed and deaired it for 24 hours. Finally, the slurry was filled into the 250 and 400 mm diameter oedometer tubes directly from the vacuum mixer with the contractor method as shown in Fig. 3.8b. The clay was incrementally loaded up to a consolidation pressure of 200 kPa. Afterwards, the reconstituted sample blocks were extruded from the consolidometer as done with the natural samples, described in the previous Chapter (Fig. 3.5). The triaxial specimens were prepared immediately after extrusion. A more detailed description of the preparation of the reconstituted samples is given in Kueng (2003).

(a)	(b)

Fig. 3.8:   Reconstituted sample preparation: a) sieving the slurry; b) filling the slurry into an oedometer tube.

Reconstituted samples were prepared from Birmensdorf clay (46707) and (46810). The Birmensdorf soil used for this preparation was sampled by J. Laue and P. Nater at the site described in Trausch Giudici (2004) and was also used in reconstituted form for investigations with the ETHZ Geotechnical Centrifuge (e.g.

Züst, 2000; Fauchère, 2000; Nater, 2006). The reconstituted samples of Kloten clay (46809) were prepared from the first block samples (46762).

3.4 Mineralogical investigations

The typical properties of clayey soils, such as plasticity, permeability, compressibility or shear resistance are among other characteristics such as texture or structure that are mainly influenced by the type and amount of clay minerals. The most common clay minerals are kaolinite, illite, smectite and chlorite. Although the mechanical properties (strength and stiffness) of the various clay minerals are quite different, the chemical compositions are fairly similar. A detailed description of the chemical structures of clay minerals can be found in Heim (1990), Jasmund & Lagaly (1993) or Plötze et al. (2002). A short summary of the chemical composition and the main properties of the typical clay minerals found in Swiss lacustrine clays is given in the following sections.

3.4.1 Chemical composition of clay minerals

The chemical components of clay minerals are silicon (Si^{4+}) and aluminium (Al^{3+}) cations as well as various forms of oxygen (O^{2-} and OH^{-}) anions (Fig. 3.9). Depending on the type of clay mineral, magnesium (Mg^{2+}), iron (Fe^{2+}) or manganese (Mn^{2+}) cations can be included as well. The cations are arranged either in sheets of SiO_4 tetrahedrons, which are subsequently named (T), or in sheets of $Al(O,OH)_6$ octahedrons, which are named (O). These tetrahedron and octahedron sheets sit on top of each other and are connected through shared oxygen anions. Two-sheet (TO), three-sheet (TOT) and four-sheet minerals (TOT O) can be observed (Tab. 3.1). A group of tetrahedron and octahedron sheets connected to oneanother is called a layer and several layers attracted or connected to each other are called platelets.

In the sheets, some silicon and aluminium cations may be replaced by other cations, e.g. aluminium may replace the silicon in tetrahedron sheets. In octahedron sheets, aluminium may be replaced by Mg^{2+}, Fe^{2+} or Mn^{2+} cations. This replacement causes a permanent excess negative charge of the layer

surface, in contrast to the charge at the edges of the layers, which is pH dependent; positive for low and negative for high pH values.

Interlayers are arranged between the single layers of a platelet. These interlayers can be empty, as is the case for kaolinite where the single layers are connected to each other with hydrogen bonds. Alternatively, counter ions can be attracted into the interlayer. The type and amount of counter ions that can be bound in the interlayer depend on the charge of the layers. Highly charged layers, such as e.g. in illites, form strong bonds between the layers and the potassium counter ions of the interlayer. Consequently, these counter ions become non-exchangeable. In lightly charged layers, such as in montmorillonites, the counter ions in the interlayers are weakly bonded to the layer surface and are therefore exchangeable and hydrateable. In the latter case, the thickness of the interlayer is variable, which results in a high potential for volume change, causing the mineral to swell.
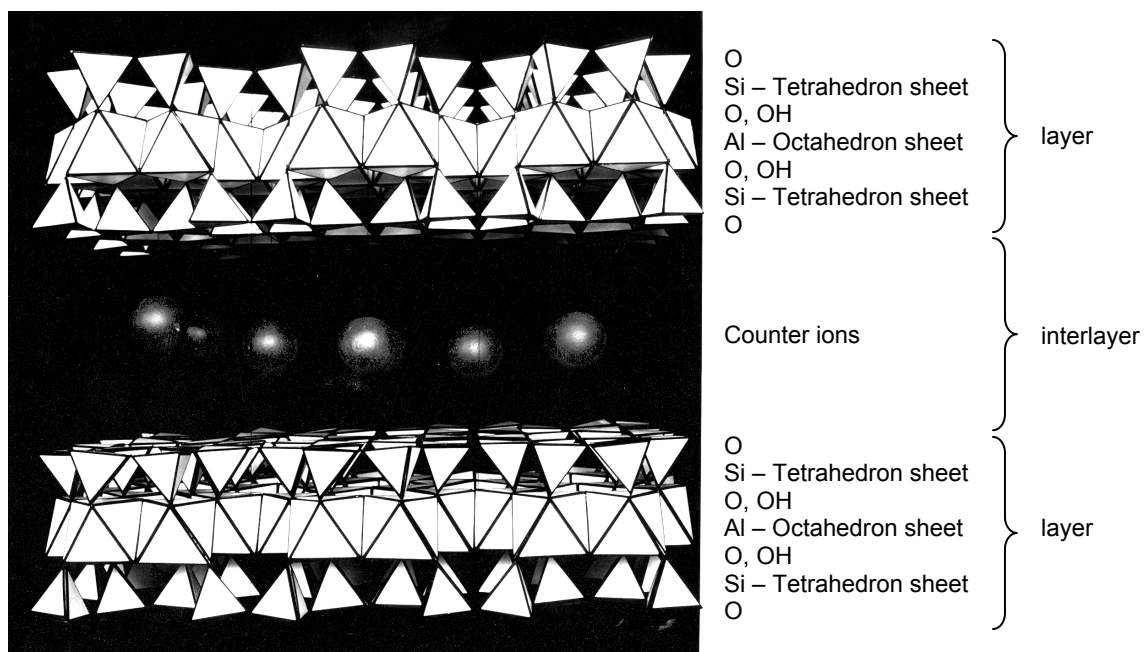
Fig. 3.9: Chemical structure of clay minerals (Picture: Günter Kahr after Hofmann et al., 1933).

Around the platelets, counter ions are attracted as well, which again attract water molecules. This formation of layer surface, counter ions and water molecules around the platelets is called an electric double layer. The thickness of this double layer depends on the type of the counter ions (defining their valence and the size;

common types are calcium (Ca^{2+}) or sodium (Na^+)) and on the concentration of electrolytes in water. The lower the negative charge of the layers, the valence of the counter ion and the concentration of electrolytes in the water, the thicker is the double layer.

The thickness of the double layer primarily defines the structure in which the platelets are arranged, next to additional forces acting between the platelets such as the Van-der-Waals force or the attraction induced by the edges due to their varying charge. Platelets with thick double layers generally form disperse structures, while platelets with thin double layers, where Van-der-Waals forces and the forces arising from the edge charge may also contribute to the formation of the structure, form flocculated structures.

3.4.2 Typical clay minerals

Some characteristics of typical clay minerals that are of interest to soil mechanics are summarised and an overview of their mineralogical properties is given in Table 3.1. More detailed information is presented, for example in Müller-Vonmoos et al. (1985).

- Kaolinite: is a 1:1 layer clay mineral. The platelets have a particle size of $0.2 - 7\ \mu m$ and a particle diameter to particle thickness ratio of about 25 : 2. Kaolinite platelets can be characterised as thick and short. The layer packages are connected through robust hydrogen bonds. The shear resistance for kaolinite, especially in the calcium environment, is comparably high as the particles orientated in a robust flocculated structure do not easily form shear surfaces. Relative to the other clay minerals, kaolinite has low compressibility and a plasticity index of about 40 %.

- Illite: is a 2:1 layer clay mineral consisting of two (T) sheets with one (O) sheet in between. The platelets are very small and thin with a particle diameter of < 2 μm and a particle diameter to thickness ratio of 100 – 300 : 1. The layer packages are connected strongly to each other due to a high layer charge arising from the K^+ ions in the interlayer. In a calcitic environment with a flocculated structure, a friction angle of 24° can be mobilised (Fig. 3.10) together with a plasticity index of ~60 %.

- Smectite: is a 2:1 layer clay mineral. The small and thin platelets are composed of a few T-O-T layers, which have low negative charge and consequently a thick double layer. The counter ions in the double layers as well as in the interlayers are easily exchangeable, which results in a high swelling potential. A low peak and a very low residual friction angle is typical as the single layers move and orientate themselves in the direction of the shear surface due to the low interlayer bonding.

- Mixed Layers: are composed of alternate layers e.g. of illite and smectite. The properties depend on the composition.

- Chlorite: is a 2:1 layer mineral. In contrast to the illite and smectite, chlorite has an additional octahedron sheet in the interlayer which reduces the cation exchange capacity and minimises potential for swelling.

The maximal and residual friction angles determined from ring shear tests on several clay minerals are shown in Fig. 3.10. Müller Vonmoos et al. (1985) pointed out that the residual friction angle for illite and kaolinite rises with higher plasticity index, whereas the residual friction angle of smectite decreases with higher plasticity index. Consequently, the friction angle does not seem to correlate with the plasticity index for natural and reconstituted soils when the clay contains montmorillonite. These observations have also been confirmed by Messerklinger et al. (2003) in the comparison of Swiss and Finnish clays. However, for artificial reconstituted soils (e.g. mixtures containing silt and kaolinite) a linear correlation between the plasticity index and the friction angle could be found (Springman, 1993 after Rossato et al., 1992).

In summary it can be said that the mineralogical composition and the properties of the liquid involved significantly influence the characteristics of clays and consequently their mechanical behaviour. Therefore, the mineralogical composition and the clay mineralogical properties of Birmensdorf clay and Kloten clay were investigated in co-operation with the clay mineralogy laboratory of the Institute for Geotechnical Engineering at ETHZ. The investigations performed and the results for the lacustrine clays derived are presented in the subsequent paragraphs.

Ca – Kaolinite
Ca – Illite
Ca – Montmorillonite 'Arizona'
Ca – Montmorillonite 'Wyoming'
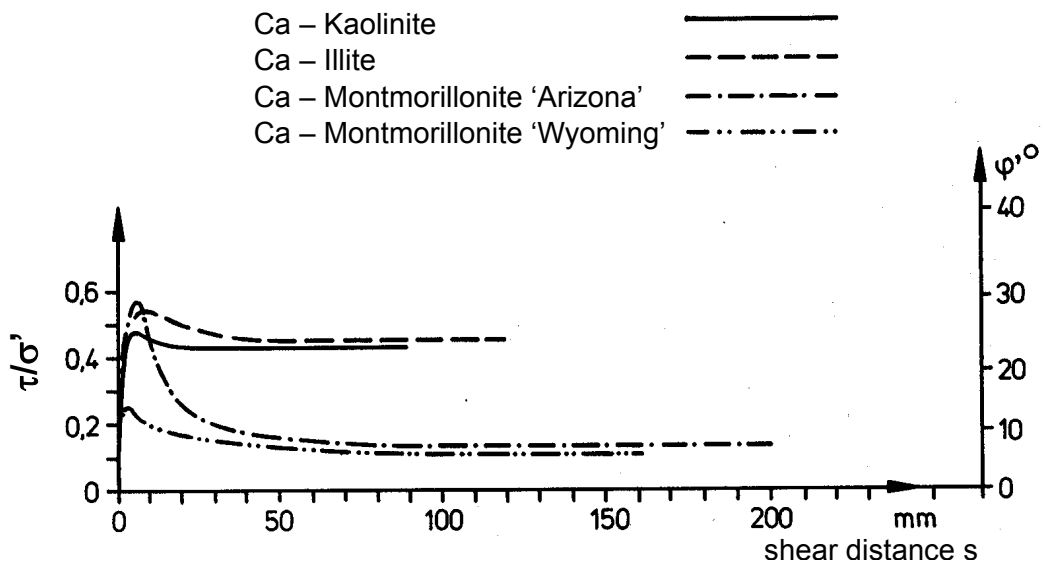
Fig. 3.10: Friction angle for different pure clay minerals determined from ring shear tests (Müller Vonmoos et al., 1985). N.B.: Montmorillonite has different peak friction angles due to variation of layer charge (Arizona $5.13 \cdot 10^4$ esE/cm^2; Wyoming: $3.24 \cdot 10^4$ esE/cm^2).

Tab. 3.1: Properties of common clay minerals, after Plötze (2002).

	Kaolinite	Illite	Smectite	Mixed Layer	Chlorite
Chemical composition					
Distance between the crystalline layers [$\overset{o}{A}$]	7	10	10 - ∞	> 10	14
Specific surface [m^2/g]	10 – 30	50 – 100	up to 800	50 – 600	5 – 30
Cation exchange capacity [meq/100g]	3 – 15	20 – 50	80 – 120	20 – 200	10 – 40
Swelling potential in water	very low	very low	very high	medium to high	very low

67

3.4.3 Mineralogical composition

The mineralogical composition of soils is investigated using X-ray diffraction analysis, which identifies the main mineral types and provides an estimate of the relative amounts of each. The diffraction of X-rays by the crystal lattice is measured and from this the distance between the atom layers in the crystal lattice is determined, which indicates the mineral type. These measurements were made with a Bragg-Brentano diffractometer (Bruker AXS D8 CuKα with automatic divergence slit, graphite monochromator and sample spinner). Randomly oriented powder specimens were used and the amount of each mineral type included in the specimen was evaluated by the Rietveld-analysis (Rietveld program BGMN®/AutoQuan).

The results of the X-ray diffractometer analysis for the Swiss lacustrine clays investigated showed that they are composed of about one third clay minerals (illite, chlorite and mixed layer), one third calcite and dolomite and one third other „grains" (mainly quartz and feldspar; Tab. 3.2). The dominant clay mineral is illite with a content of about 10 to 20 wt% (wt%: weight percent), followed by chlorite with a content of about 10 wt%. Some of the clays investigated contained mixed layers. The calcite content is dominant in all of the Swiss clays investigated, whereas the content of the so-called grain fraction is comparably low.

Tab. 3.2: Mineralogical composition of Swiss lacustrine clays in [wt%].

	quartz	dolomite	calcite	feldspar	illite	chlorite	mixed layer (J/S)	quartz & feldspar	calcite & dolomite	illite, chlorite & mixed layer
Kloten clay (46809)	17	8	45	6	13	11	-	23	53	24
Birmensdorf clay (46810)	14	5	31	6	16	19	9	20	36	44
Kloten clay (46862)	19	20	33	4	13	5	6	23	53	24

3.4.4 Grain size distribution

The grain size distribution was investigated with the laser light scattering apparatus MICROTRAC FRA from Leeds & Northrup. The method is based on the diffraction of a laser beam in a particle suspension, which depends on the particle size. The grain size distribution determined with the laser scattering method for the lacustrine specimens listed (Fig. 3.11a), gave a content of particles < 2 μm of about 44 wt% for Birmensdorf clay and 23 wt% for Kloten clay. This corresponds well with the percentage of clay minerals (illite, chlorite and mixed layers) given in Tab. 3.2. The remaining particles are of silt size and a small sand content was found in some specimens. The percentage per grain diameter is presented in more detail (from 0 μm up to 1000 μm) in Fig. 3.11b. The curves indicate that the majority of particles for Kloten clay have a size of around 10 microns, while the dominating grain size is 1 to 2 μm for Birmensdorf clay.

(a)

(b)
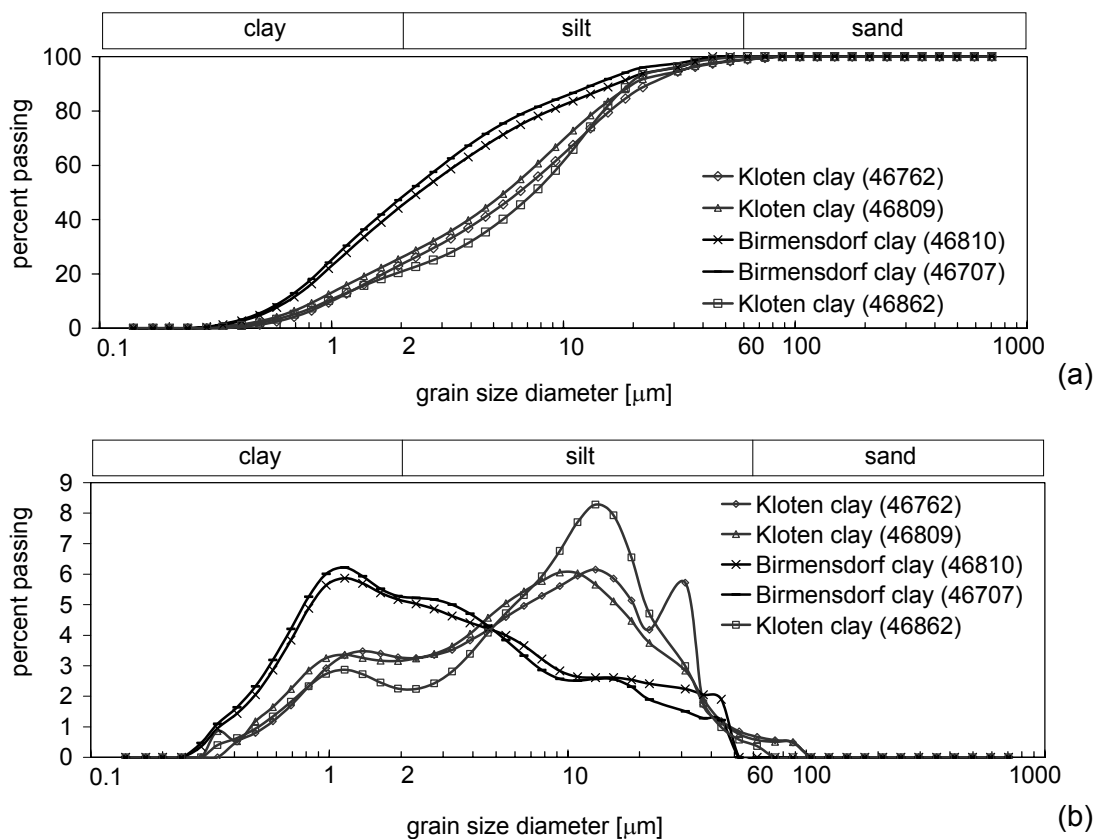
Fig. 3.11: Swiss lacustrine clays: Kloten and Birmensdorf (a) grain size distribution (b) grains passing in percent per grain diameter.

69

3.4.5 Inner, outer and total surface

The surface of the platelets is called the outer surface and is measured with the BET method after Brunauer et al. (1939). The surface of the interlayers (Fig. 3.9) is called the inner surface and its measurement is not described explicitly here. The sum of the outer and the inner surfaces is the total surface and is determined by water adsorption with the water vapour method. Consequently, the inner surface is calculated as the difference between the total and the outer surface.

Water vapour method: A dry, powdered sample of known weight is placed in an airtight box with a saturated NaCl solution in the bottom, which guarantees a relative air humidity of 75 %. The clay layers adsorb water onto the surface in this environment. Consequently, the total surface is calculated from the change of sample weight, knowing that one wt% of water covers about 35 m² (Madsen & Kahr, 1992).

Knowing the total surface the amount of water that can be chemically bonded at a maximum on the mineral surfaces can be predicted (Tab. 3.3). (N.B.: Clay minerals exposed to water vapour with 75 % relative humidity bind one water layer on each side of the mineral, whereas clay minerals in a Ca-rich environment in liquid water adsorb two water layers on each side. Therefore, the water content determined from the total surface is multiplied by two to compare the value with water contents determined from the cation exchange capacity or the water uptake capacity.)

BET – Method: Two test tubes are used, one is empty and soil is placed in the other. After evacuation, both are filled with nitrogen. The pressure level reduces in the test tube with soil due to adsorption of nitrogen at the surface of the platelets. The outer surface is calculated from the pressure difference as a measure of the amount of adsorbed nitrogen (Tab. 3.3).

The outer surface was determined for Kloten clay (46862), which was used in the triaxial test series 2, presented in Chapter 5. Comparing the outer surface determined to the total surface (Tab. 3.3) it can be seen that nearly half of the total surface is the inner surface, which may come from the 6 wt% of mixed layers contained in the specimen (Tab. 3.2). Comparing the results of the total surfaces

determined for the different specimens of lacustrine clay investigated (Tab. 3.3) to each other, it can be seen that an increasing surface correlates with an increasing amount of clay minerals and mixed layers (Tab. 3.2).

3.4.6 Cation exchange capacity (CEC)

The cation exchange capacity makes a statement about the amount of exchangeable cations in the clay mineral. The CEC determination is based on the adsorption of various solutions (e.g. complexes of copper (II) ions with triethylenetetramine and tetraethylene-pentamine (Meier & Kahr, 1999)) by the clay minerals. This adsorption is observed by means of photometric measurements of the solutions after adsorption and of water as a reference. The relationship between these intensities gives an exchange capacity, measured in milli-equivalent per 100 g of dry soil sample.

Another aim of investigating the cation exchange capacity for Swiss lacustrine clays was to estimate the amount of chemically bonded water from the number of exchangeable cations. Calcium is the exchangeable counter ion in lacustrine clays, binding 2 water layers which equals 12 water ions per cation. Consequently, the maximum amount of chemically bonded water can be calculated as:

Water bonded by calcium counter ions = 0.5 * CEC [meq/100 g] * 18 (molecular water weight [g/mol] * 12 (water ions per cation)

considering that calcium has a valence of 2 but the CEC values refer to a valence of 1. Because this water content is the maximum amount of water bindable in the inter- and double layers, all additional water is stored in voids as capillary water. It is assumed that the bond water content corresponds with the water content at the plastic limit, (Tab. 3.4; Kahr, 2003). The results (Tab. 3.3) show that this assumption is reasonable for Birmensdorf clay but did not correlate well for Kloten clay. No correlation was found between the plastic limit and the innercrystalline bindable water for the Finnish clays investigated (Messerklinger et al. 2003).

3.4.7 Water uptake capacity after Enslin-Neff

The water uptake capacity gives the maximum amount of water that can be picked up by the clay by free swelling. It is the sum of the innercrystalline bonded water

and the water that is stored in voids as capillary water. The water uptake capacity was determined by the Enslin-Neff apparatus consisting of a sample container with filter and a tube for the volume measurement. The apparatus is saturated. One gram of powdered sample material is placed on the filter plate and the time it takes to soak up the maximum possible amount of water is recorded with a stop-watch, as well as the soaked water volume. The water uptake capacity is determined from the quotient of the water taken up [ml or g] and the dry sample mass [g].

The water uptake capacity determined for the Swiss lacustrine clays is presented in Tab. 3.3. The results show that the capacity of Birmensdorf clay is up to twice as high as that of Kloten clay. This is reasonable as the Birmensdorf clay contains swelling mixed layer minerals and, additionally, the content of grains smaller than 2 μm is higher. It is assumed that the water uptake capacity correlates with the liquid limit (Tab. 3.4; Kahr, 2003). A trend is visible when comparing the results although the values differ in a range of ±10 %. This trend was also visible for the Finnish clays investigated with results, presented in Messerklinger et al. (2003).

Tab. 3.3:   Mineralogical parameters for the Swiss lacustrine clays.

	Total surface [m²/g] after water vapour method	Outer surface after BET-method [m²/g]	Water content [%] from the water vapour method (=hygroscopic water content)	Cation exchange capacity [meq/100g]	Water content [%] from the CEC	Water uptake after Enslin-Neff [ml/g]
Kloten clay (46809)	46		2.6	4.8 – 5.8	5.2 – 6.3	0.373
Birmensdorf clay (46810)	148		8.2	19.8	21.4	0.53 – 0.57
Kloten clay (46862)	53	31	3	2 - 3.6	2.2 - 3.9	0.434

3.5 Classification

The soil mechanical classification of the fine grained materials was performed using the Atterberg limits according to the Swiss Code SN 670 345a (1989).

The index properties of the Kloten clay as well as the Birmensdorf clay can vary widely over the sample field. Therefore, each time a new material was sampled or a new charge of reconstituted samples prepared, its properties were determined again. The classification results of the Swiss lacustrine clays investigated are shown in Fig. 3.12 and Tab. 3.4.

Kloten clay is classified as a low plasticity clay and the different samples of Birmensdorf clay are classified as clay of low, medium and high plasticity, respectively. Consequently the name "clay" is justified for the lacustrine soil from Kloten and Birmensdorf investigated, although the mineralogical investigation showed that the actual clay mineral content is only 24 and 44 %, respectively (Tab. 3.2). The liquidity number (Tab. 3.4) specifies a pappy plastic in-situ state for both clays.
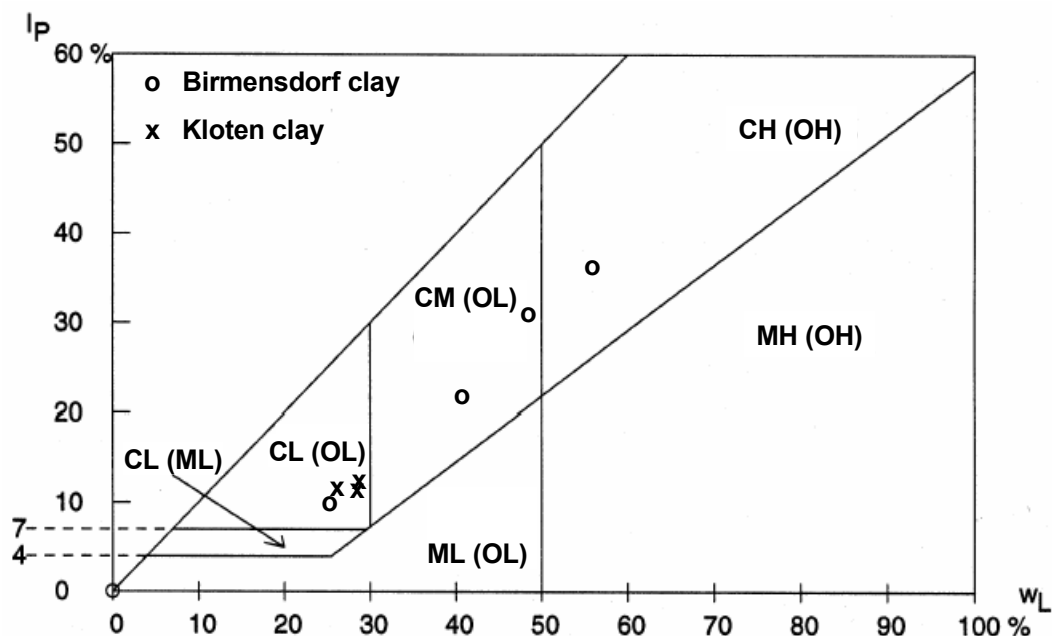
Fig. 3.12: USCS classification of the Swiss lacustrine clays.

The activity number, which is a measure of the content of swellable clay minerals, identifies Kloten clay as an inactive and Birmensdorf clay as a normally active material. The activity increasing for Kloten clay (46809), (46862) and Birmansdorf clay (46810) corresponds to the increasing content of swellable clay minerals, represented by the mixed layers, which was determined in the clay mineralogical investigations (Tab. 3.2).

Tab. 3.4: Classification results of the Swiss lacustrine clays.

	Plastic limit w_P [%]	Liquid limit w_L [%]	Plasticity index I_P [%]	USCS Classification	In-situ water content w [%]	Liquidity index I_L	Content < 0.002 mm [%]	Activity I_A	Specific density[‡] ρ_s [t/m³]
Kloten clay (46762) 1st sample	16.1	28.7	12.6	CL	28	0.94	-	-	-
Kloten clay (46862) 2nd sample	14.4	26.7	12.3	CL	26.5	0.98	21	0.59	2.74
Birmensdorf clay (upper layer)	15.3	25.3	10.0	CL	24	0.87	-	-	-
Birmensdorf clay (lower layer)	18.5	40.4	21.9	CM	34	0.71	-	-	-
Kloten clay rec. (46809)	16.1	28.3	12.2	CL	-	-	25	0.49	2.77
Birmensdorf clay rec. (46810)	18.9	55.8	36.9	CH	-	-	41	0.90	2.75
Birmensdorf clay rec. (46707)	17.3	48.4	31.1	CM	43[*]	0.83	42	0.74	-

* reconsolidated to 143 kPa; ‡ after Swiss Code SN 670 335a (1989); rec. = reconstituted

4   Triaxial test equipment

For a successful investigation of the soil behaviour during stress path reversals under triaxial stress conditions in the laboratory, the following three conditions have to be fulfilled: high sample quality, stress path test apparatus with high quality instrumentation and control systems, and accurate displacement measurement. High sample quality can be assured providing the displacements that arise in the soil during sampling are of a magnitude lower than the displacement range measured for the small strain stiffness determination. This objective was already discussed in Chapters 2 and 3.

The second condition requires the test apparatus to be able to perform stress path tests at any applied stress ratio to investigate the behaviour in the entire elastic region. The application of a constant stress ratio is possible with the use of an automated stress regulation system integrated into the triaxial test apparatus. For the performance of any stress path in extension, the axial load system has to be uncoupled from the application of radial load.

The third condition is an accurate displacement measurement system for the investigation of the stiffness degradation in the elastic region, for which the displacement measurement range of the transducer must be of the appropriate resolution and accuracy. Atkinson & Sallfors (1991) propose that the elastic stiffness degradation of clays occurs in the strain range between 10^{-3} and 1 %. This strain measurement accuracy is achievable with special triaxial apparatus or with local displacement measurement devices fixed directly on the test sample, e.g. Burland & Symes (1982), Jardine et al. (1984) or Clayton & Khatrush (1986). In summary, the soil samples as well as the test apparatus must fulfill strict criteria for the successful investigation of elastic soil behaviour.

Special triaxial test apparatuses (von Moos, 2001; Arenson, 2003; Trausch Giudici, 2004), which were designed and built in the Institute's workshop, were used in this research. The apparatuses have an automated stress regulation to apply any stress path in the triaxial stress space. Additionally, local displacement measurement devices for local axial and radial displacement measurement were implemented. These apparatuses and all additional devices are described in detail in the following section. Finally, the calibration tests performed and the accuracy determined for the different test devices are discussed.

4.1   Development of the test apparatus design

Design of the triaxial apparatuses was carried out at the Institute for Geotechnical Engineering (IGT) in 1999/2000. The first apparatus was built in the Institute's workshop for creep tests on snow samples (von Moos & Bartelt, 1998). This new apparatus offered the opportunity to perform strain-controlled as well as stress path tests. The cell pressure medium used for snow samples was air, with a special volume measurement device for determining change in air volume. The aim of that research project was to determine the visco-elastic deformation behaviour of snow by performing deformation-controlled triaxial creep tests with slow deformation speed (von Moos, 2001).

Four additional triaxial apparatuses of a similar basic design had been constructed for further research projects on permafrost and lacustrine clay. The design was adapted by replacing the air controlled cell pressure, used for tests on snow, with a standard system operating with a liquid. Three of the four new apparatuses were built for the testing of frozen soils (Arenson, 2003). Therefore they were placed in a cold chamber and equipped for a sample diameter of 74 mm. The axial load cells had a pressure range of 20 kN. One of the four apparatuses was constructed for investigations on lacustrine clays and is described in detail by Trausch Giudici (2004). This apparatus was equipped for a sample diameter of 56.4 mm, which equals a cross-sectional area of 25 cm². This is the standard in Switzerland. Additionally, bender elements were installed in the top cap and bottom plate to apply shear waves in the axial sample direction. The bender elements were

provided by ISMES (www.ismesgeo.it). The axial load cell had a pressure range of 5 kN, suitable for testing soft samples of 56.4 mm diameter.

All of these apparatuses were used for the investigations presented in this research. The three apparatuses used for permafrost (called: Triax 1, Triax 2 and Triax 3) were adapted for testing soft clay. Each top cap and bottom plate was replaced by one of a smaller diameter of 50 mm. The load cell was changed into one of smaller capacity range of up to 5 kN. The apparatuses were kept in the cold chamber (p.128ff; Arenson, 2003) under a constant temperature of 10°C ± 1°C. This test temperature of 10 °C was chosen to match the average insitu conditions of the soil since the viscosity of water varies notably with temperature. The fourth triaxial apparatus (Triax 4), which was initially constructed for clay (Trausch Giudici, 2004), was used without any further adaptations. Triax 4 was situated in a climate controlled room at a temperature of 18°C ± 1°C.

The measurement accuracy, especially measurement of the change of volume of the water in the sample, is primarily affected by temperature variation during the test period. This variation is in the same range (± 1°C) for both climate rooms used. The effect of the higher temperature level, which may have marginally influenced the viscosity of the water and consequently the drainage conditions, and was neglected in the data evaluation.

4.2   Design of the triaxial test apparatus

These special triaxial apparatuses consist of three units, as shown in Fig. 4.1(a), the cell pressure unit (A), the back pressure unit (B) and the triaxial cell (C). The design of the cell pressure and back pressure unit is the same. Each unit regulates the corresponding pressure with a piston system, whereby the change in cell and pore water volume is measured. The outer steel cylinder (1) and (5) (the following numbers in brackets refer to Fig. 4.1) of the piston system have an inner diameter of 100 mm. These outer cylinders are fixed to the load frame (10) at the top. The inner steel cylinder is fixed to the apparatus at the bottom. The load frame on which the outer cylinder is mounted, moves upwards and downwards and is powered by a stepping motor (4). The gap between the two cylinders is filled with water in these tests, because the test samples are saturated with water and the

test temperature is above freezing point. Generally, any liquid medium that is not aggressive and remains incompressible under the test temperatures can be used in the apparatus.

The sample (7) is placed in the load cell unit (C), which is a steel cylinder with an inner diameter of 300 mm and a height of 720 mm. The cell is closed at the top by a steel cupola. At the bottom, the cell is fastened to the bottom plate of the load cell (13) by 12 bolts. The cell is filled with water by an external pump and is de-aired at the top of the cupola. A load frame (10) is situated inside the cell on which the load cell (9) and the top cap (11) are fixed. The tie bars of the load frame (10) pass through the bottom plate of the pressure cell via a hermetically sealed bearing. The friction occurring in this bushed bearing does not influence the load measurement as the load cell (9) is mounted inside the pressure cell.

Tab. 4.1: Technical details of the measurement devices used in the various triaxial test apparatuses (after Arenson, 2003).

Transducer:	Test apparatus	Measurement range	Precision	Resolution	Sensor
External LVDT	1 to 3	100 mm	± 0.1 % of end value	0.003 mm	HBM WA100
	4	50 mm	± 0.1 % of end value	0.003 mm	HBM WA100
Load cell	1 to 4	5 KN	± 0.1 % of end value	0.2 N	HBM U2B
PWP (top & bottom) Cell pressure	1 to 4	1 MPa	± 0.1 % of end value	0.03 kPa	SENSTEC 8267

Fig. 4.1: Schematic cross-section through the triaxial test apparatus (after Arenson, 2003).
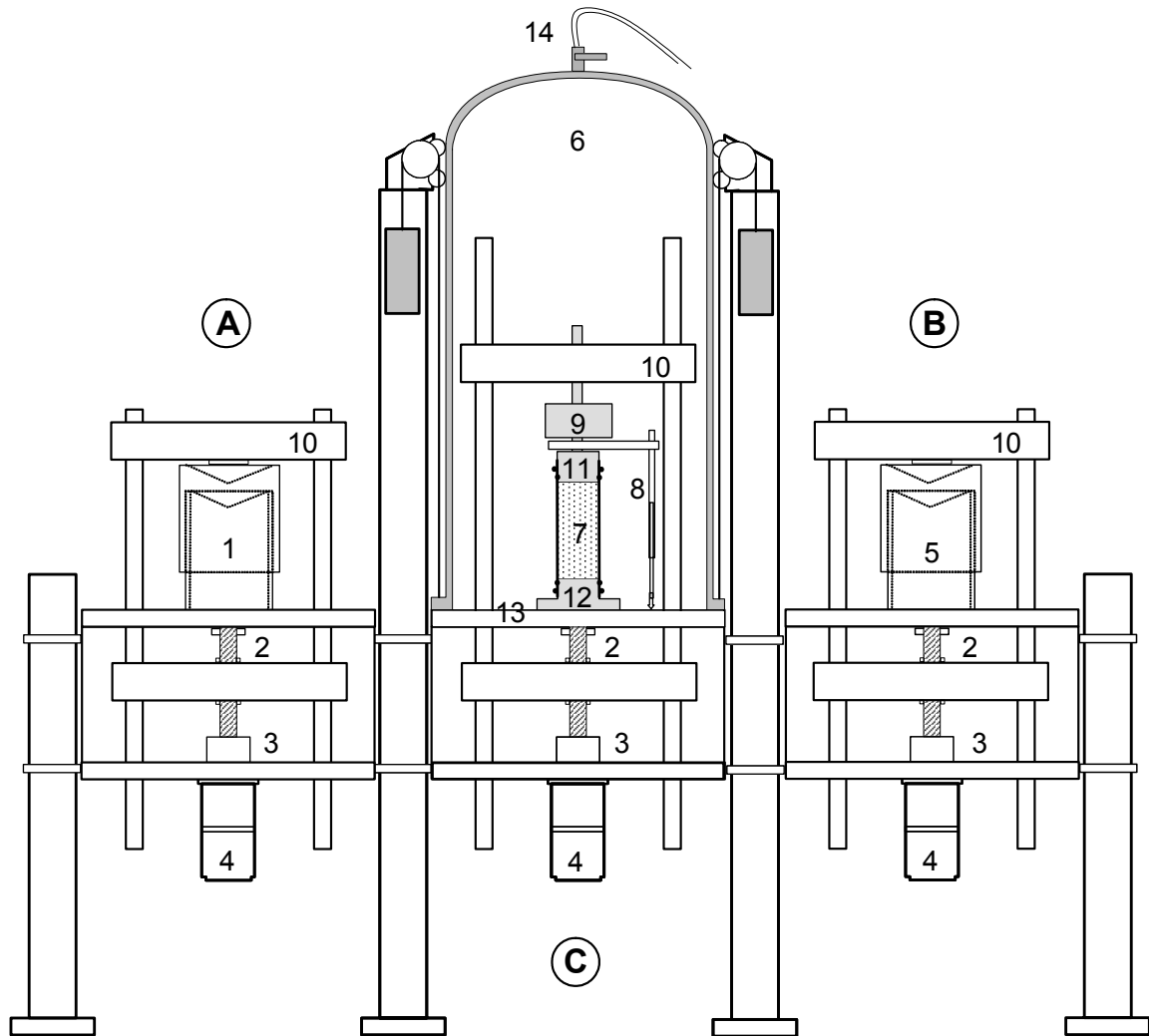
A – Back pressure unit   1 – Back pressure cylinder   8 – External LVDT

B – Cell pressure unit   2 – Lead screw   9 – Load cell

C – Triaxial cell   3 – Shaft coupling   10 – Load frame

4 – Stepping motors   11 – Top cap

5 – Cell pressure cylinder   12 – Bottom plate

6 – Pressure cell   13 – Bottom plate of the cell

7 – Sample with rubber membrane and sealing rings   14 – Deairing valve

The mounting of the external LVDT (8) is fixed between the load cell (9) and the top cap (11). The properties of the load cell and the LVDT are summarized in Tab. 4.1. The bottom plate (12) is screwed to the bottom plate of the pressure cell (13),

and the test sample (7) is bolted between the top cap (11) and the bottom plate (12). The axial load is applied to the sample through the top cap (11), via the load cell (9) and the loading frame (10). The top cap is mounted on the loading frame so that extension tests can be performed easily.

All three units are powered by stepping motors (4), which have a resolution of 400 steps per millimetre. They power a lead screw (2) with a screw pitch of 1 mm per rotation. Between the stepping motor and the lead screw, a gear box (3) is installed, which reduces the vertical movement per step by a factor of 16. The resulting step size is $1.56 \cdot 10^{-4}$ mm/step for axial movement and 1.227 mm^3/step for the volume measurement.

The pressure supply between the back and cell pressure unit and the triaxial cell is established by PVC tubes with an inner diameter of 4 mm (14) & (15) (numbers refer to Fig. 4.1 & Fig. 4.2). The current pressure is measured with the corresponding pressure transducers (16), (17) & (18), which are connected to the tubes. The cell pressure transducer (18) measures the current cell pressure. The tube supplying the fluid with a back pressure is split into a pipe for the bottom and a pipe for the top back pressure, with separate pressure measurement at the top and the bottom via the corresponding transducer (16) & (17). The measurements of the bottom back pressure transducer are used for the back pressure regulation, which is described in the next section. Each pressure supply system may be closed by a separate valve to allow saturation of all parts of the hydraulic system. The properties of the pressure transducers are described in Table 4.1.

The pressure supplies are led through the bottom plate of the load cell (13). The water supply for the bottom back pressure is led through a pipe into a connection in the bottom plate (12). Grooves on the top side of the bottom plate distribute the pressure uniformly over the cross-sectional area to the filter plate (20) and further to the bottom end of the sample. The top back pressure control is arranged in a similar way to the top end of the sample. The metal filter stones are made of bronze and have a porosity of 38 %.

Analysing the displacement measurement devices with respect to their accuracy, the following potential inaccuracies are recognisable. In the axial direction, the LVDT (8) is mounted above the top cap (but below the load cell (6)) and measures

down to the bottom of the pedestal. Therefore compliance in the top cap and pedestal, seating errors of the top cap on the porous stone and bedding errors due to surface irregularities are incorporated into the measured data. In the measurement of pore water volume, the main error is assumed to be due to the expansion of the tubes and the regulation piston system itself.
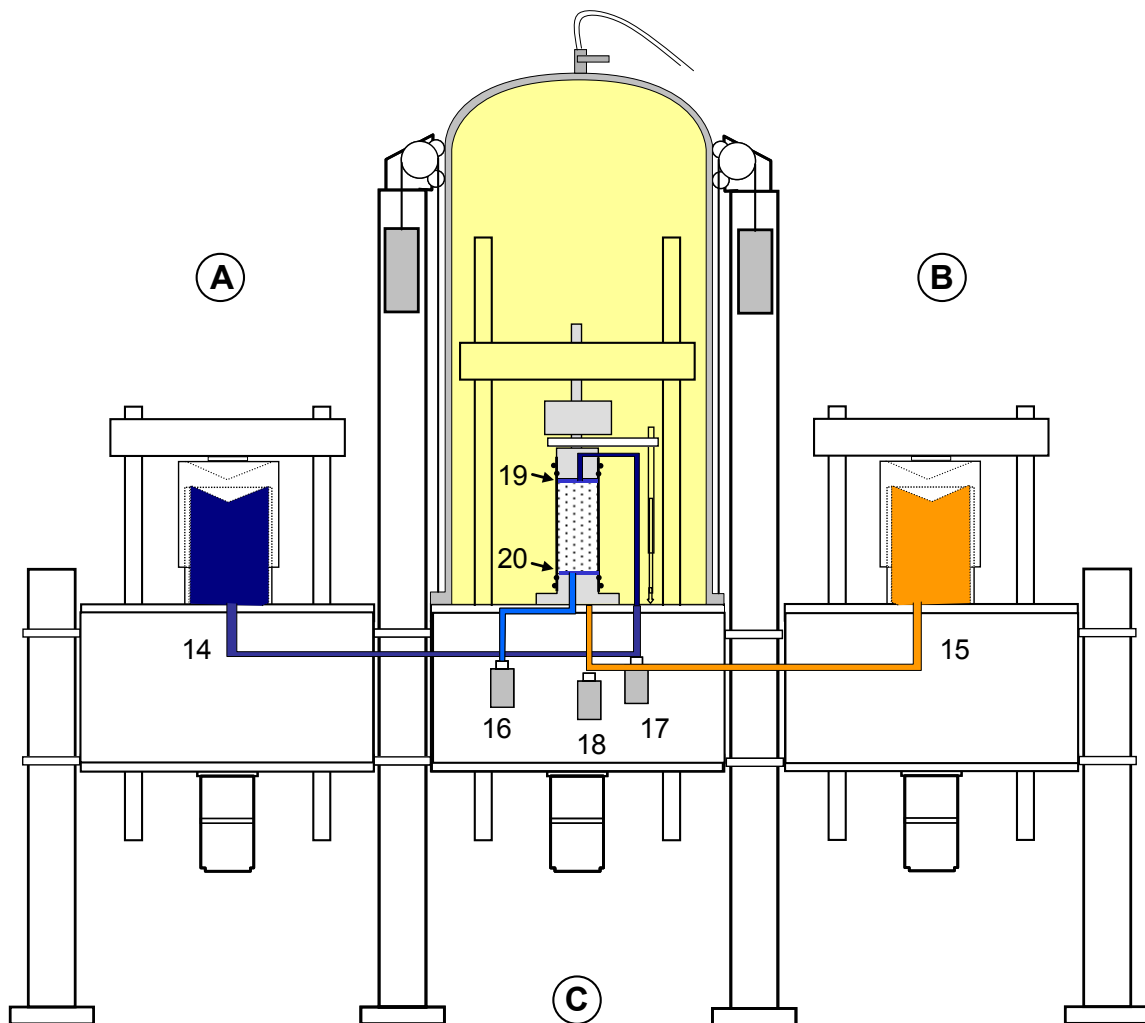
A – Back pressure unit   14 – Back pressure supply

B – Cell pressure unit   15 – Cell pressure supply

C – Triaxial cell   16 – Pore pressure transducer bottom

                            17 – Pore pressure transducer top

                            18 – Cell pressure transducer

                            19 – Filter plate on top of the sample

                            20 – Filter plate at the bottom of the sample

Fig. 4.2:   Schematic cross-section through the pressure regulation system of the triaxial test apparatus (after Trausch Giudici, 2004).

In order to investigate the small strain stiffness response of soft Swiss lacustrine clays, options for more accurate displacement measurement methods were considered. Scholey et al. (1995) present a comprehensive review of local strain measurement devices for triaxial tests, pointing out that LVDTs mounted "locally" on the sample will give the best results for axial displacement measurement. Four methods were discussed for measurement of radial displacement, although the authors did not specify the accuracy for any of them.

4.3 Local axial strain measurement device

Consequently, it was expedient to install local LVDTs for local axial displacement measurement in the triaxial apparatus. The local LVDTs were sourced from Precisor Messtechnik München. The sensor type TK-5 was used, which has a nonlinearity of ± 0.05 % of the measurement range, which is ± 5 mm.

The electrical cable was connected to the top of the LVDT to avoid bending moments being applied by the self weight of the cable and connection. Cuccovillo & Coop (1997) suggested placing the electrical connection at the side of the LVDT and the use of a type of LVDT that has an open top end, so that the measurement rod can pass through the top when larger strains are applied. Due to the small measurement range of ± 5 mm, such restrictions in the maximum applicable strains did not occur, as the test were mainly carried out in extension. For the few compression tests conducted, it was seen that convex bending of the sample surface had such a large influence that the measurement rod slipped off the bottom fixity during large deformations.

Mountings were constructed similar to those described in Cuccovillo & Coop (1997) to fix these LVDTs to the soil sample, although the pins used to secure the connection with the sample through the membrane were omitted in this case. Gens (1982) deduced that the rubber membrane does not slide on the sample surface, and so the displacement measurement is not improved by putting pins through the rubber membrane into the soil sample. However the risk of creating a leak is much higher when using pins. Therefore, the mountings were stuck onto the rubber membrane with the superglue "LOCTITE 460", which is effective in

water and under pressure, and is very stiff. The detailed design of the local LVDT mounting plates is given in Fig. 4.3.

bottom mounting: top view B – B   top mounting: top view C – C

bottom mounting: front view   top mounting: front view
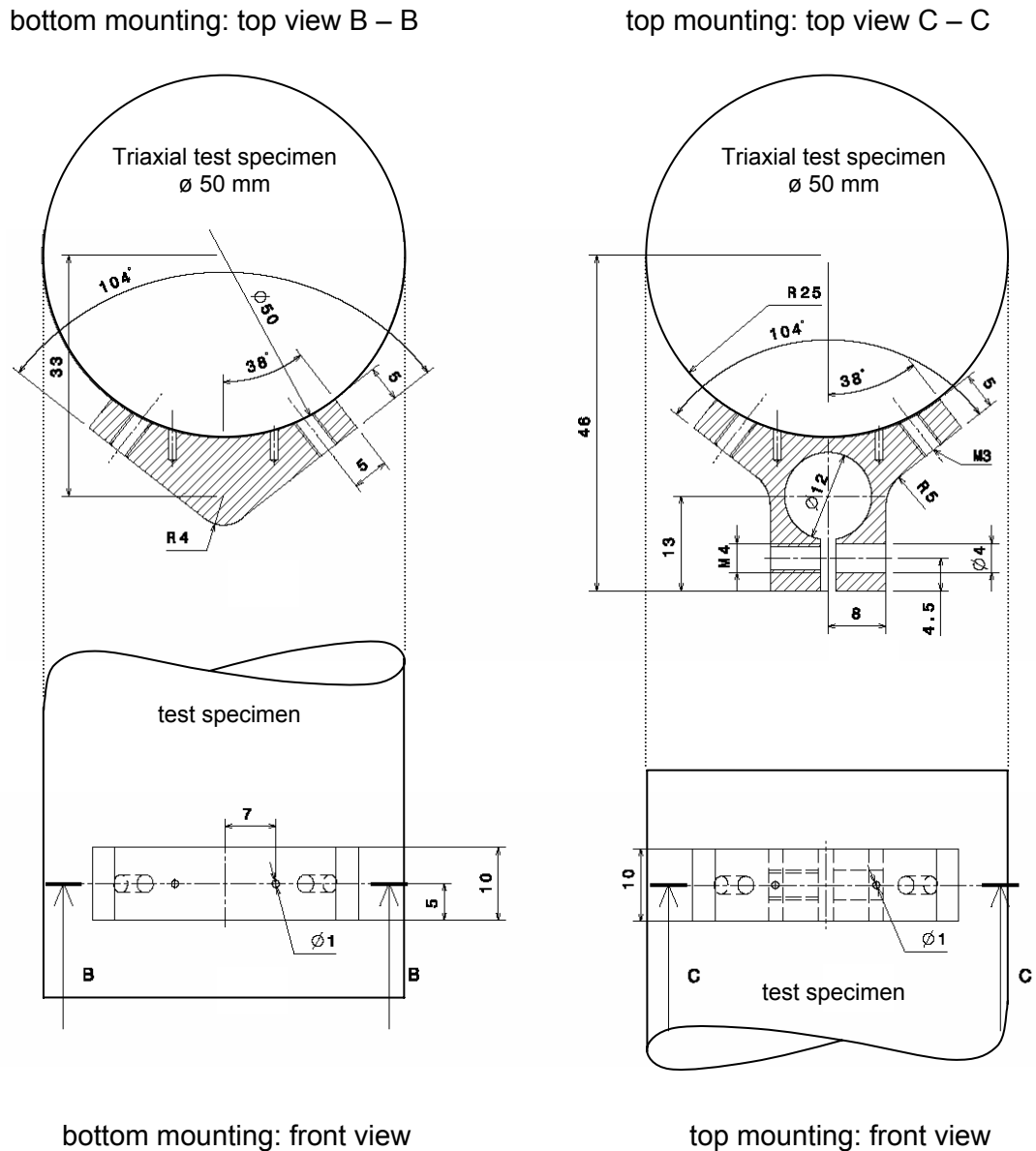
Fig. 4.3:   Construction of the bottom and the top mounting plates, dimensions in millimetre, scale 1 : 1 (drawing by A. Zweidler).

An initial axial distance of 70 mm was guaranteed because a stiff spacer was fixed between the mountings while they were being glued onto the rubber membrane.

Fig. 4.4a shows the local strain measurement device during mounting on the sample, with the spacer located between the top and the bottom mounting. Unlike

Cuccovillo & Coop (1997), who suggested two separate distance holders, only one large distance holder was used to stabilise the measurement device during mounting. The local strain measurement device during testing is shown in Fig. 4.4b. The bottom mounting supports the measurement rod and the top mounting restrains the LVDT. The measurement rod touches the bottom mounting but is not fixed any further.

local LVDT

top mounting

spacer screwed on the top and the bottom mounting

bottom mounting

$h_0 = 70$ mm

a)

b)
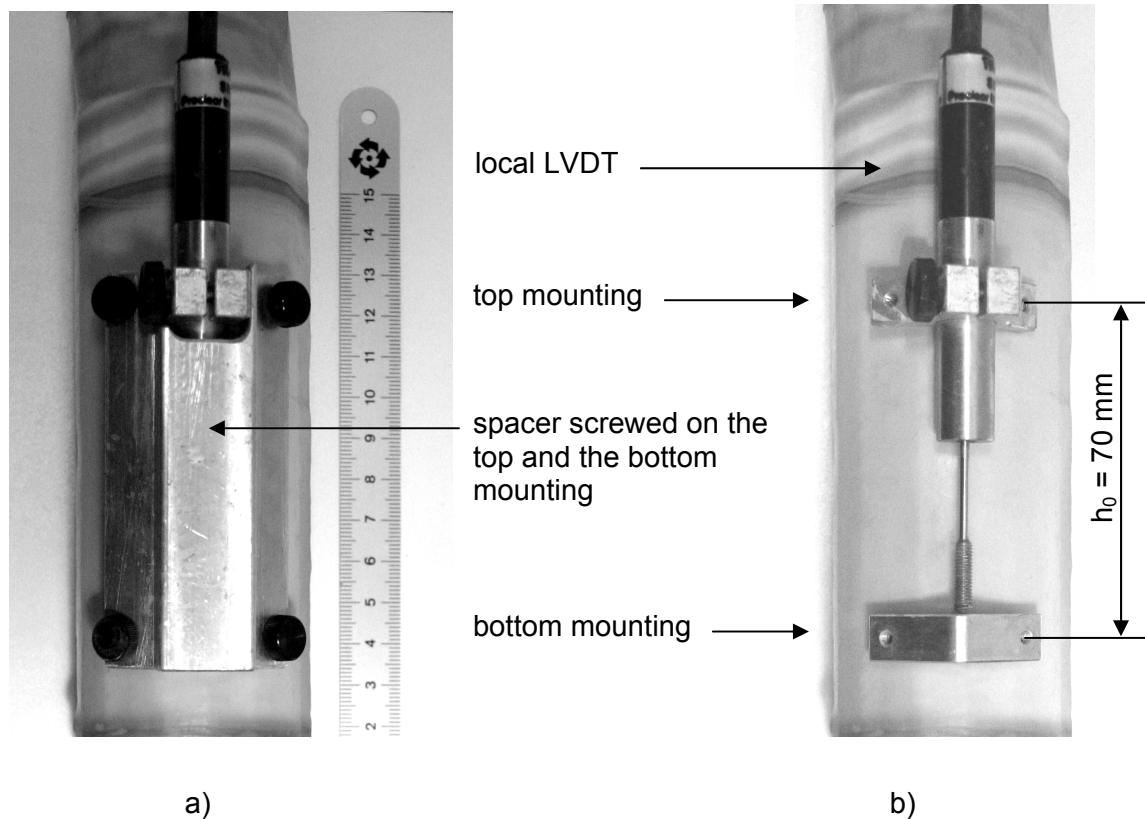
Fig. 4.4: Fixture of the local LVDT's on the triaxial sample: a) with the spacer screwed to the mountings b) the device set-up during testing.

4.4 Local radial strain measurement device

Methods of carrying out radial displacement measurement without disturbing the sample were considered. A discussion of the advantages and disadvantages of the commonly used methods for radial displacement measurement in triaxial test apparatuses is given in Chapter 2. It was highlighted therein that a laser scanning device has the advantage of contactless displacement measurement over the entire sample height. Measuring the radial displacements over the full range of the

axial extent is particularly important for the investigation of natural samples, especially for undisturbed lacustrine clays that have distinct stratification. Romero et al. (1997) used a laser scan device in order to investigate unsaturated soils under non-isothermal conditions, as discussed in Chapter 2. They mounted lasers outside the Perspex triaxial cell and used them to scan the sample to obtain radial measurement of displacement. This system was not directly implementable within the IGT triaxial testing apparatuses as the cell was made of steel rather than of Perspex. Therefore two possibilities remained to incorporate a radial laser scanning device within the existing triaxial apparatuses: either the triaxial cell should be newly manufactured out of transparent material or the laser scanning device should be installed inside the triaxial cell. The first option could be adopted by replacing the steel cell with a Perspex cell or by making "windows" in the steel cell. Using Perspex in the triaxial cell has the disadvantage of cell pressure limitations and creep (Tab. 4.2).

Tab. 4.2:   Advantages and disadvantages of a Perspex triaxial cell.

Advantages	Disadvantages
Transparent	Cell pressure limitations
Laser does not need to be packed in watertight housing	Creep influences
	Refraction of the ray at the cell wall
	Larger distance between laser and sample – less accurate

The second option could be made available by packing the lasers in a specially designed watertight housing. This method has the additional advantage that the lasers can be placed closer to the test sample, which results in higher measurement accuracies as the non-linearity that defines the measurement accuracy is related to the measurement range, and becomes larger with increasing measurement distance. Therefore it was decided to apply the second method.

The housings were designed to retain the lasers so that the ray passed through a transparent window and the cell fluid to strike the sample normally. The reflected ray was then captured by the device. Additionally, the lasers were mounted on a frame with lead screws permitting controlled movement in the axial direction. The sensor type ME ILD1400_10 with a measurement range of ± 5 mm, an initial distance to the sample of 20 mm, a nonlinearity of ± 0.2 % of the measurement range and a resolution of 1 micrometre was selected (Micro-Epsilon Ortenburg, Germany). The design of the watertight laser housing is shown in Fig. 4.5. This laser box is millcut from an aluminium block with a glass window facing towards the soil sample and with a sealed exit for the electrical supply and the data output at the rear. The two sides are protected by plates, which are glued into the frame after the laser is placed inside and connected.
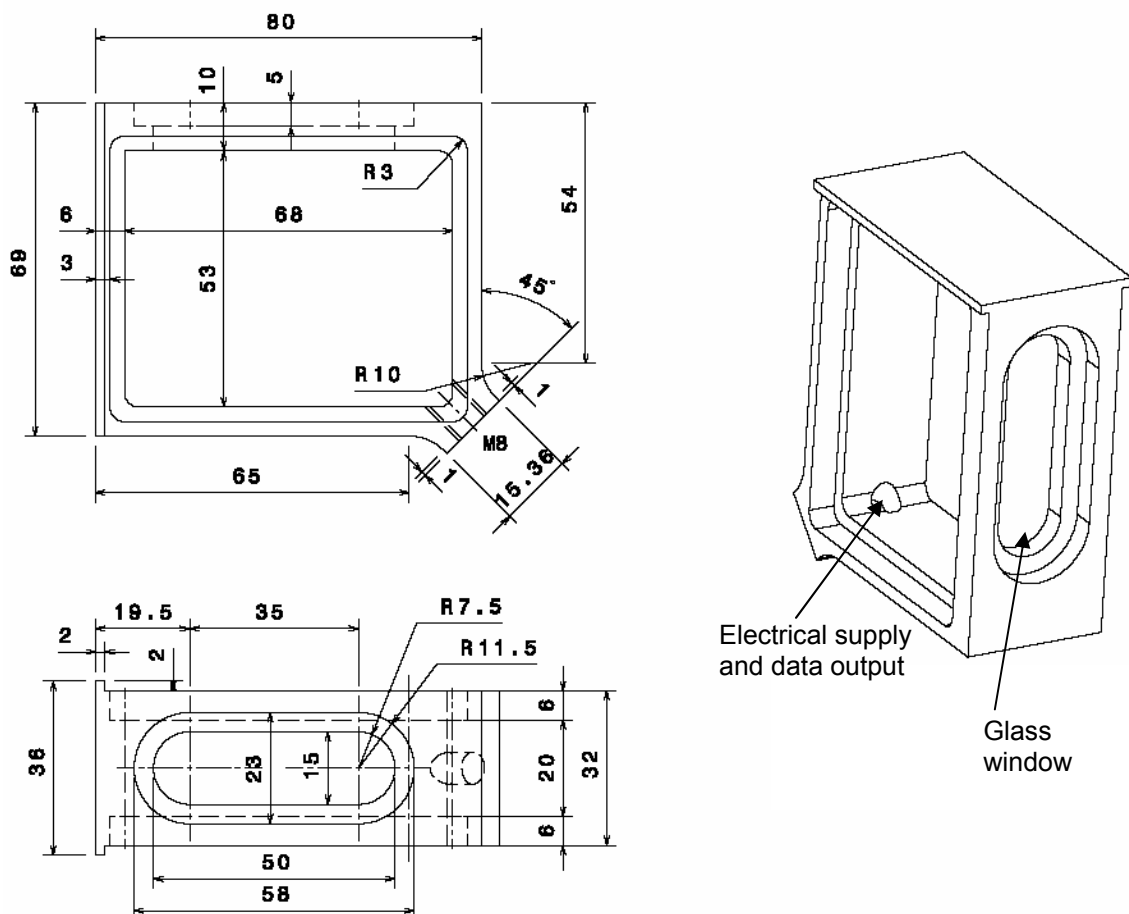
Fig. 4.5:   Laser housing, dimensions in millimetre (drawing by A. Zweidler).

A frame was constructed inside the triaxial cell, consisting of two lead screws (diameter 20 mm; pitch 4 mm/rotation), which are hermetically sealed while passing through the bottom plate of the pressure cell, and a connecting plate (Fig. 4.6 and Fig. 4.7). Each of these two lead screws is powered by a stepping motor (PHYTRON ZSH57/2.200.4,2) with a gear (PLE60 i=16), which has a transmission ratio of 16, resulting in a step size of 0.000625 mm. The connection plate is mounted on the two guiding rods of the load frame (Fig. 4.1) with a rubber slip ring to stabilise the plate in the horizontal direction. The lasers are suspended from the bottom side of the connection plate and spaced at 120° in the horizontal plane, to observe any bending or other irregularities in the sample displacements (Fig. 4.6b). The construction of the mounting unit and the arrangement of the lasers are shown in Fig. 4.6b. Three lasers were installed to enable the initial sample volume to be determined. Previously, the initial sample dimensions were measured with a sliding caliper, which is especially inaccurate for soft samples because the sample deforms as soon as the calliper touches it.

The two lead screws are rotated by two stepping motors mounted below them outside the cell, and the connection plate together with the three lasers moves upwards and downwards along them. The movement speed was chosen to be 1 mm per second. Due to the slow load ramp of radial stress applied at 0.5 to 1.0 kPa/hour for the drained stress path tests, the change of stress during each scan cycle was considered to be negligible.

The lasers were scanning continuously and the data of the radial distance was saved every second for the first two tests. For the following tests, the data logging frequency was increased and 12 readings per second (or per millimetre sample height) were performed.

Additionally, it was decided to do the data logging during upwards movement of the lasers and to move them back down without data logging to avoid any hysteretic effects from slip on the driving screws, due to the change of direction. The vertical zero position of the lasers was set below the bottom of the sample, to exclude end effects due to the initiation of movement by the stepping motors.
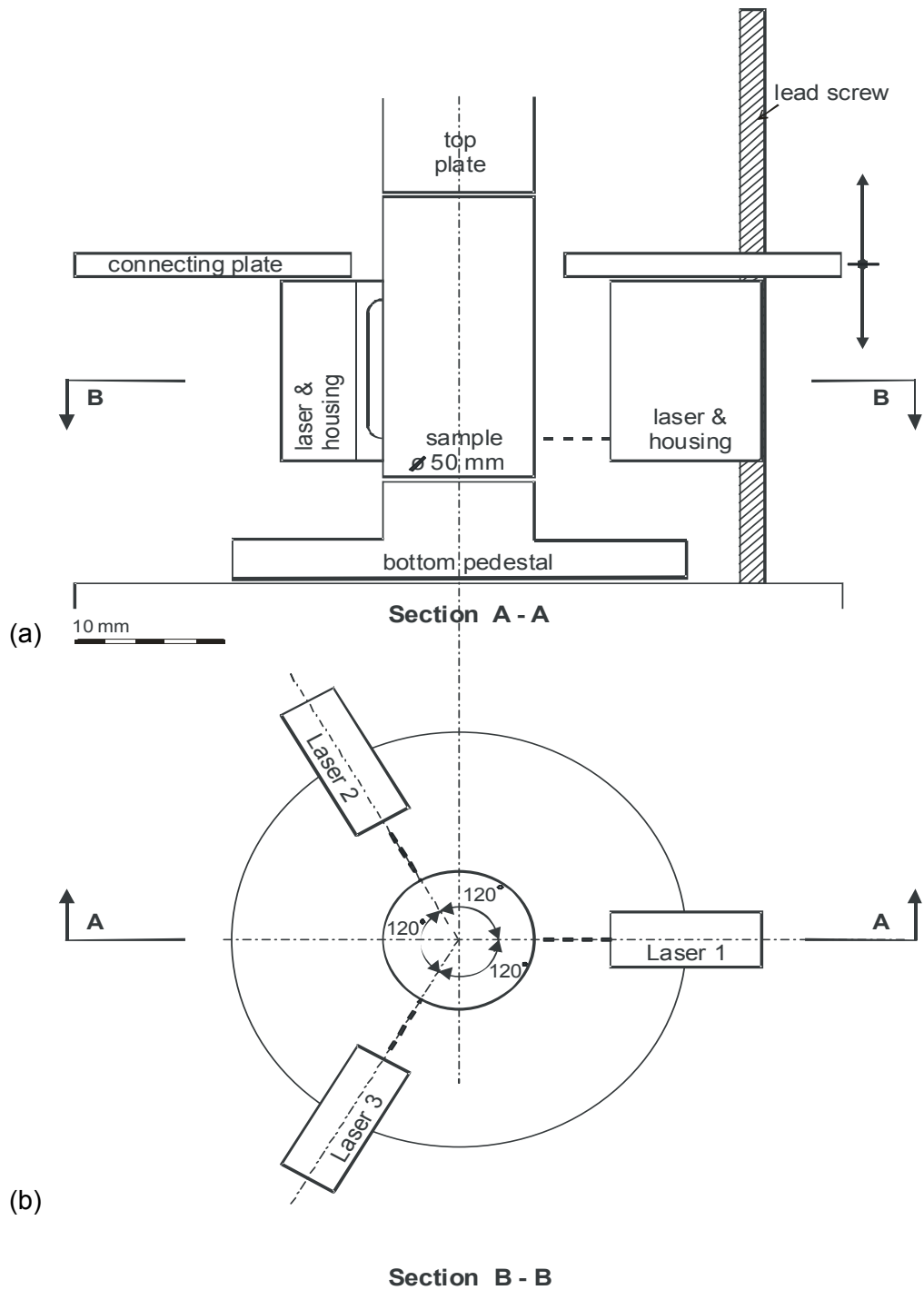
Fig. 4.6:   (a) Front view and (b) top view of the construction of the laser scanning device (Messerklinger et al., 2004).

A – Back pressure unit

B – Cell pressure unit

C – Triaxial cell

4 – Stepping motors

7 – Sample

9 – Laser measurement device

10 – Lead screw

11 – Connecting plate
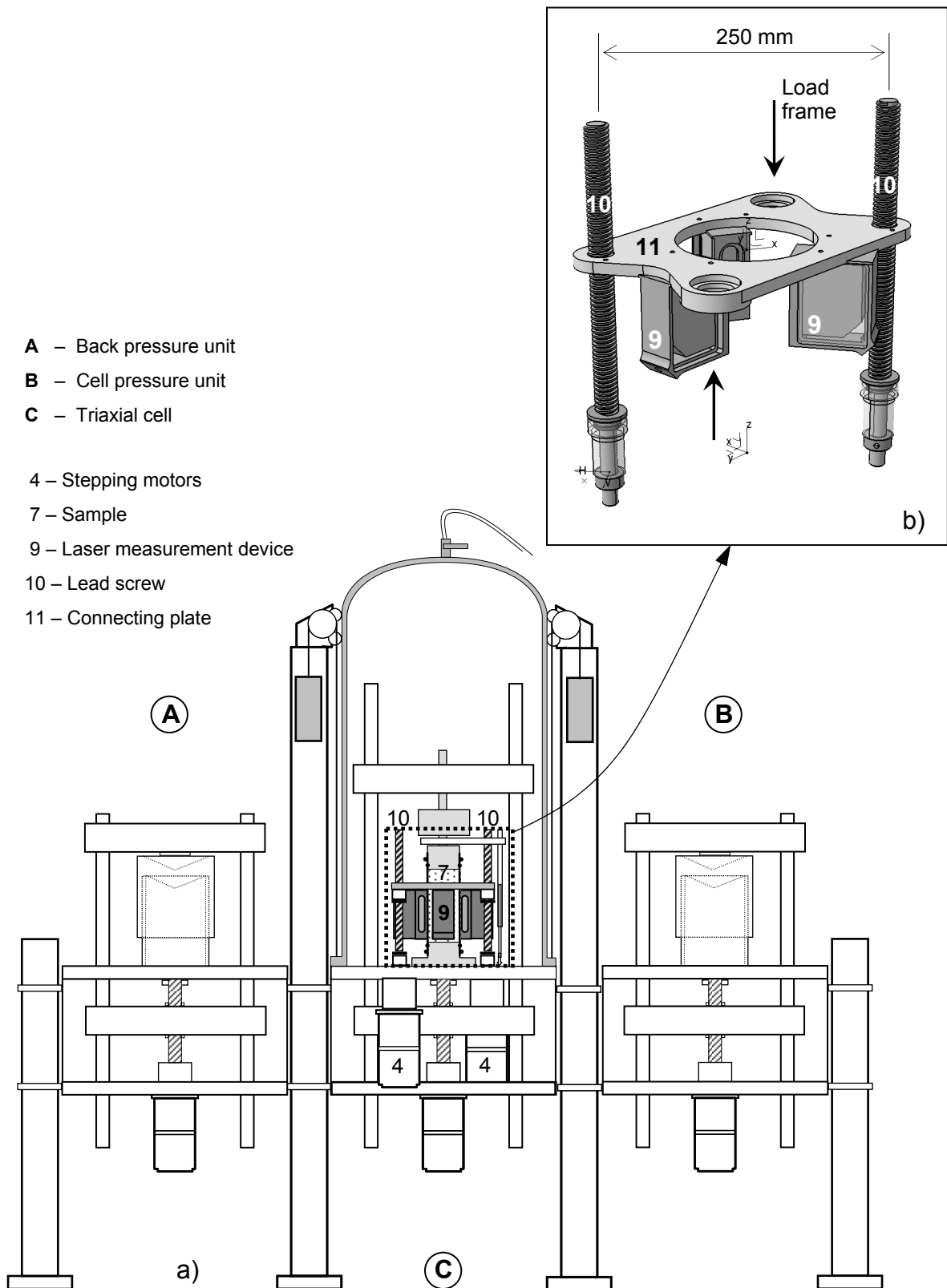
Fig. 4.7:   Standard triaxial testing apparatus (a) with radial displacement measurement system (b) construction of the radial displacement measurement device (Messerklinger et al., 2004).

4.5 Automated regulation control

The devices are computer-controlled by software developed by the Institute for Geotechnical Engineering at ETH Zurich. The program is based on the Laboratory software package „LabView" and operates all three units separately. The desired load path (stress or strain controlled) can be applied by four different possible control options:

- Panel Mode: allows the regulation with a joy stick next to the apparatus to regulate the sample in the cell during set-up.
- Regulating Mode: The pressure can be kept constant. Additionally, within this mode the rate of pressure applied in kPa per unit time can be set to load a sample along a specific load path.
- Move Velocity Mode: applies a constant strain rate.
- Move Position Mode: applies a relative or absolute change in position, which is mainly used during set-up of the test.

As these modes can be set for each unit separately, various stress paths can be performed. The regulation of the pressure is managed via a PID-controller[†]. The regulation parameters are given in Tab. 4.3.

Tab. 4.3:   Regulation constants for the PID-controller.

	Proportional	Integral	Differential	Dead band	Integral limit
Vertical movement	400	0.04	10	600	100,000
Cell pressure	400	0.20	10	600	100,000
Back pressure	200	0.20	10	300	100,000

[†] A Proportional-Integral-Derivative controller or PID controller is a common feedback loop component in industrial control applications. The controller compares a measured value from a process with a reference set-point value. The difference or "error" signal is then processed to calculate a new value for a manipulated process input, which new value then brings the process measured value back to its desired set-point. Unlike simpler control algorithms, the PID controller can adjust process inputs based on the history and rate of change of the error signal, which gives more accurate and stable control. (http://en.wikipedia.org/wiki/PID_controller)

4.6   Calibration and accuracy

Resolution, accuracy and precision are expressions that are widely used in discussions about the quality of a measurement device. Therefore, these expressions will be defined first.

Precision is a measure of repeatability. It gives the degree of agreement between individual measurements in a set of measurement data, all of the same quality. Accuracy is the measure of reliability. It is the difference between the true value of a measured quantity and the most probable value that has been derived from a series of measurements. The resolution is the smallest amount that a sensor can detect and is typically smaller than the accuracy.

Manufacturers often use the term linearity for laser sensors instead of accuracy, which defines the largest deviation of a set of measurements from a best-fit straight line over the measurement range in this case.

4.6.1 Axial strain measurement

The axial displacements are measured with external and local LVDTs. The external LVDTs are mounted on the load frame and have a measurement range of ± 50 mm and ± 25 mm respectively (Tab. 4.1). The local LVDTs are mounted directly on the soil sample and have a measurement range of ± 5 mm (Chapter 4.3).

The external LVDTs were calibrated by the stepping motor of the apparatus. The accuracy of the external LVDTs is ± 0.1 % of the measurement range (manufacturer information), which equals ± 0.1 mm and ± 0.05 mm respectively. The accuracy of each LVDT over the whole measurement range was investigated by calibration to improve this value (Fig. 4.8). A measurement range of 10 mm was found within certain zones for each LVDT in which the accuracy was within ± 0.01 mm. The LVDT was then placed in the triaxial apparatus in such a way that the start position of each test lay in the middle of this more accurate measurement range. Thus it could be ensured that the measurement accuracy for axial strains is 0.01 % within a strain measurement range of 5 %.
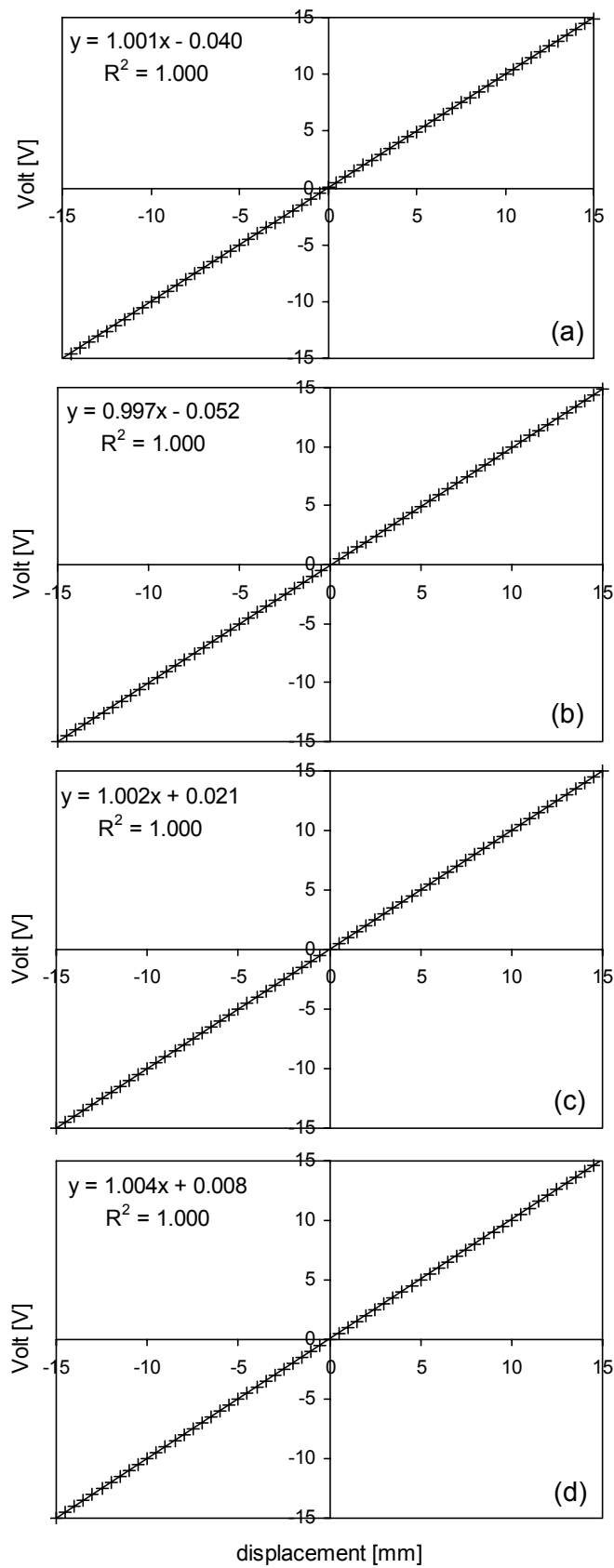
Fig. 4.8: Calibration of the external LVDT in triaxial apparatus (a) 1; (b) 2; (c) 3 and (d) 4 leading to improvement in accuracy.

The manufacturer's calibration report was assessed by measuring the response of the local LVDTs with the use of micrometer screw. The results are plotted in (Fig. 4.9). The accuracy was found to be ± 0.05 % of the measurement range, which equals ± 0.005 mm. This results in an accuracy of 0.014 %.
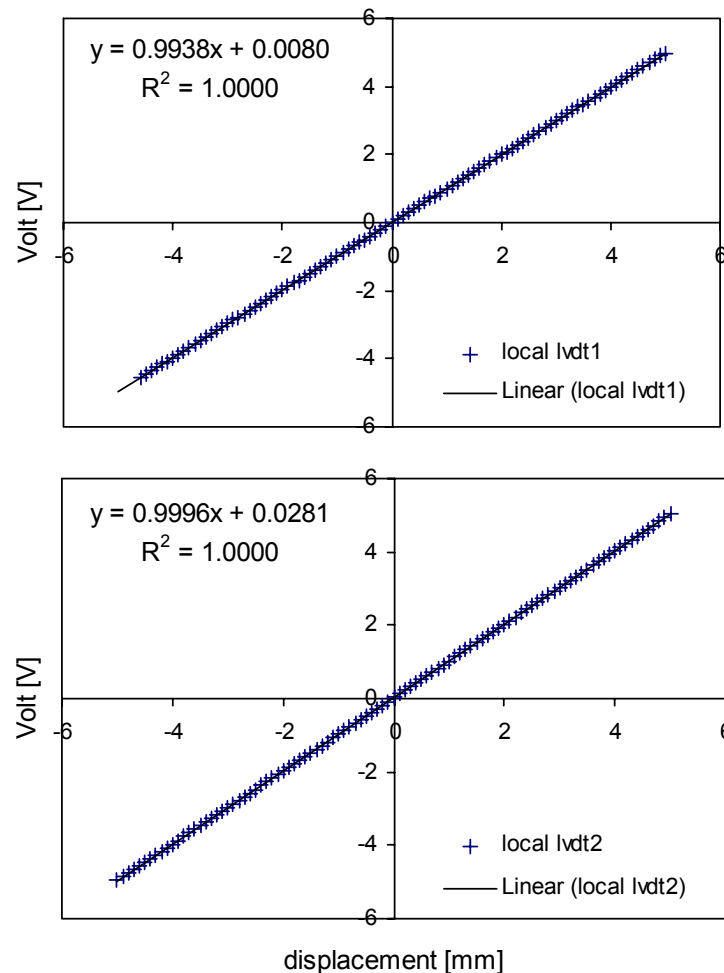
Fig. 4.9:   Calibration of the local LVDTs in triaxial apparatus 1, leading to improvement in accuracy.

The compliancy of the load system in the axial direction was investigated by placing an aluminium cylinder in the test apparatus between the top cap and the bottom plate. The cylinder had a diameter of 50 mm, a height of 100 mm and a Young's modulus of 69 kN/mm^2. This cylinder was loaded in compression up to 1.5 kN, which corresponds to an axial stress of 764 kPa. The resulting axial displacements measured by the external LVDT lay between 0.015 mm and 0.028 mm. The elastic displacement of the aluminium cylinder for this stress is calculated

to be 0.00111 mm. The elastic displacements of the top cap and the bottom plate, which have a total height of 135 mm and are both made of steel with a Young's modulus of 210 kN/mm^2, are 0.00049 mm. Consequently, the net displacements of the system were in a range of 0.013 to 0.026 mm or 0.013 to 0.026 %, which is close to the axial displacement measurement accuracy, therefore the system was assumed to be stiff.

During the calibration, it was seen that the major influence on the displacement measurements were temperature fluctuations, which cause expansion and shrinkage of the material constituting the apparatus and the control system, in particular all metals and the water.

4.6.2 Load cell

The load cell has a measurement range of 5 KN and an accuracy of ± 0.1 % of the measurement range (manufacturer information), which corresponds to a stress variation of ± 2.55 kPa for a sample diameter of 50 mm. The load cell is placed between the load frame and the top cap in the triaxial cell and so the cell pressure also acts on the surface of the load cell (Fig. 4.10).

The top and bottom areas of the load cell are not the same due to the mounting of the load frame on one side and the top cap on the other, a net force acts on the load cell due to cell pressure. A calibration factor was implemented to account for this additional force and was determined by filling the empty triaxial cell with cell liquid. Cell pressure was applied, the force was measured and the factor in N/kPa$_{cell\ pressure}$ was determined and incorporated in the data evaluation so that for any cell pressure applied to an empty cell, the measured force was zero. This calibration step meant that the load cell in these triaxial test apparatuses measured the deviator force.

4.6.3 Pressure transducer

The pressure transducers (SENTEC 8267) have a measurement range of 1 MPa and an accuracy of ± 0.1 % of the measurement range (manufacturer information), which equals a pressure variation of 1 kPa. The manufacturer's calibration report was verified using the calibration apparatus „Druck" DPI 610.
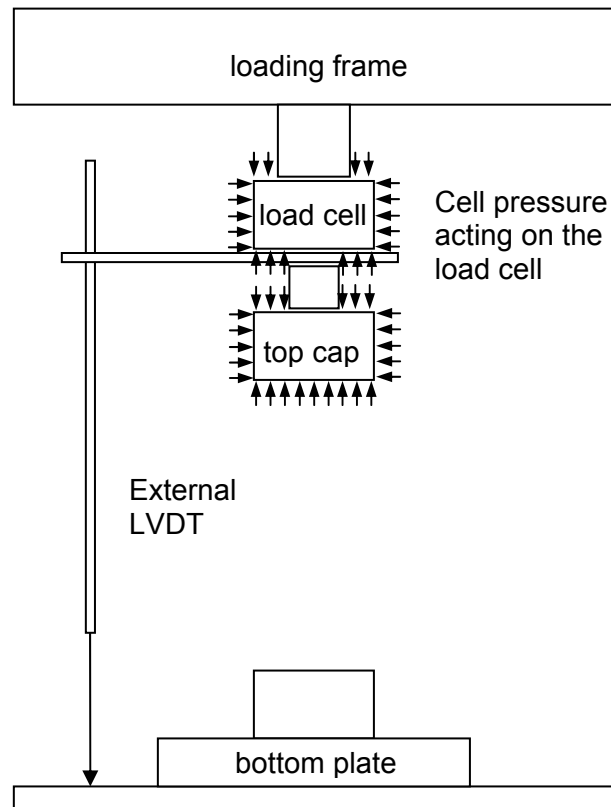
Fig. 4.10:   Pressure acting on the load cell during the calibration process.

4.6.4 Radial strain measurement

The lasers (Micro-Epsilon ILD1400-10) have a resolution of 1 μm. The measurement range is ± 5 mm, the mean measurement distance to the sample is 25 mm and the non-linearity is ± 0.2 % of the measurement range. The calibration of the lasers was performed on an aluminium cylinder with varying diameters, as shown in Fig. 4.11b, in the filled triaxial cell to include any refractions of the laser beam occurring due to the front glass window of the laser box (Fig. 4.5) and the cell liquid. The laser measurement was calibrated from the known change in cylinder radius. The diameter of the cylinder was determined with a micrometer to an accuracy of 10 μm. After calibration, the cylinder surface was scanned and the laser non-linearity was determined. The results are presented in Fig. 4.11a.

Finally, the influences of the laser mounting on the measurement data were neglected. Therefore an aluminium cylinder with a constant diameter of 50 mm (±

10 μm) over the entire height of 120 mm was placed in the triaxial cell and the scan data were used as a zero-reading in the data evaluation.
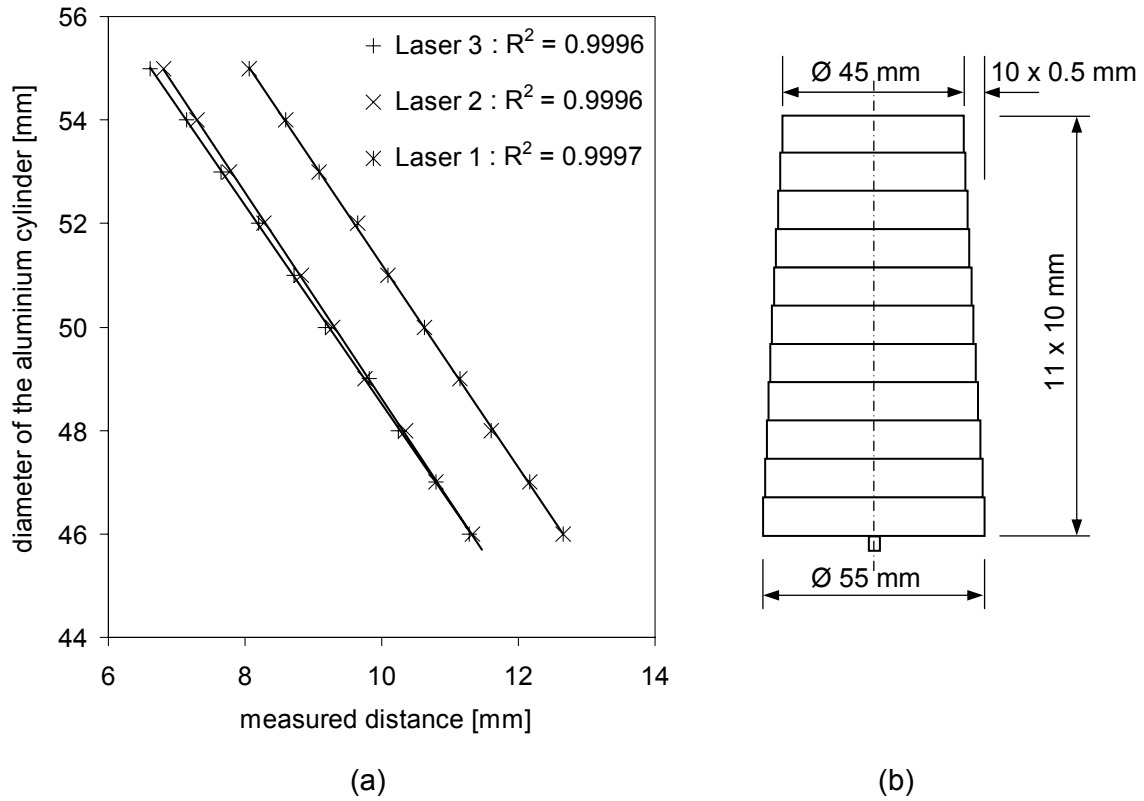
Fig. 4.11: Calibration of the laser scanning device; a) non linearity of the laser sensors; b) stepped aluminum cylinder used for laser calibration.

4.6.5 Cell pressure volume measurement

The cell pressure regulation and the change in cell volume measurement are achieved by the cell pressure piston system (Fig. 4.1). The piston system is powered by a stepping motor with a resolution of 0.156 μm/step for the axial movement and 1.227 mm^3/step for the volume measurement. But the accuracy of the volume measurement is not dictated by the resolution of the stepping motor, nor by the accuracy of the dimensions of the piston system, but by the stiffness of the triaxial cell and the pipes that connect the cell pressure system to the triaxial cell. With increasing pressure levels, these components may undergo elastic deformations.

For the investigations of the elastic apparatus deformations occurring with increasing stress, the triaxial cell and the cell pressure system were filled with water, the pressure in the system was increased stepwise and the corresponding volume change for each step was registered (Fig. 4.12).
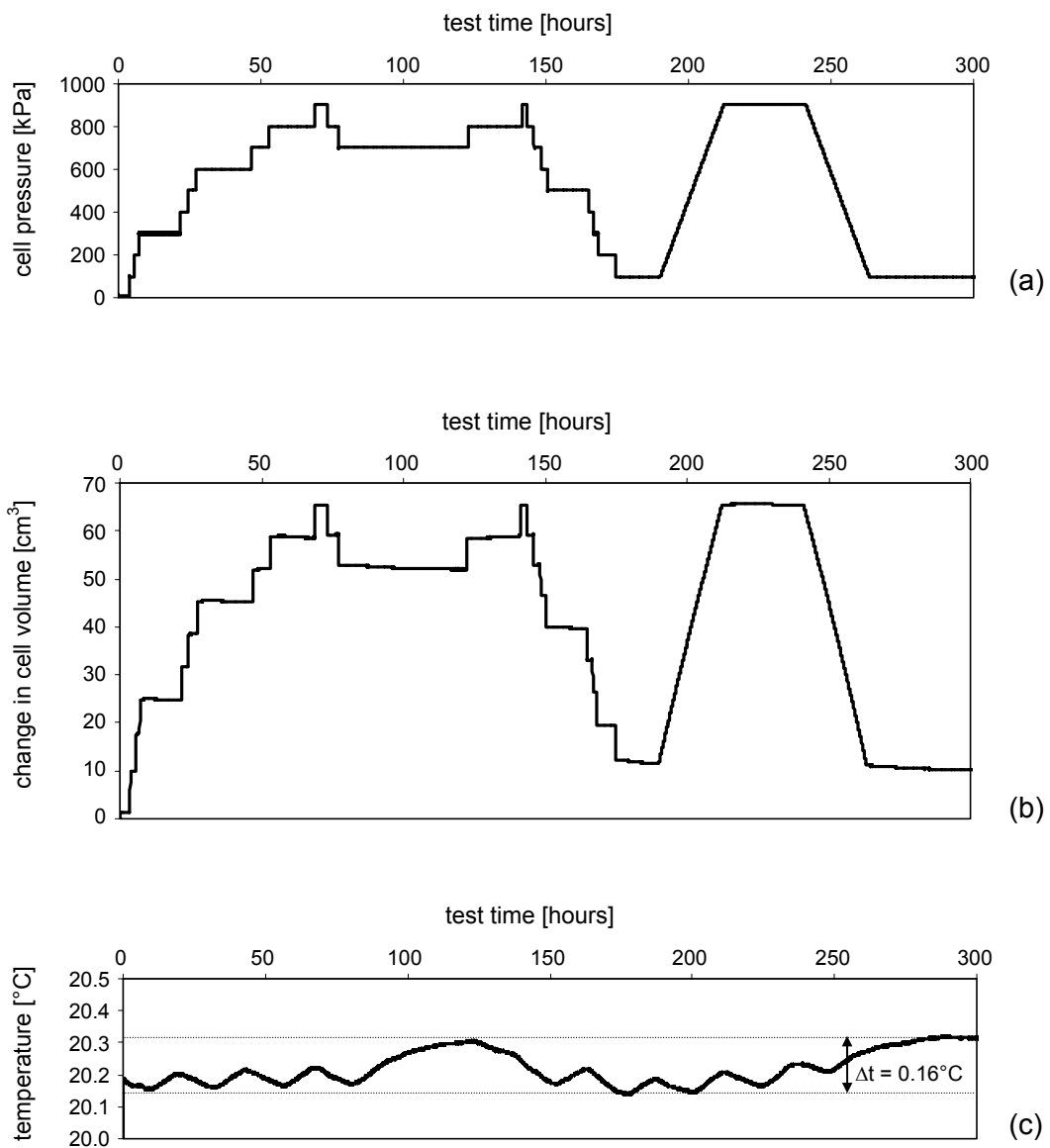
Fig. 4.12: Pressure – volume – temperature correlation of the cell volume measurement in triaxial test apparatus 4: (a) stress levels applied (b) change in cell volume (c) temperature progression.

This investigation was performed with test apparatus 4 first. The stress was increased in steps of 100 kPa up to 900 kPa, subsequently decreased to 700 kPa and again increased to 900 kPa before the stress was reduced to 100 kPa again in steps of 100 kPa. Subsequently, the system was loaded with a stress ramp up to 900 kPa and unloaded. The various stress steps applied to the system are shown in Fig. 4.12a. The change in volume of the system due to stress change is plotted over the test time in Fig. 4.12b.

The pressure was plotted over the average change in volume for this pressure level (Fig. 4.13) for the determination of the volume – pressure calibration factor. The linear calibration curve plotted in Fig. 4.13 gives a calibration factor of 0.0678 cm^3 / kPa with a correlation coefficient R^2 of 0.9982.
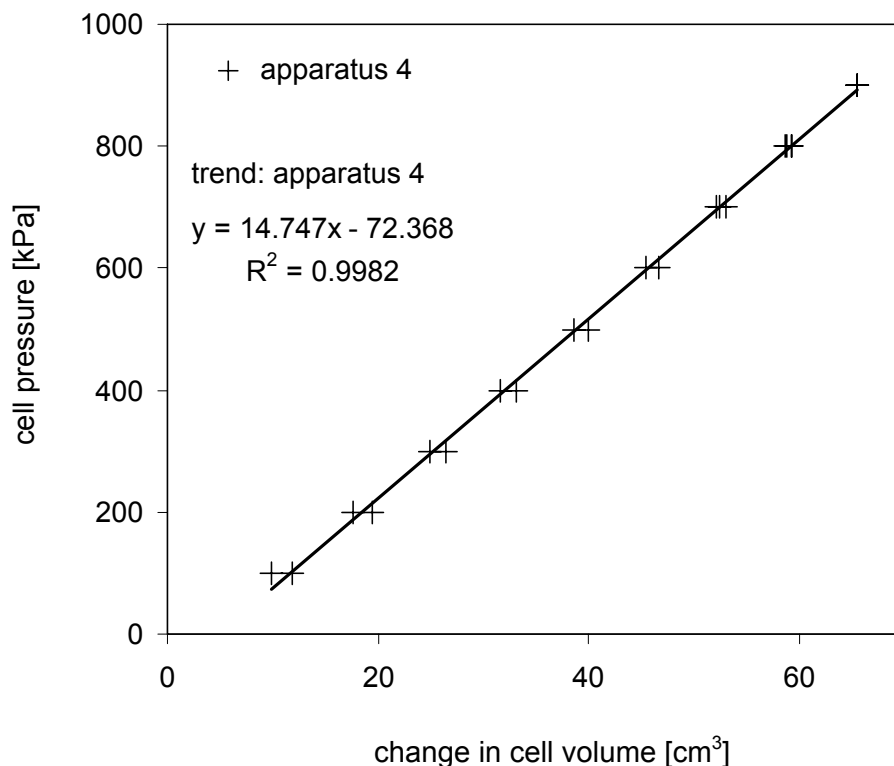
Fig. 4.13:   Calibration curve of the cell pressure volume measurement.

Additionally, the effect of temperature fluctuation on the cell volume measurement was investigated. The temperature is measured with a sensor (PHILIPS PT100) in the triaxial cell. This sensor has an accuracy of <0.1°C in a temperature range of -45 to +100°C. Further details are described in Arenson (2003). The temperature

fluctuation in the cell water observed during the cell volume calibration (Fig. 4.12c) gave a variation in cell water temperature (Δt) of 0.16°C. The triaxial cell, with its height of 70 cm and diameter of 30 cm, has a volume (V) of about 50 litres, not considering the volume of the cell pressure system. Water has a volumetric expansion coefficient (k) of 20·10^{-5} per °C. Consequently, the volume change due to 0.16 °C temperature fluctuation is:

$$\Delta V = Vk\Delta t = 1.656 \, cm^3 \qquad\qquad \text{Eq. 4.1}$$

This equals volumetric strains of 0.84 % for a test specimen of 50 mm in diameter and 100 mm in height. The error is much too high for the required accuracy.

This investigation was performed on test apparatus 4, which is placed in the climate room. Consequently, the temperature fluctuation in the cell water of a triaxial apparatus placed in the cold chamber (Fig. 4.14) was investigated next. The fluctuation measured in two tests in apparatus 2 is in the same range.
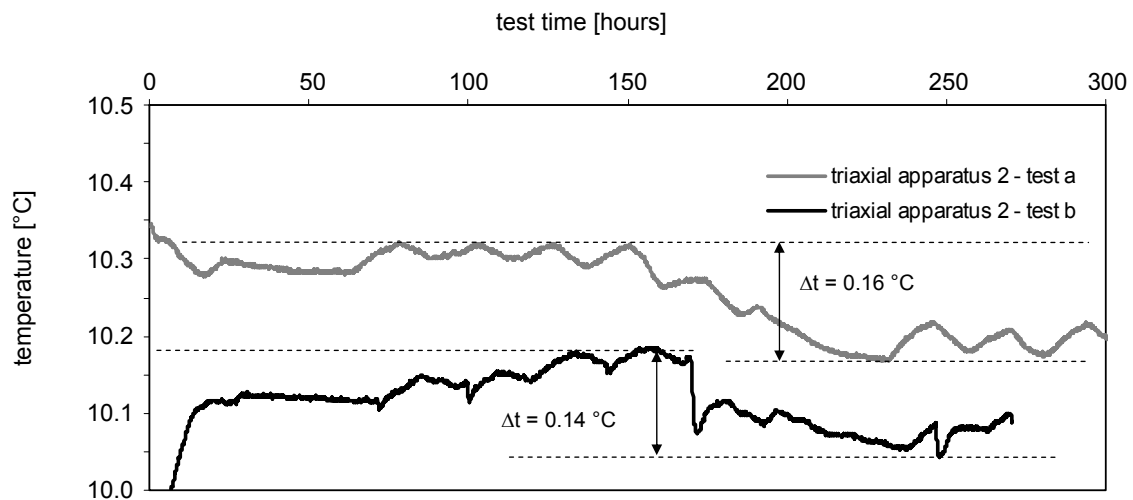
Fig. 4.14: Temperature progression of the cell water over time for triaxial tests in apparatus 2.

Therefore, the cell volume measurement could not be used for the determination of volumetric strain and consequently, its accuracy was not investigated further.

4.6.6 Back pressure volume measurement

The remaining device for the sample volume measurement is the back pressure unit, which regulates the back pressure in the sample and measures the back pressure of liquid flowing into or out of the sample, corresponding to the change in sample volume (Fig. 4.2, A, 14). The back pressure piston system is the same as that of the cell pressure system. It is also powered by a stepping motor with a resolution for the axial movement of $1.56 \cdot 10^{-4}$ mm/step, which corresponds to a resolution of the volume measurement of 1.227 mm^3/step. The volume of water, retained in the back pressure system is much less than that in the cell pressure system, with about 800 cm^3 in the cylinder of the back pressure unit, another 100 cm^3 in the sample and some water in the connection tubes. This results in a volume change due to previously mentioned temperature fluctuations ($\Delta t = 0.16°C$) of:

$$\Delta V = Vk\Delta t = 0.03\ cm^3 \qquad\qquad \text{Eq. 4.2}$$

This corresponds to a possible sample volume measurement resolution of 0.003 %. The back pressure system (the cylinder of the pressure unit and the tubes up to the triaxial cell) was filled with water, pressure was applied and the corresponding change in volume was measured in order to calibrate the back pressure volume measurement. This test was performed with all four apparatuses. All apparatuses were loaded with a constant ramp up to 900 kPa, the pressure level was kept constant and then it was unloaded stepwise (Fig. 4.15a). The corresponding change in volume is shown in Fig. 4.15b.

The change in volume at constant stress level (Fig. 4.15b) is not constant for all tests and has the tendency to decrease. This may result from the pressure regulation. Pressure states higher than the set ones can occur when the pressure is applied fast, which is subsequently regulated to the given value.

The pressure was plotted over the average change in volume for each pressure level in order to determine the volume – pressure calibration factor (Fig. 4.16). The linear calibration curves are plotted for each apparatus separately and the equations give the corresponding calibration factors.
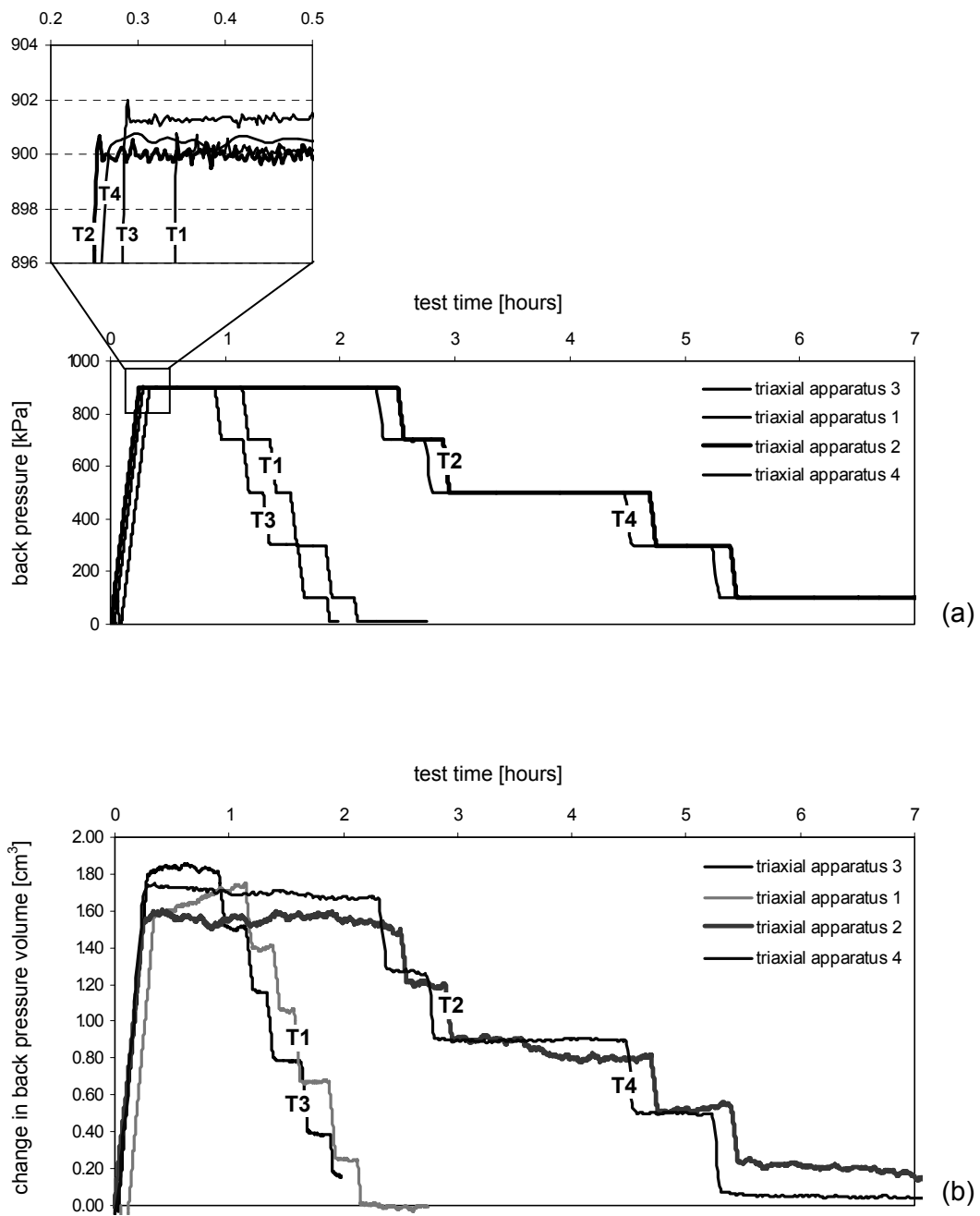
Fig. 4.15: Pressure – volume correlation of the sample volume measurement with the back pressure system.
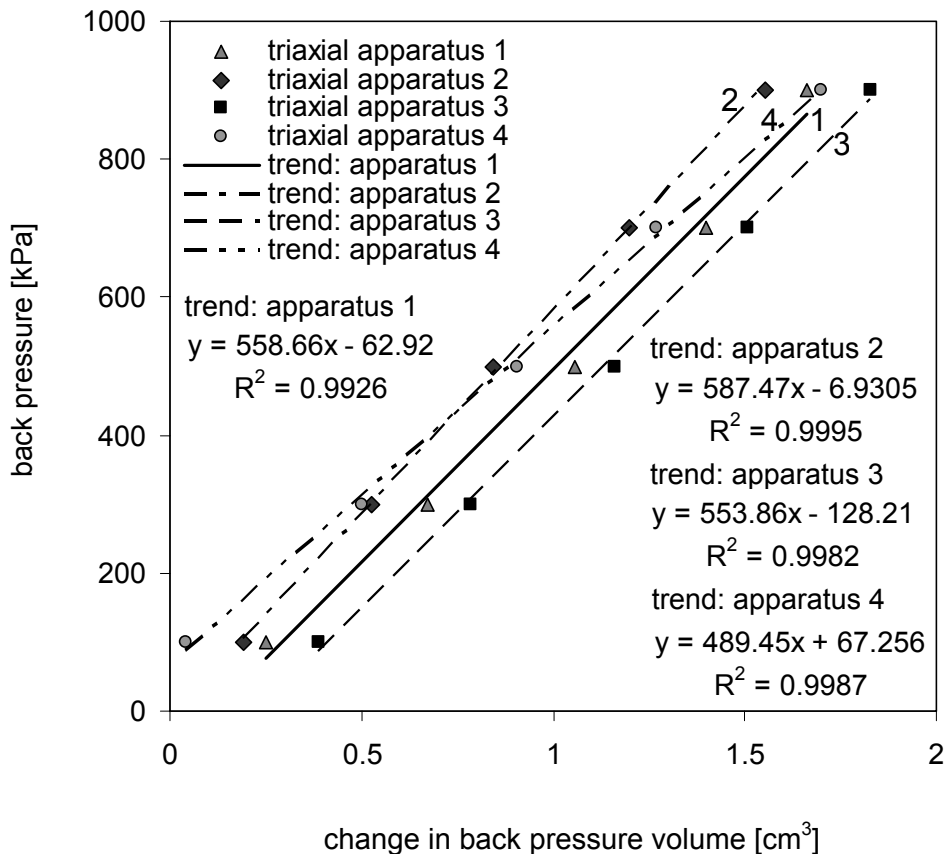
Fig. 4.16: Calibration curves of the back pressure volume.

5 Triaxial test programme

The test performance and data evaluation will be described before the triaxial test series and the test data will be illustrated.

5.1 Sample preparation procedure

The triaxial test samples were prepared from blocks of clay. Reconstituted clay blocks were used for series 1 and 3. The preparation of these materials is described in detail in Chapter 3.3. Natural lacustrine clay blocks, sampled as described in Chapter 3.2.1, were taken for series 2. The clay blocks were either prepared in 400 mm diameter steel oedometers (reconstituted samples) or sampled and stored with 200 mm diameter steel tubes (natural samples). A block was extruded from the tube before test set-up. Tests in all four test apparatuses were set up on the same day to avoid influences on the initial conditions of the sample due to storage effects on the extruded samples. The clay block was cut with a steel wire into smaller rectangular blocks and on after the other was used, while the remaining pieces were covered with cling film wrap. The triaxial sample was trimmed with a steel wire to its corresponding diameter (50 mm for tests in apparatus 1 to 3 and 56.4 mm for tests in apparatus 4). The clay that was cut off during the sample trimming was used for the determination of the water content (w). The water content was determined 3 times for each test and the mean value was used. The test specimen was then cut so that the sample finally had a height (H_0) of twice the diameter (D) and pieces of filter paper placed on the top and the bottom ends. The final sample dimensions were determined with a sliding calliper. The height and the top, middle and bottom diameter of the sample was measured three times each and the mean value was used for the data evaluation. In the

measurement of the diameter, the cylindrical surface of the soft specimens may have been flattened locally where the calliper touched the soil. This may have lead to a certain degree of inaccuracy in these measurements, but this cannot be determined exactly.

Finally the sample was weighed (m_f), then it was placed on a pedestal to pull over the rubber membrane. No filter paper was smoothed onto the surface around the sample because Head (1986) pointed out that additional radial drainage affects the distribution of the excess pore pressure in the specimen and hence influences its deformation response. The relationship between the horizontal and vertical strains would be different compared to tests where drainage is only progressing vertically.

A former was used to pull the rubber membrane over the sample with minimal disturbance, to situate the sample in the triaxial apparatus, and to fix the O-rings over the rubber membrane, the pedestal and the top platens in the triaxial apparatus. The former consists of two half shells of inner diameter 2 mm larger than the corresponding sample diameter, and a plug. Three O-rings are placed temporarily over the two shells to keep them together on one side of the former, and a rubber membrane is placed inside the former with both ends pulled over the ends. The plug is installed on the outside face of the former through which vacuum can be applied between the rubber membrane and the former to expand the rubber membrane so that there is sufficient space between membrane and soil for it to be slipped over the specimen.

When the rubber membrane is slipped over the specimen, the former, together with the specimen, is placed on the pedestal of the bottom plate in the triaxial cell on which a saturated filter plate has already been placed. The rubber membrane on the former is now pulled over the pedestal of the bottom plate followed by the three O-rings to seal the rubber membrane at the base end. The O-rings for sealing the top end are placed on the top cap, and are pulled over the rubber membrane after saturation.

The former is then removed. The set-up is saturated with pore water applied from the bottom end. The second saturated filter plate is placed on top of the sample,

the top cap is moved down onto the sample and the rubber membrane is pulled over the pedestal of the top cap. The set-up is again saturated, with the pore water supply on the top side, before the O-rings are pulled over the rubber membrane.

The local LVDTs are glued to the sample on the rubber membrane for test apparatus 1, as described in Chapter 4.1.1. Then the cell is closed and slowly filled with cell water. The two valves that connect the test sample with the back pressure unit are opened and the cell pressure is increased stepwise. The saturation of the test specimen and the back pressure unit was determined with the measurement of the back pressure. Therefore, cell pressure was increased stepwise and the corresponding back pressure increase was determined. This procedure was continued until a cell pressure increase resulted in the same size of back pressure increase, which indicates that the sample and the back pressure unit are fully saturated. A fully saturated system is necessary because the change in sample volume during test performance is measured by the change in water volume in the back pressure system. This volume measurement at changing pressure levels is possible only for a fully saturated sample because water is incompressible compared with air, which is compressible and even dissolves in water under certain pressure-temperature conditions.

For example 0.0223 cm^3 air per gram of water is dissolved in water with a temperature of 10°C at atmospheric pressure (Lange's Handbook of Chemistry, 1973; assuming that air consists of 78 % nitrogen and 21 % oxygen). The amount of air that can be dissolved in the water at a temperature of 10 °C increases with increasing pressure to 0.171 cm^3/g at 1 MPa, 0.962 cm^3/g at 5 MPa and 1.89 cm^3/g at 10 MPa pressure (Handbook of Chemistry and Physics, 1989).

Back pressure is applied in the triaxial tests to dissolve any air that is remaining in the sample and in the back pressure unit. The disadvantage of high back pressure is that it is possible that the fabric or structure can be disturbed for natural samples (Trausch Giudici, 2003). Heil (2003) recommended a back pressure of 200 kPa, with which he had good experience in his extensive triaxial testing programme on soft Swiss lacustrine clays. According to the correlations given above, 0.03 cm^3/gram water can be dissolved for a pressure of 200 kPa. The back pressure unit together with the connecting pipes and the water in the sample has a net

volume of about 700 cm^3, which implies theoretically that 21 cm^3 of air can be dissolved. A back pressure of 200 kPa was applied to the sample for one night and was found to be high enough to achieve B values (Skempton, 1954) of 0.98 in the worst case for some natural samples and 1 for the remoulded specimens, where the B value is defined as the ratio of the pore pressure increase due to the cell pressure increase and gives information about the saturation status. A value of B = 1 indicates full saturation.

Then the test was started and the load path applied. The start stress state was at the isotropic mean effective stress of p' = 5 kPa.

5.2 Interpretation procedure

The following data are measured in the triaxial apparatus with the accuracy discussed above: the axial displacement (Δh), the change in sample volume (ΔV), the cell pressure (σ_r), the back pressure (PWP) and the axial deviator force (P). The pore water pressure is measured at the top and bottom of the sample and the mean value of these two measurements is adopted for subsequent analysis. Positive stresses are assigned in compression and positive strains are assigned in compaction.

5.2.1 Stress analysis

The effective radial stress (σ_r') is calculated as the difference between the cell pressure (σ_r) and the pore water pressure (PWP). The cross-sectional area (A) of the sample is needed for determination of the total axial stress (σ_a) from the measured deviator force (P). A common approach (Bishop & Henkel, 1957), which is used here too, is to assume that the sample keeps the original cylindrical shape during deformation. According to this assumption, the cross-sectional area of the sample is described by the following equation:

$$A = \frac{V_0 - \Delta V}{H_0 - \Delta H}$$

Eq. 5.1

where: A   is the current cross-sectional area of the sample

V_0 is the initial sample volume

ΔV is the change of sample volume

H_0 is the initial sample height and

ΔH is the change of sample height.

Now the deviator stress (q) is determinable, as well as the axial effective stress (σ_a') and the mean effective stress p':

$$q = \frac{P}{A} = \sigma_a' - \sigma_r' \quad \rightarrow \quad \sigma_a' = q + \sigma_r' \quad \& \quad p' = \frac{\sigma_a' + 2\sigma_r'}{3}$$

5.2.2 Strain analysis

The measured displacements are evaluated in terms of natural strains, which means that the displacement of the sample is related to the current sample dimension (e.g. H_{act} or V_{act}) and not to the initial value (e.g. H_0 or V_0), as assumed for the calculation of engineering strains. This means that the axial strains (ε_a) are defined as the ratio of measured axial displacements ΔH to the current sample height (H_{act}) and the volumetric strains (ε_v) are defined as the measured change in sample volume (ΔV) to the current sample volume (V_{act}).

Evaluation of the axial strains from the local axial displacement measurement is done by using the current distance between the fixities of the local strain measurement devices, instead of the current sample height. The radial strains (ε_r) and the shear strains (ε_s) are determined from the axial and the volumetric strains:

$$\varepsilon_r = \frac{\varepsilon_v - \varepsilon_a}{2} \qquad\qquad\qquad \text{Eq. 5.2}$$

$$\varepsilon_s = \frac{2}{3}\left(\varepsilon_a - \varepsilon_r\right) \qquad\qquad\qquad \text{Eq. 5.3}$$

The initial void ratio (e_0) and subsequently the void ratio during the test (e) are defined as the ratio of the pore volume to the volume of solids in the sample and are determined from the following equation:

$$e = \frac{V_{act} - V_s}{V_s}$$ Eq. 5.4

where V_s is the volume of the solids, which is described for the fully saturated samples as:

$$V_s = \frac{m_f}{\rho_s (1 + w_0)}$$ Eq. 5.5

where: m_f is the mass of the saturated sample

w_0 is the initial water content and

ρ_s is the density of the solids.

Laser scan data evaluation

The radial distance ($m_{1,2,3}$) between the three lasers and the sample, covered by a 0.3 mm thick rubber membrane, is measured over the sample height. The zero-readings on an aluminium cylinder with a diameter of 50 mm are known from the laser calibration. Therefore, the current sample radius ($R_{L1, L2, L3}$) at each laser scan profile can be calculated, assuming the sample is centred on the bottom plate:

$$R_{L1, L2, L3} = 25 + zero\ reading - current\ reading(m_{1,2,3}) - 0.3 \quad [mm] \quad \text{Eq. 5.6}$$

The development of natural strains can be determined along the three vertical profiles, 120° apart, as the change of the sample dimension in a radial direction divided by the current sample radius:

$$\varepsilon_{r\ L1, L2, L3} = \frac{R_{0\ L1, L2, L3} - R_{act\ L1, L2, L3}}{R_{act\ L1, L2, L3}}$$ Eq. 5.7

where R_0 is the initial and R_{act} the current sample radius at the corresponding laser scan profile. Positive radial strain corresponds to radial contraction.

To determine the sample volume from the three laser scans, the cross-sectional area of the sample has to be determined from the three sets of data. Several possibilities arise. An average radius can be used or the cross-sectional area can

be divided into three thirds. Grün (2004) suggested that the most straightforward solution was to introduce a coordinate plane in each scan cross-section and to place a circle through the three points. A circular cross-section was taken to be the most appropriate approach, assuming cross-anisotropic material in a pressure cell.

A coordinate system is defined on each horizontal plane and the data were logged initially every 1 mm and susequently 12 times per millimetre of sample height, so that approximately 100 or 1200 planes were introduced over the whole sample. The origin of the coordinate system on these planes was defined to be in the bottom right corner with a distance of 100 mm to the centre of the sample $[x_0, y_0]$ (Fig. 5.1). The coordinates of the sample surface $[x_1, y_1]$, $[x_2, y_2]$ and $[x_3, y_3]$ were determined on each of these coordinate planes as follows:

$$x_1 = 100 \quad [mm]$$ Eq. 5.8

$$y_1 = 100 - R_{L1} \quad [mm]$$ Eq. 5.9

$$x_2 = 100 + R_{L2} \cdot \cos(30°) \quad [mm]$$ Eq. 5.10

$$y_2 = 100 + R_{L2} \cdot \sin(30°) \quad [mm]$$ Eq. 5.11

$$x_3 = 100 - R_{L3} \cdot \cos(30°) \quad [mm]$$ Eq. 5.12

$$y_3 = 100 + R_{L3} \cdot \sin(30°) \quad [mm]$$ Eq. 5.13

where R_{L1}, R_{L2} and R_{L3} are the current sample radii, defined by Eq. 5.6.

Now the coordinate pairs of the three points are known, and a circle with a radius R is drawn through these three points, which is defined by the following equations:

$$R^2 = (x_1 - x_0)^2 + (y_1 - y_0)^2$$
$$R^2 = (x_2 - x_0)^2 + (y_2 - y_0)^2$$
$$R^2 = (x_3 - x_0)^2 + (y_3 - y_0)^2$$
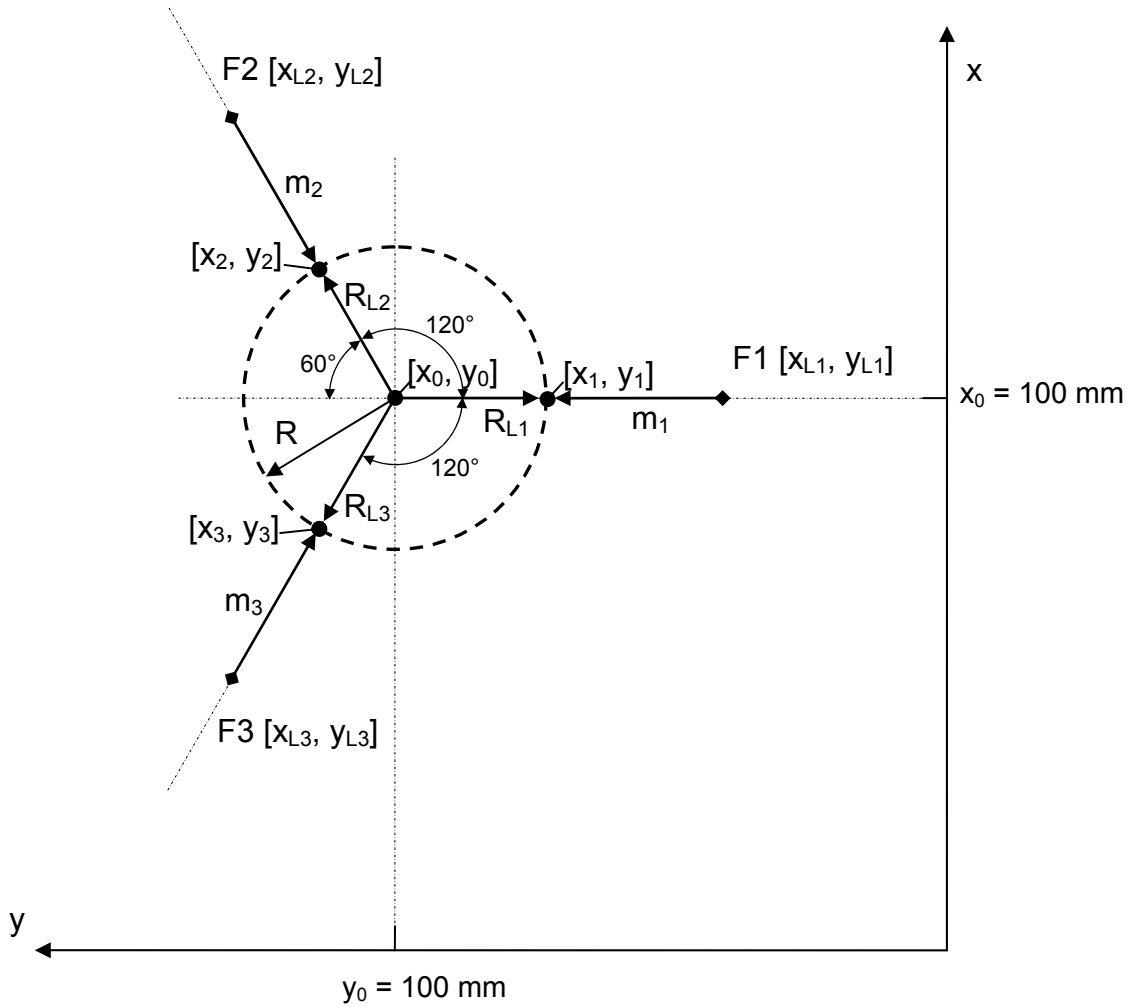
Eq. 5.14

Fig. 5.1: Top view of the horizontal coordinate plane, which was constructed for each measurement cross-section.

The coordinates of the circle origin $[x_0, y_0]$ are calculated from these three equations (Eq. 5.14) as:

$$x_0 = \frac{(x_1^2 + y_1^2)(y_3 - y_2) + (x_2^2 + y_2^2)(y_1 - y_3) + (x_3^2 + y_3^2)(y_2 - y_1)}{2(x_1(y_3 - y_2) + x_2(y_1 - y_3) + x_3(y_2 - y_1))} \qquad \text{Eq. 5.15}$$

$$y_0 = \frac{(x_1^2 + y_1^2)(x_3 - x_2) + (x_2^2 + y_2^2)(x_1 - x_3) + (x_3^2 + y_3^2)(x_2 - x_1)}{2(y_1(x_3 - x_2) + y_2(x_1 - x_3) + y_3(x_2 - x_1))} \qquad \text{Eq. 5.16}$$

The equivalent radius R can then be determined from one of the Eqs. 5.14.

The radial strains can be calculated, in each cross-section, as the change of the sample dimension in a radial direction divided by the current sample radius at that profile:

$$\varepsilon_r = \frac{R_0 - R_{act}}{R_{act}}$$

Eq. 5.17

Where R_0 is the initial and R_{act} is the current sample radius.

The cross-sectional area at every laser scan cross-section was calculated from the radius R and the deviator stress distribution over the sample height was determined from the axial force, which was assumed to be equal across all horizontal planes.

The volume of the sample slice was calculated from the radius of the circle. The net sample volume was determined by summing the volume of all slices over the sample height (considering the top slice height corresponding to the actual sample height). This method was implemented in the test control programme "Labview".

5.2.3 Bender element data analysis

The bender elements that were fitted to triaxial apparatus 4 by Trausch Giudici (2004) were used. A piezoceramic plate is installed in the top cap as well as in the bottom plate of the triaxial sample pedestal. The plate protrudes by 2 mm above the surface of both the top cap and the bottom plate. A detailed description of the development of the bender element method, and the implementation of the bender elements in the triaxial apparatus, is presented in Trausch Giudici (2004).

A sine wave impulse with a chosen frequency, as recommended by Viggiani & Atkinson (1995), is sent from the bottom piezoceramic plate and is received by the piezoceramic plate installed in the top cap. The wave travel time (t) is measured and the shear modulus can be determined from the known travel distance (l) as:

$$G = \rho v_s^2 = \rho \left(\frac{l}{t}\right)^2$$

Eq. 5.18

where ρ is the density of the sample and v_s is the shear wave velocity through the sample, which is determined from the travel distance and the travel time.

The optimum frequency depends on the current stress state and on the sample stiffness (Mohsin & Airey, 2003). Therefore, each measurement was performed at three frequencies of 5, 10 and 20 kHz. The travel distance (l) was determined from the current sample height (H_{act}) as:

$$l = H_{act} - 4 \quad [mm]$$
<div align="right">Eq. 5.19</div>

The reduction of 4 mm arises from the net length of the two bender elements that protrude into the sample. The determination of the travel time followed the recommendations of Jovicic et al. (1996). The time between the start of the first strong amplitude of the transmitted wave to the first strong amplitude of the received wave (Fig. 5.2) was used.
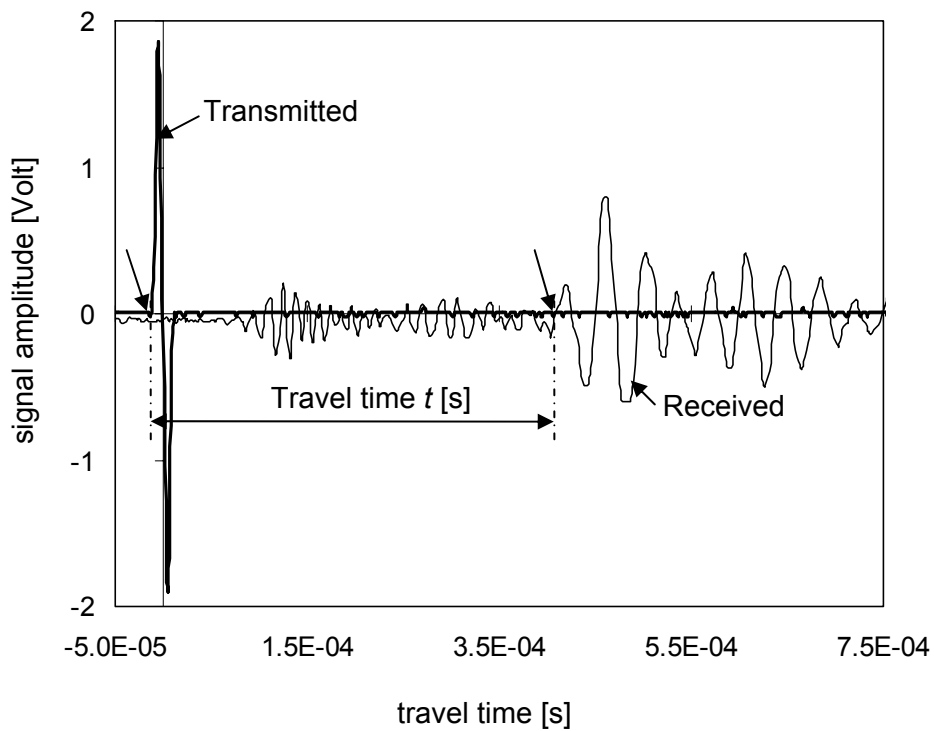
Fig. 5.2   Evaluation of bender element measurement data.

5.3 Evaluation of sample quality

Block samples were used for the investigations of natural lacustrine clay. These blocks of clay were sampled as described and discussed in Chapter 3.2. Comparative studies were performed to compare the quality of these block samples with those from conventional tube samples. Unconfined compression tests were carried out initially and the data are presented in Chapter 3.3. The results indicated that the peak deviator stress measured in the block samples was more than 20 % higher than the equivalent failure values derived in the tube samples. This confirmed the conclusions from the literature study, as discussed in Chapter 2.1.4, that a much higher sample quality can be obtained by sampling clay in blocks.

Finally, triaxial tests were performed to confirm the results of the unconfined compression tests under controlled test conditions. All samples were anisotropically reconsolidated and sheared under undrained conditions in compression, as shown in Fig. 5.3.
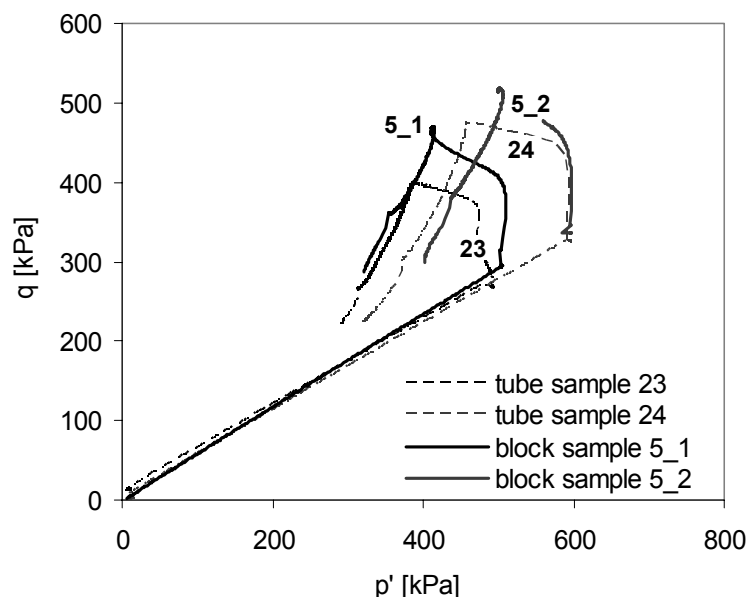
Fig. 5.3   Results of undrained triaxial compression tests on various natural Birmensdorf clay samples: stress paths in the anisotropically consolidated triaxial compression tests.

Tests B5_1 to B5_2 were performed on block samples and tests 23 & 24 were performed on tube samples of Birmensdorf clay. The samples B5_1 and 23 were consolidated anisotropically along the same path to approximately the same stress state, and subsequently sheared undrained under strain control in compression at the same cell pressure and strain rate. This was also done with samples B5_2 and 24, but at a higher stress level. This allowed comparative data to be obtained for the two datasets.

Comparison of the stress paths in the p'-q diagram (Fig. 5.3) shows that both block samples have a steeper stress path up to the peak value of the deviator stress. But the stress path is close to horizontal near to failure for the tube samples, which results in lower undrained shear strength.

Evaluation of the initial void ratio of the four test specimens (Fig. 5.4) shows that the two specimens cut from block samples, taken with a 200 mm diameter tube, have smaller values than the two specimens from the tube samples taken with a 65 mm diameter tube. The magnitude of change in initial void ratio is in a range of 5 to 10%. This clearly indicates that the soil undergoes more loosening during the sampling process when tubes of smaller diameter are used.
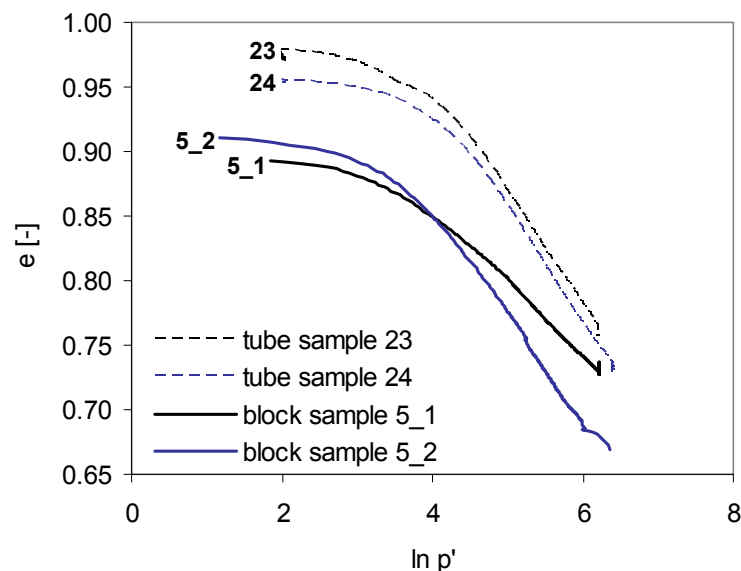
Fig. 5.4:   Results of triaxial compression tests on various natural Birmensdorf clay samples: void ratio reduction curve.

The plot of shear stress against shear strain (Fig. 5.5) of the two pairs of tube and block samples, B5_1 & 23 and B5_2 & 24, shows that higher peak and residual deviator stresses are mobilised for the block samples. The magnitude of this difference is around 20%. These results are comparable to those given by the unconfined compression tests discussed in Chapter 3. They confirm that the quality of 200 mm diameter tube samples is apparently higher, with respect to shear resistance and density, than the quality of 65 mm diameter tube samples.
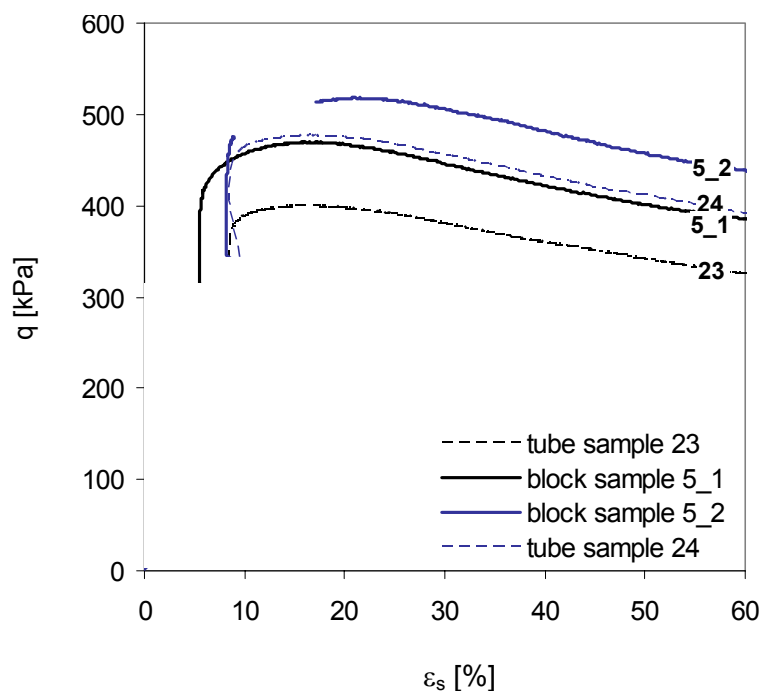
Fig. 5.5:   Results of triaxial compression tests on various natural Birmensdorf clay samples: deviator stress versus shear strain.

An additional advantage of performing the following investigations on block samples is that 4 triaxial samples can be cut out of one block, which avoids variation in test results due to inhomogeneities and layering over depth.

5.4 Triaxial test series

Triaxial stress path tests with various stress increment ratios can be carried out to investigate the stress-strain characteristics in the stress space. To perform a stress path test at constant $\eta = \delta q / \delta p'$, the conditions have to be drained without excess pore pressure occurring anywhere in the sample. For low permeability samples such as clays, achieving these drained conditions is not possible in a practicable time span. Therefore, a compromise in the loading rate has to be found to perform a test within a reasonable time period and not generate high excess pore pressures. The development of excess pore pressures at different loading rates was investigated in test series 1. The corresponding test data are shown in the following sections and the data analysis is presented in Chapter 6.

In test series 2, drained stress path tests were performed at the pre-determined loading rate. The aim was to investigate the stress-strain characteristics of natural Swiss lacustrine clays for very small to larger strains. Therefore the samples were consolidated on an anisotropic path with $\eta = 0.75$ and then drained swelling was permitted along the same anisotropic path to an overconsolidation ratio of two. Finally, the samples were reloaded along the probing stress path, with different stress increment ratios for each test. The stress path dependent stiffness, the stress history surface, the stiffness degradation in the elastic region and the elasto-plastic surface were investigated.

Large plastic deformations occur when the sample is loaded close to the failure stress state. The sample diameter reduces in extension tests in one region of the sample and necking occurs before failure, leading to an increase in the axial stress in the necking zone. This stress increase is not measurable with the conventional evaluation method, in which it is assumed that the sample retains its cylindrical shape during the entire test. The actual stress distribution over the sample height at stress states close to failure were investigated with the laser scan device in test series 3.

Each triaxial test performed in one of the various test series got an alpha-numeric code to be able to distinguish between them later in the data analysis. This code was composed of the test series (e.g.: S2 for test series 2) and the triaxial

apparatus the test was performed with (e.g.: T1 for triaxial apparatus number 1). When a second test within a series was performed with the same apparatus, a letter was added to the series name (e.g. S6a_T3 for the second test with apparatus 3 in series 6).

5.4.1 Series 1

The excess pore pressure development in lacustrine clay samples was investigated in the first triaxial test series for various loading rates. When stress is applied continuously along a stress path at a constant loading rate, excess pore water pressure builds up while the consolidation process is going on in parallel.

Triaxial stress path tests with the following test set-up were performed to investigate the excess pore pressure development during these parallel processes. Triaxial samples with half the height of normal samples of reconstituted Birmensdorf clay (46707) were used in this test series. The sample preparation is described in Chapter 3.3 and the classification results are given in Chapter 3.4. Filter paper was put on the top and bottom ends of the sample to distribute the pore pressure equally over the entire cross-sectional area. No filter paper strips were put on the curved surface of the sample, to avoid any connection between the top and the bottom pore water pressure. The sample was placed in the triaxial apparatus like a conventional triaxial test sample. The sample was drained from the bottom during test performance and the pore water pressure was measured at top of the sample. This pore pressure is assumed to equal the excess pore pressure that will develop in the middle of a drained triaxial test sample during loading.

The samples were isotropically loaded with different constant stress rates with consolidation breaks in between. The tests were performed at different back pressure levels. Additionally, tests with non-isotropic stress paths were performed, in which the loading rate can be described either by the applied increment of p' or by the increment of q. This can result in significantly different loading rates for different stress increment ratios, when the stress increment ratio $\Delta\eta$ is not equal to 1 or -1. For example, for stress paths with a stress increment ratio of $\Delta\eta = 3$, the load increment ratio of a stress path, which is described by $\Delta p' = 1\,kPa$ would be

three times faster than the load increment ratio described by $\Delta q = 1\,kPa$. Stress increment ratios of $\Delta\eta$ = 1.43 and 1.1 were chosen to investigate this effect.

Six tests were performed in the triaxial apparatuses 2, 3 & 4. The sample data and tests results for these six tests (S1T2, S1aT2, S1T3, S1aT3, S1bT3 & S1T4) are given in the Appendix. Unfortunately, no displacement measurement data are specified for the two tests carried out in apparatus 2, because in this apparatus the displacement measurement devices did not operate correctly. This did not affect the pressure measurement, therefore the data were still used for the analysis.

The method of test evaluation is presented in Fig. 5.6. The maximum value of excess pore water pressure and the asymptotic excess pore water pressure level during the pauses for consolidation is determined for each loading rate. For test S1T3, in which no consolidation break was permitted, the pore water pressure measurement on the drained bottom end of the sample was used as a reference value.

A constant excess pore water pressure plateau developed for the slower loading rates, while for faster loading rates (e.g. 26 kPa/day in Fig. 5.6), the pore pressure dropped after reaching a peak value. This effect occurred in test S1aT3 for a loading rate of 103.7 kPa/day, in test S1bT3 for a loading rate of 24 kPa/day and in test S1T4 for 47.5 kPa/day. A constant pore pressure plateau after a small pressure drop was only visible in test S1aT2 for the loading rate of 12 kPa/day. In test S1bT3, loaded at 6.12 kPa/day and in test S1T4, loaded at 3.96 kPa/day, the stress path was only continued for a short time period so that the development of a drop in the pore water pressure did not occur. For data analysis for fast loading rates, values at peak and the last one before consolidation were determined. Finally, the excess pore pressure Δu was calculated as the difference between the reference pore pressure and the pore pressure that develops during constant loading rate. The values determined for the different tests are given in Fig. 5.6 and in the Appendix, and analysis of the data is discussed in Chapter 6.2: Analysis of the drained loading rate.
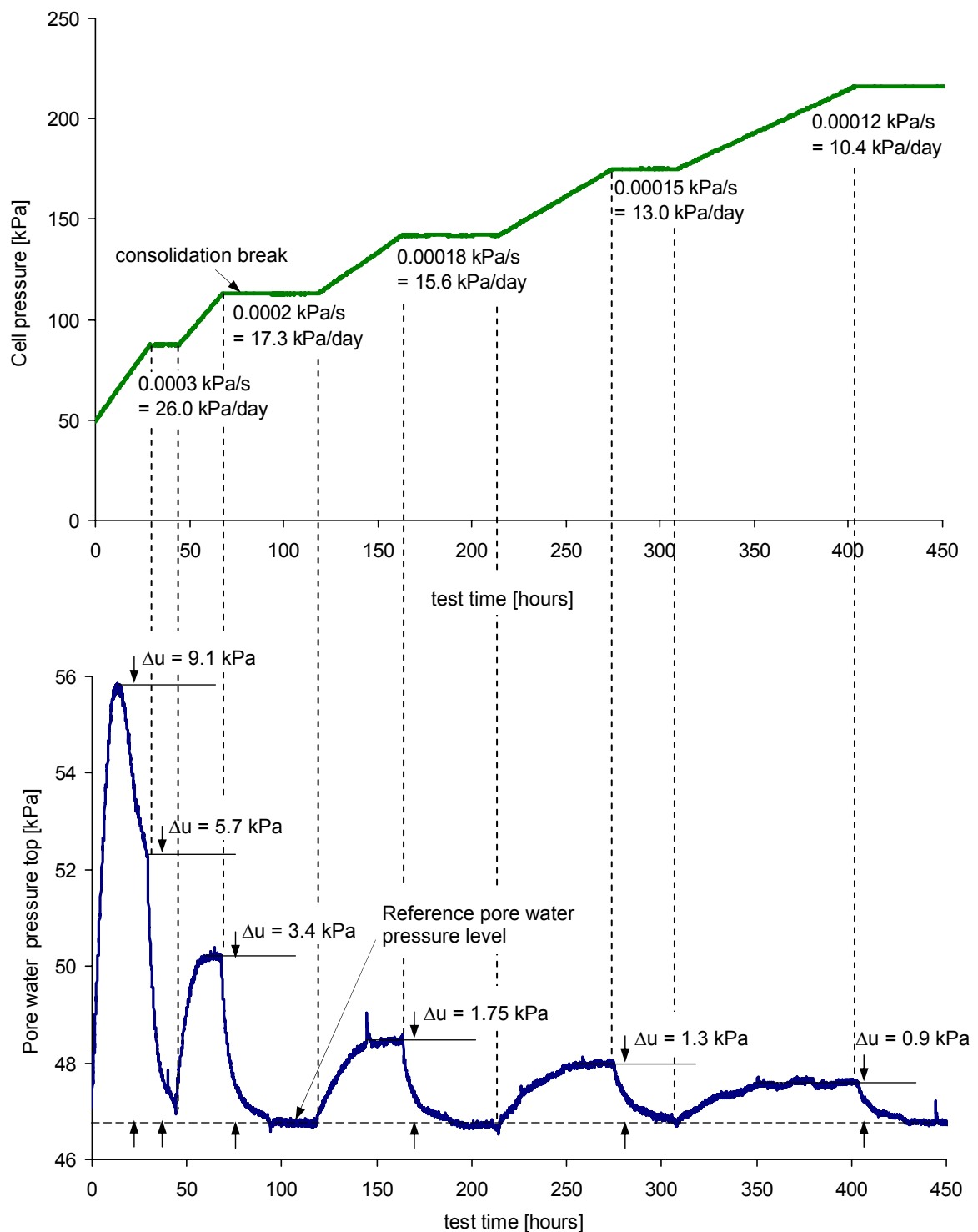
Fig. 5.6: Evaluation of the excess pore pressure development in triaxial test S1T2 during the given loading rates: a) the cell pressure plotted over the test time with the applied stress rate b) the excess pore water pressure measured at the top end of the triaxial sample during the various loading rates applied and the ongoing consolidation plotted over the test time.

5.4.2 Series 2

The aim of the series was to investigate the stiffness degradation and stress path dependency of natural Swiss lacustrine clay. Therefore natural Kloten clay (sample No. 46862) was used for this investigation. The test samples were reconsolidated in the triaxial apparatuses to a stress state beyond the in-situ pre-consolidation stress, unloaded to a common stress state for all tests of this series, and finally reloaded along various paths of constant stress increment ratios to failure. The stress paths for this series are illustrated in Fig. 5.7 and the details are listed in the following section:

First set of tests: S2T1, S2T2, S2T3, S2T4

- Consolidation along the stress ratio η_{Ko} = 0.75 with a loading rate of $\Delta p'$ = 0.5 kPa/h to a stress state of q = 225 kPa, p' = 300 kPa.
- Drained swelling along the stress ratio η_{Ko} = 0.75 with a swelling rate of $\Delta p'$ = 0.5 kPa/h to a stress state of q = 112.5 kPa, p' = 150 kPa.
- Drained probing stress path along the stress increment ratio $\Delta\eta$ = 0 (tests: S2T2 & S2T3) and η = ∞ (tests: S2T1 & S1T4) respectively, with a loading rate of $\Delta p'$ = 0.5 kPa/h and Δq = 0.5 kPa/h respectively.
- Test S2T3: Undrained shear in compression with a constant displacement rate of 0.0005 mm/sec.

Second set of tests: S2aT1, S2aT2, S2aT3, S2aT4

- Consolidation along the stress ratio η_{Ko} = 0.75 with a loading rate of $\Delta p'$ = 1.0 kPa/h to a stress state of q = 225 kPa, p' = 300 kPa.
- Drained swelling along the stress ratio η_{Ko} = 0.75 with a loading rate of $\Delta p'$ = 1.0 kPa/h to a stress state of q = 112.5 kPa, p' = 150 kPa.
- Drained probing stress path until failure: two samples along the stress increment ratio $\Delta\eta$ = 0.75 (test: S2aT1) and $\Delta\eta$ = -0.75 (test: S2aT2) respectively, with a loading rate of $\Delta p'$ = 0.5 kPa/h and a corresponding Δq = 0.375 kPa/h and two samples with the stress increment ratio of $\Delta\eta$ = 1.33 (test: S2aT4) and η = -1.33 (test S2aT3) respectively, with a loading rate of $\Delta p'$ = 0.5 kPa/h and Δq = 0.66 kPa/h.

Third set of tests: S2bT1, S2bT3, S2bT4

- Consolidation along the stress ratio η_{Ko} = 0.75 with a loading rate of $\Delta p'$ = 1.0 kPa/h to a stress state of q = 225 kPa, p' = 300 kPa.

- Drained swelling along the stress ratio η_{Ko} = 0.75 with a loading rate of $\Delta p'$ = 1.0 kPa/h to a stress state of q = 112.5 kPa, p' = 150 kPa.

- Drained probing stress path with the following stress increment ratios and loading rates until failure: stress increment ratio $\Delta\eta$ = -0.5 with a loading rate of $\Delta p'$ = 1.0 kPa/h and Δq = 0.5 kPa/h (test: S2bT3); stress increment ratio $\Delta\eta$ = -1.0 with a loading rate of $\Delta p'$ = 1.0 kPa/h and Δq = 1.0 kPa/h (test: S2bT4); stress increment ratio $\Delta\eta$ = -1.5 with a loading rate of $\Delta p'$ = 1.0 kPa/h and Δq = 1.5 kPa/h (test: S2bT1).

- Test S2bT3: Undrained shear in compression with a constant displacement rate of 0.0001 mm/sec.

Fourth set of tests: S2cT1, S2cT4

- Consolidation along the stress ratio η_{Ko} = 0.75 with a loading rate of $\Delta p'$ = 1.0 kPa/h to a stress state of q = 225 kPa, p' = 300 kPa.

- Drained swelling along the stress ratio η_{Ko} = 0.75 with a loading rate of $\Delta p'$ = 1.0 kPa/h to a stress state of q = 112.5 kPa, p' = 150 kPa.

- Drained probing stress path with the following stress increment ratios and loading rates until failure: stress increment ratio $\Delta\eta$ = 0.6 with a loading rate of $\Delta p'$ = 1.0 kPa/h and Δq = 0.6 kPa/h (test: S2cT4); The stress was applied stepwise in this test; stress increment ratio $\Delta\eta$ = 0.9 with a loading rate of $\Delta p'$ = 1.0 kPa/h and Δq = 0.9 kPa/h (test: S2cT1).

The test data are presented in the Appendix, via a data sheet with sample and test data. The evaluation method is presented in Chapter 5.2. A comparison of the results of all tests performed in series 2 is given in the following paragraph and some material parameters are determined from an overview of the results.

Stress paths of all tests in series 2 are presented in q – p' space (Fig. 5.7). It can be seen that all test samples were consolidated to a similar stress state of q = 225 kPa and p' = 300 kPa. Then all test samples were unloaded to the stress state of q = 112.5 kPa and p' = 150 kPa. Finally, each sample was reloaded along an

individual stress path as described above. Depending on the stress path direction, some tests were loaded straight towards failure (S2T2, S2aT3, S2T4, S2bT4, S2aT4, S2bT1 & S2T1) while others became recompressed (S2aT1, S2cT1, S2cT4, S2T3 & S2bT3). The latter tests were reloaded to stress states past the previous maximum consolidation stress and two of them (S2bT3 & S2T3) were then sheared under undrained conditions to failure, with a constant displacement rate.
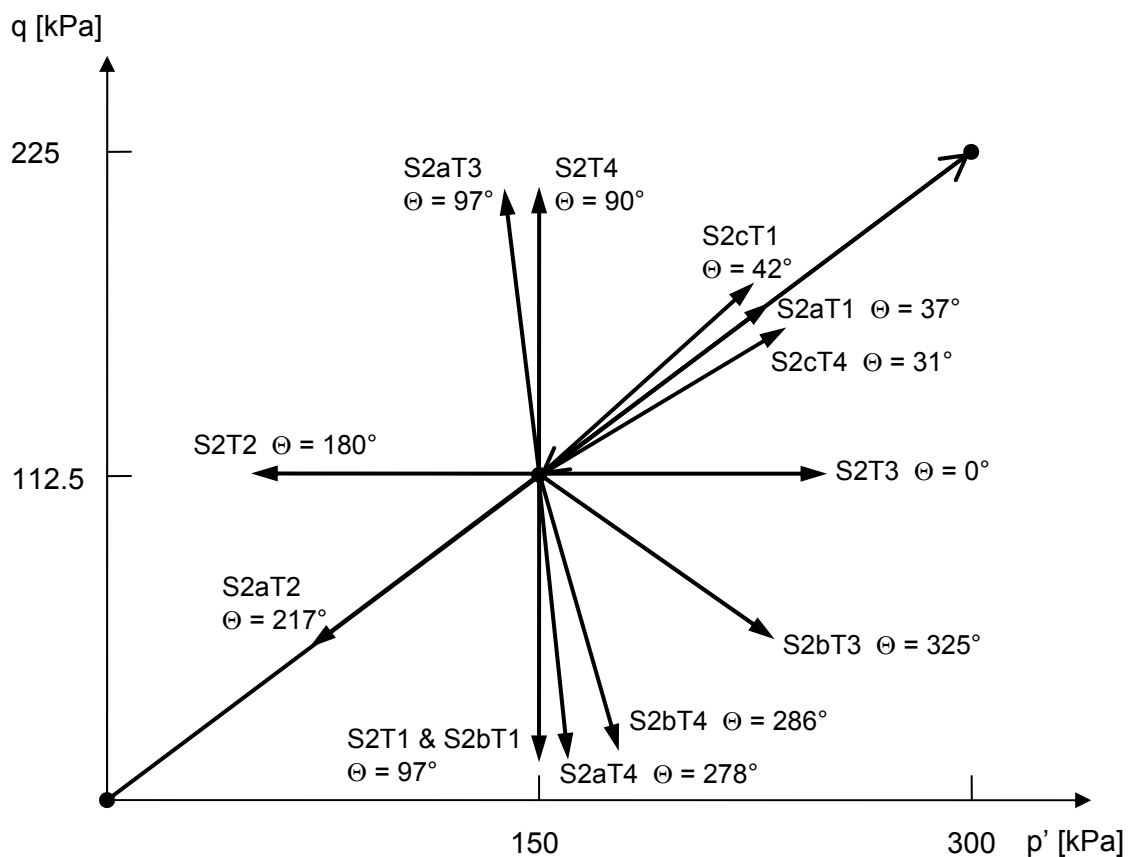
Fig. 5.7:   Stress paths imposed for test series 2.

Applied stress paths and failure stress states are shown in the q – p' plot in Fig. 5.8. For the evaluation of the failure parameters, it is necessary to distinguish between the peak failure stress state and the failure stress state at constant volume. Failure at peak is expected to occur when clays are sheared from an overconsolidated stress state. After reaching the peak failure stress state, under deformation controlled shearing, the stress decreases with increasing shear

strains to the failure stress state at constant volume (softening). When clays are sheared from a normally consolidated stress state, failure is expected to occur at constant volume without reaching an earlier peak (hardening). According to critical state theory (Schofield & Wroth, 1968), the failure stress state at constant volume is critical for the description of "failure". The stress state at constant volume occurs after having reached a peak value, therefore it can only be determined from tests on normally consolidated soils or in strain path tests where the stress decrease with increasing displacement is logged.

The series 2 tests are performed as stress path tests (stress controlled) from an overconsolidation stress state of 2. Therefore failure occurs abruptly when the peak failure stress is reached. Consequently, the post peak behaviour (constant volume) cannot be investigated from the drained stress path tests but from undrained strain controlled shear tests (S2T3 and subsequently S2bT3).

For undrained tests, constant volume at failure is reached when the pore water pressure becomes constant. This occurred at axial strains of 25 to 28 % for both tests S2T3 and S2bT3 (Fig. 10.26 & Fig. 10.83). The corresponding stress state is p' = 311 kPa and q = 403 kPa for test S2T3 and p' = 383 kPa and q = 460 kPa for test S2bT3. This leads to a critical state parameter of M = q / p' of 1.3 and 1.2 respectively. For test S2T3, a small peak in the deviator stress develops before it drops and the volume change ceases, while for test S2bT3 the deviator stress increases continuously until a constant volume is reached. The higher value of the critical state parameter M of test S2T3 might be due to sample inhomogeneities or because of the higher shear strain rate. The mean value of $\mathrm{M}_{comp} = 1.25$ was used for further evaluations.

The friction angle at constant volume (φ_{cv}') was calculated from the critical state parameter in compression (M_{comp}) as:

$$\mathrm{M}_{comp} = \frac{6\sin\varphi_{cv}'}{3 - \sin\varphi_{cv}'} \quad \rightarrow \quad \varphi_{cv}' = \arcsin\left(\frac{3M_{comp}}{6 + M_{comp}}\right) = 31° \qquad \text{Eq. 5.20}$$

where the corresponding critical state parameter in extension (M_{ext}) can be calculated as:

$$\mathrm{M}_{ext} = -\frac{6\sin\varphi_{cv}'}{3+\sin\varphi_{cv}'} \quad \rightarrow \quad M_{ext} = -0.88 \qquad \text{Eq. 5.21}$$

These critical state lines have been added in the q – p' plot in Fig. 5.8 and correlate well with the failure stress states of the shear tests in compression and extension. This indicates that the overconsolidation ratio of 2 does not increase the peak failure stress much above the constant volume stress state at failure.
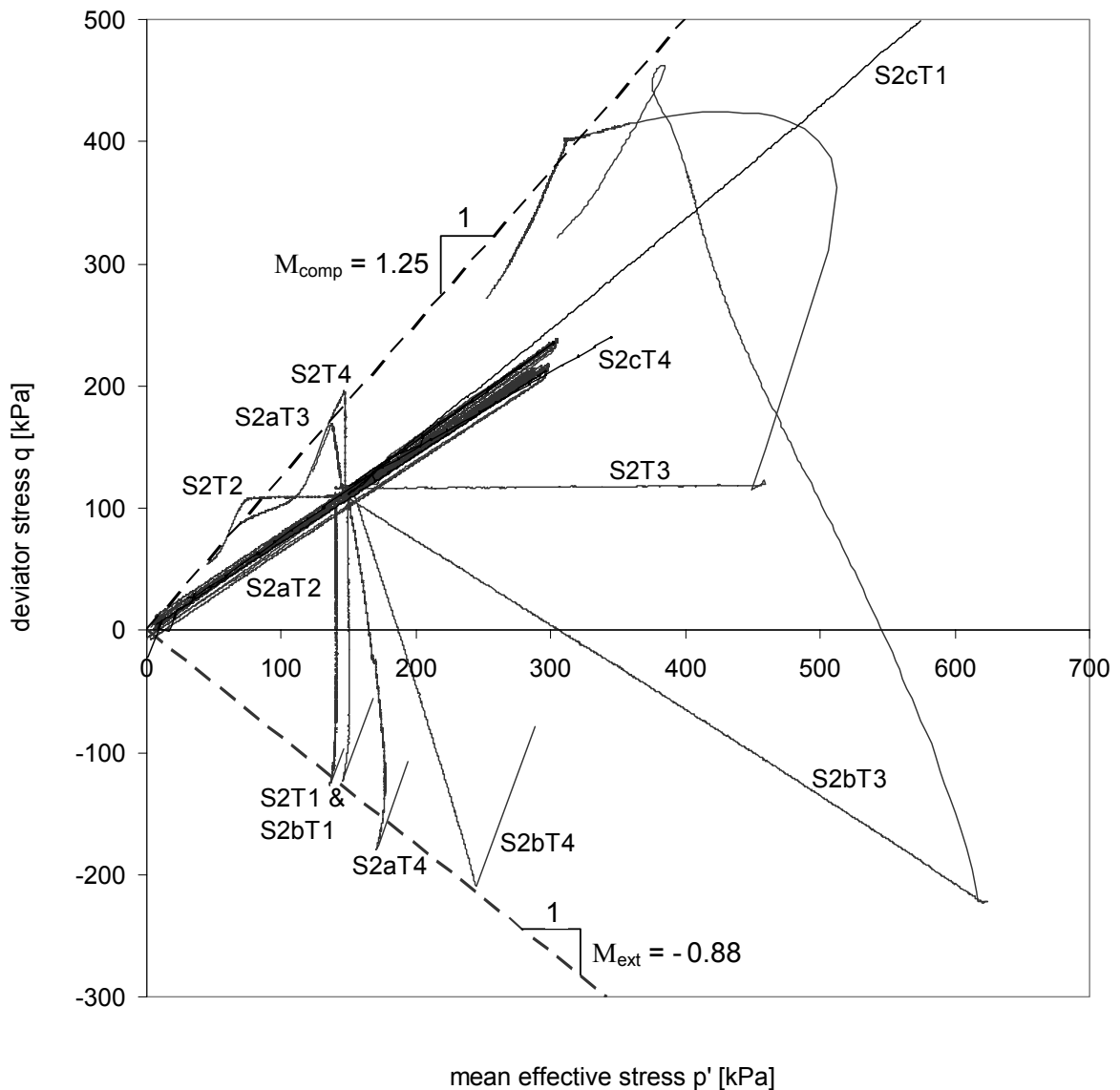
Fig. 5.8:   Applied stress paths and failure stress states of the tests from series 2.

The volume – mean effective stress relationship is shown for each stress path test in the e – ln p' plot (Fig. 5.9), from which the sample quality can also be judged. The initial void ratio, as well as the change of void ratio during reconsolidation, are indicators of sample loosening (Lo Presti et al., 1999b). Additionally, the form of the knick at the transformation from recompression to the virgin compression state reflects the sample quality (Jamiolkowski, 2003).

Comparing the results presented in Fig. 5.9 and the corresponding plots in the Appendix, it can be seen that the initial void ratio varies between 0.70 and 0.75, which can easily result from sample inhomogeneities. The inclination of the reconsolidation path is more significant for the determination of the sample quality. In Fig. 5.9 in particular, 3 tests have a disproportionately steep reconsolidation path. A more specific analysis shows that these tests are S2T3, S2T4 & S2T1.

All three are from the first test set-up, which indicates that the block sample that was used for the first test set-up may have had slightly differing properties. A kink in the line at the transition from recompression to the virgin compression state is visible for all tests, which leads to the conclusion that the test samples were all of a similar good quality. Consequently, the swelling index (κ) and the compression index (λ) were derived as well as the void ratio at the stress state of p' = 1 kPa (e_λ). The range of values is given in Fig. 5.9.

Alongside the stiffness response of the natural clay samples, radial strain development during testing was also investigated in series 2 using the laser scan device. Laser scans were performed in tests S2T1, S2aT1, S2bT1 & S2cT1. The data evaluation was performed as described in Chapter 5.2. The measurement data as well as the evaluation results are shown in the Appendix. The volume measurement results, which were calculated from the circle-fitting approach as discussed in Chapter 5.2, are presented and compared together with the conventional volume measurement data.

The data from the radial displacement measurements are given separately for the consolidation, swelling and probing stress paths. Laser scans are presented at intervals of $\Delta p'$ = 50 kPa during consolidation and swelling. Sets of scans at specified stress states are given along the probing paths. The measured radius

and the derived radial strain distribution from the three laser scan data sets are shown over the sample height.
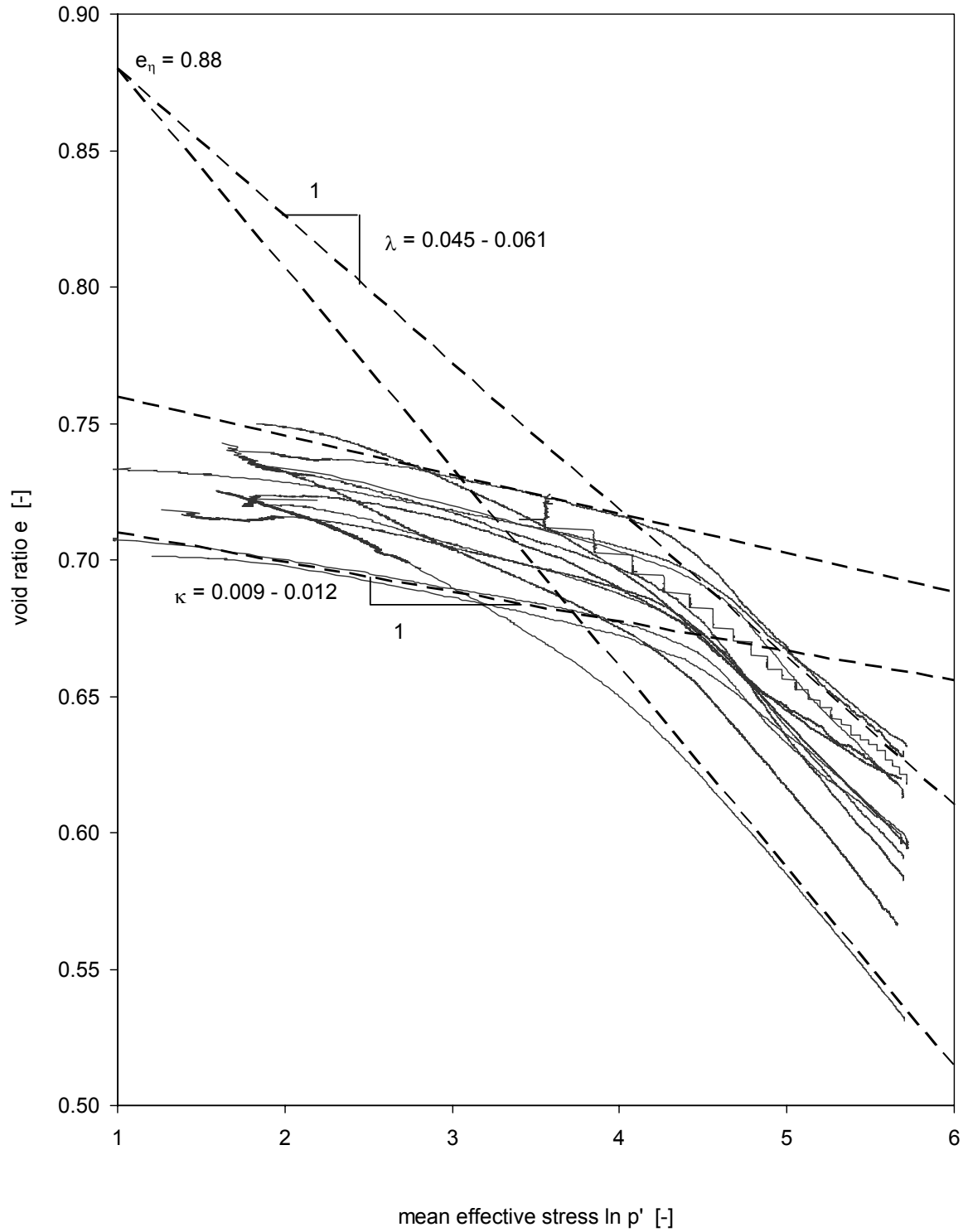
Fig. 5.9: Volume compression curves and stiffness parameters of the series 2 tests.

The radius (R), derived from the circular-fit approach through the three measured points in the horizontal plane as discussed in Chapter 5.2, is plotted and the derived cross-sectional area of the sample over the sample height is shown. The deviator stress is calculated, assuming a constant force acting through the sample, with the cross-sectional area and plotted over the sample height.

The sample midpoint $[x_0, y_0]$ is calculated from the radius R, and the resulting movement of the midpoint during the load paths is given for several cross-sections. Finally, the axial strains are plotted with the corresponding radial strains for a range of measurement cross-sections in the middle of the sample.

Local axial displacement measurements were performed in tests S2aT1 & S2bT1. The data evaluation was carried out as described in Chapter 5.2. The measurement data, as well as the evaluation results, are presented in the Appendix together with the results of the external axial strain measurement.

Bender element measurements have been performed in test S2bT4. The data evaluation was carried out as described in Chapter 5.2. The measurement data, as well as the evaluation results, are presented in the Appendix. Three measurements at different frequencies were performed after the swelling path had been followed and before the probing stress path was applied. The shear moduli determined at this mean effective stress state of p' = 150 kPa vary between 94 and 105 MPa (Fig. 10.124) and result in an average value for the nominal maximum shear modulus G_{max} of 98 MPa.

5.4.3 Series 3

The aim of this test series was to investigate differences between the laser scans measured on reconstituted and natural samples and to investigate the development of the necking zone during shearing in extension. A test with the same consolidation history as in series 2 but applied to a reconstituted sample was necessary to perform the comparative study. Therefore a reconstituted sample of Kloten clay (sample No. 46809) was used for this investigation instead of a natural sample.

The sample was consolidated and drained swelling was applied in the same way as for the tests in series 2. In the subsequent probing path, the sample was sheared undrained under displacement control in extension:

- Consolidation along the stress ratio η_{Ko} = 0.75 with a loading rate of $\Delta p'$ = 1.0 kPa/h to a stress state of q = 225 kPa, p' = 300 kPa.
- Drained swelling along the stress ratio η_{Ko} = 0.75 with a loading rate of $\Delta p'$ = 1.0 kPa/h to a stress state of q = 112.5 kPa, p' = 150 kPa.
- Undrained shear in extension with a constant axial displacement rate of 0.0001 mm/sec.

The data are evaluated as discussed in Chapter 5.2 and the resulting stress-strain plots are presented in the Appendix. The stress paths of the consolidation and swelling paths applied as well as the stress path resulting from undrained, strain controlled shearing in extension and the failure stress state are given in Fig. 5.10.
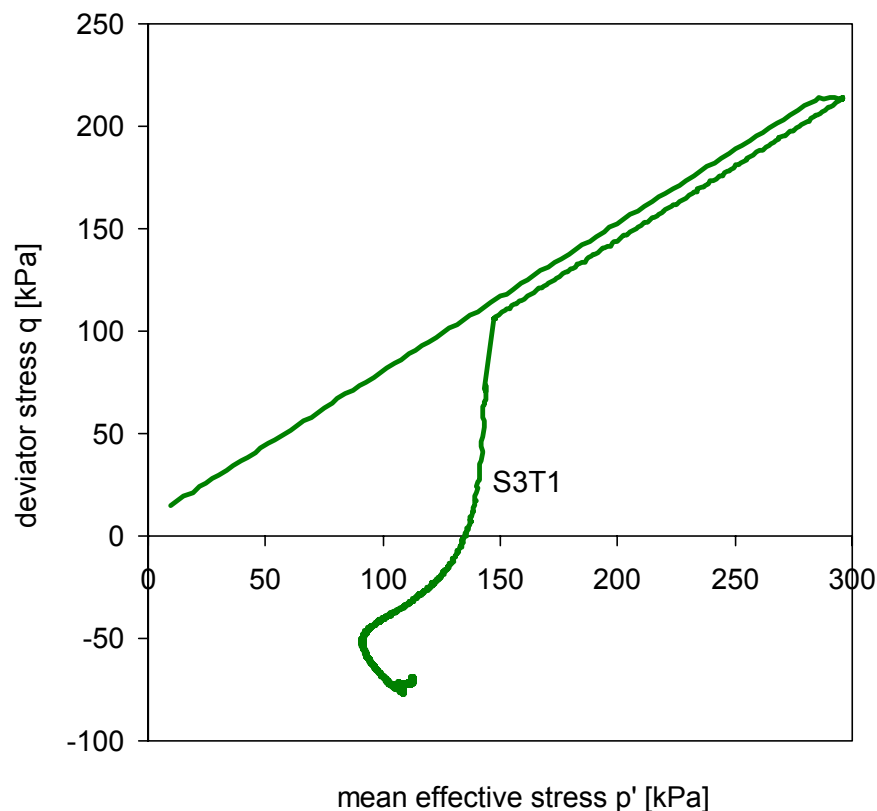
Fig. 5.10: Stress path and failure stress state of the test on reconstituted Kloten clay of series 3.

128

The comparative study of radial strain distribution over the sample derived in test series 3 on reconstituted samples, and in test series 2 on natural samples, is presented and discussed in Chapter 5.5.3 (Fig. 5.11 to Fig. 5.21). The investigation of the necking zone and the resulting failure stress is presented in Chapter 6.3 (Fig. 6.30 to Fig. 6.33).

5.5 Discussion of series 2 & 3

The measurement and evaluation data of the tests performed in series 2 & 3 are discussed and analysed in the following Chapter.

5.5.1 Sample volume measurement

The initial sample volume was determined with a sliding calliper during sample preparation, before the sample set-up. The volume decrease during the test was measured by the pore pressure and cell pressure units. Additionally, the radial sample dimensions were scanned with the laser scan device, in 4 tests (S2aT1, S2bT1, S2cT1 & S3T1). The initial sample volume and the volume degradation during test performance were determined from these data with the use of the laser scan data evaluation method, which was discussed in Chapter 5.2.2. The results are presented in the Appendix and compared to the data measured by the pore pressure unit.

Comparison of the initial sample volume shows that the result from the laser scans is the same (tests S2aT1 & S2bT1) or slightly higher (tests S2cT1 & S3T1) than the initial sample volume measured with the sliding calliper. Recalling the sample set-up procedure (Chapter 5.1), the sample dimensions were determined before test set-up with the sliding calliper. The sample was placed on the saturated filter plate during test set-up in the triaxial cell, the rubber membrane was fixed onto the bottom pedestal with O-rings and the contact areas between the sample, the rubber membrane, the bottom pedestal and top plate were saturated before the rubber membrane was fixed to the top plate to create a watertight seal. Water was added during this process, which may be soaked up by the sample or could have remained between the rubber membrane and the sample or in the system. Therefore a higher value for the initial sample volume determined from the laser

scan data is realistic. Fast decreases of sample volume at the test start are to be expected due to the drainage of any surplus pore water, which may have remained inside the rubber membrane during test set-up.

Comparison of the volume degradation curves measured with the back pressure unit to those calculated from the laser scans applying the circular slice approach shows that the stress state at which transition from recompression to the normal compression state occurs is the same for both methods. Comparing the stiffness response measured by these two methods, it can be seen that the laser data give a stiffer response for the recompression curves and a less stiff response for the normal compression state (Fig. 10.37, Fig. 10.66, Fig. 10.94 & Fig. 10.115).

5.5.2 Axial displacement measurement

The axial sample displacement was measured with the external LVDT (Fig. 4.1) and in 3 tests (S2aT1, S2bT1 & S3T1) two additional LVDTs were mounted locally on the sample, as discussed in Chapter 4.3. The measurement data and strain evaluation results are presented in the Appendix (Fig. 10.37, Fig. 10.38, Fig. 10.66, Fig. 10.67, Fig. 10.115 & Fig. 10.116). Comparison of the axial strains determined from the external LVDT and the local LVDTs show that the strain magnitude measured by both devices is remarkably similar. Therefore, it is assumed that the effects of seating and bedding errors are not that dominant for these triaxial test apparatuses.

Comparing the measurement data in terms of noise, it is visible that the stress-strain curves of the data measured by the local LVDTs are much smoother than the curves that are plotted from data of the external LVDT (Messerklinger et al., 2004). The noise inherent in the stress-strain curve is of particular importance when the stiffness degradation is derived.

5.5.3 Radial displacement measurement

Laser scans were performed in 4 tests of series 2: S2T1, S2aT1, S2bT1 & S2cT1. Data were logged every millimetre in the axial direction in tests S2T1 & S2aT1. The data evaluation of the three laser measurements in terms of radial strains

showed significant fluctuation in radial strain (zigzag line) for the sample profiles in Fig. 5.11a-c and Fig. 5.12a-c (Messerklinger et al., 2004).
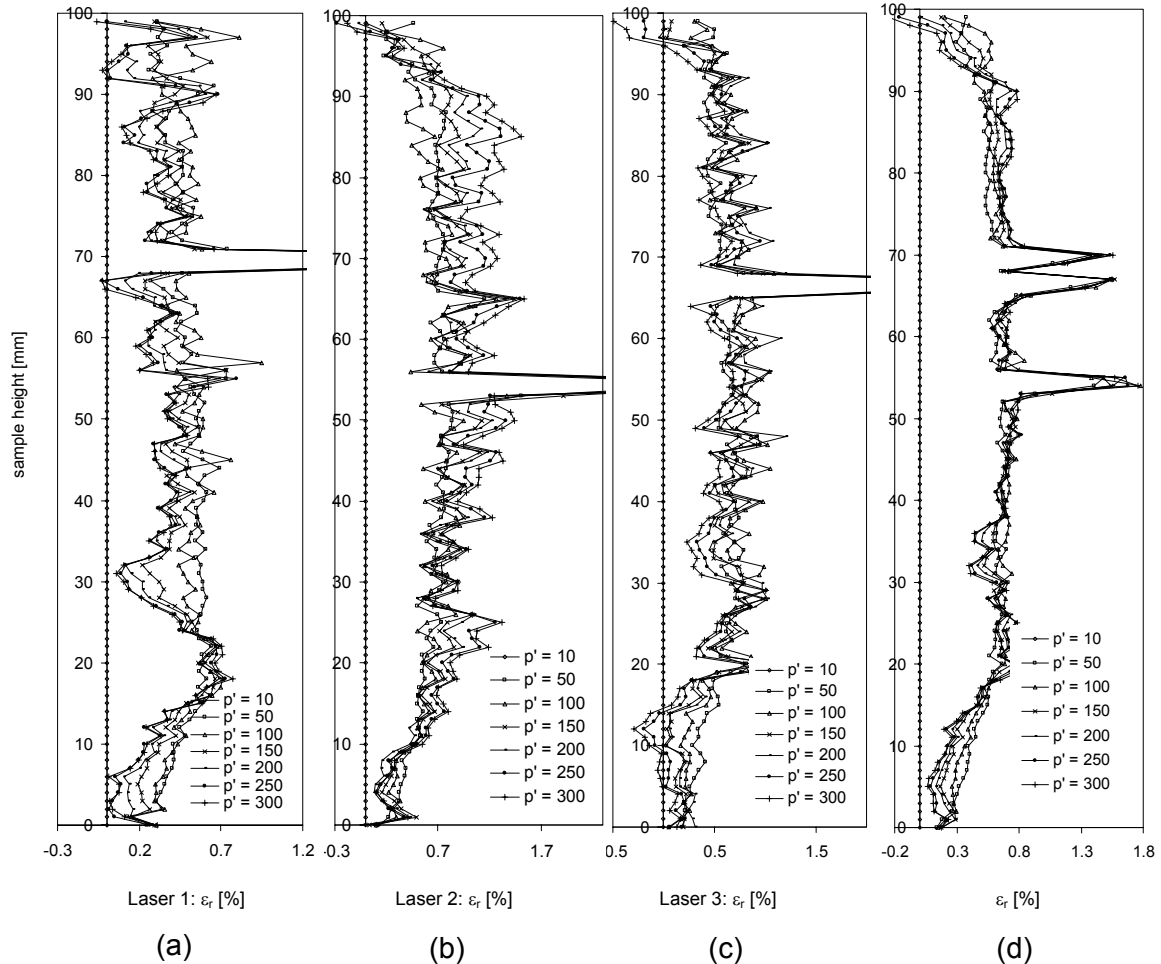
Fig. 5.11: Radial strains evaluated for the consolidation stress path of test S2T1 at the specified mean effective consolidation stress p' given in [kPa]. The radial strains calculated from the measurement data of (a) Laser 1, (b) Laser 2, (c) Laser 3 are plotted over the sample height. (d) radial strains calculated from the equivalent sample radius, determined by the circular slice approach, plotted over the sample height.

The radial strains calculated from the equivalent sample radius (R), determined using the circular slice approach, and plotted over the sample height (Fig. 5.11d and Fig. 5.12d) resulted in a smoother line. The large radial strains at a sample height of 50 to 70 mm may result from water bubbles or wrinkles in the rubber membrane.

131
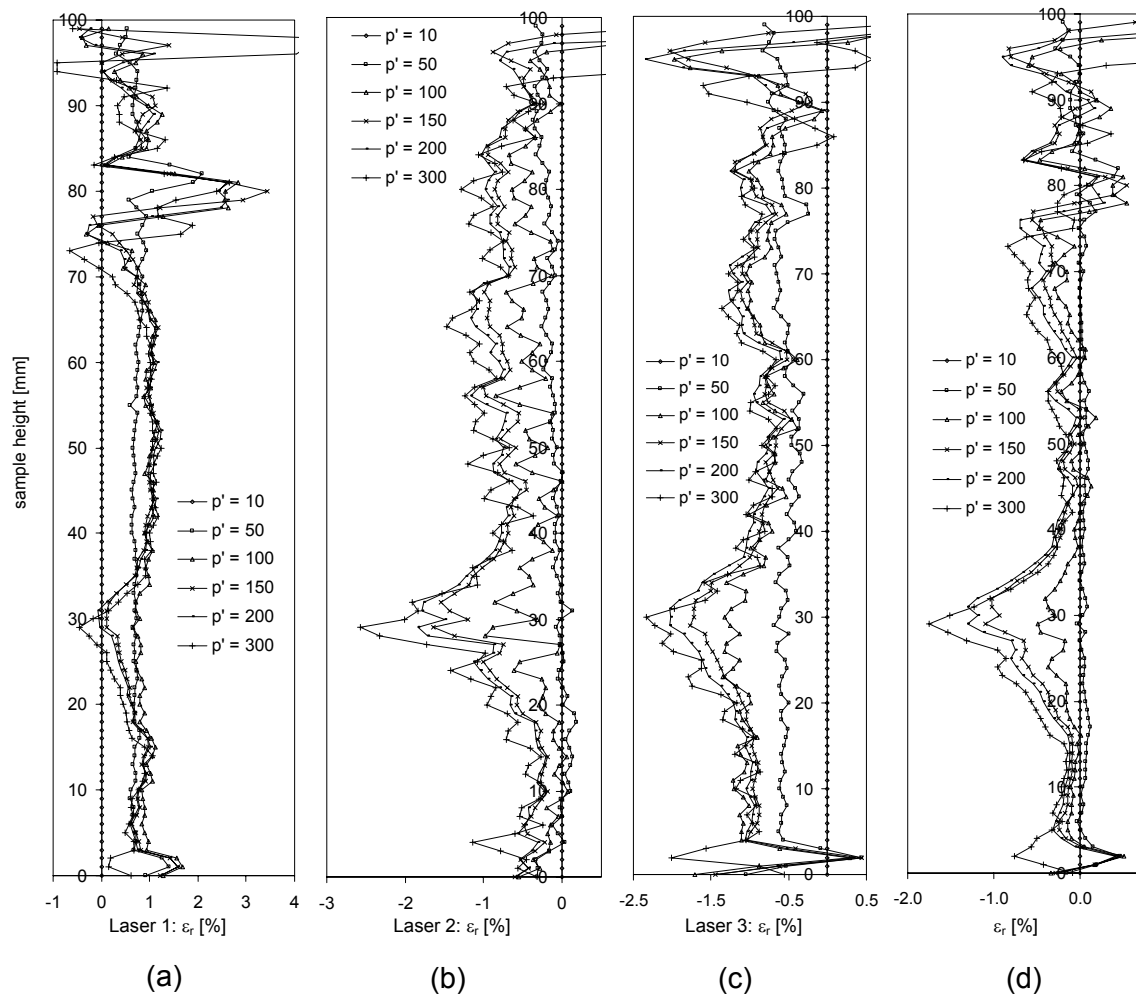
Fig. 5.12: Radial strains evaluated for the consolidation stress path of test S2aT1 at the specified mean effective consolidation stress p' given in [kPa]. The radial strains calculated from the measurement data of (a) Laser 1, (b) Laser 2, (c) Laser 3 are plotted over the sample height. (d) radial strains calculated from the equivalent sample radius, determined from the circular slice approach, plotted over the sample height.

Due to the spacing of 2 to 3 mm in the axial direction between local peaks in radial strain, it was assumed that this might be due to the stratification of the natural samples. But an exact determination of the distribution of the layers was not possible from the few measurement points. Therefore, the frequency of the data logging was increased, and in the following two tests (S2bT1, Fig. 5.13 & S2cT1, Fig. 5.15), the radial displacement was measured 12 times per millimetre in the

axial direction. The scan results show a continuous wavy line varying over the entire sample height, with a wave length in the axial direction of circa 4 mm.
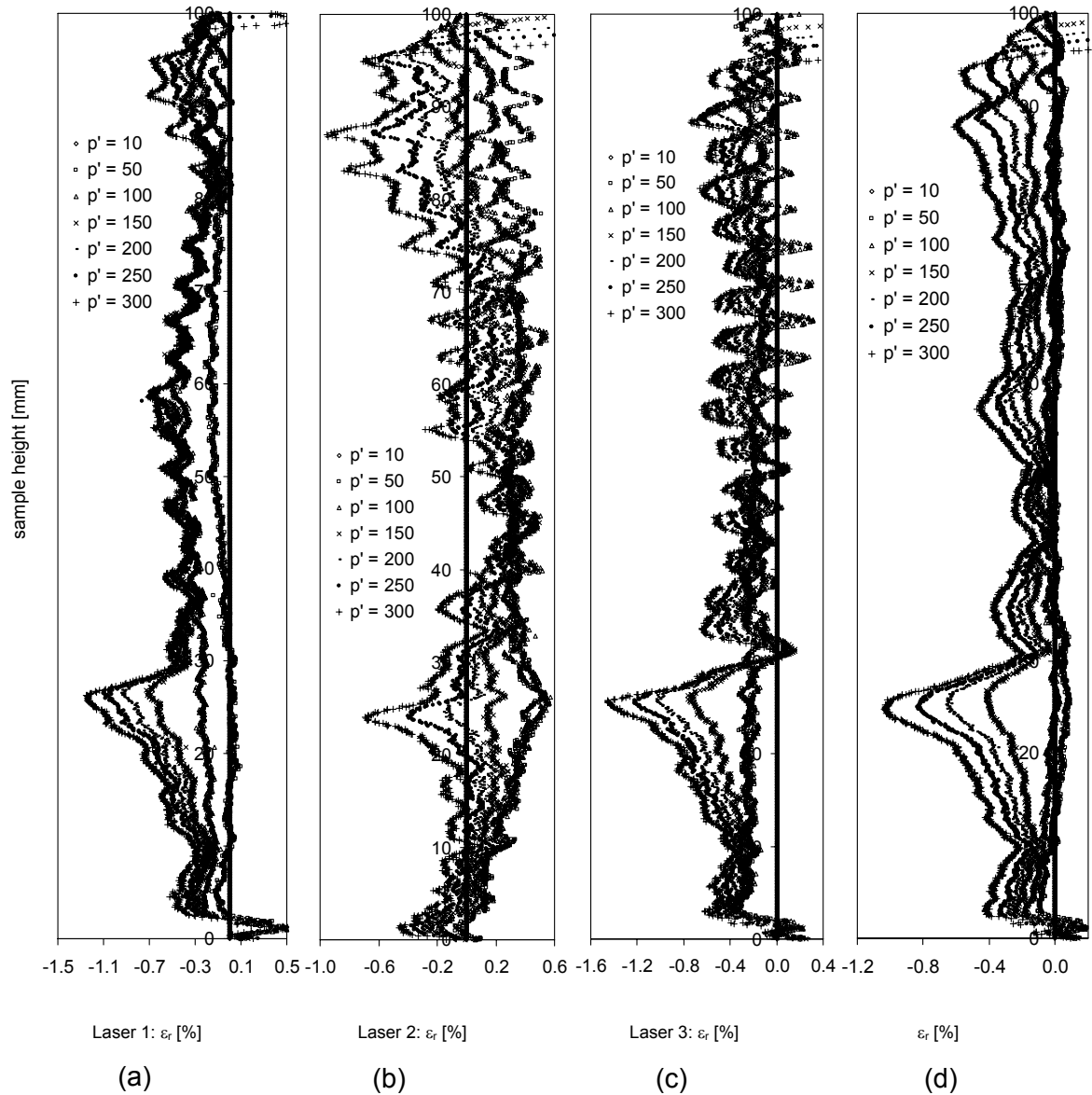
Fig. 5.13: Radial strains evaluated for the consolidation stress path of test S2bT1 at the specified mean effective consolidation stress p' given in [kPa]. The radial strains calculated from the measurement data of (a) Laser 1, (b) Laser 2, (c) Laser 3 are plotted over the sample height. (d) radial strains calculated from the equivalent sample radius, determined from the circular slice approach, plotted over the sample height.
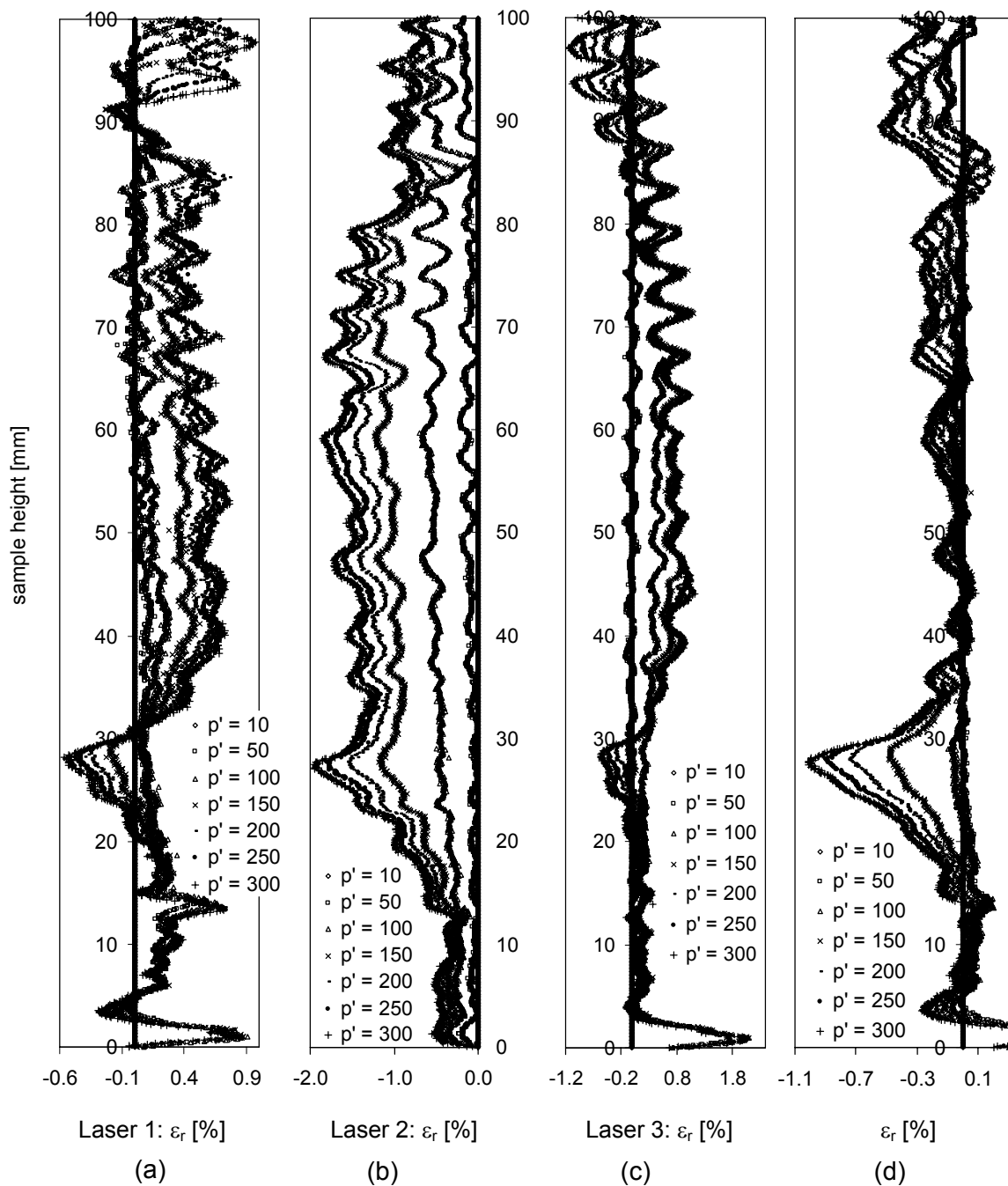
Fig. 5.14: Radial strains evaluated for the consolidation stress path of test S2cT1 at the specified mean effective consolidation stress p' given in [kPa]. The radial strains calculated from the measurement data of (a) Laser 1, (b) Laser 2, (c) Laser 3 are plotted over the sample height. (d) radial strains calculated from the equivalent sample radius, determined from the circular slice approach, plotted over the sample height.

The change in sample radius is more than 0.2 mm (see Appendix Fig. 10.69 to Fig. 10.71 & Fig. 10.75; Fig. 10.95 to Fig. 10.97 & Fig. 10.101). The regularity of the fluctuations, and the period of the waves of 4 mm in the axial direction, equalling the change in height for one rotation of the screw, looked suspicious.

Therefore, the test S3T1 was performed on a remoulded sample in a third test series, with no varving or layers or other inhomogeneities. Unfortunately, Laser 3 was out of order in this test, therefore, the results of only Laser 1 & 2 are presented (Fig. 5.15) and the equivalent radius was not determinable. The evaluation of the radius measured by these two lasers still gave fluctuations in sample radius over the sample height. The change in sample radius is up to 0.1 mm (see Appendix Fig. 10.117 & Fig. 10.118). The data from Laser 2 shows a wavy surface with increasing wave size from the bottom to the top. This clearly indicates an influence of the laser scan device on the data. Therefore the identification of layering from the laser scan data might be difficult.

The increase in magnitude of the waves with sample height is because, at the hermetically sealed joint passing through the bottom plate of the triaxial pressure cell (Fig. 4.7a&b), the lead screws and consequently the connecting plate with the three lasers are stabilised. It is assumed that the magnitude of oscillation of the lead screws, and with them the connection plate and the lasers, increases with increasing distance from the bottom plate.

Local LVDTs were mounted in three (S2aT1, S2bT1 & S3T1) of the five tests of series 2 and 3 on which laser scans were performed. Due to the fact that some laser scan tests have been performed with, and some without, local LVDTs, it was possible to investigate the influence of the LVDT mounting on the radial displacements. The equivalent radius data are compared for this investigation. No LVDTs were mounted in the first laser scan test (S2T1, Fig. 10.15).

The radial displacement measurement data show continuous radial deformation of the sample radius over the middle part of the sample. The radial deformations were restricted at the bottom and top ends because of the friction between sample, filter paper and top cap or bottom plate. This influence decreased away from the platens within the bottom and top 20 mm of the sample. The initial sample height was 112.5 mm and the height increased during shearing in extension.

Therefore, this influence is not fully visible on the top end of the sample because the laser scan was initially performed on the bottom 100 mm of the sample only.
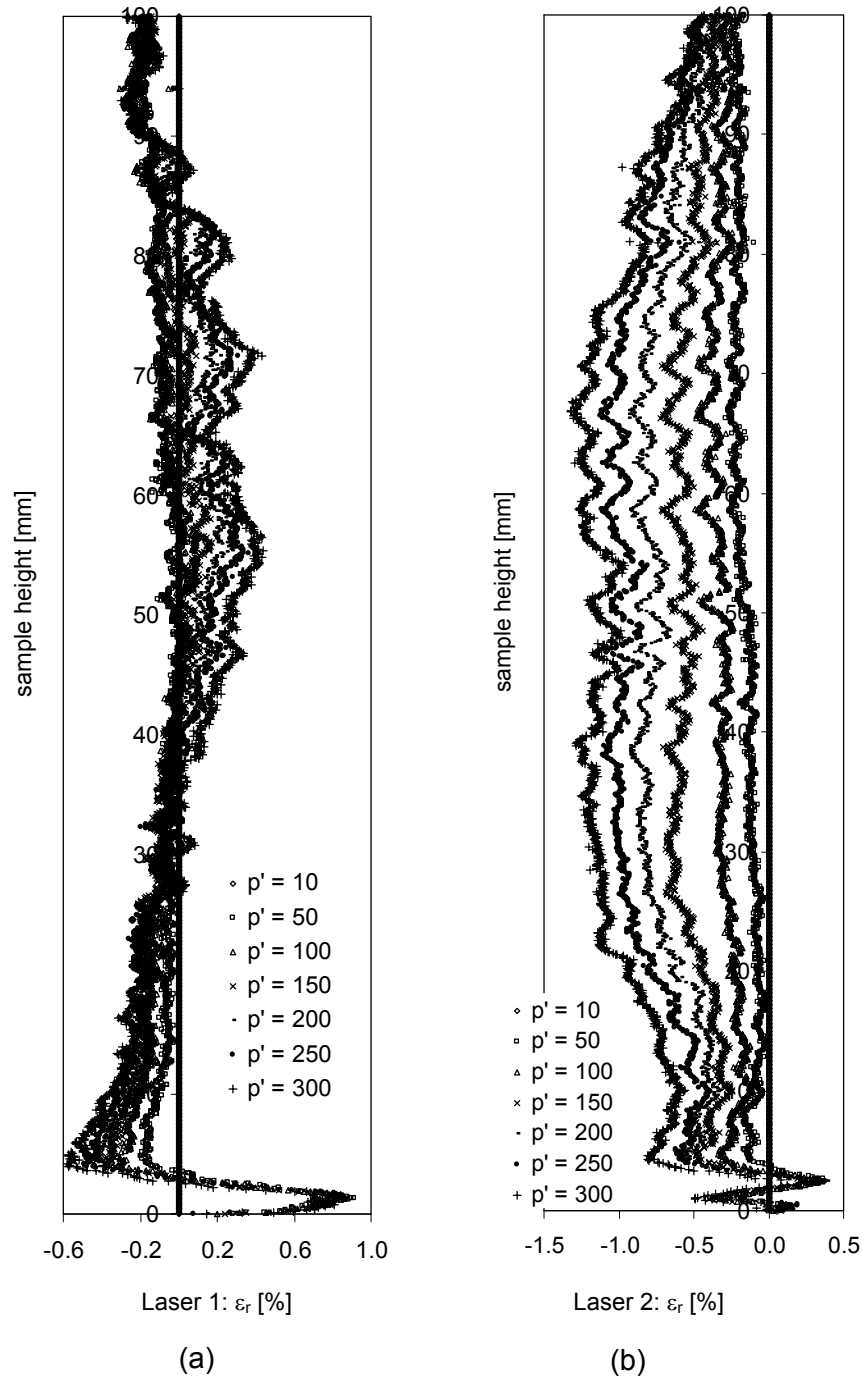
Fig. 5.15: Radial strains evaluated for the consolidation stress path of test S3T1 at the specified mean effective consolidation stress p' given in [kPa]. The radial strains calculated from the measurement data of (a) Laser 1, (b) Laser 2 are plotted over the sample height.
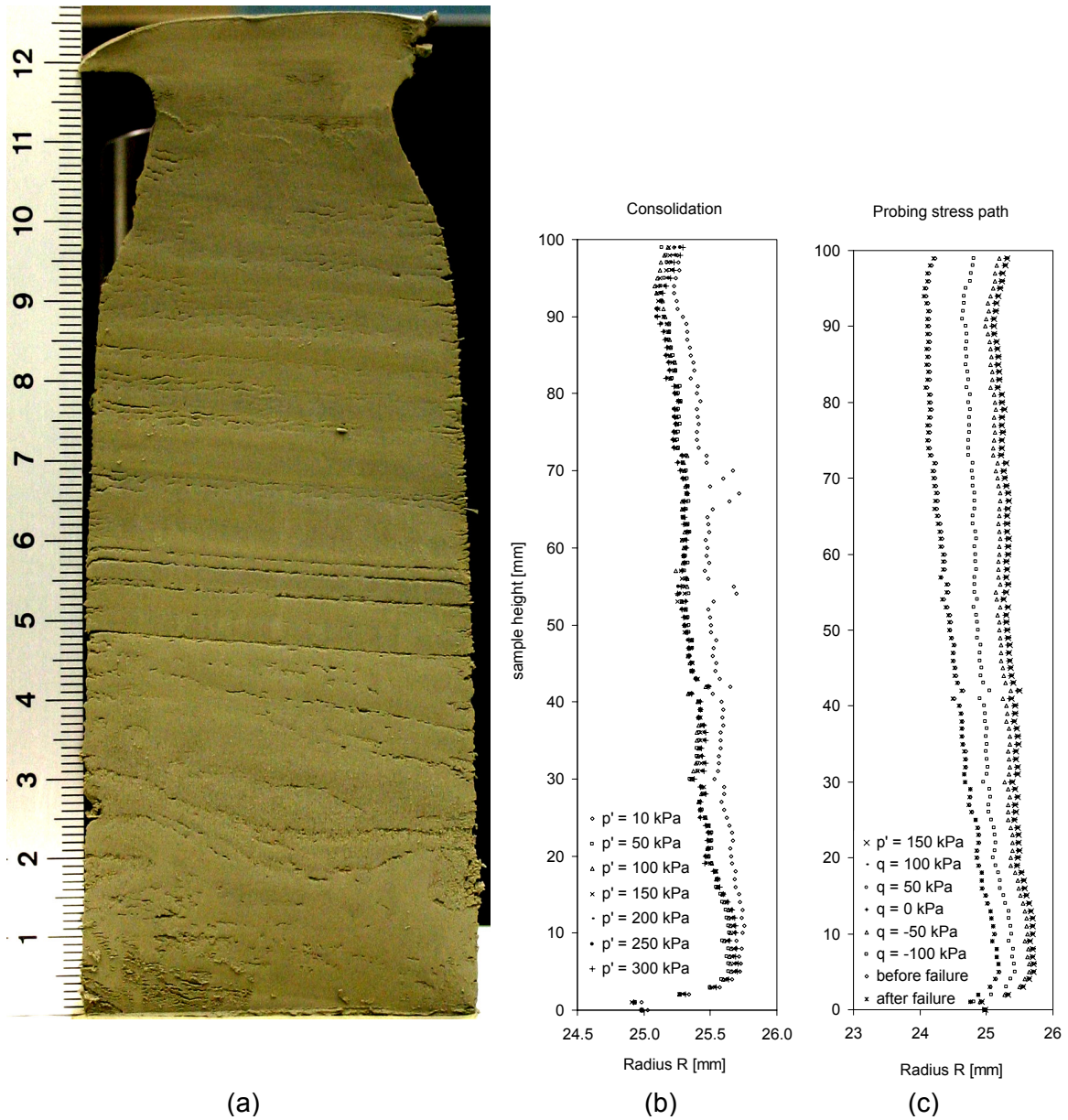
Fig. 5.16: Test S2T1: a) Picture of the section of the test sample after the probing stress path was applied and the specimen was extracted from the triaxial test apparatus; (the ruler unit is centimetres). The measured sample radius, calculated from the three laser scans using the circular slice approach, is plotted over the sample height at the given stress states in [kPa] (b) for the consolidation stress path; (c) for the probing stress path.

Two local LVDTs were mounted on the sample surface in the second and third laser scan test (S2aT1, Fig. 5.17 & Fig. 10.45; and S2bT1, Fig. 5.18 & Fig. 10.75). The scan data of both tests (S2aT1 & S2bT1) showed an increase of the sample

radius during consolidation at a height of around 30 mm, which equals the height of the top side of the bottom LVDT mounting. The radial increase is stretched over more than 10 mm of the sample height, which is equal to the height of the mountings. But these radial displacements could also be due to a weak layer in the natural specimen. Consequently, no local LVDTs were used in test S2cT1 (Fig. 10.101).

(a)   (b)   (c)
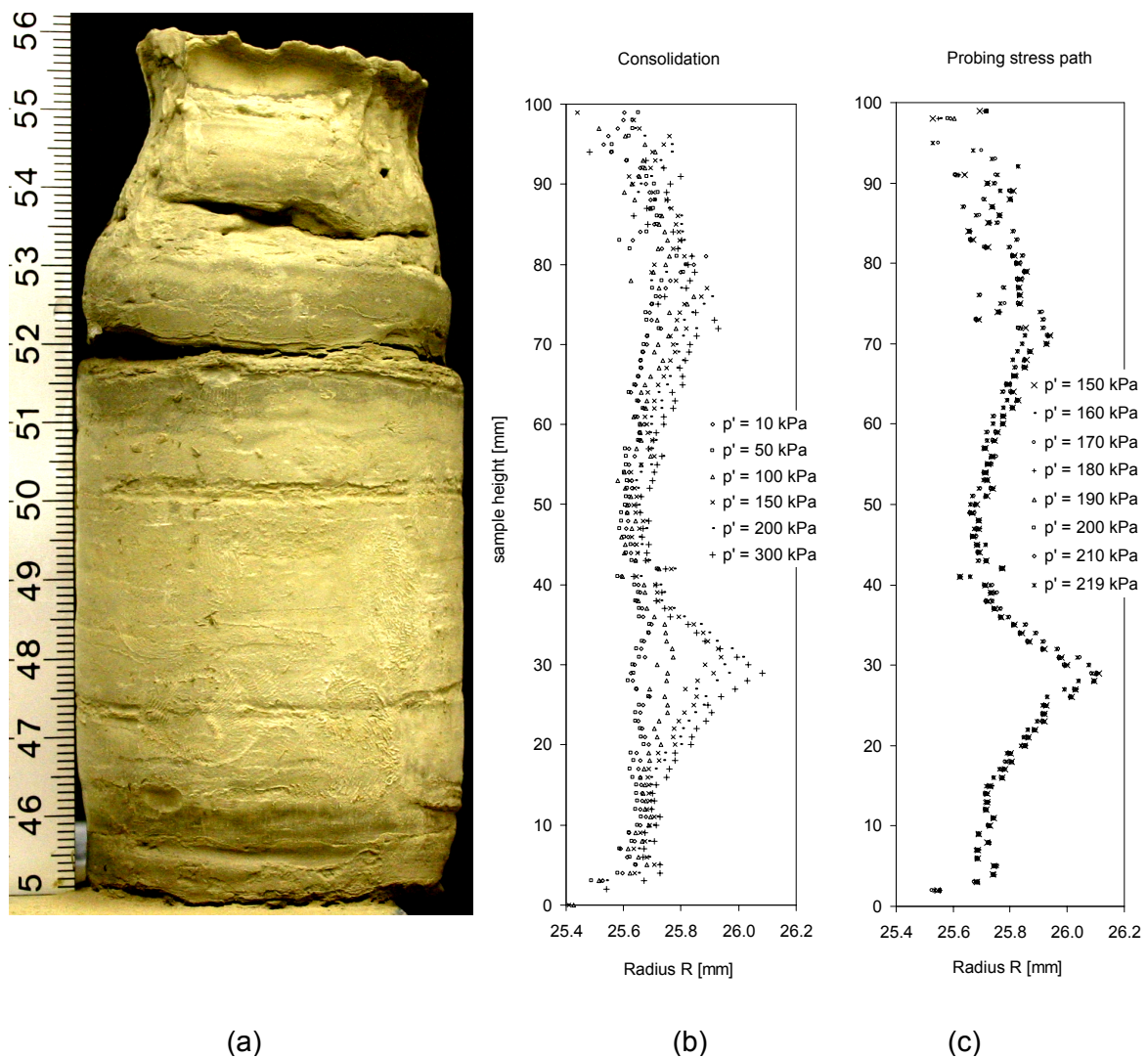
Fig. 5.17: Test S2aT1: a) Picture of the test sample after the probing stress path was applied and the specimen was extracted from the triaxial test apparatus; (the ruler units are centimetres). The measured sample radius, calculated from the three laser scans using the circular slice approach, is plotted over the sample height at the given stress states in [kPa] (b) for the consolidation stress path; (c) for the probing stress path.
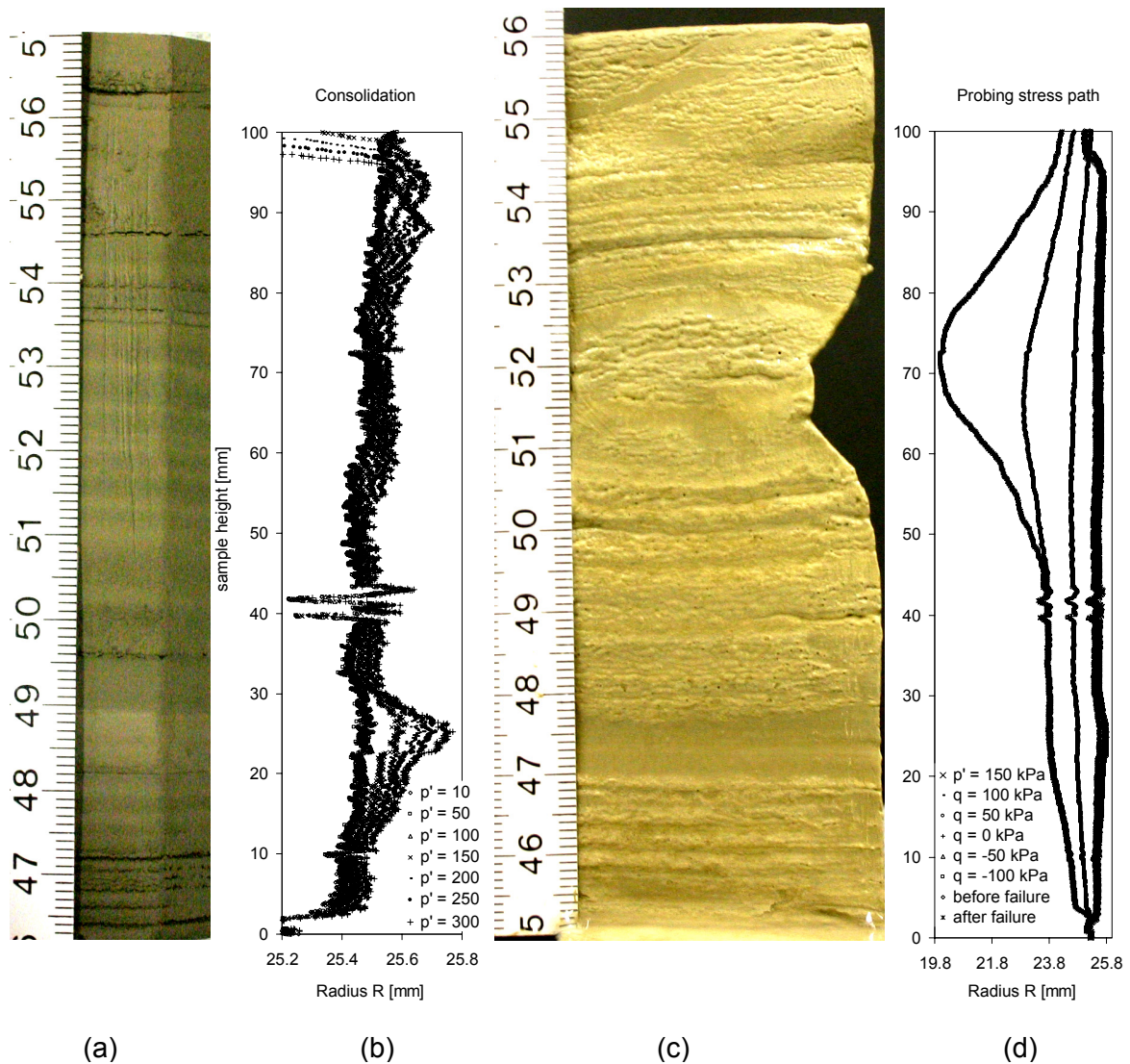
Fig. 5.18: Test S2bT1: (a) Picture of the test sample during sample preparation. (c) Picture of the section of the test sample after the probing stress path was applied and the specimen was extracted from the triaxial test apparatus; (the ruler units are centimetres). The measured sample radius, calculated from the three laser scans using the circular slice approach, is plotted over the sample height at the given stress states in [kPa] (b) for the consolidation stress path; (d) for the probing stress path.

The radial displacement measurement data show an increase in the sample radius occurring again at a height of around 30 mm. Therefore a layer of material of varying compressibility may be found at this height.
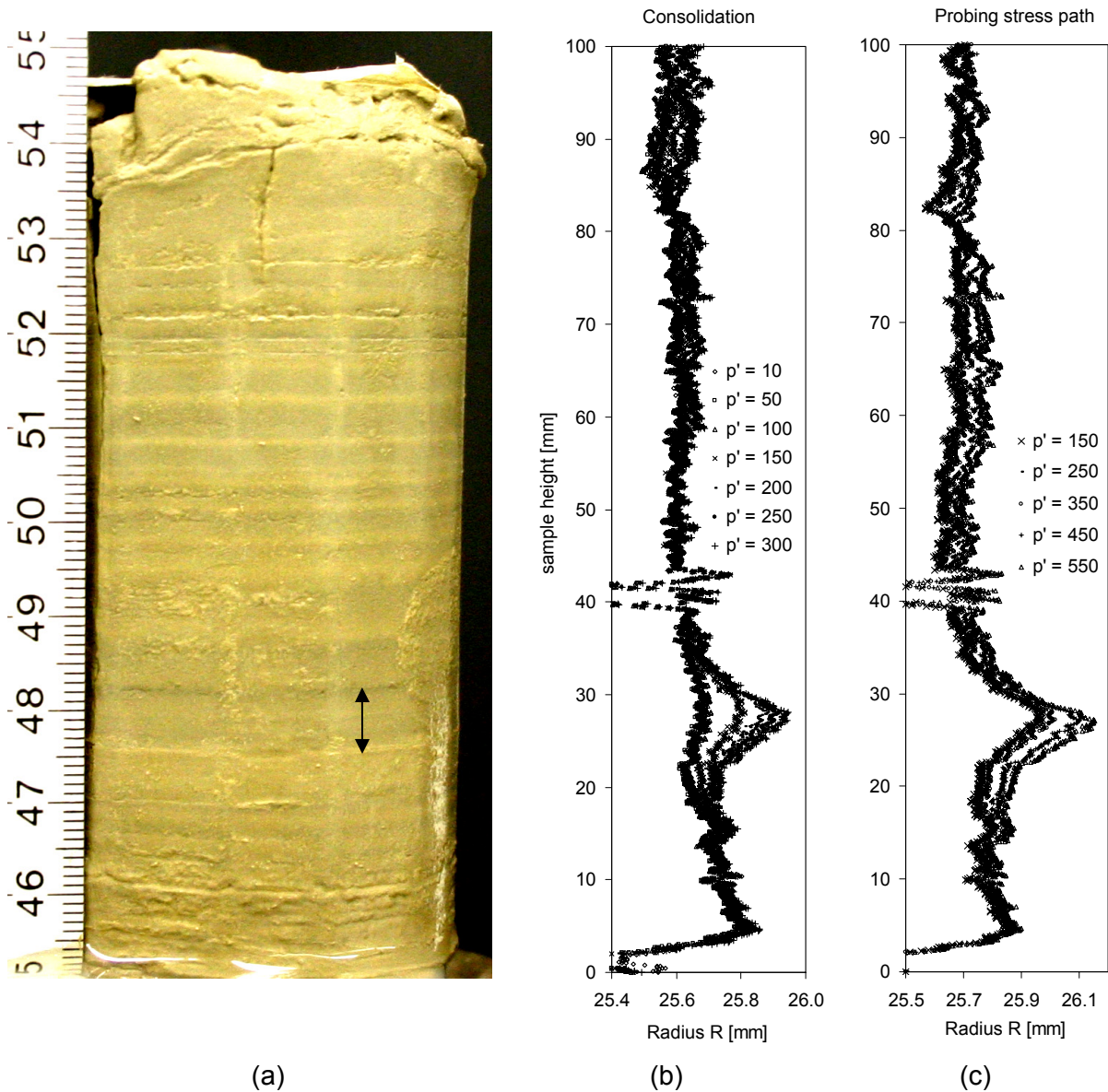
Fig. 5.19: Test S2cT1: (a) Picture of the test sample after the probing stress path was applied and the specimen was extracted from the triaxial test apparatus (the ruler units are centimetres). The measured sample radius, calculated from the three laser scans using the circular slice approach, is plotted over the sample height at the given stress states in [kPa] (a) for the consolidation stress path; (c) for the probing stress path.

The extent to which the LVDT mounting influences the radial deformation behaviour and how much the natural sample inhomogeneities contribute to the scatter cannot be defined in this case. Therefore an additional laser scan test with

local LVDTs was performed on a reconstituted sample: test S3T1 (Fig. 5.20, Fig. 5.21, Fig. 10.117 & Fig. 10.118).

(a) (b) (c)
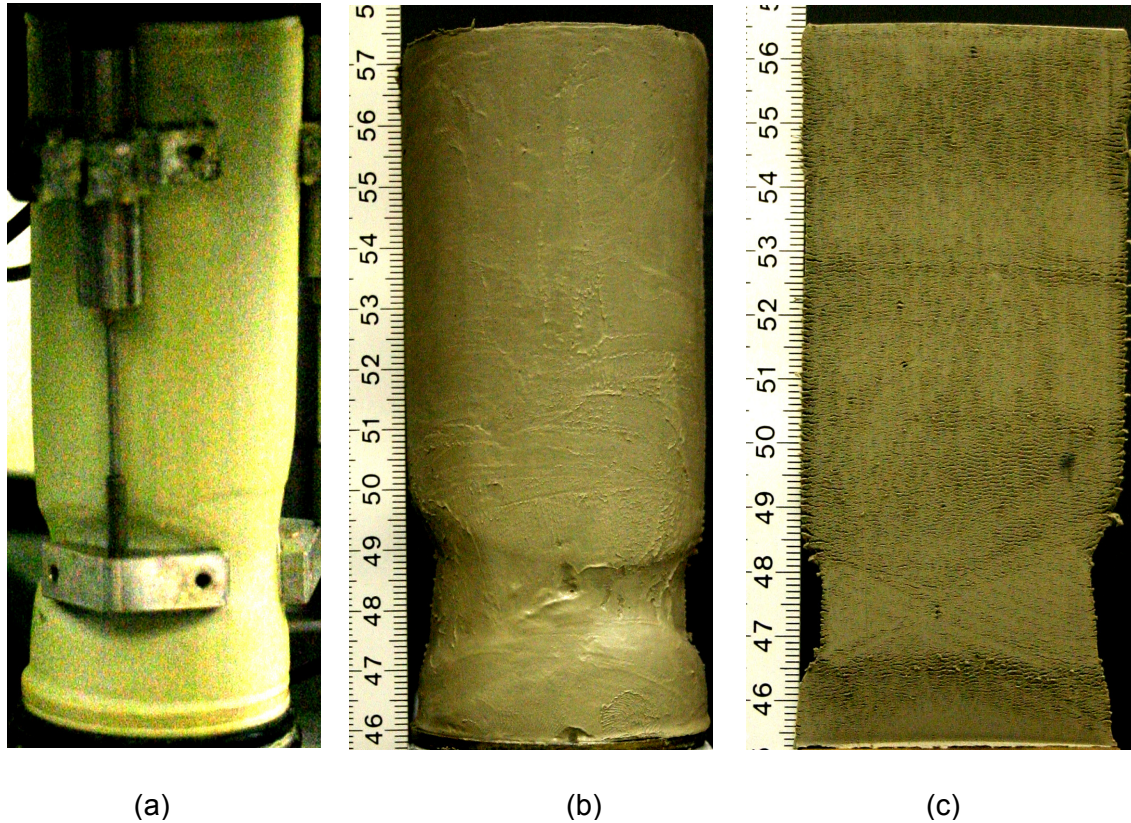
Fig. 5.20: Pictures of test S3T1 during dismounting: a) local LVDT mounted on the sample; b) failed sample with the failure shear zone developed at the location of the LVDT mounting; c) section through the sample and failure zone.

Here the radial laser scan data show a continuous radial sample deformation over the sample height for the consolidation and swelling stress path. No influence of the LVDT mounting on the radial displacement measurements is visible. Therefore it is assumed that the local LVDT mountings do not influence the deformation behaviour of the test sample at "small" strains. An undrained strain path was applied for the probing path. In the stress states close to failure, larger plastic strains occurred and necking developed around the bottom mounting of the LVDT. In test S2bT1, however, necking occurred in the middle of the sample and was not influenced by the LVDT mounting but most probably by the natural layering of the specimen. This indicates the difference in the failure behaviour between reconstituted and natural samples.
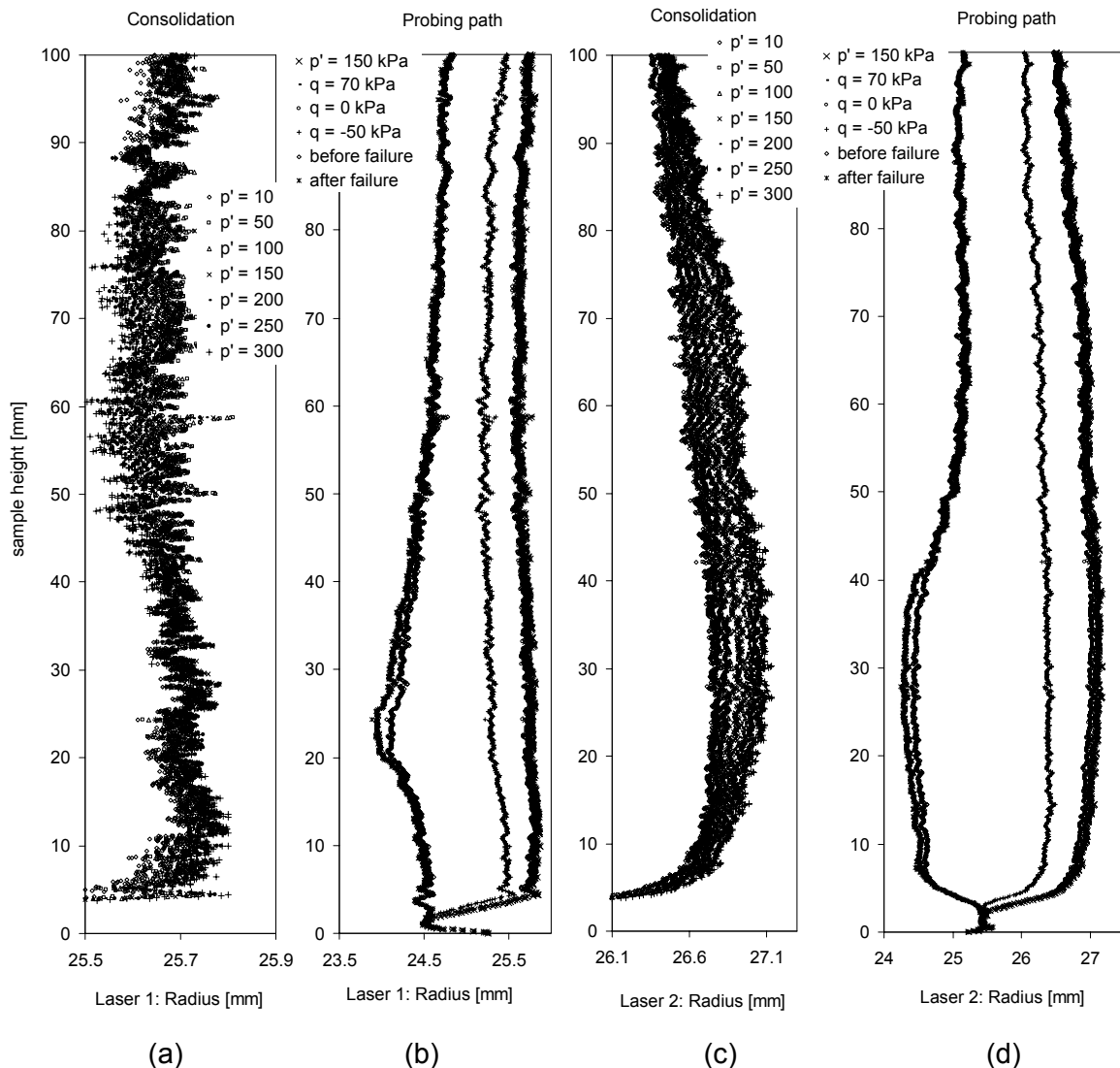
Fig. 5.21: Test S3T1: The sample radius calculated from the two laser scan data is plotted over the sample height at the given stress states (in [kPa]): (a) & (c) for the consolidation stress path; (b) & (d) for the probing stress path.

This difference is particularly visible in the extension tests. While the reconstituted sample failed at a location with stress concentration (in this case at the stiff LVDT mounting) and a shear zone developed (Fig. 5.20c), natural samples tend to fail along a weak layer e.g. Fig. 5.16 or Fig. 5.18, without developing a shear zone. This failure behaviour has previously been observed in compression tests on natural lacustrine clay samples (Plötze et al., 2003). The failure behaviour of lacustrine clay when sheared in extension was observed by the laser scan device

during the tests performed. The investigations are described in the following paragraph.

Two of the four tests in series 2 on which laser scans were performed were sheared in extension (S2T1 and S2bT1) to failure, where necking occurred in the sample. The development of necking could be observed due to the ability to scan the radial displacements over the entire sample height. Although only stress path tests were performed in test series 2 in extension, which lead to an abrupt failure of the sample, the development of necking just prior to failure was clearly visible. Unfortunately this necking developed in test S2T1 at the top of the sample and radial displacements were only measured over the bottom 100 mm sample height, so the entire magnitude was not measured. But in test S2bT1, as well as in test S3T1 of series 3, very promising data were measured and these are presented in the Appendix and analysed in Chapter 6.

6   Analysis of triaxial test results

6.1   Drained loading rate

The manual of soil laboratory testing (Head, 1986) defines a test as drained when: "the rate of strain is slow enough to ensure dissipation of any excess pore pressure." Different empirical formulations are suggested for the determination of this strain rate (e.g. Bucher, 2000), which give an estimation of the test time to failure depending on the drainage conditions, the consolidation coefficient of the tested material, the height of the sample and the desired degree of consolidation. The drained loading rate e.g. in m/s can be determined by assuming the displacements at failure, which tend to be dependent on the degree of overconsolidation of the tested sample. This is a very convenient and successful method for setting up a drained *strain path* test, which was originally the most common type of triaxial testing. With the improvement of stress regulation systems for triaxial test apparatuses, it is now possible to apply almost any triaxial *stress path* with the principal stress axis in axial and radial direction. But for drained *stress* path tests, it is necessary to define the stress rate e.g. in kPa/hour for which the excess pore pressure is dissipating. Trausch Giudici (2004) suggested a mean effective stress rate ($\dot{p}'$) of 2 kPa/hour for drained stress path tests on Swiss lacustrine clays. No verification of the drainage state in the sample was specified, however, a small degree of excess pore pressure build-up was indicated by deformations occurring during the pause following consolidation (Trausch Giudici, 2002).

Consequently, the pore pressure development during a constant stress path was investigated. Isotropically drained triaxial stress path tests were carried out to

determine the excess pore pressure developed as a function of loading rate. In parallel, Terzaghi′s one-dimensional consolidation theory was applied.

Birmensdorf clay (46707) was used for this study, which has the lowest permeability of all Swiss lacustrine clays investigated. The consolidation coefficient (c_v) of reconstituted Birmensdorf clay in a normally consolidated state was determined after Küng (2003) to be c_v = 0.1 mm^2/s for vertical effective stresses from 100 to 400 kPa. Therefore, the time period (t) after loading that is necessary to reach a degree of consolidation of 95 % in the middle of a 100 mm high triaxial sample, drained on both sides, can be calculated as:

$$t = T_v \frac{d^2}{c_v} = 1.129 \frac{50^2}{0.1} = 28\,222 \text{ sec} = 7.8 \text{ hours}$$

Eq. 6.1

But for drained stress path tests, the consolidation time is less important. More crucial is the magnitude of the excess pore water pressure e.g. after an hour, when the next load step is applied. This can be determined after Terzaghi′s one-dimensional consolidation theory by calculating the current time factor (T_v), the degree of consolidation (U) e.g. in the middle of the sample drained on both sides ($U_{z=d}$) and thus the excess pore pressure at this location. The excess pore pressure remaining in the middle of the previously described triaxial test sample after 1 hour′s consolidation can be calculated from:

$$T_v = \frac{tc_v}{d^2} = 0.144 \quad \rightarrow \quad U_{z=d} = 13 \text{ \%}$$

Eq. 6.2

Thereafter, the excess pore pressure in the middle of a 100 mm high Birmensdorf clay sample after 1 hour consolidation, with drainage at the top and bottom is 0.87 kPa for a vertical stress increment of 1 kPa. The question now is how the excess pore pressure develops when an additional vertical stress increment of 1 kPa is applied after another hour.

Therefore, the differential equation of the one-dimensional consolidation theory (Terzaghi, 1943)

$$\frac{\partial u}{\partial t} = c_v \frac{\partial^2 u}{\partial z^2}$$

Eq. 6.3

was numerically solved for these varying boundary conditions:

$$\frac{\partial u}{\partial t} = \frac{c_v}{\partial z^2}\left[u_{(z=i-1)} - 2u_{(z=i)} + u_{z=i+1}\right] \quad \rightarrow \quad u_{(z=1),t+\Delta t} = M\left[u_{(z=i-1)} - 2u_{(z=i)} + u_{(z=i+1)}\right]_t + u_{(z=i),t}$$

Eq. 6.4

Using:

$$M = \frac{\Delta t c_v}{\Delta z^2}$$

Eq. 6.5

where (Δt) is a function of the constant time step, (c_v) is the consolidation coefficient and (Δz) is a constant increment of sample height. This calculation converges for values of $M < 0.5$. A value for M of 0.384 was used with a time step Δt of 600 seconds and a height increment Δz of 12.5 mm. The pore pressure distribution $u_{(z=i),t+\Delta t}$ over the sample height was calculated for each time step (Fig. 6.1a). One kPa was added to the calculated pore pressure distribution every sixth time step, which equals a loading period of 1 hour (Fig. 6.1b). The calculation was done for 96 time steps or 16 hours in total and the result is shown in Fig. 6.2. The excess pore pressure converges towards 3 kPa in the middle of the sample, when applying a vertical stress increment of 1 kPa/hour and Terzaghi's consolidation theory.
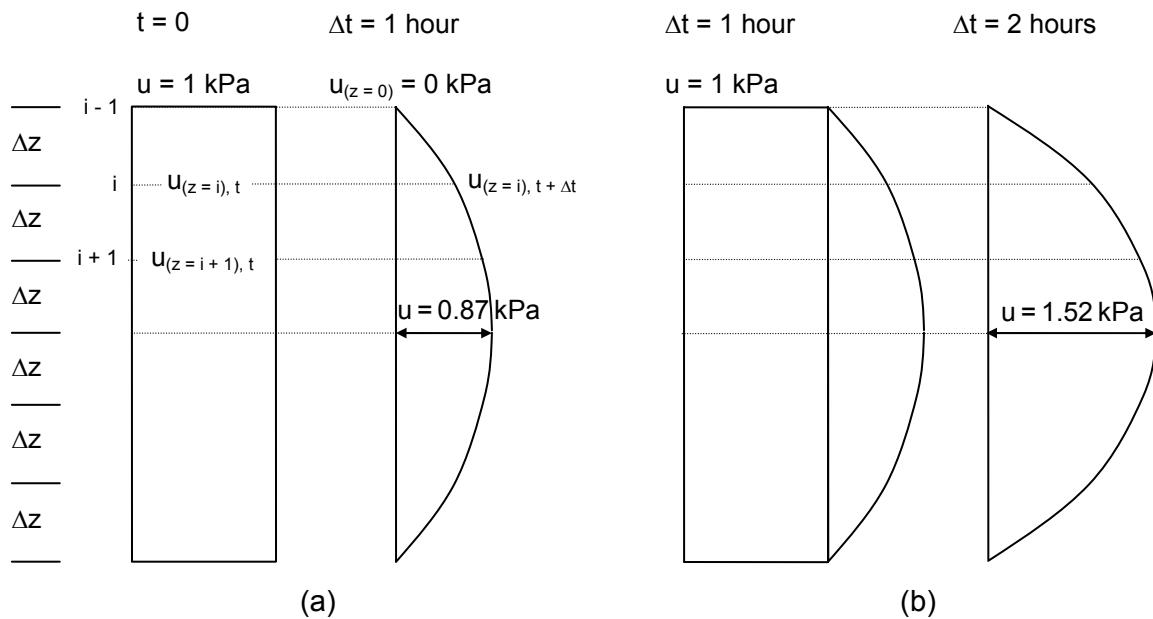
Fig. 6.1: Pore pressure distribution in a triaxial sample during a constant stress path.
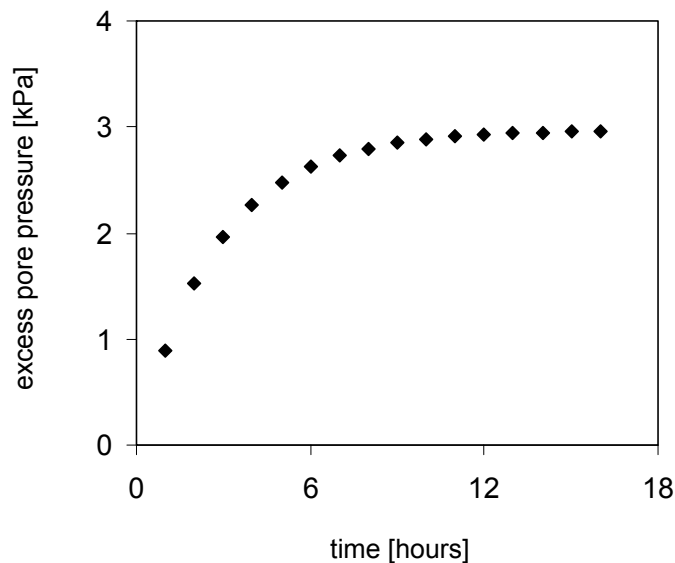
Fig. 6.2:   Development of the excess pore pressure in the middle of a 100 mm high triaxial sample of Birmensdorf clay, which is drained at both ends and loaded with a constant vertical stress rate of 1 kPa/hour.

These results refer to one-dimensional consolidation, whereas isotropic consolidation was applied in these experimental investigations. Triaxial samples with half the height of normal samples were placed in the triaxial apparatus. The sample was drained at the bottom and the pore water pressure was measured at the top. Filter paper was put on the top and bottom ends to distribute the pore pressure equally over the entire cross-sectional area. No filter paper was put on the surface of the sample to avoid any direct connection between the top and bottom pore water pressures. Each sample was loaded isotropically at different mean effective stress rates, with consolidation breaks in between. The development of the excess pore water pressure at the top of the sample was evaluated for the different stress rates and the results are shown in Fig. 6.3.

Additionally, drained tests were performed with an anisotropic stress path. In this case, the loading rate can either be described by the increment of p' or by the increment of q. This can result in significantly differing loading rates for different stress increment ratios ($\Delta\eta = q/p'$) when they are not equal to 1, 0 or -1. For example, for stress paths with a stress increment ratio of $\Delta\eta = 3$, the deviatoric

loading ratio described by $\Delta q = 1\,kPa$ would be three times faster than the loading ratio that is described by the increment $\Delta p' = 1\,kPa$.
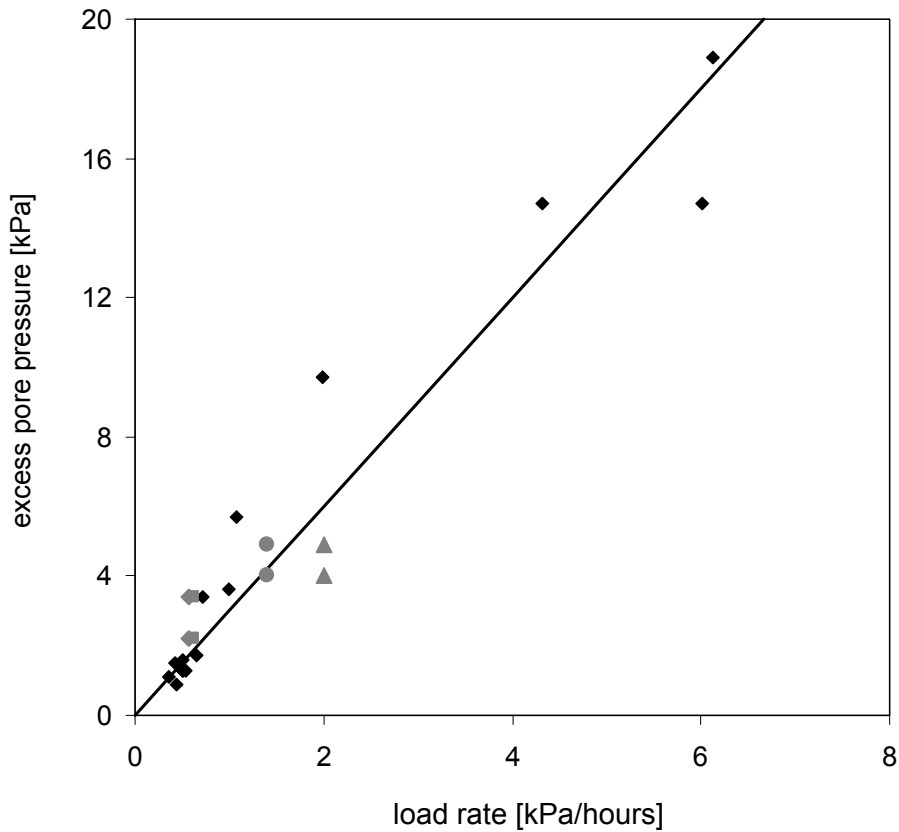
◆   isotropic stress path

———   theoretical solution after Terzaghi's one-dimensional consolidation theory

▲ $\eta = 1.4$: rate determined from the deviatoric stress increment

● $\eta = 1.4$: rate determined from the mean effective stress increment

■ $\eta = 1.1$: rate determined from the deviatoric stress increment

◆ $\eta = 1.1$: rate determined from the mean effective stress increment

Fig. 6.3:   Experimental results from the investigation of the development of excess pore water pressure for different loading rates in drained stress path tests and the theoretical solution after Terzaghi's one-dimensional consolidation theory.

Stress increment ratios of $\Delta\eta$ = 1.5 and 1.1 were chosen to investigate this behaviour. The results are also presented in Fig. 6.3. It can be seen that the pore pressure development for anisotropic stress paths differs only in the range of variation of the pore pressure measurement. Consequently, it was decided that for stress paths with $1 > \Delta\eta > -1$, an increment $\Delta p'$ should be set according to the drainage conditions and the deviatoric loading increment Δq then determined. The increment Δq is set for those stress paths with $\Delta\eta < -1$ or $\Delta\eta > 1$ according to the consolidation conditions, and the corresponding increment $\Delta p'$ is calculated from the stress increment ratio of the stress path applied.

Examination of the results of the experimental investigation and theoretical derivation shows despite assuming isotropic and one-dimensional consolidation respectively, both investigations give an excess pore pressure development of a similar magnitude at a common loading rate. Thus it is possible to choose a loading rate corresponding to an acceptable excess pore pressure build-up following a nominal drained loading increment at a specific stress increment ratio.

6.2   Yield characteristics of lacustrine clay

The stiffness response is highly non-linear during loading of soil. For a mechanical description of this behaviour, the stress-strain response curve is typically divided into zones with similar stiffnesses, and the boundary of these zones is identified by kinks in the stress-strain curve.

The number of zones selected for analysis depends on the desired accuracy of the material description. The most significant kink in the stress – strain curves is the transition from the "elastic" zone, where recoverable strains dominate, to the plastic zone, where irrecoverable strains dominate. The stress at this kink is called the yield stress and defines the yield surface in terms of the stress variants adopted, e.g. $q - p'$, $\sigma_v' - \sigma_h'$ or $\sigma_a' - \sigma_r'$ space. Additional zones can be defined around the current stress state inside this yield surface, e.g. Mröz (1967). Jardine (1992) defined two additional surfaces.

6.2.1 Yielding

The triaxial test data of the probing stress paths were analyzed according to the stiffness framework proposed by Jardine (1992) and introduced in Chapter 1. The location of the yield surfaces was evaluated by identifying the corresponding kinks in the stress-strain plots, as described by Smith et al. (1992). The stress-strain invariants δq - $\delta \varepsilon_s$ and $\delta p'$ - $\delta \varepsilon_v$ of the probing stress paths were plotted for the evaluation and are presented in the Appendix. Consequently, the origin of stresses in these plots is the consolidation stress ($p' = 150\,kPa$ and $q = 112.5\,kPa$) and the strains are set to zero at the start of the probing stress path.

For those probing stress paths where the deviator stress stayed constant during reloading (S2T2 & S2T3), both strain invariants $\delta \varepsilon_s$ and $\delta \varepsilon_v$ were plotted versus $\delta p'$. Similarly, for those tests in which the mean effective stress remained constant during reloading (S2T4, S2T1 & S2bT1), both strain invariants were plotted over δq.

The evaluation process for the yield point determination is presented in Fig. 6.4 for the first test of series 2 (test S2T1). The δq - $\delta \varepsilon_s$ plots (Fig. 6.4a) are presented at different scales (Fig. 6.4b-d) as well as the $\delta p'$ - $\delta \varepsilon_v$ plot (Fig. 6.4e). From the largest scale δq - $\delta \varepsilon_s$ plot (Fig. 6.4b), it can be seen that the resolution of the test data is not high enough to permit determination of the exact location of Y1. This was subsequently assumed to be circular and was located around the current stress state in the $q - p'$ space, with a circle radius of 0.5 kPa for Bothkennar clay (Smith et al., 1992). The δq - $\delta \varepsilon_s$ plot for $0 \leq |\delta q| \leq 40\,kPa$ indicates a kink in the curve at a deviator stress increment of -17 kPa with a corresponding shear strain increment of -0.043 % (Fig. 6.4c). This stress state was taken to be the Y2 point. The third plot (Fig. 6.4d) of the δq - $\delta \varepsilon_s$ data for $0 \leq |\delta q| \leq 180\,kPa$ indicates the start of the transition from zone 3 to zone 4, but does not show a distinct kink in this test. Therefore, the δq - $\delta \varepsilon_v$ plot was analysed, which shows a significant kink at a deviator stress increment of -163 kPa. This stress state was taken to define the Y3 point. Typically, both yield points (Y2 & Y3) are not visible in every stress-strain increment plot of all the tests.
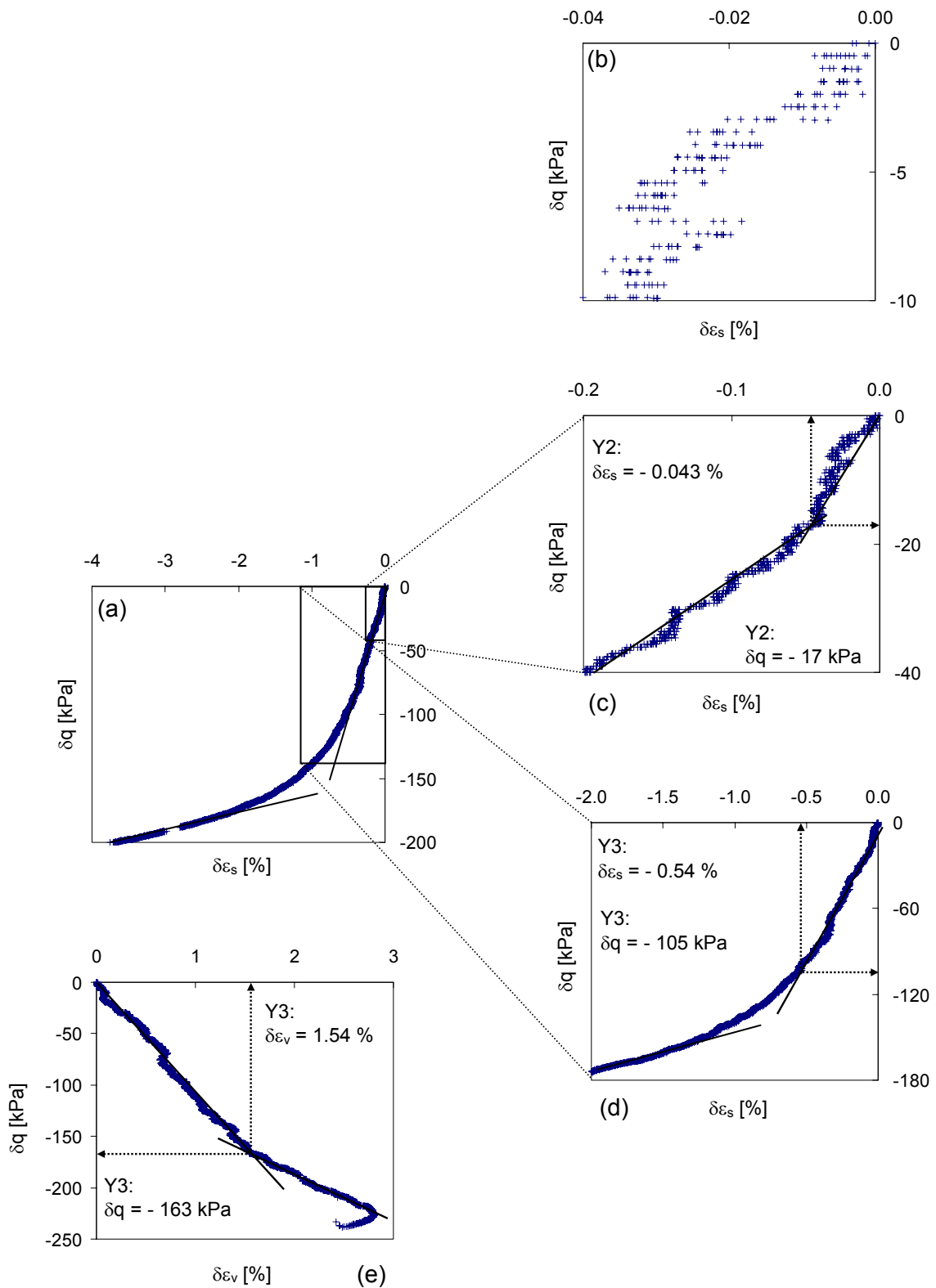
Fig. 6.4: Yield point evaluation method presented on the data of test S2T1; (a) $\delta q - \delta \varepsilon_s$ plot; (b) $\delta q - \delta \varepsilon_s$ plot at very small strains; (c) $\delta q - \delta \varepsilon_s$ plot at very small strains, Y2 determination; (d) $\delta q - \delta \varepsilon_s$ plot, Y3 determination; (e) $\delta q - \delta \varepsilon_v$ plot.

Therefore, only those stress points, where a significant kink was detected, were used for further comparative studies. All probing data of the thirteen tests of series 2 were evaluated in this way and the process and results for each test are shown in the Appendix.

For comparison, the resulting yield stress points were transferred to a q - p' plot, which is shown in Fig. 6.5, as well as the previously identified critical state line in compression and extension (Fig. 5.9). In the presentation of the yield points Y2 and Y3, a distinction is made between those points derived from the δq - $\delta \varepsilon_s$ and δq - $\delta \varepsilon_v$ plots, and those determined from the $\delta p'$ - $\delta \varepsilon_v$ and $\delta p'$ - $\delta \varepsilon_s$ plots, respectively.
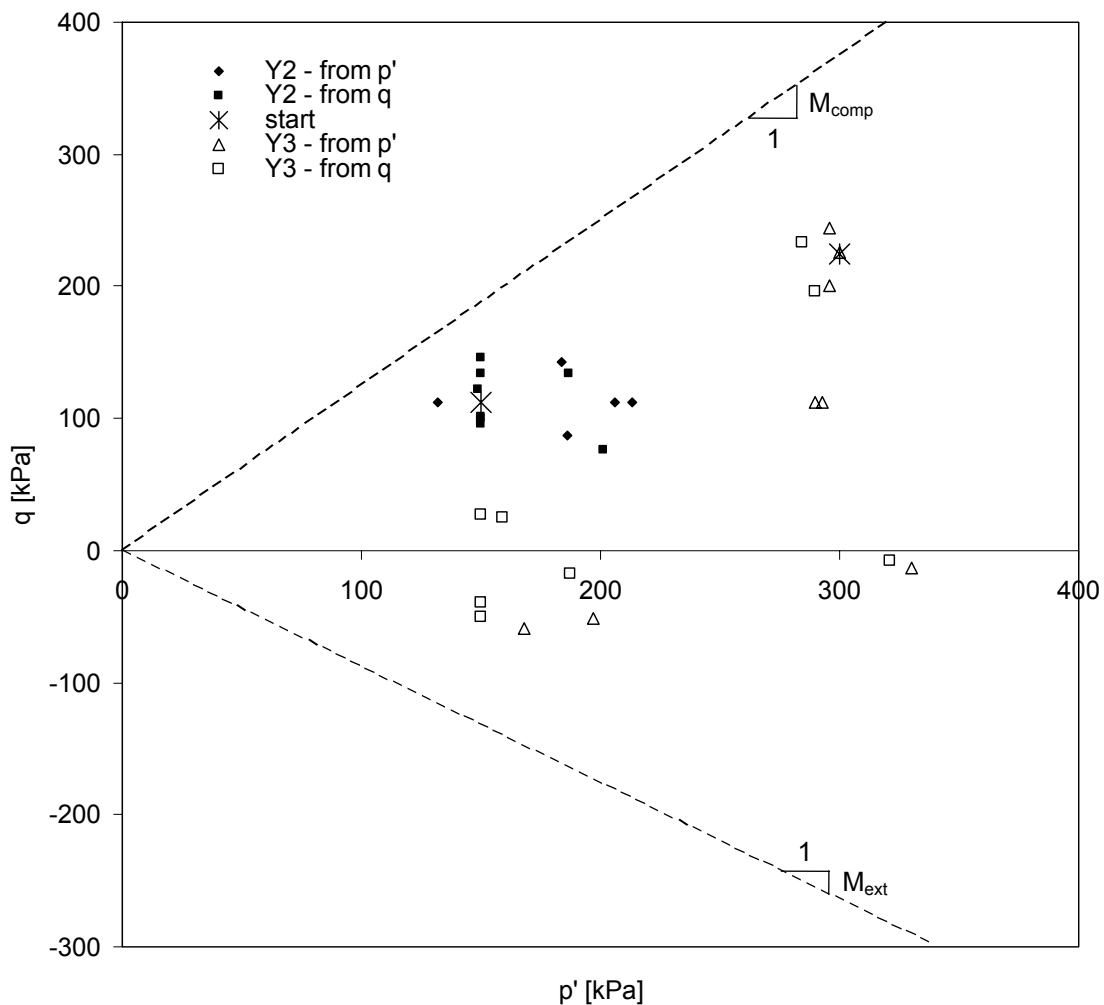
Fig. 6.5:   Comparison of the yield point analysis of test series 2 for the reload path.

Stress points derived from the δq - $\delta\varepsilon_s$ and δq - $\delta\varepsilon_v$ plot are named " from q" and those points derived from the $\delta p'$ - $\delta\varepsilon_v$ and $\delta p'$ - $\delta\varepsilon_s$ plot are named "from p' ". The crosses in Fig. 6.5 indicate the start point of the probing stress path (at q = 112.5 kPa, p' = 150 kPa), and the pre-consolidation stress state (at q = 225 kPa, p' = 300 kPa).

Comparison of the yield stress states Y2 determined from the δq - $\delta\varepsilon_s$ plot with those determined from the $\delta p'$ - $\delta\varepsilon_v$ plot shows good agreement. The same comparison for the Y3 yield points shows that the yield stress states that are derived from the δq - $\delta\varepsilon_s$ plot are closer to the stress reversal point than those derived from the $\delta p'$ - $\delta\varepsilon_v$ plots. This effect is particularly noticeable for the probing paths in extension. Remembering the evaluation of the yield points for test S2T1 presented in Fig. 6.4, in the δq - $\delta\varepsilon_s$ plot the yield stress state Y3 was not detectable although a transition zone was visible, whereas a distinct kink was visible in the δq - $\delta\varepsilon_v$ plots. This indicates that the volumetric strain increments appear to define the Y3 yield stress state more clearly. Therefore, for further evaluation and discussion of the Y3 points, the stress points that were derived from the volumetric strain increments are used for the extension tests.

The surface denoted by the Y2 stress points can be fitted by an ellipse, with the main axis parallel to the p' axis (Fig. 6.6). When trying to fit a surface through the Y3 stress points, it appears that the points derived from test S2bT3, with the probing path Θ = 325°, do not agree with the results of all other tests (Fig. 6.6). Yielding appears to start at much higher stress for this particular test. No explanation was forthcoming from further inspection of the data, but this yield point was not used for further evaluations, and a curve was fitted through the remaining Y3 points (Fig. 6.6). The shape of the curve is not congruent with the ellipse through the Y2 points.

Comparison of the test results on lacustrine clay with the data from Bothkennar clay, which are presented by Smith et al. (1992), show a similar shape of the Y3 surface on the compression side. In extension, the surface derived for Bothkennar clay is larger than the indications from Fig. 6.5 for lacustrine clay showed. The

shape of the Y2 surface for Bothkennar clay is more circular than elliptical and is centred on q = 18 kPa and p' = 33 kPa with OCR ≈ 1.5. The diameter of the Y2 surface for Bothkennar clay is about 12 kPa and the maximum extension of the Y3 surface in the direction of the p' axis is 50 kPa. The Y2 surface for the lacustrine clay has an extension of 65 to 80 kPa in the direction of the p' axis and the Y3 surface passes through q = 225 kPa and p' = 300 kPa due to the preconsolidation stress. The size of the Y2 surface of the lacustrine clay, measured parallel to the p' axis is a quarter of the Y3 surface whereas the comparable ratio for the Y2 surface of the Bothkennar clay, in the stress states quoted above, is a fifth. Consequently, the size of the Y2 surface of the lacustrine clay investigated, is large compared to that of Bothkennar clay.
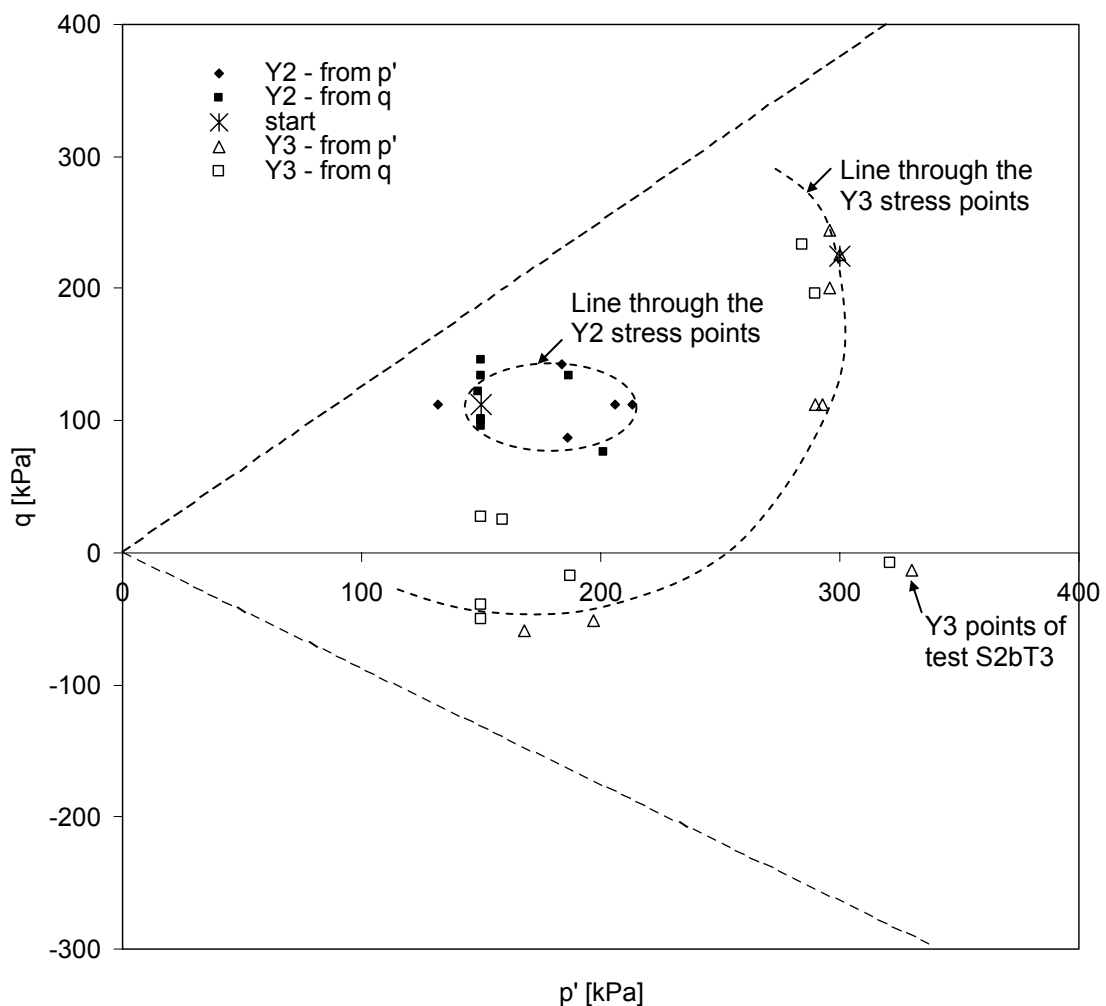
Fig. 6.6: Specification of the yield points and surfaces of test series 2 for the probing stress paths.

155

It was therefore of interest to verify the size of the Y2 surface. The Y2 surface is crossed by any stress path with an extension larger than the Y2 surface. All tests were first consolidated and allowed to swell before the probing stress path was applied. During consolidation in the triaxial apparatus, the influence on the strain of sample preparation and test setup is large, so the Y2 points are not detectable for this consolidation path. But the Y2 points are visible along the subsequent the swelling path. Consequently, the stress-strain increment curves of the swelling path were evaluated. This evaluation was performed with the same method as for the probing path (Fig. 6.4), by detecting the kink in the δq - $\delta \varepsilon_s$ and $\delta p'$ - $\delta \varepsilon_v$ plots.
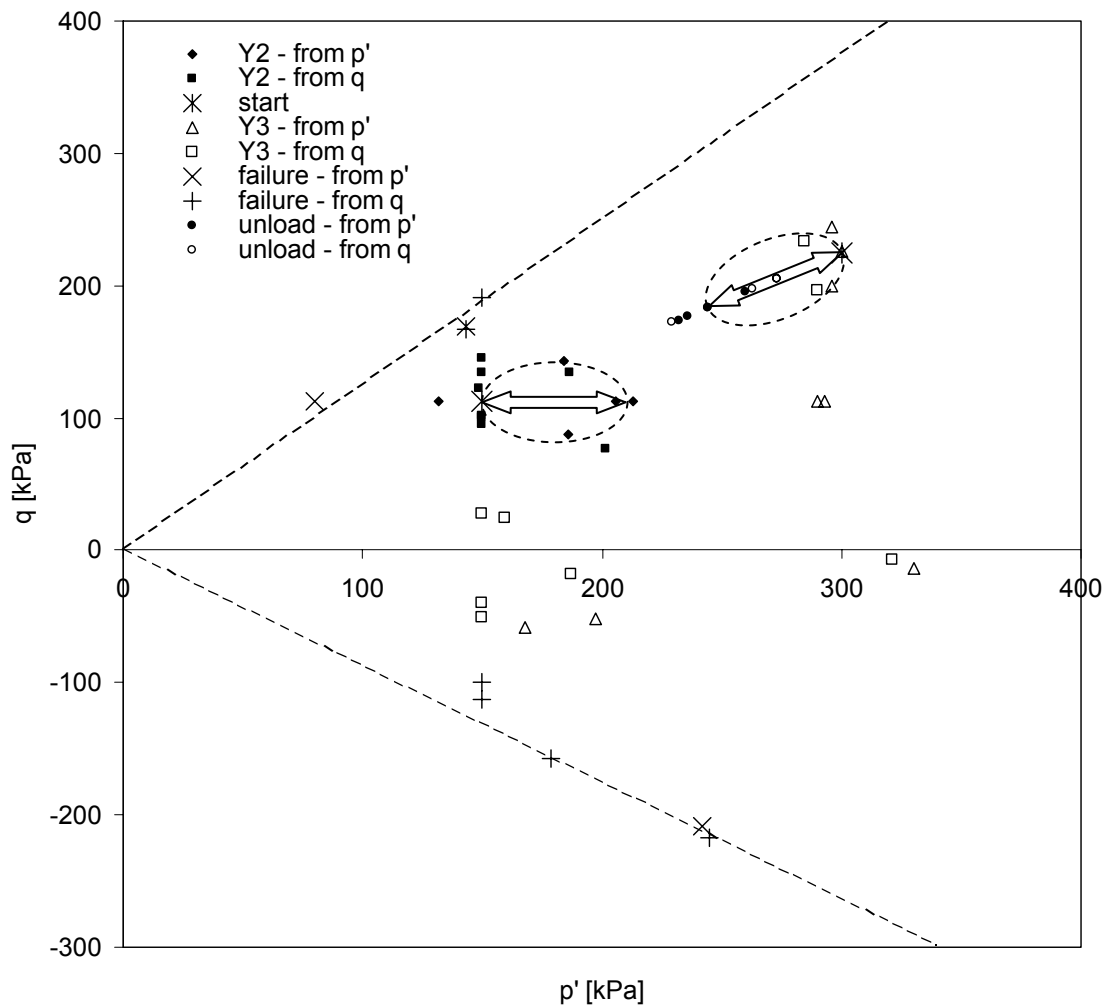
Fig. 6.7: Comparison of the yield point analysis of test series 2 for the swelling and probing path.

Unloading gives less stable responses, so the fluctuations in the results are greater. However, the yield stress states determinable in the data evaluation for each test are presented in the Appendix and shown in Fig. 6.7. The two arrows with the same length in Fig. 6.7 show that the Y2 surface for the unloading path has the same extension on average as the Y2 surface of the probing paths allowing the size of the Y2 surface to be verified.

6.2.2 Strain increment ratio at yielding

The plastic strain increment ratio is needed for the identification of the shape of the plastic potential surface. The plastic strain increment ratio cannot be derived directly from the displacement measurement data of the tests, because only the total displacements (plastic and elastic components) are measured in the tests. Some authors assume that for straining in zone 4, the elastic component of strains is small enough compared to the plastic component to be ignored, e.g. Wheeler (1997). This might be acceptable for straining in zone 4 (Fig. 1.2), but it is definitely not true for straining in zone 1, where only elastic strains are assumed to occur.

However, to derive the plastic strain increment[‡] ratios at the yield surfaces, the total strain increment ratios[§] at the yield points Y2 and Y3 are determined first. This was done in the invariant strain formulation: ε_s & ε_v. The $\delta\varepsilon_s$ - $\delta\varepsilon_v$ plots were generated, and at the strain levels corresponding to the yield stress states the inclination of the strain curves, which equal the strain increment ratios, were determined. The evaluation process for test S2T1 is presented in Fig. 6.8. At the yield stress states ($\delta\varepsilon_s = -0.043$ % for Y2 and $\delta\varepsilon_v = 1.54$ % for Y3), the strain increment ratios were determined to be $\delta\varepsilon_s / \delta\varepsilon_v = -0.42$ and $\delta\varepsilon_s / \delta\varepsilon_v = -2.3$, respectively.

[‡] Although some of the changes in strains might be negative, and therefore should be described as decrements, for simplicity the general term increment will be used to signify a change in strain.

[§] The term „total strain increment ratio" is used for the strain increment ratio composed of the elastic and the plastic components.
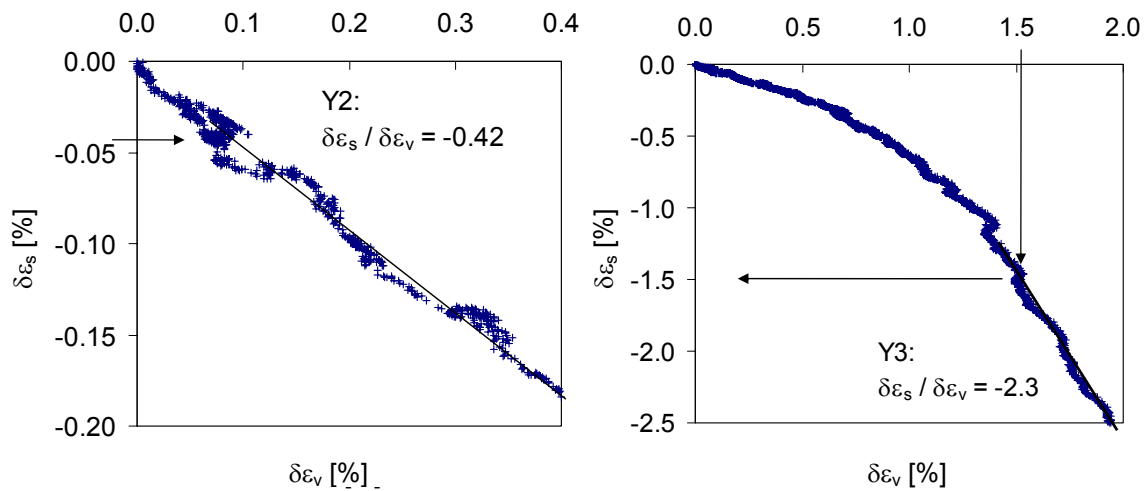
Fig. 6.8: Strain increment ratio evaluation method presented on the data of test S2T1.

The results of all tests are plotted at the corresponding yield points in the q - p' plot, Fig. 6.9. The length of the vectors plotted is not related to the test results.

The horizontal component dominates the strain increment ratio at the Y2 yield points, indicating that greater volumetric strain components are mobilised than shear strains. It can be seen that the volumetric strains are positive for probing stress paths with increasing mean effective stresses, and negative for probing stress paths with decreasing mean effective stresses. This was expected as positive volumetric strains correspond to volume decrease of the sample.

Analysis of the strain increment ratio at the Y3 yield points shows that their direction depends on the probing stress path. The shear strains dominate for the shear tests in extension and the volumetric compressive strains control the deformation behaviour for the recompression stress path.

6.2.3 Components of the strain increment ratio: elastic - plastic

The next step in the evaluation of the plastic strain increment ratio is the determination of the elastic component of the total strain increment ratio. Pure elastic strains are assumed to develop in zone 1. Unfortunately, the resolution of the load and displacement measurement data of the tests performed is not high enough to derive any results for zone 1. Therefore, other techniques have to be used for the determination of the elastic stiffness. Possible methods include

oedometer tests with a suitable resolution of the load and displacement measurement, resonant column tests or bender element tests. A new triaxial apparatus with bender elements installed in the top cap and bottom pedestal of the cell (Trausch Giudici, 2004) was available and an intensive investigation, in terms of evaluation method applied to the bender element test data, was performed by Trausch Giudici (2004). Bender elements apply a shear wave, which implies shear strains of less than 10^{-3} %, and the shear modulus can be calculated from the travel time and distance of the applied wave through the test sample.
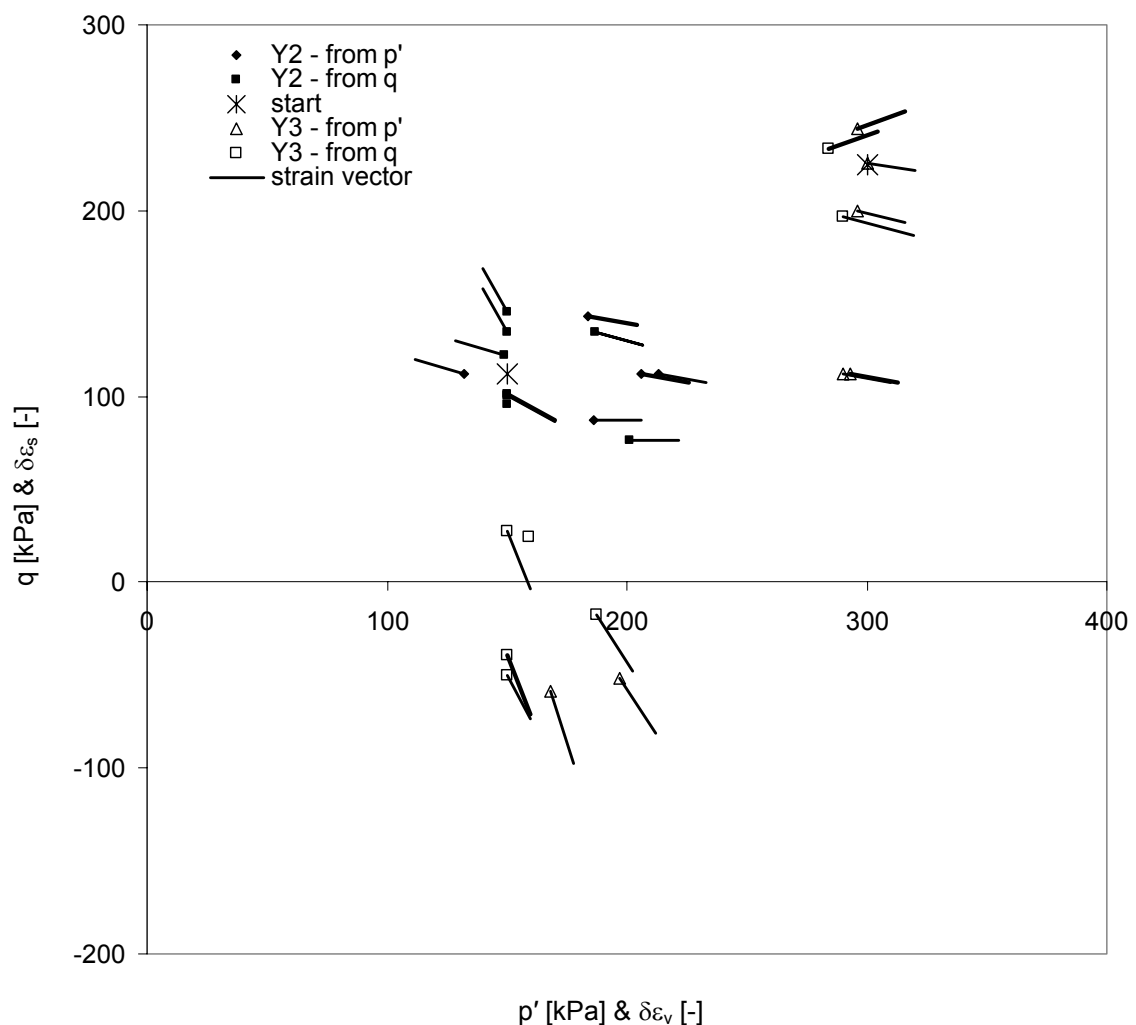
Fig. 6.9: Total strain increment ratios at the yield points of the probing path of tests of series 2.

The question is whether a strain level of 10^{-3} % is small enough to detect the purely elastic stiffness. Linear elastic response occurs in zone 1, according to the stiffness framework proposed by Jardine (1992), which is applied here. The size of zone 1 is given in the literature for a range of soils. Smith et al. (1992) defined zone 1 for Bothkennar clay, based on triaxial test results, as $\Delta\varepsilon_s$ = 0.001 % and Δq = 0.5 kPa. Jardine (1992) presented the analysis of torsional shear test results on Toyoura sand, carried out by Teachavorasinskun (1989) and reported elastic strains at the boundary of zone 1 of $\Delta\varepsilon_s$ = $6\cdot10^{-4}$ % at Δq = 1 kPa.

Therefore, the stiffness in zone 1 for clays can be measured with bender elements, although whether this stiffness represents the maximum stiffness of the soil following reloading is not specified. But when assuming that the behaviour in zone 1 is linear elastic, by applying the stiffness framework of Jardine (1992), any stiffness detected within the zone is assigned as the "elastic" stiffness.

Jardine (1992) discussed contact mechanics theories (Bowden & Tabor, 1964; Johnson, 1985) that throw doubt on the existence of a linear elastic region and propose that any response has to be non-linear elastic. Unfortunately, measurement of this response is not possible yet with a sufficient degree of accuracy. Therefore, it is not further considered here and the shear modulus determined by the bender elements is adopted for the calculation of elastic strains.

Bender element tests were performed on triaxial test S2bT4. The data evaluation method is presented in Chapter 5.2.3 and the results are shown in the Appendix. An average G_{max} value of 98 MPa was determined for natural Kloten clay, at a stress state of q = 112.5 kPa and p' = 150 kPa with a previous one-dimensional consolidation history to greatest stresses of q = 225 kPa and p' = 300 kPa and subsequent drained swelling.

This is one of the parameters used to describe the elastic material behaviour. Assuming the soil behaves isotropically, only one more parameter is necessary to determine the elastic component of a strain increment ratio. This parameter can either be the compression modulus (K) or the Poisson's ratio (v'). The compression modulus can be measured in oedometer tests to a certain degree of accuracy or with piezoceramic transducers, which produce compression waves.

But as discussed in Trausch Giudici (2004), measurement of the compression modulus with the piezoceramic elements installed in the top cap and bottom pedestal of the triaxial apparatus, which apply compression waves with the aim of measuring the travel time, was not successful. The Poisson's ratio can either be estimated by empirical correlations based on soil plasticity e.g. Wroth (1975) or Lade (1979), or it can be determined from displacement measurement data from laboratory tests. As the radial strains were measured by the laser scan device, these data were used. Isotropic elastic material is described by the following stiffness matrix (Timoshenko & Goodier, 1951):

$$
\begin{bmatrix} \delta\varepsilon_1 \\ \delta\varepsilon_3 \end{bmatrix} = \frac{1}{E} \cdot \begin{bmatrix} 1 & -2v' \\ -v' & 1-v' \end{bmatrix} \cdot \begin{bmatrix} \delta\sigma_1' \\ \delta\sigma_3' \end{bmatrix}
\qquad\text{Eq. 6.6}
$$

Axial and radial stresses are applied in triaxial tests and it is assumed that these are aligned with the principal stress directions 1 and 3. However, the subscripts a (axial) and r (radial) are adopted instead of 1 and 3 for greater clarity in the following evaluations.

$$
\begin{bmatrix} \delta\varepsilon_a \\ \delta\varepsilon_r \end{bmatrix} = \frac{1}{E} \cdot \begin{bmatrix} 1 & -2v' \\ -v' & 1-v' \end{bmatrix} \cdot \begin{bmatrix} \delta\sigma_a' \\ \delta\sigma_r' \end{bmatrix}
\qquad\text{Eq. 6.7}
$$

Eq. 6.6 shows that the Poisson's ratio for unconfined compression tests ($\delta\sigma_r' = 0$) is defined as $v' = -\delta\varepsilon_r / \delta\varepsilon_a$ and for one-dimensional conditions ($\delta\sigma_r' = K_0\delta\sigma_a'$ & $\delta\varepsilon_r = 0$) the Poisson's ratio is $v' = K_0 / (1 + K_0)$. For tests with stress paths other than one-dimensional or unconfined compression, the Poisson's ratio is defined as a function of the stress and strain increment ratios:

$$
v' = \frac{1 - \dfrac{\delta\varepsilon_r}{\delta\varepsilon_a} \dfrac{\delta\sigma_a'}{\delta\sigma_r'}}{1 + \dfrac{\delta\sigma_a'}{\delta\sigma_r'} - 2\dfrac{\delta\varepsilon_r}{\delta\varepsilon_a}}
\qquad\text{Eq. 6.8}
$$

The Poisson's ratio can then be calculated from Eq. 6.8 for various stress path directions ($\delta\sigma_a'/\delta\sigma_r'$), or vice versa, the strain increment ratio ($\delta\varepsilon_r/\delta\varepsilon_a$) can be calculated for a given Poisson's ratio and compared to data from measurements:

$$\frac{\delta \varepsilon_r}{\delta \varepsilon_a} = \frac{1 - v' \dfrac{\delta \sigma_a'}{\delta \sigma_r'} - v'}{\dfrac{\delta \sigma_a'}{\delta \sigma_r'} - 2v'}$$

Eq. 6.9

Before the strain increment ratio is determined from the laser scan data, it must be ascertained that the Poisson's ratio is determinable from the strain increment data arising from any stress path direction. Therefore, Eq. 6.9 is rewritten as:

$$\frac{\delta \sigma_a'}{\delta \sigma_r'} \frac{\delta \varepsilon_r}{\delta \varepsilon_a} - 2v' \frac{\delta \varepsilon_r}{\delta \varepsilon_a} = 1 - v' \frac{\delta \sigma_a'}{\delta \sigma_r'} - v'$$

Eq. 6.10

This shows that if:

$$2 \frac{\delta \varepsilon_r}{\delta \varepsilon_a} = \frac{\delta \sigma_a'}{\delta \sigma_r'} + 1$$

Eq. 6.11

or:

$$\frac{\delta \varepsilon_r}{\delta \varepsilon_a} \frac{\delta \sigma_a'}{\delta \sigma_r'} = 1$$

Eq. 6.12

the strain increment ratio is independent of the Poisson's ratio. So, the Poisson's ratio cannot be determined from the strain increment ratio of these particular stress paths. By solving Eq. 6.12 and Eq. 6.11 for the stress increment ratio: $\dfrac{\delta \sigma_a'}{\delta \sigma_r'} \left(\dfrac{\delta \sigma_a'}{\delta \sigma_r'} + 1 \right) = 2$, the two roots give effective stress increment paths $\dfrac{\delta \sigma_a'}{\delta \sigma_r'} = 1$ and $\dfrac{\delta \sigma_a'}{\delta \sigma_r'} = -2$ from which the Poisson's ratio is indeterminable.

The stress increment ratio $\dfrac{\delta \sigma_a'}{\delta \sigma_r'} = 1$ corresponds to an isotropic load path, and the strain increment ratio is $\dfrac{\delta \varepsilon_r}{\delta \varepsilon_a} = 1$, which is independent of the Poisson's ratio. The stress increment ratio $\dfrac{\delta \sigma_a'}{\delta \sigma_r'} = -2$ represents the shear path in extension, and the corresponding strain increment ratio is $\dfrac{\delta \varepsilon_r}{\delta \varepsilon_a} = -\dfrac{1}{2}$. These calculations are based on isotropic elastic material behaviour.

Now the strain increment ratio determined from the assumption of isotropic elastic material behaviour can be compared to the measured test data. Thirteen probing stress path tests were performed in test series 2. Laser scanning was done on four of these tests: test S2T1, S2aT1, S2bT1 & S2cT1. The nominal probing effective stress increment ratio was -2 in the tests S2T1 and S2bT1, 2 in test S2aT1, and 2.23 in test S2cT1. So for two tests, the Poisson's ratio can not explicitly be determined but the strain increment ratio has to be -0.5 according to isotropic elastic theory. For the remaining two tests, the Poisson's ratio can be calculated from the stress and strain increment ratios. Consequently, the strain increment ratio is determined for all four tests, either to compare the measured values with the theoretical calculated values (for tests S2T1 & S2bT1), or to determine the Poisson's ratio (from tests S2aT1 & S2cT1). Determination of the strain increment ratio, with the axial strain increments $\delta\varepsilon_a$ plotted over the radial strain increments $\delta\varepsilon_r$, is presented in Fig. 6.10 to Fig. 6.13.

The same sign convention is applied to the laser data, meaning that positive radial strain increments (Fig. 6.10 & Fig. 6.12) imply radial compression and negative axial strain increments (Fig. 6.10, Fig. 6.11 & Fig. 6.12) imply axial extension. The data are plotted for a selection of horizontal cross-sections. The number in the legend gives the height in millimetres from the bottom of the sample at which the measurements were taken. The data from each plot are evaluated by deriving an average inclination of the strain increment ratio, which is given by a thick line in each of the plots from Fig. 6.10 to Fig. 6.13.

An average ratio of radial to axial strain increments of -0.68 was determined for the tests S2T1 and S2bT1 with a probing stress path of $\delta\sigma_a'/\delta\sigma_r' = -2$ and $\delta q/\delta p' = -\infty$. The radial strain increments were zero for test S2aT1, with a probing stress path of $\delta\sigma_a'/\delta\sigma_r' = 2$ and $\delta q/\delta p' = 0.75$. The strain increment ratio was determined as 0.09 on average for test S2cT1, with a probing stress path of $\delta\sigma_a'/\delta\sigma_r' = -2.23$ and $\delta q/\delta p' = 0.9$.

The probing stress path was applied after the consolidation and swelling path at an initial stress state of $p' = 150\,kPa$ and $q = 112.5\,kPa$ for all four tests, as descried in Chapter 5.
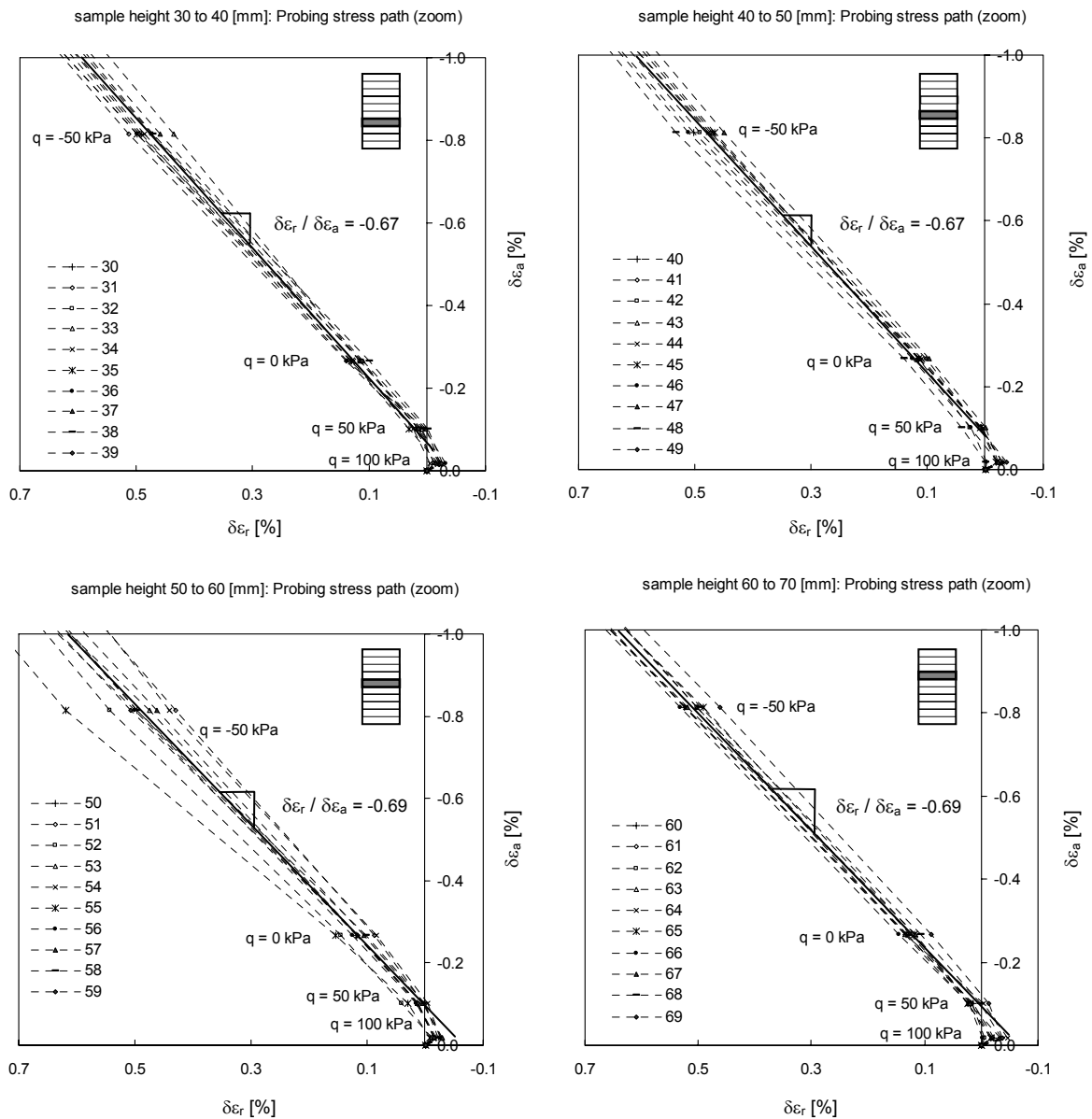
Fig. 6.10: Radial laser scan data from test S2T1 ($\delta\sigma_a'/\delta\sigma_r' = -2;\ \delta q/\delta p' = -\infty$) plotted versus the axial strain increment data for selected stress states over the middle 40 mm of the sample height.

The strain plots of the two extension tests S2T1 & S2bT1 (Fig. 6.10 & Fig. 6.12) have a "crook" at the start of the probing path. For the analysis of anisotropy in the small strain region, it is important to consider the strain increment ratio at small strains. Therefore this "crook" was further investigated to examine how the strain increment ratio changes following the beginning of the probing path. The data of

every laser scan at the start of the probing test was plotted (Fig. 6.14) and the strain state at the predetermined Y2 yield point was marked.

sample height 30 to 40 [mm]: Probing stress path (zoom)

sample height 40 to 50 [mm]: Probing stress path (zoom)

sample height 50 to 60 [mm]: Probing stress path (zoom)

sample height 60 to 70 [mm]: Probing stress path (zoom)
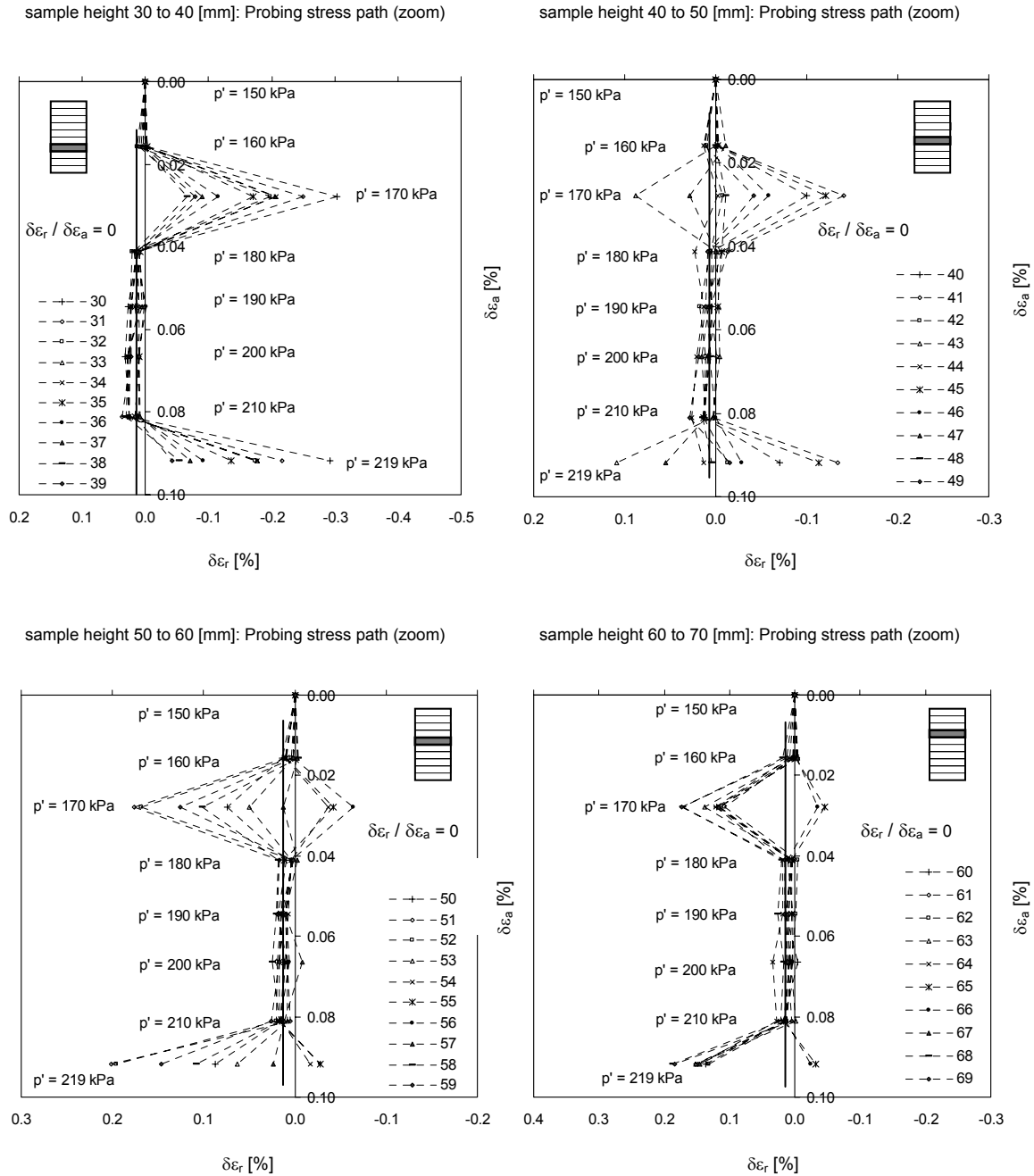
Fig. 6.11: Radial laser scan data from test S2aT1 ($\delta\sigma_a' / \delta\sigma_r' = 2$; $\delta q / \delta p' = 0.75$) plotted versus the axial strain increment data for selected stress states over the middle 40 mm of the sample height.

sample height 50 to 50.96 [mm]: Probing stress path (zoom)
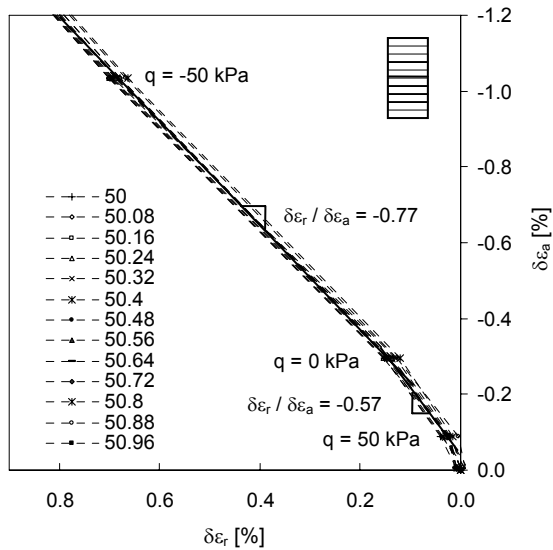
sample height 51.04 to 52 [mm]: Probing stress path (zoom)
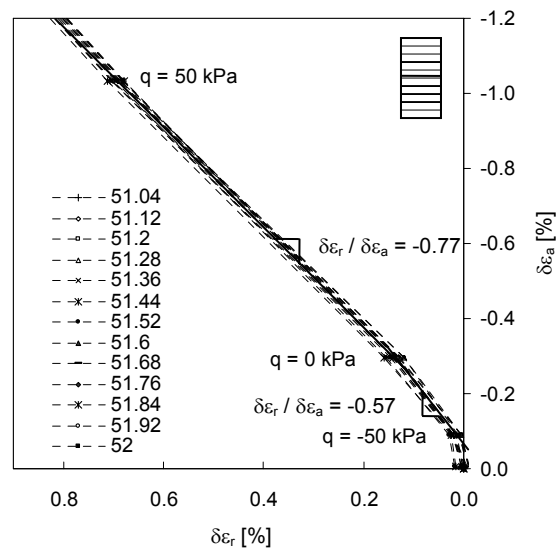
sample height 52.08 to 53.04 [mm]: Probing stress path (zoom)
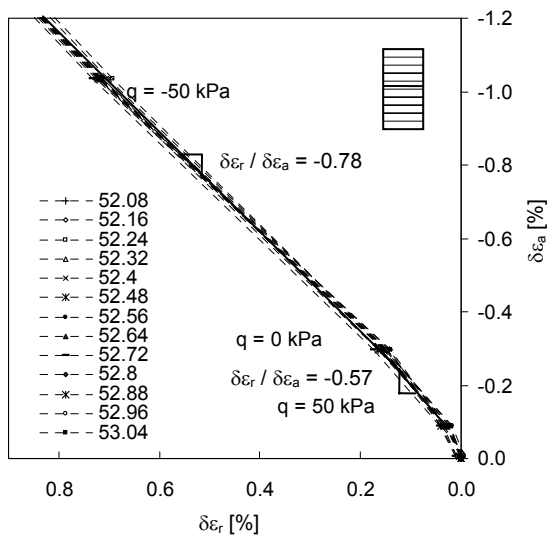
sample height 53.12 to 54.08 [mm]: Probing stress path (zoom)
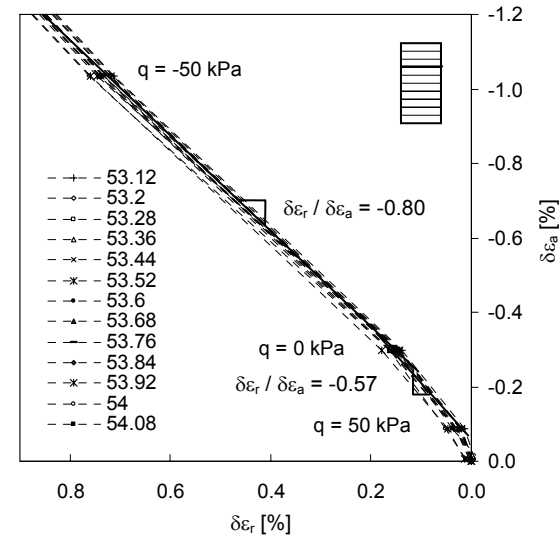
Fig. 6.12: Radial laser scan data from test S2bT1 ($\delta\sigma_a' / \delta\sigma_r' = -2$; $\delta q / \delta p' = -\infty$) plotted versus the axial strain increment data for selected stress states for a vertical length of 4 mm near the middle of the sample.

The curves (Fig. 6.14) show that at the very beginning of the probing stress path, the axial and radial strain increments are negative, representing an expansion of the sample radius and axial extension. This equals the strain direction that occurred during swelling in the previous unloading path. In the newly applied extension stress path, the sample will continue to expand in the axial direction

while the sample deformations will change from expansion to compression in the radial direction.
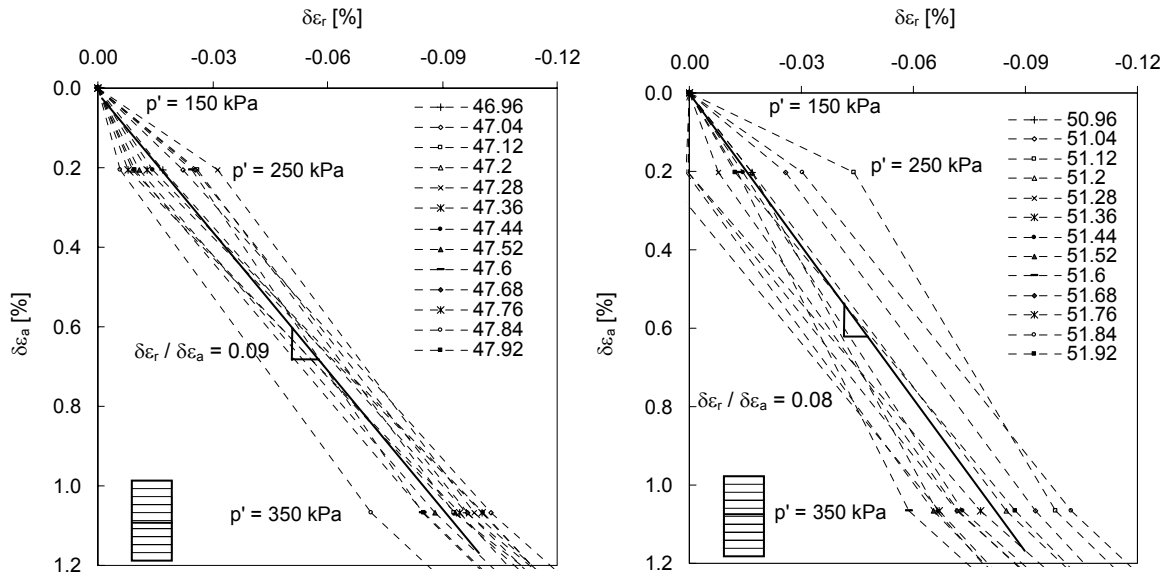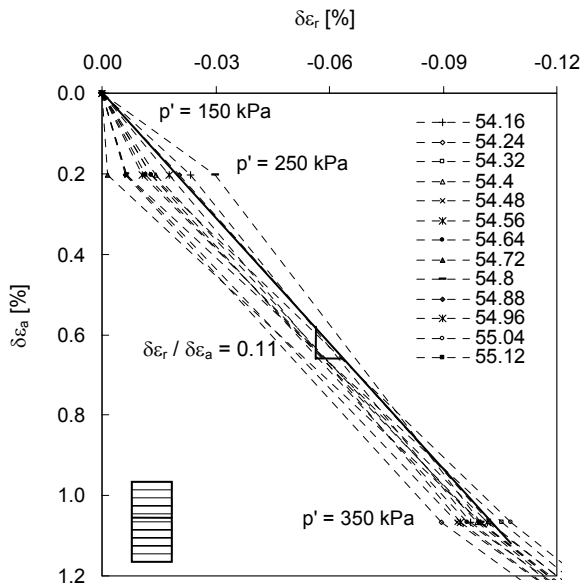
Fig. 6.13: Radial laser scan data from test S2cT1 ($\delta\sigma_a' / \delta\sigma_r' = 2.23;\ \delta q / \delta p' = 0.9$) plotted versus the axial strain increment data for selected stress states over 3 increments of one millimetre near the middle of the sample.
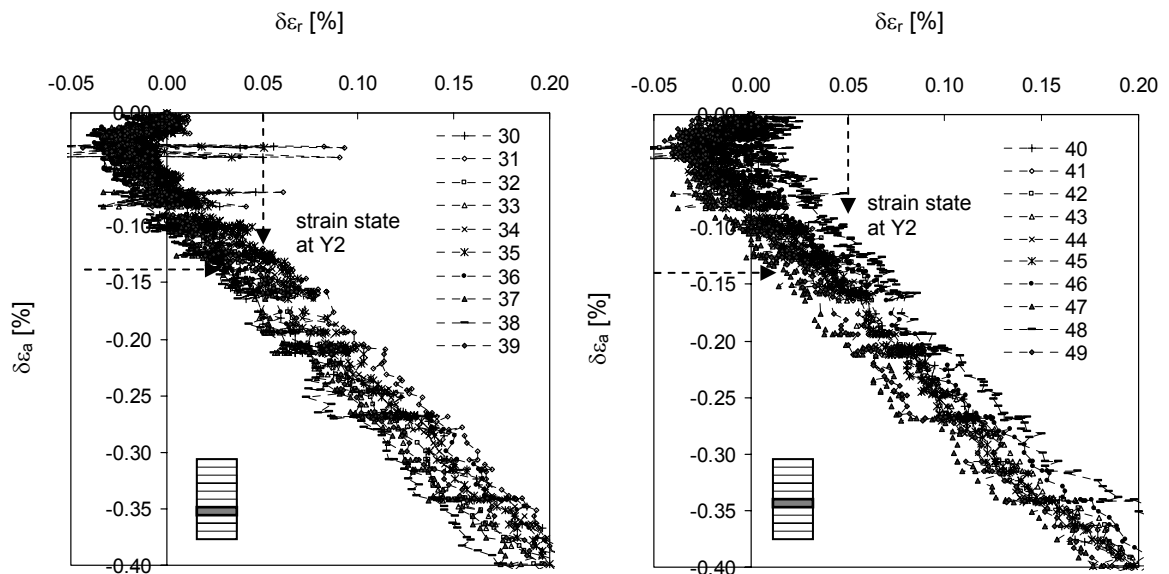
Fig. 6.14: Radial laser scan data from all measured laser scans of test S2T1 ($\delta\sigma_a{}'/\delta\sigma_r{}' = -2$; $\delta q / \delta p' = -\infty$) plotted versus the axial strain increment data over the middle 40 mm of the sample height.

But this change in direction of the radial strain requires some combination of time, stress and strain to occur, therefore the sample is continuously expanding

although the new stress increment ratio is already applied. But after reaching the middle of the Y2 yield strain state, the strain increment ratio has already rotated to the values obtained from Fig. 6.10 & Fig. 6.12, which are consequently valid for the small strain region.

Comparison of the strain increment ratios measured in the tests S2T1 & S2bT1 with a probing stress path of $\delta\sigma_a'/\delta\sigma_r' = -2$ and $\delta q/\delta p' = -\infty$ to the strain increment ratios that were calculated from the elastic isotropic behaviour for the corresponding stress path, shows that the values do not coincide. A strain increment ratio of -0.68 was measured in the tests while isotropic elastic behaviour gave a strain increment ratio of -0.5. This discrepancy indicates that adopting isotropic elastic theory to describe the small strain response of these lacustrine clays might not be the right solution.

Calculating the Poisson's ratio (Eq. 6.8) from test S2aT1, which had a probing stress path ratio of $\delta\sigma_a'/\delta\sigma_r' = 2$ and a strain increment ratio of $\delta\varepsilon_r/\delta\varepsilon_a = 0$, gives a value of $v' = 0.33$. The Poisson's ratio calculated from test S2cT1 with a probing stress path ratio of $\delta\sigma_a'/\delta\sigma_r' = 2.23$ and the strain increment ratio of $\delta\varepsilon_r/\delta\varepsilon_a = 0.09$ is $v' = 0.26$. These two Poisson's ratios were used to calculate the strain increment ratio for further tests. The three tests performed in apparatus 4 were chosen for this comparison because the most accurate external LVDT is installed in this device (see Chapter 4). They are test S2T4 with $\delta\sigma_a'/\delta\sigma_r' = -2$ and $\delta q/\delta p' = \infty$, test S2aT4 with $\delta\sigma_a'/\delta\sigma_r' = -1.3$ and $\delta q/\delta p' = -9.5$ and test S2bT4 with $\delta\sigma_a'/\delta\sigma_r' = -0.61$ and $\delta q/\delta p' = -3.5$.

The corresponding strain measurement data of these tests are shown in Fig. 6.15 and compared to the results of the strain increment ratios predicted, by applying isotropic elastic theory and two different values for the Poisson's ratio of $v' = 0.26$ and $v' = 0.33$. The comparison shows that neither of the calculated strain increment ratios fit the test data perfectly, which was to be expected given the sample structure and in particular the fabric. This conclusion finally confirms that the lacustrine clays investigated do not adhere to isotropic elastic behaviour.
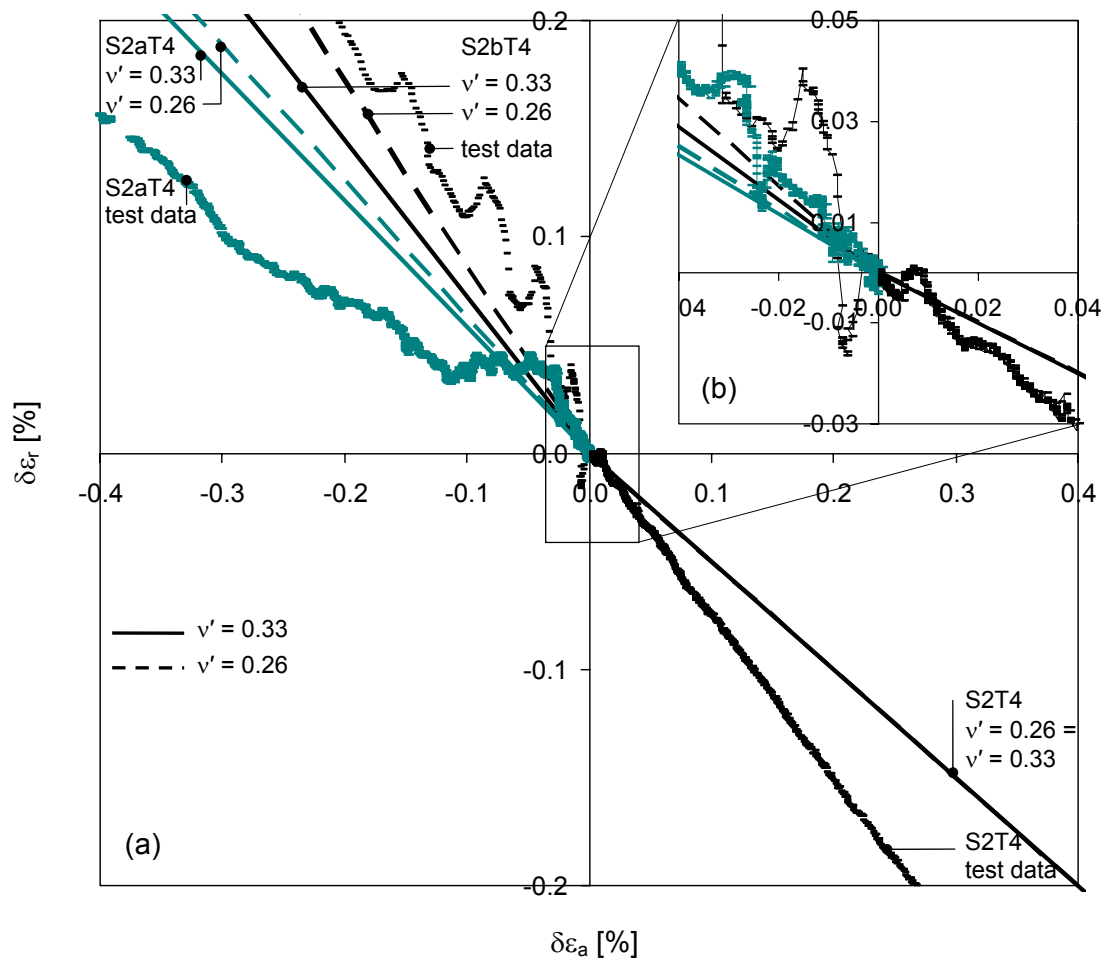
Fig. 6.15: Radial strain increments versus axial strain increments measured in the triaxial tests S2T4 ($\delta\sigma_a'/\delta\sigma_r' = -2$; $\delta q / \delta p' = \infty$), S2aT4 ($\delta\sigma_a'/\delta\sigma_r' = -1.3$; $\delta q / \delta p' = -9.5$) & S2bT4 ($\delta\sigma_a'/\delta\sigma_r' = -0.61$; $\delta q / \delta p' = -3.47$) compared to the isotropic elastic strain increment ratios for the corresponding tests using Poisson′s ratio 0.33 (straight line) and 0.26 (dotted line); (a) for a strain increment range of $\delta\varepsilon_a = \pm 0.4\ \%$ and $\delta\varepsilon_r = \pm 0.2\ \%$; (b) for a strain increment range of $\delta\varepsilon_a = \pm 0.04\ \%$ and $\delta\varepsilon_r = -0.03\ \%$ to $+0.05\ \%$.

6.2.4 Analysis of cross-anisotropy in the small strain region of natural Kloten clay

A cross-anisotropic model is applied next, which needs more than the two independent material parameters that the isotropic elastic model is defined with. Transverse isotropic (= cross-anisotropic) elastic material is defined by 5

independent parameters. Three of them can be determined from triaxial stress path tests (Graham & Houlsby, 1983). In triaxial stress conditions, the cross-anisotropic elastic material is defined as:

$$\begin{bmatrix} \delta\varepsilon_a \\ \delta\varepsilon_r \end{bmatrix} = \begin{bmatrix} \dfrac{1}{E_a} & -2\dfrac{v'_{ar}}{E_a} \\ -\dfrac{v'_{ar}}{E_a} & \dfrac{1}{E_r}\left(1-v'_{rr}\right) \end{bmatrix} \begin{bmatrix} \delta\sigma_a' \\ \delta\sigma_r' \end{bmatrix}$$

Eq. 6.13

where E_a is the stiffness in the axial direction. Here $E_a = E_v$, the stiffness in the vertical direction, due to the soil sample setup in the test apparatus. Similarly, the radial stiffness E_r is equal to the horizontal soil stiffness E_h. The Poisson's ratio v'_{ar} is the same as v'_{vh} and gives the strain relationship between the axial (vertical) and radial (horizontal) directions. v'_{rr} is the same as v'_{hh} and describes the strain relationship between two orthogonal radial (horizontal) directions. In triaxial conditions, where the same cell pressure is applied around the sample, this Poisson's ratio v'_{hh} is not determinable.

The stiffness matrix for triaxial conditions (defining the axial and radial normal stress-strain relationship and omitting the deviator stress-strain relations) contains four parameters, from which three can be defined. Therefore the term $\dfrac{1}{E_r}\left(1-v'_{rr}\right)$, which includes two parameters that can not be found independently, is summarized as the variable b.

The three cross-anisotropic elastic stiffness parameters E_a, v'_{ar} and b can be defined with data from three independent stress path tests. Tests with local strain measurement (S2T1, S2aT1, S2bT1 & S2cT1) and those performed in apparatus 4 (S2T4, S2aT4, & S2bT4) were used for this evaluation. The reason for selecting these tests is the higher accuracy of these apparatus measurement systems, as discussed previously.

-   Condition 1: test S2aT1, presented in Fig. 6.11: $\dfrac{\delta\sigma_a'}{\delta\sigma_r'} = 2$, $\dfrac{\delta\varepsilon_r}{\delta\varepsilon_a} = 0$:

    which is, in the general case: $\dfrac{\delta\sigma_a'}{\delta\sigma_r'} = \dfrac{1}{K_0}$

- Condition 2: tests S2T1 & S2bT1, presented in Fig. 6.10 & Fig. 6.12:

$$\frac{\delta\sigma_a{}'}{\delta\sigma_r{}'} = -2 \,, \quad \frac{\delta\varepsilon_r}{\delta\varepsilon_a} = -0.68$$

The stiffness matrix (from Eq. 6.13), rewritten in terms of stress and strain increment ratios, is:

$$\frac{\delta\varepsilon_r}{\delta\varepsilon_a} = \frac{-\dfrac{v'_{ar}}{E_a}\dfrac{\delta\sigma_a{}'}{\delta\sigma_r{}'} + b}{\dfrac{1}{E_a}\dfrac{\delta\sigma_a{}'}{\delta\sigma_r{}'} - 2\dfrac{v'_{ar}}{E_a}} \qquad \text{Eq. 6.14}$$

The term b is calculated from Eq. 6.14 with condition 1:

$$b = 2\frac{v'_{ar}}{E_a} \quad \text{or in the general case,} \quad b = \frac{v'_{ar}}{E_a}\frac{1}{K_0} \qquad \text{Eq. 6.15}$$

Substituting Eq. 6.15 into Eq. 6.14, the parameter E_a in Eq. 6.7 disappears:

$$\frac{\delta\varepsilon_r}{\delta\varepsilon_a} = \frac{-\dfrac{v'_{ar}}{E_a}\dfrac{\delta\sigma_a{}'}{\delta\sigma_r{}'} + \dfrac{v'_{ar}}{E_a}\dfrac{1}{K_0}}{\dfrac{1}{E_a}\dfrac{\delta\sigma_a{}'}{\delta\sigma_r{}'} - 2\dfrac{v'_{ar}}{E_a}} \quad \rightarrow \quad \frac{\delta\varepsilon_r}{\delta\varepsilon_a} = \frac{-v'_{ar}\dfrac{\delta\sigma_a{}'}{\delta\sigma_r{}'} + v'_{ar}\dfrac{1}{K_0}}{\dfrac{\delta\sigma_a{}'}{\delta\sigma_r{}'} - 2v'_{ar}} \qquad \text{Eq. 6.16}$$

and the only remaining unknown parameter, the Poisson's ratio v'_{ar}, can be calculated as:

$$v'_{ar} = \frac{\dfrac{\delta\varepsilon_r}{\delta\varepsilon_a}\dfrac{\delta\sigma_a{}'}{\delta\sigma_r{}'}}{\dfrac{1}{K_0} - \dfrac{\delta\sigma_a{}'}{\delta\sigma_r{}'} + 2\dfrac{\delta\varepsilon_r}{\delta\varepsilon_a}} \qquad \text{Eq. 6.17}$$

The Poisson's ratio v_{ar}' can be determined explicitly for Kloten clay, from condition 2 ($\frac{\delta\sigma_a{}'}{\delta\sigma_r{}'} = -2$, $\frac{\delta\varepsilon_r}{\delta\varepsilon_a} = -0.68$) and with $\frac{1}{K_0} = 2$ from condition 1, as $v'_{ar} = 0.52$. This value looks rather high compared for example to the valid values for the Poisson's ratio of isotropic material, in the range $-1 \le v' \le 0.5$, obtained from ensuring that the determinant of the stiffness matrix in Eq. 6.7 and Eq. 6.8 is positive. Therefore the equivalent limit is verified by determining the valid range of value for the cross-

anisotropic Poisson's ratio v'_{ar}. The determinant of the cross-anisotropic stiffness matrix (Eq. 6.13) is:

$$\frac{1}{E_a}b - 2\frac{v'^2_{ar}}{E_a^2} \geq 0$$

Eq. 6.18

and substituting b from Eq. 6.15 reduces Eq. 6.18 to:

$$\frac{v'_{ar}}{E_a^2}\frac{1}{K_0} - 2\frac{v'^2_{ar}}{E_a^2} \geq 0$$

Eq. 6.19

from which the maximum valid Poissons ratio v'_{ar} can be calculated for Kloten clay with $\frac{1}{K_0} = 2$ (Condition 1) as $v'_{ar} \leq 1$. A value of $v'_{ar} = 0.52$ is therefore thought to be valid.

- Condition 3: tests S2T4, S2aT4 & S2bT4, presented in Fig. 6.16:

The last remaining parameter, the axial stiffness E_a is determined from the upper line of Eq. 6.13 by referring to the data from condition 3:

$$\delta\varepsilon_a = \frac{1}{E_a}\delta\sigma_a' - 2\frac{v'_{ar}}{E_a}\delta\sigma_r'$$

Eq. 6.20

Which is solved for the axial stiffness E_a:

$$E_a = \frac{\delta\sigma_a' - 2v'_{ar}\delta\sigma_r'}{\delta\varepsilon_a}$$

Eq. 6.21

Results of three stress path tests were used for this final evaluation, which was performed graphically. The terms of Eq. 6.21 are plotted in Fig. 6.16 for the tests S2T4, S2aT4 & S2bT4, where the inclination of the curves in Fig. 6.16 equals the axial stiffness. A trend line is plotted with the test data of these three tests, indicating an average axial stiffness for Kloten clay of $E_a = 120\,MPa$, for axial strains smaller than 0.007 %. Finally, the value of the term b can be determined from Eq. 6.15:

$$b = 2\frac{v'_{ar}}{E_a} = 8.7 \cdot 10^{-6} \quad [1/kPa] \hspace{3cm} \text{Eq. 6.22}$$
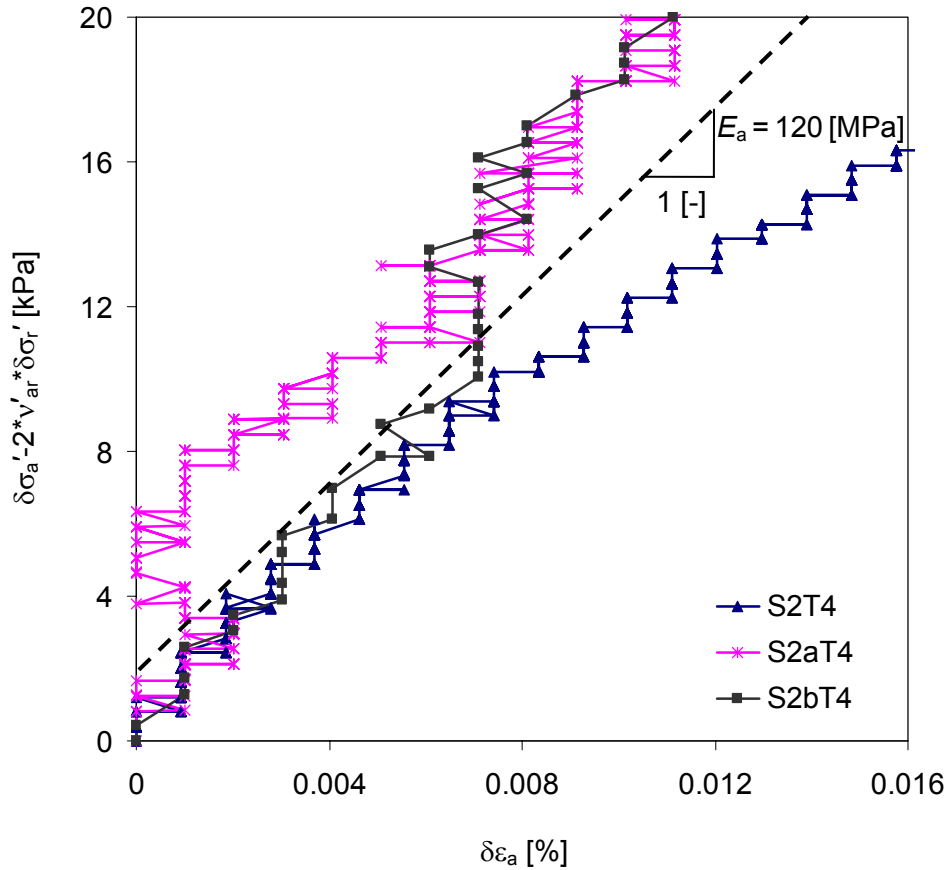
Fig. 6.16: Plot of Eq. 6.21 for the data from the three triaxial tests S2T4 ($\delta\sigma_a' / \delta\sigma_r'$ = - 2; $\delta q / \delta p'$ = ∞), S2aT4 ($\delta\sigma_a' / \delta\sigma_r'$ = - 1.3; $\delta q / \delta p'$ = - 9.5) & S2bT4 ($\delta\sigma_a' / \delta\sigma_r'$ = - 0.61; $\delta q / \delta p'$ = - 3.47) and the determination of the axial stiffness E_a.

Consequently the cross-anisotropic stiffness matrix (Eq. 6.13) for Kloten clay, evaluated at the start of the probing stress path at the stress state $p' = 150\,kPa$ and $q = 112.5\,kPa$ and, an overconsolidation ratio of 2, for the strain increment ranges shown in Fig. 6.10 to Fig. 6.14 and Fig. 6.16, is:

$$\begin{bmatrix} \delta\varepsilon_a \\ \delta\varepsilon_r \end{bmatrix} = \begin{bmatrix} \dfrac{1}{E_a} & -2\dfrac{v'_{ar}}{E_a} \\ -\dfrac{v'_{ar}}{E_a} & \dfrac{1}{E_r}(1-v'_{rr}) \end{bmatrix} \begin{bmatrix} \delta\sigma_a' \\ \delta\sigma_r' \end{bmatrix} \text{ with } \begin{aligned} E_a &= 120 \; [MPa] \\ v'_{ar} &= 0.52 \; [-] \\ b = \frac{1}{E_r}(1-v'_{rr}) &= 8.7 \cdot 10^{-6} \; [1/kPa] \end{aligned}$$

174

This evaluation was carried out on test data from local radial and axial displacement measurements. No results of volumetric displacement measurements are involved. These are less accurate than local displacement measurements because of fluctuations in the pressure regulation system. In addition, temperature fluctuations affect the outsourced back pressure unit (Chapter 4, e.g. Fig. 4.1 or Fig. 4.7) much more than they do the devices placed in the triaxial cell surrounded by the cell water.

In the next evaluation step, the b value determined is verified on test data, including the radial strains ε_r calculated from the volumetric displacement measurement with the back pressure unit, and axial strains measured with the external LVDT. It is visible that the resolution of strain data measured directly on the specimen (ε_a and ε_r) is higher than the resolution of strain data derived with the help of volumetric displacement measurements (ε_v and ε_s).

Again, the evaluation of the parameter b is done graphically. The term b is solved from the second line of Eq. 6.13 as:

$$b = \frac{\delta\varepsilon_r + \dfrac{v'_{ar}}{E_a}\delta\sigma_a'}{\delta\sigma_r'} \qquad \text{Eq. 6.23}$$

and the terms of Eq. 6.23 are plotted in Fig. 6.17, for the three tests carried out in apparatus 4, together with the b value of $8.7 \cdot 10^{-6}$ [1/kPa] determined previously.

Comparison of the b value calculated with the plot of the corresponding measurement data (Fig. 6.17) shows that the b value calculated fits the data of test S2aT4 and S2bT4 fairly well, in that the measured data fluctuate more or less about the line described. Only the response at the start of the curve for test S2T4 corresponds remotely to the plotted b line, then the radial strain increments exceed the predicted values. The radial strains are calculated from the volumetric displacement measurement and it was highlighted previously in the data evaluation in Chapter 5 (Fig. 5.9) that the volumetric strains were disproportionately high in test S2T4 (see $e - \ln p'$ plot of every test in the Appendix). The comparison in Fig. 6.17 indicates that $b = 8.7 \cdot 10^{-6}$ [1/kPa]

corresponds with the test data when the disproportionately large volumetric and consequently radial strain data of test S2T4 are ignored.
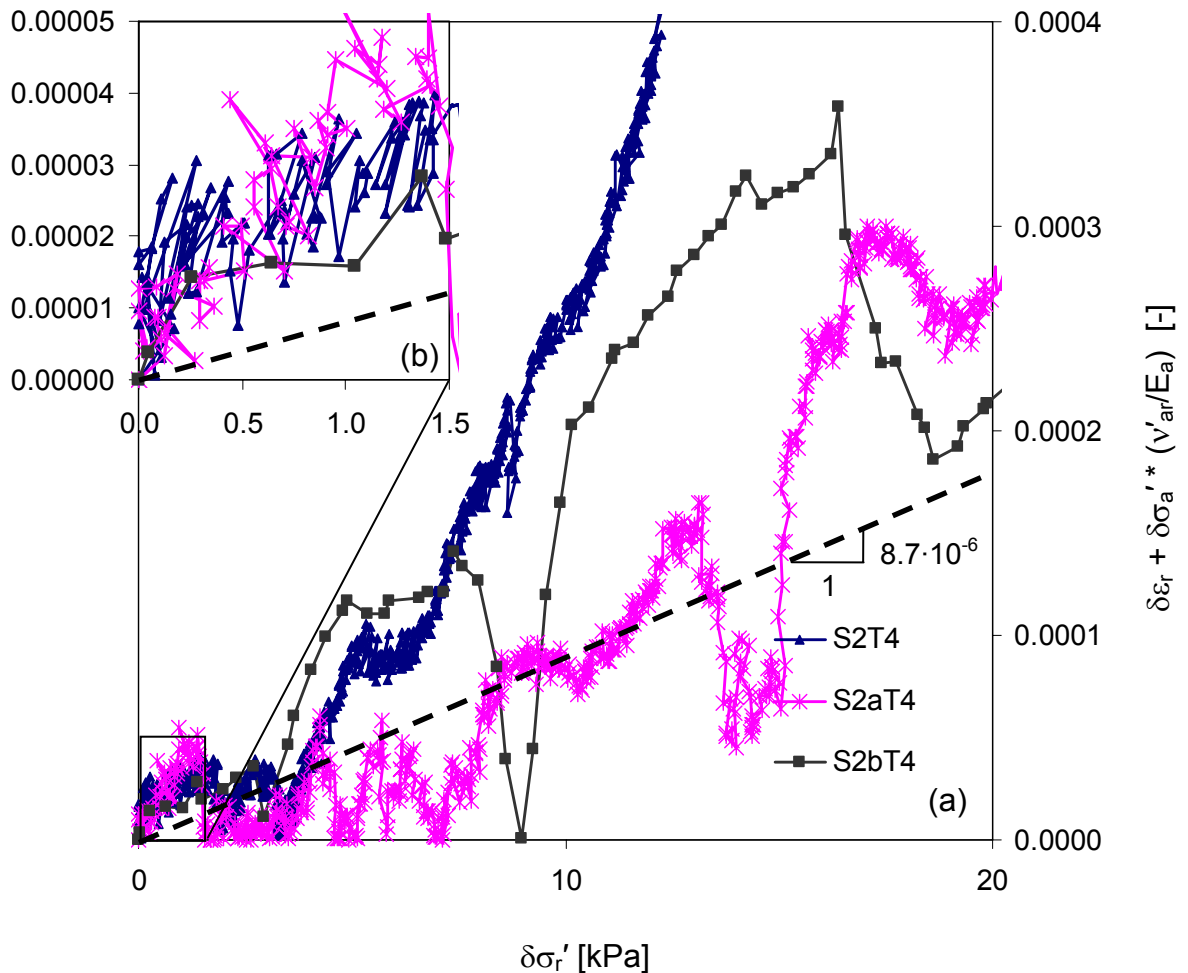
Fig. 6.17: Plot of Eq. 6.23 for the three triaxial tests S2T4 ($\delta\sigma_a' / \delta\sigma_r' = -2$; $\delta q / \delta p' = \infty$), S2aT4 ($\delta\sigma_a' / \delta\sigma_r' = -1.3$; $\delta q / \delta p' = -9.5$) & S2bT4 ($\delta\sigma_a' / \delta\sigma_r' = -0.61$; $\delta q / \delta p' = -3.47$) to verify the stiffness parameter b; (a) for a stress range of $\delta\sigma_r' = 20\ kPa$ and (b) for a stress range of $\delta\sigma_r' = 1.5\ kPa$.

Due to the high fluctuation of b in the previous comparison, it is interesting to check the value of b at which the material behaves isotropically. Therefore, the parameters for isotropic behaviour are determined by comparing the isotropic elastic stiffness matrix (Eq. 6.7) to the cross-anisotropic elastic stiffness matrix (Eq. 6.13):

$$\frac{1}{E}\begin{bmatrix} 1 & -2v' \\ -v' & 1-v' \end{bmatrix} \leftrightarrow \begin{bmatrix} \dfrac{1}{E_a} & -2\dfrac{v'_{ar}}{E_a} \\ -\dfrac{v'_{ar}}{E_a} & \dfrac{1}{E_r}\left(1-v'_{rr}\right) \end{bmatrix}$$

<div align="right">Eq. 6.24</div>

The comparison shows that the behaviour is isotropic when $E_a = E$, $v'_{ar} = v'$ and

$$b = \frac{1-v'}{E} = \frac{1}{E_a} - \frac{v'_{ar}}{E_a}$$

<div align="right">Eq. 6.25</div>

This is the case for b = 4·10^{-6} [1/kPa] for Kloten clay, which is named b_{iso} in the following section. Comparing the value of b_{iso} to the b value determined for natural Kloten clay (Fig. 6.17), shows that the b values vary by a factor of approximately two.

Finally, after all these derivations leading to the determination of the elastic soil properties, firstly for isotropic and secondly for cross-anisotropic material, it would be interesting to investigate whether Kloten clay is stiffer in the axial or in the radial direction. This is not determinable so far, as the stiffness in the horizontal direction cannot be evaluated alone but is included in parameter b. Additionally, the cross-anisotropic stiffness matrix needed to determine the elastic strain components has to represent the soil stiffness in zone 1 (Fig. 1.2). Only measurement data at a strain range representing zone 2 were evaluated, as the resolution of the tests was not high enough to derive data for zone 1. The only stiffness parameter derived from measurement data at a strain range representing zone 1 was the shear modulus G_{max} (Chapter 6.2.3), which is not used in data evaluation in the triaxial stress space.

Therefore, the modified stiffness matrix for cross-anisotropic material in triaxial stress space, as proposed by Houlsby (1981), is applied to solve these two previously mentioned requirements to derive the ratio of axial to radial stiffness explicitly and find the elastic stiffness matrix, representing the stiffness behaviour in zone 1 (Fig. 1.2).

Houlsby's aim in deriving this matrix was to determine cross-anisotropic elastic stiffness behaviour from triaxial stress path tests. Therefore the anisotropy is described by one "anisotropy factor" α, which is incorporated in an isotropic

matrix by multiplying the second to the sixth column and the second to the sixth row by the anisotropy factor. The proposed cross-anisotropic stiffness matrix is shown in Eq. 6.26. The common Young's modulus (E) and the Poisson's ratio (v') are renamed as E^* and v^* to indicate their different use.

$$
\begin{bmatrix} \delta\sigma_1' \\ \delta\sigma_2' \\ \delta\sigma_3' \\ \delta\tau_{23} \\ \delta\tau_{13} \\ \delta\tau_{12} \end{bmatrix} = \frac{E^*}{(1+v^*)(1-2v^*)}
$$

$$
\begin{bmatrix} 1-v^* & \alpha v^* & \alpha v^* & & & \\ \alpha v^* & \alpha^2(1-v^*) & \alpha^2 v^* & & & \\ \alpha v^* & \alpha^2 v^* & \alpha^2(1-v^*) & & & \\ & & & \alpha^2(1-2v^*) & & \\ & & & & \alpha(1-2v^*) & \\ & & & & & \alpha(1-2v^*) \end{bmatrix} \begin{bmatrix} \delta\varepsilon_1 \\ \delta\varepsilon_2 \\ \delta\varepsilon_3 \\ \delta\gamma_{23} \\ \delta\gamma_{13} \\ \delta\gamma_{12} \end{bmatrix}
$$

Eq. 6.26

The connection between the commonly used cross-anisotropic stiffness parameters E_a, E_r, v'_{ar}, v'_{rr} and G_{ar}, and the newly introduced stiffness parameters α, E^* and v^* can be established when this stiffness matrix is transformed into a compliance matrix and compared to the conventional cross-anisotropic compliance matrix (Houlsby & Graham, 1983).

$$
E_a = E^*; \; E_r = \alpha^2 E^*; \; v'_{ar} = \frac{v^*}{\alpha}; \; v'_{rr} = v^*; \; 2G_{ar} = \frac{\alpha E^*}{(1+v^*)}
$$

Eq. 6.27

Thus the correlations describing the anisotropy factor α can be derived as:

$$
\alpha^2 = \frac{E_r}{E_a} \text{ and } \alpha = \frac{v'_{rr}}{v'_{ar}}
$$

Eq. 6.28

The behaviour is isotropic when $\alpha = 1$. For $\alpha > 1$, the material is stiffer horizontally than vertically, and for $\alpha < 1$, the material is stiffer vertically than horizontally.

The radial stiffness E_r and the Poisson's ratio for the radial direction v'_{rr} can be determined explicitly and the shear stiffness G_{ar} can be calculated from the

previously derived stiffness parameters E_a, v'_{ar} & b, from the relationships given in Eq. 6.27.

By inserting the formulations of Eq. 6.27 into the equation for b, the radial stiffness E_r, the Poisson's ratio for the radial direction v'_{rr} and the anisotropy factor α are determined:

$$b = \frac{1}{E_r}\left(1 - v'_{rr}\right) = \frac{1}{\alpha^2 E^*}\left(1 - v^*\right) = \frac{1}{\alpha^2 E_a}\left(1 - \alpha v'_{ar}\right) = \frac{1}{\alpha^2}\frac{1}{E_a} - \frac{1}{\alpha}\frac{v'_{ar}}{E_a} \qquad \text{Eq. 6.29}$$

This formulation confirms that for $\alpha = 1$, the term $b_{(\alpha=1)} = \frac{1}{E_a} - \frac{v_{ar}}{E_a} = b_{iso}$. It can be seen that for $\alpha > 1$, which describes a material that is horizontally stiffer than vertically, $b < b_{iso}$ and subsequently for $\alpha < 1$, $b > b_{iso}$, which is the case for Kloten clay. Therefore α must be smaller than 1, which indicates that the material has a greater vertical then radial stiffness (Fig. 6.18), applying the modified cross-anisotropic stiffness matrix proposed by Houlsby (1981).

The value of α is calculated by transforming Eq. 6.29 into:

$$\alpha^2 + \alpha \frac{v'_{ar}}{bE_a} - \frac{1}{bE_a} = 0 \qquad\qquad \text{Eq. 6.30}$$

Solving Eq. 6.30 for the positive value of α for Kloten clay gives $\alpha_{Kloten\ clay} = 0.76$.

From $\alpha^2 = \frac{E_r}{E_a}$ the radial stiffness $E_r = \alpha^2 E_a = 69.5\,MPa$ can be determined from the cross-anisotropic stiffness matrix proposed by Houlsby & Graham (1983).

The shear modulus (G_{ar}), corresponding to the elastic shear modulus measured by the bender elements ($G_{max} = 98\,MPa$ at p' = 150 kPa and q = 112.5 kPa) can be calculated from the formulations (Eq. 6.27) for Kloten clay as:

$$G_{ar} = \frac{\alpha E^*}{2\left(1 + v^*\right)} = 32.7\,MPa \qquad\qquad \text{Eq. 6.31}$$

The result gives a shear stiffness three times lower than the stiffness measured by the bender elements. This was expected because the yield surface (Y1) in Fig. 6.4 was not determinable from the measurement data, whereas it was possible to

determine stiffness in zone 2 (Fig. 1.2). But the stiffness matrix can be scaled when one stiffness parameter of zone 1 (G_{max}) is known, assuming that the anisotropy is the same for zone 1 and zone 2. This assumption is realistic because no plastic straining is assumed to have occurred in the material at small strains within zone 2.
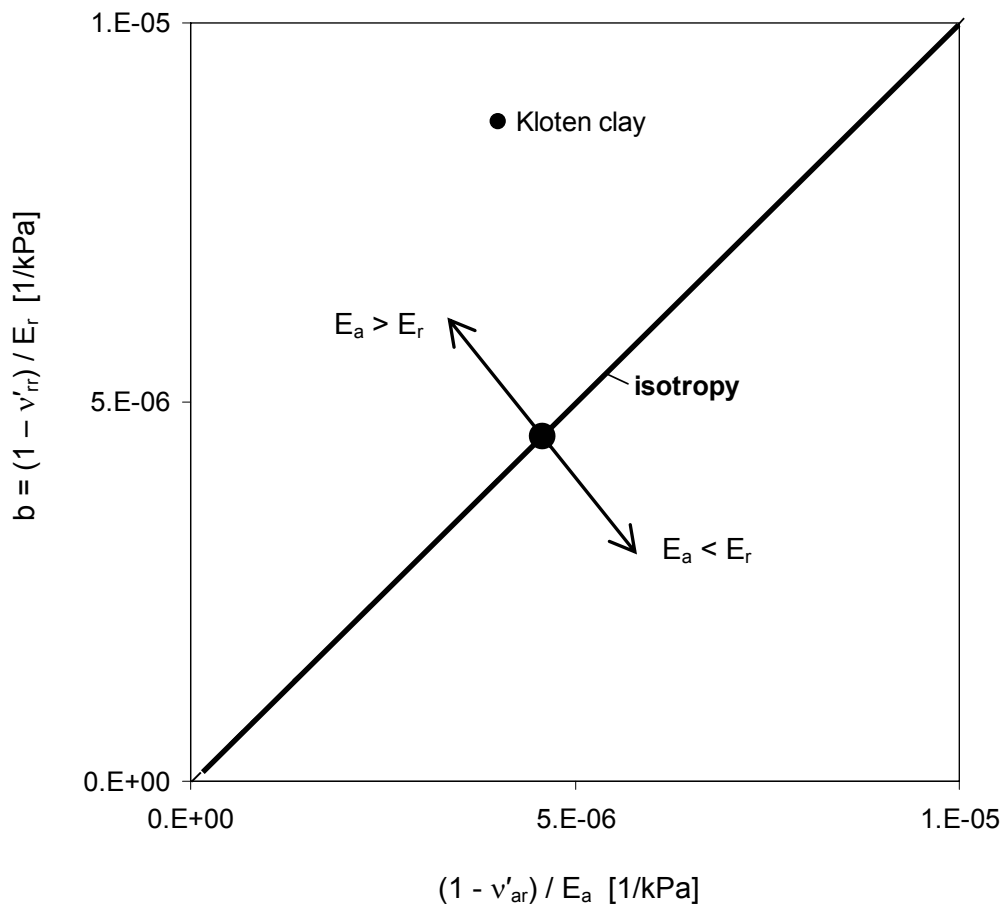
Fig. 6.18: Comparison of cross-anisotropic to isotropic material behaviour.

Consequently, the stiffness parameters for Kloten clay, derived at the stress and strain conditions described previously and in Chapter 5, are scaled by a factor of 3, while the anisotropy parameters, such as the Poisson's ratios, are kept the same. Therefore the cross-anisotropic stiffness matrix of Kloten clay in zone 1 is:

$$
\begin{bmatrix} \delta\varepsilon_a \\ \delta\varepsilon_r \end{bmatrix} = \begin{bmatrix} \dfrac{1}{E_a} & -2\dfrac{v'_{ar}}{E_a} \\ -\dfrac{v'_{ar}}{E_a} & \dfrac{1}{E_r}\left(1-v'_{rr}\right) \end{bmatrix} \begin{bmatrix} \delta\sigma_a' \\ \delta\sigma_r' \end{bmatrix} \quad \text{with} \quad \begin{array}{l} E_a = 360\,MPa \\ v'_{ar} = 0.52 \\ v'_{rr} = 0.40 \\ E_r = 208\,MPa \end{array} \qquad \text{Eq. 6.32}
$$

6.2.5 Plastic strain increment ratio

The plastic strain increment ratio can finally be determined with the identification of the elastic strain increment ratio, as discussed in Chapter 6.2.2. The elastic strain increment ratio is described by the stiffness matrix given in Eq. 6.32. This stiffness matrix represents a cross-anisotropic material response and is defined in the triaxial stress space σ_a' versus σ_r'. Therefore, the following evaluation will be performed in this stress space.

To calculate the plastic strain increment ratio at the yield stress states Y2 and Y3, the corresponding stress states and total strain increment ratios must be known. These were derived in the previous Chapter in the invariant stress space q versus p'. But these stress invariants cannot be used any more for the evaluation of cross-anisotropic elasticity, therefore the derived yield points Y2 and Y3 and strain increment ratios must either be transformed to the triaxial stress space by assuming that the principal stresses are in the axial and radial directions, or by redefining the yield points and strain increment ratios in the σ_a' and σ_r' space. Because not all yield points could be successfully identified in the δq - $\delta\varepsilon_s$ and $\delta p'$ - $\delta\varepsilon_v$ plots and the fact that data from axial displacement measurement are more accurate than data of the volume displacement measurement, the determination of the yield points and strain increment ratios was repeated in the triaxial stress space (σ_a' - σ_r'). The plastic components of the axial and radial strain increments $\delta\varepsilon_a^p$ and $\delta\varepsilon_r^p$ respectively, were used. This is possible because the elastic component is described by a cross-anisotropic **linear** elastic stiffness matrix. Yield point evaluation in the stress versus plastic strain increment plot has the advantage that the derived strain increments at yield are already plastic and

can be used directly to find the strain increment ratio at yielding in the plot $\delta\varepsilon_r^p$ versus $\delta\varepsilon_a^p$.

The yield point identification and strain increment ratio determination at yield are as discussed in Chapter 6.2.1. The stress-strain increments curves $\delta\sigma_a'$ - $\delta\varepsilon_a^p$ and $\delta\sigma_r'$ - $\delta\varepsilon_r^p$ are plotted for the probing stress paths of the tests in series 2 and the stress states of visible kinks are identified for the yield point detection. The strain level at the yield stress state is defined for the evaluation of the corresponding strain increment ratio and the direction of the plastic strain increment ratio is identified on the $\delta\varepsilon_a^p$ - $\delta\varepsilon_r^p$ strain curve at the yield strain state. Kinks in the stress-strain curve are not visible in every plot for all tests. Therefore, only those stress points where a significant kink was detected were used for further comparative studies. The evaluation process is demonstrated in Fig. 6.19 to Fig. 6.21 on the data of test S2T1.

The $\delta\sigma_a'$ - $\delta\varepsilon_a^p$ plot is presented in Fig. 6.19 at different scales with the entire set of data given in Fig. 6.19a. The stress-strain increment curve in Fig. 6.19b shows the change in inclination at an axial effective stress increment of approximately -11 kPa, which is identified as the Y2 stress state.

The corresponding axial strain increment is about -0.01 %. No distinct kink in the curve is visible in the next scale of the $\delta\sigma_a'$ - $\delta\varepsilon_a^p$ plot (Fig. 6.19c), but the start of the transition from zone 3 to zone 4, in which the yield point Y3 is located, can be recognised at an axial effective stress increment of -58 kPa. Thus the $\delta\sigma_r'$ - $\delta\varepsilon_r^p$ plot is analysed at different scales from the entire set of data given in Fig. 6.20a.

Fig. 6.20b shows a distinct kink in the stress-strain increment curve at a radial effective stress increment of 6 kPa and corresponding radial strain increment of 0.05 %. The curve in Fig. 6.20c indicates a change in inclination of the curve at a radial effective stress increment of 48 kPa. The radial strain increment developed at this Y3 stress state is 0.8 %.
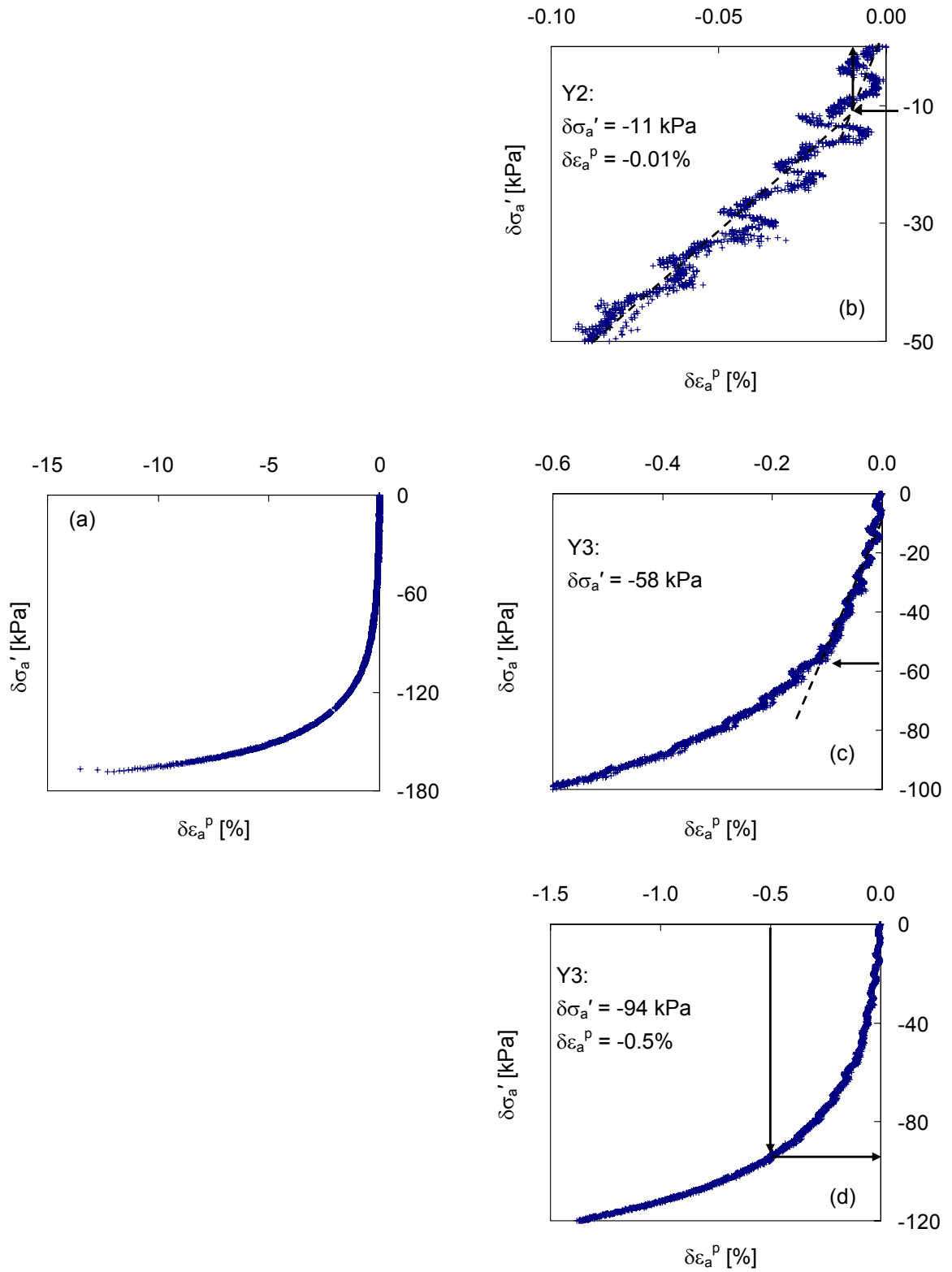
Fig. 6.19: Yield point evaluation method presented for the data from test S2T1.
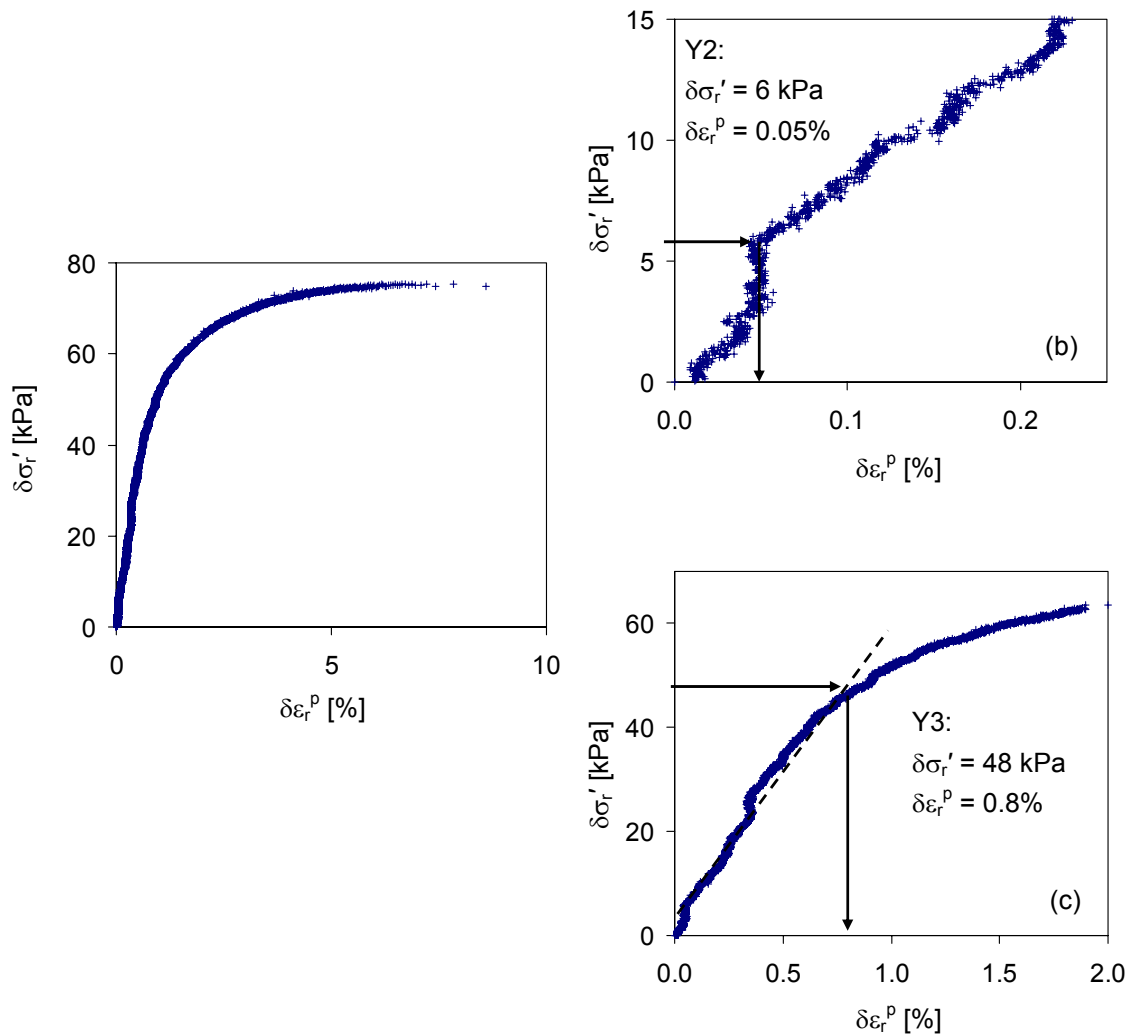
Fig. 6.20: Yield point evaluation method presented for the data from test S2T1.

The direction of the plastic strain increment ratio is determined from the $\delta\varepsilon_r^p$ - $\delta\varepsilon_a^p$ plot (Fig. 6.21a&b) as $\delta\varepsilon_a^p / \delta\varepsilon_r^p$ = -0.23 for Y2 and $\delta\varepsilon_a^p / \delta\varepsilon_r^p$ = -1.33 for Y3 with the strain increment levels identified at the corresponding Y2 and Y3 stress states. Finally, the plastic axial strain increment at Y3 is determined from Fig. 6.21b as -0.5 % and the corresponding axial effective stress increment at Y3 is derived from Fig. 6.19d as -94 kPa.

The test data of all probing stress paths for series 2 have been analyzed in this way in the σ_a' - σ_r' stress space. The analysis and the results are shown in the Appendix (Fig. 10.143 to Fig. 10.155) and a comparative study is given in the following paragraphs.
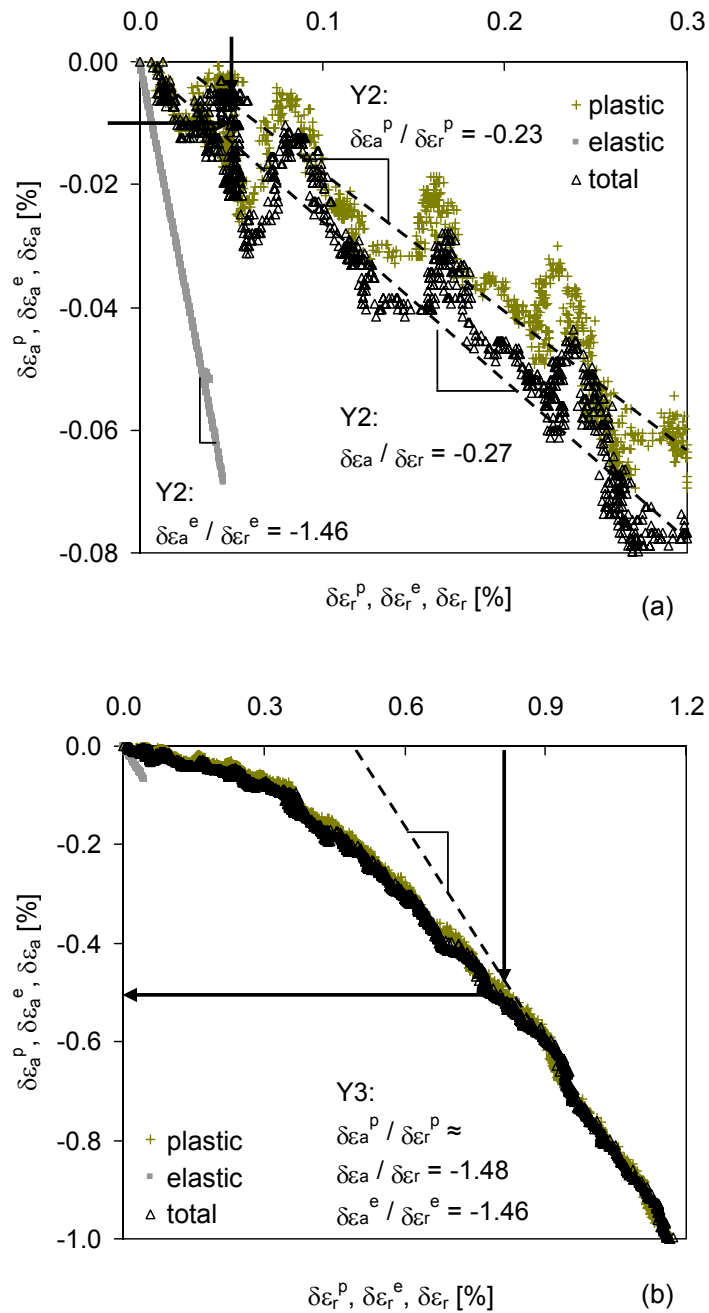
Fig. 6.21: Strain increment ratio evaluation method presented for the data from test S2T1.

The probing stress path directions of the tests in series 2, given in the $\sigma_a' - \sigma_r'$ stress space, are presented in Fig. 6.22. The isotropic stress path is indicated by the dot-dash line and the critical state lines are shown by the dashed lines. The

start stress state of probing path in the σ_a' - σ_r' stress space is at σ_a' = 225 kPa and σ_r' = 112.5 kPa.
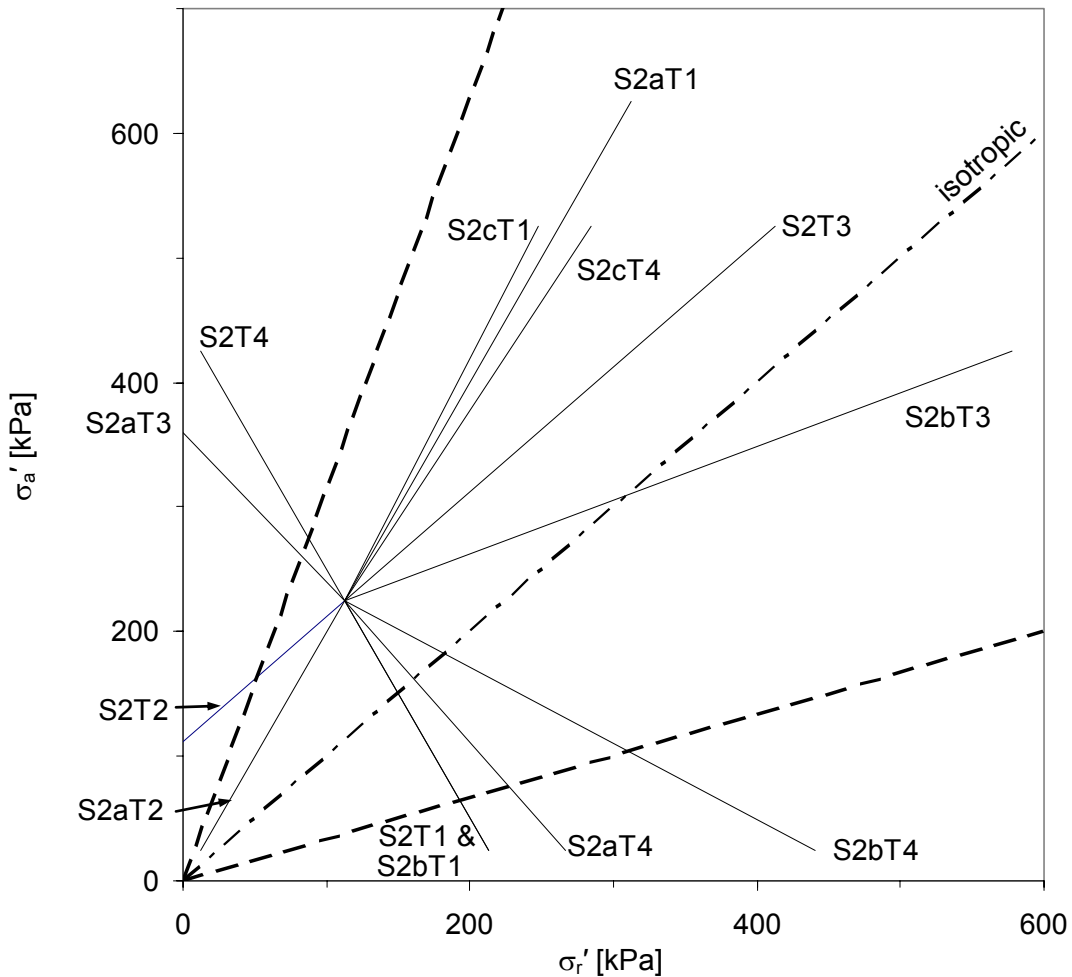
Fig. 6.22: Probing stress path in the σ_a' - σ_r' stress space for the triaxial tests in series 2.

An overview of the yield points Y2 and Y3 is shown in Fig. 6.23. Yield points derived from the $\delta\sigma_a'$ - $\delta\varepsilon_a^p$ or $\delta\sigma_r'$ - $\delta\varepsilon_r^p$ curve are differentiated from one another. Those that are obtained from the $\delta\sigma_a'$ - $\delta\varepsilon_a^p$ plot are called "from σ_a'", and those that are determined from the $\delta\sigma_r'$ - $\delta\varepsilon_r^p$ plot are called "from σ_r'". Additionally, the start point of the probing path (σ_a' = 225 kPa) and the preconsolidation stress state (σ_a' = 450 kPa) are indicated.
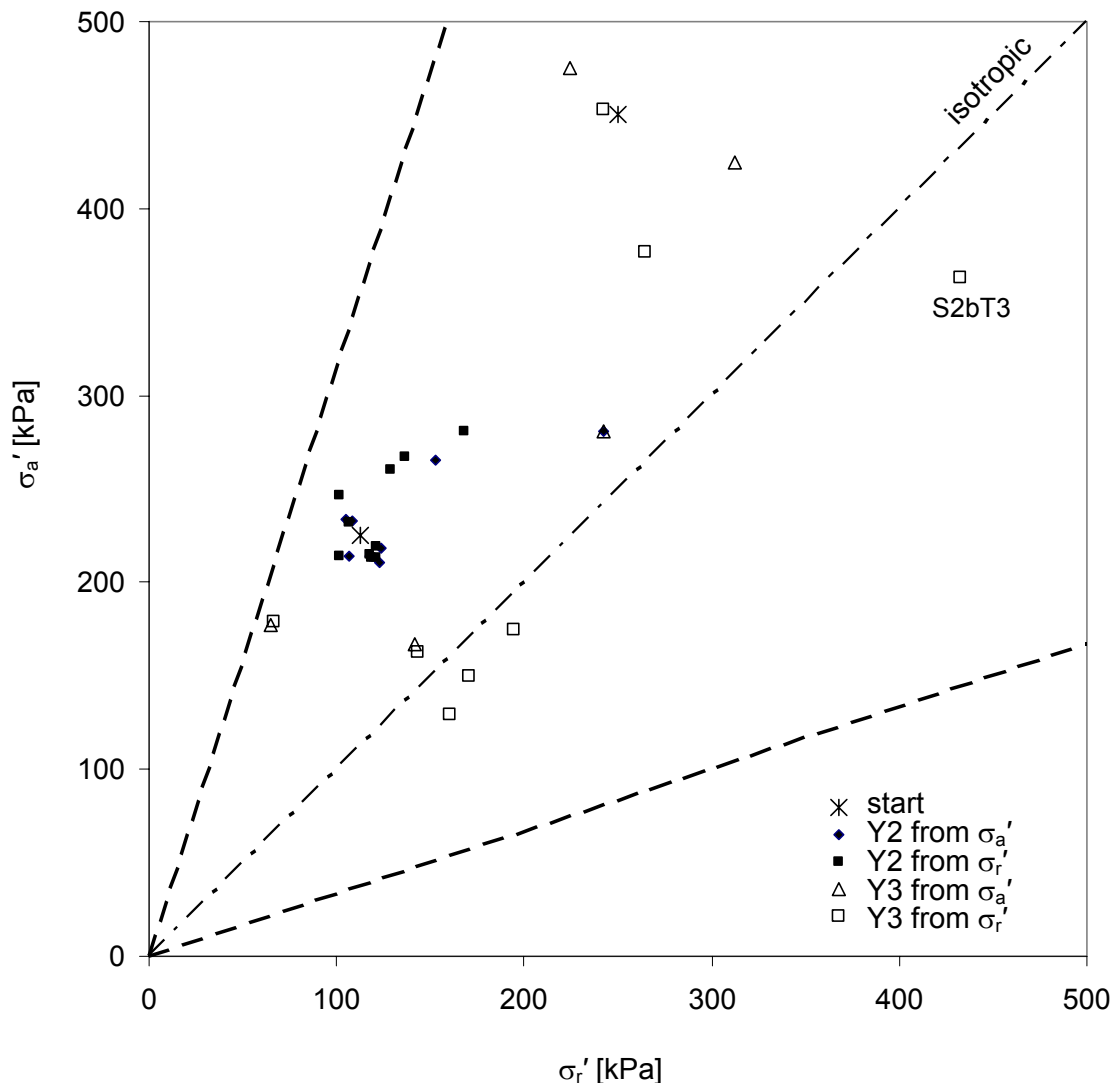
Fig. 6.23: Comparison of the yield point analysis of the probing paths for test series 2 in the σ_a' - σ_r' stress space.

Analysis of the yield point data shows that the yield stress states derived from test S2bT3 overestimate the yield stress by the same magnitude as previously found in the yield point analysis in q - p' stress space (Fig. 6.6). Therefore, these data are ignored in the subsequent comparative studies. When putting a curve through the Y2 and Y3 yield points, e.g. as shown in Fig. 6.24, it can be seen that the newly derived yield points give similar shapes for the yield surfaces. The Y2 points are fitted best by an ellipse with the main axis parallel to the isotropic stress ratio ($\sigma_a' = \sigma_r'$). The shape of the curve indicated by the Y3 points may be elliptical but

the main axis of the ellipse is not parallel to the isotropic axis, instead inclined through 10 to 20° towards the axial stress axis.
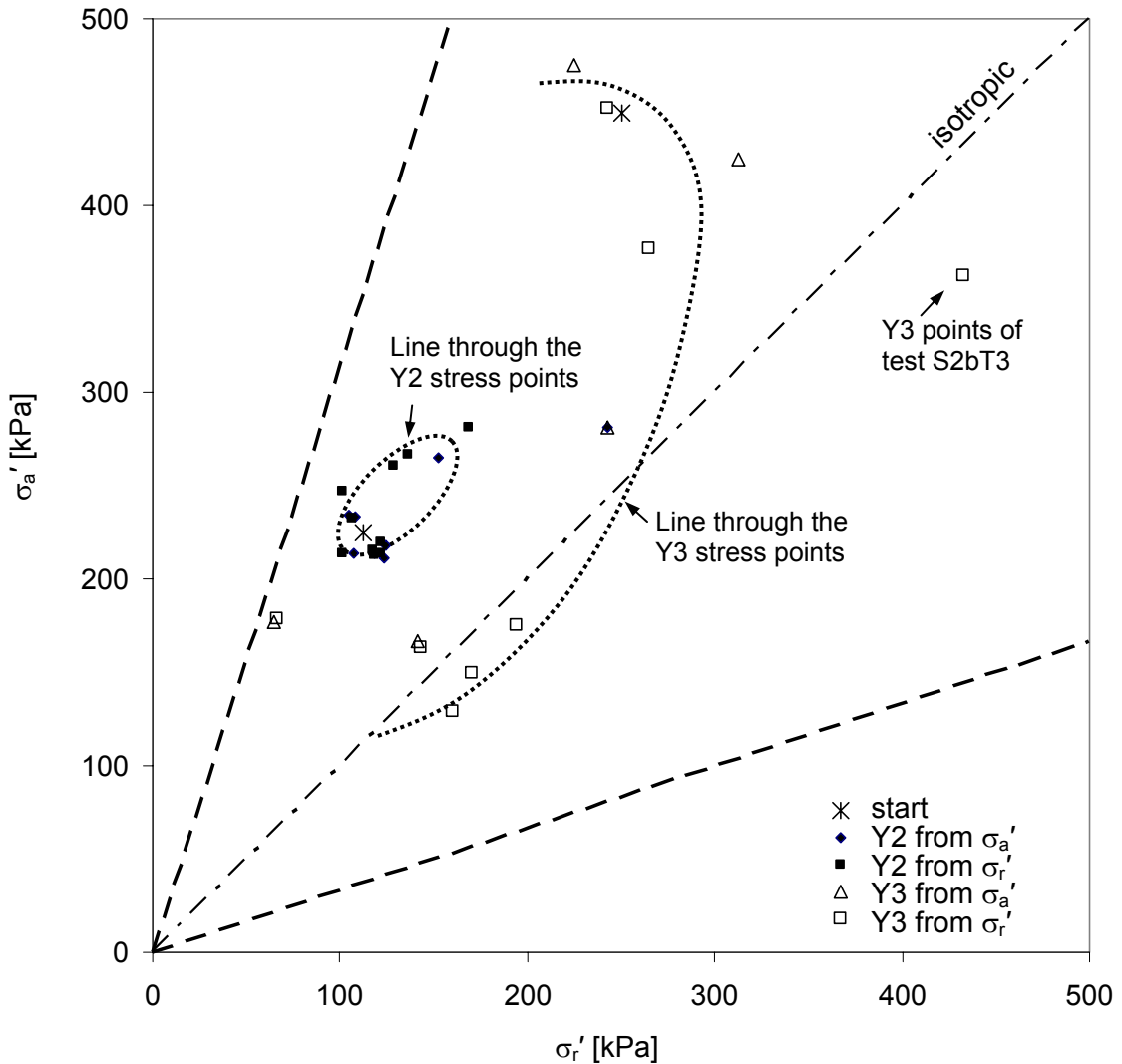
Fig. 6.24: Proposed Y2 & Y3 yield surfaces through the yield points for the probing paths of test series 2 in the σ_a' - σ_r' stress space.

The shape of the Y3 yield surface is only given for the probing stress path with increasing radial stress. For the probing stress path with decreasing radial stress that stays above the isotropic stress axis, the Y3 surface may be given by the critical state line. As discussed in Chapter 5, no pre-failure stress states above the yield surface were recognised.

Finally the directions of the plastic strain increment ratios for the probing stress paths of tests in series 2 are given. The determination of the strain increment

ratios is shown in Fig. 6.21 and the results of analysis of all test data are shown in Fig. 6.25. The plastic strain increment ratios are plotted for the corresponding yield stress states Y2 and Y3 in the triaxial stress and strain space, respectively. The length of the vectors given is not related to the test data, therefore no units are given for the strain increment axis $\delta\varepsilon_a^p$ and $\delta\varepsilon_r^p$.
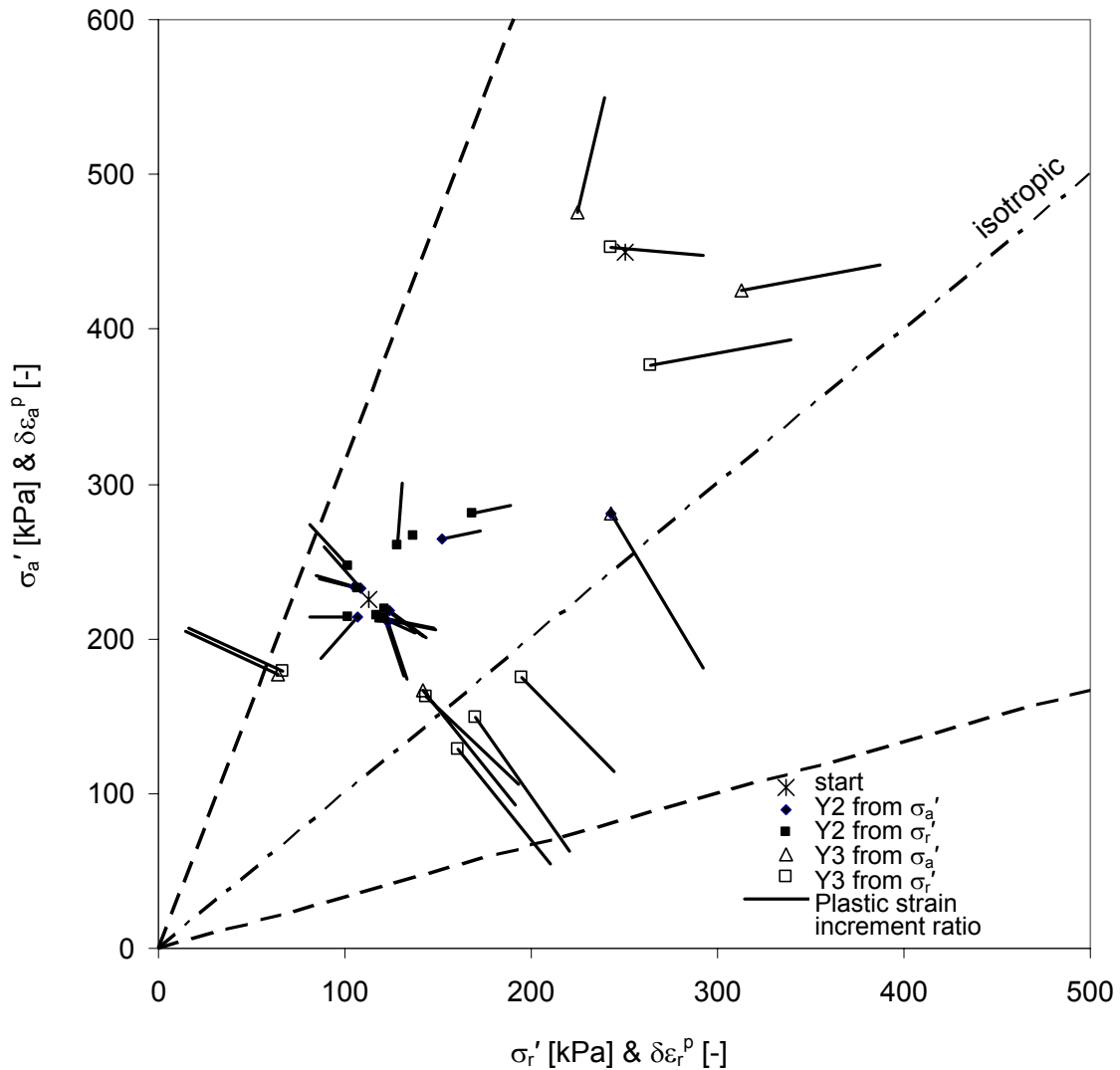
Fig. 6.25: Plastic strain increment ratios at the yield points of the probing paths of test series 2 in the $\sigma_a' - \sigma_r'$ stress space and $\delta\varepsilon_a^p - \delta\varepsilon_r^p$ strain space.

The plastic strain increment vector is perpendicular to the plastic potential surface. Therefore, the tangent to the plastic potential surface at the corresponding stress point is given by a line normal to the plastic strain increment vector. Lines perpendicular to the plastic strain increment vectors at the Y3 yield points are

plotted in Fig. 6.26, which indicate the shape of the plastic potential surface (dashed line) similar to the presumed yield surface (dotted line, and Fig. 6.24).
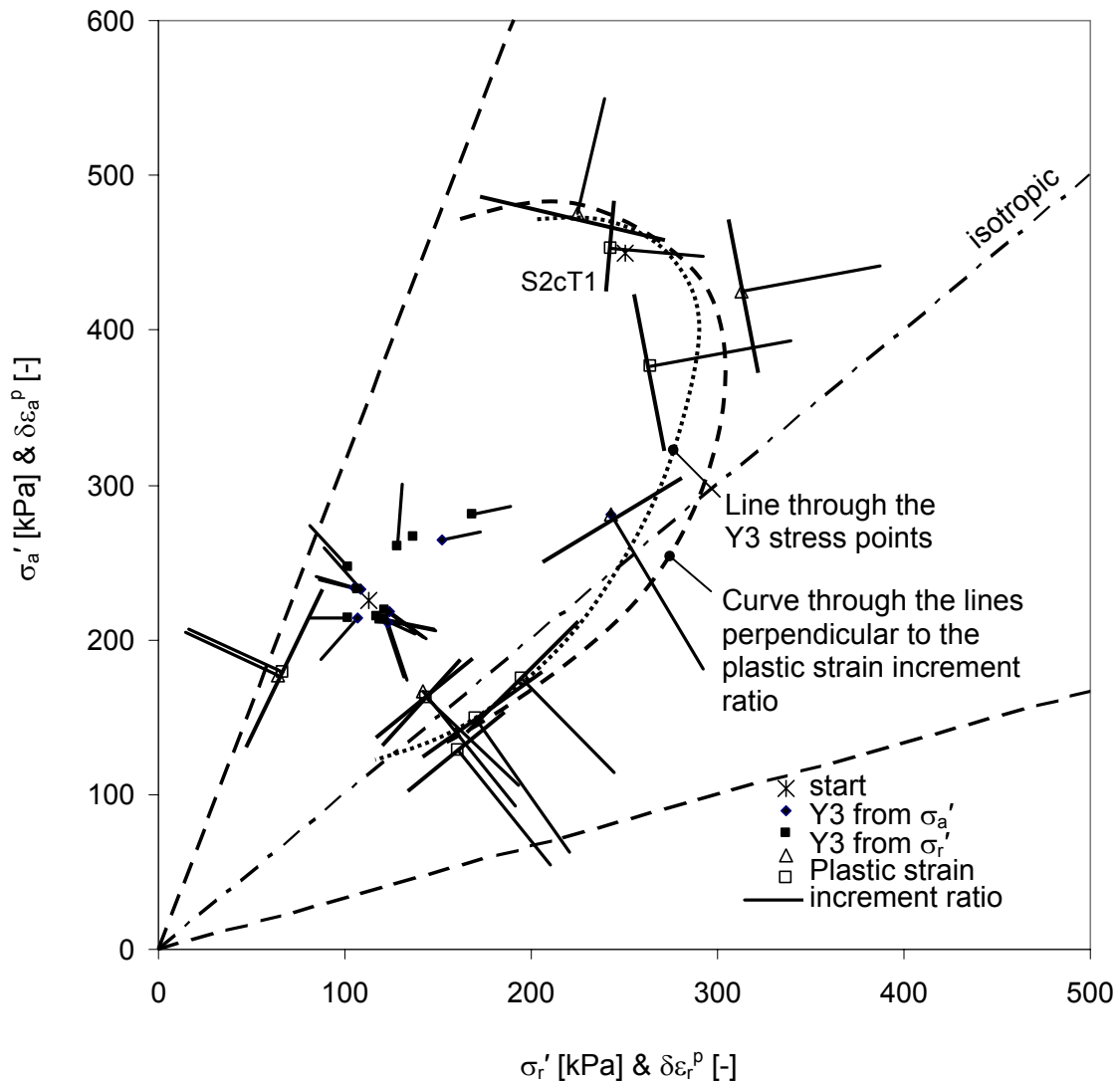
Fig. 6.26: Determination of the plastic potential surface at the Y3 yield points of the probing paths of test series 2 in the σ_a' - σ_r' stress space and $\delta\varepsilon_a^p - \delta\varepsilon_r^p$ strain increment space.

The same analysis is done for the Y2 yield points (Fig. 6.27). The resulting tangents to the plastic potential surface fit well with the shape of the proposed yield surface. Only the strain increment vector given by test S2cT1 does not correspond. Many test results are given for the left hand side of the curve for the Y2 yield surface, which was not possible for the Y3 surface. All these results

confirm a shape of the plastic potential surface similar to the proposed elliptical yield surface.
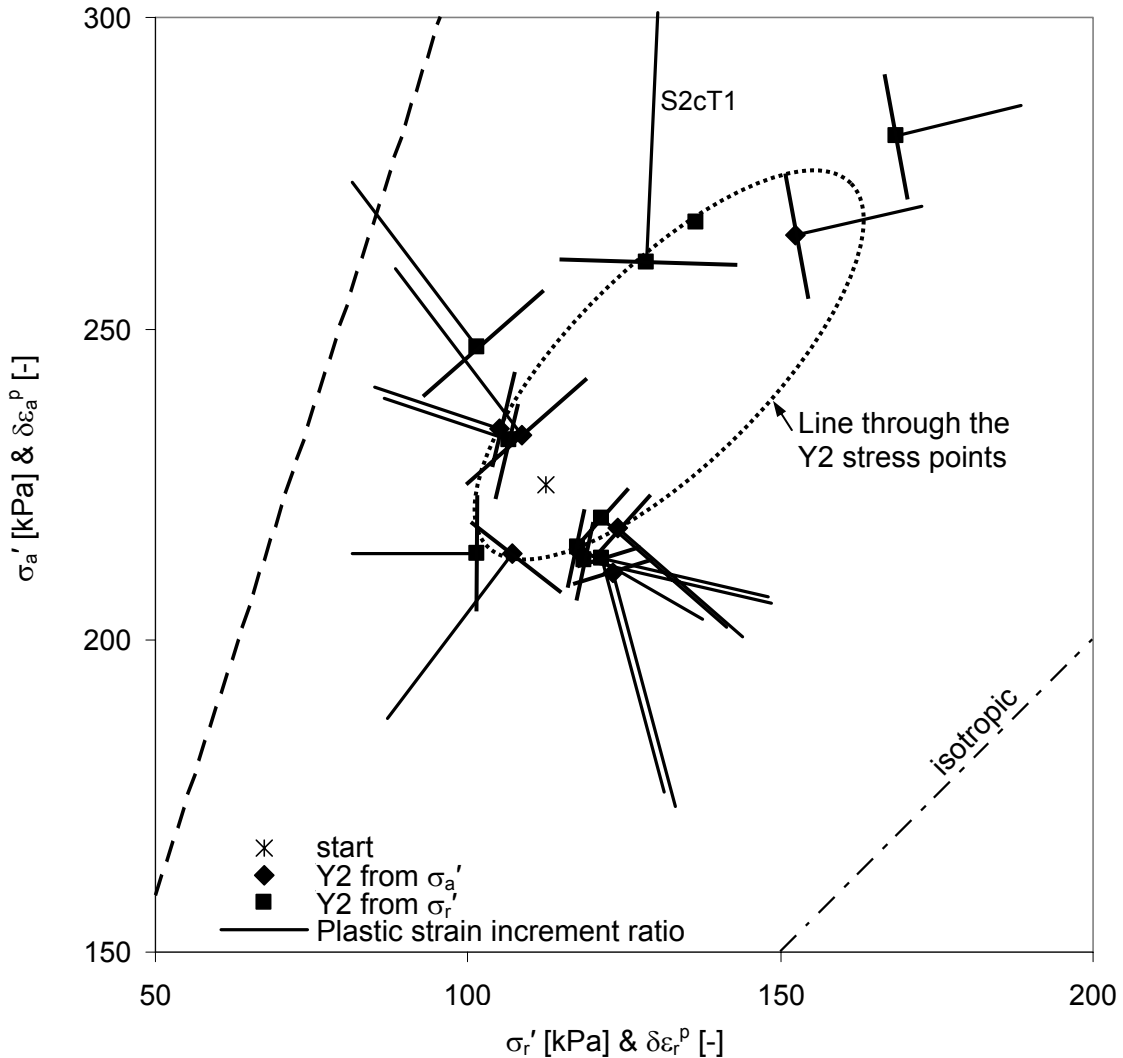
Fig. 6.27: Determination of the plastic potential surface at the Y2 yield points of the probing paths of test series 2 in the σ_a' - σ_r' stress space and $\delta\varepsilon_a^p - \delta\varepsilon_r^p$ strain increment space.

The plastic and cross-anisotropic elastic strain increment ratios, calculated from Eq. 6.32 at the Y3 yield points are plotted in Fig. 6.28. The comparison shows that the cross-anisotropic strain increment ratio corresponds to the plastic strain increment ratios determined for the extension tests. For those stress path tests with a stress increment ratio between isotropic and one-dimensional, the cross-anisotropic elastic matrix underpredicts the absolute axial strain component and

for stress increment ratios higher than the one-dimensional stress increment ratio, the cross-anisotropic elastic matrix overpredicts the axial strain component (Fig. 6.28).
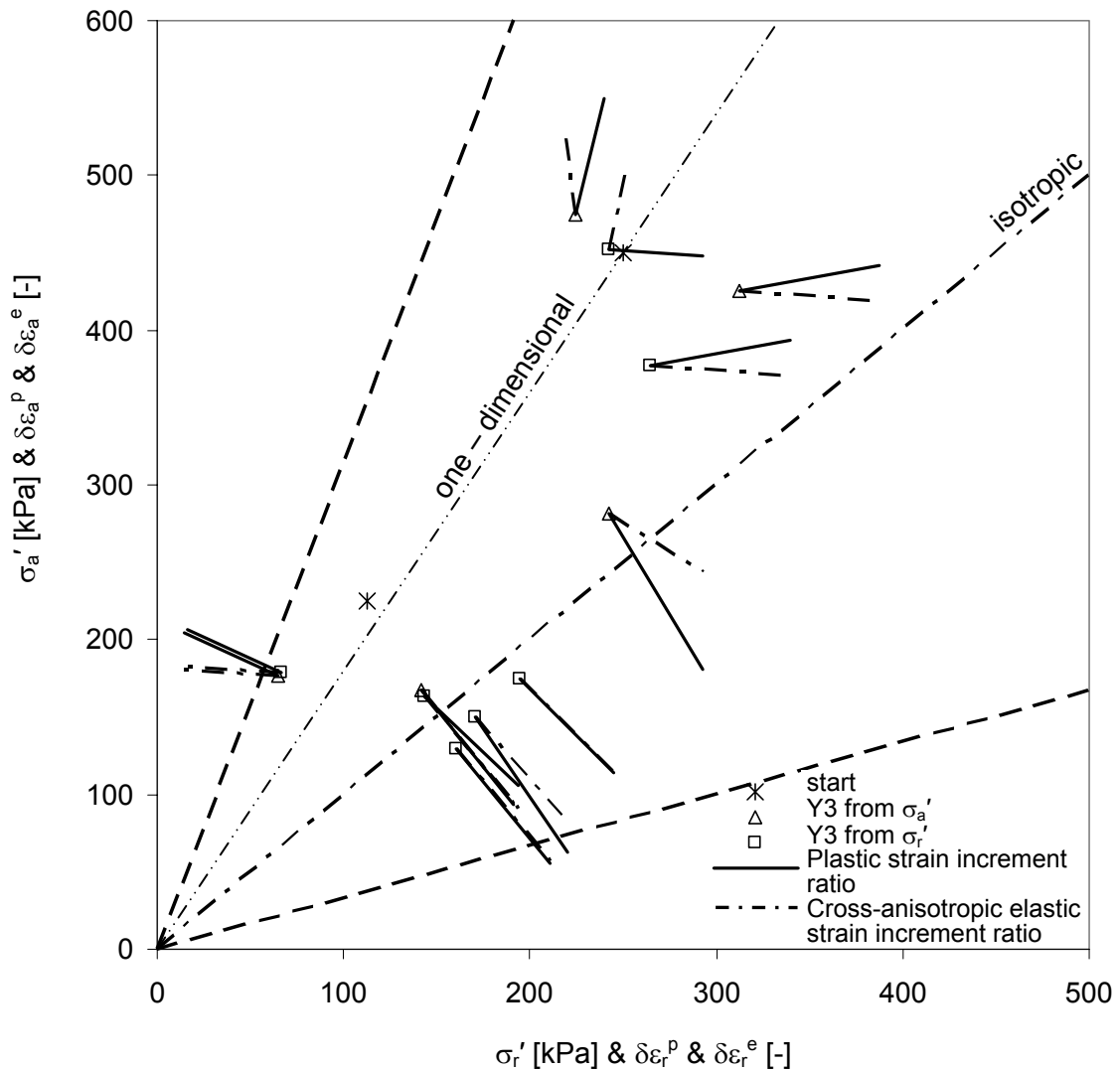
Fig. 6.28: Comparison of the cross-anisotropic elastic to the plastic strain increment ratio at the Y3 yield points of the probing paths of test series 2 in the $\sigma_a{}'$ - $\sigma_r{}'$ stress space and $\delta\varepsilon_a{}^p$ – $\delta\varepsilon_r{}^p$ strain increment space.

The strain ratios of cross-anisotropic elastic, plastic and total strain increments are plotted at the corresponding Y2 yield points (Fig. 6.29). Comparison of the plastic to the total strain increment ratios shows that the ratios differ by up to 25% (see also Appendix Fig. 10.143 to Fig. 10.155). The comparison of the cross-

anisotropic elastic to the plastic strain increment vectors shows good agreement between the ratios, with the same tendencies as discussed previously for the Y3 points.
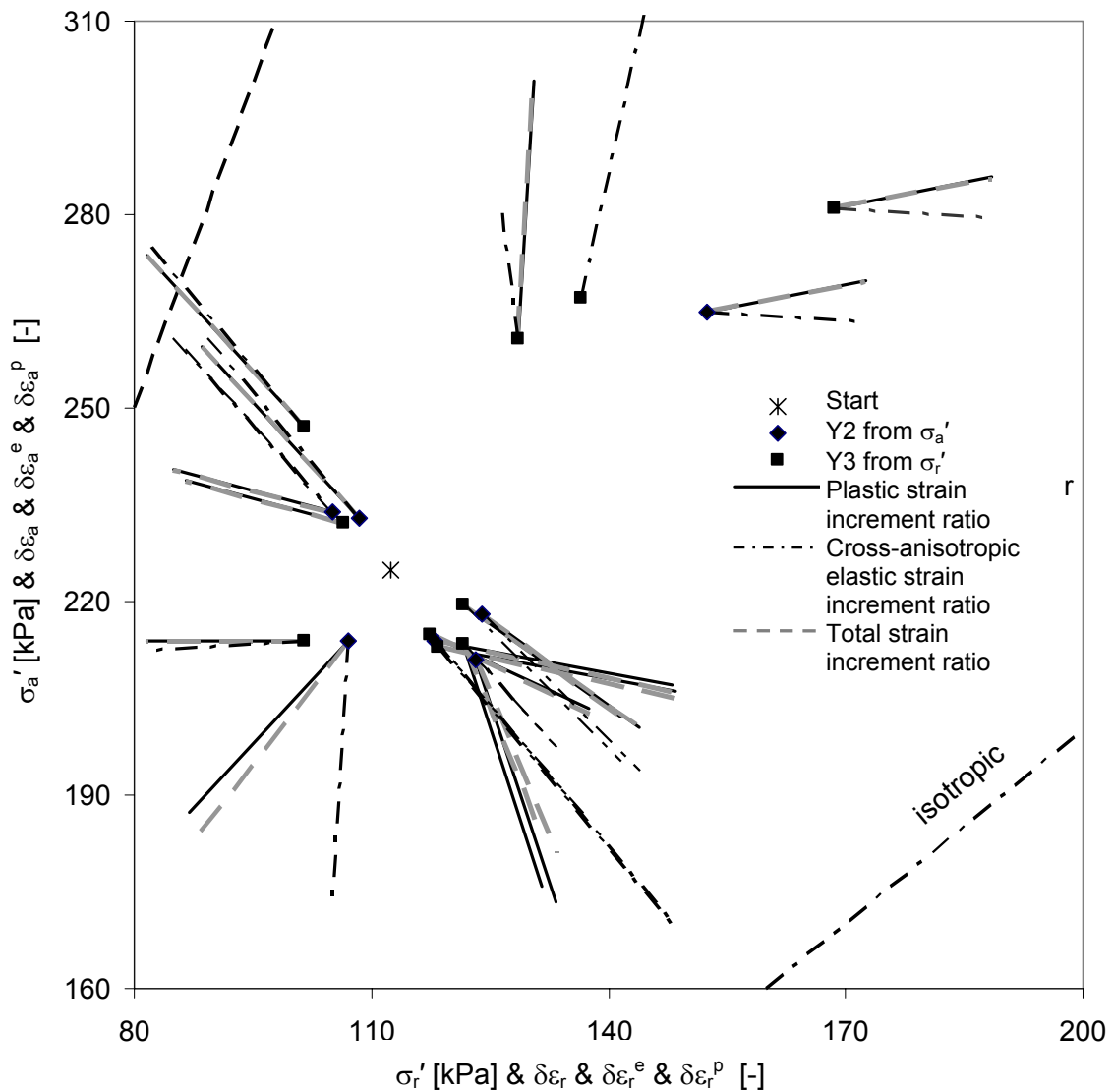
Fig. 6.29: Comparison of the cross-anisotropic elastic, plastic and total strain increment ratios at the Y2 yield points of the probing paths for test series 2 in the σ_a' - σ_r' stress space and total ($\delta\varepsilon_a - \delta\varepsilon_r$), elastic ($\delta\varepsilon_a^e - \delta\varepsilon_r^e$) and plastic ($\delta\varepsilon_a^p - \delta\varepsilon_r^p$) strain increment spaces.

The analysis and discussion of the elasto-plastic behaviour of natural Kloten clay under probing stress conditions is complete, and the behaviour at failure will now be investigated.

6.3   Analysis of the failure behaviour of Kloten clay

Significant necking is shown by the test specimens to which a probing stress path was applied in extension. This necking was observed during extraction of the sample from the triaxial cell after the test procedure. Necking causes a reduction in the sample diameter and consequently a reduction in the cross-sectional area. For tests where the axial force is kept constant, or is increased along a constant stress ramp, the reduction in cross-sectional area results in a local stress increase. Consequently, necking of the sample at stress states close to failure would cause a higher failure stress compared to the failure stress that is determined by the data evaluation method presented in Chapter 5.2.1, in which it is assumed that the sample keeps the original cylindrical shape during deformation. The magnitude of necking in the sample during test performance is not determinable from the axial and volume displacement measurement. Radial displacements have to be observed and because it is not known at which height necking will occur in the sample, radial displacement observation over the entire sample height is required.

The radial sample displacements over the entire sample height are measured by the laser scan device (Chapter 4.4), in a selection of the triaxial tests. The measurement range of the lasers is ± 5 mm, which equals a radial strain range of ± 20 %. Consequently, displacement observation at the strain magnitude expected at failure is possible. The triaxial tests of series 2 and 3, in which laser scans have been performed in apparatus 1, are presented in Chapter 5.5.3 and a discussion of the measurement data is given. It is shown that the development of necking was recorded in test S2bT1. The probing stress path for this test was achieved under drained conditions along a stress increment ratio in extension by applying a deviator stress increment of Δq = -1.5 kPa/hour, while the mean effective stress was kept the same. Laser scans have been performed every hour. The detailed test description, the sample data and the test results are presented in the Appendix (Fig. 10.64 – Fig. 10.86).

The stress is continuously increased in the stress path tests and the resulting displacements are recorded. When the failure stress state is reached while the force is increased continuously, the sample collapses and large displacements

occur suddenly. Consequently, the stress, and especially the strain state, *at* failure is difficult to observe, and so the data before and after failure are presented, i.e. the last laser scan before and the first scan after the failure.

The deviator stress at failure usually lies between these two sets of data and, due to the applied stress increment ratio and the laser scan regularity, it can vary by a maximum of Δq = 1.5 kPa for test S2bT1. The radial displacement measurement data of the three lasers are evaluated, as described in Chapter 5.2.2, to determine the equivalent sample radius (R) and, consequently, the distribution of the current cross-sectional area over the sample height. With the knowledge of the current deviator force at the stage where the laser scan is performed, the deviator stress distribution over the sample height can be determined.

These results are presented in Fig. 6.30 for test S2bT1. Additionally, the average deviator stress at failure, evaluated by applying the conventional method that assumes a cylindrical sample shape, is shown. The scan data before failure indicates a necking area at a sample height of 60 to 70 mm, in which the average deviator stress is exceeded by 7 kPa. Analyzing this in terms of shear resistance (Fig. 6.31) shows that the internal angle of friction determined from the "true" deviator stress, derived from the laser scan data, is 2.2° or 7.5 % larger than the friction angle calculated from the average deviator stress. The analysis of the laser scan data after failure (Fig. 6.30) gives a deviator stress in the necking zone that is 38 kPa larger than the average. The sample has experienced approximately 20 % axial strains at this test state and is most probably fractured along a weak horizontal layer. The assumption that a crack along a horizontal layer developed is additionally confirmed by the step in the data (marked x) at a sample height of about 73 mm (Fig. 6.30). Additionally, due to the fast deformations, the sample state might not be fully drained anymore. However, this stress state, determined from the laser scan after failure, is not exactly representative of the failure conditions. Also, it is not known how much more necking developed between the scan before failure and the sample collapsing. Although the axial *force* between the scan before and after failure is only increased by 1.5 kPa, with ongoing necking, the failure *stress* can increase significantly.
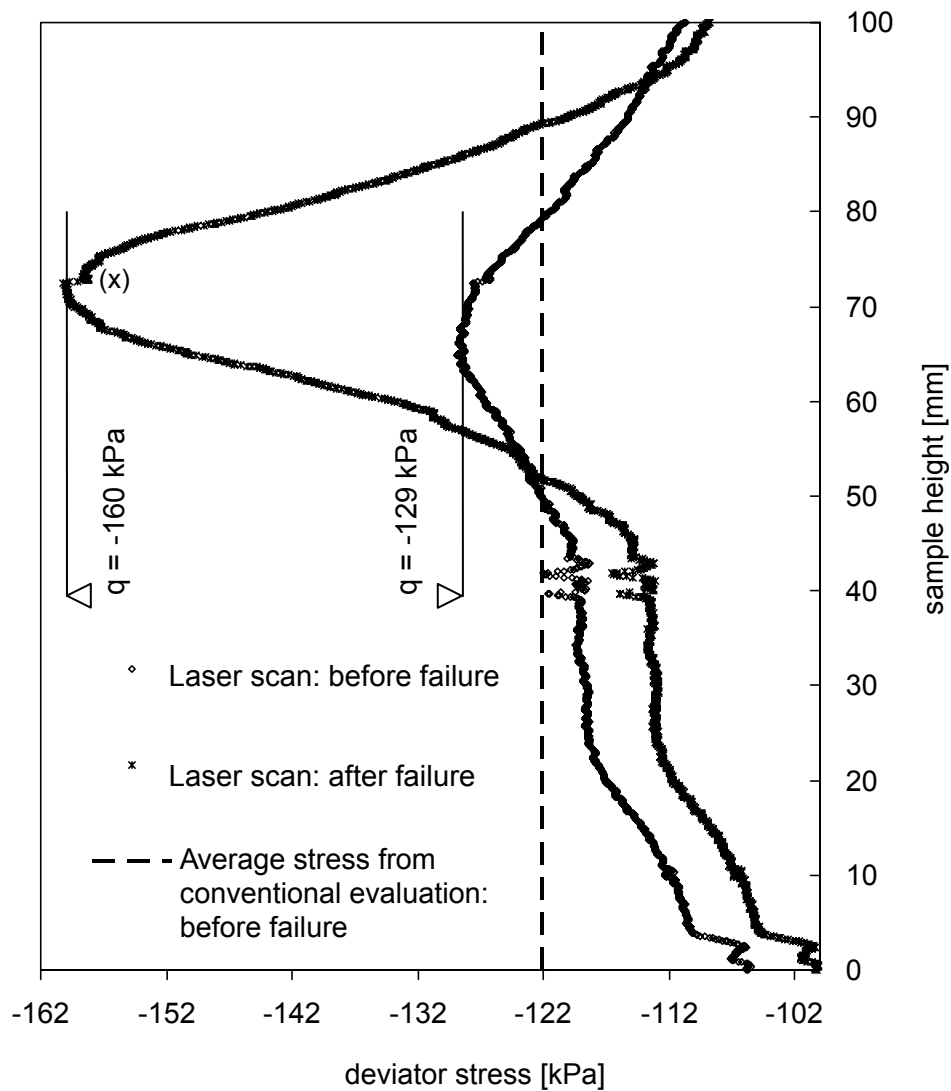
Fig. 6.30: Deviator stress distribution over the sample height for test S2bT1.

Therefore a strain path test (test S3T1) was performed, where a constant strain rate was applied while the developing force and stress were recorded. A reconstituted sample was used to avoid any influences due to sample inhomogeneities. The test details are described in Chapter 5.4.3 and the data are presented in the Appendix. An axial deformation rate of $-1 \cdot 10^{-4}$ mm/sec was applied under undrained sample conditions for this probing path. Consequently, observation of the sample volume change is not necessary for the failure stress analysis. Also, the drained strain increment ratio necessary to assure drained conditions in the entire sample is not known for stress or deformation changes

occurring suddenly at failure. Consequently, an undrained strain path test was the most straightforward solution and the results are presented in Fig. 6.32 and Fig. 6.33.
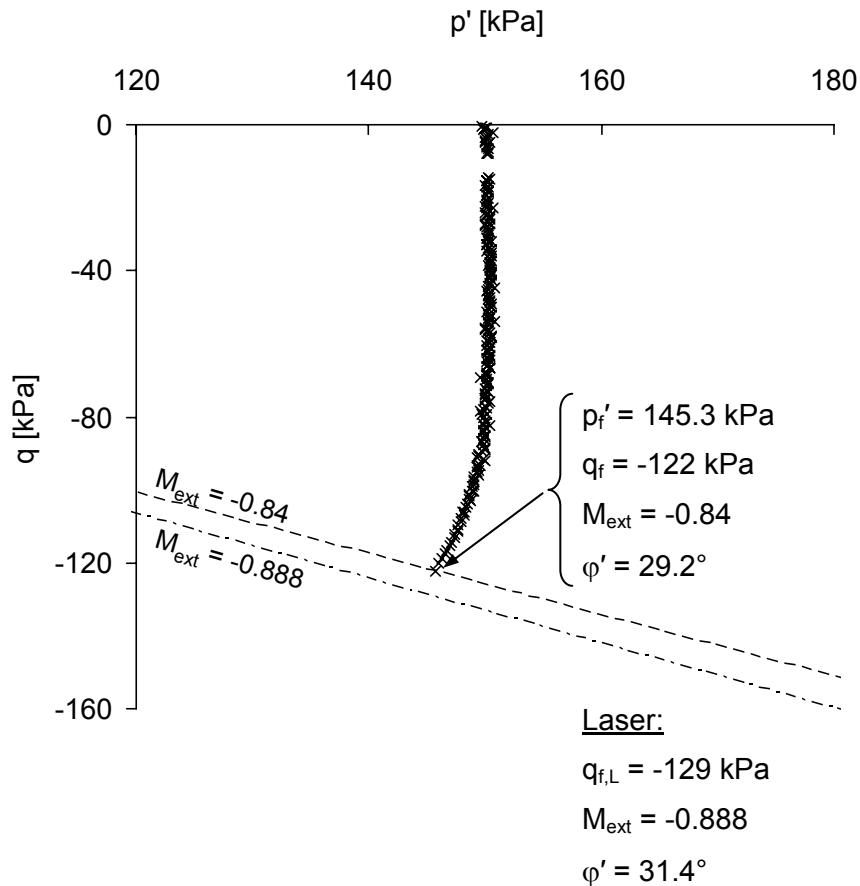
Fig. 6.31: Shear resistance analysis of measurement data performed on test S2bT1 (natural specimen); N.B.: p' axis does not extend to the origin $p' = 0$.

The stress path resulting from the deformation path applied in test S3T1 is shown in Fig. 6.33 in the q - p' space. The deviator stress distributions over the sample height determined from the laser scan at failure and after additional axial displacements of -0.391 mm are compared to the equivalent average deviator stress (Fig. 6.32). Since the third laser was not functioning in this test, the equivalent radius could not be determined, but the data are evaluated separately for each laser according to the evaluation method of Chapter 5.2.2.

The scan data from both lasers, presented in Fig. 6.32, show the development of a necking zone at a sample height of 20 to 30 mm. While the profile of laser 1

indicates a more concentrated necking zone at the sample height of 20 mm, it is spread over a range of 30 mm in the profile of laser 2. These different responses along the two profiles measured may result from the influence of the bottom fixity of the local LVDTs (Fig. 5.20).
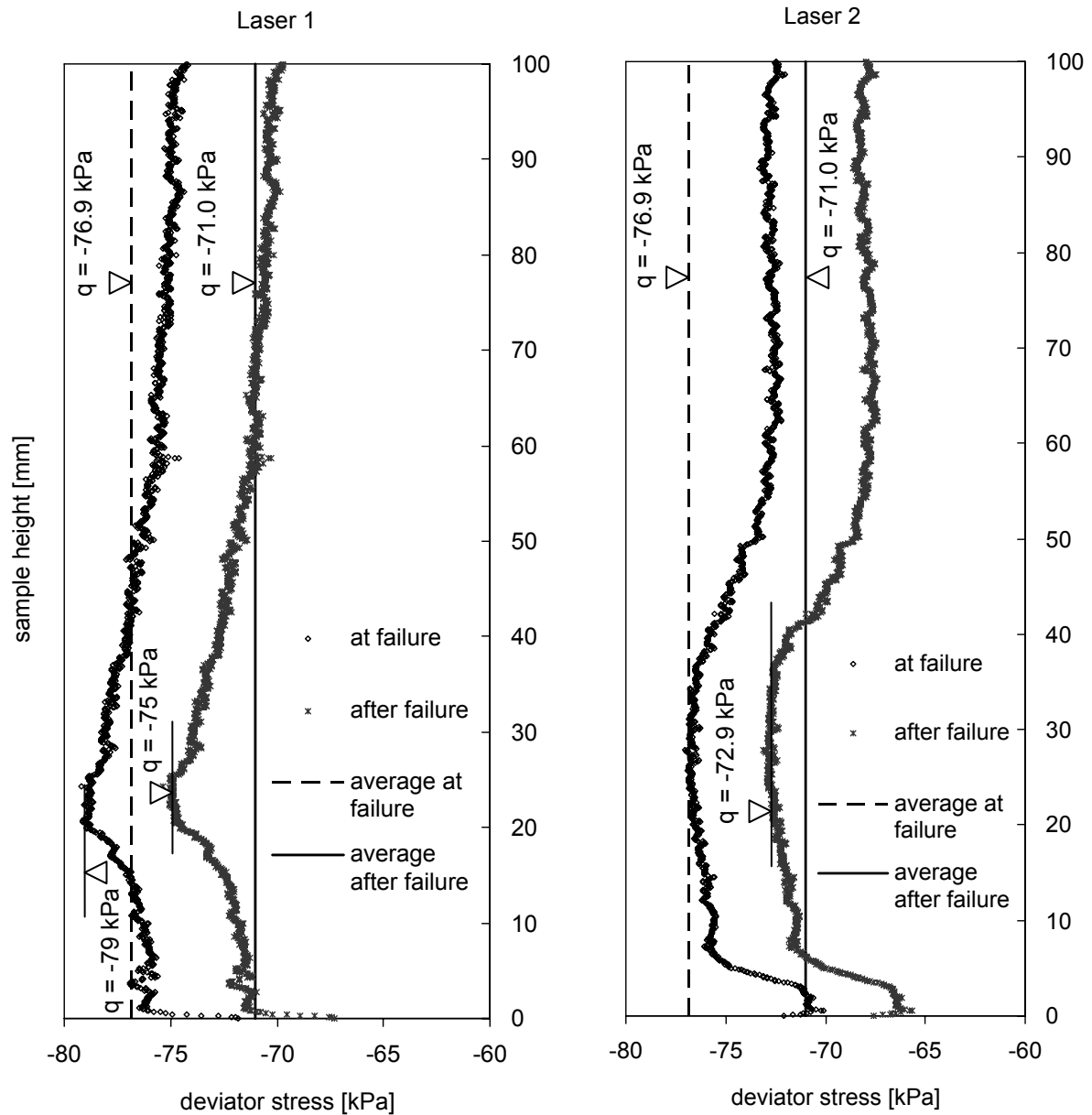
Fig. 6.32:   Deviator stress distribution over the sample height for test S3T1.

The comparison of the deviator stress, derived from the laser scan data, to the average deviator stress shows that at failure in laser profile 1, the deviator stress

calculated in the necking zone is 2.1 kPa higher than the average value, while there appears to be no difference in laser profile 2. Additionally, it can be seen that the deviator stress decreases with increasing axial strains. After additional 0.391 mm axial displacements are applied, the average deviator stresses reduce by 5.9 kPa and the difference between the deviator stress in the neck at failure and the average stress increases to 4 kPa for Laser 1 and 1.9 kPa for Laser 2.
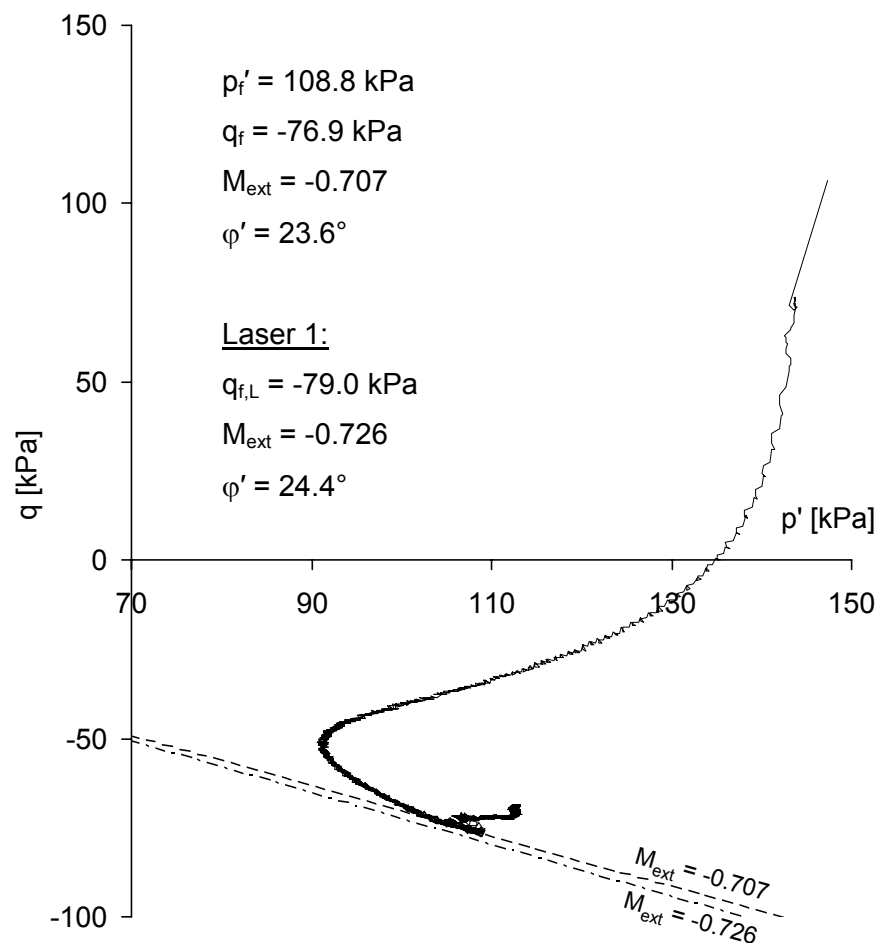
Fig. 6.33: Shear resistance analysis of measurement data performed on test S3T1 (reconstituted specimen); N.B.: *p'* axis does not extend to the origin *p'* = 0.

Analyzing the increased deviator stress in the necking zone at failure in terms of shear resistance again (Fig. 6.33), shows that the friction angle derived from the laser scan data of laser 1 is 0.8° or 3.4 % larger than the one determined from the average deviator stress. In general, the shear resistance of the reconstituted sample is smaller than that of the natural samples of Kloten clay, which indicates

that the natural varving may also act as reinforcement for shearing applied in triaxial extension.

This investigation showed that 95 % of the necking visible in a sample, for example after a stress path with shear in extension, develops after the peak deviator stress is passed. Therefore, the increase of deviator stress locally at the necking zone is not significant. Consequently, the standard evaluation method of triaxial test data for the determination of deviator stress, which assumes a cylindrical specimen shape up to failure, is valid for all stress states before failure.

6.4 Conclusion and Outlook

The analysis of the triaxial stress path tests on natural lacustrine clay establishes the complex deformation behaviour of these varved soils. It was found that the stress-strain behaviour is already nonlinear after the development of very small strains and that plastic strains develop not only in zone 4 but in zone 3 as well (Fig. 1.2). The natural stratification of the lacustrine clay samples influence the material behaviour from the small strains stage, due to the anisotropy in the elasticity, up to the large strain stage at failure, where the friction resistance is increased by the silt layers reinforcing the material and where the failure surface is changed from a shear zone to a crack or slip zone along a weak layer.

In summary, the deformation behaviour of lacustrine clays is significantly different in some aspects from that of natural marine or reconstituted clays.

In the following Chapter, the usability of a selection of the most recent and most commonly used constitutive models is discussed with respect to modelling the deformation behaviour of lacustrine clays.

7 Numerical modelling

7.1 Introduction

The aim of this research is to investigate the small strain stiffness behaviour of Swiss lacustrine clays, as outlined in the introduction in Chapter 1. Consequently, a series of advanced triaxial stress path tests, with accurate displacement measurement devices, have been performed on specimens obtained from block samples of Swiss lacustrine clays. The evaluation of the elastic stiffness response from these investigations resulted in the identification of the shape of two yield surfaces with corresponding plastic strain increment vectors, the establishment of anisotropic elastic stiffness properties and the determination of the failure condition in the triaxial stress space (Chapters 5 & 6). Hence, both the elasto-plastic stiffness response and the failure behaviour was established for the lacustrine clay investigated.

Finally, it is intended to introduce these findings into geotechnical design to improve predictions of deformations and the design process for serviceability limit state (SLS). The determination of the soil deformations for the SLS design is still a challenge in geotechnical design, which is addressed with the application of numerical methods. But a numerical simulation is only as good as the incorporated constitutive model and, of course, the quality of the input parameters. Therefore, some widely used and some newly developed constitutive models are investigated in terms of their application for modelling the deformation behaviour established for Swiss lacustrine clay.

One of the widely used constitutive models for simulating the deformation behaviour of soft clays is the Modified Cam Clay model (Roscoe & Burland, 1968). This model is also the basis of many subsequent developments and represents a

useful comparative reference. Therefore, this model is applied for simulating the deformation behaviour of lacustrine clay.

Two of these advanced constitutive models, which are based on the Modified Cam Clay model, are entitled 3-SKH (Three Surface Kinematic Hardening; Stallebrass, 1990; Stallebrass & Taylor, 1997) and S_CLAY1 (Soft Clay1; Wheeler, 1997; Näätänen et al., 1999). The 3-SKH model incorporates two kinematic yield surfaces (equivalent to Y1 & Y2) within the Modified Cam Clay bounding surface (Y3) with which non-linear elastic and stress path dependent stiffness behaviour is simulated. The kinematic yield surface, representing the stress path dependency, has the same shape as the Y2 surface, analysed for lacustrine clay (Chapter 6). Therefore this model seems to be the most appropriate to simulate this behaviour. In the S_CLAY1 model, the elliptical bounding surface of the Modified Cam Clay model, which represents isotropic elasto-plastic behaviour, is changed into an elliptical bounding surface "inclined" in the $p'–q$ stress space, to simulate anisotropic elasto-plastic behaviour. An inclined bounding surface (Y3) was established as well in the data analysis of the triaxial stress path tests (Chapter 6). Therefore this model seems to be the most appropriate to simulate the anisotropic plastic deformation behaviour.

Most of the major drawbacks of the Modified Cam Clay model, in terms of simulating the pre-failure deformation behaviour, are overcome with these two advanced constitutive models. But one unfavourable aspect of the model, which is also outlined in the discussion of the constitutive models in the literature review, remains. This is the description of the failure behaviour with the Drucker-Prager criterion. Therefore, another basic constitutive model, which shares similar features with the Modified Cam Clay model, is the Soft Soil model (Brinkgreve, 1994), and is also applied in the simulations. The Soft Soil model (SS) describes the failure behaviour with the Mohr-Coulomb failure criterion. The elasto-plastic behaviour is described by an elliptical yield surface, which is only active on the "wet" side (Roscoe & Burland, 1968) of the critical state line (CSL). The shape of this yield surface is not dependent on the critical state parameter, as in the Modified Cam Clay model, but can be defined by an independent parameter. Therefore, the strain increment ratio for plastic straining on the wet side can be

varied in order to adjust the strain increment ratio e.g. for one-dimensional conditions.

These are the four constitutive models selected for the numerical simulation of the deformation and failure behaviour of lacustrine clay. Finally, a simulation code has to be chosen and the model parameters determined before the simulations can be performed.

7.2   Numerical methods

Numerical methods have become a widely used tool in geotechnical design. Consequently, a variety of commercial finite element and finite difference codes have been developed. These can be grouped into those programs that are specifically developed for geotechnical applications such as PLAXIS (Brinkgreve et al., 2004), Flac (Itasca Consulting Group, 2002) or SAGE CRISP (Britto & Gunn, 1987; Woods & Rahim, 2001) and those which are applicable for numerical analysis of a range of different materials, also including soils; for example ABAQUS (Hibbitt, Karlsson & Sorensen, Inc., 2002). Finite elements or finite differences are used by all of these programs, but each program incorporates various element types, constitutive models and solving algorithms. The programs have primarily been chosen by the constitutive models available in the codes because the aim of the numerical modelling was to find the most appropriate model to simulate the lacustrine clay response. The accuracy of the simulations and the stability of the analysis is influenced, in particular, by the algorithm, and this was also considered. Consequently, a list of codes (Tab. 7.1) is given, in which the 4 constitutive models, mentioned above, are implemented.

The Modified Cam Clay (MCC), the three surface kinematic hardening (3-SKH) and a beta version of the S_CLAY1 model are implemented in CRISP. A modified version of the Modified Cam Clay model, a user defined soil model of the S_CLAY1 model and the Soft Soil model (SS) are implemented in PLAXIS. Consequently, these two codes are used for the numerical simulations.

Tab. 7.1:   Available finite element and difference codes and their constitutive models.

Codes – Models:	MCC	3-SKH	S_CLAY1	SS
Abaqus	x			
Sage CRISP	x	x	(x)	
Flac	x			
PLAXIS	(x)		x	x

N.B.: Brackets indicate that the models are a beta version such the S_CLAY1 model in CRISP or that the model formulation incorporated in the code diverges from the original formulation (MCC in PLAXIS).

7.3 Constitutive models and their parameters

The constitutive model formulations are briefly outlined, before the model parameters are determined.

7.3.1 Modified Cam Clay model (MCC)

The Modified Cam Clay elasto-plastic bounding surface (Roscoe & Burland, 1968) is defined by Eq. 7.1, which represents an ellipse in the triaxial stress space q – p′.

$$q^2 - \mathrm{M}^2 p'\left(p_0{}'-p'\right) = 0 \qquad\qquad \text{Eq. 7.1}$$

where p_0' is the mean effective preconsolidation stress (Fig. 7.1). The elastic stiffness response inside the bounding surface is described by the isotropic elastic stiffness matrix (Eq. 7.2). The formulation is given in the triaxial stress space where K' is the bulk modulus and G' is the shear modulus.

$$\begin{bmatrix} \delta\varepsilon_v^e \\ \delta\varepsilon_s^e \end{bmatrix} = \begin{bmatrix} \dfrac{1}{K'} & 0 \\ 0 & \dfrac{1}{3G'} \end{bmatrix} \begin{bmatrix} \delta p' \\ \delta q \end{bmatrix} \qquad\qquad \text{Eq. 7.2}$$

The plastic straining is described by an associated flow rule, which results in a plastic strain increment ratio for the MCC yield surface (Eq. 7.1) of:

$$\frac{\delta\varepsilon_s^p}{\delta\varepsilon_v^p} = \frac{2\eta}{M^2 - \eta^2}$$

Eq. 7.3

The MCC model is formulated within the critical state concept (Roscoe et al., 1963), which defines a unique relationship between the volumetric deformation behaviour and the deviator and mean effective stresses at failure. An outline of the critical state concept and its parameter definition is given in Fig. 7.1.
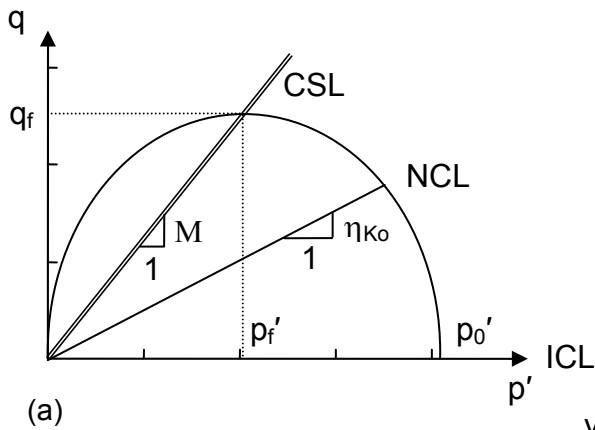
Modified Cam Clay:

bounding surface:

$$q^2 - M^2 p'\left(p_0' - p'\right) = 0$$

Critical State Line:

$$q_f = M p_f'$$

$$v = \Gamma - \lambda \, ln\left(p'\right)$$
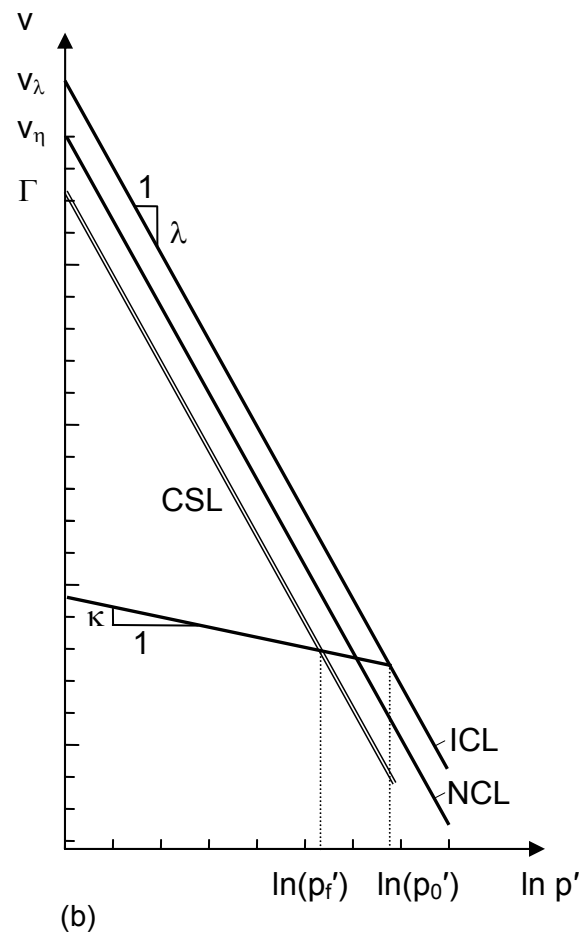
Fig. 7.1:   Critical state concept shown in a) $q - p'$ space b) $v - ln\,p'$ space.

Consequently, the bulk modulus (K') derived from the critical state theory is described by Eq. 7.4:

$$\delta\varepsilon_v^e = \frac{\kappa}{v}\frac{\delta p'}{p'} \quad \rightarrow \quad K' = \frac{vp'}{\kappa}$$

Eq. 7.4

where v is the pore volume and κ is the swelling index defined in the $v - \ln p'$ space (Fig. 7.1). The resulting volumetric hardening law is:

$$\delta p_o' = \frac{vp_0'}{\lambda - \kappa}\delta\varepsilon_v^p \quad \rightarrow \quad \delta\varepsilon_s^p = \frac{2\eta}{M^2 - \eta^2}\delta\varepsilon_v^p$$

Eq. 7.5

where λ is the compression index defined in the $v - \ln p'$ space (Fig. 7.1). The failure stress state is described by the critical state line in the triaxial stress space, which represents a Drucker-Prager failure cone in the general stress space.

Modified Cam Clay parameters

Five parameters are required for the Modified Cam Clay model, which include the four critical state parameters M, λ, κ, Γ and the elastic shear modulus G'. The self weight of the sample is neglected in the triaxial test simulations presented, with specimen dimensions of 5 cm in diameter and 10 cm in height and mean effective stress levels of 150 to 300 kPa. Therefore, the unit weight of the soil (γ) does not need to be specified.

The gradient of the critical state line in the q – p' space for compression tests was determined in Chapter 5 (Fig. 5.8) as $M_{comp} = 1.25$ for Kloten clay. The swelling index κ and the compression index λ were determined from the plot of the volume compression curves during consolidation and swelling along a stress ratio of $\eta_{Ko} = 0.75$, presented in Chapter 5 (Fig. 5.9), and gave values of $\lambda = 0.045 - 0.061$ and $\kappa = 0.009 - 0.012$. The volume at $p' = 1\,kPa$ was determined as $e_\eta = 0.88$ (Fig. 5.9). Consequently, the specific volume intercept in *ln p'* space (Γ) can be calculated from the critical state theory combined with the Modified Cam Clay yield surface as:

$$v_\eta - \lambda\,ln\,p' + \kappa\left(ln\,p' - ln\frac{p_0'}{2}\right) = \Gamma - \lambda\,ln\frac{p_0'}{2}$$

Eq. 7.6

$$\Gamma = v_\eta - (\lambda - \kappa) \ln\left(2\frac{p'}{p_0'}\right)$$

Eq. 7.7

With the transformation of the Modified Cam Clay yield surface (Eq. 7.1) into a stress ratio dependent formulation:

$$\frac{\eta^2}{M^2} + 1 = \frac{p_0'}{p'}$$

Eq. 7.8

and the use of the mean values for the compression and swelling indices of $\lambda = 0.053$ and $\kappa = 0.01$ and a specific volume of $v_\eta = 1.88$ for the consolidation stress path with $\eta = 0.75$, the specific volume intercept for the critical state line Γ for Kloten clay can be calculated as $\Gamma = 1.86$.

Finally, the description of the elastic stiffness has to be completed, either by giving a value for the elastic shear modulus or for the Poisson's ratio of Kloten clay. While it is optional to give the shear modulus or the Poisson's ratio as an input parameter in CRISP in the model version implemented in PLAXIS, the elastic properties can only be described via the Poisson's ratio. In order to get the same set of elastic parameters in all simulations, the Poisson's ratio is selected as the input parameter and the shear modulus will then be a function of the stress state. The Poisson's ratio for Kloten clay was determined in Chapter 6.2.3 from the radial and axial displacement measurement data, assuming isotropic elastic material behaviour, as $v' = 0.26 - 0.33$. But it was also shown that Kloten clay does not respond isotropically but anisotropically. However, only an isotropic stiffness matrix is implemented in the MCC model to simulate the elastic material response, so an appropriate isotropic Poisson's ratio had to be chosen for the simulations. Therefore a parametric study was performed on this parameter (Chapter 7.5.4; Fig. 7.23 & Fig. 7.22). The ranges of values applied in the parametric study are given in Tab. 7.2 and the value chosen for the subsequent simulations is underlined.

A summary of all the parameters of the MCC model and their values for natural Kloten clay is given in Tab. 7.2:

Tab. 7.2: Material parameters of Kloten clay for the Modified Cam Clay model.

Gradient of the critical state line in the q – p′ space	M_{comp}	1.25
Compression index, defined in the v – ln p′ space	λ	0.053
Swelling index, defined in the v – ln p′ space	κ	0.01
Poisson's ratio	ν'	0.1 - 0.2 - 0.3
Specific volume at intercept of critical state line when p′ = 1 kPa	Γ	1.86

7.3.2 Three surface kinematic hardening model (3-SKH)

The Modified Cam Clay yield surface is extended by two kinematic surfaces within the bounding surface in the 3-SKH model (Stallebrass, 1990). These two kinematic surfaces are called the history and the yield surfaces (Fig. 7.2). They have the same shape as the Modified Cam Clay bounding surface (Eq. 7.1), but their size is scaled by the factors T^2 for the history surface and S^2 for the yield surface.

The mean effective preconsolidation stress p_0' in the MCC model equals the parameter p_c' in the 3-SKH model (see Fig. 7.1 & Fig. 7.2) and the parameter p_0' equals $p_c'/2$ in the 3-SKH model in the formulation of the yield surfaces (Eq. 7.1, Eq. 7.9 & Eq. 7.10). These changes in the use of the parameters were applied in the 3-SKH model in order to simplify the term on the right hand side in Eq. 7.9 and Eq. 7.10.

Consequently, the formulation of the history surface becomes:

$$\left(p'-p_a'\right)^2 + \frac{\left(q^2 - q_a^{\,2}\right)}{M^2} = T^2 p_0'^{\,2}$$

Eq. 7.9

and the corresponding formulation for the yield surface is:

$$\left(p'-p_b'\right)^2 + \frac{\left(q^2 - q_b^{\,2}\right)}{M^2} = T^2 S^2 p_0'^{\,2}$$

Eq. 7.10

where (q_a, p_a') and (q_b, p_b') are the locations of the centres of the history and yield surfaces, respectively (Fig. 7.2).

The movement of the centre of the two kinematic surfaces inside the bounding surface is described by a translation rule for each surface. Each translation rule consists of two components. The first component describes the movement of the kinematic surface due to the expansion or contraction of the bounding surface. The second component describes the movement of the kinematic surface when it is dragged by the current stress state.
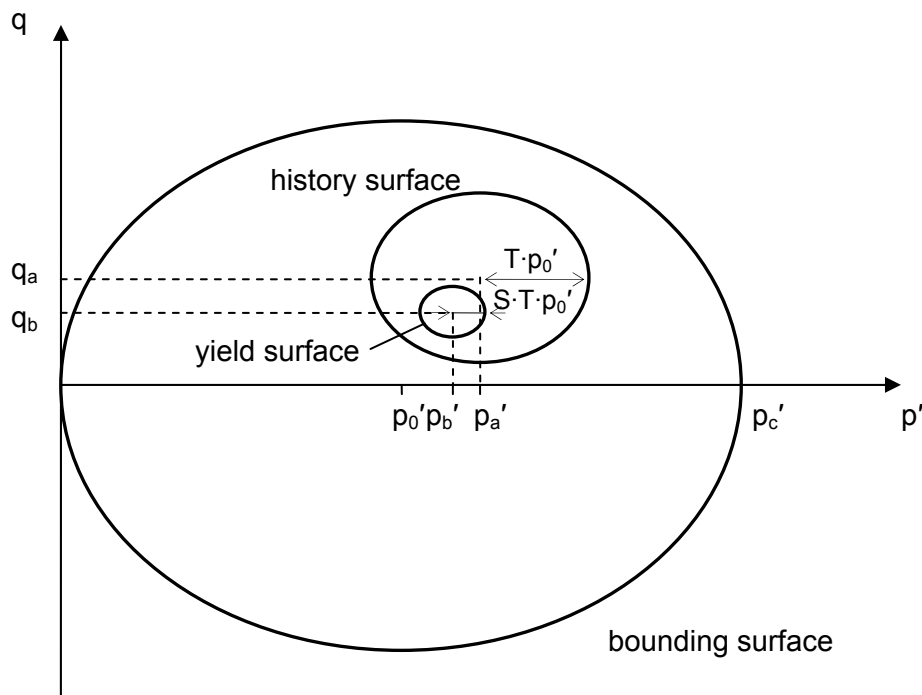
Fig. 7.2:   The three yield surfaces that constitute the 3-SKH model, presented in the q – p′ stress space, after Stallebrass (1990).

The two components of the translation rule for the history surface are shown in Eq. 7.11, which combine expansion or contraction of the surfaces as well as the translation:

$$\begin{bmatrix} \delta p_a' \\ \delta q_a \end{bmatrix} = \frac{\delta p_0'}{p_0'} \begin{bmatrix} p_a' \\ q_a \end{bmatrix} + W \begin{bmatrix} \dfrac{p'-p_a'}{T} - (p'-p_0') \\ \dfrac{q-q_a}{T} - q \end{bmatrix} \qquad \text{Eq. 7.11}$$

where W is determined from the consistency equation as:

$$W = \frac{\left(p'-p_a'\right)\left(\delta p' - \dfrac{\delta p_0'}{p_0'}p'\right) + \dfrac{(q-q_a)}{M^2}\left(\delta q - \dfrac{\delta p_0'}{p_0'}q\right)}{\left(p'-p_a'\right)\left(\dfrac{p'-p_a'}{T} - \left(p'-p_0'\right)\right) + \dfrac{(q-q_a)}{M^2}\left(\dfrac{q-q_a}{T} - q\right)}$$

Eq. 7.12

and the corresponding translation rule for the yield surface is shown in Eq. 7.13:

$$\begin{bmatrix} \delta p_b' \\ \delta q_b \end{bmatrix} = \frac{\delta p_0'}{p_0'}\begin{bmatrix} p_b' \\ q_b \end{bmatrix} + Z\begin{bmatrix} \dfrac{p'-p_b'}{S} - \left(p'-p_a'\right) \\ \dfrac{q-q_b}{S} - \left(q-q_a\right) \end{bmatrix}$$

Eq. 7.13

where Z is again derived from the consistency equation as:

$$Z = \frac{\left(p'-p_b'\right)\left(\delta p' - \dfrac{\delta p_0'}{p_0'}p'\right) + \dfrac{(q-q_b)}{M^2}\left(\delta q - \dfrac{\delta p_0'}{p_0'}q\right)}{\left(p'-p_b'\right)\left(\dfrac{p'-p_b'}{S} - \left(p'-p_a'\right)\right) + \dfrac{(q-q_b)}{M^2}\left(\dfrac{q-q_b}{S} - \left(q-q_a\right)\right)}$$

Eq. 7.14

The deformations inside the yield surface are described by the same isotropic elastic constitutive equations as here used inside the bounding surface of the Modified Cam Clay model (Eq. 7.2).

The plastic straining in the 3- SKH model is described by the formulation given in Eq. 7.15:

$$\begin{bmatrix} \delta\varepsilon_v^p \\ \delta\varepsilon_s^p \end{bmatrix} = \frac{1}{h}\begin{bmatrix} \left(p'-p_b'\right)^2 & \left(p'-p_b'\right)\dfrac{(q-q_b)}{M^2} \\ \left(p'-p_b'\right)\dfrac{(q-q_b)}{M^2} & \left(\dfrac{(q-q_b)}{M^2}\right)^2 \end{bmatrix}\begin{bmatrix} \delta p' \\ \delta q \end{bmatrix}$$

Eq. 7.15

where h is defined as:

$$h = h_0 + H_1 + H_2$$

Eq. 7.16

with:

$$h_0 = \frac{\left(p'-p_b'\right)}{(\lambda-\kappa)}\left(p'\left(p'-p_b'\right) + q\frac{(q-q_b)}{M^2}\right)$$

Eq. 7.17

$$H_1 = S^2 \left(\frac{b_1}{b_{1\,max}} \right)^\psi \frac{1}{\lambda - \kappa} p_0{'}^3 \qquad\qquad \text{Eq. 7.18}$$

$$H_2 = \left(\frac{Tb_2}{b_{2\,max}} \right)^\psi \frac{1}{\lambda - \kappa} p_0{'}^3 \qquad\qquad \text{Eq. 7.19}$$

The variables b_1 and b_2 describe the degree of approach of the history to the bounding surface and the yield surface to the history surface, respectively. The formulations of the two variables are determined geometrically and are given in Eq. 7.20 and Eq. 7.21.

$$b_1 = \frac{1}{Tp_0{'}} \left(\frac{(p'-p_b')}{S} \left(\frac{(p'-p_b')}{TS} - \left(\frac{(p'-p_b')}{S} + p_a'-p_0' \right) \right) + \frac{(q-q_b)}{SM^2} \left(\frac{(q-q_b)}{ST} - \left(\frac{(q-q_b)}{S} + q_a \right) \right) \right)$$

$$\text{Eq. 7.20}$$

$$b_2 = \frac{1}{STp_0{'}} \left((p'-p_b') \left(\frac{(p'-p_b')}{S} - (p'-p_a') \right) + \frac{(q-q_b)}{M^2} \left(\frac{(q-q_b)}{S} - (q-q_a) \right) \right) \quad \text{Eq. 7.21}$$

When the two kinematic surface are in contact, b_2 becomes zero. The variables have their maximum ($b_{1\,max}$ and $b_{2\,max}$) for isotropic consolidation, when all three surfaces are in contact. The parameter ψ is called the "exponent in the hardening function" and is not determinable from laboratory investigations, and can only be chosen by trial and error (Stallebrass, 1990).

3-SKH parameters

The 3-SKH model requires 8 material parameters, including the 4 critical state parameters M, λ^*, κ^* and Γ. The elastic behaviour inside the Y1 yield surface is defined by the shear modulus G'. Additionally, 3 model-specific parameters are required. The parameters T and S, which define the size of the kinematic surfaces, and the exponent of the hardening function ψ, which defines the rate of hardening of the kinematic hardening law.

The values of the gradient of the critical state line in the $q - p'$ space (M) and the volume at critical state Γ for Kloten clay are the same as for the Modified Cam

Clay model and were determined in the previous section (Tab. 7.2). In principle, the stiffness inside the Y1 yield surface should be represented by the very small strain "elastic" stiffness, therefore the values of G' obtained from the bender element tests at the start of the probing stress path ($p' = 150\ kPa$, $q = 112.5\ kPa$ & $OCR = 2$) was selected. The swelling and compression indices in the 3-SKH model are defined in the $\ln v$ - $\ln p'$ space and are therefore named κ^* and λ^*, respectively. This change in the formulation was done following the recommendations of Butterfield (1979), who highlighted that the stiffness indices defined in the v - $\ln p'$ space may result in unrealistic values for the void ratio for certain stress paths.

The values of this newly defined compression index λ^* and the swelling index κ^* can not be derived explicitly from the compression and swelling indices κ and λ (Tab. 7.2) by equalizing their definitions because this leads to an equation in which the indices are a function of the current specific volume. Consequently, the newly defined indices are determined directly from the test data as well, as shown in Fig. 7.3, and only the ratio between λ^* and κ^* is kept the same.

The model parameters T and S are evaluated indirectly in the data analysis in Chapter 6, where it was found that the history surface Y2 has an extension in the direction of the p' axis of 65 to 80 kPa with $\Delta p' = 10\ kPa$ on the left side and the remaining $\Delta p' = 55 - 70\ kPa$ on the right side of the final unloading stress state, $p' = 150\ kPa$ and $q = 112.5\ kPa$. The bounding surface of the 3-SKH model, after consolidation along a stress ratio of $\eta = 0.75$ to a mean effective stress of $p' = 300\ kPa$, has an extension in the direction of the p' axis of 408 kPa, using $M = 1.25$.

The model is formulated in such a way that during kinematic hardening, which occurs e.g. during swelling from $p' = 300\ kPa$ to $p' = 150\ kPa$, the stress state is at the boundary of the internal kinematic surfaces. The additional enlargement of the history surface to the left side of the final swelling stress state, observed in the test evaluations, may have occurred in the soil due to aging during the consolidation pause between swelling and applying the probing stress path. This aspect is not incorporated in the model formulation and can therefore not be considered in the

T parameter determination. Consequently, the extension of the history surface on the right side of the final swelling stress state is used, which equals 6.5 times the size of the bounding surface. The value of the parameter T, which describes the ratio between the size of the history and the bounding surface is 0.15.
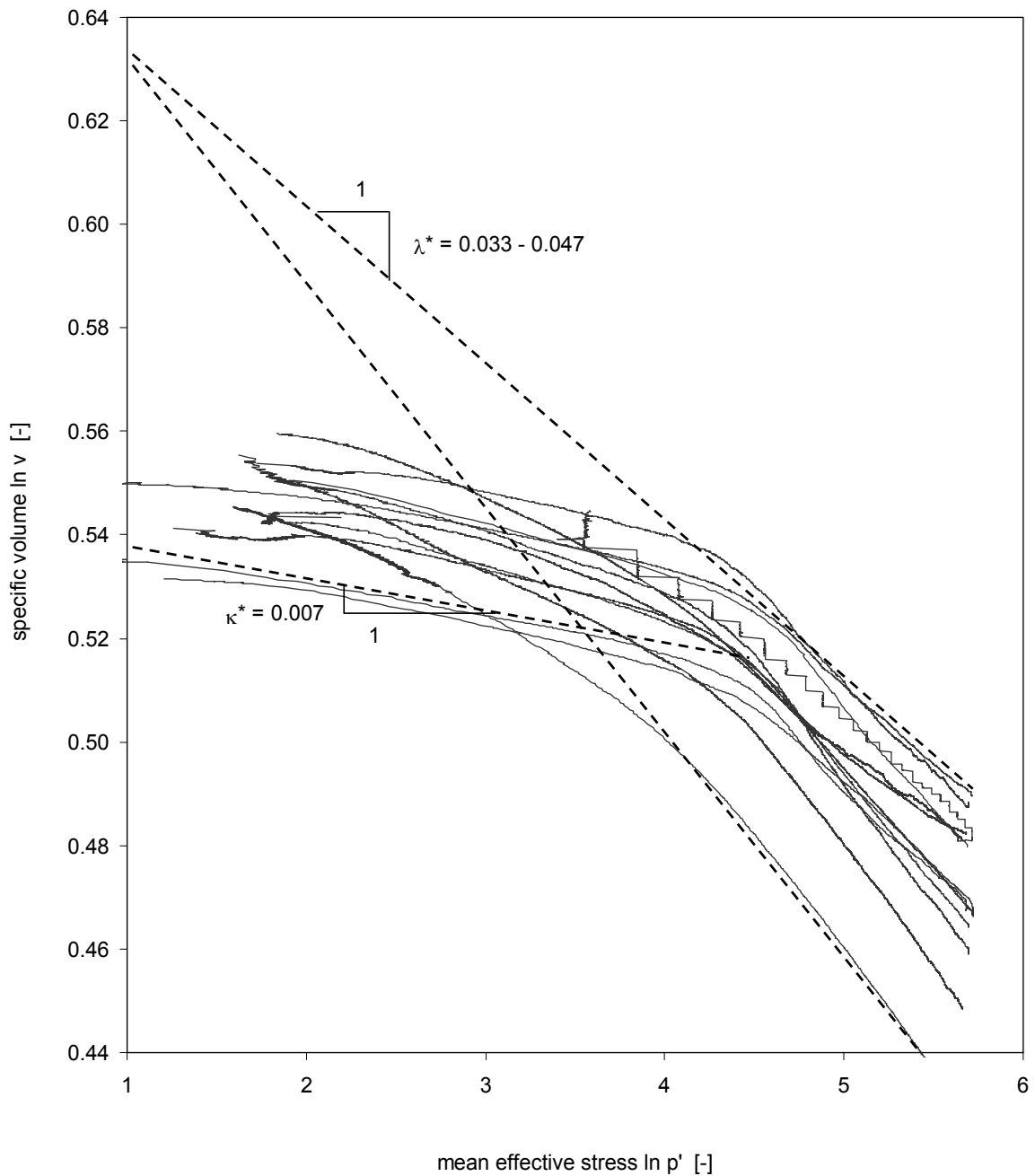
Fig. 7.3:   3-SKH stiffness parameter determination of Kloten clay from triaxial tests.

The size of the circular Y1 yield surface was not determinable from the data analysis, but the literature study indicated an extension of 0.5 and 1 kPa, which

results in a value for the parameter S, describing the ratio between the elastic surface Y1 and the history surface Y2, of 0.008 to 0.016. Consequently, an average of S = 0.012 was chosen for this Kloten clay.

The value of the exponent of the hardening function is not determinable from laboratory investigations (Stallebrass, 1990) but has to be chosen from parametric studies. Stallebrass (1990) performed such parametric studies and varied the values of the parameter ψ between 1.5 and 3.0, whereupon the plastic strain development was compared. It was found that with increasing values for ψ, the stiffness decreased more rapidly while kinematic hardening of the history surface occurred. Subsequent parametric studies for the ψ parameter for different clay types (Masin, 2004) showed that values for ψ between 1.5 and 2.75 are most suitable for the simulation of elasto-plastic deformations during plastic hardening for various clays. Consequently, a parameter study for lacustrine clay was also performed within the range of $1 \leq \psi \leq 2.8$ (Fig. 7.16 to Fig. 7.18).

A summary of all the 3-SKH model parameters and their values for natural Kloten clay is given in Tab. 7.3.

Tab. 7.3:   Material parameters of Kloten clay for the 3-SKH model in CRISP.

Gradient of the critical state line in the q – p′ space	M_{comp}	1.25
Compression index, defined in the ln v – ln p′ space	λ^*	0.04
Swelling index, defined in the ln v – ln p′ space	κ^*	0.007
Specific volume at intercept of critical state line when p′ = 1 kPa	Γ	1.86
Elastic shear modulus	G′	98 MPa
Ratio between the size of the history and the bounding surface	T	0.15
Ratio between the size of the elastic and the history surface	S	0.012
Exponent of the hardening function (1.0 - 1.5 - 1.7 - <u>2.0</u> - 2.8)	ψ	2.0

The yield surface can be drawn and compared to the test results (Fig. 7.4), with the parameters given in Tab. 7.3 and the pre-consolidation stress

($p_0{'}_{(MCC)} = p_c{'}_{(3-SKH)}$) calculated from the equation of the yield surface (Eq. 7.1) for the stress state $p' = 300 \, kPa$ and $q = 225 \, kPa$ as $p_0{'}_{(MCC)} = 408 \, kPa$.

Comparing the Modified Cam Clay bounding surface to the Y3 yield points derived from the test data analysis (Chapter 6), it can be seen that the model will predict the yield stress well for the normal consolidation stress path but will overpredict the stresses imposed before yielding occurs, when the applied stress ratio moves away from the normal consolidation path towards the extension path. The model simulation for stress increment ratios higher than the normal consolidation ratio cannot be investigated from the test results of stress path tests.
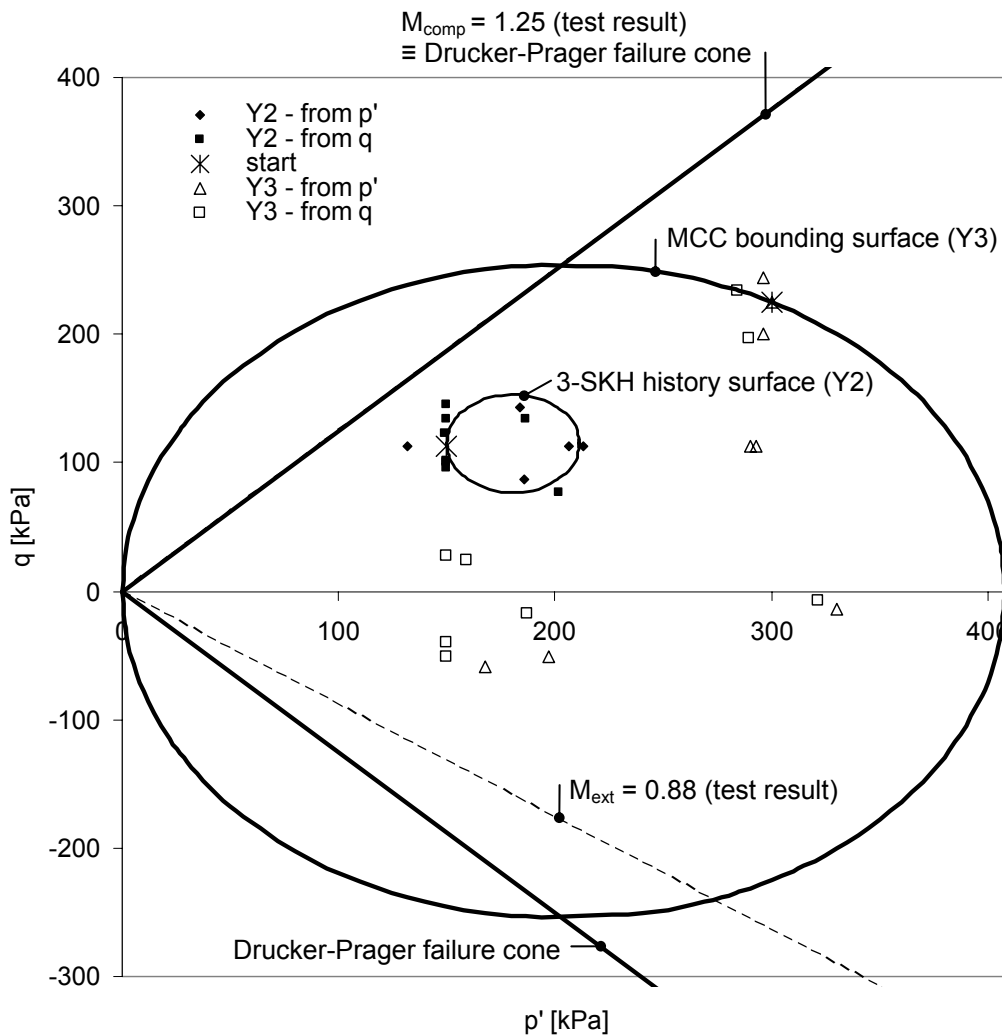
Fig. 7.4:   3-SKH yield surfaces compared to the triaxial test data.

The corresponding parameter (M) was chosen for the failure criterion in order to match the test data for failure stress paths in compression. This results in a disagreement between the failure stress states investigated and those simulated for stress paths in extension and would lead to an overprediction of the failure stress state. For the simulation of extension tests with the Modified Cam Clay model, the gradient of the critical state line in the q – p′ space M , representing the parameter of the failure criterion, can be reduced to M_{ext} (Fig. 7.5).
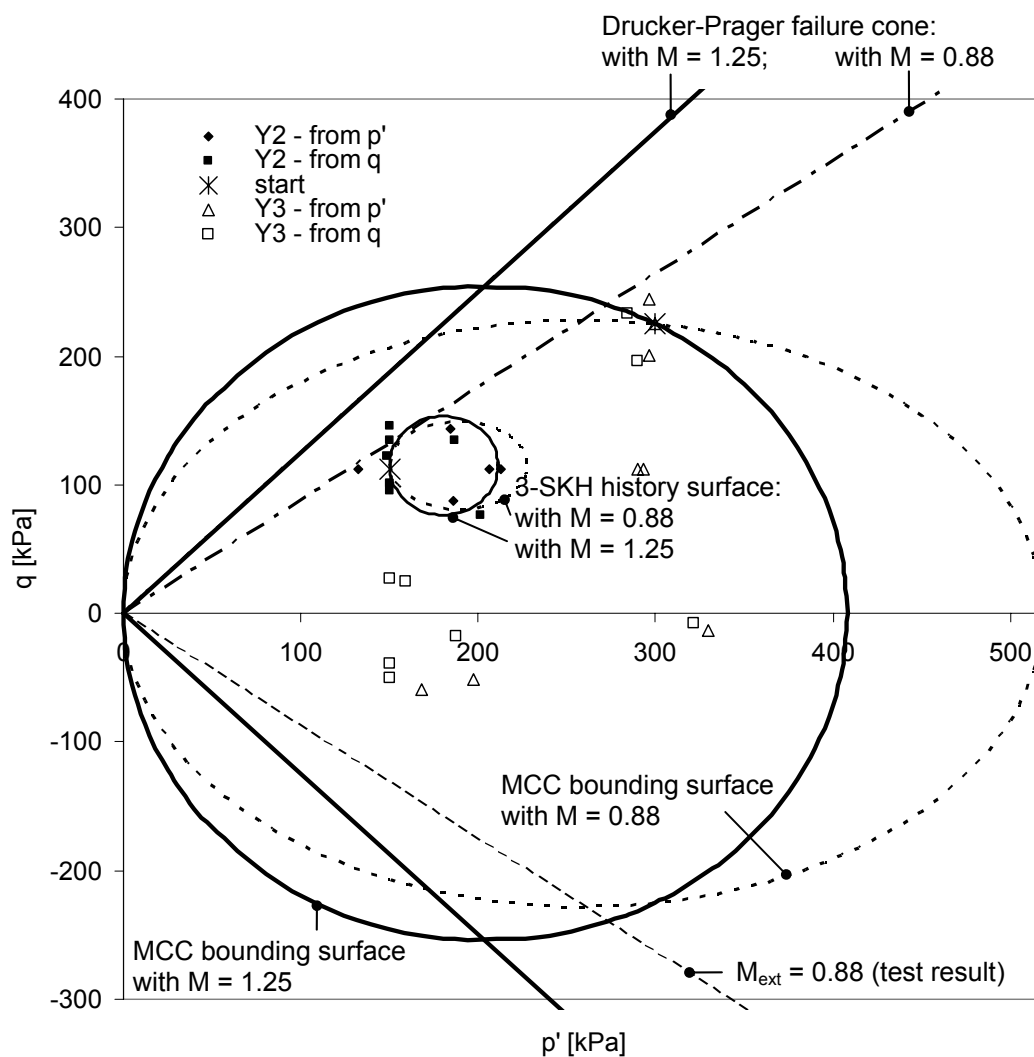
Fig. 7.5:   Comparison between the possible 3-SKH bounding and history surfaces with the triaxial test data.

This is, of course, only a solution for simulating a single stress path test. The application of a reduced value for the gradient of the critical state line in the

simulations of a boundary value problem, in which a range of stress paths in compression to extension could develop, may lead to significantly underpredicted failure stress states and the inability to predict the actual failure mechanism.

The comparison of the 3-SKH history surface for the parameters given in Tab. 7.3, to the Y2 yield points derived from the test data analysis (Chapter 6) gives good agreement (Fig. 7.4), although the history surface plotted with M_{ext} used for the critical state parameter (M) (Fig. 7.5) gives even better agreement.

But the yield and failure conditions of an elasto-plastic model represent only a part of the overall model behaviour, which is additionally specified by the elastic stiffness properties, the hardening rule and the flow rule. With the simulation of a selection of characteristic triaxial stress path tests using finite element codes, the suitability of these three latter aspects, describing the recoverable and non-recoverable deformation behaviour, in modelling the stress-strain behaviour of lacustrine clay will be investigated. The constitutive models selected, together with their model parameters, are applied in these finite element simulations, and the results are compared to the test data.

7.3.3 S_CLAY1 model

The symmetrical elliptical Modified Cam Clay bounding surface is changed into a bounding surface with the shape of a distorted ellipse (Fig. 7.6) in the S_CLAY1 model (Wheeler, 1997; Näätänen et al., 1999). The degree of distortion in the triaxial stress space is represented by the parameter α, which defines the inclination between the hydrostatic axis and the principal axis of the distorted ellipse. Consequently, the equation of the bounding surface in the triaxial stress space becomes:

$$\left(q - \alpha p'\right)^2 - \left(\mathrm{M}^2 - \alpha^2\right)\left(p_m' - p'\right)p' = 0 \qquad\qquad \text{Eq. 7.22}$$

Where p_m' is the mean effective preconsolidation stress (Fig. 7.6), which equals p_0' in the MCC and p_c' in the 3-SKH model. The term $\left(q - \alpha p'\right)$ represents the distortion of the ellipse and the term $\left(\mathrm{M}^2 - \alpha^2\right)$ describes the change of the ratio of the two principal axes of the ellipse in order to guarantee a horizontal tangent to the ellipse at the intersection with the critical state line. This latter condition has to

be guaranteed for bounding surfaces of constitutive models that apply an associated flow rule and are defined within the critical state concept.

Two further characteristics of the model are already anticipated. The model uses an associated flow rule that results in plastic strain increment ratio of:

$$\frac{\delta\varepsilon_s^p}{\delta\varepsilon_v^p} = \frac{2(\eta - \alpha)}{M^2 - \eta^2}$$

Eq. 7.23

and the model is formulated within the critical state concept, which defines the volumetric deformation and failure state.
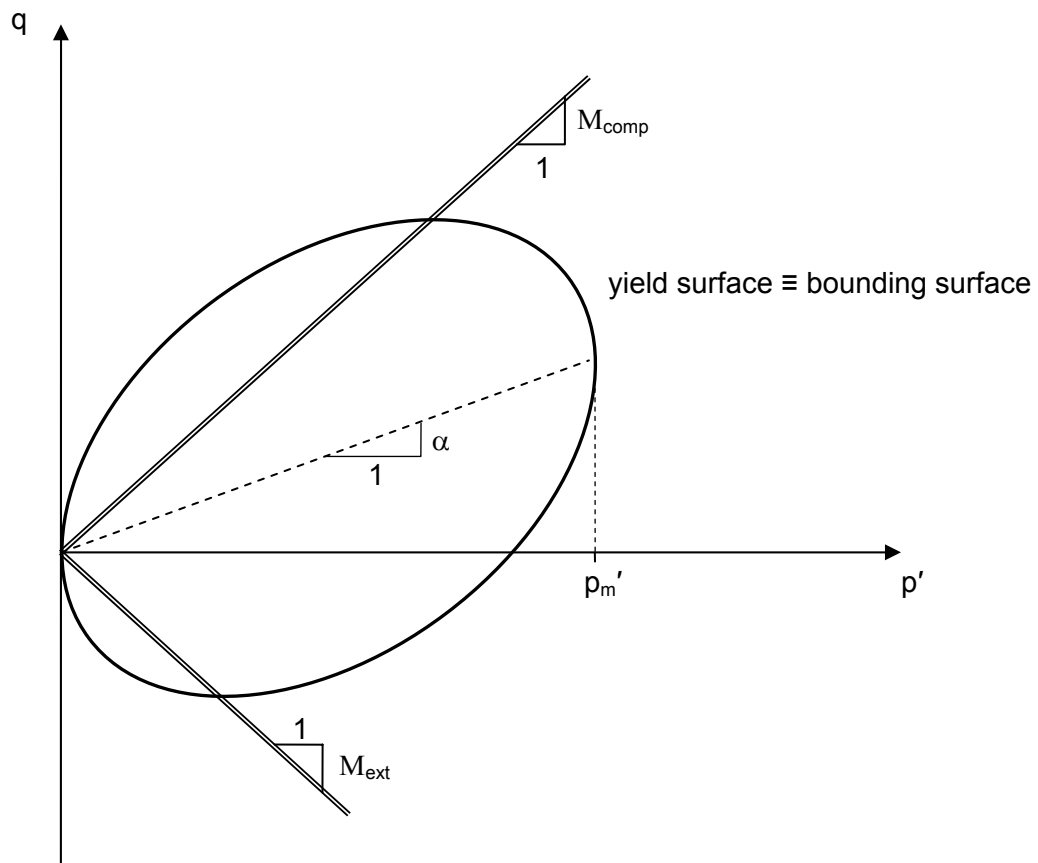
Fig. 7.6: The yield surface that constitutes the S_CLAY1 model, defined in the invariant $q - p'$ stress space, after Wheeler (1997).

Consequently the elastic straining is described by Eq. 7.2 & Eq. 7.4 and the volumetric hardening law is:

$$\delta p_m' = \frac{v p_m'}{\lambda - \kappa}\delta\varepsilon_v^p$$

Eq. 7.24

The failure criterion is the critical state line, which represents a Drucker-Prager failure cone.

Additionally, the model incorporates a second hardening law, which defines the change in inclination ($\delta\alpha$) of the bounding surface during plastic straining. This is called a rotational hardening law and is described by Eq. 7.25:

$$\delta\alpha = \mu\left[\left(\chi_v(\eta) - \alpha\right)\left\langle\delta\varepsilon_v^p\right\rangle + \beta\left(\chi_d(\eta) - \alpha\right)\left|\delta\varepsilon_s^p\right|\right]$$

Eq. 7.25

Two hardening parameters, the "rate of rotation" (μ) and the "proportional constant" (β) are incorporated in the hardening rule. The variables $\chi_v(\eta)$ and $\chi_d(\eta)$ represent target values, which are functions of the applied stress ratio η. As increments of plastic volumetric strains and plastic shear strains develop, this hardening law drags the inclination of the bounding surface towards the corresponding target value. The Macaulay brackets for the plastic volumetric strain component and the modulus symbol for the plastic shear strain component guarantee that, for negative strain increments, the inclination does not move away from the target value but stays the same or moves towards the target value.

S_CLAY1 parameters

The S_CLAY1 model requires 9 parameters. The gradient of the critical state line in the $q - p'$ space (M) and the compression index (λ) and swelling index (κ), both defined in the $v - \ln p'$ space. The values of these parameters for Kloten clay were already determined for the Modified Cam Clay model (Chapter 7.3.1, Tab. 7.2). Two parameters of the S_CLAY1 model describe the initial conditions, the "in-situ" void ratio (e_0) and the pre-consolidation stress (p_m'). The volume at critical state for $p' = 1\,kPa$ (Γ) is the input parameter in the MCC and the 3-SKH model and the current void ratio is calculated internally with the preconsolidation stress given. The void ratio at the start of the test (e_0) is the parameter that defines the volume state for the S_CLAY1 model. This parameter, e_0, is always related to a defined mean effective preconsolidation stress. Therefore, the strain and stress states given to the S_CLAY1 model at the start of the simulation have to correspond in order to obtain correct volumetric strain predictions.

The pre-consolidation stress for Kloten clay is determined from data plotted in the $v - \ln p'$ space (Fig. 5.9), as the mean effective stress state at which the reconsolidation path transforms into the virgin normal compression path. This is indicated by a kink of the data curve in the $v - \ln p'$ plot and gives a value of $p_m' = 80 \, kPa$. But the determination of the pre-consolidation stress from the $e - \ln p'$ plot of the consolidation path is not straightforward. A range of methods are proposed in the literature and a discussion of their applicability for the determination of parameters for numerical simulations is given in Messerklinger (2002). However, a parametric study was performed in order to investigate the magnitude of the influence of the preconsolidation pressure on the strain prediction.

The initial void ratio is calculated with the use of the critical state theory as:

$$v_\kappa = v_\eta - (\lambda - \kappa)\ln p_m'$$
Eq. 7.26

giving $v_\kappa = 1.69$, which corresponds to an initial void ratio of $e_0 = 0.69$. The definition of the elastic stiffness response is then completed with the Poisson's ratio (v'). The selection of an appropriate value for the isotropic Poisson's ratio for Kloten clay is discussed in the parameter determination of the Modified Cam Clay model paragraph 7.3.1 and a parametric study is performed (Fig. 7.23 & Fig. 7.22).

The three remaining model parameters of the S_CLAY1 model are the inclination of the yield surface (α), and the two hardening parameters, the proportional constant (β), and the rate of rotation (μ). These are model-specific parameters that define the initial anisotropy (α) and the change in anisotropy during plastic straining (β and μ). Two of these parameters can be derived from the special conditions of one-dimensional consolidation, when it is assumed that the plastic strain component dominates over the elastic strain component. This assumption can be made for the simulation of normally and lightly overconsolidated soft soils.

With the one-dimensional condition, the strain invariants become:

$$\delta\varepsilon_v = \delta\varepsilon_1 \text{ and } \delta\varepsilon_s = \frac{2}{3}\delta\varepsilon_1$$
Eq. 7.27

With the second assumption of a negligible elastic strain component during plastic straining the strain increment ratio becomes:

$$\frac{\delta\varepsilon_s}{\delta\varepsilon_v} = \frac{\delta\varepsilon_s^p}{\delta\varepsilon_v^p}$$

Eq. 7.28

Based on the two assumptions outlined above (Eq. 7.27 & Eq. 7.28), the formulation of the plastic strain increment ratio (Eq. 7.23) can be rewritten as:

$$\frac{2\left(\eta_{K_0} - \alpha_{K_0}\right)}{M^2 - \eta_{K_0}^2} = \frac{2}{3}$$

Eq. 7.29

Consequently, for determining the initial inclination of the yield surface, α_{K_0}, only the stress ratio (η_{K_0}) at which one-dimensional conditions occur, has to be known.

The stress ratio for one dimensional consolidation, $K_0 = \dfrac{\sigma_3{}'}{\sigma_1{}'}$, can be derived from the empirical formula, $K_0 = 1 - \sin\varphi'$, of Jaky (1944). This results in a principal effective stress ratio K_0 of 0.48, which equals a stress path in the q - p' stress space of $\eta_{K_0} = \dfrac{3(1 - K_0)}{1 + 2K_0} = 0.78$. The laser scan measurements (Fig. 6.11) confirmed that no radial displacements were measured for the stress path ratio of radial to axial effective stresses ($\sigma_r{}'/\sigma_a{}'$), which equals the principal stress ratio in triaxial stress space ($\sigma_3{}'/\sigma_1{}'$), of 0.5. This leads to a one-dimensional stress path of $\eta_{K_0} = 0.75$, which is close to the empirical one defined above from K_0 and which is used for the subsequent evaluations. Consequently, the initial inclination of the yield surface α_{K_0} can be calculated from Eq. 7.29 as 0.417.

The value for the parameter β is derived by assuming that the in situ anisotropy was developed during deposition and one-dimensional consolidation, which implies that there will be no change in anisotropy during plastic straining for ongoing consolidation of the sample along the same one-dimensional stress path, η_{K_0}. In this case, no rotational hardening ($\delta\alpha$) will develop and $\delta\alpha = 0$. With the target values given in Eq. 7.30 & Eq. 7.31 for initial conditions (Näätänen, 1999):

$$\chi_v(\eta) = \frac{3\eta}{4} \qquad\qquad\qquad \text{Eq. 7.30}$$

$$\chi_d(\eta) = \frac{\eta}{3} \qquad\qquad\qquad \text{Eq. 7.31}$$

the parameter β can be determined from Eq. 7.25 as $\beta = 1.31$ for Kloten clay.

The remaining model parameter, μ, can only be determined from parametric studies. Such parametric studies have been performed for Finnish clays (Wheeler et al., 1999). Values for μ of 10, 20 and 50 were applied and the best fit to the test data was found with the highest value of μ. Finnish clays are marine clays with significantly different properties to the lacustrine clays and therefore, a parametric study for Kloten clay was also performed on the hardening parameter, μ (Fig. 7.21).

A summary of all parameters for the S_CLAY1 model, and their values for natural Kloten clay is given in Tab. 7.4.

Tab. 7.4:   Material parameters of Kloten clay for the S_CLAY1 model.

Gradient of the critical state line in the q – p′ space	M	1.25
Compression index, defined in the v – ln p′ space	λ	0.053
Swelling index, defined in the v – ln p′ space	κ	0.01
Poisson's ratio	ν′	0.1
Initial void ratio	e_0	0.693
Initial inclination of the yield surface	α_{Ko}	0.42
Initial size of the yield surface	p_m'	80 kPa
Proportional constant (hardening parameter)	β	1.31
Rate of rotation (hardening parameter) $(0.05 - 0.5 - \underline{5} - 50 - 500)$	μ	5

The yield surface can be drawn and compared to the test results (Fig. 7.7), with the parameters given in Tab. 7.4 and the pre-consolidation stress (p_m') calculated

from the equation of the yield surface (Eq. 7.22) for the stress state $p' = 300\,kPa$ and $q = 225\,kPa$ as $p_m' = 324\,kPa$.

Comparison of the S_CLAY1 bounding surface with the test data (Fig. 7.7) gives a much better agreement than the MCC bounding surface that was also adopted for the 3-SKH model (Fig. 7.4). This is especially the case for the extension tests, due to the distorted form of the bounding surface. However, the rotational hardening law may have a negative influence because plastic straining during the extension stress path reduces the distortion of the bounding surface and consequently enlarges the elastic space on the extension side.
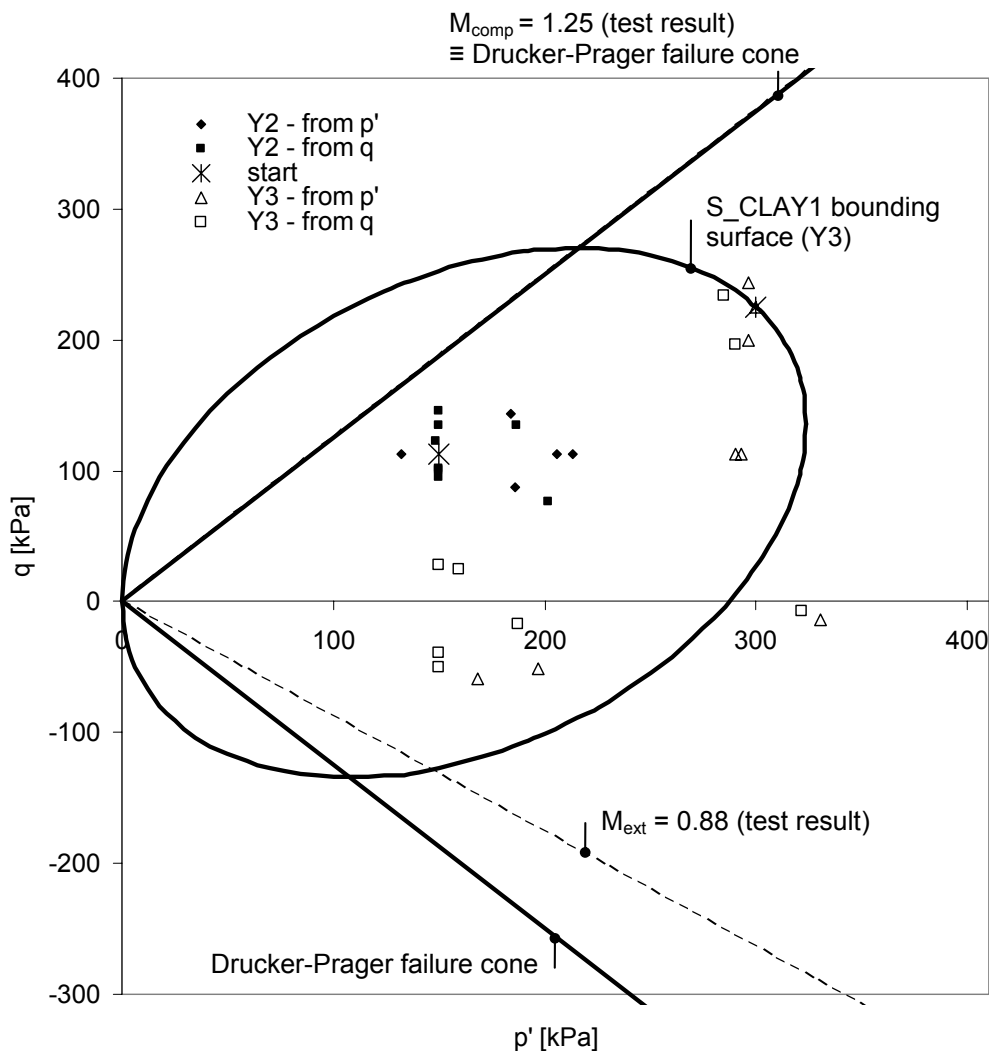
Fig. 7.7:   S_CLAY1 yield surface compared to the triaxial test data.

Failure is simulated by the Drucker-Prager failure criterion because the model is formulated in the critical state concept, which overpredicts the failure stress for the

extension stress path as discussed for the 3-SKH model. The gradient of the critical state line in the q – p′ space derived from extension tests (M_{ext}), when applied to this model, results in a decrease of the width of the failure cone and yield ellipse and represents both, the yielding and failure in the extension tests more accurately (Fig. 7.8). However, this change of shape and size of the bounding surface has a negative effect on the predictions on the compression side.
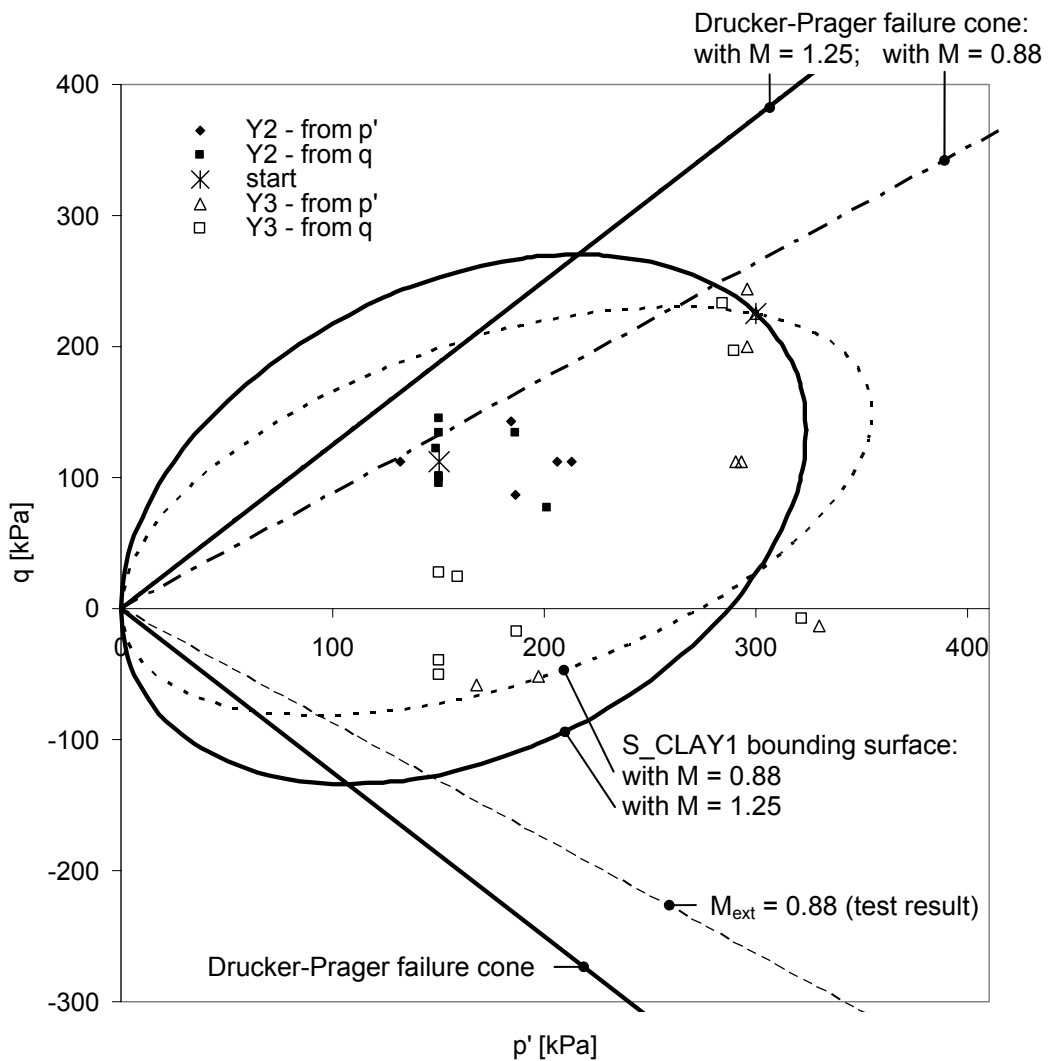
Fig. 7.8: Comparison between possible S_CLAY1 yield surfaces and the triaxial test data.

The suitability of the elasto-plastic strain development and the flow and hardening rule of the S_CLAY1 model for simulating lacustrine clay response will again be evaluated by finite element simulations.

7.3.4 Soft Soil model

The yield surface is composed of two parts in the Soft Soil model (Brinkgreve, 1994). In lightly to highly overconsolidated states, the yield surface is represented by the Mohr Coulomb failure criterion with elastic-ideal plastic deformation behaviour. For normally consolidated states, the yield surface is described by a yield cap, with the formulation given in Eq. 7.32:

$$\frac{q^2}{M^2\left(p'+c'\cot\varphi'\right)} + p' - p_0' = 0 \qquad\qquad \text{Eq. 7.32}$$

where p_0' is the mean effective pre-consolidation stress (Fig. 7.9). M describes the height of the ellipse, which is defined by the function given in Eq. 7.32. The formulation can additionally account for a value of cohesion (c'), which results in an enlargement of the ellipse towards the tension side of the p' axes (Fig. 7.9). The formulation of the ellipse in the Soft Soil model (Eq. 7.32) is the same as the Modified Cam Clay bounding ellipse (Eq. 7.1) when the cohesion is zero.
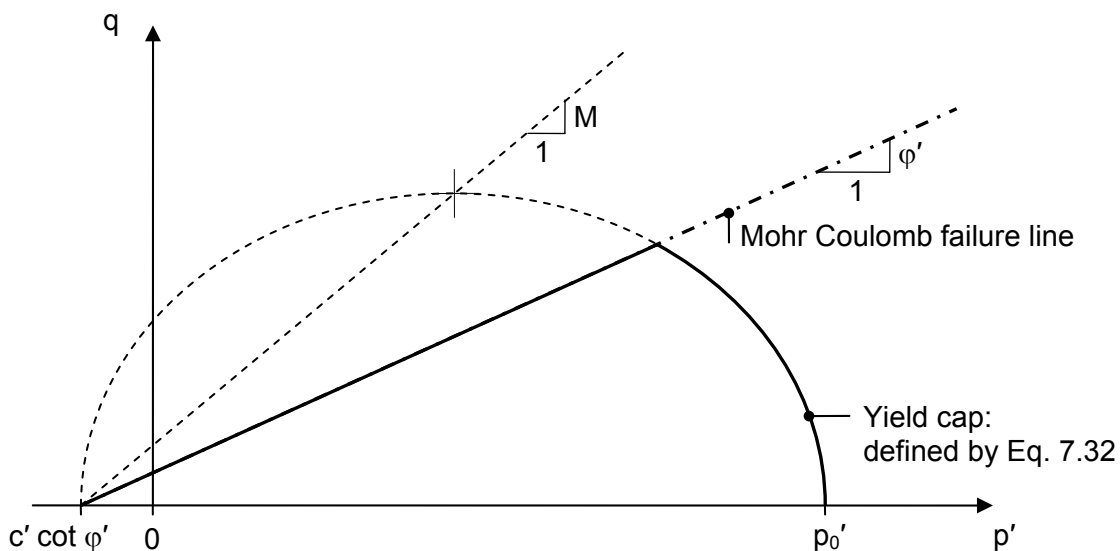
Fig. 7.9: Yield surfaces constituting the Soft Soil model, presented in the q – p' stress space, after Brinkgreve et al. (2004).

The elastic stiffness response inside the yield surfaces is described by the isotropic elastic stiffness matrix (Eq. 7.2) and the plastic straining on the yield cap is described by an associated flow rule, which results in a plastic strain increment ratio of:

$$\frac{\delta\varepsilon_s^p}{\delta\varepsilon_v^p} = \frac{2q(p'+c\cot\varphi')}{M^2(p'+c\cot\varphi')^2 - q^2}$$

Eq. 7.33

The failure stress state is defined by the Mohr Coulomb failure criterion as mentioned above and the volumetric deformation behaviour is defined as:

$$\varepsilon_v - \varepsilon_v^0 = -\lambda^\otimes \ln\left(\frac{p'}{p_0'}\right)$$

Eq. 7.34

$$\varepsilon_v^e - \varepsilon_v^{e0} = -\kappa^\otimes \ln\left(\frac{p'}{p_0'}\right)$$

Eq. 7.35

where the modified compression ($\lambda^\otimes$) and swelling ($\kappa^\otimes$) indices are defined as a straight line in the $\varepsilon_v - \ln p'$ space. Consequently, the elastic bulk modulus is:

$$K' = \frac{p'}{\kappa^\otimes}$$

Eq. 7.36

These two modified indices are called λ^* and κ^* in the PLAXIS manual. They are now renamed as $\lambda^\otimes$ and $\kappa^\otimes$ because the compression and swelling indices for the 3_SKH model, which are defined in the $\ln v - \ln p'$ space, have already been allocated the symbols λ^* and κ^*. This formulation of the volumetric behaviour (Eq. 7.34 & Eq. 7.35) used for the Soft Soil model in PLAXIS is applied for the Modified Cam Clay model, also implemented in PLAXIS, and the transformation between the original compression and swelling index and the newly defined ones is given in the PLAXIS Manual as:

$$\lambda^\otimes = \frac{\lambda}{v}; \; \kappa^\otimes = \frac{\kappa}{v}$$

Eq. 7.37

An average value for the specific volume during the test is recommended for this transformation. A brief comparison is shown in Fig. 7.10 to analyse the differences of the formulation implemented in PLAXIS to the original formulation, e.g. as implemented in CRISP.

Critical state concept:

Formulation in PLAXIS:

$$\Delta\varepsilon_v = \frac{\Delta v}{v} \rightarrow \lambda^{\otimes} = \frac{\lambda}{v} \quad \text{with: } v = 1 + e$$
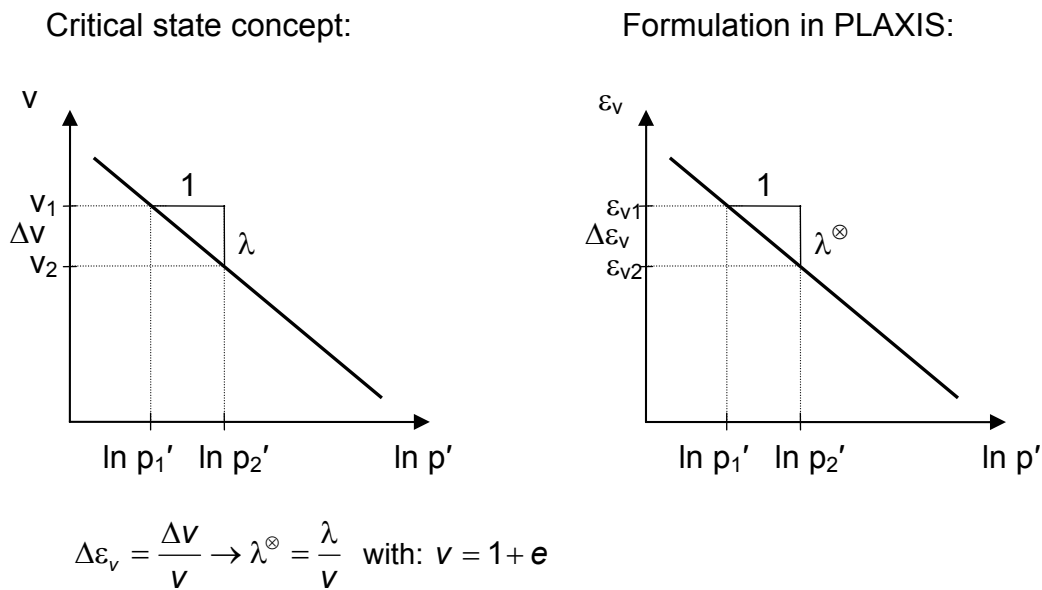
Fig. 7.10: Comparison of the volumetric deformation behaviour of different formulations.

As the volumetric strains in the critical state concept are formulated as natural strains, the modified indices are strain-dependent parameters. This is not taken into account in the PLAXIS formulation. Consequently, the strains predicted with the Modified Cam Clay model in PLAXIS will vary from strain predictions calculated e.g. with CRISP. A comparison of the magnitude of the differing predictions is given in Fig. 7.11.

Soft Soil parameters

7 parameters are required for the Soft Soil model. The friction angle (φ'), the dilatancy angle (ψ) and the cohesion (c') to define the failure criterion, the modified compression ($\lambda^{\otimes}$) and swelling index ($\kappa^{\otimes}$) to define the volumetric deformation behaviour, the Poisson's ratio (v') to complete the description of the deformations and the model parameter (M) to define the size of the ellipse (Eq. 7.32) in the direction of the deviator stress axis and hence the shape of the yield cap.

The test results at failure were evaluated for Kloten clay in Chapter 5 and gave a friction angle of 31° and zero cohesion. The dilatancy angle is set zero. The modified compression and swelling indices are calculated from Eq. 7.37 with the compression and swelling indices determined in the $v - \ln p'$ plot (Fig. 5.9). A

parametric study is performed to select the specific volume to be applied in Eq. 7.37. The initial specific volume, $v_0 = 1.88$ (Fig. 5.8), the specific volume after consolidation up to $p' = 300 \, kPa$ and unloading to $p' = 1 \, kPa$, $v_\kappa = 1.635$, and the specific volume after consolidation to $p' = 300 \, kPa$ and unloading to $p' = 150 \, kPa$, $v_0 = 1.585$, were adopted and the resulting volumetric strain predictions of a drained stress path test similar to those performed in test series 2 (Chapter 5) were compared to the volumetric strains calculated from the critical state theory combined with the Modified Cam Clay yield surface and parameters of Tab. 7.2. The results are presented in Fig. 7.11.
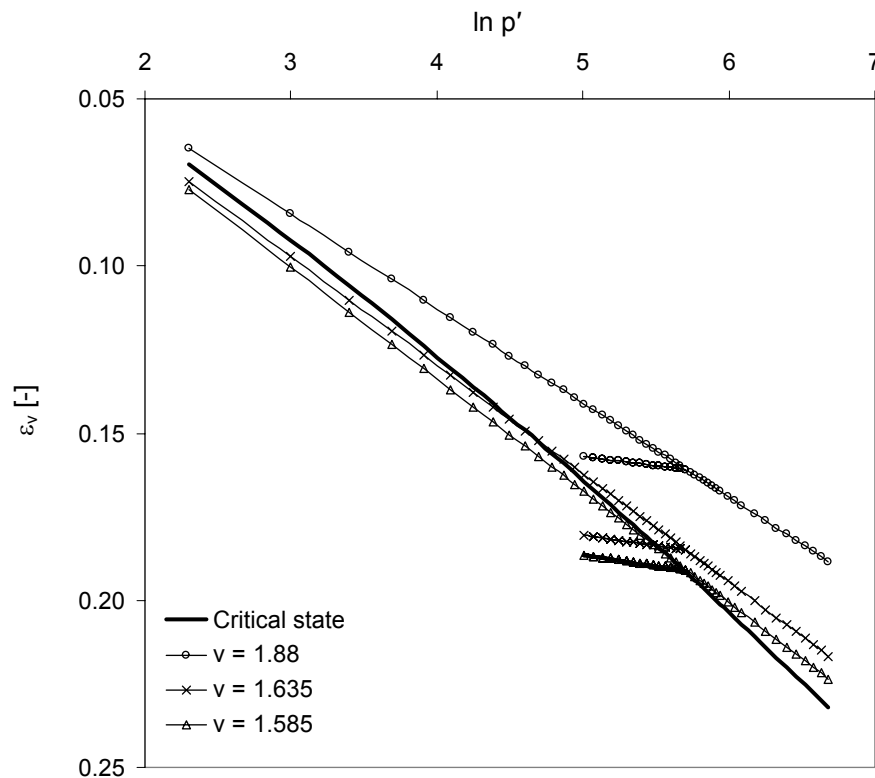
Fig. 7.11: Validation of the modified compression and swelling index for use in PLAXIS.

It can be seen that with $v_0 = 1.585$ the volumetric strain predictions of the Soft Soil model are closest to the calculated result of the critical state theory combined with the MCC yield surface, which is called "Critical state" in Fig. 7.11. In particular, the results in the unloading-reloading path are well predicted, which is the most interesting for further comparisons.

Consequently, values of $\lambda^{\otimes} = 0.033$ and $\kappa^{\otimes} = 0.006$ are applied for the simulations of Kloten clay with the Soft Soil as well as the Modified Cam Clay model in PLAXIS. The value determined in the parametric study (Fig. 7.23 & Fig. 7.22) is applied again for the Poisson's ratio of Kloten clay. Finally, the model parameter M is derived. Separation of the size of the yield cap from the failure criterion allows the shape of the yield cap to be defined in such a way that a plastic strain increment ratio of 2/3 is achieved for the normal consolidation stress path as proposed when using the associated flow rule. Therefore, the value of M is estimated from the plastic strain increment ratio (Eq. 7.33), initially by assuming that the elastic strain component is small compared to the plastic strain component. For zero cohesion, Eq. 7.33 simplifies to Eq. 7.38 and can be set equal to 2/3 to derive the parameter M.

$$\frac{\delta \varepsilon_s^p}{\delta \varepsilon_v^p} = \frac{2\eta}{M^2 - \eta^2} = \frac{2}{3} \quad \rightarrow \quad M = \sqrt{3\eta_{K_0} + \eta_{K_0}^2} \qquad \text{Eq. 7.38}$$

With a normal consolidation stress ratio of $\eta_{K_0} = 0.75$, determined from the laser scan data as discussed for the parameter determination of the S_CLAY1 model, the parameter M becomes 1.72 for Kloten clay.

A more sophisticated formulation, which incorporates the influence of the elastic strain component, is given (Eq. 7.39) in the PLAXIS manual, and the value of M becomes 1.65, assuming a K_0^{nc} value of 0.5 and the other parameters as given above for Kloten clay: $v' = 0.3$, $\lambda^{\otimes} = 0.033$ and $\kappa^{\otimes} = 0.006$.

$$M \approx 3 \sqrt{\frac{\left(1 - K_0^{nc}\right)^2}{\left(1 + 2K_0^{nc}\right)^2} + \frac{\left(1 - K_0^{nc}\right)\left(1 - 2v'\right)\left(\dfrac{\lambda^{\otimes}}{\kappa^{\otimes}} - 1\right)}{\left(1 + 2K_0^{nc}\right)\left(1 - 2v'\right)\dfrac{\lambda^{\otimes}}{\kappa^{\otimes}} - \left(1 - K_0^{nc}\right)\left(1 + v'\right)}} \qquad \text{Eq. 7.39}$$

This value is close (-4 %) to the previously estimated one and is used for the simulations. A summary of all parameters of the Soft Soil model and their values for natural Kloten clay is given in Tab. 7.5. With the parameters given in Tab. 7.5 and a preconsolidation stress p_0' of 362 kPa, calculated from Eq. 7.32 for the consolidation stress state $p' = 300\,kPa$ and $q = 225\,kPa$, the yield surface can be drawn and compared to the triaxial test results (Fig. 7.12).

Tab. 7.5:   Material parameters of Kloten clay for the Soft Soil model.

Modified compression index, defined in the $\varepsilon_v - \ln p'$ space	$\lambda^{\otimes}$	0.033
Modified swelling index, defined in the $\varepsilon_v - \ln p'$ space	$\kappa^{\otimes}$	0.006
Friction angle	φ'	31°
Cohesion	c'	0 kPa
Dilatancy angle	ψ	0°
Poisson's ratio	v'	$\underline{0.1} - 0.2 - 0.3$
Model parameter, K_0^{nc} - parameter	M	1.65
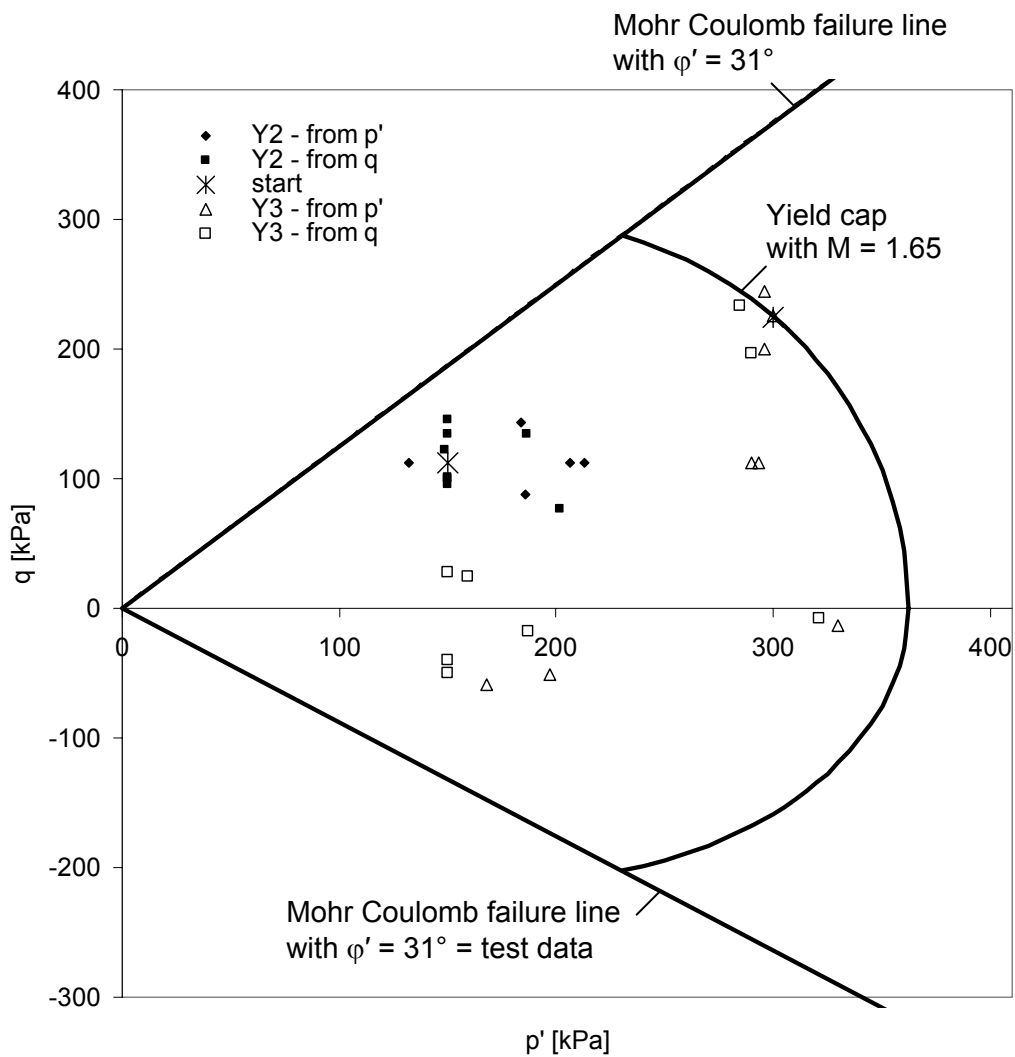
Fig. 7.12:   Soft Soil yield surfaces compared to the test data.

The comparison of the Soft Soil bounding surface to the test data (Fig. 7.12) shows reasonable agreement on the compression side, where the location of the bounding surface is defined by the consolidation stress state. On the extension side, the bounding surface of the Soft Soil model is located between the well fitting S_CLAY1 and the poorly matching MCC bounding surfaces. The plastic strain increment ratio will be simulated well with the associated flow rule for stress paths that reach the bounding surface close to its intersection with the failure line. The failure stress states simulated with a Mohr Coulomb failure criterion in the Soft Soil model fit the test results well (Fig. 7.12).

7.4   Stress path test simulation in CRISP

The finite element programme CRISP was developed at Cambridge University, initially by Mark Zytynski in 1976 (Woods & Rahim, 2001) with subsequent adaptions and developments by Britto & Gunn (1987), who founded the company CRISP users group and eventually sold on the rights to Sage consulting. Sage distributes the programme commercially. The version used for the simulations presented here is version 5.1b. This 2D code was adequate for the objectives of simulating small strain deformation behaviour rather than failure conditions.

A domain with a width of 2.5 cm and a height of 10 cm (Fig. 7.13) is modelled axisymmetrically around a vertical symmetry axis to simulate the triaxial test. The domain was built of two 2D non-consolidating cubic strain triangle elements, which have 15 nodes and 16 integration points each. The boundary conditions restrict axial displacement on the horizontal bottom edge and radial displacements on the left vertical edge of the domain. The loads are applied in order to simulate the stress paths of the triaxial tests. The domain, with the two triangular finite elements chosen and the boundary conditions and loads applied, is shown in Fig. 7.13.

7.4.1 Parametric study of the elastic shear modulus in the 3_SKH model

Before the final simulations were performed, a couple of parametric studies were done in order to confirm the values of the parameters selected. The first study was carried out for the elastic shear modulus of the 3-SKH model. A value for the

elastic shear modulus at the start of the probing stress path of $G_{bender} = 98\,MPa$ was measured with bender elements.
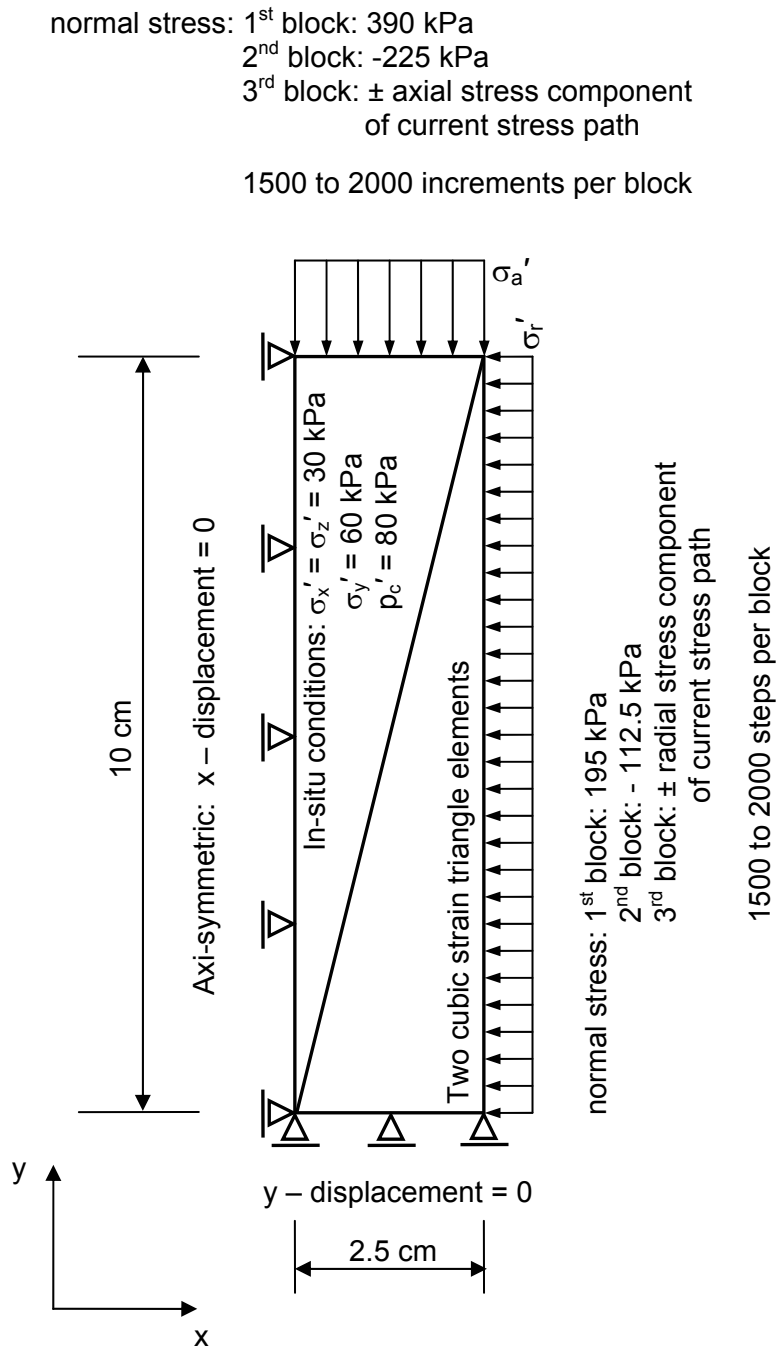
Fig. 7.13: Input data for the simulation of the triaxial tests in CRISP.

The isotropic elastic properties of $\kappa = 0.01$ and $v' = 0.3$ were determined from the triaxial test measurements, which give an equivalent shear modulus at the start of the probing stress path ($p' = 150\,kPa$, $v = 1.585$) of $G = 11\,MPa$. These two values of the shear modulus were taken as the upper and lower boundaries in the parametric study and additional values for G' in between these boundaries were selected.

Thereafter, three probing stress paths representing the triaxial tests of series 2 were simulated with the 3-SKH model in CRISP using the parameters given in Tab. 7.3. The selected tests are S2T4 with $\Theta = 90°$, S2cT1 with $\Theta = 42°$ and S2aT4 with $\Theta = 278°$. These probing stress paths represent stress increment ratios of shearing in compression, one-dimensional consolidation and shearing in extension, respectively.

The comparison of the simulation to the test results of test S2T4 with $\Theta = 90°$ (Fig. 7.14a) show that a shear modulus of 98 MPa represents the shear stiffness inside the history surface, while the results determined with a shear modulus of 11 MPa equal the stiffness observed in the strain range between the history surface and the bounding surface and critical state line. The comparison of the data of test S2cT1 with $\Theta = 42°$ (Fig. 7.14b) shows that, for this stress path, shear moduli between 30 and 98 MPa represent the stiffness inside the history surface. But the decrease in stiffness at the boundary of the history surface simulated by the 3-SKH model, applying any value for the shear modulus, is much too significant and does not represent the data observed. This aspect is related to the parameter ψ (exponent of the hardening function) and will be investigated in a subsequent parametric study. Again shear moduli between 50 and 98 MPa, depending on the critical state value chosen (Fig. 7.15a&b), give simulation results that represent the stiffness observed inside the history surface for test S2aT4, with the stress path in extension.

For all three stress paths investigated, the elastic shear modulus of $G' = 98\,MPa = G'_{bender}$ simulates the stiffness observed at the start of the probing stress path in the triaxial tests well. Therefore this value was taken for the simulations performed subsequently with the 3-SKH model.
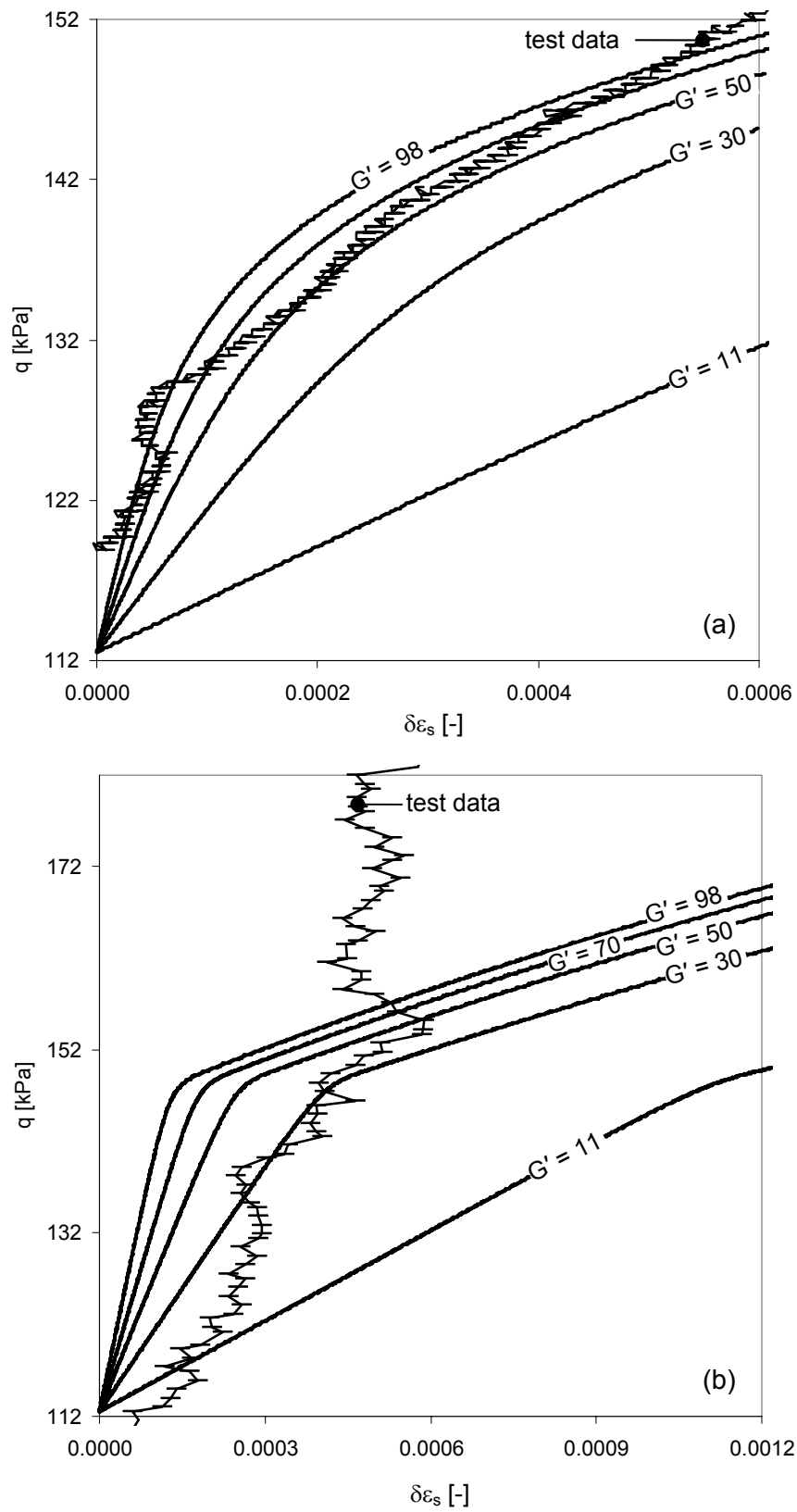
Fig. 7.14: Parametric study on the elastic shear modulus G' with the 3-SKH model in CRISP. Simulation results of test (a) S2T4 with $\Theta = 90°$ and (b) S2cT1 with $\Theta = 42°$ for a range of shear moduli given in MPa.
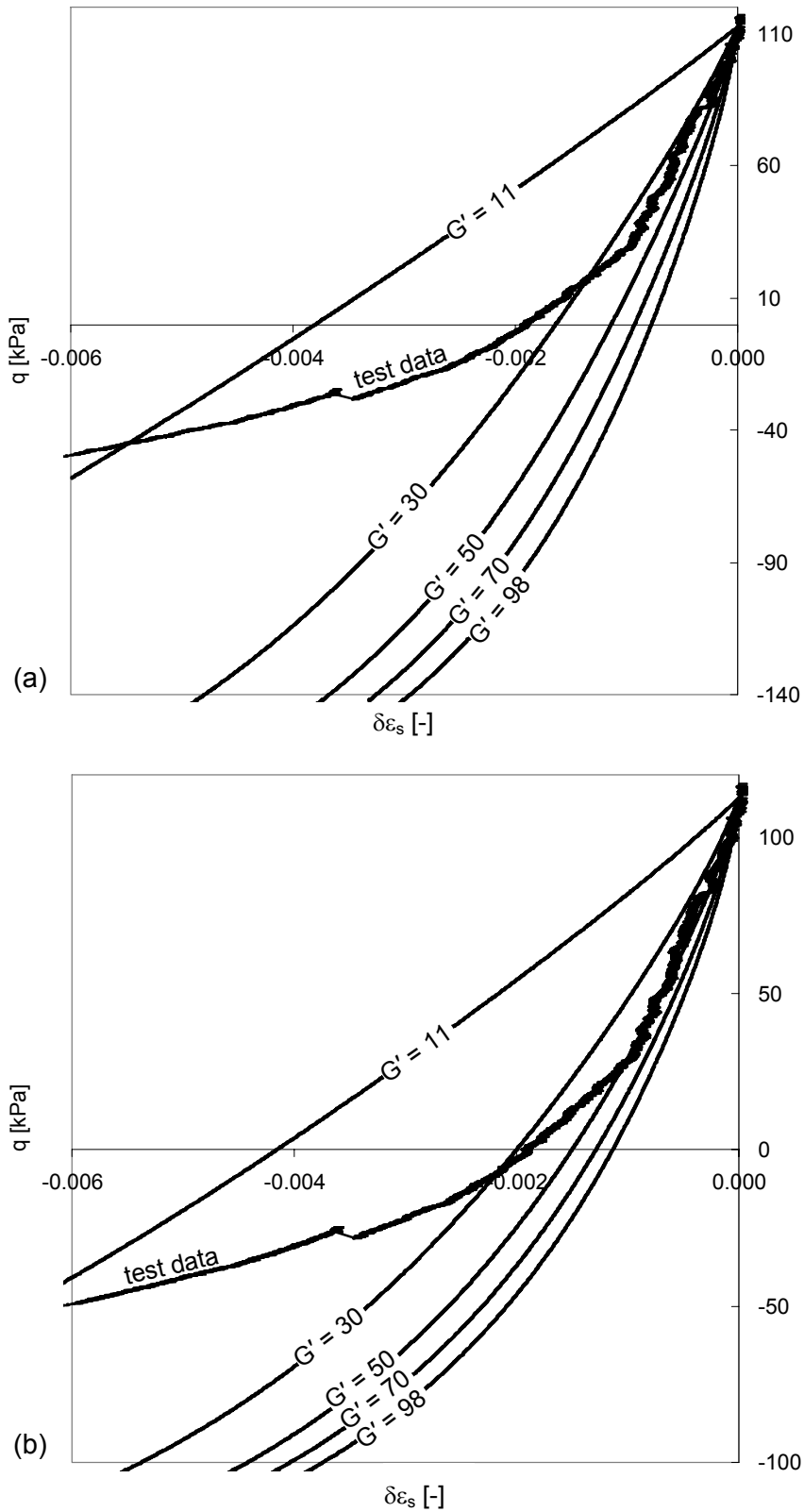
Fig. 7.15: Parametric study on the elastic shear modulus G′ with the 3-SKH model in CRISP. Simulation results of test S2aT4 with $\Theta = 278°$ for a critical state value of (a) $M_{comp} = 1.25$ and (b) $M_{ext} = 0.88$ for a range of shear moduli given in MPa.

7.4.2 Parametric study of the hardening parameter ψ in the 3-SKH model

The hardening parameter (ψ) in the 3-SKH model defines the rate of decrease of stiffness with kinematic hardening and can only be determined by parametric studies (Stallebrass, 1990). Parametric studies performed on speswhite Kaolin clay and a range of marine clays showed that values for ψ of 1.5 to 3.0 are most suitable (Stallebrass, 1990; Masin, 2004).

To determine an optimal value for lacustrine Kloten clay, a parametric study was performed on three different probing stress paths. Tests in shearing and compression were selected in order to verify the rate of decrease of shear and bulk modulus, respectively. The tests simulated are S2T4 with Θ = 90°, S2cT1 with Θ = 42° and S2T3 with Θ = 0° and the simulation results are presented in Fig. 7.16, Fig. 7.17 and Fig. 7.18.

The comparison of the simulation to the test results of the shear test in compression (S2T4, Fig. 7.16a) shows that a hardening exponent between $\psi = 1.7$ and 2.0 is most suitable for modelling the decrease of the shear modulus. While for the corresponding decrease of the bulk modulus (Fig. 7.16b), none of the simulations fits the bi-linear form of the data well.

The comparison for the one-dimensional compression path (test S2cT1; Fig. 7.17a) shows that the shear modulus decreases very slowly so that a hardening exponent of $\psi = 1.0$ is still too high. The degradation of the bulk modulus for test S2cT1 (Fig. 7.17b) is simulated best with a value for the hardening exponent of $\psi = 1.0$. The degradation of the bulk modulus is simulated best in the isotropic probing stress path (test S2T3; Fig. 7.18b) with a rather higher hardening exponent of $\psi = 2.8$. The shear strain predictions (Fig. 7.18a) do not fit the test data, which is due to the definition of the flow rule.

The analysis of these three test simulation results lead to the conclusion that there is no unique value for this parameter.
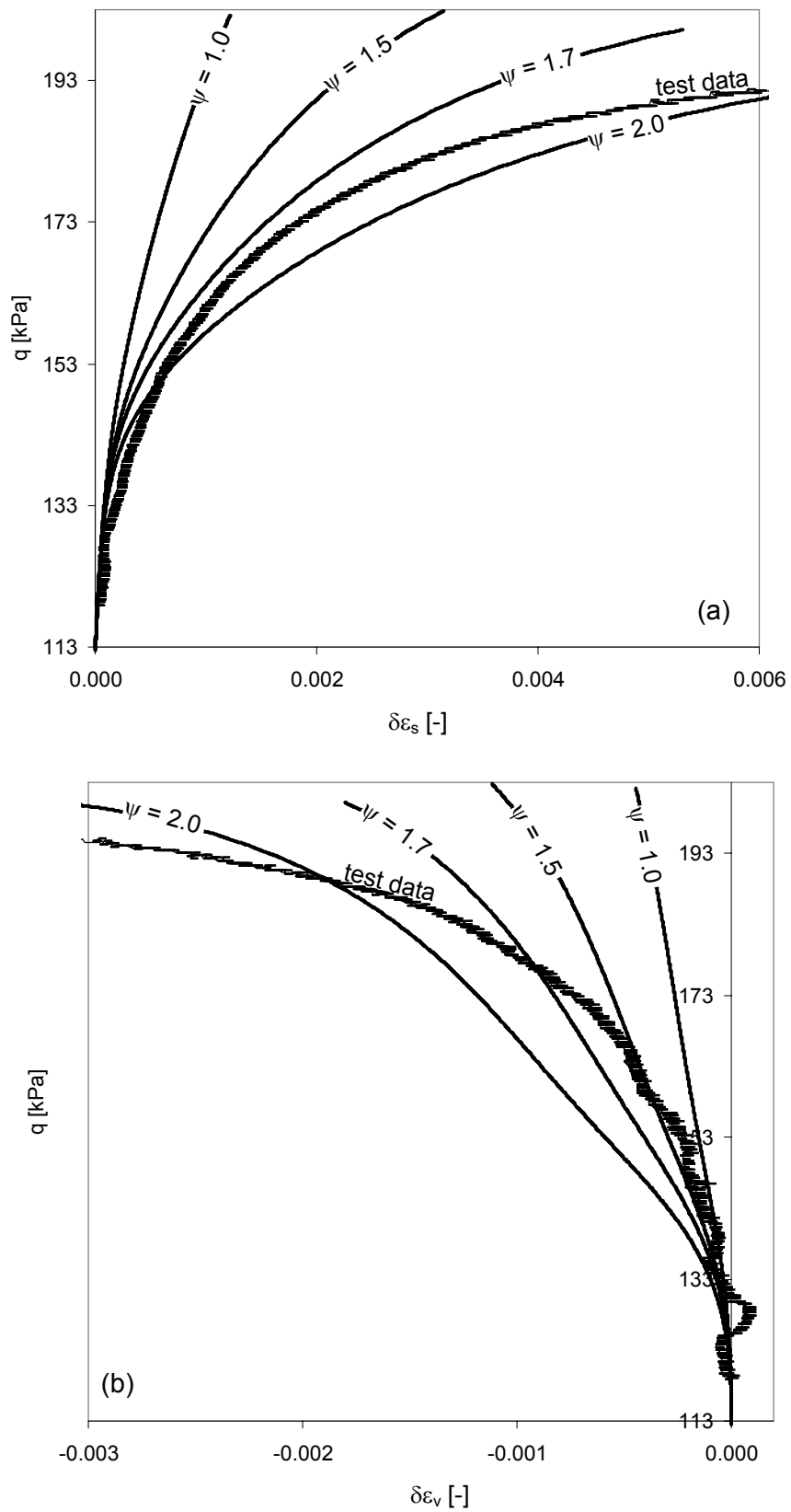
Fig. 7.16: Parametric study on the exponent of the hardening function in the 3-SKH model. Simulation results of test S2T4 with $\Theta = 90°$ are given in the (a) $q - \delta\varepsilon_s$ (for G') and (b) $q - \delta\varepsilon_v$ (for K') plots.

237
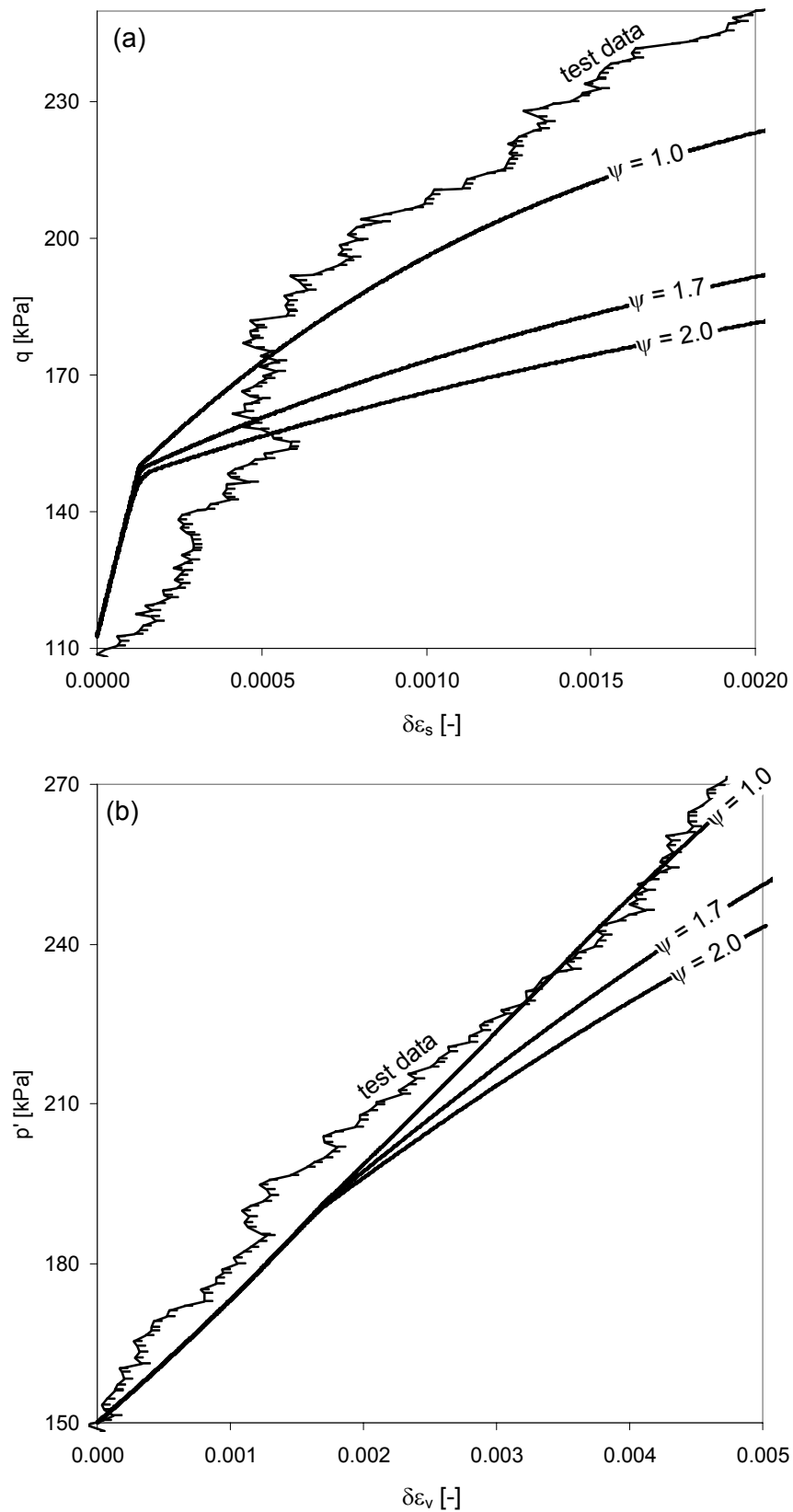
Fig. 7.17: Parametric study on the exponent of the hardening function in the 3-SKH model. Simulation results of test S2cT1 with $\Theta = 42°$ are given in the (a) $q - \delta\varepsilon_s$ (for G') and (b) $p' - \delta\varepsilon_v$ (for K') plots.
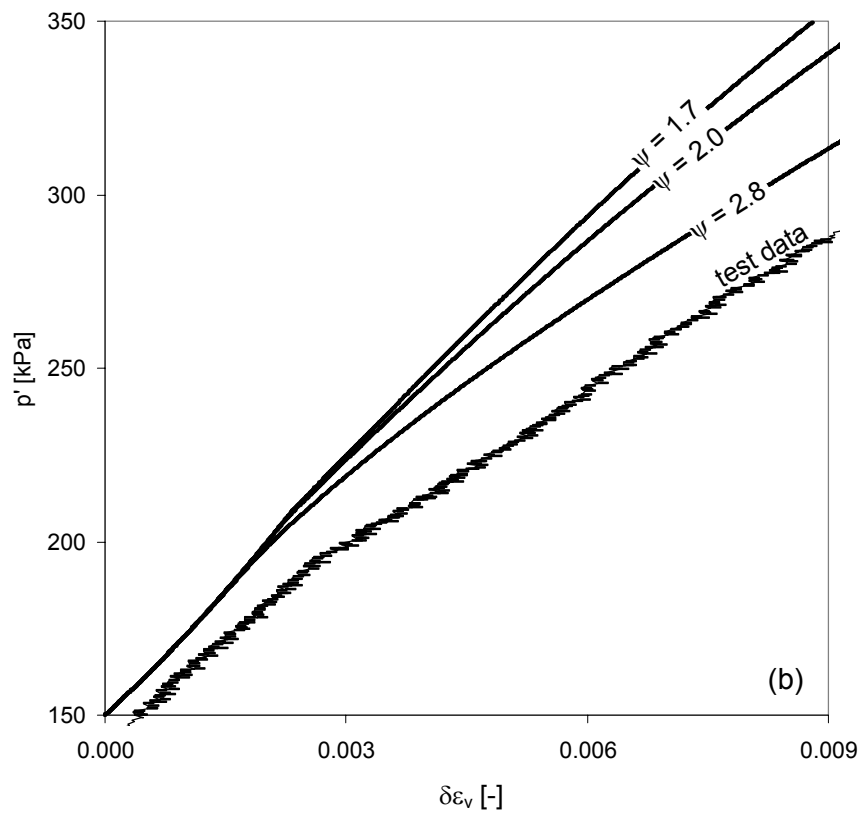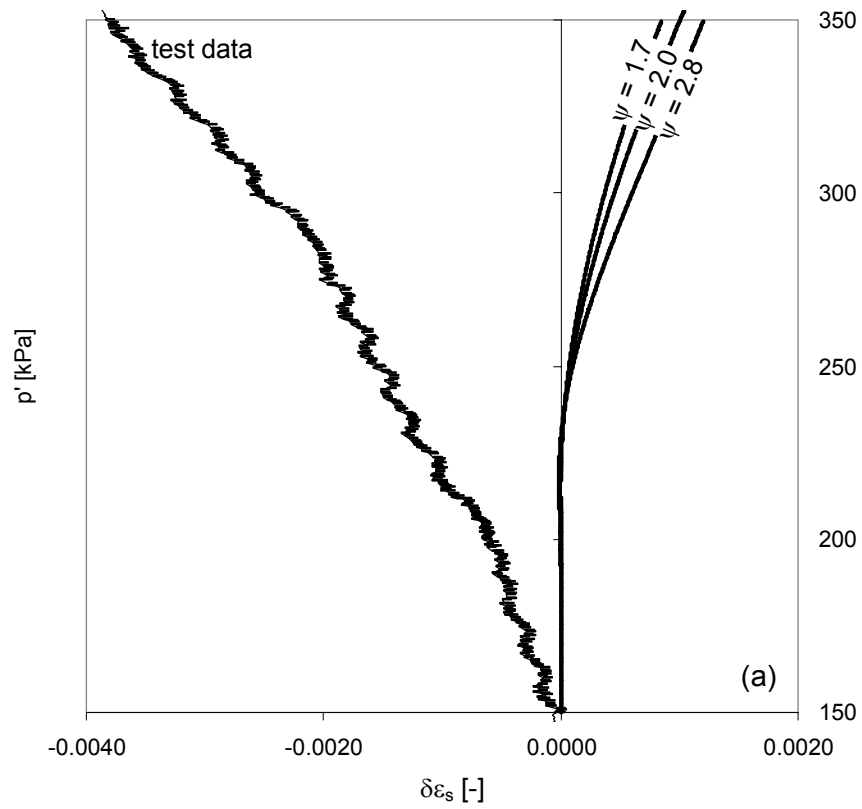
Fig. 7.18: Parametric study on the exponent of the hardening function in the 3-SKH model. Simulation results of test S2T3 with $\Theta = 0°$ are given in the (a) $p' - \delta\varepsilon_s$ (for G') and (b) $p' - \delta\varepsilon_v$ (for K') plots.

The only tendency resulting from the comparisons is that higher values of ψ give better predictions of the decrease in the bulk modulus and lower values of ψ give better predictions of the change in the shear modulus. Therefore an average value for the exponent of the hardening function of $\psi = 2.0$ was applied for the subsequent simulations.

7.5 Stress path test simulation in PLAXIS

The development of the Finite Element programme PLAXIS started at the Technical University of Delft and led consequently to the formation of the company PLAXIS b.v., which is developing the code and selling it for commercial and research purposes. The version used for the simulations performed with the Soft Soil model and the S_CLAY1 model is version 8.2, with service pack 4. The simulations with the Modified Cam Clay model were performed with service pack 6.

The triaxial test specimen is modelled axisymmetrically around a vertical symmetry axis with a rectangular domain with a width of 2.5 cm and a height of 10 cm. The domain is built of two 15 node triangle elements. Drained simulations were performed with the water level at the bottom of the element. The loads for the triaxial stress paths were applied with the "incremental multiplier" module, which allows defined load increment sizes.

In order to keep the size of the increment the same during the simulation process, the parameters of the automated step size procedure, "desired minimum" and "desired maximum", were set to 2 and 100, respectively (Scharinger, 2005). The tolerated error was also reduced to 0.1% and the maximum number of iterations was set to 100 to improve the accuracy of the results. Before the final simulations were performed, a couple of parametric studies were done in order to confirm the values of the parameters selected.

7.5.1 Parametric study of the step size parameter of the S_CLAY1 routine in PLAXIS

In the S_CLAY1 model, which was implemented as a user-defined soil model by Wiltafsky (2003b) in PLAXIS, the step size can be modified by the parameter "StepSize". This parameter was added in order to allow control of the automatic step size generation in PLAXIS. With a value for the StepSize parameter of greater than one, the parameter acts as a divisional factor of the automatically generated step size. A value for the StepSize parameter that is smaller than zero acts as a step size length controller and defines the maximum step size. Wiltafsky (2003b) recommends the latter method.

A parametric study was performed to investigate the influence of this parameter and to choose an appropriate value. The test S2cT1 was simulated with the S_CLAY1 model in PLAXIS using the parameters given in Tab. 7.4, with step size factors of 0, -0.1 and -0.01. A step size factor of zero represents no additional regulation of the step size. The resulting stress-strain curves are presented in Fig. 7.19a&b and show that the strain prediction is independent of the step size parameter. This means that the chosen load increment is already sufficiently small.
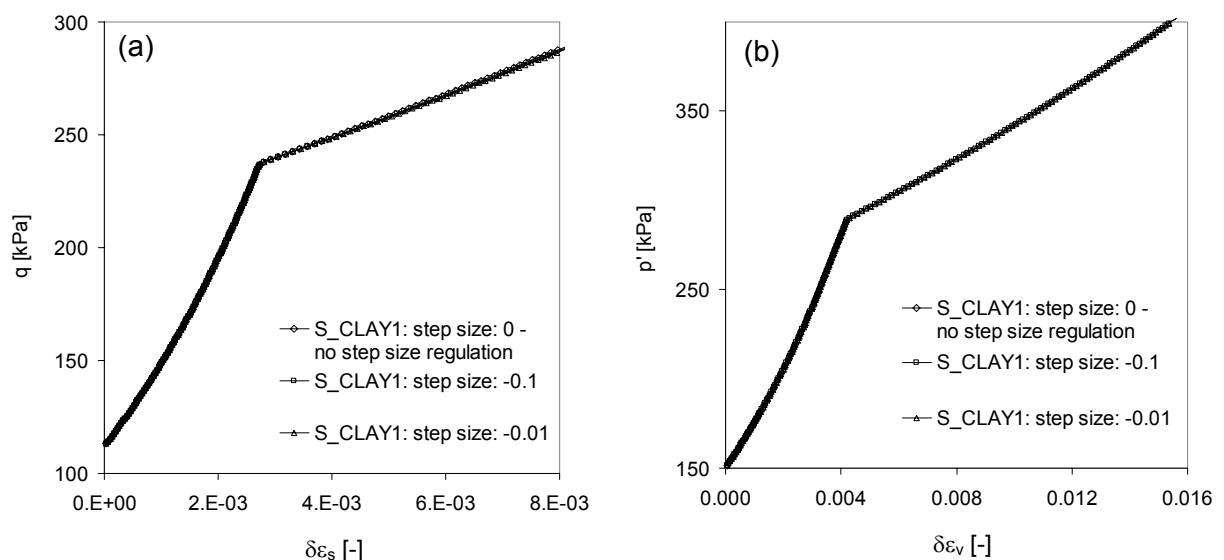
Fig. 7.19: Parametric study on the StepSize factor of the user-defined S_CLAY1 model in PLAXIS. Simulation results of test S2cT1 with $\Theta = 42°$ given in the (a) $q - \delta\varepsilon_s$ and (b) $p' - \delta\varepsilon_v$ plots.

7.5.2 Parametric study of the sensitivity of the in-situ parameter POP in the S_CLAY1 model

The preconsolidation stress state (p_m') is an input parameter for the S_CLAY1 model. It indirectly influences the volumetric strain predictions in all subsequent simulation stages, but, as discussed in Chapter 7.3.3, its value is difficult to determine from test data. A value of around $p_m' = 80\,kPa$ was determined for Kloten clay (Fig. 5.9).

Therefore a parametric study (Fig. 7.20) was performed. The probing stress path of test S2cT1 was simulated with the parameters given in Tab. 7.4 and values for POP of 60, 120 and 180 kPa. POP is the preoverburden pressure and corresponds to the effective vertical preconsolidation stress.
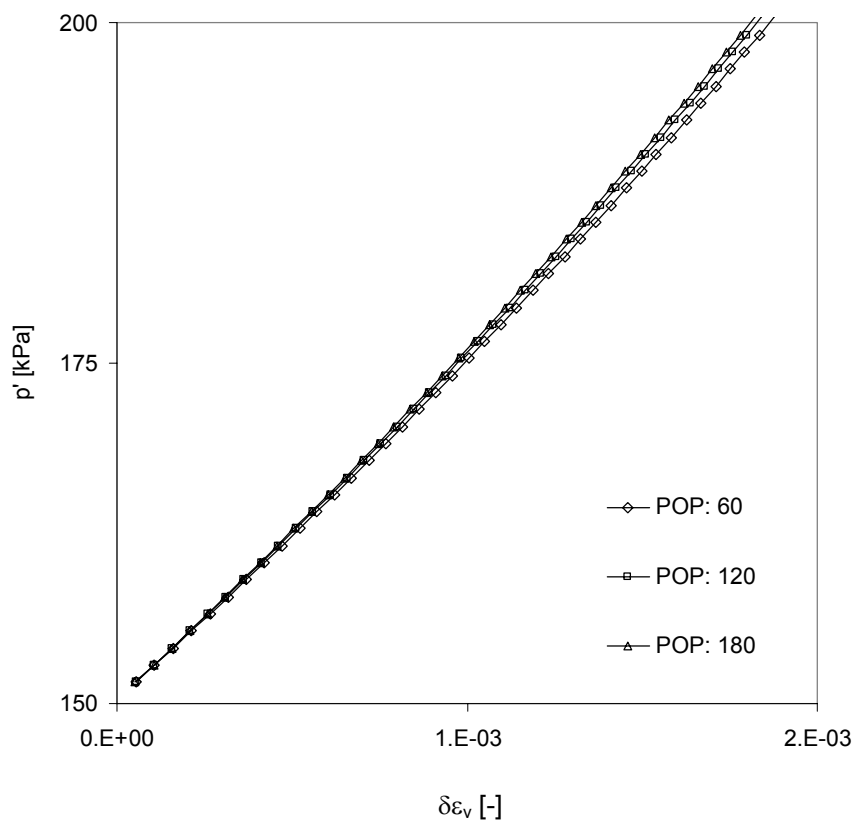
Fig. 7.20: Parametric study of the influence of the preconsolidation pressure on the volumetric strain increment development. POP is the pre-overburden pressure in kPa, which equals the pre-consolidation pressure and is the maximum vertical effective stress experienced by the soil.

Assuming a normal consolidation K_0 of 0.5 these POP values correspond to mean effective stresses of p' equal to 40, 80 and 120 kPa, which covers a range of $\pm$ 50 % of p_m' evaluated for Kloten clay. The results are presented in Fig. 7.20 and confirm that the predicted volumetric strains decrease with increasing POP. This is expected as the current specific volume (v), which is in the denominator of the volumetric strain increment formulations (Eq. 7.4 & 7.24), remains larger. The magnitude of the variation in volumetric strain increment prediction with the change of the POP of 50 % is 0.005 %, which is small. Consequently a pre-overburden pressure of -120 kPa, which represents approximately the in situ stress state of the test specimens shown in (Fig. 5.9), was applied in the simulations without further discussion of the accuracy of the POP determination method.

7.5.3 Parametric study of the hardening parameter μ "rate of rotation" in the S_CLAY1 model

μ describes the rate of rotation in the rotational hardening law (Eq. 7.25) and its value can not be determined from test data but has to be defined using parametric studies. Comparative studies of this parameter for soft and sensitive marine clays from Finland led to recommendations of a value of 50 (Wheeler et al., 1999). The tests S2aT4 with Θ = 278° and S2T3 with Θ = 0° were simulated in the parametric study for Kloten clay in order to validate the parameter for different magnitudes of rotation. The values for μ were varied between 0.05 and 500. The results are presented in Fig. 7.21 and show that a value for μ of 5 or smaller fits the data best. Therefore $\mu = 5$ was chosen in the subsequent simulations.

7.5.4 Parametric study of the Poisson′s ratio

The value of the Poisson′s ratio was determined from the test data as v' = 0.3, assuming isotropic elastic material behaviour, but it was also seen that an isotropic elastic response does not fit the data well. However, as all the constitutive models used apply isotropic elastic material responses, an appropriate value for this parameter has to be defined as discussed in Chapter 7.3.1: Modified Cam Clay parameters.
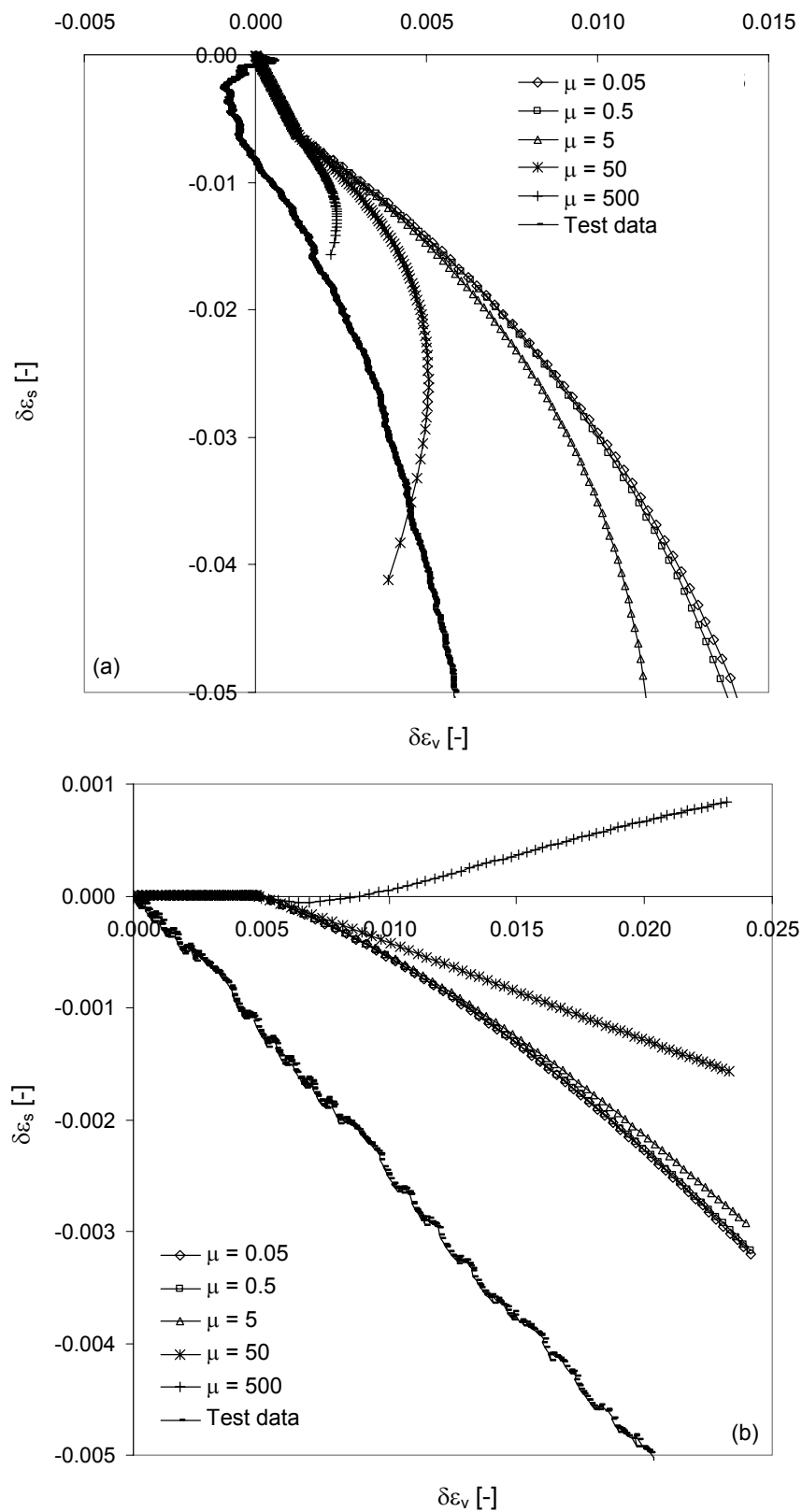
Fig. 7.21: Parametric study on the hardening parameter μ of the S_CLAY1 model for the simulation of test (a) S2aT4 with $\Theta = 278°$ and (b) S2T3 with $\Theta = 0°$. Shear strain increments plotted versus volumetric strain increments.

Therefore a parametric study was performed in which three probing stress paths were simulated with the Modified Cam Clay model, using three different values for the Poisson's ratio.

The simulated tests include tests S2T4 (shearing in compression with $\Theta = 90°$), S2cT1 (one-dimensional loading with $\Theta = 42°$) and S2aTa (shearing in extension with $\Theta = 278°$). The results are presented in Fig. 7.22 and Fig. 7.23 and show that the simulations with the smallest value for the Poisson's ratio fit the test data best for all simulated stress increment ratios. Therefore, a value of $\nu' = 0.1$ was applied in the subsequent simulations.
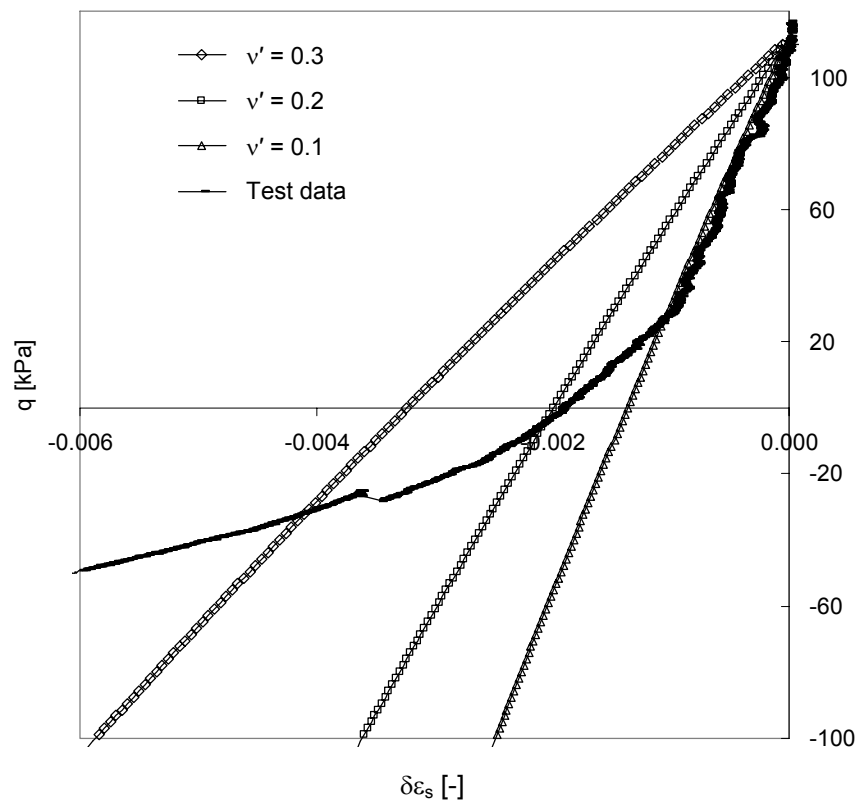
Fig. 7.22: Parametric study on the Poisson's ratio with the Modified Cam Clay model. Simulation and test results for triaxial test S2aT4 with $\Theta = 278°$.
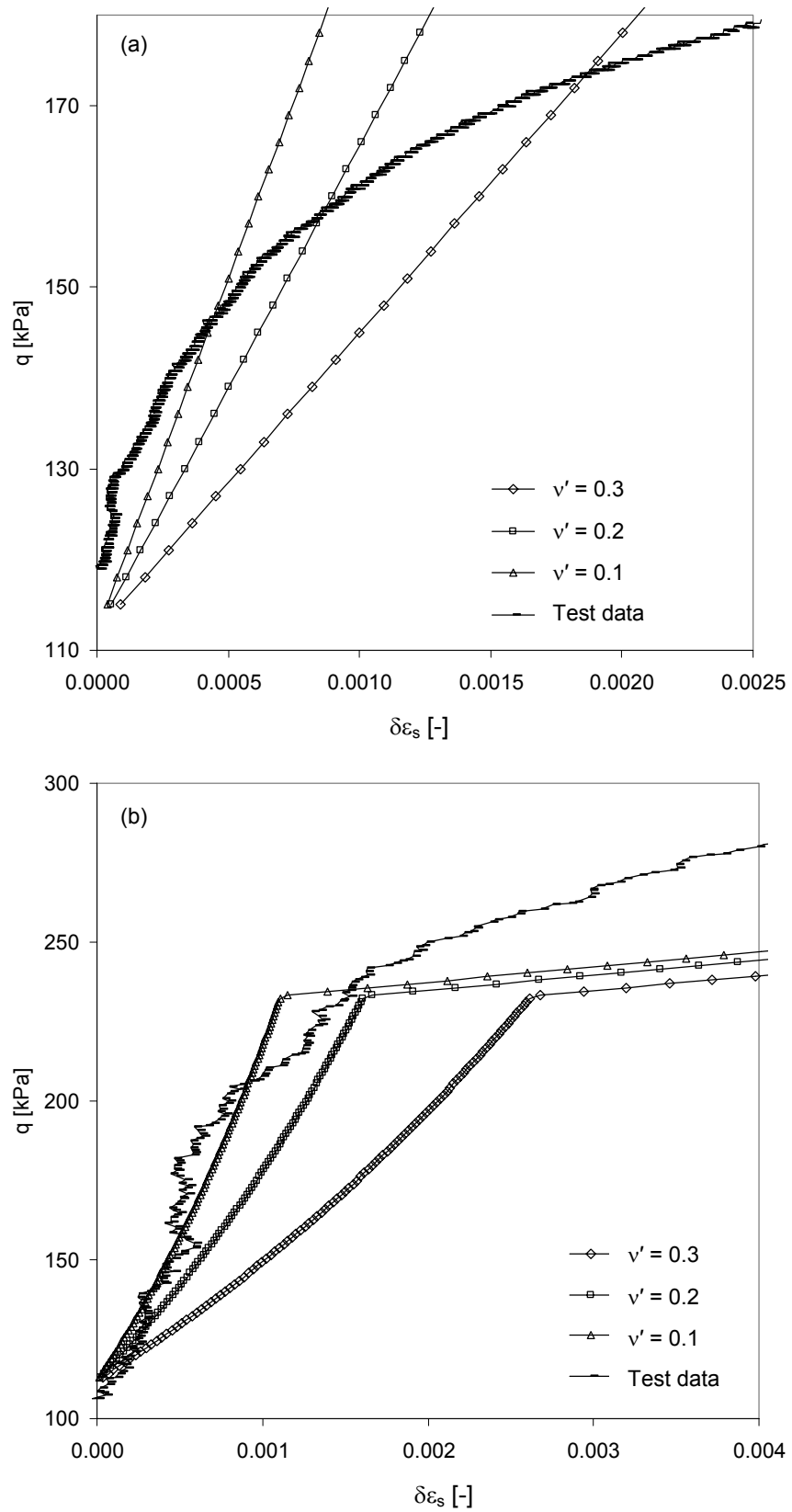
Fig. 7.23: Parametric study on the Poisson's ratio with the Modified Cam Clay model. Simulation and test results for triaxial test (a) S2T4 with $\Theta = 90°$ and (b) S2cT1 with $\Theta = 42°$.

7.6 Simulation results

Four triaxial tests from series 2, which represent four major stress paths in the triaxial stress space (compression, one-dimensional, isotropic and extension) are simulated using the 5 constitutive models introduced above.

The simulation results are presented and compared to the experimental data in the following paragraphs. First the probing stress path and the consolidation history is given in the q – p′ plot to verify the simulated stress paths. The yield surfaces of the constitutive models applied, with an extent corresponding to the consolidation history induced, are also presented in this plot.

Thereafter, only the data from the probing stress path are presented. The plot of the deviator or mean effective stress versus the volumetric and shear strain increments respectively is given to investigate the deformation behaviour, yield states and failure conditions. Finally, a plot of the shear versus volumetric strain increments is presented to determine the strain increment ratio.

7.6.1 Test S2T4: $\Delta p'$ = constant (compression)

The first test simulated is a shear test in compression with the stress paths and peak failure stress states shown in Fig. 7.24. As well as the stress path applied in the test and the simulations the yield surfaces of the various models, representing the consolidation history performed, are also presented.

The failure behaviour simulated by each model is also visible in the corresponding stress-strain plots, given in Fig. 7.25. Comparison of the failure simulation with the Modified Cam Clay and the S_CLAY1 models, specifically the yield surface and failure cone, shows that the stress path is simulated up to a peak deviator stress of about 250 kPa, where the bounding surface is reached (Fig. 7.4). The subsequent softening, back to the failure criterion, described by the critical state line, is not simulated by any of the codes applied.

The deviator stress versus shear strain increment curves of the probing stress path are shown in Fig. 7.25a. The simulation results compared to each other show the same linear elastic response for the MCC and S_CLAY1 model, the Soft Soil

model behaves slightly more stiffly due to the modified strain definition, as discussed in Chapter 7.3.4 and outlined in Fig. 7.11.
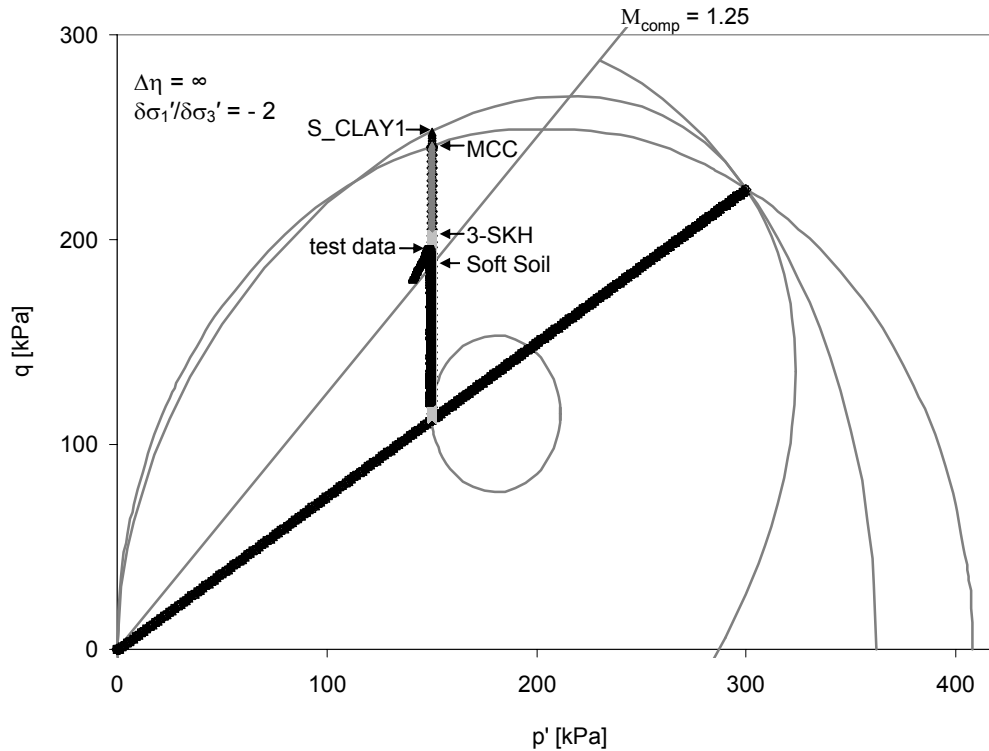
Fig. 7.24: Numerical simulation and experimental test results for triaxial test S2T4. Deviator versus mean effective stress. (N.B.: The arrows indicate the failure stress state simulated by the model.)

The 3-SKH deviator stress versus shear strain increment curve starts with a high initial shear stiffness, which decreases with increasing shear strain, and is the only model that follows the test data at all stages from small strain up to failure remarkably well. This is because 3-SKH is the only model which incorporates special formulations simulating non-linearity and stress path dependency in addition to the logarithmic non-linear elastic formulations used in the other models. Therefore, the remaining simulations are characterised by a bilinear deviator stress versus shear strain relationship incorporating elastic straining moving directly on to failure, without any plastic straining and hardening for this probing stress path and the consolidation history applied.

The development of volumetric strains is shown for the compression shear path in Fig. 7.25b.
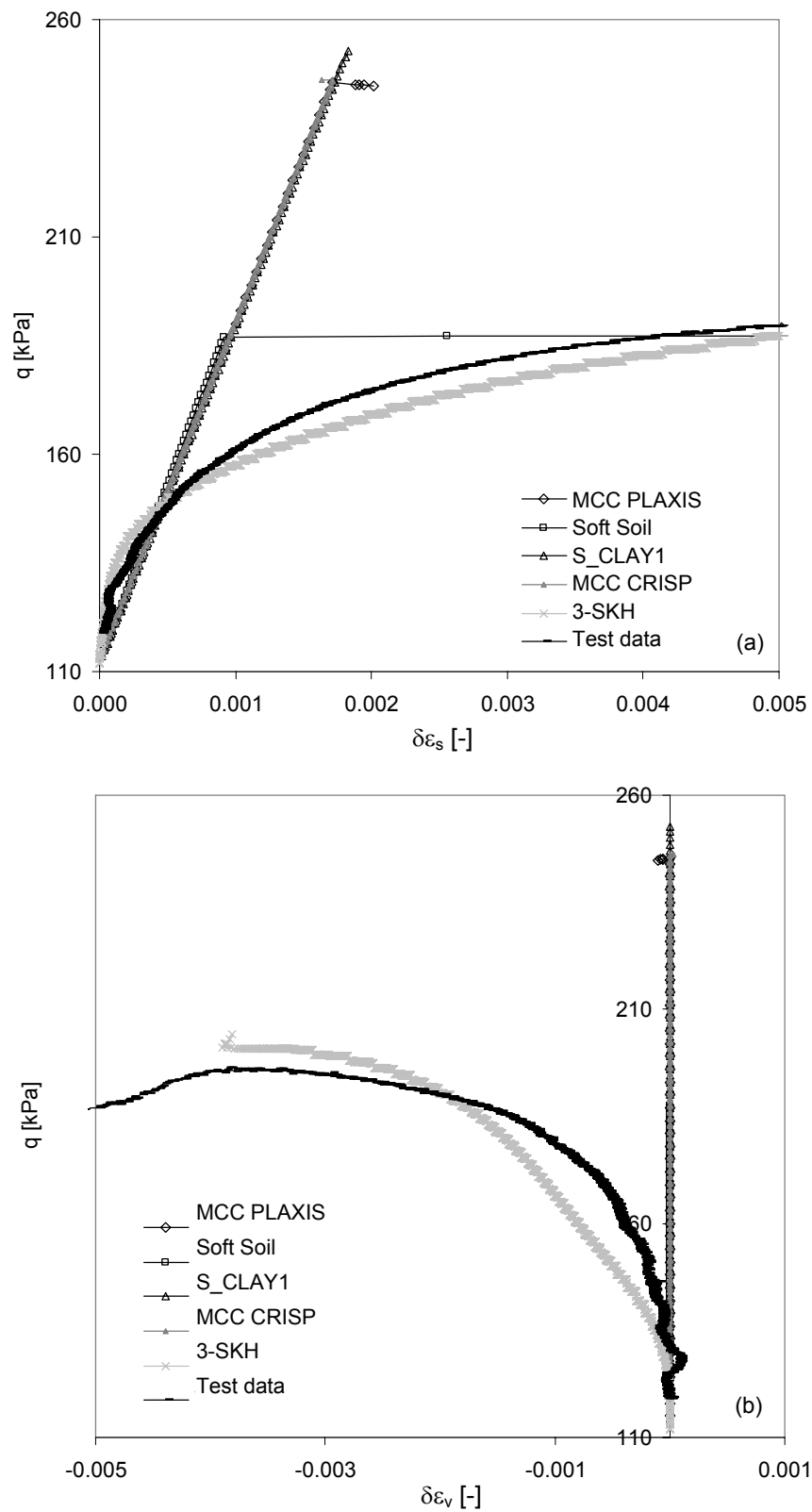
Fig. 7.25: Numerical simulation and experimental test results of test S2T4. Deviator stress versus (a) shear strain increments; (b) volumetric strain increments.

Zero volumetric strains are measured in the test and predicted in the simulations by all models in the first Δq = 20 kPa of the probing path. Volumetric expansion is measured in the test specimen thereafter and this is simulated quite effectively by the 3-SKH model.

The models that are based on the critical state theory couple the development of volumetric strains to the change in mean effective stress only and are therefore not able to simulate the observed response. This drawback can be overcome with the application of an anisotropic elastic, instead of an isotropic elastic, formulation. E.g. with the cross-anisotropic matrix, derived in Chapter 6 for Kloten clay (p. 172) and applied to this stress increment ratio of constant p' in compression, the elastic volumetric strain increment per deviator stress increment is $-3.1 \cdot 10^{-6}$.

The shear strain versus the volumetric strain increments are plotted in Fig. 7.26 and represent a composition of the data given above.
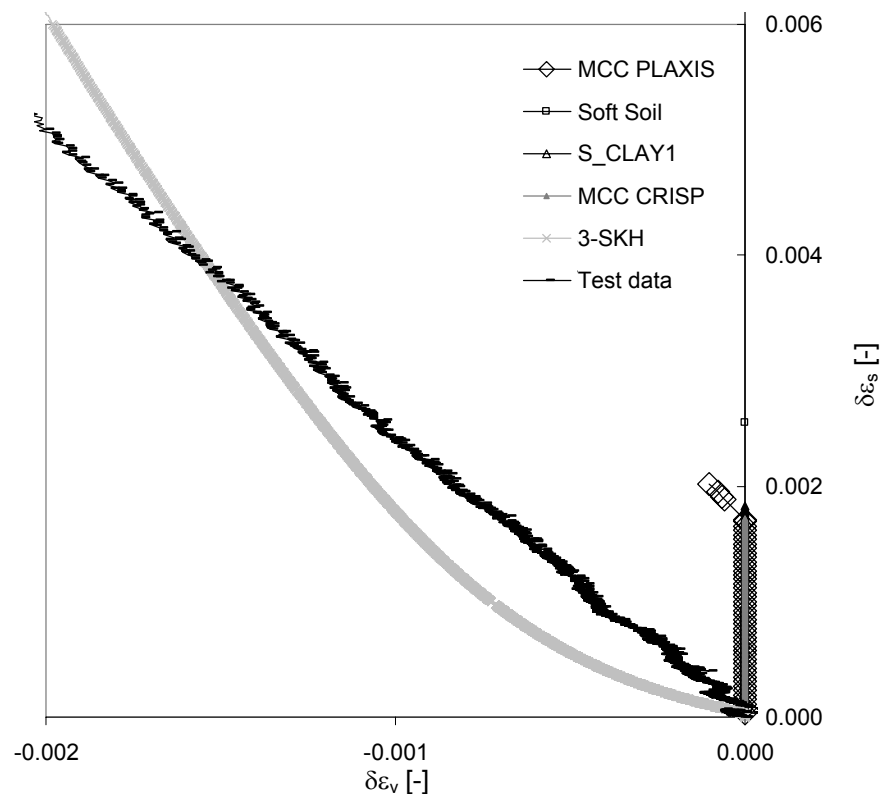
Fig. 7.26: Numerical simulation and experimental test results for triaxial test S2T4. Shear versus volumetric strain increments.

Therefore, the results given in Fig. 7.26 highlight again that due to the lack of volumetric strain predictions of the MCC, S_CLAY1 and Soft Soil model the measured strain increment ratios are not simulated well, whereas the 3-SKH model more or less captures the trend in the shear versus volumetric strain increment plot.

The 3-SKH model is the most appropriate for this stress path in compression followed by the Soft Soil model only in respect of average stiffness and failure state. The Modified Cam Clay and the S_CLAY1 model highly overpredict the failure stress state.

7.6.2 Test S2cT1: $\Delta\eta$ = 0.9 (compression)

The stress paths of the consolidation history and the probing stress path, as well as the yield surfaces of the models applied, are given in Fig. 7.27. With this stress path simulated no failure occurs. Therefore, the stress path in the simulations is applied beyond the consolidation stress state reached in the laboratory test.

The stress-strain plots are presented in Fig. 7.28a&b. The bilinear representation from the S_CLAY1 and the Soft Soil models correspond well with test observations in the deviator stress versus shear strain increment space and both MCC analyses perform acceptably (Fig. 7.28a). This observation would imply that the aspect of non-linearity in the elasticity is not dominant in the deformation behaviour and that a logarithmic linear elastic-plastic model simulates the response observed better than a model which considers stress path history and non-linear elasticity like the 3-SKH model.

The stiff response inside the history surface and the rapid decrease in shear stiffness with kinematic hardening is clearly visible in the simulation data from the 3-SKH model. But both aspects, the initial stiffness and the stiffness decrease, are simulated too significantly. A lower value of G' and a smaller value for the exponent of the hardening function ψ than the applied 2.0 would give simulation results that agree better with the test data of this stress path.

The volumetric response is presented in Fig. 7.28b. The comparison shows good agreement between the simulation data and the test data for all models at the start of the probing stress path. Again, the bi-linear elasto-plastic formulation without

any additions to describe non-linear elasticity or stress history, such as it is used in the Modified Cam Clay, the S_CLAY1 and the Soft Soil models, simulate the deformation behaviour observed as well as the 3-SKH model, which does consider these additions. The stiffness in the model decreases more rapidly than in the test with the onset of the kinematic hardening in the 3-SKH model.

The strain increment ratios are compared in Fig. 7.29. Elastic straining is well predicted by all models except the 3-SKH model, which significantly underpredicts the shear strains. The shear strain increments are overpredicted by all models in plastic straining beyond the Y3 bounding surface and most of all by the two analyses using the MCC model.
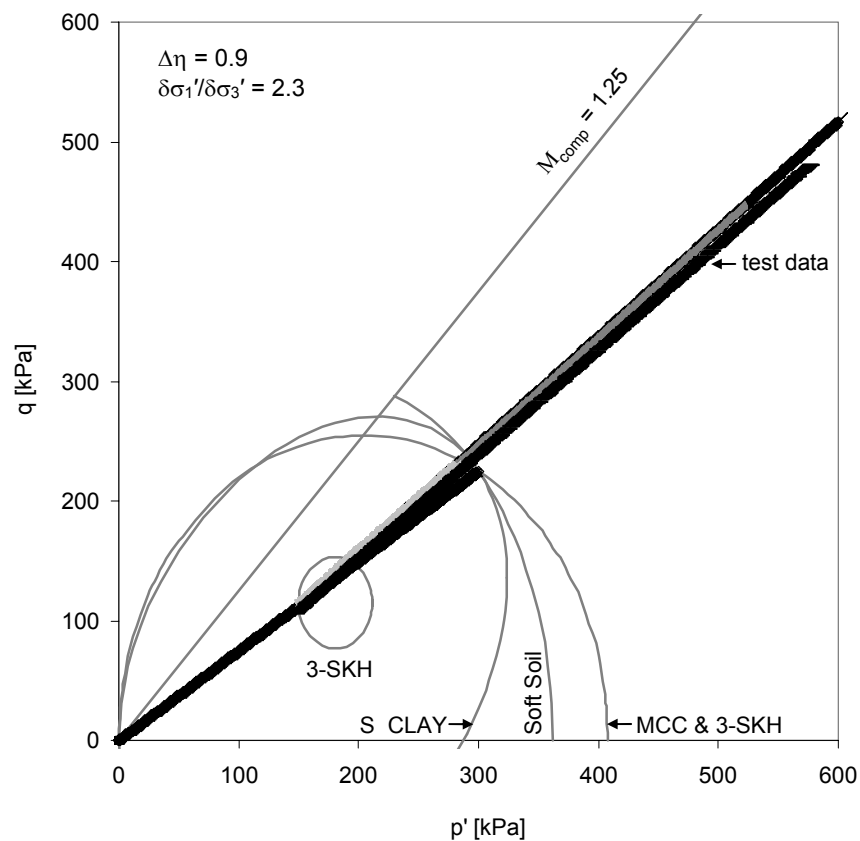
Fig. 7.27: Numerical simulation and experimental test results for triaxial test S2cT1. Deviator versus mean effective stress.

The deformations are simulated quite well for this stress path by all models, independent of their ability to model small strain and stress history dependent stiffness behaviour.
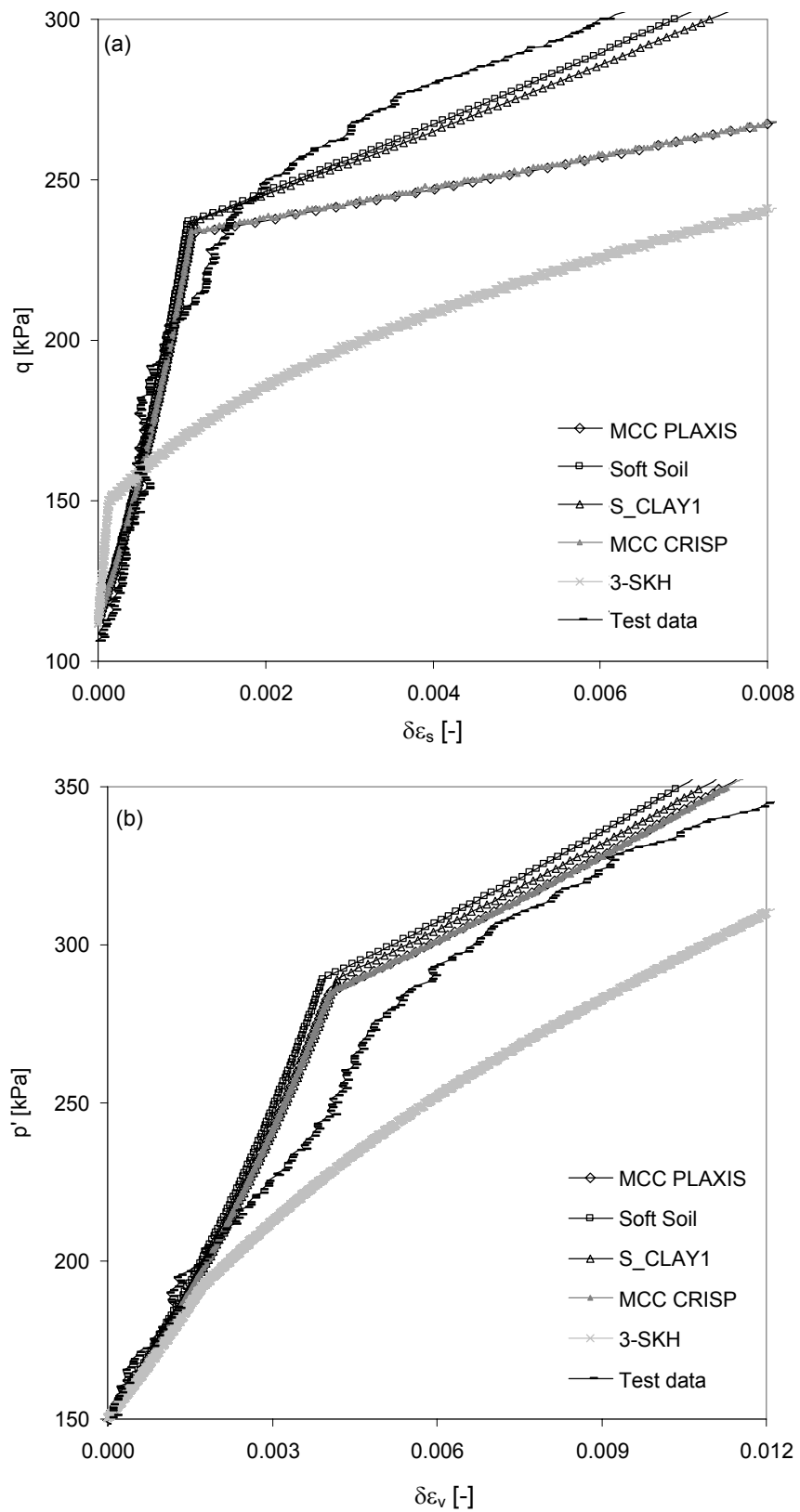
Fig. 7.28: Numerical simulation and experimental test results for triaxial test S2cT1. (a) deviator stress versus shear strain increments. (b) mean effective stress versus volumetric strain increments.
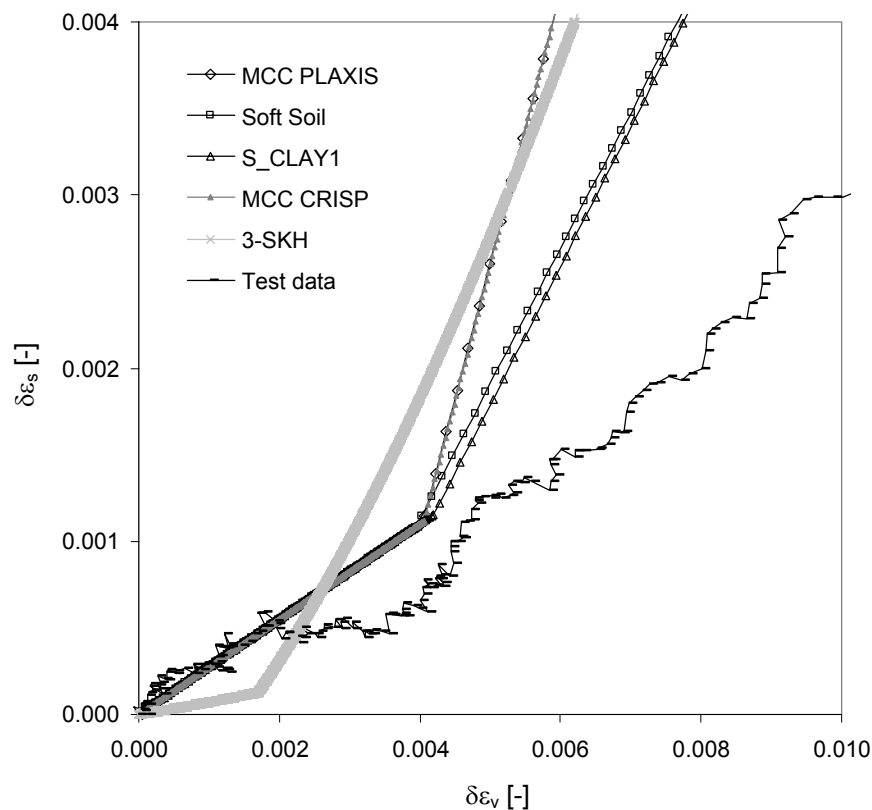
Fig. 7.29: Numerical simulation and experimental test results for triaxial test S2cT1. Shear versus volumetric strain increments.

7.6.3 Test S2T3: Δq = constant (isotropic compression)

The stress paths of the consolidation history and the probing stress path are given in Fig. 7.30, together with the stress-strain plots in Fig. 7.31. The test data show negative shear strain increments developing immediately (Fig. 7.31a). The only model to respond with negative shear strain increments in plastic straining is S_CLAY1, due to the inclination of the tangent to the plastic potential having a positive gradient and hence a negative shear strain increment.

S_CLAY1, as well as the MCC and the Soft Soil models, simulates isotropic elastic behaviour inside the Y3 bounding surface, which gives zero shear strain increments for loading in isotropic compression. This can be changed with the application of an anisotropic elastic instead of an isotropic elastic formulation. E.g. with the cross-anisotropic matrix, derived in Chapter 6 for Kloten clay (p. 172) and applied to this stress increment ratio of constant q, the elastic shearing strain

increment per mean effective stress increment is $-3.1 \cdot 10^{-6}$. Comparing this increment to the test data presented in Fig. 7.31a shows that the shear strain increment has the same sign as the test data, only the magnitude is not well represented. The magnitude is related to the stiffness applied, which is nonlinear and strain level dependent, and can therefore not be described by a unique value.
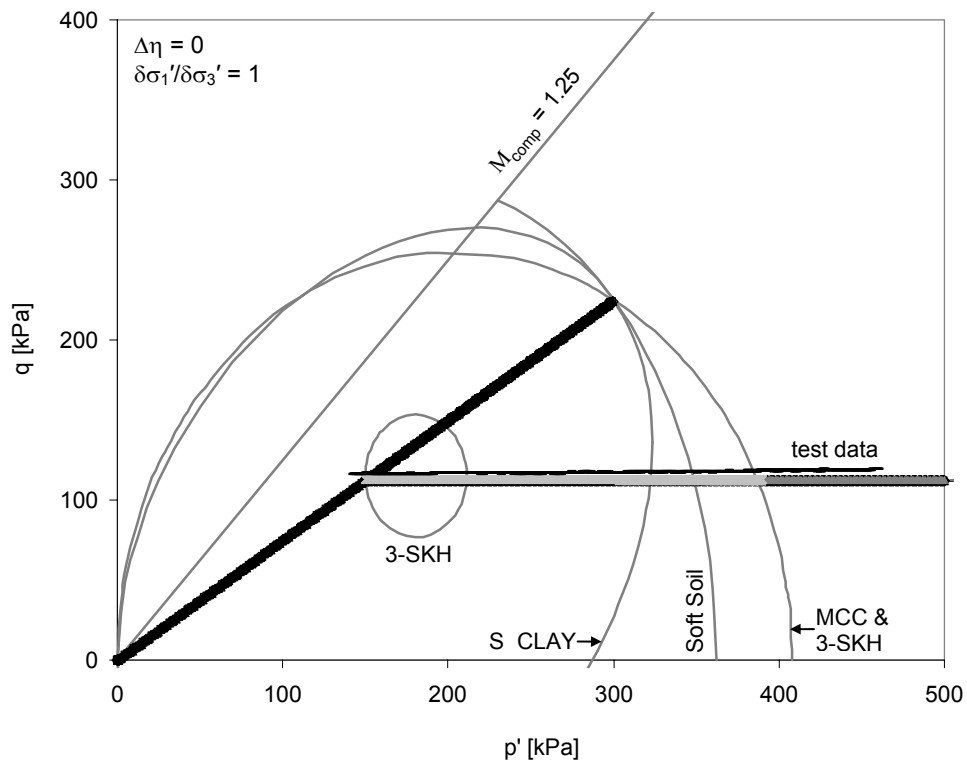
Fig. 7.30: Numerical simulation and experimental test results for triaxial test S2T3. Deviator versus mean effective stress.

The only model predicting shear strains before reaching the Y3 bounding surface is the 3-SKH model, which simulates positive shear strain increments during kinematic hardening of the history surface.

The volumetric response is presented in Fig. 7.31b. The comparison shows that the elastic volumetric strains are underpredicted by all models. The magnitude of plastic strains, predicted for stress states beyond the preconsolidation bounding surface Y3, is simulated well by all models except the 3-SKH model, which also underpredicts the volumetric strains at these stress states.
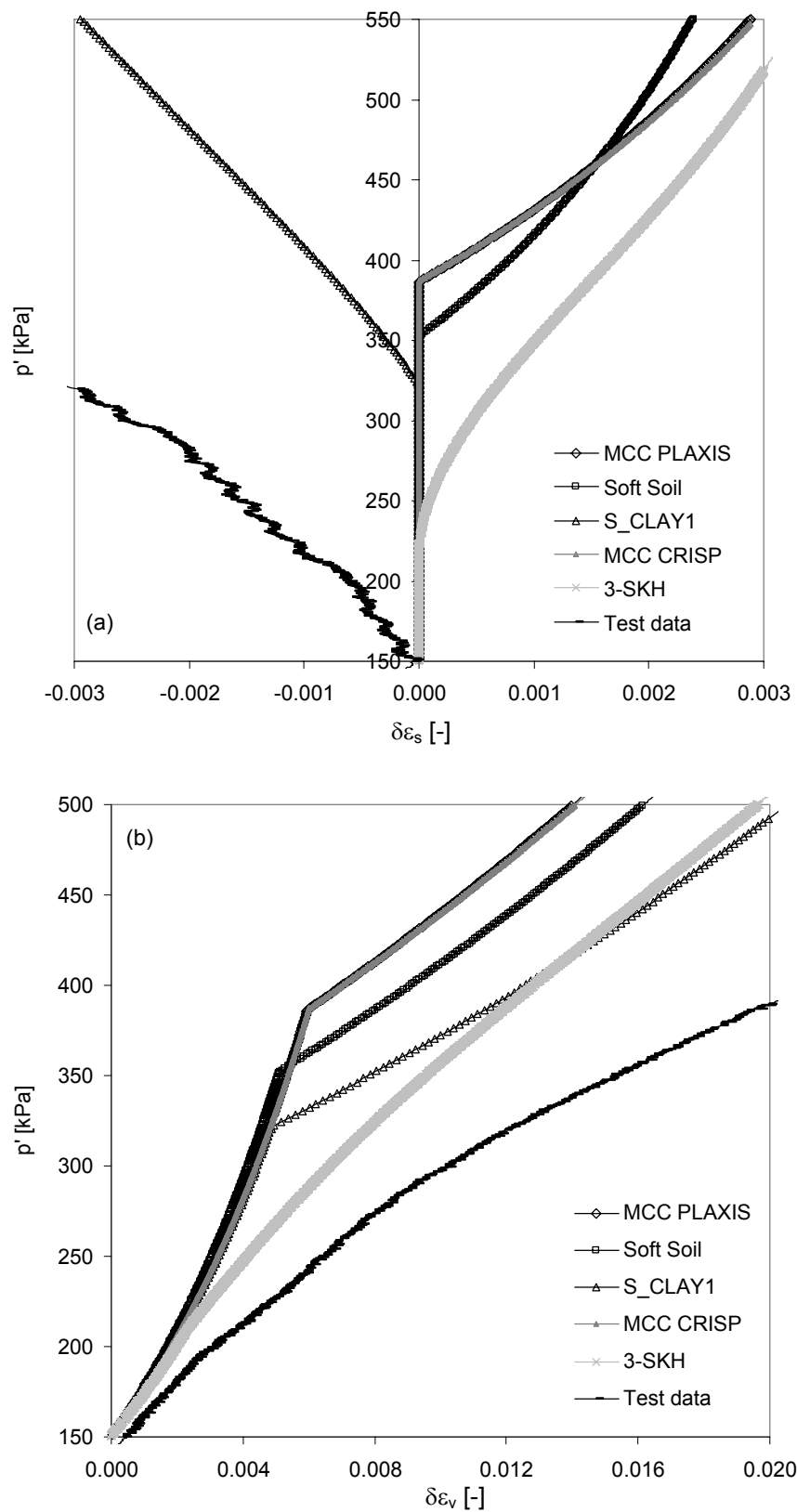
Fig. 7.31: Numerical simulation and experimental test results for triaxial test S2T3. Mean effective stress versus (a) shear strain increments; (b) volumetric strain increments.

The shear strain versus the volumetric strain increments are presented in Fig. 7.32. As discussed above, predictions from all models except the S_CLAY1 model give positive shear strain increments. Therefore, these models are not able to predict the strain increment ratio for isotropic load paths. Normally consolidated soils in general, and lacustrine clays in particular, have a distinct inherent anisotropy due to the deposition mode, which is increased by subsequent natural one-dimensional consolidation. This generates additional induced anisotropy.
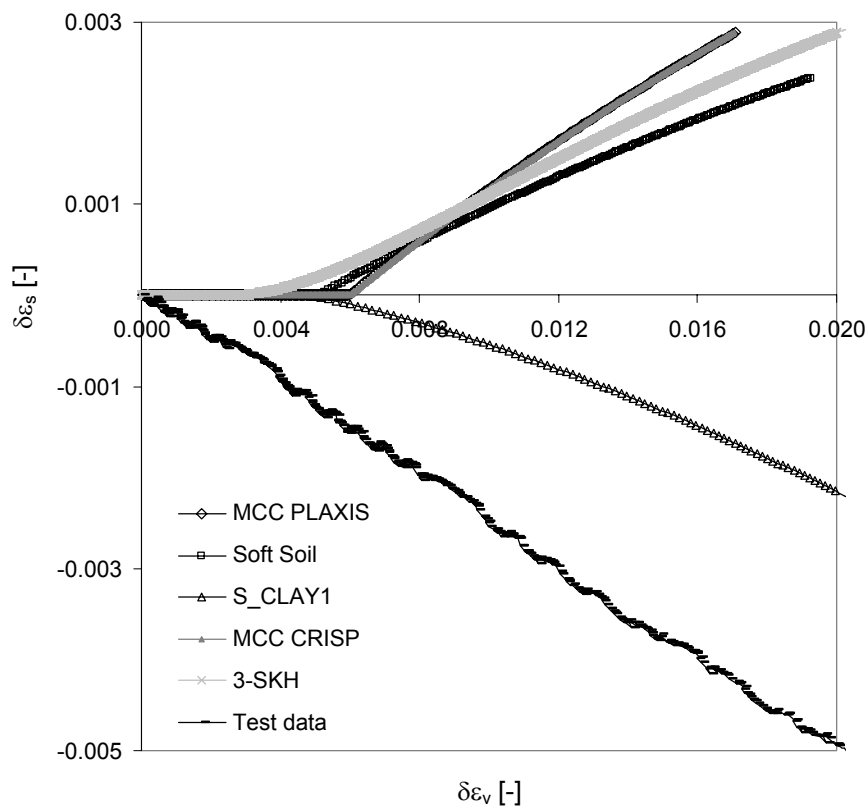
Fig. 7.32: Numerical simulation and experimental test results for triaxial test S2T3. Shear versus volumetric strain increments.

Consequently, all natural clays can only be simulated by constitutive models that consider this aspect in the model formulation, as done in the S_CLAY1 model, using an inclined yield surface.

The trend of the strain response to this isotropic stress path is simulated only well by the S_CLAY1 model, but even here, the rate of straining was underpredicted. The others were incapable of representing the strains observed.

7.6.4 Test S2aT4: Δp′ = constant (extension)

The stress paths of the consolidation history and the probing stress path are given in Fig. 7.33 and the stress-strain plots are presented in Fig. 7.34. The comparison between the model responses for the shear strain development (Fig. 7.34a) shows that the models which simulate logarithmic linear elastic stiffness response inside the bounding surface simulate the shear stiffness well within the first $\Delta q \approx 100 \, kPa$. After that, a non-linear response with stiffness decrease is measured, which cannot be simulated by the Modified Cam Clay, the S_CLAY1 and the Soft Soil model as this aspect is not incorporated in the model formulations. With ongoing loading, the shear strains measured in the test increase rapidly, while the MCC and the Soft Soil models predict elastic straining until the failure stress state, which is about twice the failure stress measured in the test. This is because of the greater extent of the bounding surface in extension for these models.

The 3-SKH model, which incorporates a formulation for non-linear elastic stiffness response, appears to predict non-linear but too high stiffness throughout failure. Due to the application of the Drucker-Prager failure cone, the failure stress is overpredicted by the corresponding models as well.

A smaller failure cone, e.g. using M_{ext} instead of M_{comp}, would not only improve the simulation of the failure state but would also result in a smaller extent of the yield surface in extension for the MCC, the 3-SKH and the S_CLAY1 models (e.g. see Fig. 7.5 & Fig. 7.8). This would result in a faster stiffness decrease during kinematic hardening in the 3-SKH model as well, because the strain magnitude predicted increases with the proximity of the kinematic surface to the failure state (Chapter 7.3.2).

The volumetric response is presented in Fig. 7.34b. The comparison shows that the elastic volumetric strains are well approximated by all models, but none of the models generate significant plastic volumetric straining with the exception of the S_CLAY1 model, which predicts the volumetric straining very well once the stress path reaches the inclined, but marginally oversized, yield surface in extension

space. Therefore the simulated magnitude of volumetric strains at failure is underpredicted by all models except the S_CLAY1 model.
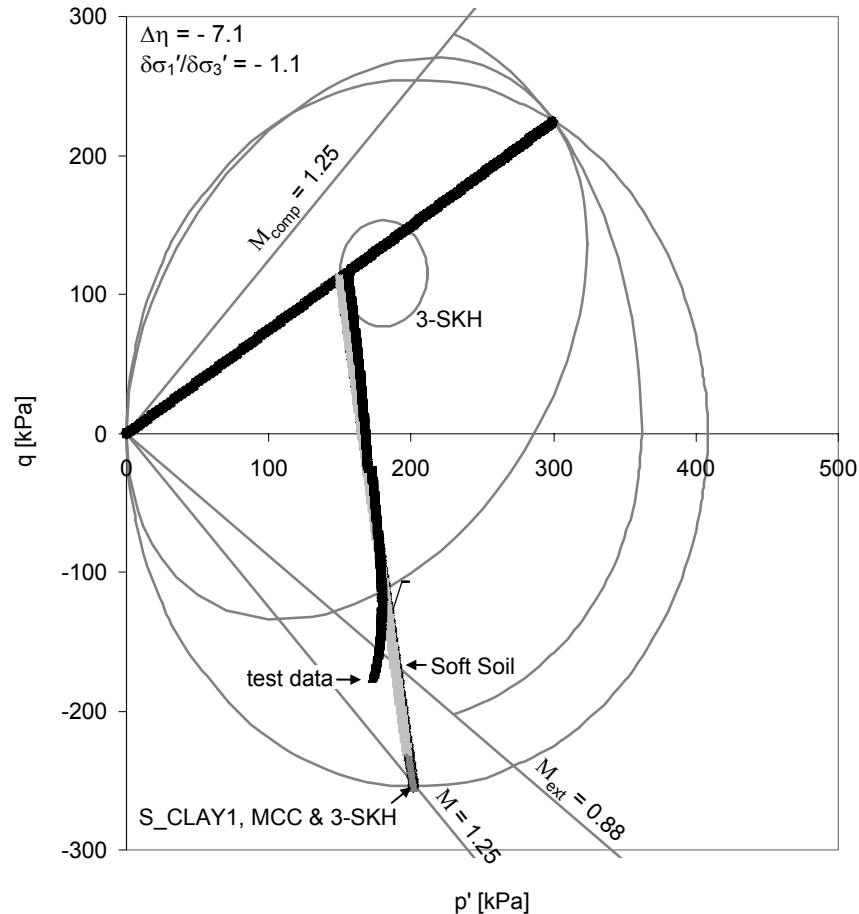
Fig. 7.33: Numerical simulation and experimental test results for triaxial test S2aT4. Deviator versus mean effective stress. (N.B.: The arrows indicate the failure stress state simulated by the model.)

The shear versus volumetric strain increments are presented in Fig. 7.35. But before the simulation results are compared, a comment on the test data is given. At the start of the test, the specimen undergoes small volumetric compression followed by a small expansion, which probably represents zero volumetric strains within the accuracies given for the measurement device. However, this small volumetric expansion of the sample has a major influence on the shear versus volumetric strain increment curve in Fig. 7.35 but is not considered in the data discussion.
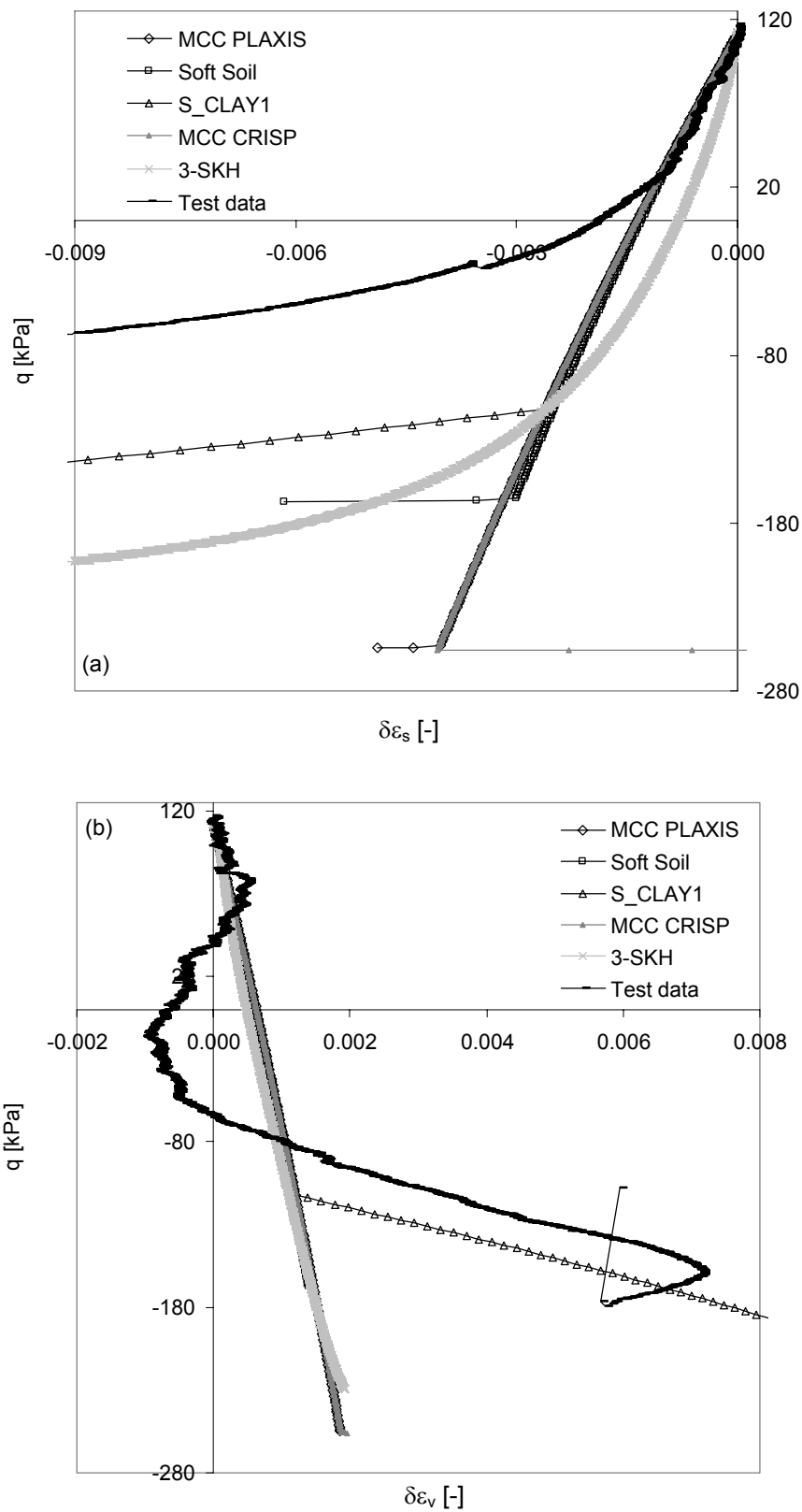
Fig. 7.34: Numerical simulation and experimental test results for triaxial test S2aT4. Deviator stress versus (a) shear strain increments; (b) volumetric strain increments.

The comparison of the simulation results to the test data shows that all models except the 3-SKH model simulate the strain increment ratio quite well, although they overpredict the volumetric strain increment. While the MCC and the Soft Soil model only simulate elastic straining and failure the S_CLAY1 model simulates both elastic and plastic straining, with a strain increment ratio corresponding to the test data.
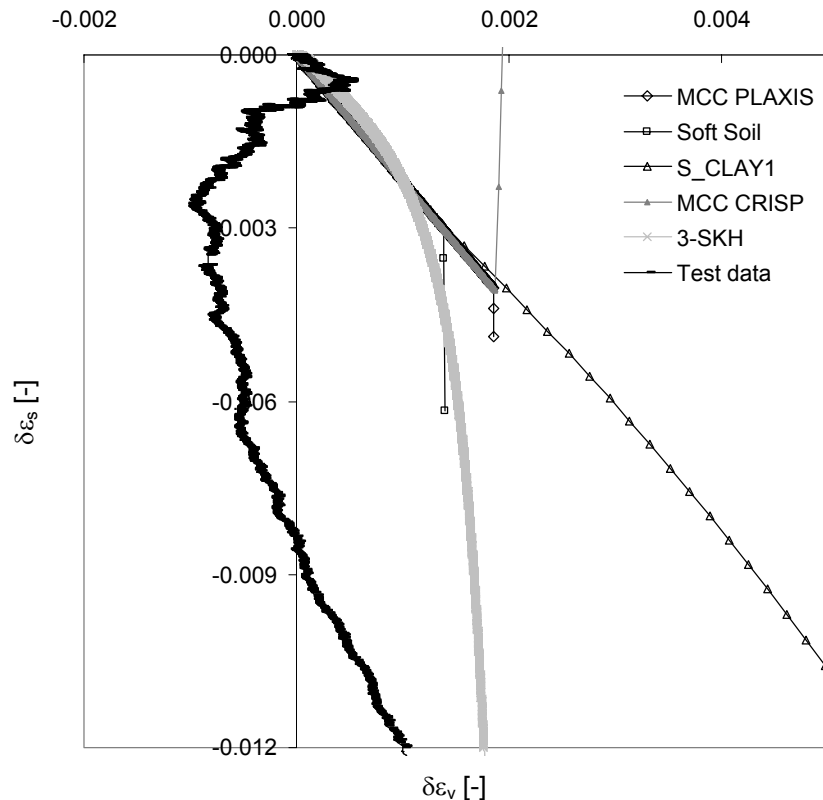
Fig. 7.35: Numerical simulation and experimental test results for triaxial test S2aT4. Shear versus volumetric strain increments.

This stress path in extension is simulated best by the S_CLAY1 model. With the exception of the Soft Soil model, all models incorporate the Drucker-Prager failure criterion, which does not represent the failure state well in extension. This problem can be overcome for simulating single element tests by applying a different failure parameter for the stress paths in extension. The results of the simulations after applying a critical state value of M_{ext} = 0.88 is shown in Fig. 7.37 and Fig. 7.38.

The stress-strain plots are given in Fig. 7.37 and from the plot of the deviator stress versus the shear strain increments (Fig. 7.37a) it can be seen that, although

the failure stress is still overpredicted, the magnitude has been reduced for all models except the Soft Soil model, where the failure criterion is not defined by the critical state parameter M but by the internal friction angle φ'.
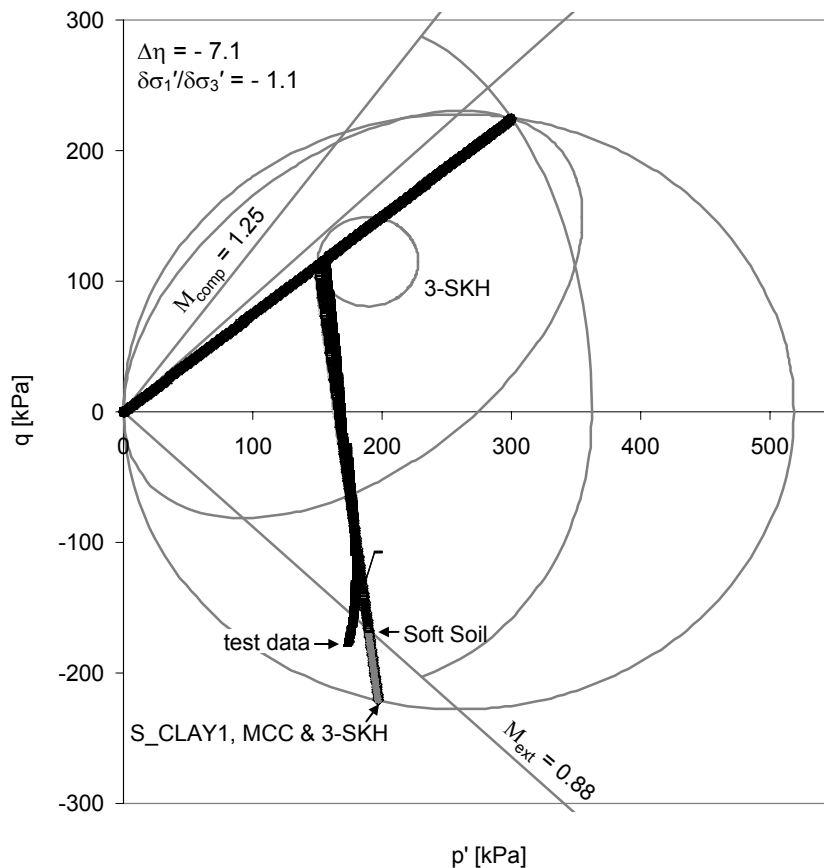
Fig. 7.36: Numerical simulation applying M_{ext} = 0.88 and experimental test results for triaxial test S2aT4. Deviator versus mean effective stress. (N.B.: The arrows indicate the failure stress state simulated by the model.)

The volumetric strain predictions (Fig. 7.37b) show that the 3-SKH model simulates volumetric expansion close to the failure state, which does not represent the test measurements, while the S_CLAY1 models predicts yielding and plastic volumetric compression, which represents the test data almost perfectly.

The comparison of the shear versus volumetric strains, presented in Fig. 7.38, gives good agreement with the test data for the S_CLAY1 model, after neglecting the expansion at the start of the test. The strain increment ratio is less well predicted for the 3-SKH model.
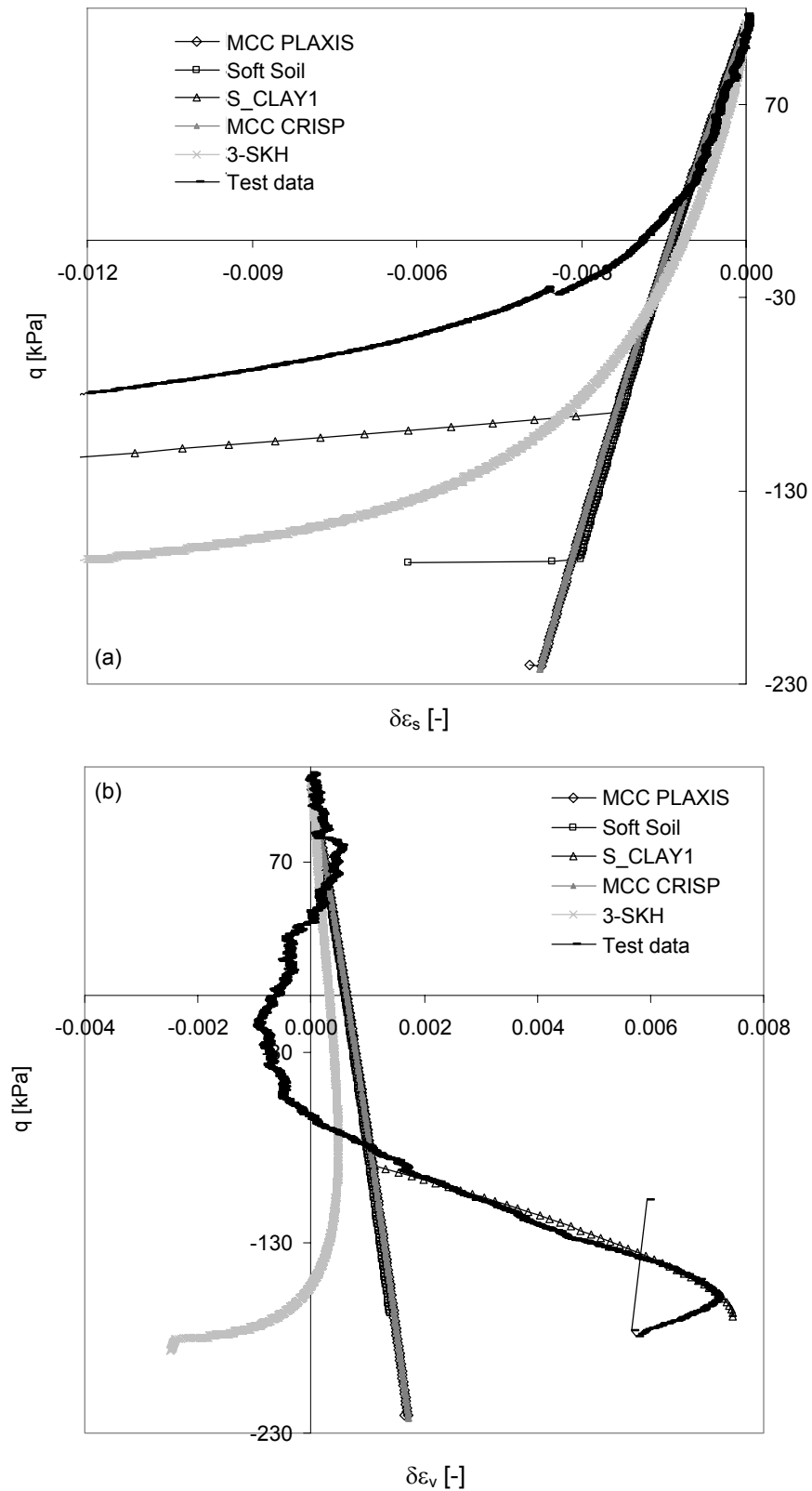
Fig. 7.37: Numerical simulation and experimental test results for triaxial test S2aT4. A critical state parameter of M = 0.88 was applied for the numerical simulations with critical state based models.
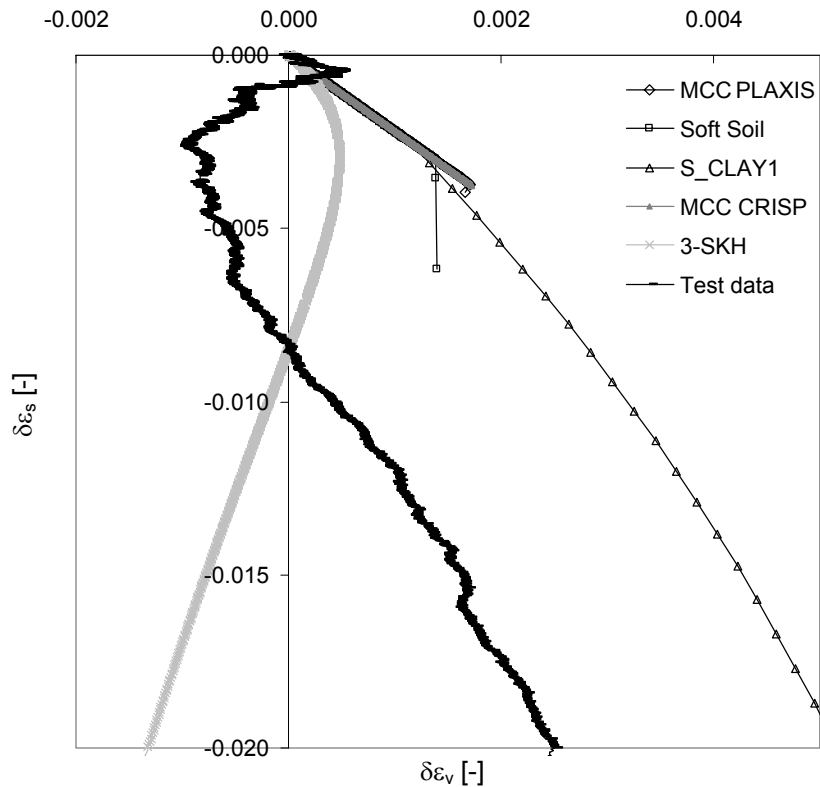
Fig. 7.38: Numerical simulation and experimental test results for triaxial test S2aT4. A critical state parameter of $M = 0.88$ was applied for the numerical simulations with critical state based models.

7.7 Discussion of the numerical simulations

The comparison of the simulation results with the test data shows that each model is able to simulate one stress path well but all four stress increment ratios can not be simulated equally well with one model.

All four models (assuming that the MCC model in CRISP and PLAXIS is the same) gave results that demonstrated the right tendencies for the two stress increment ratios in compression, but either over or underpredicted the measured strain magnitude. However, some models also gave the wrong tendencies for the isotropic stress increment ratio and the stress path in extension, especially for the shear strain predictions. Only the S_CLAY1 model was capable of strain predictions corresponding to test data for these stress increment ratios.

This inability of the Modified Cam Clay, the 3-SKH and the Soft Soil model, to predict the strain increment ratio trend can be overcome by defining an additional

plastic potential surface and incorporating a non-associated flow rule, but the plastic potential surface only changes the direction and not the magnitude of strains. The magnitude is a function of the elastic and plastic stiffnesses, but is also significantly influenced by the onset of yielding, defined by the location of the yield surface. Therefore, a yield surface that corresponds to the test data is as important as a plastic potential surface corresponding to the test data. The evaluation of the test data on lacustrine clay showed that for a yield surface that fits the test data, an associated flow rule is also most appropriate for a good prediction of the strain increment ratios. The model that comes closest to this approach is the S_CLAY1 model.

This is important for a successful simulation of plastic straining which may represent the major component of strains in elasto-plastic straining. But in this research the elastic behaviour in terms of non-linearity and stress path dependency was established for lacustrine clays. A formulation, describing these aspects is only incorporated in one model, the 3-SKH model. The simulations showed that this formulation, using kinematic hardening, incorporated in the 3-SKH model in order to simulate non-linear elastic behaviour, can give good simulation results for a set of data but often has difficulties in representing the non-linear elastic behaviour observed. The simulation results highlighted that the small strain stiffness, representing the stress history dependent initial stiffness, is higher than observed while the drop in stiffness with ongoing straining is less significant in the test data than in the model.

This drop in stiffness is described by the kinematic hardening rule using the parameter ψ. This hardening parameter ψ influences the degradation of the shear and the bulk modulus in the same way and this does not always represent the test data. With an uncoupled set of parameters, one for the decrease of the bulk modulus and one for the decrease of the shear modulus, the kinematic hardening law might give better results. However, due to the constitution of the translation and hardening rules incorporated in the 3-SKH model it might be difficult to split the hardening parameter ψ into two independent parameters. Probably the most straight forward solution would be to formulate the change in shear and bulk stiffness with ongoing straining in two separate laws.

The failure stress states were, in general, not very well predicted and were highly overpredicted for the extension stress path simulated by those models that apply the Drucker-Prager failure criterion (Fig. 7.39). This even results in predictions on the unsafe side. Therefore the application of a failure criterion that considers the difference in response for compression and extension, is a necessity for all models that are applied to simulations that may include failure stress states in extension. Models which account for this aspect are e.g. the Mohr Coulomb failure criterion, Lade's failure surface (Lade & Duncan, 1975) or the Matsuoka-Nakai failure cone (Matsuoka & Nakai, 1974; Fig. 7.39).
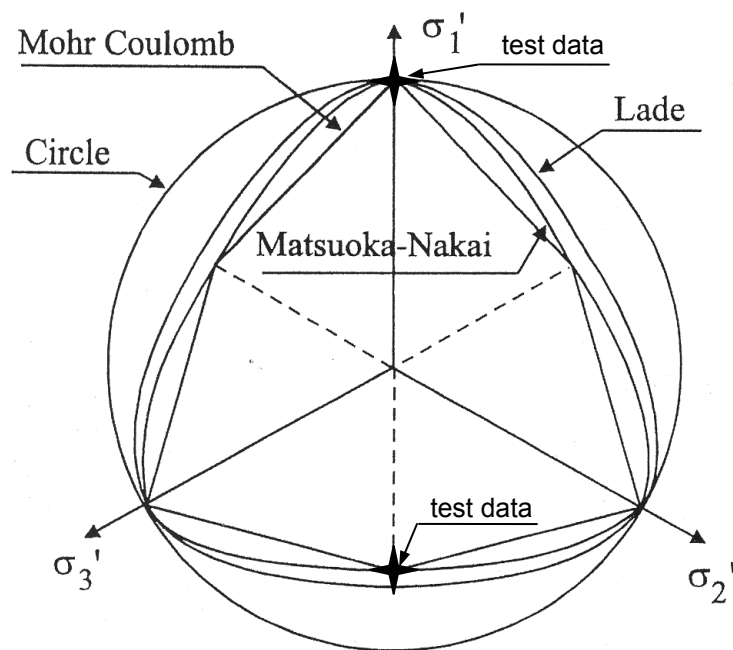
Fig. 7.39: Failure surfaces in the deviatoric plane compared with the two failure states in compression and extension obtained from the laboratory investigations on Kloten clay (after Potts & Zdravkovic, 1999b; p. 166).

8 Summary and Conclusion

The deformation characteristics of varved Swiss lacustrine soils were investigated by means of drained triaxial stress path tests. Special emphasis was put on the observation of stiffness response in the small strain region and investigation of the influence of anisotropic soil texture on the stiffness behaviour.

8.1 Local displacement measurement in the triaxial test apparatus

Consequently, displacement measurement methods that fulfill the requested accuracy criteria, and that are applicable in triaxial test apparatuses, were evaluated. It was found that the most appropriate method for axial displacement measurement is the linear variable differential transducer (LVDT), directly mounted on the test specimen. The study of radial displacement measurement methods showed that none of the methods that would fulfill the desired accuracy were appropriate to apply to varved soils, although radial displacements had been measured successfully over the entire sample height with the use of laser transducers for unsaturated soil samples. Consequently, this method was adapted and applied herein for the radial displacement measurement of highly varved lacustrine soils.

Both types of transducers, the LVDTs for the axial and the lasers for the radial displacement measurement, had to be installed in the triaxial apparatuses and located optimally in relation to the test sample. It was found that the LVDTs were attached most appropriately with the help of small mountings glued on to the rubber membrane of the test specimen, to hold the transducer. With respect to the installation of the laser transducers, the literature recommended placing the

transducer outside a triaxial Plexiglas cell. But the Institute's triaxial cell was made of steel. A comparative survey was performed on whether the steel cell should be replaced by a Plexiglas cell or the lasers should be placed in the cell liquid inside the existing cell. This study confirmed that the option of placing the transducers inside the triaxial cell was more favourable. Therefore, a water- and pressure-tight housing for each laser, together with a mounting for them inside the triaxial apparatus, were designed, constructed and installed. Three laser transducers were individually housed and were mounted from the top to a rigid plate, which was itself connected to two lead screws. These were each powered by a stepping motor, to move the entire system (rigid plate and three laser transducers and their housings) in an axial direction up and down along the height of the test specimen. It was possible to measure the radial displacements without contact with this newly designed laser scanning device, on three profiles over the entire sample height, at any state of the stress path tests.

Additional to the development and installation of new local displacement measurement tools for the existing triaxial test apparatuses, these apparatuses were adapted for testing soft soils. The load cells were changed to ones with an appropriate measurement range and the corresponding required accuracy. The top platen and bottom pedestals were reduced in size to a diameter of 50 mm. Bender elements, which were installed in one of the triaxial apparatuses (Trausch Giudici, 2004), were also used. Finally, the newly installed displacement measurement devices and the rebuilt triaxial test apparatuses were calibrated with all their components.

8.2   Extraction of natural lacustrine clay samples

It was possible to investigate the load-displacement response over a wide displacement range with this equipment. But for a successful investigation of soil stiffness, not just the apparatuses but also the soil specimens tested have to be of a corresponding quality. Therefore, a preliminary literature review on sampling methods for clays was performed. This showed that block samples carved out of the deposit give the highest quality of test specimens. This method was applied in sampling lacustrine clay at a site in Kloten (Switzerland), but some drawbacks

were experienced due to the softness of the normally consolidated Swiss lacustrine soils. In a subsequent literature study, it was found that test specimens that were carefully sampled with thin-walled tubes with diameters of 200 mm or more were able to mobilise higher strength than samples obtained by different techniques. Protecting the sides of the horizontally layered soils with the sample tube has the additional advantage of preventing the more permeable layers from draining the sample. Therefore, a sample tube with an inner diameter of 196 mm, an area ratio of 4 % and an outer cutting edge angle of 11° was designed and built.

A comparative study on samples taken with the new sampler and conventionally sampled soil specimens was performed to establish the relative degree of disturbance, by comparing the strength parameters derived. Sampling was performed at a site in Birmensdorf (Switzerland) with sample tubes of three different diameters. Test specimens were cut from these soil samples, all taken from the same soil layer, and were subsequently investigated in the laboratory by means of unconfined compression and undrained triaxial shear tests. The results showed that the undrained shear strength of the specimens cut from the samples that were taken with the new sample tube was consistently around 20 % higher than that of specimens cut from conventional thin-walled soil samplers with tube diameters of 65 mm. This confirmed that less sample disturbance occurred with the newly designed sample tubes. Consequently, a series of such samples was taken from a fine grained lacustrine sediment field in Kloten (Switzerland). These samples were subsequently used for investigation of the non-linear stiffness response in triaxial stress path tests. Additionally, some soil was taken from both sites, Birmensdorf and Kloten, from which reconstituted samples were prepared and consolidated in large scale oedometer apparatuses.

8.3   Triaxial test series

Eventually, three test series, each with three different objectives, were performed in the newly equipped apparatuses on reconstituted and natural lacustrine soil specimens. The aim of the investigation in the first test series was to explore the influence of the load rate on the pore pressure development in specimens drained

at the top and bottom. Therefore, reconstituted samples were loaded isotropically at different mean effective stress rates. Half height specimens were drained at one end and the pore pressure development was measured at the other end. The test results showed an approximately linear relationship between the mean effective stress rate and the excess pore pressure. It was found that a stress rate of 1 kPa per hour will result in an excess pore pressure of 3 kPa in the middle of the sample, which was considered to be an acceptable compromise between total test time and excess pore water pressure to achieve nominal "drained" test conditions. In the subsequent data analysis, it was found that calculation results based on Terzaghi's one-dimensional consolidation theory fitted the data very well.

Natural samples from Kloten were investigated in terms of their non-linear elasto-plastic response in the second test series. The specimens were cut from the block samples, reconsolidated and allowed to swell under drained conditions along the same one-dimensional stress increment ratio. Subsequently, the probing stress path was applied, also under drained conditions, with various stress increment ratios. Thirteen drained triaxial stress path tests were performed in this series. Two of the samples were subsequently sheared, undrained, under strain control to failure in compression.

The test data were evaluated in terms of natural strains and the results of each test are presented separately in a data sheet attached in the Appendix. A method was proposed for the evaluation of the laser scan data in terms of volumetric observations, with which the initial sample volume as well as the volumetric displacements during the test can be calculated from the three line profiles taken by the laser scans. The method is based on the summation of thin cylindrical slices, which are fitted through the three measurement points of each scan plane. The verification of the laser volume measurement results with volume displacement measurements of the pore water expressed from the sample confirmed that the stiffness derived from scanning was higher than the stiffness obtained from the pore water volume measurements. This indicates that the circular slice approach is likely to be more accurate than the pore water volume measurement, which may be subjected to losses additional to those arising from the sample alone.

The comparison of the initial sample volume measured with the sliding caliper before the test setup to the sample volume calculated from the first laser scan showed that the latter method gives the same or slightly higher sample volumes. The slight increase of volume after test setup may result from water that is added during this phase. It was found that the laser scanning system placed inside the triaxial test apparatus is a very convenient and accurate method to determine the actual volume of the specimen at the start of the test. It revealed a completely original picture of the effect of the different properties of the layers as well as the detrimental effect of fixing LVDTs to the rubber membrane.

8.4   Analysis of the triaxial test data

The analysis of the elasto-plastic stiffness properties for the test data evaluated from the thirteen drained loading stress paths was done by identifying the yield points and the direction of the strain increment ratio at these yield points from the stress-strain plots. This yield point and strain increment ratio evaluation is shown for each test separately in the Appendix. The yield point determination was done in the deviator stress versus shear strain as well as in the mean effective stress versus volumetric strain plots for each test. Each stress state that was detected as a yield stress in one of the curves was plotted in a deviator versus mean effective stress diagram. The strain increment ratio was determined in the shear versus volumetric strain plot at the corresponding yield stress and was also added to the deviator versus mean effective stress plot, with the deviator stress axis corresponding to the shear strain increment axis and the mean effective stress axis corresponding to the volumetric strain increment axis. The shapes of the yield surfaces and the total strain increment ratios at yield were established in this way for the soil investigated with the stress history applied.

8.4.1 Yield surfaces

It was found that the history surface has an elliptical shape oriented in the direction of the mean effective stress axis with an extent in this direction of around 60 kPa. The elliptical shape of the bounding surface was found not to be symmetric about the mean effective stress axis, but inclined from the mean effective stress axis

towards the positive deviator stress axis. The direction of the strain increment ratio was determined at each yield point, as outlined above.

8.4.2 Elastic and plastic strain increment ratios

For the identification of the shape of the plastic potential from the plastic strain increment ratios, the total strain increment ratio had to be split into the elastic and the plastic components. This was achieved by determining the elastic component and substracting it from the total increment ratio. Isotropic elastic material response was assumed initially, which is defined by two of the three independent material parameters, e.g. the shear stiffness and the Poisson's ratio. The shear stiffness was derived from the bender element measurements and the Poisson's ratio was determined from the radial and axial displacement measurements with lasers and LVDTs. But comparison of the calculated strain increment ratios to those measured for a range of tests indicated that isotropic elastic material response is not an appropriate model for the soil investigated.

Therefore, cross-anisotropic elastic stiffness response was assumed, and from the corresponding five stiffness parameters, three were calculated from the triaxial strain measurements. The remaining parameters were calculated with the application of a simplified cross-anisotropic stiffness matrix for the triaxial stress space after Houlsby & Graham (1983). The ratio of axial to radial stiffness was determined to be 1.7. This cross-anisotropic elastic stiffness matrix calculated from the triaxial strain measurements represents the stiffness at small, but not elastic (entirely recoverable) strains. Therefore, these parameters were scaled up by a factor derived from the shear modulus measured with the bender elements, which was assumed to represent the very small strain elastic stiffness properties. The degree of anisotropy was taken to be the same for the elastic and small strain regions, which was thought to be justified because changes in anisotropy result only from plastic straining.

The plastic strain increment ratio was then derived from the total strain increment ratio. Consequently, the shape of the plastic potential was determined. The comparison between the plastic potential surface derived and the previously analyzed yield surface showed that an associated flow rule is most appropriate for

the bounding surface. An associated flow rule is only appropriate for probing stress paths with decreasing mean effective stress for the history surface, whereas the volumetric component dominates over the deviatoric one for probing stress paths with increasing mean effective stress.

8.4.3 Development of the necking zone in triaxial extension tests

The development of deformation in the extensional failure stress state was investigated more specifically in a third test series because significant necking had been observed for the specimens in the extension tests from series 2. Conventional evaluation methods assume a cylindrical shape of the specimen during the entire test period but with the new laser scan device, there was potential to measure the reduction in the effective cross-sectional area in the necking zone and deduce the resulting increase of effective axial stresses in the failure zone.

A reconstituted sample was taken for the investigation of the necking, and the same one-dimensional consolidation history as adopted in test series 2 was applied. Subsequently, the specimen was sheared undrained in extension with displacement control. Displacement-controlled shearing results in a continuous development of the failure zone rather than catastrophic failure, which may occur in stress-controlled shear tests. The development of the failure zone was observed during shearing with the help of the laser scan device and it was found that the majority of displacements that led to necking of the sample occurred when the peak deviator stress state had already passed. It was shown that the peak shear strength determined with the conventional stress evaluation method, assuming a cylindrical shape of the test specimen, gives values that are 5 to 10 % smaller than the strength evaluated from the local radial displacement measurements with the laser scan device at the failure state.

8.5 Numerical simulation results

Finally, the observed deformation behaviour was modelled using the finite element method. A literature review was performed for the selection of constitutive models which could represent the soft clay response most effectively and a combination of

the most widely used and some appropriate, recently developed, advanced constitutive models were chosen. These constitutive models were described in detail and the parameters of each model were obtained from the test data from the second triaxial test series. The steps adopted to simulate the triaxial stress path tests were outlined in a summary about the capabilities of the selected numerical codes, before the simulation results of four triaxial tests were presented and compared to the test data. The comparison of the simulation results with the test data shows that a model that incorporates an inclined yield surface, such as in the S_CLAY1 model, combined with a kinematic hardening law for non-linear elastic straining, with a modified description of the hardening law, and a Mohr Coulomb failure criterion would simulate the test data best.

8.6   Recommendations for future research

The automated triaxial test apparatuses were very useful for the performance of stress path tests at any possible stress increment ratio, bearing in mind that the principal stresses were vertical and horizontal. It was very convenient to apply the desired stress paths via the automated regulation routine, using stepping motors to adjust the pressures. This regulation system has a certain tolerated error, which was 0.5 kPa for the pressure regulation. However, it was found during the data evaluation process that this regulation may have led to periodic fluctuations in the load displacement curves. A dead weight loading may reduce these effects but of course brings other disadvantages such as e.g. only stepwise load application and possible stress path limitations.

The new laser scanning device gave useful additional information about the radial displacement development over the entire sample height during the test performance and very promising results were obtained in the determination of the initial sample volume and the volumetric displacements. But a careful investigation of the radial displacement measurement plots of natural as well as reconstituted specimens indicated that although the device was directed along the load frame and was calibrated versus a steel cylinder, with ongoing test performance the displacement measurements at small strain level might have been influenced by

the thread of the lead screw. This could be overcome by using a hydraulic cylinder instead of the lead screw and the stepping motors.

Sampling with the newly designed larger diameter sample tube was very convenient and successful and gave good sample qualities in comparison with conventionally sampled soil specimens. But this is only a relative comparison, and a more absolute sample quality determination can only be achieved by comparing laboratory investigation results to field measurement data. In this respect, Jamiolkowski (2003) suggested that comparison of the shear wave velocity measured in situ with that measured in the laboratory might be a suitable method for sample quality assessment. This could be used to determine the extent of sample disturbance in relation to the completely undisturbed state in-situ.

The natural soil specimens had a highly varved texture. These structural aspects were investigated in terms of elastic and elasto-plastic anisotropy. But further investigations of the influence of this layered structure e.g. on the failure behaviour and the residual strength of the clay layers, might be necessary for a full understanding of its influence on all aspects of mechanical behaviour.

In the simulation of the stiffness response of the Swiss lacustrine clays investigated using the finite element method with a range of different constitutive models, it was observed that none of the models gave an equally good agreement with the test data for all stress increment ratios investigated. This showed that even more care should be taken of the selection of an appropriate constitutive model for the problem investigated. Another possibility is to modify the constitutive models so that a more realistic response is given for the entire stress space.

One possible modification is to introduce a cross-anisotropic elastic formulation instead of isotropic elasticity in the linear isotropic elastic–plastic hardening models such as the Modified Cam Clay, the Soft Soil or the S-CLAY1 model.

The consideration of anisotropic elasto-plastic stress-strain behaviour is indispensable for a successful prediction of deformations in normally consolidated varved soft soils such as the lacustrine clay investigated, especially when the stresses applied correspond to extension stress increment ratios. This aspect was very well represented by the yield formulations of the S_CLAY1 model, therefore

this model can build a good base for subsequent developments in modelling lacustrine clay response.

A stress history dependent stiffness and a non-linear stress-strain response before the elasto-plastic Y3 stress states is indicated in the test data analysis. This aspect was simulated in the 3-SKH model with kinematic hardening, but the results showed that the hardening rules incorporated do not represent the bulk and shear modulus decrease properly. These hardening rules might have to be extended, in order to represent real soil behaviour, before they are applied in new developments.

The adoption of failure conditions which can distinguish between stress states in compression and extension, such as the Mohr-Coulomb or the Matsuoka-Nakai failure cone (Fig. 7.39), would bring a major improvement to all models that use the Drucker-Prager failure criterion i.e. all critical state based models.

9 References

Ackerley, S.K., Hellings, J.E. & Jardine, R.J. (1987). Discussion on a new device for measuring local axial strains on triaxial specimens. Géotechnique. 37(3): 413-417.

Addenbrooke, T.I. & Potts, D.M., (1996). Twin tunnel construction - ground movements and lining behaviour. Proceeding of the International Symposium on Geotechnical Aspects of Underground Construction in Soft Ground, London, Great Britain, April 1996. Editors: R.J. Mair & R.N. Taylor, Balkema: 441-446.

Al-Tabbaa, A. (1987). Permeability and stress-strain response of speswhite Kaolin. PhD thesis, University of Cambridge.

Al-Tabbaa, A. & Wood, D.M. (1989). An experimental based "bubble" model for clay. Proceedings of the Third Conference on Numerical Models in Geomechanics, Niagara Falls, Canada: 91-99.

Amann, P., Bucher, F., & Heil, H.M. (1992). Untersuchungen an Seebodenlehm. Mitteilungen des Institutes für Geotechnik No. 4391, ETH-Zürich, Switzerland.

Amann, P. & Heil, H.M. (1995). Cone penetration testing in Switzerland. Proceedings of the International Symposium on Cone Penetration Testing, Linköping, Swedish Geotechnical Society, Vol. 1: 235-242.

Arenson, L. (2003). Unstable Alpine Permafrost: a Potentially Important Natural Hazard - Variations of Geotechnical Behaviour with Time and Temperature. PhD thesis, ETH Zurich, No. 14801.

Atkinson, J.H. & Sällfors, G. (1991). Experimental determination of stress-strain-time characteristics in laboratory and in situ tests. Proceedings of the Tenth European Conference on Soil Mechanics and Foundation Engineering, Florence, Italy. 3: 915-956.

Atkinson, J.H. (2000). Non-linear soil stiffness in routine design. Rankine Lecture, Géotechnique. 50(5): 487-508.

Baldi, G., Hight, D.W. & Thomas, G.E. (1988). State-of-the-art paper: A Re-evaluation of Conventional Triaxial Test Methods. Advanced Triaxial Testing of Soil and Rock. Editors: R.T. Donaghe, R.C. Chaney & M.L. Silver, American Society of Testing and Materials, Philadelphia, United States: 219-263.

Baligh, M.M. (1985). Strain Path Method. Journal of Geotechnical Engineering. 111(9): 1108-1136.

Baligh, M.M., Azzouz, A.S. & Chin, C.-T. (1987). Disturbance due to "Ideal" tube sampling. Journal of Geotechnical Engineering. 113(7): 739-757.

Banerjee, P.K. & Yousif, N.B. (1986). A plasticity model for the mechanical behaviour of anisotropically consolidated clay. International Journal for Numerical and Analytical Methods in Geomechanics. 10: 521-541.

Bates, R.L. & Jackson, J.A. (1984). Dictionary of Geological terms. Third Edition prepared by the American Geological Institute. Doubleday Dell Publishing Group, Inc.: 551.

Bazant, Z.P. & Oh, B.H. (1986). Efficient Numerical Integration on the Surface of a Sphere. Zeitschrift für angewandte Mathematik und Mechanik. 66(1): 37-49.

Berre, T. (1982). Triaxial Testing at the Norwegian Geotechnical Institute. Geotechnical Testing Journal. 5(1/2): 3-17.

Bishop, A.W. & Henkel, D.J. (1957). The Measurement of Soil Properties in the Triaxial Test. Edward Arnold Ltd., London.

Bishop, A.W. & Wesley L.D. (1975). A hydraulic triaxial apparatus for controlled stress path testing. Géotechnique. 25(4): 657-670.

Bolton, M.D., Dasari, G.R. & Britto, A.M. (1994). Putting small strain non-linearity into the Modified Cam Clay model. Proceedings of the Eighth International Conference on Computer Methods and Advances in Geomechanics, Morgantown, West Virginia, United States: 537-542.

Bowden, F.P. & Tabor, D. (1964). The friction and lubrication of solids. Oxford University Press, London.

Brinkgreve, R.B.J. (1994). Geomaterial models and numerical analysis of softening. PhD thesis, TU Delft.

Brinkgreve, R.B.J., Broere, W. & Waterman, D. (2004). Plaxis 2D - Version 8, Manual, www.plaxis.nl.

Britto, A.M. & Gunn, M.J. (1987). Critical State Soil Mechanics via Finite Elements, Ellis Horwood, Chichester.

Brown, S.F. & Snaith, M.S. (1974). The Measurement of Recoverable and Irrecoverable Deformations in Repeated Load Triaxial Tests. Géotechnique. 24(2): 255-259.

Brunauer, S., Emmet, P.H. & Teller, E. (1938). Adsorption of Gases in Multimolecular Layers. Journal of American Chemical Society. 60(1-6): 309-319.

Bucher F. (1975). Die Restscherfestigkeit natürlicher Böden, ihre Einflussgrössen und Beziehungen als Ergebnis experimenteller Untersuchungen. PhD thesis, Nr.: 5523. Mitteilungsheft Nr.: 103, Institut für Geotechnik, ETH-Zürich, Schweiz.

Bucher, F. (2000). Experimentelle Bodenmechanik. Skriptum Wintersemester 2000/01, Institut für Geotechnik, ETH-Zürich, Schweiz.

Burghignoli, A., Pane, V. & Cavalera, L. (1991). Modelling stress-strain-time behaviour of natural soils. Monotonic loading. Proceedings of the Tenth European Conference on Soil Mechanics and Foundation Engineering, Florence, Italy. 3: 961-979.

Burland, J.B. & Hancock, R.J.R. (1977). Underground car park at the House of Commons, London: geotechnical aspects. Structural Engineering. 55: 87-100.

Burland, J.B., Simpson, B. & St. John, H.D. (1979). Movements around excavations in London clay. Proceedings of the Seventh European Conference of Soil Mechanics, Brighton, Great Britain. 1: 13-30.

Burland, J.B. & Symes, M. (1982). A simple axial displacement gauge for use in the triaxial apparatus. Géotechnique. 32(1): 62-65.

Burland, J.B., & Karla, J.C. (1986). Queen Elizabeth II Conference Centre: geotechnical aspects. Proceedings of the Institution of Civil Engineering. 80: 1479-1503.

Burland, J.B. (1989). „Small is beautiful" - the stiffness of soils at small strains. Ninth Laurits Bjerrum Memorial Lecture. Canadian Geotechnical Journal. 26: 499-516.

Burland, J.B. (1990). On the compressibility and shear strength of natural clays. Rankine Lecture, Géotechnique. 40(3): 329-378.

Butterfield, R. (1979). A natural compression law for soils. Géotechnique. 29(4):469-480.

Callisto, L. & Calabresi, G. (1998). Mechanical behaviour of a natural soft clay. Géotechnique. 48(4): 495-513.

Callisto, L. & Rampello, S. (2002). Shear strength and small-strain stiffness of a natural clay under general stress conditions. Géotechnique. 52(8): 547-560.

Clayton, C.R.I. & Khatrush, S.A. (1986). A new device for measuring local axial strains on specimens. Géotechnique. 36(4): 593-597.

Clayton, C.R.I., Khatrush, S.A., Bica, A.V.D. & Siddique, A. (1989). The Use of Hall Effect Semiconductors in Geotechnical Instrumentation. Geotechnical Testing Journal. 12(1): 69-76.

Clayton, C.R.I., Siddique, A. & Hopper, R.J. (1998). Effects of sampler design on tube sampling disturbance - numerical and analytical investigations. Géotechnique. 48(6): 847-867.

Clough, R.W. (1960). The Finite Element in Plane Stress Analysis. Proceedings of the Second American Society of Civil Engineers Conference on Electronic Computation, Pittsburg.

Cole, K.W. & Burland, J.B. (1972). Observations of retaining wall movements associated with a large excavation. Proceedings of the Fifth European Conference on Soil Mechanics and Foundation Engineering, Madrid, Spain. 1: 445-453.

Cole, D.M. (1978). A Technique for Measuring Radial Deformation during Repeated Load Triaxial Testing. Canadian Geotechnical Journal. 15: 426-429.

Costa-Filho, L.F. & Vaughan P.R. (1980). Discussion on a computer model for the analysis of ground movements in London clay. Géotechnique. 30: 336-339.

Costa-Filho, L. de M. (1985). Measurement of axial strains in triaxial tests on London Clay. Geotechnical Testing Journal. 8(1): 3-13.

Cuccovillo, T. & Coop, M.R. (1997). The measurement of local axial strains in triaxial tests using LVDT's. Géotechnique. 47(1): 167-171.

Cundall, P.A. & Strack, O.D.L. (1979). A discrete numerical model for granular assemblies. Géotechnique. 29(1): 47-65.

Dafalias, Y.F. (1975). On cyclic and anisotropic plasticity: (i) A general model including material behaviour under stress reversal, (ii) Anisotropic hardening for initially orthotropic materials, PhD Thesis, University of California, Berkeley.

Dafalias, Y.F. & Popov, E.P. (1975). A model of nonlinearly hardening materials for complex loadings. Acta Mechanica. 21: 173-192.

Dafalias, Y.F. & Popov, E.P. (1976). Plastic internal variables formalism of cyclic plasticity. Journal of Applied Mechanics. 98(4): 645-650.

Dafalias, Y.F. & Herrmann, G.R. (1982). Bounding surface formulation of soil plasticity. Soil Mechanics, Transient and Cyclic Loads. Editors: G.N. Pande & O.C. Zienkiewicz, Wiley and Sons: 253-282.

Dafalias, Y.F. (1987). An anisotropic critical state clay plasticity model. Proceedings of the Second International Conference on Constitutive Laws for Engineering Materials, Tucson, Arizona, United States: 513-521.

Dasari, G. (1996). Modelling the variation of soil stiffness during sequential construction. PhD Thesis, University of Cambridge.

Davies, M.C.R. & Newson, T.A.A. (1993). Critical state constitutive model for anisotropic soils. Predictive Soil Mechanics. Editors: G.T. Houlsby & A.N. Schofield, Thomas Telford, London, 219-229.

DeGroot, D. J. & Lutenegger, A. J. (2003). Geology and engineering properties of Connecticut Valley Varved Clay. Proceedings of the Conference on Characterisation and Engineering Properties of Natural Soils, Singapore. Editors: T.S. Tan, K.K. Phoon, D.W. Hight, & S. Leroueil. Balkema. 1: 693-724.

Diaz-Rodriguez, J.A., Leroueil, S. & Aleman, J.D. (1992). Yielding of Mexico city clay and other natural clays. Journal of Geotechnical Engineering. 118(7): 981-995.

Diaz-Rodriguez, J. A. (2003). Characterization and engineering properties of Mexico city lacustrine soils. Proceedings of the Conference on Characterization and Engineering Properties of Natural Soils, Singapore. Editors: T.S. Tan, K.K. Phoon, D.W. Hight, & S. Leroueil. Balkema. 1: 724-756.

Dimmock, P.S., Mair R.J. & Standing J.R. (2002). Ground movements caused by tunnelling with an earth pressure balance machine: a greenfield case study at Southwark Park, London. Proceedings of the Third International Symposium on Geotechnical Aspects of Underground Construction in Soft Ground, Toulouse, France, October 2002.

Dr von Moos AG (1995). Baugrunduntersuchung Flughafenautobahn Überdeckung Opfikon. Dr. von Moos AG, Beratende Geologen und Ingenieure, Zürich, Schweiz.

Duncan, J.M. & Chang, C.-Y. (1970). Nonlinear analysis of stress and strain in soils. Journal of the Soil Mechanics and Foundation Division. 96(SM5): 1629-1653.

Farnell (1980). Instruction manual: Autographic unconfined clay compression test apparatus A3070 series, 1-6.

Fauchère, A. (2000). Preliminary Studies for Simulation of a Spread Base Bridge Abutment on Lacustrine Clay in the ETHZ Geotechnical Centrifuge. Diplomarbeit. ETH-Zürich.

Fearon, R.E. & Coop, M.R. (2000). Reconstitution: what makes an appropriate reference material? Géotechnique. 50(4): 471-477.

Franz, A. & Göbbels, D. (2000). N20 Umfahrung Birmensdorf Dreieck Zürich West, Grenzen der Konsolidationsbeschleunigung. Mitteilung der Schweizerischen Gesellschaft für Boden- und Felsmechanik 140: Spezielle geotechnische Lösungen bei der Umfahrung Zürich West.

Ganendra, D. & Potts, D.M. (1995). Discussion: Evaluation of a constitutive model for overconsolidated clays. Géotechnique. 45(1): 169-173.

Gens, A. (1982). Stress-strain and strength characteristics of a low plasticity clay. PhD thesis, London University.

Geologische Karte der Schweiz (1980). Massstab 1 : 500,000. 2. Ausgabe. Herausgegeben von der Schweizerischen Geologische Kommission.

Germaine, J.T. & Ladd, C.C. (1988). Triaxial testing of saturated cohesive soils: State-of-the-Art Paper. Proceedings of the Symposium on Advanced Triaxial Testing of Soil and Rock. Editors: R.T. Donaghe, R.C. Chaney & M.L. Silver, American Society of Testing and Materials, Philadelphia, STP 977: 421-459. 421-459.

Goto, S., Tatsuoka, F., Shibuya, S., Kim, Y.-S. & Sato, T. (1991). A Simple Gauge for Local Small Strain Measurements in the Laboratory. Soils and Foundations. 31(1): 169-180.

Graham, J. & Houlsby, G.T. (1983). Anisotropic elasticity of a natural clay. Géotechnique. 33(2): 165-180.

Graham, J., Noonan, M.L. & Lew, K.V. (1983). Yield states and stress-strain relationships in a natural plastic clay. Canadian Geotechnical Journal. 20: 502-516.

Grün A. (2004). Personal Communication. Professor for Photogrammetry at the Institute of Geodesy and Photogrammetry, ETH Zurich.

Gyger, M., Müller-von Moos, M. & Schindler, K. (1976). Untersuchungen zur Klassifikation spät- und nacheiszeitlicher Sedimente aus dem Zürichsee. Schweizerische mineralogische und petrographische Mitteilungen, Heft 56: 387-406.

Haefeli, R. (1951). Investigation and measurement of shear strength of saturated cohesive soils. Géotechnique. 2(3): 186-208.

Handbook of Chemistry and Physics (1989 - 1990) 70th Edition. Editors: D.R. Lide & R.C. Weast, CRC Press Inc. Boca Rato, Florida: B-457.

Hardin, B.O. & Drnevich, V.P. (1972). Shear modulus and damping in soils: measurement and parameter effects. Journal of Geotechnical Engineering Division. 98(SM 6): 603-624.

Head, K.H. (1986). Manual of soil laboratory testing 3: Effective stress tests. Pentech Press, London.

Heil, H.M., Huder, J. & Amann, P. (1997). Determination of shear strength of lacustrine clays. Proceedings of the Fourteenth International Conference on Soil Mechanics and Foundation Engineering, Hamburg, Germany. Balkema, Rotterdam. 1: 507-510.

Heil, H.M. (2002). Localization and critical state. Proceedings of the Workshop on Constitutive and Centrifuge Modelling: Two Extremes. Monte Verita, Ascona. Editor: S.M. Springman, Balkema: 199-208.

Heil, H.M. (2003). Personal communication. Institute for Geotechnical Engineering, ETH-Zurich.

Heil, H.M. (2006). Ermittlung der Scherfestigkeit sensitiver Tone. PhD thesis, ETH Zurich.

Heim, D. (1990). Tone und Tonminerale: Grundlagen der Sedimentologie und Mineralogie. Ferdinand Enke Verlag, Stuttgart.

Hibbitt, Karlsson & Sorensen, Inc. (2002). ABAQUS/CAE User's Manual, Version 6.3. http://www.abaqus.com.

Hight, D.W. & Leroueil, S. (2003). Characterization of soils for engineering purposes. Proceedings of the Conference on Characterization and Engineering Properties of Natural Soils, Singapore. Editors: T.S. Tan, K.K. Phoon, D.W. Hight, & S. Leroueil. Balkema. 1: 255-360.

Hird, C.C. & Yung, P.C.Y. (1989). The use of proximity transducers for local strain measurements in triaxial tests. Geotechnical Testing Journal. 12(4): 292-296.

Hofmann, U., Endell, K. & Wilm, D. (1933). Kristallstruktur und Quellung von Montmorillonit. Zeitschrift für Kristallographie. 86: 340-348.

Houlsby, G.T. (1981). A study of plasticity theories and their applicability to soils. PhD thesis, University of Cambridge.

Hueckel, T. & Nova, R. (1979). Some hysteresis effects of the behaviour of Geological Media. International Journal of Solids and Structures. 15: 625-642.

Hvorslev, M.J. (1937). Über die Festigkeitseigenschaften gestörter bindiger Böden. Danmarks naturvidenskabelide Samfund, Kobenhaven.

Itasca Consulting Group (2002). FLAC Fast Lagrangian Analysis of Continua. Minneapolis, Minnesota.

Jaecklin, F. (1964). Standardversuche im Erdbaulaboratorium. Versuchsanstalt für Wasserbau und Erdbau, Interner Bericht Nummer 217J, ETH-Zürich, Schweiz.

Jaky, J. (1944). The Coefficient of Earth Pressure at Rest. Journal of the Hungarian Society of Engineers and Architects. 7: 355–358.

Jamiolkowski, M., Ladd, C.C., Germaine. J.T. & Lancellotta, R. (1985). New developments in field and laboratory testing of soils. Proceedings of the Eleventh International Conference on Soil Mechanics and Foundation Engineering, San Francisco, United States: 57-153.

Jamiolkowski, M., Lancellotta, R. & Lo Presti, D.C.F. (1995). Remarks on the stiffness at small strains of six Italian clays. Proceedings on the Symposia on Geotextiles, Geomembranes and other Geosynthetics in Ground Improvement on Deep Foundations and Ground Improvement Schemes, Bangkok, Thailand. Editor: A.S. Balasubramaniam, Balkema: 197-216.

Jamiolkowski, M. (2003). Suspension Bridge over the Messina Straits. Colloquium, Institute for Geotechnical Engineering, ETH, Zurich, Switzerland, November 6th.

Jardine, R.J., Symes, M.J. & Burland, J.B. (1984). The measurement of soil stiffness in the triaxial testing apparatus. Géotechnique. 34(3): 323-340.

Jardine, R.J. (1985). Investigations of pile-soil behaviour with special reference to the foundations of offshore structures. PhD. thesis, University of London, United Kingdom.

Jardine, R.J., Fourie, A.B., Maswoswe, J. & Burland, J.B. (1985a). Field and laboratory measurements of soil stiffness. Proceedings of the Eleventh International

Conference on Soil Mechanics and Foundation Engineering, San Francisco, United States. Balkema, Rotterdam. 2: 511-514.

Jardine, R.J., Brooks, N.J. & Smith P.R. (1985b). The use of Electro-level Transducers for strain measurement in triaxial tests on weak rock. International Journal of Rock Mechanics, Mineral Science and Geomechanic Abstracts. 22(5): 331-337.

Jardine, R.J., Potts, D.M., Fourie, A.B. & Burland, J.B. (1986). Studies of the Influence of Non-Linear Stress Strain Characteristics in Soil-Structure Interaction. Géotechnique. 36(3): 377-396.

Jardine, R.J. (1992). On the kinematic nature of soil stiffness. Soils and Foundations. 32(2): 111-124.

Jasmund, K. & Lagaly, G. (1993). Tonminerale und Tone: Struktur, Eigenschaften, Anwendung und Einsatz in Industrie und Umwelt. Steinkopf Verlag, Darmstadt.

Jovicic, V., Coop, M.R. & Simic, M. (1996). Objective criteria for determining G_{max} from bender element tests. Géotechnique. 46(2): 357-362.

Kahr, G. (2003). Personal communication. Institute for Geotechnical Engineering, ETH-Zurich, Switzerland.

Karstunen, M. (1998). Numerical modelling of strain localisation in dense sands, PhD thesis, University of Wales, Swansea, United Kingdom.

Kavvadas, M.J. (1982). Non-linear consolidation around driven piles in clays. ScD Thesis, Massachusetts Institute of Technology, Cambridge, United States.

König, M.A. (1978). Kleine Geologie der Schweiz. Ott Verlag Thun.

Kolymbas, D. (1977). A rate-dependent constitutive equation for soils. Mechanics Research Communications. 4: 367-372.

Koskinen, M. (2001). Anisotropy and destructuration of Soft Clays. Master's thesis, Helsinki University of Technology, Finland.

Koskinen, M., Karstunen, M. & Wheeler, S.J. (2002). Modelling destructuration and anisotropy of a natural soft clay. Proceedings of the Fifth European Conference on Numerical Methods in Geotechnical Engineering, Paris, France: 11-20.

Krajewski, W. (1986). Mathematisch-numerische und experimentelle Untersuchungen zur Bestimmung der Tragfähigkeit von in Sand gegründeten, vertikal belasteten Pfählen. Veröffentlichungen des Instituts für Grundbau, Bodenmechanik, Felsmechanik und Verkehrswasserbau der RWTH Aachen, Deutschland, Heft 13.

Krieg, R.D. (1975). A practical two-surface plasticity theory. Journal of Applied Mechanics. 42: 641-646.

Kueng, H. (2003). Undrainierte Scherfestigkeit an aufbereitetem Seebodenlehm. Diplomarbeit, Institut für Geotechnik, ETH-Zürich, Schweiz.

Labhart, T.P. (1995). Geologie der Schweiz. 3. Auflage, Ott-Verlag, Thun.

Lacasse, S., Berre, T. & Lefebvre, G. (1985). Block sampling of sensitive clays. In Proceedings of the Eleventh International Conference on Soil Mechanics and Foundation Engineering, San Francisco, United States. 2: 887-892.

Lade, P.V. & Duncan, J.M. (1975). Elasto-plastic stress-strain theory for cohesionless soil. Journal of the Geotechnical Engineering Division. 101:1037-1053.

Lade, P.V. (1979). Stress-strain theory for normally consolidated clay. Third International Conference on Numerical Methods in Geomechanics, Aachen, Germany, 2-6 April: 1325-1337.

Ladd, C.C. & Foott, R. (1974). New Design Procedure for Stability of Soft Clays. Journal of the Geotechnical Engineering Division. 100(GT7): 763-786.

Landkarte der Schweiz (1994). Massstab 1 : 25,000. Blatt 1071: Bülach. Herausgegeben vom Bundesamt für Landestopographie, Wabern, Schweiz.

Lang, H.J. (1976). SBB - Flughafenlinie, Baulos 8: Geotechnische Untersuchungen. Bericht Nr.: 3615, Institut für Bodenmechanik und Grundbau, ETH-Zürich.

Lange's handbook of chemistry (1973). 11th Edition, Editor: J.A. Dean. Formerly composed and edited by N.A. Lange. McGraw-Hill New York. Section 10, page 10-5 to 10-7.

La Rochelle, P. & Lefebvre, G. (1971). Sampling disturbance in Champlain clays. In Sampling of soil and rock. American Society for Testing and Materials; Special Technical Publication; (483): 143-163.

La Rochelle, P. (1973). Discussion on the State-of-the-Art Report to Session 4: "Problems of soil mechanics and construction on soft clays." by Bjerrum. Proceedings of the 8th International Conference on Soil Mechanics and Foundation Engineering; (4.2):102-108.

La Rochelle, P., Sarrailh, J., Tavenas, F., Roy, M. & Leroueil, S. (1981). Causes of disturbance and design of a new sampler for sensitive soils. Canadian Geotechnical Journal. 18(1): 52-66.

Lefebvre, G. & Poulin, C. (1979). A new method of sampling in sensitive clay. Canadian Geotechnical Journal. 16: 226-233.

Leroueil, S. (2003). Personal communication at the International Workshop on Geotechnics of Soft Soils - Theory and Practice in The Netherlands in September 2003.

Lings, M.L., Pennington, D.S. & Nash, D.F.T. (2000). Anisotropic stiffness parameters and their measurement in a stiff natural clay. Géotechnique. 50(2): 109-125.

Long, M. (2003). Characterization and engineering properties of Athlone laminated clay. Proceedings of the Conference on Characterization and Engineering Properties of Natural Soils, Singapore. Editors: T.S. Tan, K.K. Phoon, D.W. Hight, & S. Leroueil. Balkema. 1: 757-790.

Lo Presti, D.C.F. (1991). Behaviour of sand at small strain. Proceedings of the Tenth European Conference on Soil Mechanics and Foundation Engineering, Florence, Italy. 3: 961-979.

Lo Presti, D.C.F., Pallara, O., Cavallaro, A. & Jamiolkowski, M. (1999a). Influence of reconsolidation techniques and strain rate on the stiffness of undisturbed clays from triaxial tests. Geotechnical Testing Journal. 22 (3): 211-226

Lo Presti, D.C.F., Jamiolkowski, M., Pallara, O., & Tordella, M.L. (1999b). Assessment of sample disturbance in the laboratory. Proceedings of the Second International Symposium on Pre-failure Deformation Characteristics of Geomaterials, Torino, Italy, September 1999. 1: 11-18.

Madsen, F.T. & Kahr, G. (1992). Wasserdampfadsorption und spezifische Oberfläche von Tonen. Bericht der DTTG, Hannover. Band 2:165-179.

Masin, D. (2003). A kinematic hardening critical state model for anisotropic clays. Proceedings of the Conference on Constitutive Modelling an Analysis of Boundary Value Problems in Geotechnical Engineering. Napoli, Italy.

Masing, G. (1926). Eigenspannungen und Verfestigung bei Messung. Proceedings of the Second International Congress of Applied Mechanics, Zurich, Switzerland: 332-335.

Matsuoka, H. & Nakai, T. (1974). Stress-deformation and strength characteristics of soil under three different principal stresses. Japanese Society of Civil Engineers. 232: 59-70.

Maurer, H., Giudici Trausch, J., Roth, M., Hollinger, K., Springman, S.M. & van der Veen, M. (2000). Bestimmung elastischer Bodeneigenschaften bei kleinen Verformungen. Felsbau, Rock and Soil Engineering. 5: 129-133.

McDowell, G.R. & Hau, K.W. (2003). A simple non-associated three surface kinematic hardening model. Géotechnique. 53(4): 433-437.

McGinty, K., Karstunen, M. & Wheeler, S.J. (2001). Modelling the stress-strain behaviour of Bothkennar clay. Proceedings of the Third International Conference on Soft Soil Engineering, Hong Kong: 263-268.

Meier, L.P. & Kahr, G. (1999). Determination of the cation exchange capacity (CEC) of clay minerals using the complexes of copper (II) ion with triethylenetetramine and tetraethylenepentamine. Clays and Clay Minerals. 47: 386-388.

Messerklinger, S. (2001). Numerical modelling of anisotropy of soft clays. Diploma thesis, Institute for Soil Mechanics and Foundation Engineering, Graz University of Technology, Austria.

Messerklinger, S. & Springman, S.M. (2003). Modelling soft lacustrine clay. Proceedings of the Second M.I.T. Conference on Computational Fluid and Solid Mechanics. June 17 – 20, Boston; (1): 447-450.

Messerklinger, S., Kahr, G., Plötze, M., Trausch Giudici, J., Springman, S.M. & Lojander, M. (2003). Mineralogical and mechanical behaviour of soft Finnish and Swiss clays. International Workshop on Geotechnics of Soft Soils - Theory and Practice, Noordwijkerhout, The Netherlands, September 17-19. Editors: P.A. Vermeer, H.F. Schweiger, M. Karstunen & M. Cudny, Verlag Glückauf, Essen: 467-472.

Messerklinger, S., Bleiker, E., Zweidler, A. & Springman, S.M. (2004). Displacement measurement with laser scanning in triaxial testing apparatuses. Proceedings of the Sixteenth European Young Geotechnical Engineers' Conference, Vienna, Austria, July 8-10: 251-260.

Miller, C.J. (1980). The laboratory determination of the small strain behaviour of Lias clay, and its significance to settlement analysis. MSc thesis, University of London, United Kingdom.

Mitchell, J.K. (1976). Fundamentals of soil behaviour. New York: John Wiley & Sons.

Mohsin, A.K.M. & Airey, D.W. (2003). Automating G_{max} measurement in triaxial tests. Proceedings of the Conference on Deformation Characteristics of Geomaterials, Lyon, France. Editors: H. Di Benedetto, T. Doanh, H. Geoffroy, & C. Sauzéat: 73-80.

Mröz, Z. (1967). On the description of anisotropic work hardening. Journal of the Mechanics and Physics of Solids. London. 15: 163-175.

Mröz, Z., Norris, V.A. & Zienkiewicz, O.C. (1978). An anisotropic hardening model for soils and its application to cyclic loading. International Journal for Numerical and Analytical Methods in Geomechanics. 2: 203-221.

Mröz, Z., Norris, V.A. & Zienkiewicz, O.C. (1979). Application of an anisotropic hardening model in the analysis of elasto-plastic deformation of soils. Géotechnique. 29(1): 1-34.

Müller-Vonmoos, M., Honold, P. & Kahr, G. (1985). Das Scherverhalten reiner Tone. Mitteilung des Institutes für Grundbau und Bodenmechanik, Nr. 128, ETH-Zürich, Schweiz.

Müller-Vonmoos, M. & Loken, T. (1988). Das Scherverhalten der Tone. Tagung: Tonmineralogie und Tonmechanik, Mitteilungsheft Nr. 133, Institut für Grundbau und Bodenmechanik, ETH-Zürich.

Näätänen, A., Wheeler, S.J., Karstunen, M. & Lojander, M. (1999). Experimental investigation of an anisotropic hardening model for soft clays. Second International Symposium on Pre-failure Deformation Characteristics of Geomaterials, Torino, Italy: 541-548.

Nater, P. (2005). Belastungs- und Verformungsverhalten von geschichteten Bodensystemen unter starren Kreisfundamenten. Disstertation No. 16319. ETH-Zürich.

Neher, H., Sterr, C., Messerklinger, S. & Koskinen, M. (2003). Numerical modelling of the anisotropy of Otaniemi clay. International Workshop on Geotechnics of Soft Soils - Theory and Practice, Noordwijkerhout, The Netherlands, September 17-19. Editors: P.A. Vermeer, H.F. Schweiger, M. Karstunen & M. Cudny, Verlag Glückauf, Essen: 217-224.

Ng, C.W.W., Simpson, B., Lings, M.L. & Nash, D.F.T. (1998). Numerical analysis of a multipropped excavation in stiff clay. Canadian Geotechnical Journal. 35: 115-130.

Pande, G.N. & Sharma, K.G. (1983). Multi-laminate model of clays - a numerical evaluation of the influence of rotation of the principal stress axes. International Journal for Numerical and Analytical Methods in Geomechanics. 7: 397-418.

Panduri, R. (2000). Versuchsschüttung Nordwestumfahrung Zürich: Auswertung von Laborversuchen. Diplomarbeit, Institut für Geotechnik, ETH-Zürich, Schweiz.

Parry, R. H. G., & Wroth, C. P. (1981). Shear properties of soft clays. Soft clay engineering. Elsevier, Amsterdam: 311-364.

Penck, A. (1925). Glazialgeologische Beobachtungen in den bayerischen Hochalpen: Alte Breccien u. junge Krustenbewegungen in d. bayerischen Hochalpen; Die Eiszeit in den bayerischen Hochalpen. Sitzungsberichte d. Preuss. Akad. d. Wiss. Physik.-math. Klasse 17. Akademie d. Wissenschaften; Berlin. Verlag: W. de Gruyter & Co.

Pennington, D.S., Nash, D.F.T. & Lings, M.L. (1997). Anisotropy of G_0 shear stiffness in Gault Clay. Géotechnique. 47(3): 391-398.

Pestana, J.M. & Whittle, A.J. (1999). Formulation of a unified constitutive model for clays and sands. International Journal for Numerical and Analytical Methods in Geomechanics. 23: 1215-1243.

Pestana, J.M., Whittle, A.J. & Gens, A. (2002). Evaluation of a constitutive model for clays and sands: Part II - clay behaviour. International Journal for Numerical and Analytical Methods in Geomechanics. 26: 1123-1146.

Plaxis b.v. (1998). Plaxis Version 8: Material Models Manual: 7-1. http://www.plaxis.nl.

Plötze, M. (2002). Skriptum: Umweltgeotechnik, Kapitel T2: Eigenschaften von Tonen und Tonmineralen. T2.2.

Plötze, M., Giudici Trausch, J., Messerklinger, S. & Springman, S.M. (2003). Swiss Lacustrine Clay: mineralogical and mechanical characteristics. International Workshop on Geotechnics of Soft Soils - Theory and Practice, Noordwijkerhout, The Netherlands, September 17-19, Editors: P.A. Vermeer, H.F. Schweiger, M. Karstunen & M. Cudny, Verlag Glückauf, Essen: 473-478.

Potts, D.M. & Zdravkovic, L. (1999). Some Pitfalls when using Modified Cam Clay. Proceedings of the Workshop on Soil and Structure Interaction (COST C7), Thessaloniki, Greece.

Potts, D.M. & Zdravkovic, L. (1999b). Finite element analysis in geotechnical engineering: theory. Thomas Telford Ltd, London.

Potts, D.M. & Zdravkovic, L. (2001). Finite element analysis in geotechnical engineering: application. Thomas Telford Ltd, London.

Prévost, J.H. (1977). Mathematical modeling of monotonic and cyclic undrained clay behaviour. International Journal for Numerical and Analytical Methods in Geomechanics. 1: 195-216.

Prévost, J.H. (1978). Anisotropic undrained stress-strain behaviour of clays. Journal of Geotechnical Engineering Division. 104(GT8): 1075-1090.

Prévost, J.H. (1982). Two-Surface versus Multi-Surface Plasticity Theories: A critical assessment. International Journal for Numerical and Analytical Methods in Geomechanics. 6: 323-338.

Puzrin, A.M. & Burland, J.B. (1996). A logarithmic stress-strain function for rocks and soils. Géotechnique. 46(1): 157-164.

Puzrin, A.M. & Burland, J.B. (1998). Non-linear model of small-strain behaviour of soils. Géotechnique. 48(2): 217-233.

Puzrin, A.M. & Houlsby, G.T. (2001). Strain-based plasticity models for soils and the BRICK model as an example of the hyperplasticity approach. Géotechnique. 51(2): 169-172.

Rendulic, L. (1937). Ein Grundgesetz der Tonmechanik und sein experimenteller Beweis. Bauingenieur. 18: 459-467.

Rey, R. (1994). Geotechnische Folgen der glazialen Vorbelastung von Seebodenablagerungen. PhD thesis Nr. 10631. ETH-Zurich, Switzerland.

Richardson, D. (1988). Investigations of threshold effects in soil deformations, PhD thesis, City University, London, United Kingdom.

Romero, E., Lloret, F., Gens, J.A. & Alonso, E.E. (1997). A new suction and temperature controlled triaxial apparatus. Proceedings of the Fourteenth International Conference on Soil Mechanics and Foundation Engineering. Hamburg, Germany, September 6-12, A.A. Balkema, Rotterdam. 1: 185-188.

Roscoe, K.H., Schofield, A.N. & Wroth, C.P. (1958). On the yielding of soils. Géotechnique. 8(2): 22-53.

Roscoe, K.H. & Schofield, A.N. (1963). Mechanical behaviour of an idealised "wet" Clay. Proceedings of the Second European Conference on Soil Mechanics and Foundation Engineering, Wiesbaden, Germany: 47-54.

Roscoe, K.H., Schofield, A.N. & Thurairajah, A. (1963). Yielding of clays in states wetter than critical. Géotechnique. 13: 211-240.

Roscoe, K.H. & Burland, J.B. (1968). On the generalized stress-strain behaviour of „wet" clay. Engineering Plasticity. Editors: J. Heyman & F.A. Leckie, Cambridge University Press: 535-609.

Rossato, G., Ninis, N.L. & Jardine, R.J. (1992). Properties of some kaolin-based model clay soils. Geotechnical Testing Journal. 15(2): 166-179.

Rowe, P.W. (1972). Theoretical meaning and observed values of deformation parameters for soil. Proceedings of the Roscoe Memorial Symposium, Cambridge: 143-194.

Sadrnejad, S.A. & Pande, G.N. (1989). A multilaminate model for sands. Proceedings of the Third Conference on Numerical Models in Geomechanics, Niagara Falls, Canada. Editors: S. Pietruszczak & G.N. Pande: 17-27.

Santagata, M.C. (1999). Factors affecting the initial stiffness and stiffness degradation of cohesive soils. PhD Thesis, Massachusetts Institute of Technology, Boston, United States.

Scharinger, F. (2004). Further Development of a Multilaminate Model for Soils. Sixteenth European Young Geotechnical Engineers Conference, Vienna, Austria.

Scharinger, F. (2005). Personal communication. Research Assistant at the Institute for Soil Mechanics and Foundation Engineering, Graz University of Technology, Austria.

Scherzinger, T. (1991). Materialverhalten von Seetonen - Ergebnisse von Laboruntersuchungen und ihre Bedeutung für das Bauen im weichen Baugrund. Veröffentlichungen des Inst. für Boden- und Felsmechanik, Karlsruhe, Deutschland. Heft: 122.

Schofield, A.N. & Wroth, C.P. (1968). Critical State Soil Mechanics. McGraw Hill, London.

Scholey, G.K., Frost, J.D., Lo Presti, C.F. & Jamiolkowski, M. (1995). A review of instrumentation for measuring small strains during triaxial testing of soil specimens. Geotechnical Testing Journal. 18(2): 137-156.

Schuller, H. (2000). A Multilaminate Model for Soils and its Application to Numerical Analysis of Tunnel Excavation. PhD thesis. Graz University of Technology, Austria.

Simpson, B., O'Riordan, N. J. & Croft, D. D. (1979). A computer model for the analysis of ground movements in London clay. Géotechnique. 29: 149-175.

Simpson, B. (1992). Retaining structures: displacement and design. Rankine Lecture, Géotechnique. 42(2): 541-576.

Skempton, A.W. (1954). The pore pressure coefficients A and B. Géotechnique. 4: 143–147.

Smith, P.R., Jardine, R.J. & Hight, D.W. (1992). The yield of Bothkennar clay. Géotechnique. 42(2): 257-274.

SN 670 335a: Dichte des Bodens. Schweizer Norm, Vereinigung Schweizer Strassenfachleute (VSS), Ausgabe November 1989.

SN 670 345a: Konsistenzgrenzen. Schweizer Norm, Vereinigung Schweizer Strassenfachleute (VSS), Ausgabe November 1989.

Soccodato, F.M. (2003). Geotechnical properties of Fucino clayey soil. Characterisation and engineering properties of natural soils. Proceedings of the Conference on Characterization and Engineering Properties of Natural Soils, Singapore. Editors: T.S. Tan, K.K. Phoon, D.W. Hight, & S. Leroueil. Balkema. 1: 791-808.

Springman, S.M. (1993). Centrifuge modelling in clay: Marine applications. Proceedings of the Fourth Canadian Marine Geotechnical Conference. St Johns', Newfoundland. Editor: J.L. Clarke et al. 3: 853-896.

Springman, S.M., Giudici Trausch, J., Heil, H.M. & Heim, R. (1999). Strength of a soft Swiss lacustrine clay: cone penetration and triaxial test data. Journal of the Transportation Research Board 1675: 1-9.

Stallebrass, S.E. (1990). Modelling the effect of recent stress history on the deformation of overconsolidated soils. PhD thesis, Civil Engineering Department, The City University, London, United Kingdom.

Stallebrass, S.E. & Taylor, R.N. (1997). The development and evaluation of a constitutive model for the prediction of ground movements in overconsolidated clay. Géotechnique. 47(2): 235-253.

Sture, S., Costes, N. C., Alshibli, K. A., Batiste, S. N., Frank, M., Lankton, M. R. & Swanson, R. A. (1999). Summary Results Report STS-79/Mir 4 and STS-89/Mir8 Missions - Mechanics of Granular Materials (MGM). Laboratory for Atmospheric and Space Physics, University of Colorado.

Tanaka, H. & Tanaka, M. (1999). Key factors governing sample quality. Characterization of soft marine clays. International Symposium on Coastal Engineering in Practice, IS-Yokohama: 57-82.

Tavernas, F. & Leroueil, S. (1977). Effects of stresses and time on yielding of clays. Proceedings of the Ninth International Conference on Soil Mechanics and Foundation Engineering, Tokyo, Japan: 319-326.

Tatsuoka, F. (1988). Some Recent Developments in Triaxial Testing Systems for cohesionless Soils. Advanced Triaxial Testing of Soil and Rock. Editors: R.T. Donaghe, R.C. Chaney & M.L. Silver, American Society of Testing and Materials, Philadelphia: 7-67.

Tatsuoka, F. & Kohata, Y. (1995). Stiffness of hard soils and soft rocks in engineering applications. Proceedings of the International Symposium on Pre-failure Deformation of Geomaterials. Sapporo, Japan. Balkema. 2: 947-1063.

Taylor, G.I. (1938). Plastic strains in metals. Journal of the Institute of Metals. 62, 307-324. Reprinted in: The Scientific Papers of G.I. Taylor 1 (1958). Cambridge University Press, United Kingdom.

Teachavorasinskun, S. (1989). Stress-Strain and Strength Characteristics of Granular Materials in Simple Shear. MEng. Thesis, University of Tokyo, Japan.

Terzaghi, K. (1923). Die Berechnung der Durchlässigkeitsziffer des Tones aus dem Verlauf der hydrodynamischen Spannungserscheinungen. Sitzungsbericht der Akademie der Wissenschaften, Wien, Math.-Nat. Kl., Abt. IIA, 132(3-4): 125-138.

Terzaghi, K. (1943). Theoretical Soil Mechanics. John Wiley and Sons, New York.

Timoshenko, S. & Goodier, J.N. (1951). Theory of Elasticity, second edition. New York: McGraw-Hill Book Company, Inc.

Thornton, C. (2000). Numerical simulations of deviatoric shear deformation of granular media. Géotechnique. 50(1): 43-53.

Trausch Giudici, J. L. (1999). Strength and Deformation Characteristics of a Soft Swiss Lacustrine Clay for a Railway Underpass. Proceedings of the Eighth Young Geotechnical Engineers Conference, Santorini, Greece.

Trausch Giudici J. (2002). Deformation behaviour of a Swiss Lacustrine Clay. Proceedings of the Workshop on constitutive and centrifuge geotechnical modelling: two extremes. Monte Verità, Ascona, Balkema: 277-284.

Trausch Giudici, J. (2002 & 2003). Personal communication. Institute for Geotechnical Engineering, ETH-Zurich, Switzerland.

Trausch Giudici, J. (2004). Stress-strain characteristics of Seebodenlehm. PhD thesis, ETH Zürich. Veröffentlichung des Instituts für Geotechnik, Band 223, vdf, Zürich.

Van Husen, D. (1987). Die Ostalpen in den Eiszeiten. Populärwissenschaftliche Veröffentlichungen der geologischen Bundesanstalt, Wien.

Viggiani, G. & Atkinson, J.H. (1995). Interpretation of bender element tests. Géotechnique. 45(1): 149-154.

von Moos, M. & Bartelt, P. (1998). Creep behaviour of snow investigated by triaxial testing. Proceedings of the Twelfth European Young Geotechnical Engineers' Conference, September, Tallinn, Estonia. Estonian Geotechnical Society.

von Moos, M. (2001). Untersuchungen über das visko-elastische Verhalten von Schnee auf der Grundlage von triaxialen Kriechversuchen. PhD thesis. No. 13725, ETH Zürich. Veröffentlichung des Instituts für Geotechnik, Band 214, vdf, Zürich.

Vucetic, M & Dobry, R. (1991). Effect of soil plasticity on cyclic response. Journal of Geotechnical Engineering. 117(1): 89-107.

Wheeler, S.J. (1997). A rotational hardening elasto-plastic model for clays. Proceedings of the Fourteenth International Conference on Soil Mechanics and Foundation Engineering, Hamburg, Germany (1): 431-434.

Wheeler, S.J., Karstunen, M. & Näätänen, A. (1999). Anisotropic hardening model for normally consolidated soft clays. Proceedings of the Seventh Conference on Numerical Models in Geomechanics, Graz, Austria: 33-40.

White D.J., Take W.A. & Bolton M.D. (2003). Soil deformation measurement using particle image velocimetry (PIV) and photogrammetry. Géotechnique. 53(7): 619-631.

Whittle, A.J. (1987). A constitutive model for overconsolidated clays with application to the cyclic loading of friction piles. ScD Thesis, Massachusetts Institute of Technology, Cambridge, United States.

Whittle, A.J. (1993). Evaluation of a constitutive model for overconsolidated clays. Géotechnique. 43(2): 289-313.

Whittle, A.J., Hashash, Y.M.A. & Whitman, R.V. (1993). Analysis of Deep Excavation in Boston. Journal of Geotechnical Engineering. 119(1): 69-90.

Whittle, A.J., DeGroot, D.J., Ladd, C.C. & Seah, T.-H. (1994). Model Prediction of Anisotropic Behaviour of Boston Blue Clay. Journal of Geotechnical Engineering. 120(1): 199-224.

Whittle, A.J. & Kavvadas, M.J. (1994). Formulation of MIT-E3 Constitutive Model for Overconsolidated Clays. Journal of Geotechnical Engineering. 120(1): 173-198.

Wiltafsky, C., Messerklinger, S. & Schweiger, H.F. (2002). An advanced multilaminate model for clay. Proceedings of the Seventh Conference on Numerical Models in Geomechanics, Rome, Italy: 67-74.

Wiltafsky, C. (2003a). A Multilaminate Model for Normally Consolidated Clay. PhD thesis, Graz University of Technology, Austria.

Wiltafsky, C. (2003b). S_CLAY1S User defined soil model for Plaxis – Documentation. University of Glasgow, United Kingdom.

Wiltafsky, C., Scharinger, F., Schweiger, H.F., Krenn, H., Zentar, R., Karstunen, M., Cudny, M., Neher, H. & Vermeer, P.A. (2003). Results from a geotechnical benchmark exercises of embankment on soft clay. International Workshop on Geotechnics of Soft Soils - Theory and Practice, Noordwijkerhout, The Netherlands, September 17-19, Editors: P.A. Vermeer, H.F. Schweiger, M. Karstunen & M. Cudny, Verlag Glückauf Essen: 381-388.

Woods, R. & Rahim, A. (2001). SAGE CRISP Technical Reference Manual. The CRISP Consortium Ltd.

Wroth, C.P. (1975). In-situ measurement of initial stresses and deformation characteristics. Proceedings of the Special Conference on In-Situ Measurement of Soil Properties, Raleigh, North Carolina, United States. 2: 181-230.

Yu, Y. & Axelsson, K. (1994). Constitutive modelling of Swedish cohesive soils accounting for anisotropy. Proceedings of the Conference on Computer Methods and Advances in Geomechanics, Manchester, United Kingdom. Balkema, Rotterdam. 1: 737-743.

Zienkiewicz, O.C. (1967). The Finite Element Method, 1st edition. McGraw Hill, London.

Zienkiewicz, O.C. & Pande, G.N. (1977). Time dependent Multilaminate model of rocks - a numerical study of deformation and failure of rock masses. International Journal of Numerical and Analytical Methods in Geomechanics. 1: 219-247.

Züst, Y. (2000). Vorstudien zur Simulation einer Dammschüttung als Strassendamm auf Seebodenlehm in der geotechnischen Grosszentrifuge Zürich. Diplomarbeit. ETH-Zürich.

10 Appendix

Outline:

Series 1: Load rate for drained stress paths:

Series 2: Non-linearity and small strain plasticity:

Series 3: Failure behaviour:

Bender element measurement data and evaluation

Data Evaluation of series 2:

Data Evaluation of series 2:

Triaxial Test   S1T2

Test aim: Investigation of the drained load ratio
Material number: 46707   Birmensdorf clay: reconstituted and consolidated in the centrifuge pot
Test apparatus: HIF B 24: Triax 2 (red)
File: 30_kpa_p_d_Birm_1.PRB
   test start: 05.08.2003   12:52:56   test stop: 27.08.2003   09:47:34
Comments:

Measured sample data:	**Determined sample data:**	**Material parameter:**

Measured sample data:			Determined sample data:			Material parameter:		
Height H_0	49.25 [mm]		Cross-sectional area:	A	20.52 [cm²]	density	ρ_s	2.75 [g/cm³]
Diameter D	5.11 [cm]		Volume: f(H_0, D)	V_0	101.08 [cm³]	specific gravity of water ρ_w		1 [g/cm³]
Weight m_f	188.08 [g]		Water content	w	41.84 [%]			
			Volume: f(m_f, w, ρ_s, S_r=1)	V_0	103.70 [cm³]			
			Void ratio: f(m_f, w, ρ_s, S_r=1)	e_0	1.151 [-]			

Test data:

test-time [hours]	force [kN]	cell-pressure [kPa]	PWP bottom [kPa]	PWP top [kPa]
0.0	0.016	49.451	46.899	47.067
14.9	0.016	69.119	46.939	55.798
28.1	0.016	86.095	46.732	52.504
43.5	0.016	87.314	46.695	47.113
67.8	0.016	112.958	46.672	50.224
117.3	0.016	112.912	46.983	46.799
163.7	0.016	142.323	46.686	48.511
216.0	0.016	142.839	46.669	46.880
274.8	0.016	175.021	46.979	48.041
308.2	0.016	174.904	46.768	46.768
378.4	0.015	205.295	46.750	47.679
450.2	0.017	216.118	46.779	46.721
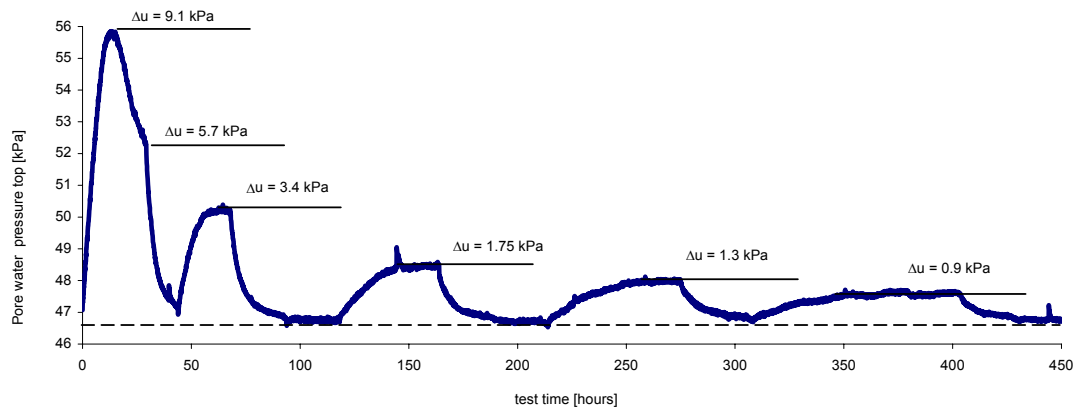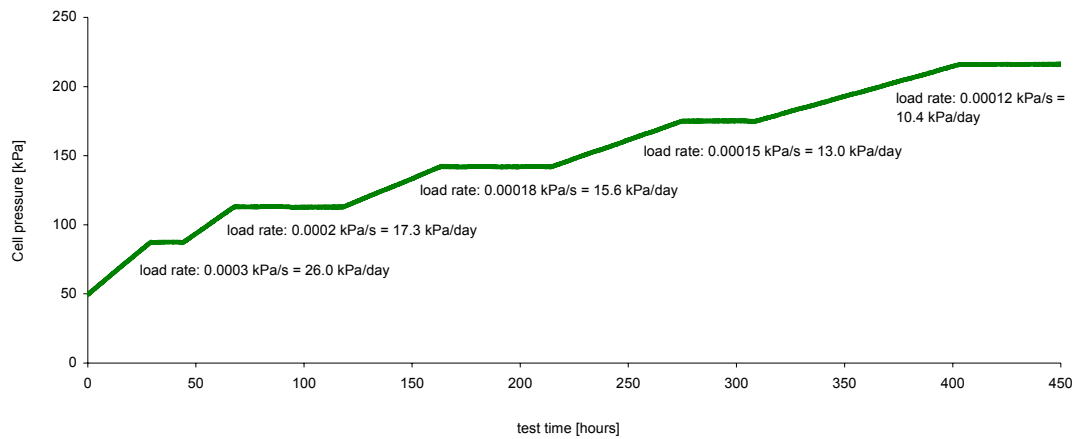
Fig. 10.1:   Triaxial test data of test S1T2 on reconstituted Birmensdorf clay (46707): excess pore water pressure at the given load rate.

298

Triaxial Test $\qquad$ S1aT2

Test aim: Determination of the drained load ratio
Material number: 46707 Birmensdorf clay: reconstituted and consolidated in the centrifuge pot
Test apparatus: HIF B 24: Triax 2 (red)
File name: Birm07.PRB
    test start: 07.09.2003 12:53:35   test stop: 24.09.2003 11:05:58
Comments:

Measured sample data:			Determined sample data:				Material parameter:		
Height H_0	52.55 [mm]		Cross-sectional area:	A	20.27 [cm^2]		density	ρ_s	2.75 [g/cm^3]
Diameter D	5.08 [cm]		Volume: f(H_0, D)	V_0	106.51 [cm^3]		specific gravity of water ρ_w		1 [g/cm^3]
Weight m_f	193.61 [g]		Water content	w	43.05 [%]				
			Volume: f(m_f, w, ρ_s, S_r=1)	V_0	107.48 [cm^3]				
			Void ratio: f(m_f, w, ρ_s, S_r=1)	e_0	1.184 [-]				

Test data:

test-time [hours]	force [kN]	cell-pressure [kPa]	PWP bottom [kPa]	PWP top [kPa]
0.0	0.012	275.688	239.229	239.082
19.4	0.012	295.370	239.209	242.679
46.1	0.012	304.915	239.189	238.834
72.5	0.012	317.609	239.122	240.164
94.4	0.011	328.456	239.175	240.016
109.6	0.012	329.904	239.186	238.440
134.4	0.012	436.775	239.024	252.969
187.5	0.012	450.125	239.203	238.422
220.0	0.137	483.240	239.111	243.404
240.0	0.217	504.500	239.024	243.280
260.0	0.295	525.900	238.789	243.283
360.0	0.395	590.204	238.753	238.509
380.0	0.395	589.973	239.186	238.252
400.0	0.396	590.367	239.182	238.371
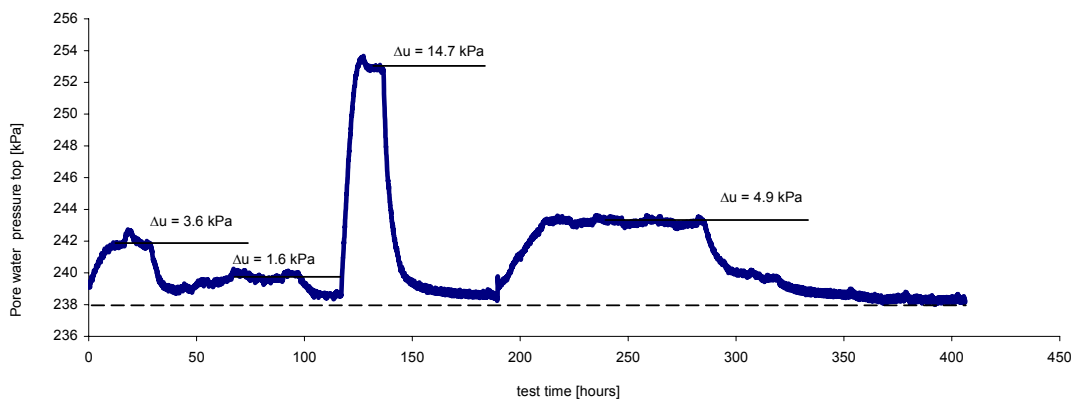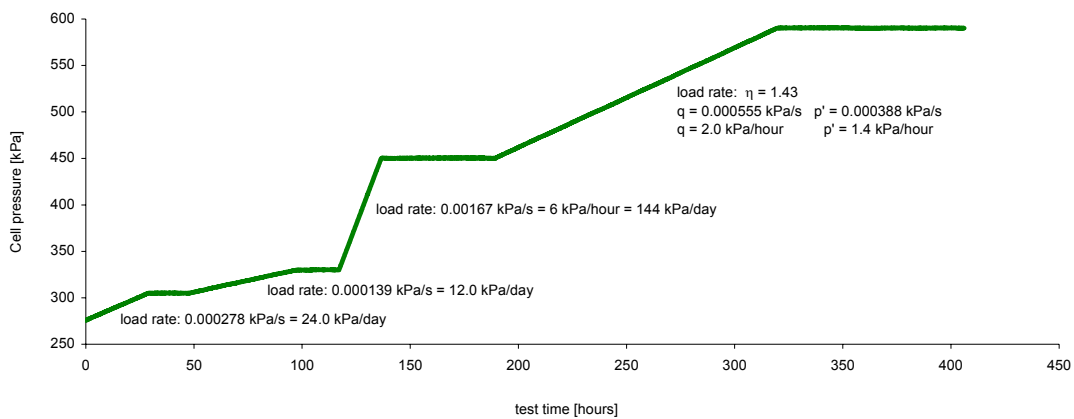
Fig. 10.2: Triaxial test data of test S1aT2 on reconstituted Birmensdorf clay (46707): excess pore water pressure at the given load rate.

Triaxial Test   S1T3

Test aim: Determination of the drained load ratio
Material number: 46707   Birmensdorf clay: reconstituted and consolidated in the centrifuge pot
Test apparatus: HIF B 24: Triax 3 (yellow)
File name: Birm01.PRB
     test start: 03.08.2003   11:42:51   test stop: 06.08.2003   08:21:01
Comments:

Measured sample data: **Determined sample data:**   **Material parameter:**
Height H_0 52.50 [mm]   Cross-sectional area: A   20.85 [cm^2]   density ρ_s 2.75 [g/cm^3]
Diameter D   5.15 [cm]   Volume: f(H_0, D) V_0 109.45 [cm^3]   specific gravity of water ρ_w 1 [g/cm^3]
Weight m_f 198.53 [g]   Water content   w   40.54 [%]
                                         Volume: f(m_f, w, ρ_s, S_r=1) V_0 108.64 [cm^3]
                                         Void ratio: f(m_f, w, ρ_s, S_r=1) e_0 1.115 [-]

Test data:

testtime	dH	force	cell-pressure	PWP bottom	PWP top	dV backpr.	H_{act}	V_{act}	A_c	σ_1'	σ_3'	q	p'	ε_1	ε_3	ε_s	ε_v	e
[sec]	[mm]	[kN]	[kPa]	[kPa]	[kPa]	[ccm]	[mm]	[ccm]	[cm^2]	[kPa]	[kPa]	[kPa]	[kPa]	[%]	[%]	[%]	[%]	[-]
00:00:00	0.000	0.006	78.508	49.136	50.780	0.000	52.50	108.64	20.69	31.4	28.6	2.9	29.5	0.000	0.000	0.000	0.000	1.115
02:03:45	0.075	0.000	79.073	49.049	51.129	-0.117	52.43	108.52	20.74	29.0	29.0	0.0	29.0	0.143	-0.018	0.107	0.108	1.113
04:03:45	0.073	0.002	80.037	49.017	50.737	-0.167	52.43	108.47	20.75	31.1	30.2	1.0	30.5	0.139	0.007	0.088	0.154	1.112
06:03:45	0.072	0.003	81.117	49.249	50.732	-0.230	52.43	108.41	20.76	32.6	31.1	1.4	31.6	0.137	0.037	0.067	0.212	1.110
08:03:45	0.070	0.005	81.848	49.046	50.694	-0.275	52.43	108.36	20.77	34.4	32.0	2.4	32.8	0.134	0.060	0.049	0.254	1.109
10:03:45	0.068	0.005	82.458	48.842	50.543	-0.323	52.43	108.31	20.78	35.2	32.8	2.4	33.6	0.130	0.084	0.030	0.298	1.109
12:03:45	0.066	0.006	83.318	49.036	50.552	-0.364	52.43	108.27	20.79	36.4	33.5	2.9	34.5	0.126	0.105	0.014	0.336	1.108
14:03:45	0.065	0.007	84.157	49.055	50.580	-0.413	52.44	108.22	20.80	37.7	34.3	3.4	35.5	0.124	0.129	-0.003	0.382	1.107
16:03:45	0.063	0.008	85.045	49.223	50.586	-0.475	52.44	108.16	20.81	39.0	35.1	3.8	36.4	0.120	0.160	-0.026	0.439	1.106
18:03:45	0.059	0.009	86.021	49.252	50.655	-0.540	52.44	108.10	20.82	40.4	36.1	4.3	37.5	0.113	0.194	-0.054	0.500	1.104
20:03:45	0.052	0.010	86.577	48.949	50.456	-0.583	52.45	108.05	20.82	41.7	36.9	4.8	38.5	0.099	0.220	-0.081	0.540	1.104
22:03:45	0.050	0.011	87.517	48.975	50.470	-0.638	52.45	108.00	20.83	43.1	37.8	5.3	39.6	0.095	0.248	-0.102	0.591	1.102
00:03:45	0.047	0.012	88.292	48.784	50.368	-0.703	52.45	107.93	20.85	44.5	38.7	5.8	40.6	0.090	0.281	-0.128	0.651	1.101
02:03:45	0.044	0.012	89.049	49.063	50.392	-0.748	52.46	107.89	20.85	45.1	39.3	5.8	41.2	0.084	0.305	-0.147	0.693	1.100

load rate: 10 kPa/day = 0.00011574 kPa/s = 0.42 kPa/hour

$\Delta u = 1.6$ kPa
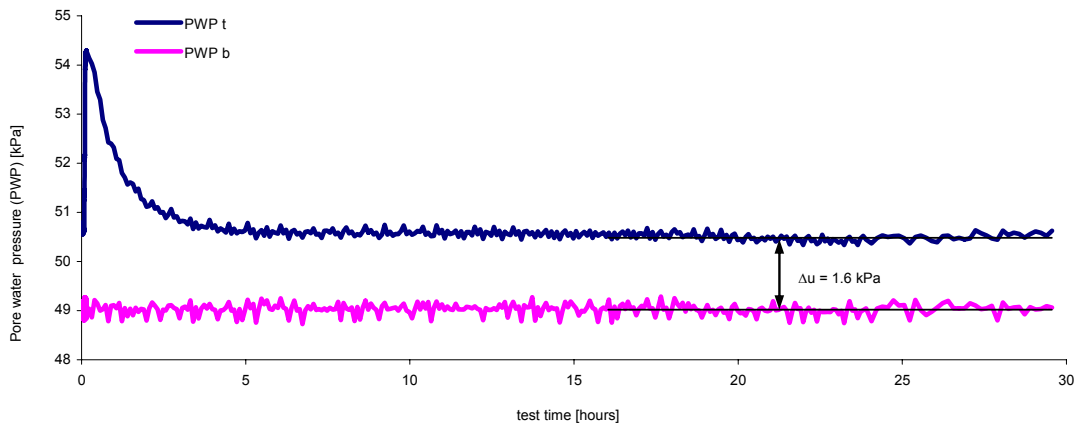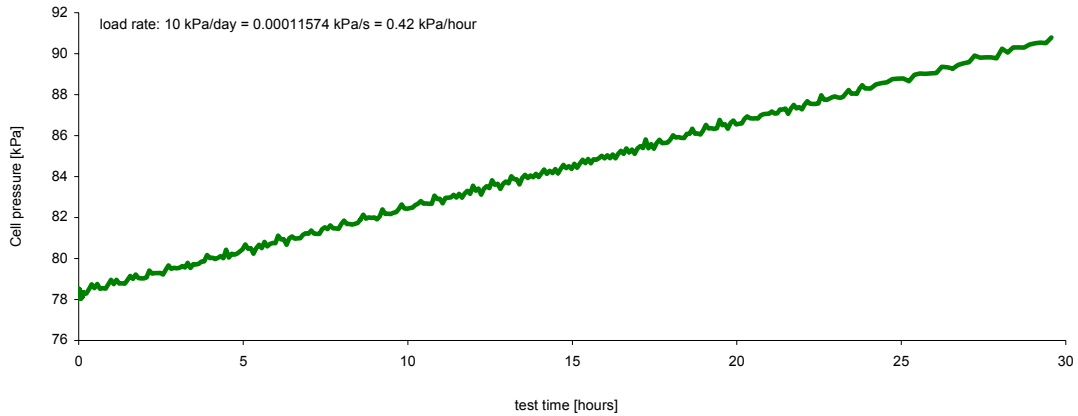
Fig. 10.3:   Triaxial test data of test S1T3 on reconstituted Birmensdorf clay (46707): excess pore water pressure at the given load rate.

Triaxial Test   S1aT3

Test aim: Determination of the drained load ratio
Material number: 46707   Birmensdorf clay: reconstituted and consolidated in the centrifuge pot
Test apparatus: HIF B 24: Triax 3 (yellow)
File name: Birm06.PRB
     test start: 07.09.2003   12:53:35   test stop: 24.09.2003   11:05:58
Comments:

Measured sample data:

			Determined sample data:				**Material parameter:**		
Height H_0	50.00 [mm]		Cross-sectional area:	A	20.35 [cm^2]		density	ρ_s	2.75 [g/cm^3]
Diameter D	5.09 [cm]		Volume: f(H_0, D)	V_0	101.74 [cm^3]		specific gravity of water ρ_w		1 [g/cm^3]
Weight m_f	185.59 [g]		Water content	w	41.93 [%]				
			Volume: f(m_f, w, ρ_s, S_r=1)	V_0	102.38 [cm^3]				
			Void ratio: f(m_f, w, ρ_s, S_r=1)	e_0	1.153 [-]				

Test data:

test-time	dH	force	cell-pressure	PWP bottom	PWP top	dV backpr.	H_{act}	V_{act}	A_c	σ_1'	σ_3'	q	p'	ε_1	ε_3	ε_s	ε_v	e
[hours]	[mm]	[kN]	[kPa]	[kPa]	[kPa]	[ccm]	[mm]	[ccm]	[cm^2]	[kPa]	[kPa]	[kPa]	[kPa]	[%]	[%]	[%]	[%]	[-]
0.0	0.000	0.002	100.980	99.687	101.256	0.000	50.00	102.38	20.48	1.5	0.5	1.0	0.8	0.000	0.000	0.000	0.000	1.153
12.3	0.517	0.003	139.778	100.748	133.449	-6.774	49.48	95.60	22.06	24.0	22.7	1.4	23.1	1.045	3.020	-1.317	7.085	1.011
25.8	1.469	0.003	197.946	100.583	115.256	-11.380	48.53	91.00	23.44	91.3	90.0	1.3	90.5	3.027	4.739	-1.142	12.506	0.914
40.0	1.606	0.002	199.828	100.597	102.147	-11.977	48.39	90.40	23.63	99.3	98.5	0.8	98.7	3.319	4.965	-1.098	13.249	0.901
60.0	1.640	0.003	205.859	100.725	102.051	-12.006	48.36	90.37	23.65	105.7	104.5	1.3	104.9	3.391	4.947	-1.037	13.285	0.901
80.0	1.681	0.003	213.014	100.908	101.781	-12.070	48.32	90.31	23.69	112.9	111.7	1.3	112.1	3.479	4.943	-0.976	13.365	0.899
100.0	1.716	0.002	220.251	100.581	101.852	-12.170	48.28	90.21	23.72	119.9	119.0	0.8	119.3	3.554	4.969	-0.943	13.491	0.897
120.0	1.770	0.001	227.533	100.546	101.524	-12.337	48.23	90.04	23.78	126.9	126.5	0.4	0.0	3.670	5.016	-0.897	13.702	0.894
140.0	1.829	0.002	234.779	100.610	101.990	-12.545	48.17	89.83	23.86	134.3	133.5	0.8	133.8	3.797	5.084	-0.858	13.965	0.889
160.0	1.863	0.002	235.103	100.551	100.508	-12.468	48.14	89.91	23.86	135.4	134.6	0.8	134.9	3.870	4.998	-0.752	13.867	0.891
167.0	1.865	0.002	234.891	100.641	100.378	-12.424	48.14	89.95	23.85	135.2	134.4	0.8	134.7	3.875	4.968	-0.729	13.811	0.892
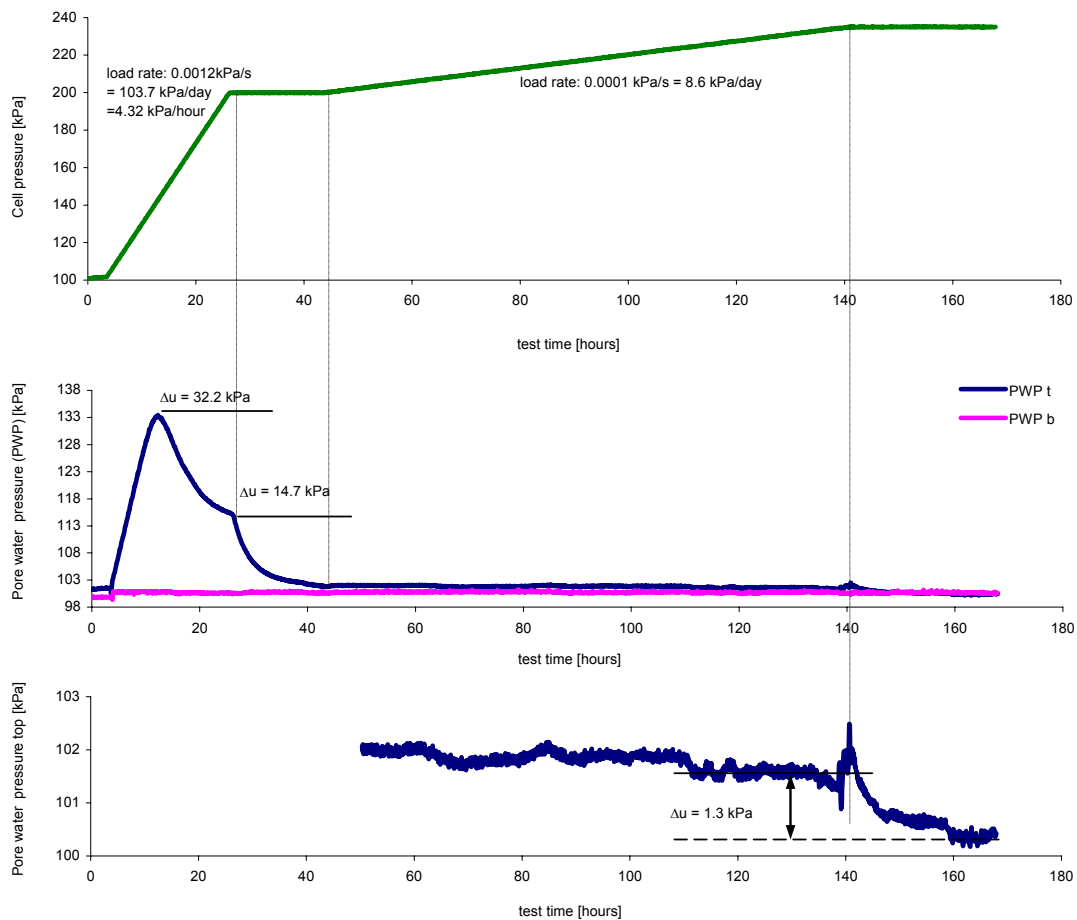
Fig. 10.4:   Triaxial test data of test S1aT3 on reconstituted Birmensdorf clay (46707): excess pore water pressure at the given load rate.

Triaxial Test S1bT3

Test aim: Determination of the drained load ratio
Material number: 46707 Birmensdorf clay: reconstituted and consolidated in the centrifuge pot
Test apparatus: HIF B 24: Triax 3 (yellow)
File name: Birm09.PRB
test start: 05.09.2003 08:57:54 test stop: 23.09.2003 08:48:38
Comments:

Measured sample data:

Height H_0 52.60 [mm]
Diameter D 5.12 [cm]
Weight m_f 196.70 [g]

Determined sample data:

Cross-sectional area: A 20.59 [cm^2]
Volume: f(H$_0$, D) V_0 108.30 [cm^3]
Water content w 42.32 [%]
Volume: f(m_f, w, ρ_s, S_r=1) V_0 108.75 [cm^3]
Void ratio: f(m_f, w, ρ_s, S_r=1) e_0 1.164 [-]

Material parameter:

density ρ_s 2.75 [g/cm^3]
specific gravity of water ρ_w 1 [g/cm^3]

Test data:

test-time	dH	force	cell-pressure	PWP bottom	PWP top	dV backpr.	H_{act}	V_{act}	A_c	σ_1'	σ_3'	q	p'	ε_1	ε_3	ε_s	ε_v	e
[hours]	[mm]	[kN]	[kPa]	[kPa]	[kPa]	[ccm]	[mm]	[ccm]	[cm^2]	[kPa]	[kPa]	[kPa]	[kPa]	[%]	[%]	[%]	[%]	[-]
0.0	0.000	0.010	250.014	246.902	247.490	0.000	52.60	108.75	20.67	7.7	2.8	4.8	4.4	0.000	0.000	0.000	0.000	1.164
13.7	0.340	0.009	276.830	247.188	256.735	-2.404	52.26	106.34	21.27	29.1	24.9	4.2	26.3	0.651	0.805	-0.103	2.261	1.116
48.6	0.865	0.009	299.895	247.221	247.868	-4.500	51.74	104.25	21.89	56.5	52.4	4.1	53.7	1.672	1.322	0.233	4.317	1.074
64.3	1.470	0.010	376.033	247.356	265.968	-6.907	51.13	101.84	22.62	123.8	119.4	4.4	120.8	2.875	1.954	0.614	6.782	1.026
120.0	1.839	0.009	400.171	246.849	248.096	-8.583	50.76	100.17	23.11	156.6	152.7	3.9	154.0	3.623	2.473	0.767	8.569	0.993
160.0	1.898	0.009	415.721	247.028	248.120	-8.730	50.70	100.02	23.17	172.0	168.1	3.9	169.4	3.743	2.492	0.834	8.728	0.990
180.0	1.936	0.009	419.745	246.892	247.192	-8.863	50.66	99.89	23.21	176.6	172.7	3.9	174.0	3.821	2.526	0.864	8.873	0.987
220.0	1.992	0.010	430.077	246.951	247.823	-8.883	50.61	99.87	23.24	187.0	182.7	4.3	184.1	3.936	2.479	0.971	8.895	0.987
240.0	2.036	0.009	439.990	246.846	248.055	-8.929	50.56	99.82	23.27	196.4	192.5	3.9	193.8	4.027	2.459	1.045	8.945	0.986
265.0	2.066	0.009	439.935	246.693	247.412	-9.032	50.53	99.72	23.31	196.7	192.9	3.9	194.2	4.088	2.485	1.069	9.058	0.984
295.0	2.081	0.008	440.102	246.764	247.397	-9.117	50.52	99.63	23.33	196.5	193.0	3.4	194.2	4.119	2.516	1.069	9.151	0.982
335.0	1.678	-0.138	480.858	246.851	251.178	-9.186	50.92	99.56	23.16	172.3	231.8	-59.6	212.0	3.295	2.966	0.220	9.226	0.981
370.0	-1.438	-0.277	518.510	246.909	252.893	-10.218	54.04	98.53	22.02	142.8	268.6	-125.8	226.7	-2.661	6.516	-6.118	10.370	0.960
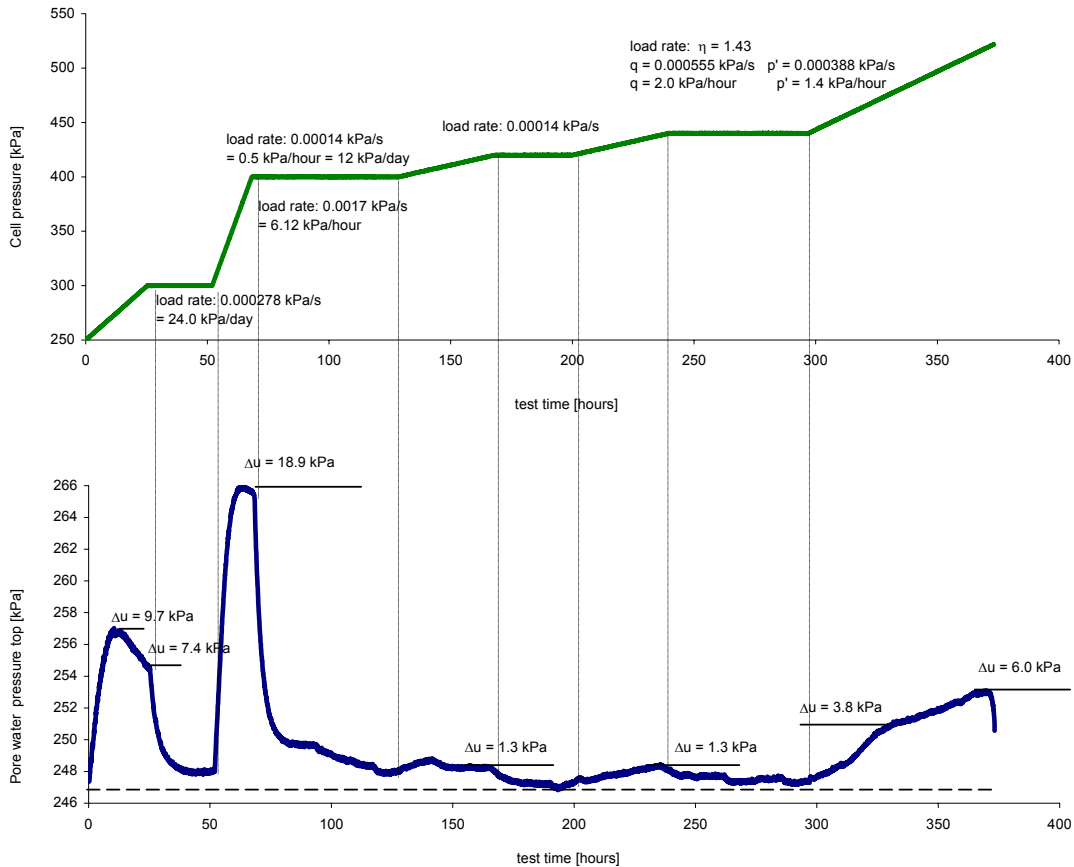
Fig. 10.5: Triaxial test data of test S1bT3 on reconstituted Birmensdorf clay (46707): excess pore water pressure at the given load rate.

Triaxial Test   S1T4

Test aim: Determination of the drained load ratio
Material number: 46707   Birmensdorf clay: reconstituted and consolidated in the centrifuge pot
Test apparatus: HIF B : Triax 4 (blue)
File name: Birm10.PRB
  test start: 08.09.2003   13:45:40   test stop: 09.11.2003   10:50:00
Comments:

Measured sample data:	**Determined sample data:**	**Material parameter:**

Measured sample data:
Height H_0 57.10 [mm]
Diameter D   5.68 [cm]
Weight m_f 266.60 [g]

Determined sample data:
Cross-sectional area: A   25.34 [cm^2]
Volume: f(H$_0$, D) V_0 144.68 [cm^3]
Water content   w   41.31 [%]
Volume: f(m$_f$, w, ρ$_s$, S$_r$=1) V_0 146.54 [cm^3]
Void ratio: f(m$_f$, w, ρ$_s$, S$_r$=1) e_0 1.136 [-]

Material parameter:
density   ρ$_s$ 2.75 [g/cm^3]
specific gravity of water ρ$_w$ 1 [g/cm^3]

Test data:

test-time	dH	force	cell-pressure	PWP bottom	PWP top	dV backpr.	H_{act}	V_{act}	A_c	σ_1'	σ_3'	q	p'	ε_1	ε_3	ε_s	ε_v	e
[hours]	[mm]	[kN]	[kPa]	[kPa]	[kPa]	[ccm]	[mm]	[ccm]	[cm^2]	[kPa]	[kPa]	[kPa]	[kPa]	[%]	[%]	[%]	[%]	[-]
25.1	0.000	0.007	249.982	238.554	239.592	0.123	57.10	146.66	25.64	13.6	10.9	2.7	11.8	0.000	-0.042	0.028	-0.084	1.138
63.2	0.660	0.007	290.895	238.583	247.351	10.966	56.44	157.51	24.02	50.8	47.9	2.9	48.9	1.169	-4.066	3.490	-6.962	1.296
120.0	1.078	0.007	309.999	238.539	239.642	15.458	56.02	162.00	23.40	73.9	70.9	3.0	71.9	1.924	-5.733	5.105	-9.542	1.361
163.0	1.225	0.007	329.976	238.548	241.013	17.833	55.88	164.37	23.04	93.2	90.2	3.0	91.2	2.192	-6.521	5.809	-10.849	1.396
210.0	1.285	0.007	329.964	238.469	239.584	18.546	55.82	165.09	22.93	94.0	90.9	3.1	92.0	2.302	-6.768	6.047	-11.234	1.406
235.0	1.652	0.007	388.182	238.257	252.402	24.821	55.45	171.36	21.95	146.0	142.9	3.2	143.9	2.979	-8.732	7.808	-14.484	1.498
290.0	2.150	0.007	430.005	238.353	239.528	33.274	54.95	179.82	20.61	194.5	191.1	3.4	192.2	3.913	-11.209	10.081	-18.505	1.621
350.0	2.181	0.007	430.081	238.550	239.545	33.233	54.92	179.77	20.63	194.4	191.0	3.4	192.2	3.971	-11.229	10.133	-18.486	1.620
430.0	2.303	0.007	467.644	238.559	240.875	33.903	54.80	180.44	20.56	231.3	227.9	3.4	229.1	4.203	-11.496	10.466	-18.789	1.630
500.0	2.371	0.007	470.117	238.496	239.487	35.241	54.73	181.78	20.34	234.6	231.1	3.4	232.3	4.332	-11.859	10.794	-19.386	1.650
650.0	3.208	0.155	540.321	238.509	242.842	42.197	53.89	188.74	19.36	379.7	299.6	80.1	326.3	5.953	-14.155	13.405	-22.357	1.751
800.0	3.602	0.182	553.152	238.509	239.340	44.509	53.50	191.05	19.07	409.7	314.2	95.4	346.0	6.733	-15.015	14.499	-23.297	1.785
900.0	3.641	0.182	553.247	238.480	239.272	44.615	53.46	191.16	19.07	409.8	314.4	95.5	346.2	6.811	-15.075	14.591	-23.340	1.786
1153.2	3.654	-0.130	698.811	238.525	241.551	54.395	53.45	200.94	17.24	383.4	458.8	-75.4	433.6	6.837	-16.954	15.860	-27.071	1.929
1400.0	3.650	-0.184	725.269	238.286	238.948	58.594	53.45	205.14	16.45	374.8	486.7	-111.8	449.4	6.829	-17.696	16.350	-28.564	1.990

Fig. 10.6:   Triaxial test data of test S1T4 on reconstituted Birmensdorf clay (46707): excess pore water pressure at the given load rate.

Triaxial Test S2T1

Test aim: Initial stiffness and stiffness degradation
Material number: 46862 Block sample of natural Kloten clay
Test apparatus: HIF B 24: Triax 1 (green)
File name: Kloten_nat_serie1_sample4_green.PRB
 test start: 28.01.2004 22:11:17 test stop: 29.03.2004 09:58:23
Comments:

Measured sample data: **Determined sample data:** **Material parameter:**

Height H_0 112.50 [mm] Cross-sectional area: A 20.33 [cm²] density ρ_s 2.77 [g/cm³]
Diameter D 5.09 [cm] Volume: f(H_0, D) V_0 228.72 [cm³] specific gravity of water ρ_w 1 [g/cm³]
Weight m_f 465.72 [g] Water content w 26.52 [%]
 Volume: f(m_f, w, ρ_s, S_r=1) V_0 230.51 [cm³]
 Void ratio: f(mf, w, ρ_s, S_r=1) e_0 0.735 [-]

Test data:

test-time [hours]	dH [mm]	force [kN]	cell-pressure [kPa]	PWP bottom [kPa]	PWP top [kPa]	dV backpr. [ccm]	H_{act} [mm]	V_{act} [ccm]	A_c [cm²]	σ_a' [kPa]	σ_r' [kPa]	q [kPa]	p' [kPa]	ε_a [%]	ε_r [%]	ε_s [%]	ε_v [%]	e [-]
19.4	0.000	0.006	15.419	10.147	9.628	0.000	112.50	230.51	20.33	8.5	5.5	3.0	6.5	0.000	0.000	0.000	0.000	0.735
68.2	1.006	0.042	32.912	10.196	9.692	-5.485	111.49	225.02	20.02	43.9	23.0	21.0	30.0	0.902	0.768	0.090	2.437	0.693
130.3	2.129	0.091	57.542	10.245	9.634	-8.577	110.37	221.93	19.95	93.2	47.6	45.6	62.8	1.929	0.968	0.641	3.865	0.670
186.8	3.175	0.131	77.815	9.998	9.523	-10.995	109.33	219.51	19.92	133.8	68.1	65.8	90.0	2.904	1.052	1.235	5.009	0.652
249.0	4.409	0.177	100.278	10.184	9.755	-13.682	108.09	216.83	19.89	179.3	90.3	89.0	120.0	4.079	1.116	1.976	6.310	0.632
310.9	5.437	0.221	122.746	10.017	9.586	-15.828	107.06	214.68	19.88	224.1	112.9	111.1	150.0	5.078	1.147	2.621	7.373	0.615
373.1	6.263	0.266	145.262	10.165	9.583	-17.538	106.24	212.97	19.88	269.2	135.4	133.8	180.0	5.895	1.170	3.150	8.235	0.603
435.6	6.948	0.311	167.627	10.158	9.541	-19.095	105.55	211.41	19.86	314.4	157.8	156.6	210.0	6.583	1.225	3.572	9.032	0.591
497.3	7.521	0.356	190.265	9.970	9.377	-20.521	104.98	209.99	19.83	360.1	180.6	179.5	240.4	7.164	1.304	3.907	9.773	0.580
559.1	8.026	0.401	212.344	10.129	9.520	-21.684	104.47	208.82	19.82	404.9	202.5	202.4	270.0	7.682	1.351	4.221	10.384	0.571
604.7	8.352	0.433	225.081	10.352	9.854	-22.502	104.15	208.01	19.80	433.7	215.0	218.7	287.9	8.019	1.399	4.413	10.818	0.565
641.7	8.430	0.405	211.668	10.202	9.621	-22.836	104.07	207.67	19.78	406.5	201.8	204.7	270.0	8.100	1.448	4.435	10.996	0.563
704.8	8.435	0.360	188.963	10.075	9.430	-23.299	104.07	207.21	19.74	361.6	179.2	182.4	240.0	8.106	1.569	4.357	11.244	0.559
766.4	8.433	0.315	166.724	10.229	9.705	-23.517	104.07	206.99	19.72	316.5	156.8	159.8	210.0	8.103	1.629	4.316	11.361	0.558
829.1	8.393	0.270	144.312	10.202	9.677	-23.761	104.11	206.75	19.69	271.5	134.4	137.1	180.1	8.062	1.715	4.231	11.493	0.556
938.5	8.351	0.225	112.706	10.237	9.641	-24.351	104.15	206.16	19.62	217.4	102.8	114.7	141.0	8.018	1.897	4.081	11.812	0.551
947.8	8.341	0.216	114.197	10.201	9.592	-24.456	104.16	206.05	19.61	214.4	104.3	110.1	141.0	8.008	1.930	4.052	11.869	0.551
958.3	8.346	0.206	115.962	10.231	9.656	-24.506	104.15	206.00	19.61	211.1	106.0	105.1	141.0	8.013	1.941	4.048	11.896	0.550
968.4	8.334	0.196	117.719	10.329	9.772	-24.513	104.17	206.00	19.60	207.6	107.7	100.0	141.0	8.001	1.949	4.034	11.900	0.550
988.0	8.329	0.177	120.755	10.152	9.557	-24.692	104.17	205.82	19.59	201.3	110.9	90.4	141.0	7.996	2.001	3.996	11.997	0.549
1007.3	8.321	0.157	124.020	10.410	9.848	-24.900	104.18	205.61	19.56	194.1	113.9	80.2	140.6	7.987	2.061	3.950	12.110	0.547
1027.7	8.303	0.137	127.455	10.214	9.633	-25.094	104.20	205.41	19.54	187.6	117.5	70.1	140.9	7.969	2.124	3.896	12.216	0.546
1047.8	8.271	0.118	130.656	10.089	9.555	-25.208	104.23	205.30	19.53	181.3	120.8	60.4	141.0	7.935	2.172	3.843	12.279	0.545
1088.2	8.244	0.078	137.473	10.034	9.486	-25.477	104.26	205.03	19.49	167.7	127.7	40.0	141.1	7.907	2.259	3.765	12.426	0.543
1126.4	8.173	0.039	143.802	10.130	9.569	-25.694	104.33	204.81	19.46	154.0	134.0	20.0	140.6	7.834	2.356	3.652	12.545	0.541
1166.7	8.049	0.000	150.540	10.236	9.679	-25.999	104.45	204.51	19.41	140.6	140.6	0.0	140.6	7.706	2.503	3.468	12.713	0.539
1206.7	7.889	-0.039	157.185	10.204	9.589	-26.299	104.61	204.21	19.35	127.1	147.3	-20.2	140.6	7.541	2.669	3.248	12.878	0.537
1244.8	7.614	-0.077	163.651	10.199	9.694	-26.607	104.89	203.90	19.27	113.7	153.7	-40.0	140.4	7.259	2.895	2.910	13.049	0.534
1283.7	7.102	-0.115	170.288	10.310	9.717	-27.076	105.40	203.43	19.13	100.2	160.3	-60.1	140.2	6.738	3.286	2.302	13.309	0.531
1349.8	4.484	-0.186	181.953	10.155	9.497	-28.361	108.02	202.15	18.55	71.9	172.1	-100.3	138.7	4.151	4.939	-0.525	14.030	0.521
1378.1	0.313	-0.214	186.508	10.168	9.575	-28.748	112.19	201.76	17.82	56.6	176.6	-120.1	136.6	0.279	6.985	-4.471	14.249	0.518
1383.2	-2.328	-0.218	187.697	10.136	9.572	-28.506	114.83	202.00	17.44	52.8	177.8	-125.0	136.2	-2.027	8.070	-6.731	14.112	0.520
1384.9	-5.100	-0.220	187.952	10.149	9.596	-28.284	117.60	202.22	17.04	49.0	178.1	-129.1	135.1	-4.337	9.162	-8.999	13.986	0.522
1385.2	-8.671	-0.204	187.947	10.524	10.011	-28.194	121.17	202.31	16.55	54.4	177.7	-123.3	136.6	-7.156	10.546	-11.801	13.936	0.522

Fig. 10.7: Triaxial test data of stress path test S2T1 on natural Kloten clay.

Fig. 10.8:   Triaxial test data of stress path test S2T1 on natural Kloten clay.

Fig. 10.9:   Laser scan data of the triaxial stress path test S2T1 on natural Kloten clay:
              radius from laser 1.

Fig. 10.10: Laser scan data of the triaxial stress path test S2T1 on natural Kloten clay: radius from laser 2.

Fig. 10.11:   Laser scan data of the triaxial stress path test S2T1 on natural Kloten clay: radius from laser 3.

Fig. 10.12: Laser scan data of the triaxial stress path test S2T1 on natural Kloten clay: radial strain from laser 1.

Fig. 10.13: Laser scan data of the triaxial stress path test S2T1 on natural Kloten clay: radial strain from laser 2.

Fig. 10.14: Laser scan data of the triaxial stress path test S2T1 on natural Kloten clay: radial strain from laser 3.
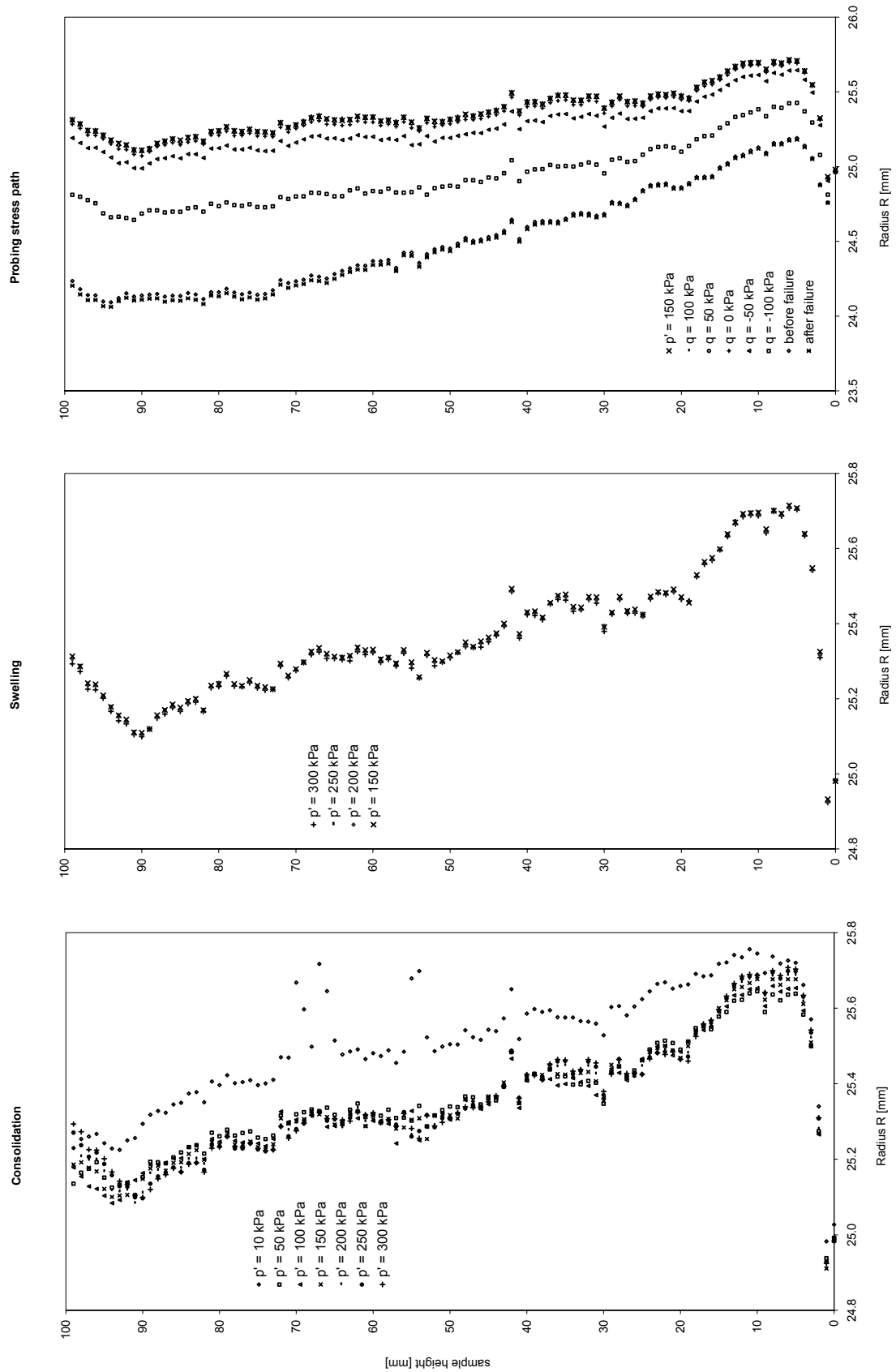
Fig. 10.15:   Laser scan data of the triaxial stress path test S2T1 on natural Kloten clay: radius determined with the circular slice approach.
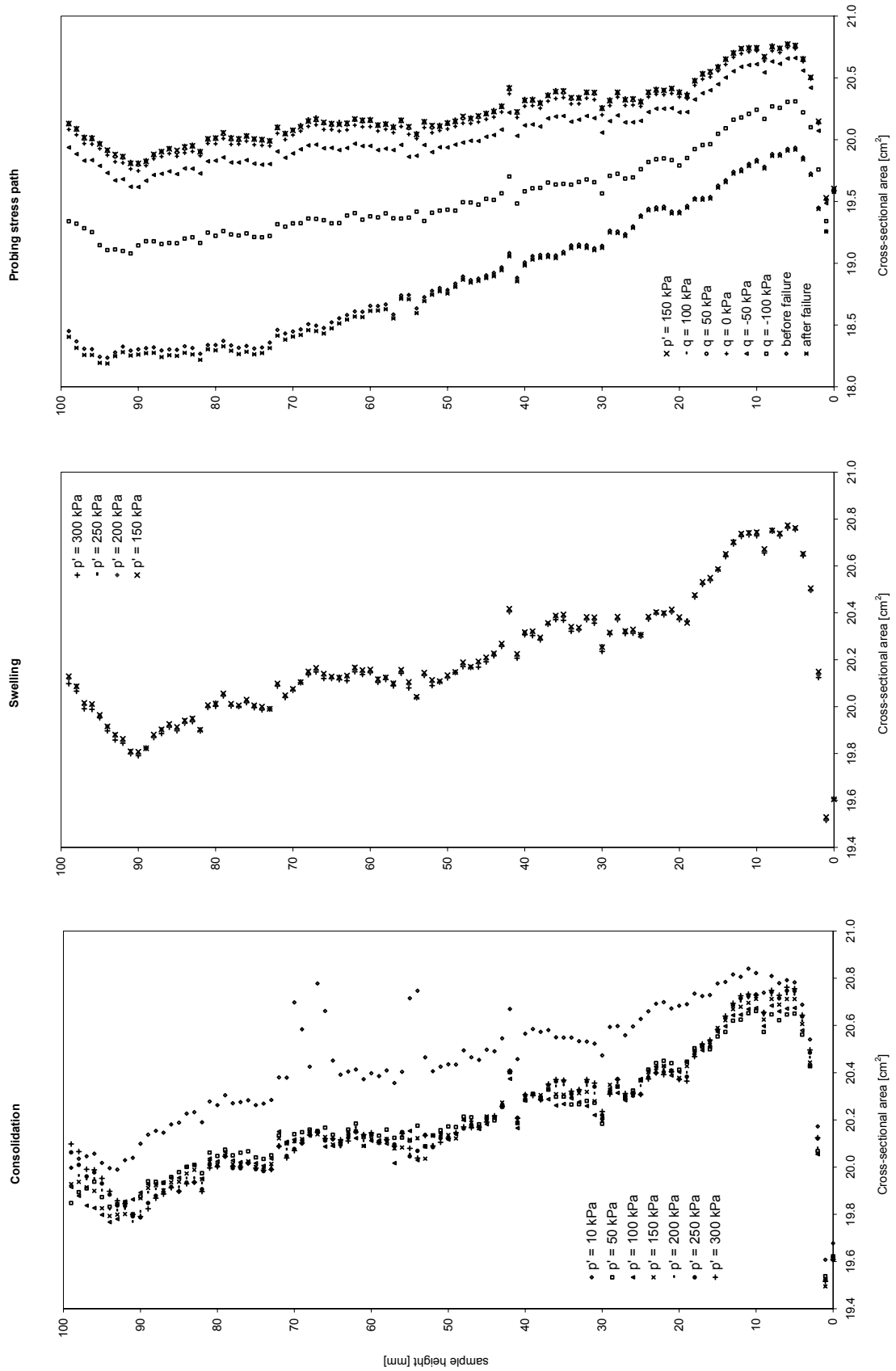
Fig. 10.16: Laser scan data of the triaxial stress path test S2T1 on natural Kloten clay:
cross-sectional area calculated from *R* (Fig. 10.15).

Fig. 10.17: Laser scan data of the triaxial stress path test S2T1 on natural Kloten clay: change of deviator stress.
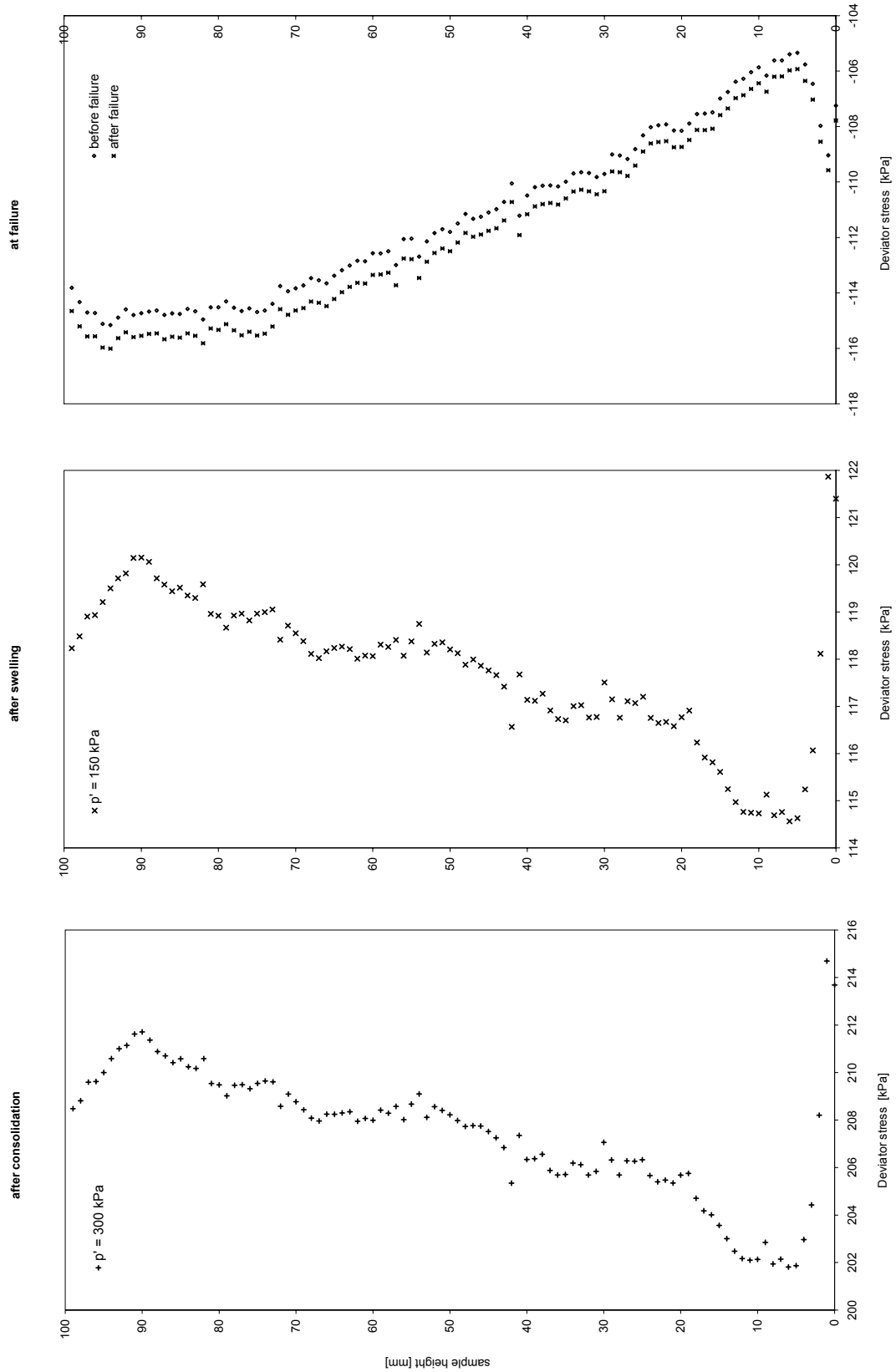
Fig. 10.18: Laser scan data of the triaxial stress path test S2T1 on natural Kloten clay: change of deviator stress (enlarged scale).
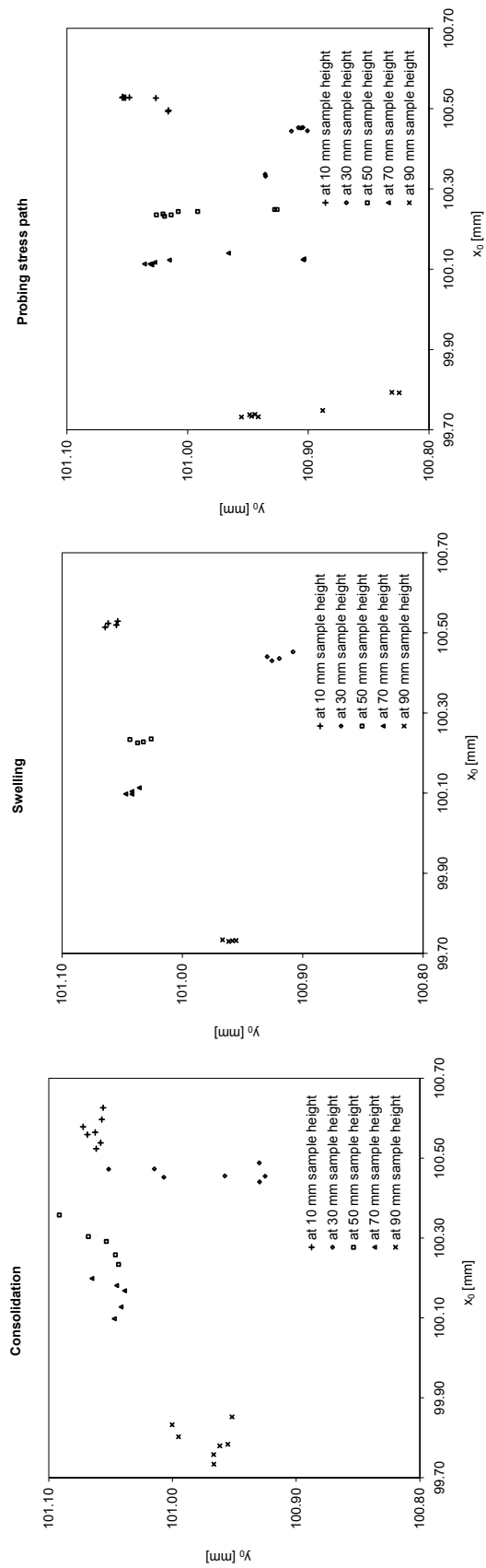
Fig. 10.19: Laser scan data of centre of each disc for the triaxial stress path test S2T1 on natural Kloten clay.

316
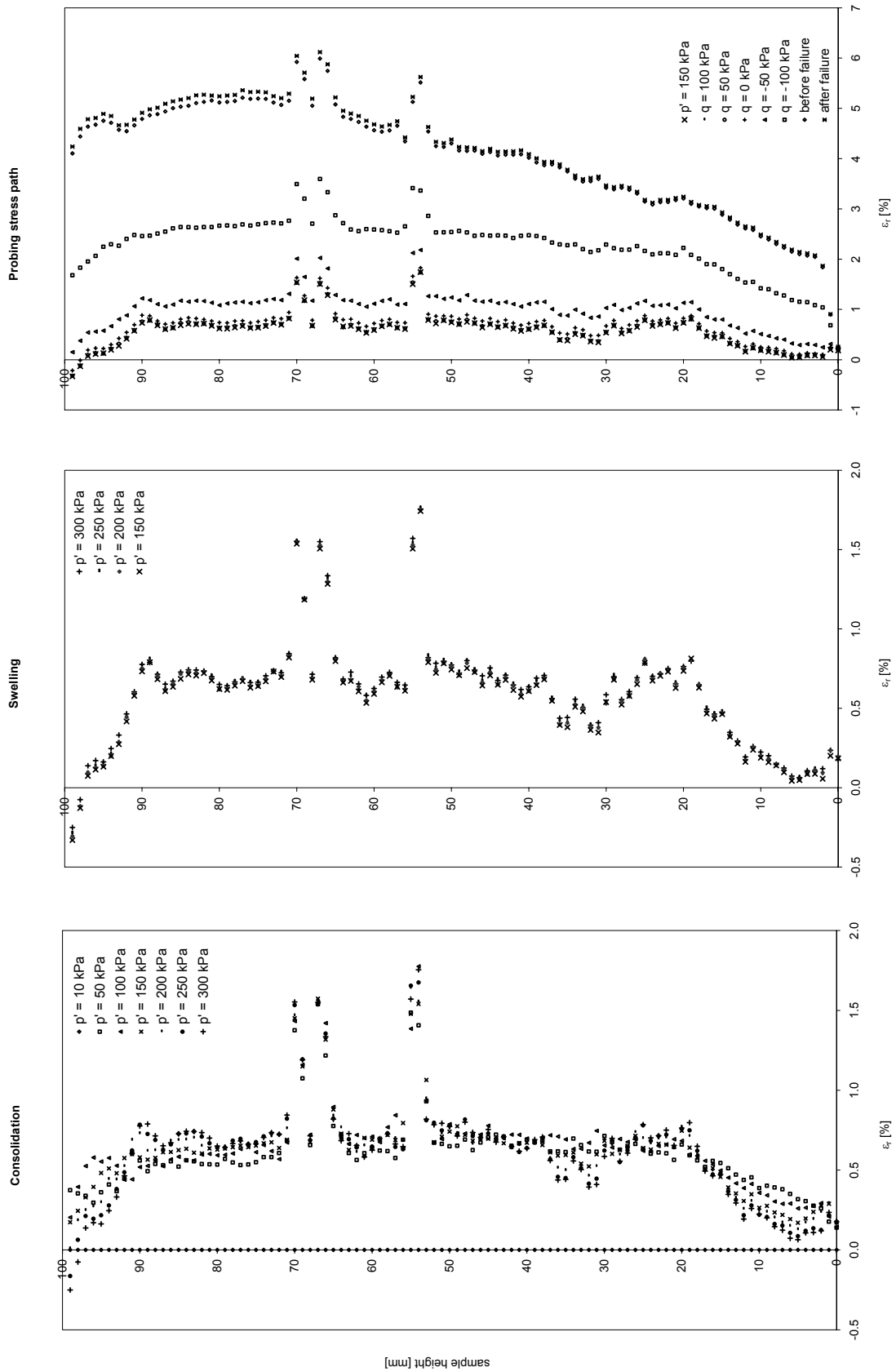
Fig. 10.20: Laser scan data of the triaxial stress path test S2T1 on natural Kloten clay: radial strain calculated from *R* (Fig. 10.15).
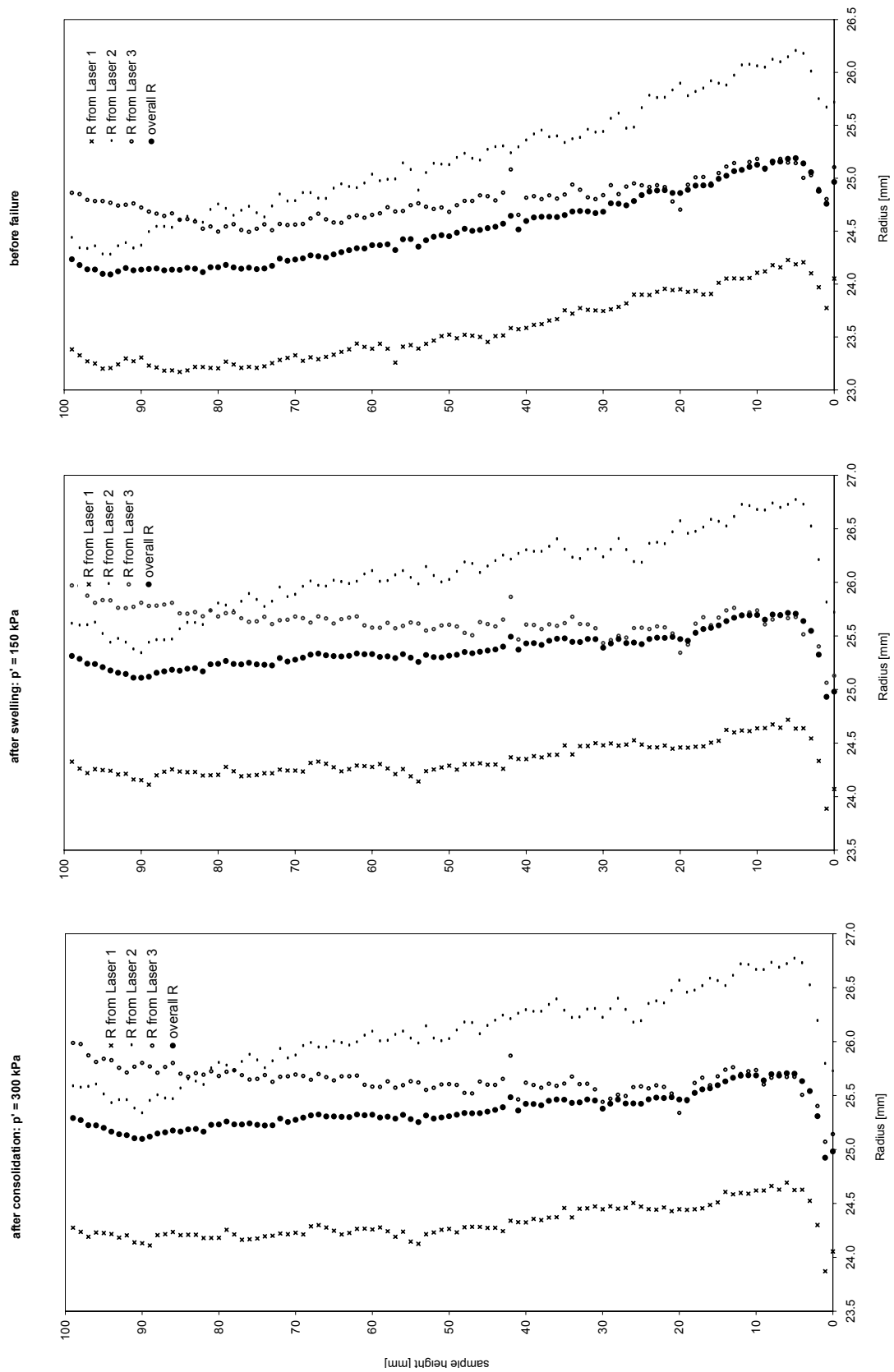
Fig. 10.21: Laser scan data of the triaxial stress path test S2T1 on natural Kloten clay: comparison of radius determined from each laser together with the radius *R* determined from the circular slice approach.
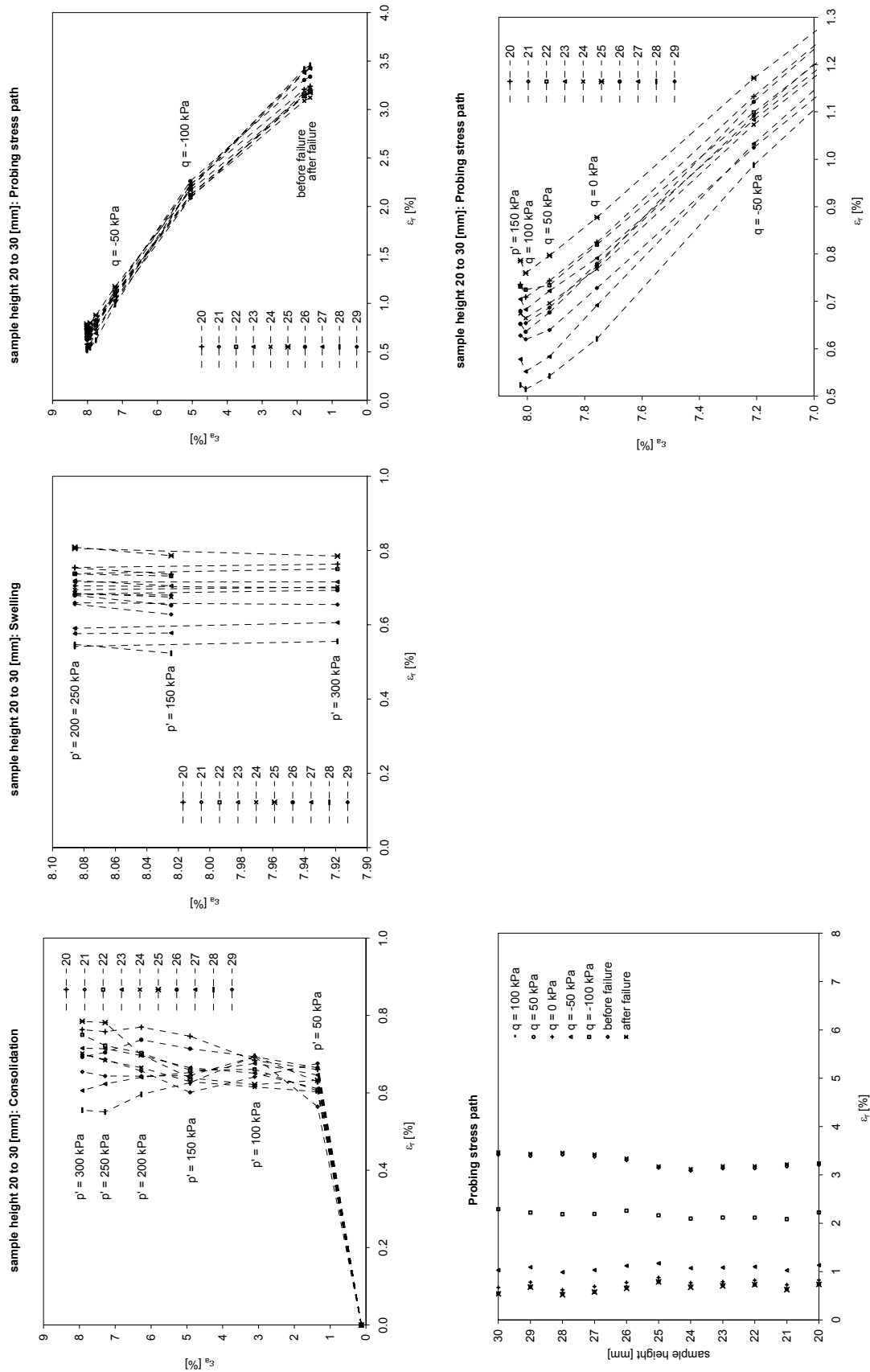
Fig. 10.22:   Laser scan data of the triaxial stress path test S2T1 on natural Kloten clay:
between sample heights (from base) 20 – 30 mm.

319
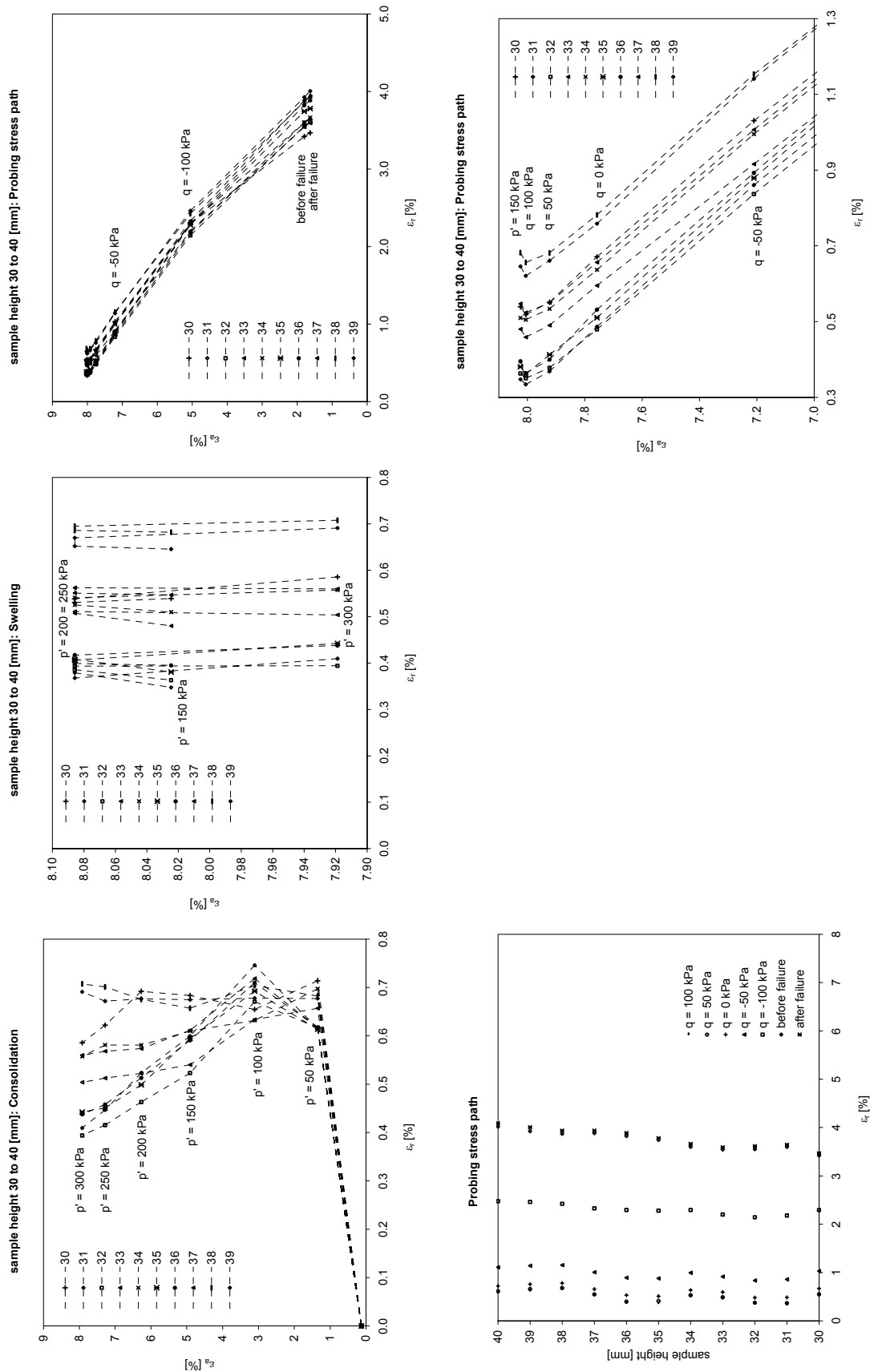
Fig. 10.23: Laser scan data of the triaxial stress path test S2T1 on natural Kloten clay: between sample heights (from base) 30 – 40 mm.
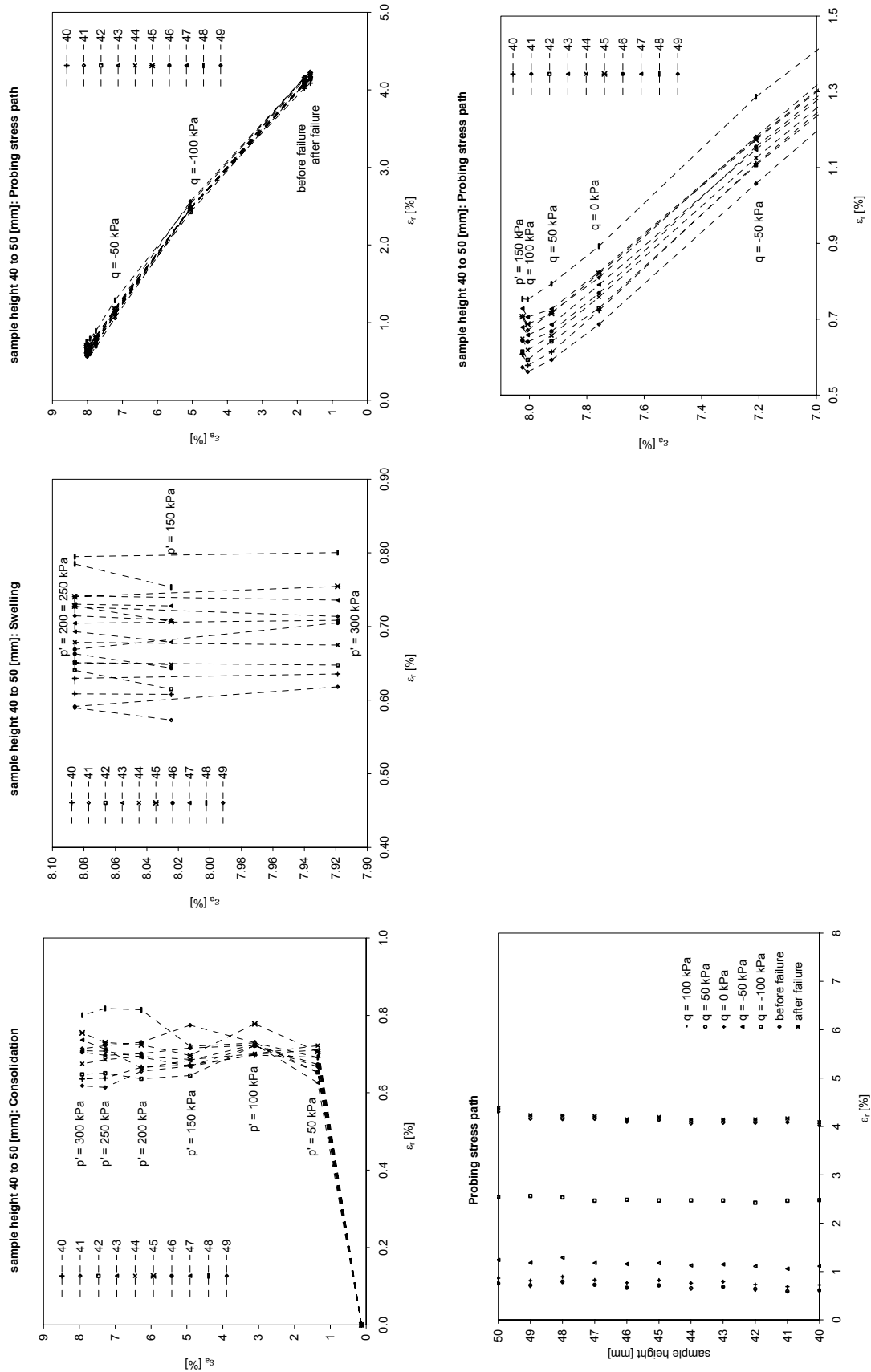
Fig. 10.24:   Laser scan data of the triaxial stress path test S2T1 on natural Kloten clay: between sample heights (from base) 40 – 50 mm.
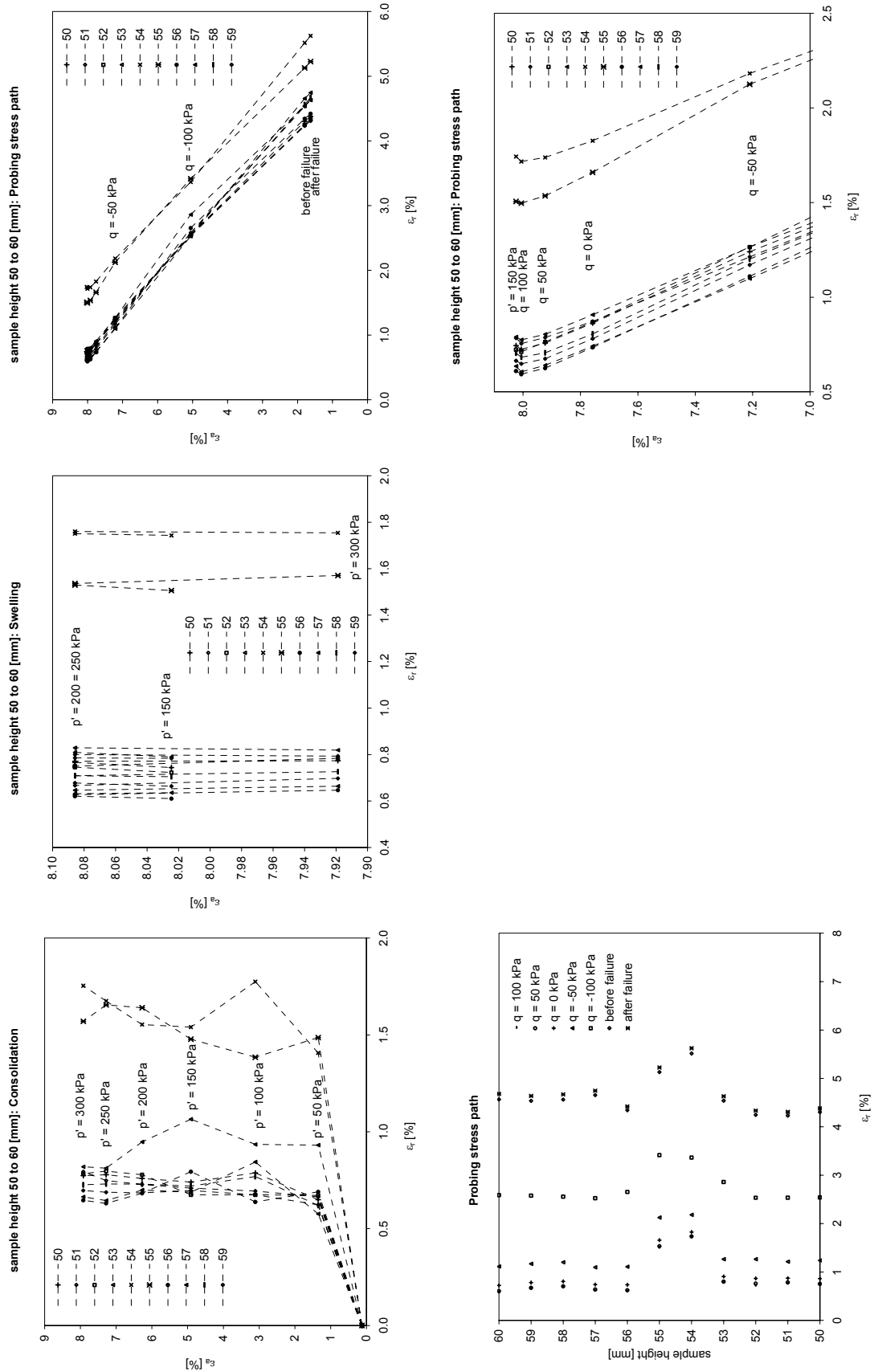
Fig. 10.25:   Laser scan data of the triaxial stress path test S2T1 on natural Kloten clay: between sample heights (from base) 50 – 60 mm.

Fig. 10.26:   Laser scan data of the triaxial stress path test S2T1 on natural Kloten clay: between sample heights (from base) 60 – 70 mm.

Fig. 10.27:   Laser scan data of the triaxial stress path test S2T1 on natural Kloten clay: between sample heights (from base) 70 – 80 mm.

Triaxial Test S2T2

Test aim: Initial stiffness and stiffness degradation
Material number: 46862 Block sample of natural Kloten clay
Test apparatus: HIF B 24: Triax 2 (red)
File name: Kloten_nat_serie_1_sample3_red
  test start: 28.01.2004   22:38:01   test stop: 26.03.2004   07:55:29
Comments:

Measured sample data:

Height H_0	111.90	[mm]
Diameter D	5.08	[cm]
Weight m_f	463.89	[g]

Determined sample data:

Cross-sectional area:	A	20.28	[cm^2]
Volume: f(H_0, D)	V_0	226.91	[cm^3]
Water content	w	26.19	[%]
Volume: f(m_f, w, ρ_s, S_r=1)	V_0	228.99	[cm^3]
Void ratio: f(m_f, w, ρ_s, S_r=1)	e_0	0.725	[-]

Material parameter:

density	ρ_s	2.77	[g/cm^3]
specific gravity of water	ρ_w	1	[g/cm^3]

Test data:

test-time [hours s]	dH [mm]	force [kN]	cell-pressure [kPa]	PWP bottom [kPa]	PWP top [kPa]	dV backpr. [ccm]	H_{act} [mm]	V_{act} [ccm]	A_c [cm^2]	σ_a' [kPa]	σ_r' [kPa]	q [kPa]	p' [kPa]	ε_a [%]	ε_r [%]	ε_s [%]	ε_v [%]	e [-]
0.0	0.000	-0.001	5.557	3.799	2.730	0.000	111.90	228.99	20.30	1.8	2.3	-0.5	2.1	0.000	0.000	0.000	0.000	0.725
46.6	1.204	0.029	24.289	9.137	8.064	-1.485	110.70	227.50	20.39	29.9	15.7	14.2	20.4	1.088	-0.217	0.870	0.653	0.714
87.8	2.240	0.059	39.192	9.319	8.235	-3.466	109.66	225.52	20.40	59.3	30.4	28.9	40.1	2.043	-0.253	1.530	1.537	0.699
129.6	3.088	0.090	54.134	9.351	8.308	-5.188	108.81	223.80	20.40	89.4	45.3	44.1	60.0	2.838	-0.260	2.065	2.318	0.686
171.4	3.921	0.120	69.319	9.303	8.252	-6.524	107.98	222.47	20.43	119.3	60.5	58.7	80.1	3.631	-0.349	2.654	2.932	0.676
213.4	4.722	0.150	84.348	9.306	8.266	-8.055	107.18	220.94	20.44	148.9	75.6	73.4	100.0	4.406	-0.380	3.191	3.646	0.665
252.5	5.427	0.178	98.744	9.242	8.209	-9.336	106.47	219.65	20.46	177.0	90.0	87.0	119.0	5.097	-0.423	3.680	4.250	0.655
296.0	6.072	0.210	114.574	9.227	8.217	-10.264	105.83	218.73	20.50	208.3	105.9	102.5	140.0	5.738	-0.523	4.173	4.692	0.648
338.3	6.615	0.241	129.623	9.212	8.154	-10.911	105.29	218.08	20.54	238.3	120.9	117.3	160.0	6.283	-0.640	4.615	5.003	0.643
380.8	7.091	0.271	144.971	9.334	8.336	-11.449	104.81	217.54	20.58	267.8	136.1	131.7	180.0	6.766	-0.751	5.011	5.263	0.639
422.2	7.531	0.301	160.065	9.302	8.267	-12.232	104.37	216.76	20.59	297.4	151.3	146.2	200.0	7.216	-0.786	5.335	5.643	0.633
464.6	7.909	0.332	175.348	9.363	8.372	-12.567	103.99	216.42	20.64	327.4	166.5	160.9	220.1	7.605	-0.899	5.670	5.807	0.631
506.3	8.251	0.362	190.511	9.407	8.392	-13.046	103.65	215.94	20.66	356.8	181.6	175.2	240.0	7.961	-0.959	5.947	6.042	0.627
547.7	8.556	0.392	205.453	9.146	8.145	-13.603	103.34	215.39	20.67	386.5	196.8	189.7	260.0	8.279	-0.982	6.174	6.316	0.623
614.1	9.002	0.442	223.698	9.340	8.351	-14.282	102.90	214.71	20.69	428.5	214.9	213.6	286.1	8.748	-1.048	6.531	6.652	0.618
667.4	9.079	0.402	204.051	9.180	8.188	-14.199	102.82	214.79	20.71	389.4	195.4	194.1	260.1	8.830	-1.110	6.626	6.611	0.618
709.5	9.083	0.372	189.122	9.358	8.376	-14.023	102.82	214.97	20.73	359.7	180.3	179.4	240.1	8.834	-1.155	6.660	6.524	0.620
751.3	9.081	0.342	173.950	9.320	8.304	-13.801	102.82	215.19	20.75	329.9	165.1	164.8	220.1	8.832	-1.209	6.694	6.413	0.621
792.8	9.067	0.312	158.835	9.344	8.325	-13.608	102.83	215.38	20.77	300.2	150.0	150.2	200.1	8.817	-1.250	6.711	6.318	0.623
834.4	9.042	0.282	143.704	9.253	8.281	-13.264	102.86	215.73	20.80	270.5	134.9	135.6	180.1	8.791	-1.321	6.741	6.148	0.626
876.3	9.023	0.252	128.554	9.297	8.336	-12.695	102.89	216.30	20.85	240.6	119.7	120.9	160.0	8.771	-1.451	6.814	5.869	0.630
908.9	9.011	0.228	116.985	9.341	8.318	-12.156	102.89	216.83	20.90	217.3	108.2	109.1	144.5	8.758	-1.576	6.889	5.606	0.634
916.0	9.011	0.228	114.458	9.328	8.281	-12.168	102.89	216.82	20.90	214.8	105.7	109.1	142.0	8.758	-1.573	6.887	5.612	0.634
931.5	9.009	0.229	112.418	9.364	8.311	-12.120	102.89	216.87	20.90	213.1	103.6	109.6	140.1	8.756	-1.584	6.893	5.588	0.634
935.5	9.007	0.229	110.553	9.352	8.315	-12.076	102.89	216.91	20.90	211.3	101.7	109.5	138.2	8.754	-1.593	6.898	5.567	0.634
939.6	9.008	0.229	108.324	9.343	8.304	-12.109	102.89	216.88	20.90	209.1	99.5	109.6	136.0	8.755	-1.586	6.894	5.583	0.634
943.1	9.004	0.229	106.378	9.373	8.363	-12.068	102.90	216.92	20.90	207.1	97.5	109.5	134.0	8.751	-1.594	6.896	5.564	0.635
946.7	8.997	0.228	104.588	9.343	8.334	-12.052	102.90	216.94	20.91	204.8	95.7	109.1	132.1	8.743	-1.594	6.891	5.555	0.635
950.9	8.995	0.228	102.438	9.258	8.255	-12.013	102.91	216.98	20.91	202.7	93.7	109.0	130.0	8.741	-1.602	6.896	5.536	0.635
970.6	8.996	0.228	92.532	9.332	8.348	-11.885	102.90	217.11	20.92	192.7	83.7	109.0	120.0	8.742	-1.634	6.917	5.474	0.636
990.6	9.006	0.228	82.617	9.343	8.293	-11.594	102.89	217.40	20.95	182.6	73.8	108.8	110.1	8.753	-1.710	6.975	5.333	0.638
1010.4	9.025	0.228	72.635	9.302	8.279	-11.409	102.87	217.58	20.97	172.6	63.8	108.7	100.1	8.773	-1.765	7.025	5.243	0.639
1030.1	9.077	0.228	62.663	9.259	8.258	-10.925	102.82	218.07	21.03	162.3	53.9	108.4	90.0	8.828	-1.909	7.158	5.010	0.643
1049.7	9.283	0.228	52.853	9.256	8.299	-10.432	102.62	218.56	21.12	152.0	44.1	107.9	80.1	9.046	-2.137	7.455	4.773	0.647
1065.3	14.225	0.228	44.986	9.332	8.354	-8.060	97.68	220.93	22.43	137.8	36.1	101.6	70.0	14.564	-5.458	13.348	3.648	0.665
1066.0	15.886	0.228	44.656	9.315	8.354	-7.731	96.01	221.26	22.86	135.6	35.8	99.8	69.1	16.546	-6.526	15.381	3.494	0.667
1066.6	17.641	0.228	44.258	9.213	8.195	-7.464	94.26	221.53	23.31	133.4	35.6	97.8	68.2	18.715	-7.673	17.592	3.369	0.669
1067.1	19.506	0.228	44.022	9.192	8.206	-7.207	92.39	221.78	23.81	131.1	35.3	95.8	67.2	21.112	-8.931	20.029	3.249	0.671

Fig. 10.28: Triaxial test data of stress path test S2T2 on natural Kloten clay.

Fig. 10.29:   Triaxial test data of stress path test S2T2 on natural Kloten clay.

Triaxial Test S2T3

Test aim: Initial stiffness and stiffness degradation
Material number: 46862 Block sample of natural Kloten clay
Test apparatus: HIF B 24: Triax 3 (yellow)
File name: sample1_yellow.PRB
  test start: 26.01.2004 14:19:36   test stop: 06.04.2004 10:27:32
Comments:

Measured sample data:

Height H_0	114.60	[mm]
Diameter D	5.09	[cm]
Weight m_f	473.54	[g]

Determined sample data:

Cross-sectional area:	A	20.35	[cm^2]
Volume: $f(H_0, D)$	V_0	233.19	[cm^3]
Water content	w	26.17	[%]
Volume: $f(m_f, w, \rho_s, S_r=1)$	V_0	233.72	[cm^3]
Void ratio: $f(m_f, w, \rho_s, S_r=1)$	e_0	0.725	[-]

Material parameter:

density	ρ_s	2.77	[g/cm^3]
specific gravity of water	ρ_w	1	[g/cm^3]

Test data:

test-time [hours]	dH [mm]	force [kN]	cell-pressure [kPa]	PWP bottom [kPa]	PWP top [kPa]	dV backpr. [ccm]	H_{act} [mm]	V_{act} [ccm]	A_c [cm^2]	σ_a' [kPa]	σ_r' [kPa]	q [kPa]	p' [kPa]	ε_a [%]	ε_r [%]	ε_s [%]	ε_v [%]	e [-]
31.3	0.000	0.011	15.092	10.393	13.303	0.000	114.60	233.72	20.35	8.6	3.2	5.4	5.0	0.000	0.000	0.000	0.000	0.725
82.2	1.849	0.048	33.324	10.483	11.842	-6.764	112.75	226.95	20.08	46.1	22.2	23.9	30.1	1.640	0.670	0.646	2.980	0.675
143.9	3.169	0.093	55.855	10.426	11.012	-10.934	111.43	222.78	19.95	91.8	45.1	46.6	60.7	2.844	1.032	1.208	4.908	0.644
204.5	4.468	0.136	77.625	10.451	10.295	-14.269	110.13	219.45	19.88	135.7	67.3	68.4	90.1	4.057	1.223	1.890	6.502	0.620
267.6	5.639	0.181	100.604	10.199	11.118	-16.996	108.96	216.72	19.84	181.2	89.9	91.2	120.4	5.175	1.334	2.561	7.842	0.599
329.2	6.586	0.226	122.946	10.429	10.722	-19.142	108.01	214.57	19.82	226.4	112.4	114.0	150.4	6.097	1.412	3.124	8.921	0.584
391.8	7.335	0.271	145.192	10.391	10.916	-20.945	107.27	212.77	19.79	271.5	134.5	137.0	180.2	6.838	1.503	3.557	9.844	0.570
453.9	7.958	0.316	167.845	10.196	10.959	-22.526	106.64	211.19	19.75	317.2	157.3	160.0	210.6	7.462	1.602	3.907	10.666	0.559
514.9	8.487	0.360	189.879	10.265	11.105	-23.858	106.11	209.86	19.73	361.7	179.2	182.5	240.0	7.998	1.685	4.208	11.369	0.549
578.5	8.952	0.406	212.770	10.295	12.408	-25.066	105.65	208.65	19.70	407.5	201.4	206.1	270.1	8.473	1.770	4.469	12.013	0.540
655.5	9.448	0.455	234.946	10.448	13.281	-26.346	105.15	207.37	19.67	454.4	223.1	231.3	300.2	8.985	1.860	4.750	12.705	0.530
731.6	9.544	0.412	211.662	10.181	12.828	-26.736	105.06	206.98	19.65	409.8	200.2	209.6	270.0	9.085	1.916	4.779	12.917	0.528
787.7	9.538	0.367	189.638	10.274	13.135	-26.809	105.06	206.91	19.64	364.8	177.9	186.8	240.2	9.078	1.939	4.759	12.957	0.527
852.0	9.520	0.321	165.974	10.268	10.527	-26.875	105.08	206.84	19.63	319.1	155.6	163.5	210.1	9.060	1.967	4.729	12.993	0.527
912.6	9.493	0.277	144.330	10.301	11.438	-26.924	105.11	206.79	19.62	274.6	133.5	141.2	180.5	9.032	1.994	4.692	13.020	0.526
975.7	9.470	0.232	121.629	10.405	11.453	-26.873	105.13	206.84	19.62	228.9	110.7	118.2	150.1	9.008	1.992	4.677	12.992	0.527
1020.7	9.459	0.227	112.646	10.408	11.154	-26.869	105.14	206.85	19.62	217.5	101.9	115.7	140.4	8.996	1.997	4.667	12.990	0.527
1021.7	9.457	0.228	112.643	10.260	11.028	-26.880	105.14	206.84	19.62	218.2	102.0	116.2	140.7	8.994	2.001	4.662	12.996	0.527
1024.6	9.456	0.228	114.392	10.304	11.165	-26.893	105.14	206.82	19.62	219.9	103.7	116.2	142.4	8.993	2.005	4.659	13.003	0.526
1028.2	9.456	0.228	116.115	10.336	11.342	-26.908	105.14	206.81	19.62	221.5	105.3	116.2	144.0	8.993	2.009	4.656	13.011	0.526
1032.1	9.457	0.228	118.112	10.228	11.197	-26.917	105.14	206.80	19.62	223.6	107.4	116.2	146.1	8.994	2.011	4.656	13.016	0.526
1036.0	9.465	0.229	120.100	10.437	11.473	-26.935	105.14	206.78	19.62	225.9	109.1	116.7	148.1	9.003	2.011	4.661	13.026	0.526
1039.7	9.467	0.229	122.044	10.403	11.560	-26.936	105.13	206.78	19.62	227.8	111.1	116.7	150.0	9.005	2.011	4.663	13.026	0.526
1050.3	9.464	0.228	127.324	10.277	11.755	-26.981	105.14	206.73	19.61	232.6	116.3	116.2	155.1	9.002	2.025	4.651	13.051	0.526
1060.1	9.470	0.228	132.240	10.297	11.705	-27.014	105.13	206.70	19.61	237.5	121.2	116.3	160.0	9.008	2.030	4.652	13.069	0.526
1080.8	9.471	0.228	142.554	10.248	11.739	-27.113	105.13	206.60	19.60	247.9	131.6	116.3	170.3	9.009	2.057	4.635	13.123	0.525
1100.7	9.472	0.228	152.466	10.269	11.995	-27.209	105.13	206.51	19.59	257.7	141.3	116.4	180.1	9.010	2.083	4.618	13.176	0.524
1101.7	9.474	0.228	152.986	10.295	11.986	-27.209	105.13	206.51	19.59	258.2	141.8	116.4	180.6	9.012	2.082	4.620	13.176	0.524
1120.3	9.481	0.228	162.180	10.266	11.452	-27.312	105.12	206.40	19.59	267.7	151.3	116.4	190.1	9.019	2.106	4.609	13.232	0.523
1138.5	9.495	0.228	171.837	10.374	10.823	-27.429	105.11	206.29	19.58	277.7	161.2	116.5	200.1	9.034	2.131	4.602	13.297	0.522
1178.0	9.499	0.228	191.394	10.257	10.080	-27.672	105.10	206.04	19.55	297.8	181.2	116.6	220.1	9.038	2.196	4.561	13.430	0.521
1217.6	9.505	0.228	211.652	10.466	10.651	-27.909	105.10	205.81	19.53	317.8	201.1	116.7	240.0	9.044	2.258	4.524	13.561	0.519
1258.7	9.523	0.228	231.978	10.274	10.864	-28.136	105.08	205.58	19.51	338.2	221.4	116.8	260.4	9.063	2.312	4.501	13.686	0.517
1299.2	9.535	0.229	252.678	10.413	11.852	-28.410	105.07	205.30	19.49	359.0	241.5	117.5	280.7	9.075	2.381	4.463	13.838	0.515
1339.6	9.537	0.228	272.664	10.277	12.184	-28.710	105.06	205.01	19.46	378.6	261.4	117.1	300.5	9.077	2.464	4.409	14.005	0.513
1379.6	9.552	0.228	292.888	10.435	12.732	-29.042	105.05	204.67	19.43	398.6	281.3	117.3	320.4	9.093	2.548	4.363	14.190	0.511
1418.7	9.566	0.228	312.177	10.271	12.126	-29.417	105.03	204.30	19.40	418.5	301.0	117.5	340.2	9.108	2.646	4.308	14.399	0.508
1458.3	9.591	0.228	332.086	10.213	12.085	-29.824	105.01	203.89	19.37	438.7	320.9	117.7	360.2	9.134	2.747	4.258	14.628	0.505
1497.4	9.610	0.228	351.790	10.223	11.554	-30.242	104.99	203.47	19.33	458.9	340.9	117.9	380.2	9.153	2.855	4.199	14.863	0.502
1537.6	9.638	0.228	371.893	10.202	12.187	-30.679	104.96	203.04	19.29	478.9	360.7	118.2	400.1	9.182	2.964	4.146	15.110	0.498
1577.5	9.656	0.228	392.368	10.216	12.646	-31.129	104.94	202.59	19.25	499.4	380.9	118.4	420.4	9.201	3.082	4.079	15.366	0.495
1616.4	9.698	0.228	411.736	10.309	11.653	-31.582	104.90	202.15	19.22	519.4	400.8	118.6	440.3	9.245	3.190	4.037	15.624	0.492
1652.6	9.725	0.229	430.078	10.362	11.386	-32.013	104.88	201.70	19.18	538.6	419.2	119.4	459.0	9.273	3.299	3.983	15.871	0.489
1667.2	9.727	0.282	429.480	18.317	19.606	-32.802	104.87	200.91	19.11	558.1	410.5	147.6	459.7	9.275	3.526	3.833	16.327	0.483
1667.3	9.868	0.595	429.449	27.246	26.909	-32.802	104.73	200.91	19.13	713.3	402.4	311.0	506.0	9.422	3.452	3.980	16.327	0.483
1667.4	10.013	0.694	429.396	39.113	36.824	-32.802	104.59	200.91	19.16	753.6	391.4	362.2	512.2	9.574	3.376	4.132	16.327	0.483
1667.4	10.162	0.742	429.419	52.579	48.621	-32.802	104.44	200.91	19.19	765.5	378.8	386.7	507.7	9.730	3.298	4.288	16.327	0.483
1667.5	10.309	0.769	429.414	66.483	61.391	-32.802	104.29	200.91	19.21	765.7	365.5	400.2	498.9	9.885	3.221	4.443	16.327	0.483
1667.6	10.457	0.790	429.451	80.350	74.568	-32.802	104.14	200.91	19.24	762.6	352.0	410.6	488.8	10.041	3.143	4.599	16.327	0.483
1667.7	10.614	0.803	429.337	94.020	88.179	-32.802	103.99	200.91	19.27	754.9	338.2	416.7	477.1	10.207	3.060	4.765	16.327	0.483
1667.9	10.922	0.818	429.434	119.371	113.785	-32.802	103.68	200.91	19.33	736.1	312.9	423.2	453.9	10.535	2.896	5.092	16.327	0.483
1668.0	11.224	0.823	429.387	141.769	136.501	-32.802	103.38	200.91	19.38	714.8	290.3	424.6	431.8	10.857	2.735	5.415	16.327	0.483
1668.4	11.965	0.823	429.329	182.851	177.989	-32.802	102.64	200.91	19.52	670.4	248.9	421.5	389.4	11.658	2.334	6.216	16.327	0.483
1668.8	12.551	0.820	429.214	203.500	199.046	-32.802	102.05	200.91	19.64	645.5	227.9	417.6	367.1	12.299	2.014	6.857	16.327	0.483

Fig. 10.30:   Triaxial test data of stress path test S2T3 on natural Kloten clay.

Fig. 10.31:   Triaxial test data of stress path test S2T3 on natural Kloten clay.

Fig. 10.32:   Triaxial test data of stress path test S2T3 on natural Kloten clay.

Triaxial Test   S2T4

Test aim: Initial stiffness and stiffness degradation
Material number: 46862   Block sample of natural Kloten clay
Test apparatus: HIL B 58: Triax 4 (blue)
File name: Kloten_nat_serie1_blue.PRB
test start: 26.01.2004   17:51:31   test stop: 26.03.2004   09:05:43
Comments:

Measured sample data:

Height H_0 131.70 [mm]
Diameter D   5.59 [cm]
Weight m_f 653.43 [g]

Determined sample data:

Cross-sectional area: A   24.57 [cm^2]
Volume: f(H_0, D) V_0 323.57 [cm^3]
Water content   w   27.07 [%]
Volume: f(m_f, w, ρ_s, S_r=1) V_0 324.84 [cm^3]
Void ratio: f(m_f, w, ρ_s, S_r=1) e_0 0.750 [-]

Material parameter:

density ρ_s 2.77 [g/cm^3]
specific gravity of water ρ_w 1 [g/cm^3]

Test data:

test-time	dH	force	cell-pressure	PWP bottom	PWP top	dV backpr.	H_{act}	V_{act}	A_c	σ_a'	σ_r'	q	p'	ε_a	ε_r	ε_s	ε_v	e
[hours]	[mm]	[kN]	[kPa]	[kPa]	[kPa]	[ccm]	[mm]	[ccm]	[cm^2]	[kPa]	[kPa]	[kPa]	[kPa]	[%]	[%]	[%]	[%]	[-]
27.9	0.000	0.003	15.204	9.764	8.940	0.000	131.70	324.84	24.57	7.1	5.9	1.2	6.3	0.000	0.000	0.000	0.000	0.750
76.7	1.961	0.048	33.022	9.753	8.932	-6.171	129.74	318.67	24.47	43.3	23.7	19.6	30.2	1.511	0.212	0.866	1.936	0.717
133.3	3.854	0.106	55.292	9.650	8.784	-10.777	127.85	314.07	24.47	89.4	46.1	43.3	60.5	3.015	0.208	1.871	3.432	0.692
194.6	5.630	0.164	77.531	9.613	8.737	-14.635	126.07	310.21	24.51	135.3	68.4	66.9	90.7	4.466	0.126	2.893	4.718	0.671
256.7	7.212	0.222	100.037	9.755	8.821	-17.893	124.49	306.95	24.56	181.1	90.7	90.4	120.9	5.793	0.018	3.850	5.829	0.653
318.7	8.468	0.280	122.391	9.685	8.737	-20.570	123.23	304.27	24.59	227.0	113.2	113.9	151.1	6.872	-0.056	4.618	6.760	0.639
380.6	9.480	0.339	144.714	9.604	8.630	-22.691	122.22	302.15	24.62	273.3	135.6	137.7	181.5	7.757	-0.123	5.253	7.510	0.628
442.2	10.320	0.397	167.023	9.480	8.505	-24.499	121.38	300.34	24.64	319.1	158.0	161.1	211.7	8.502	-0.173	5.783	8.157	0.618
504.3	11.049	0.455	189.514	9.521	8.496	-25.992	120.65	298.85	24.67	365.0	180.5	184.5	242.0	9.158	-0.230	6.259	8.697	0.610
566.5	11.683	0.514	211.960	9.578	8.517	-27.360	120.02	297.48	24.68	411.1	202.9	208.2	272.3	9.734	-0.269	6.669	9.197	0.602
658.0	12.450	0.585	234.904	9.576	8.476	-29.028	119.25	295.82	24.70	462.7	225.9	236.8	304.8	10.440	-0.314	7.169	9.813	0.593
724.5	12.553	0.522	210.974	9.718	8.611	-29.265	119.15	295.58	24.70	413.1	201.8	211.3	272.2	10.536	-0.317	7.235	9.901	0.592
786.7	12.557	0.464	188.596	9.679	8.563	-29.246	119.14	295.60	24.71	367.3	179.5	187.8	242.1	10.539	-0.323	7.241	9.894	0.592
848.5	12.540	0.405	166.125	9.616	8.423	-29.141	119.16	295.70	24.71	321.0	157.1	163.9	211.7	10.524	-0.334	7.239	9.855	0.593
910.4	12.511	0.347	143.788	9.683	8.405	-28.966	119.19	295.88	24.72	275.1	134.7	140.4	181.5	10.497	-0.354	7.234	9.790	0.594
975.7	12.464	0.293	120.190	9.869	8.556	-28.783	119.24	296.06	24.73	229.5	111.0	118.5	150.5	10.453	-0.366	7.213	9.722	0.595
1019.0	12.460	0.294	116.821	9.845	8.464	-28.755	119.24	296.09	24.73	226.6	107.7	118.9	147.3	10.450	-0.369	7.212	9.712	0.595
1024.7	12.462	0.302	115.869	9.755	8.344	-28.740	119.24	296.10	24.73	228.9	106.8	122.1	147.5	10.451	-0.373	7.216	9.706	0.595
1028.9	12.464	0.307	115.149	9.682	8.311	-28.738	119.24	296.11	24.73	230.3	106.2	124.1	147.5	10.453	-0.374	7.218	9.705	0.595
1039.0	12.469	0.320	113.434	9.688	8.353	-28.772	119.23	296.07	24.73	233.8	104.4	129.4	147.5	10.458	-0.370	7.219	9.718	0.595
1048.9	12.476	0.332	111.841	9.634	8.237	-28.731	119.22	296.11	24.73	237.1	102.9	134.2	147.7	10.464	-0.381	7.230	9.703	0.595
1058.9	12.485	0.345	110.172	9.607	8.249	-28.735	119.22	296.11	24.73	240.7	101.2	139.5	147.7	10.473	-0.384	7.238	9.704	0.595
1069.2	12.495	0.358	108.546	9.729	8.336	-28.709	119.21	296.13	24.74	244.2	99.5	144.7	147.8	10.482	-0.394	7.250	9.694	0.595
1079.9	12.509	0.371	106.659	9.718	8.344	-28.695	119.19	296.15	24.74	247.6	97.6	149.9	147.6	10.495	-0.403	7.265	9.689	0.595
1090.1	12.525	0.384	105.014	9.653	8.246	-28.679	119.18	296.16	24.75	251.2	96.1	155.2	147.8	10.510	-0.413	7.282	9.683	0.595
1100.6	12.547	0.397	103.201	9.753	8.339	-28.640	119.15	296.20	24.76	254.5	94.2	160.4	147.6	10.530	-0.431	7.307	9.669	0.596
1110.9	12.573	0.410	101.527	9.706	8.270	-28.619	119.13	296.22	24.76	258.1	92.5	165.6	147.7	10.554	-0.447	7.334	9.661	0.596
1121.4	12.609	0.423	99.748	9.589	8.159	-28.582	119.09	296.26	24.77	261.6	90.9	170.8	147.6	10.588	-0.470	7.372	9.648	0.596
1131.8	12.655	0.436	98.096	9.625	8.189	-28.517	119.05	296.33	24.79	265.1	89.2	175.9	147.8	10.630	-0.503	7.423	9.623	0.596
1142.0	12.717	0.449	96.355	9.616	8.212	-28.444	118.98	296.40	24.81	268.4	87.4	181.0	147.8	10.688	-0.546	7.489	9.596	0.597
1152.0	12.816	0.462	94.591	9.697	8.264	-28.345	118.88	296.50	24.84	271.6	85.6	186.0	147.6	10.780	-0.610	7.594	9.560	0.597
1163.2	12.985	0.476	92.807	9.625	8.147	-28.168	118.72	296.68	24.89	275.2	83.9	191.3	147.7	10.938	-0.722	7.773	9.495	0.598
1170.4	13.224	0.484	91.565	9.618	8.136	-27.986	118.48	296.86	24.95	276.7	82.7	194.0	147.3	11.162	-0.867	8.019	9.427	0.599
1175.1	13.610	0.491	90.871	9.650	8.154	-27.837	118.09	297.01	25.05	278.0	82.0	196.0	147.3	11.525	-1.076	8.401	9.372	0.600
1179.2	15.813	0.495	90.100	9.543	8.064	-27.604	115.89	297.24	25.54	275.1	81.3	193.8	145.9	13.645	-2.179	10.550	9.287	0.601
1181.0	19.113	0.498	89.818	9.544	8.080	-27.486	112.59	297.36	26.30	270.3	81.0	189.3	144.1	16.976	-3.866	13.895	9.243	0.602
1183.0	21.096	0.500	89.467	9.608	8.142	-27.373	110.60	297.47	26.78	267.3	80.6	186.7	142.8	19.073	-4.936	16.006	9.202	0.602
1190.1	27.425	0.509	88.309	9.546	8.023	-27.046	104.28	297.80	28.44	258.5	79.5	179.0	139.2	26.301	-8.609	23.273	9.082	0.604

Fig. 10.33:   Triaxial test data of stress path test S2T4 on natural Kloten clay.

Fig. 10.34: Triaxial test data of stress path test S2T4 on natural Kloten clay.

Triaxial Test   S2aT1

Test aim: Initial stiffness and stiffness degradation
Material number: 46862   Block sample of natural Kloten clay
Test apparatus: HIF B 24: Triax 1 (green)
File name: Serie4_Kloten_nat_cyl_green.PRB
    test start: 06.04.2004   21:04:59   test stop: 19.04.2004   11:13:34
Comments: LVDT & Laser measurement!

Measured sample data: **Determined sample data:**   **Material parameter:**
Height H_0 110.20 [mm]   Cross-sectional area: A   20.28 [cm^2]   density ρ_s 2.77 [g/cm^3]
Diameter D   5.08 [cm]   Volume: f(H$_0$, D) V_0 223.46 [cm^3]   specific gravity of water ρ_w 1 [g/cm^3]
Weight m_f 415.80 [g]   Water content   w   26.81 [%]
                                            Volume: f(m$_f$, w, ρ_s, S$_r$=1) V_0 206.28 [cm^3]
                                            Void ratio: f(m$_f$, w, ρ_s, S$_r$=1) e_0 0.743 [-]

Test data:

test-time	dH	force	cell-pressure	PWP bottom	PWP top	dV backpr.	H_{act}	V_{act}	A_c	σ_1'	σ_3'	q	p'	ε_1	ε_3	ε_s	ε_v	e
[hours]	[mm]	[kN]	[kPa]	[kPa]	[kPa]	[ccm]	[mm]	[ccm]	[cm^2]	[kPa]	[kPa]	[kPa]	[kPa]	[%]	[%]	[%]	[%]	[-]
0.0	0.000	0.001	54.697	50.043	49.538	0.000	110.20	206.28	20.27	5.4	4.9	0.5	5.1	0.000	0.000	0.000	0.000	0.743
33.7	1.460	0.051	71.584	50.215	49.644	-3.989	108.74	202.29	20.17	46.9	21.7	25.3	30.1	1.343	0.315	0.685	1.972	0.709
53.5	1.912	0.080	86.652	50.148	49.565	-5.181	108.29	201.10	20.15	76.5	36.8	39.7	50.0	1.766	0.405	0.907	2.576	0.699
63.4	2.068	0.095	94.249	50.226	49.709	-5.707	108.13	200.57	20.13	91.5	44.3	47.2	60.0	1.912	0.466	0.964	2.845	0.694
93.4	3.003	0.140	116.876	50.259	49.675	-7.795	107.20	198.49	20.11	136.5	66.9	69.6	90.1	2.801	0.563	1.492	3.927	0.677
103.2	3.510	0.154	124.510	50.174	49.742	-8.722	106.69	197.56	20.12	151.1	74.6	76.5	100.1	3.290	0.562	1.818	4.415	0.669
123.2	4.688	0.184	139.459	50.287	49.721	-10.536	105.51	195.74	20.17	180.7	89.5	91.2	119.9	4.443	0.470	2.649	5.382	0.654
153.2	6.030	0.228	162.366	50.230	49.649	-12.855	104.17	193.43	20.21	225.3	112.4	112.8	150.0	5.789	0.429	3.573	6.646	0.634
183.0	6.956	0.273	185.158	50.291	49.724	-14.431	103.24	191.85	20.24	270.1	135.2	134.9	180.1	6.737	0.392	4.230	7.522	0.621
203.0	7.458	0.303	200.331	50.162	49.521	-15.431	102.74	190.85	20.24	300.2	150.5	149.7	200.4	7.259	0.413	4.564	8.085	0.612
213.0	7.639	0.317	207.765	50.218	49.556	-15.832	102.56	190.45	20.23	314.5	157.9	156.7	210.1	7.448	0.432	4.677	8.313	0.609
242.8	8.178	0.361	230.440	49.991	49.373	-16.926	102.02	189.35	20.23	359.2	180.8	178.4	240.2	8.016	0.461	5.036	8.939	0.600
252.9	8.349	0.376	237.910	50.044	49.393	-17.229	101.85	189.05	20.24	374.0	188.2	185.8	250.1	8.197	0.458	5.159	9.113	0.597
272.8	8.682	0.405	253.215	50.064	49.582	-17.956	101.52	188.32	20.23	403.6	203.4	200.2	270.1	8.552	0.491	5.374	9.535	0.591
302.1	9.088	0.442	274.959	50.211	49.535	-18.786	101.11	187.49	20.23	443.6	225.1	218.5	297.9	8.988	0.516	5.648	10.019	0.584
329.6	9.293	0.441	275.157	50.165	49.527	-19.362	100.91	186.92	20.22	443.5	225.3	218.1	298.0	9.209	0.574	5.757	10.358	0.579
357.4	9.288	0.400	254.216	50.108	49.529	-19.636	100.91	186.66	20.19	402.5	204.4	198.1	270.4	9.204	0.658	5.697	10.521	0.577
386.9	9.289	0.356	231.720	50.098	49.438	-19.696	100.91	186.58	20.18	358.3	182.0	176.4	240.7	9.205	0.675	5.686	10.556	0.576
417.2	9.266	0.311	208.720	50.220	49.701	-19.967	100.93	186.31	20.15	313.1	158.8	154.3	210.2	9.180	0.768	5.608	10.717	0.574
447.3	9.227	0.267	186.197	50.232	49.588	-20.273	100.97	186.01	20.11	269.0	136.3	132.8	180.5	9.138	0.880	5.505	10.899	0.571
502.1	9.200	0.220	163.124	50.243	49.562	-20.521	101.00	185.76	20.08	222.8	113.2	109.5	149.7	9.109	0.969	5.427	11.047	0.569
506.8	9.183	0.223	164.813	50.133	49.484	-20.538	101.02	185.74	20.08	226.1	115.0	111.1	152.0	9.091	0.983	5.405	11.057	0.569
510.6	9.196	0.227	166.182	50.148	49.622	-20.637	101.00	185.64	20.07	229.4	116.3	113.1	154.0	9.105	1.006	5.399	11.116	0.568
515.1	9.189	0.229	167.914	50.252	49.612	-20.683	101.01	185.60	20.06	232.1	118.0	114.1	156.0	9.097	1.023	5.382	11.144	0.568
518.7	9.176	0.232	169.374	50.159	49.443	-20.725	101.02	185.56	20.06	235.2	119.6	115.7	158.1	9.083	1.043	5.360	11.169	0.568
522.3	9.173	0.235	170.668	50.090	49.338	-20.719	101.03	185.56	20.06	238.1	121.0	117.2	160.0	9.080	1.043	5.358	11.166	0.568
532.5	9.199	0.242	174.521	50.136	49.480	-20.880	101.00	185.40	20.05	245.4	124.7	120.7	165.0	9.108	1.077	5.354	11.262	0.566
542.3	9.187	0.250	178.313	50.215	49.553	-20.972	101.01	185.31	20.04	253.2	128.4	124.8	170.0	9.095	1.111	5.322	11.317	0.565
552.5	9.197	0.257	182.043	50.212	49.504	-21.072	101.00	185.21	20.03	260.5	132.2	128.3	175.0	9.106	1.136	5.313	11.377	0.565
562.8	9.219	0.265	185.805	50.247	49.596	-21.229	100.98	185.05	20.02	268.3	135.9	132.4	180.0	9.129	1.171	5.306	11.472	0.563
572.7	9.215	0.272	189.635	50.159	49.457	-21.327	100.99	184.95	20.01	275.8	139.8	136.0	185.1	9.125	1.203	5.281	11.531	0.562
582.9	9.249	0.280	193.437	50.381	49.898	-21.442	100.95	184.84	20.00	283.3	143.3	140.0	190.0	9.162	1.219	5.295	11.601	0.561
592.6	9.244	0.287	196.907	50.043	49.403	-21.505	100.96	184.78	19.99	290.7	147.2	143.5	195.0	9.156	1.241	5.277	11.639	0.561
603.0	9.265	0.294	200.838	50.157	49.564	-21.502	100.94	184.78	20.00	298.0	151.0	147.0	200.0	9.179	1.229	5.300	11.637	0.561
612.7	9.277	0.301	204.617	50.131	49.522	-21.630	100.92	184.65	19.99	305.4	154.8	150.7	205.0	9.192	1.261	5.287	11.714	0.560
622.8	9.280	0.309	208.426	50.282	49.680	-21.731	100.92	184.55	19.98	313.1	158.4	154.7	210.0	9.195	1.290	5.270	11.775	0.559
632.6	9.290	0.316	212.128	50.174	49.567	-21.910	100.91	184.37	19.96	320.6	162.3	158.3	215.0	9.206	1.339	5.245	11.884	0.558
640.0	9.271	0.322	214.955	50.032	49.452	-21.981	100.93	184.30	19.95	326.6	165.2	161.4	219.0	9.186	1.371	5.210	11.927	0.557

Fig. 10.35:   Triaxial test data of stress path test S2aT1 on natural Kloten clay.

Fig. 10.36:   Triaxial test data of stress path test S2aT1 on natural Kloten clay.

Test data:

test-time	dH LVDT 1	dH LVDT 2	ε_a LVDT 1	ε_a LVDT 2	ε_r LVDT 1	ε_r LVDT 2	ε_s LVDT 1	ε_s LVDT 2	V_{act} Laser	dV Laser	ε_v Laser	ε_3 LVDT 1 & Laser	ε_3 LVDT 2 & Laser	ε_s LVDT 1 & Laser	ε_s LVDT 2 & Laser	e Laser	V_{act} Cellpr.	ε_v Cellpr.
[hours]	[mm]	[mm]	[%]	[%]	[%]	[%]	[%]	[%]	[ccm]	[ccm]	[%]	[%]	[%]	[%]	[%]	[-]	[ccm]	[%]
0.0	0.000	0.000	0.000	0.000	0.000	0.000	0.00	0.00	205.99	0.00	0.00	0.00	0.00	0.00	0.00	0.74	206.28	0.00
33.7	0.794	1.255	1.147	1.826	0.412	0.073	0.49	1.17	204.87	-1.13	0.55	-0.30	-0.64	0.96	1.64	0.73	195.08	5.74
53.5	1.038	1.519	1.505	2.218	0.536	0.179	0.65	1.36	204.46	-1.53	0.75	-0.38	-0.73	1.26	1.97	0.73	191.33	7.81
63.4	1.167	1.650	1.695	2.414	0.575	0.216	0.75	1.47	204.06	-1.94	0.95	-0.37	-0.73	1.38	2.10	0.72	190.61	8.22
93.4	1.749	2.212	2.563	3.263	0.682	0.332	1.25	1.95	202.00	-3.99	1.98	-0.29	-0.64	1.90	2.60	0.71	186.76	10.45
103.2	2.072	2.538	3.050	3.762	0.682	0.326	1.58	2.29	201.04	-4.96	2.47	-0.29	-0.65	2.23	2.94	0.70	185.39	11.27
123.2	2.897	3.387	4.317	5.085	0.533	0.149	2.52	3.29	198.97	-7.03	3.53	-0.39	-0.78	3.14	3.91	0.68	182.24	13.19
153.2	3.832	4.348	5.791	6.623	0.427	0.012	3.58	4.41	197.00	-8.99	4.56	-0.61	-1.03	4.27	5.10	0.66	178.82	15.36
183.0	4.477	5.012	6.833	7.712	0.345	-0.095	4.33	5.20	195.29	-10.70	5.48	-0.68	-1.12	5.01	5.89	0.65	176.23	17.05
203.0	4.820	5.364	7.395	8.299	0.345	-0.107	4.70	5.60	194.33	-11.66	6.00	-0.70	-1.15	5.39	6.30	0.64	174.94	17.91
213.0	4.965	5.507	7.634	8.539	0.339	-0.113	4.86	5.77									174.24	18.39
242.8	5.344	5.881	8.265	9.172	0.337	-0.117	5.29	6.19									172.29	19.73
252.8	5.469	6.003	8.475	9.380	0.319	-0.134	5.44	6.34									171.93	19.98
272.8	5.695	6.233	8.856	9.775	0.339	-0.120	5.68	6.60									171.21	20.49
302.1	5.988	6.535	9.354	10.297	0.332	-0.139	6.01	6.96									170.02	21.33
329.6	6.117	6.672	9.575	10.536	0.392	-0.089	6.12	7.08	190.62	-15.37	8.06						170.50	20.98
357.4	6.134	6.686	9.604	10.560	0.458	-0.020	6.10	7.05	190.34	-15.66	8.23						170.44	21.03
386.9	6.126	6.676	9.591	10.543	0.483	0.007	6.07	7.02	190.77	-15.22	7.98						170.40	21.06
417.2	6.108	6.655	9.560	10.506	0.578	0.105	5.99	6.93	190.45	-15.55	8.16						170.68	20.86
447.3	6.084	6.630	9.519	10.462	0.690	0.218	5.89	6.83	190.58	-15.42	8.09						170.83	20.75
502.1	6.055	6.592	9.469	10.396	0.790	0.327	5.79	6.71									171.31	20.41
506.8	6.056	6.593	9.471	10.398	0.793	0.330	5.79	6.71									171.15	20.53
510.6	6.057	6.591	9.472	10.394	0.822	0.361	5.77	6.69									171.24	20.47
515.1	6.059	6.596	9.476	10.403	0.834	0.370	5.76	6.69									171.13	20.54
518.7	6.061	6.597	9.479	10.405	0.845	0.382	5.76	6.68									171.10	20.56
522.3	6.062	6.598	9.481	10.407	0.842	0.380	5.76	6.68									171.05	20.60
532.5	6.067	6.608	9.490	10.424	0.886	0.419	5.74	6.67									170.97	20.66
542.3	6.071	6.610	9.496	10.428	0.910	0.445	5.72	6.66									170.98	20.65
552.5	6.076	6.615	9.505	10.436	0.936	0.471	5.71	6.64									170.94	20.68
562.8	6.081	6.617	9.514	10.440	0.979	0.516	5.69	6.62									170.89	20.71
572.7	6.087	6.624	9.524	10.452	1.004	0.540	5.68	6.61									170.83	20.75
582.9	6.092	6.631	9.532	10.464	1.034	0.568	5.67	6.60									170.86	20.73
592.6	6.097	6.637	9.541	10.475	1.049	0.582	5.66	6.60									170.75	20.81
603.0	6.103	6.641	9.551	10.482	1.043	0.578	5.67	6.60									170.65	20.88
612.7	6.108	6.645	9.560	10.489	1.077	0.613	5.66	6.58									170.58	20.93
622.8	6.115	6.648	9.572	10.494	1.102	0.641	5.65	6.57									170.60	20.91
632.6	6.120	6.656	9.580	10.508	1.152	0.688	5.62	6.55									170.58	20.93
640.0	6.125	6.663	9.589	10.520	1.169	0.703	5.61	6.54									170.67	20.86

Fig. 10.37: Triaxial test data of stress path test S2aT1 on natural Kloten clay: comparison of strain determination with various measurement methods.

Fig. 10.38: Triaxial test data of stress path test S2aT1 on natural Kloten clay: comparison of strain determination with various measurement methods.

Fig. 10.39: Laser scan data of the triaxial stress path test S2aT1 on natural Kloten clay: radius from laser 1.

Fig. 10.40:   Laser scan data of the triaxial stress path test S2aT1 on natural Kloten clay: radius from laser 2.
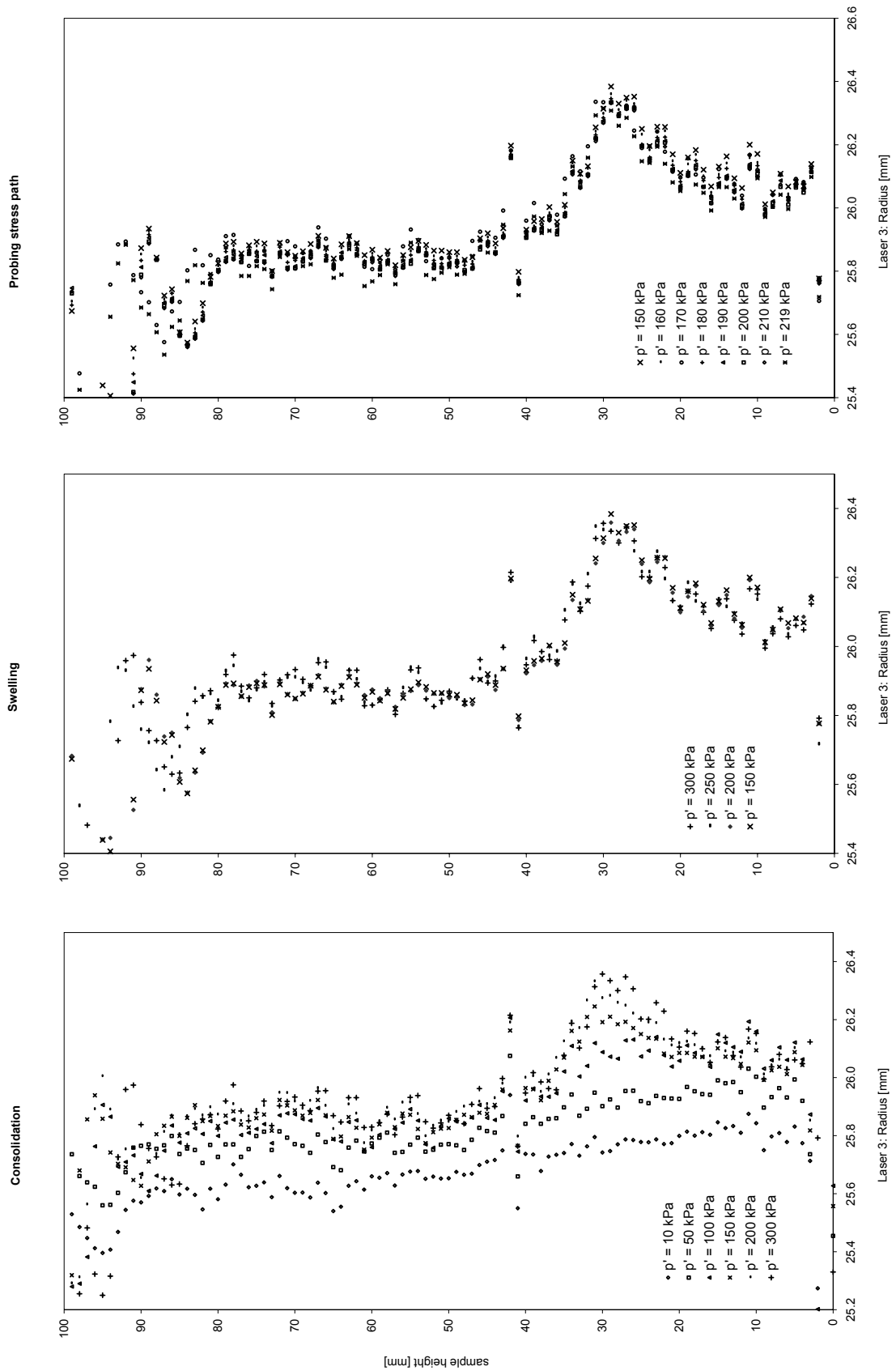
Fig. 10.41: Laser scan data of the triaxial stress path test S2aT1 on natural Kloten clay: radius from laser 3.
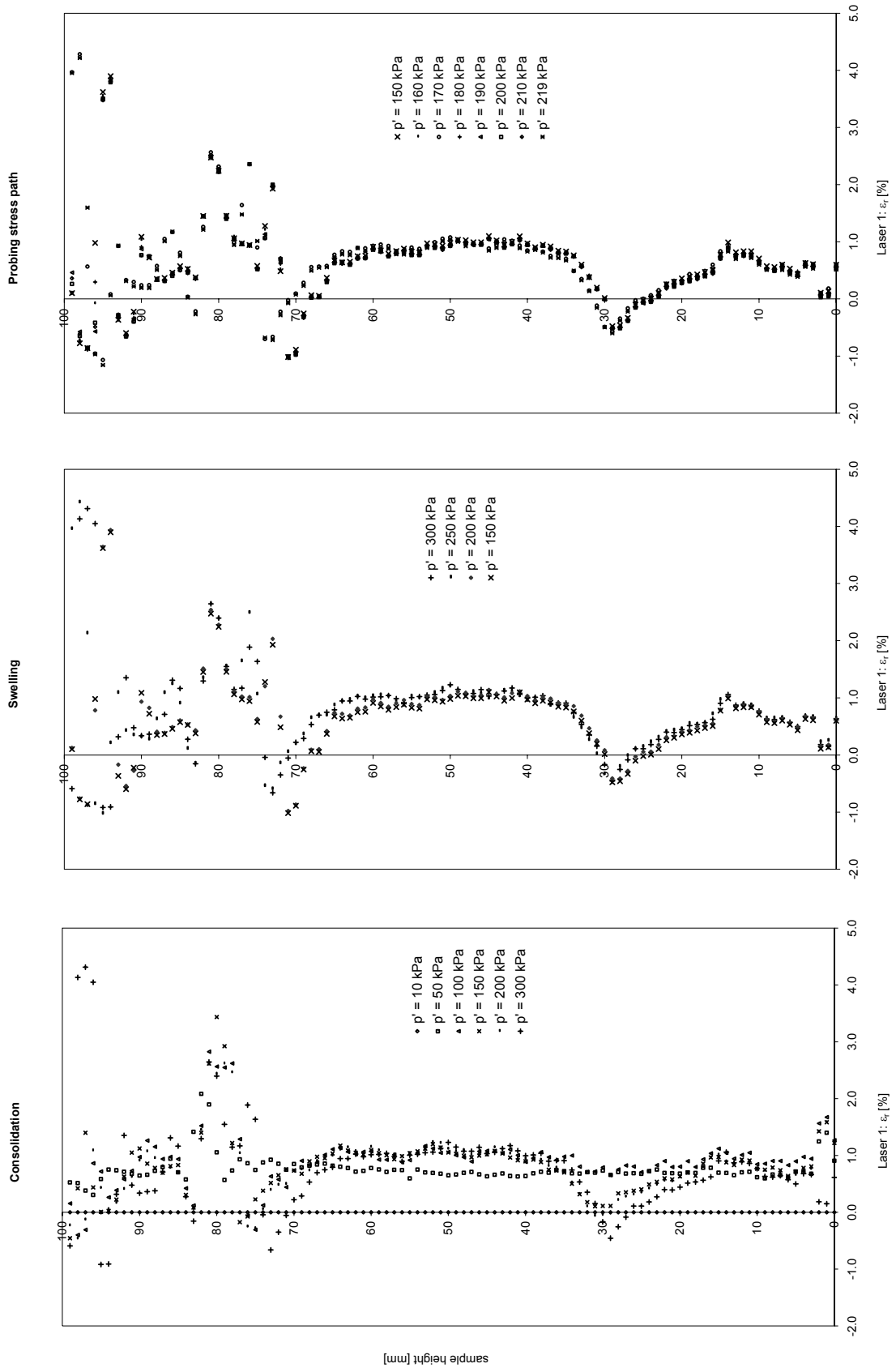
Fig. 10.42: Laser scan data of the triaxial stress path test S2aT1 on natural Kloten clay: radial strain from laser 1.
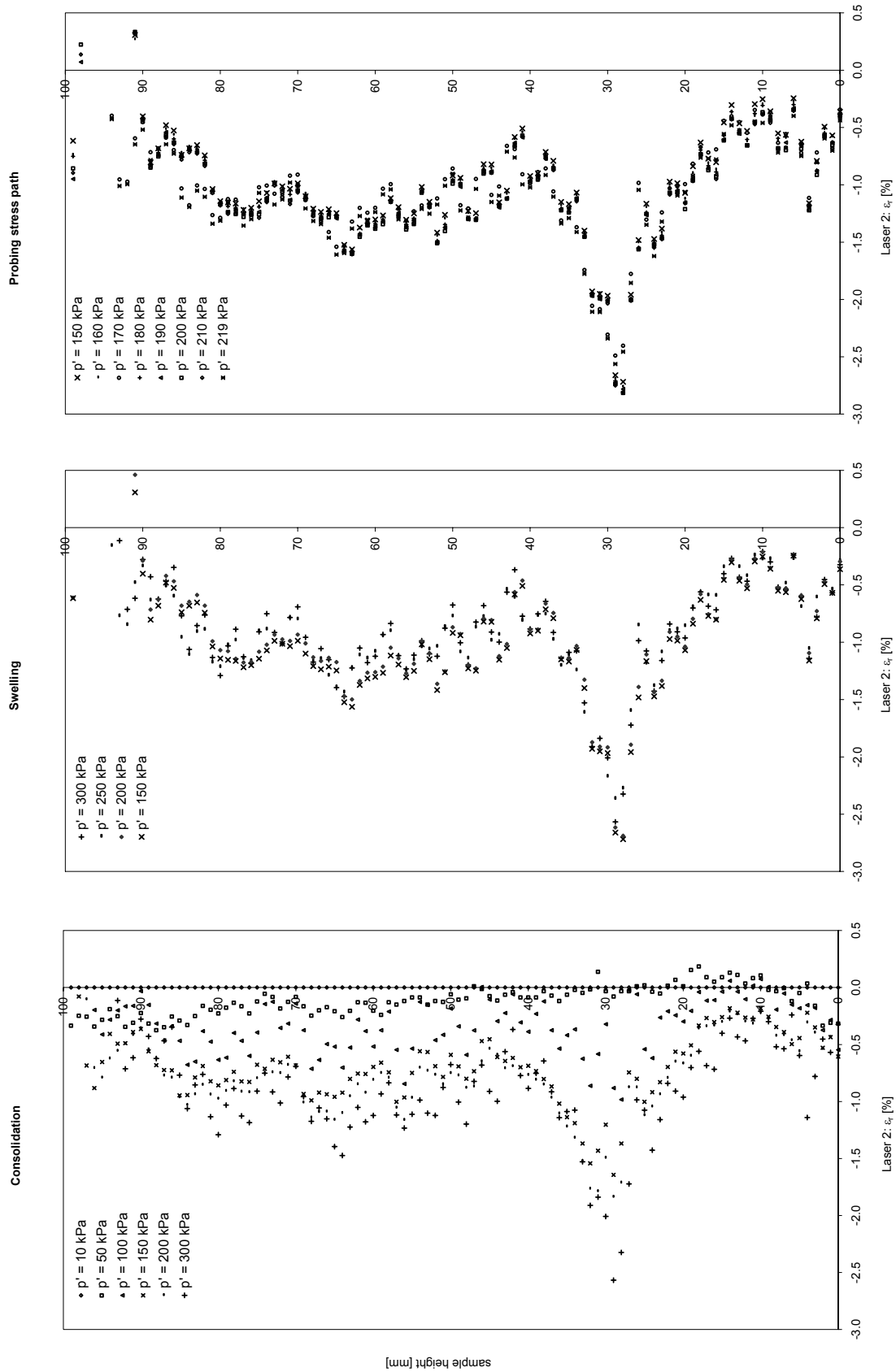
Fig. 10.43: Laser scan data of the triaxial stress path test S2aT1 on natural Kloten clay: radial strain from laser 2.
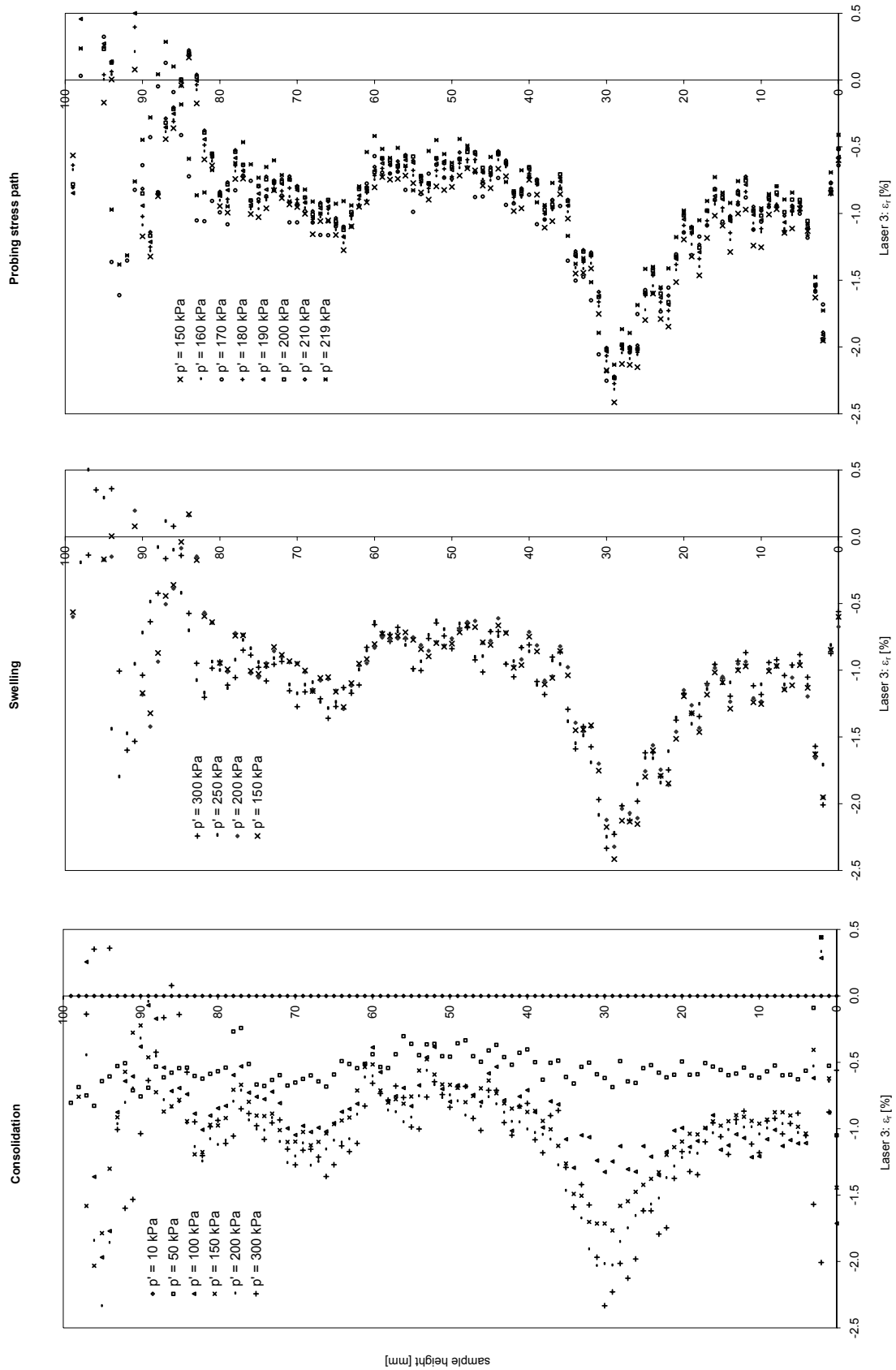
Fig. 10.44: Laser scan data of the triaxial stress path test S2aT1 on natural Kloten clay: radial strain from laser 3.
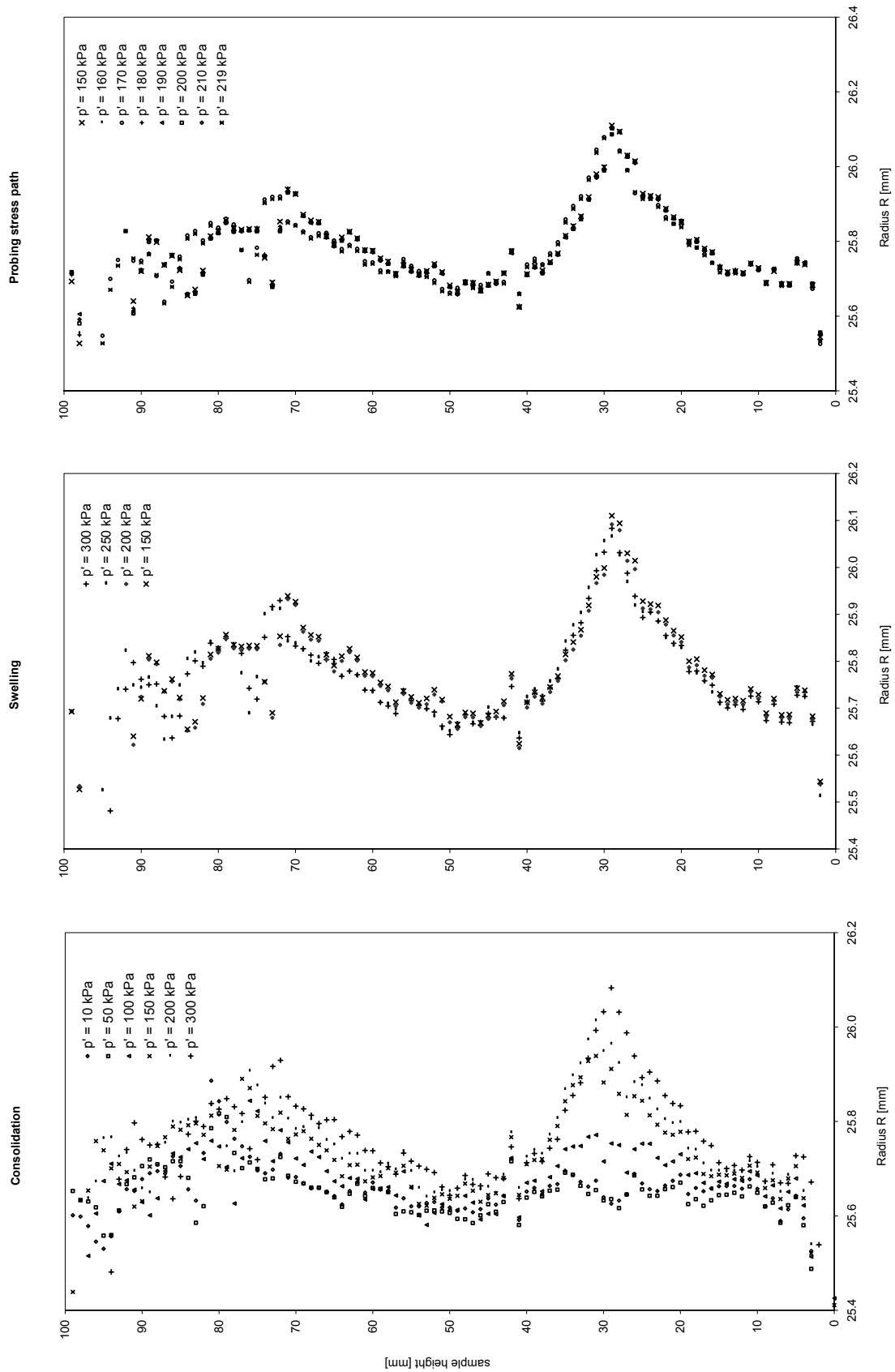
Fig. 10.45: Laser scan data of the triaxial stress path test S2aT1 on natural Kloten clay: radius determined with the circular slice approach.
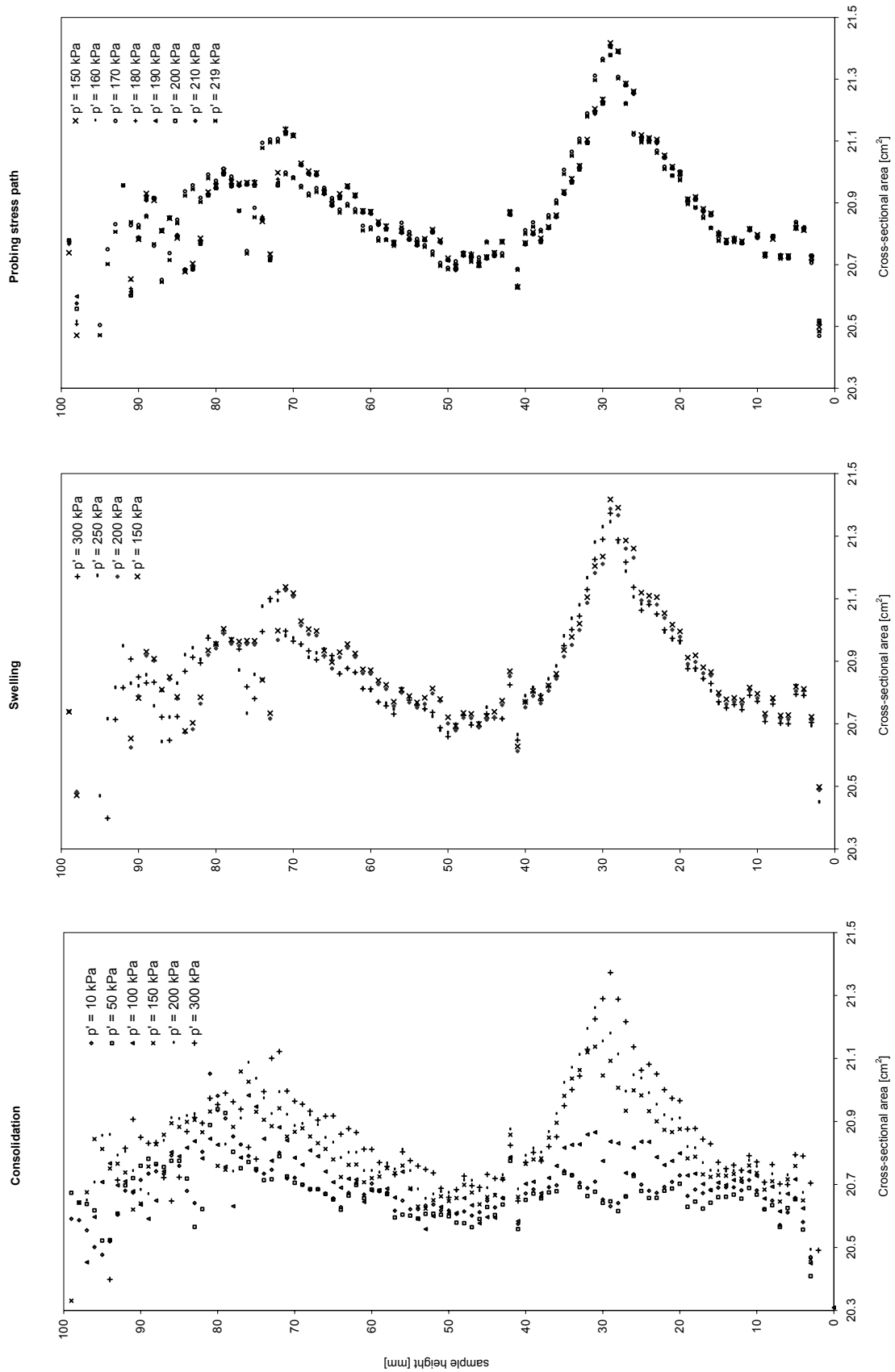
Fig. 10.46:   Laser scan data of the triaxial stress path test S2aT1 on natural Kloten clay:
cross-sectional area calculated from *R* (Fig. 10.45).
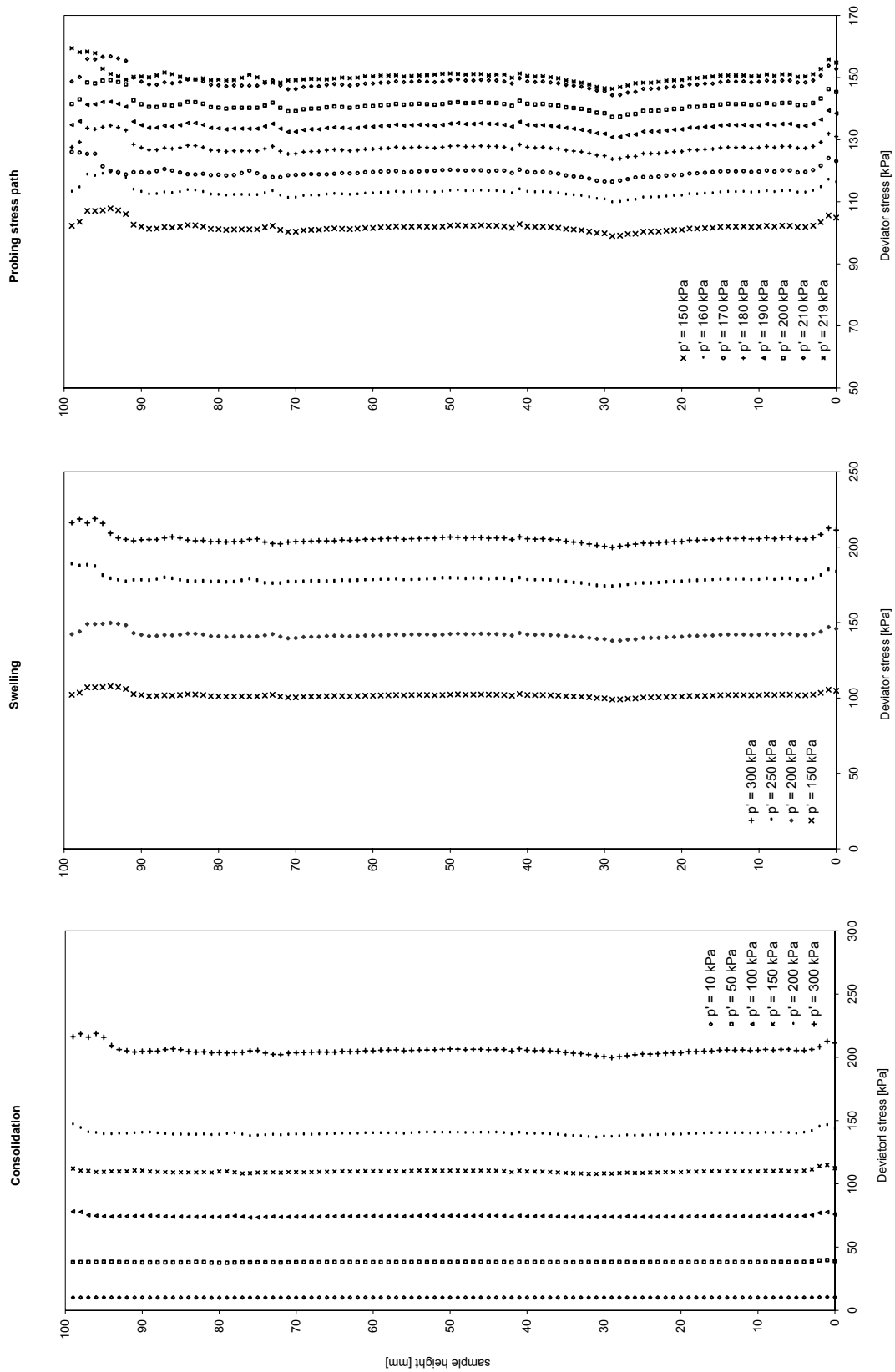
Fig. 10.47:   Laser scan data of the triaxial stress path test S2aT1 on natural Kloten clay:
change of deviator stress.
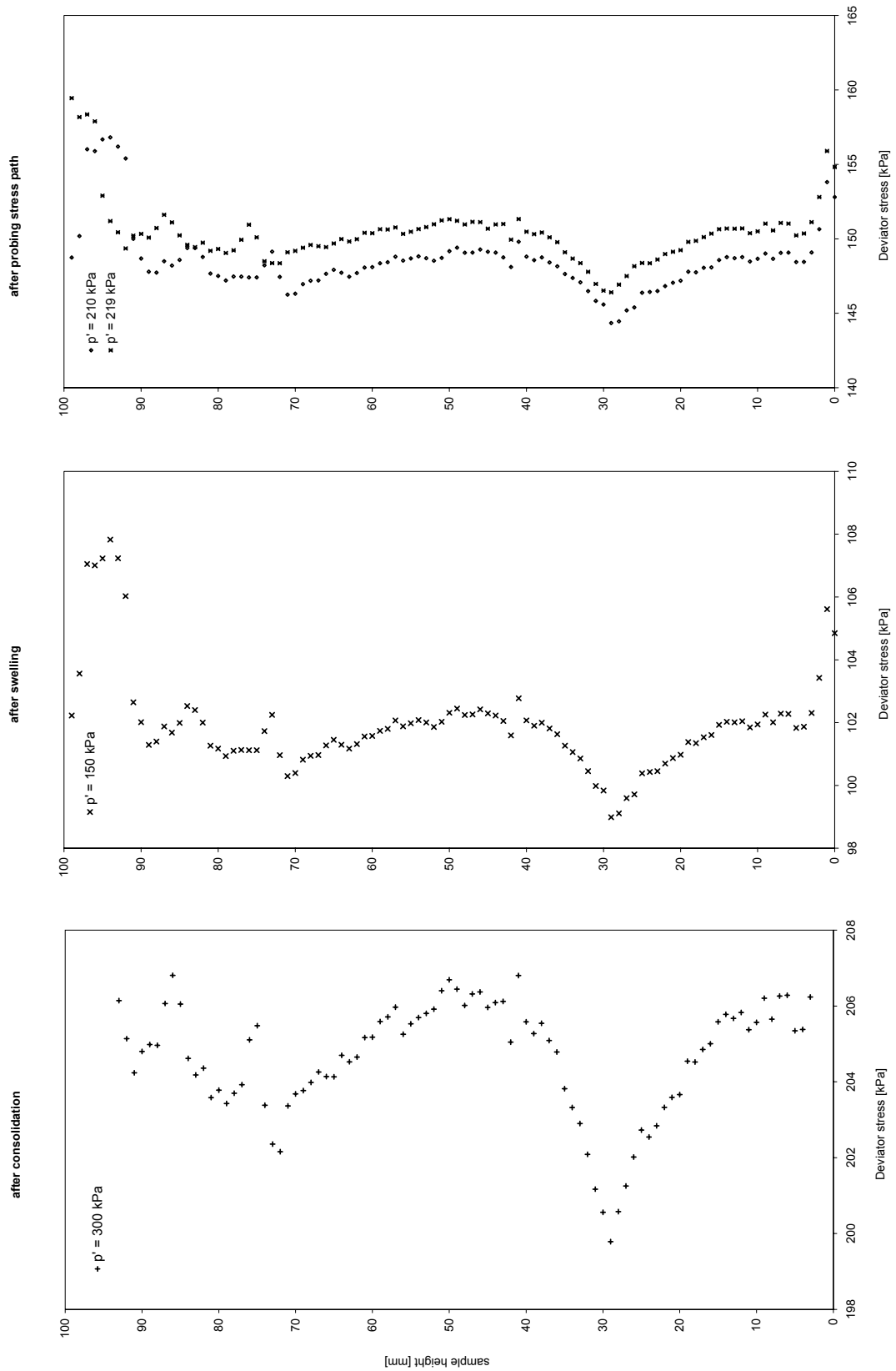
Fig. 10.48: Laser scan data of the triaxial stress path test S2aT1 on natural Kloten clay: change of deviator stress (enlarged scale).
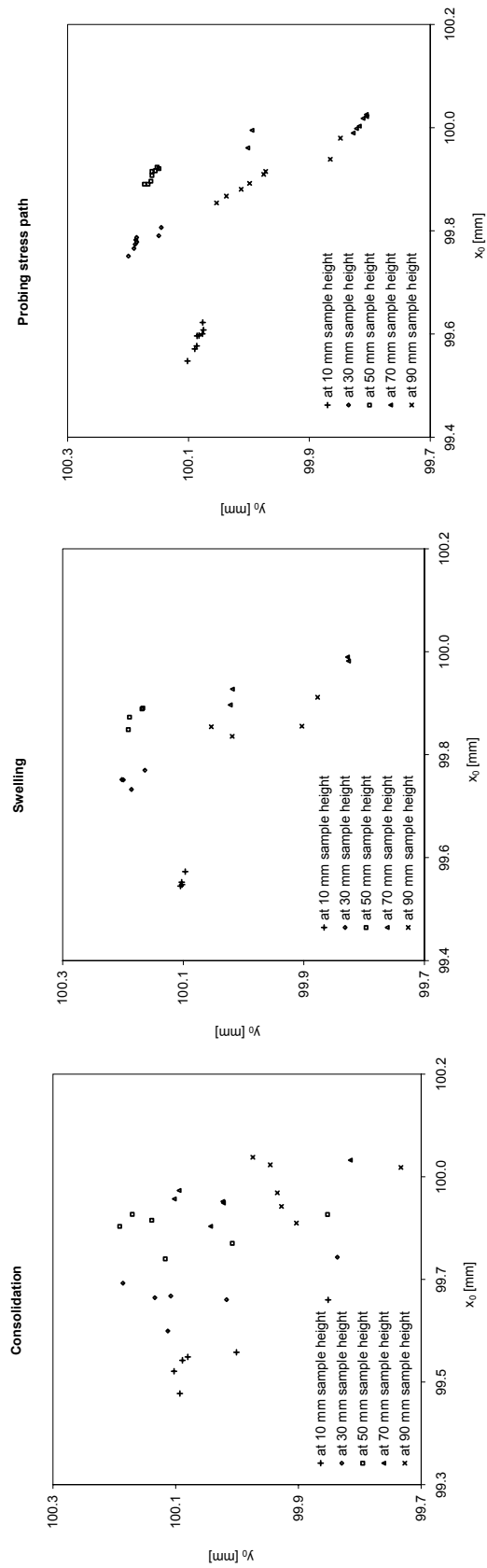
Fig. 10.49:   Laser scan data of centre of each disc for the triaxial stress path test S2aT1
on natural Kloten clay.
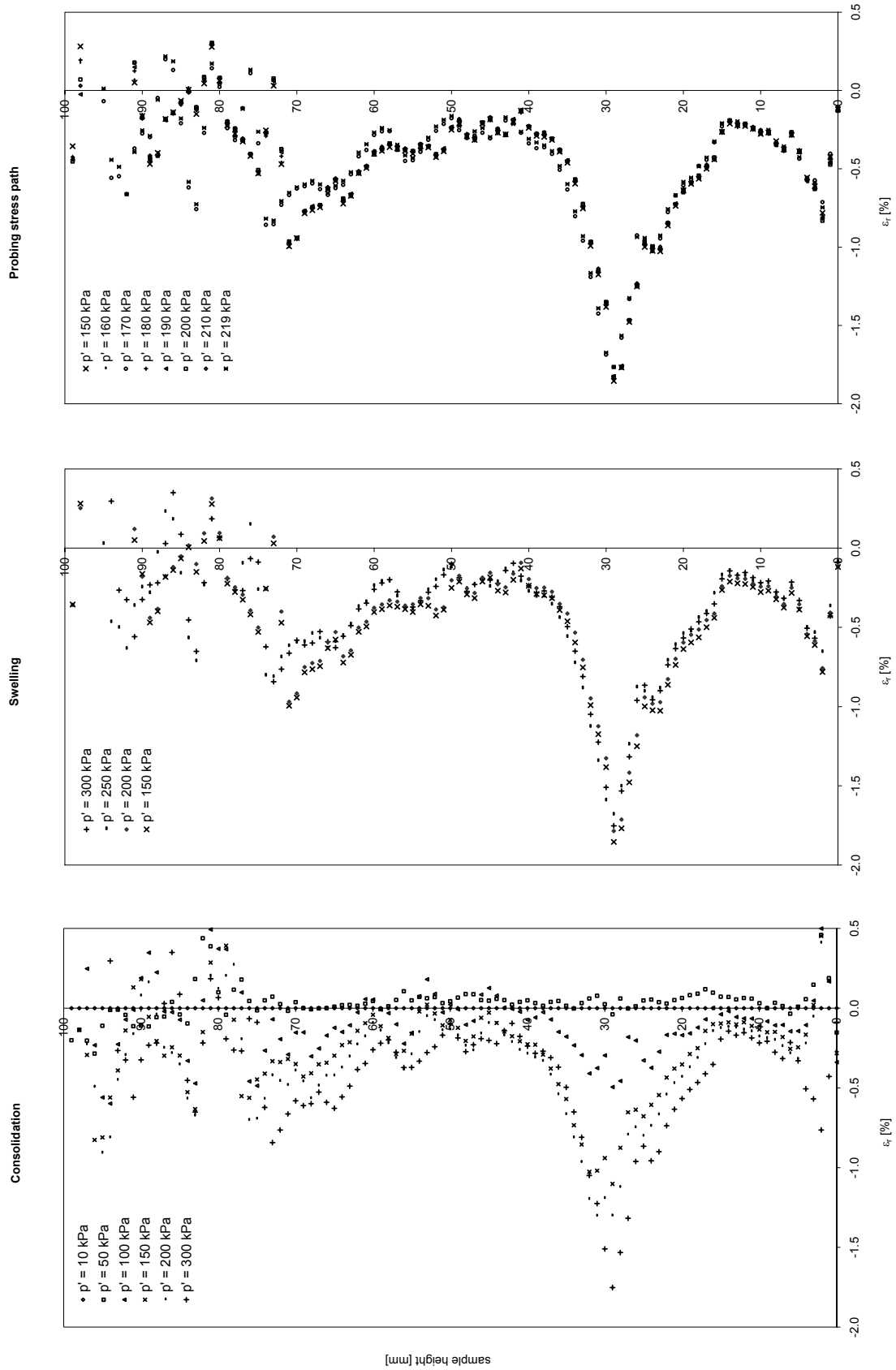
Fig. 10.50: Laser scan data of the triaxial stress path test S2aT1 on natural Kloten clay: radial strain calculated from *R* (Fig. 10.45).
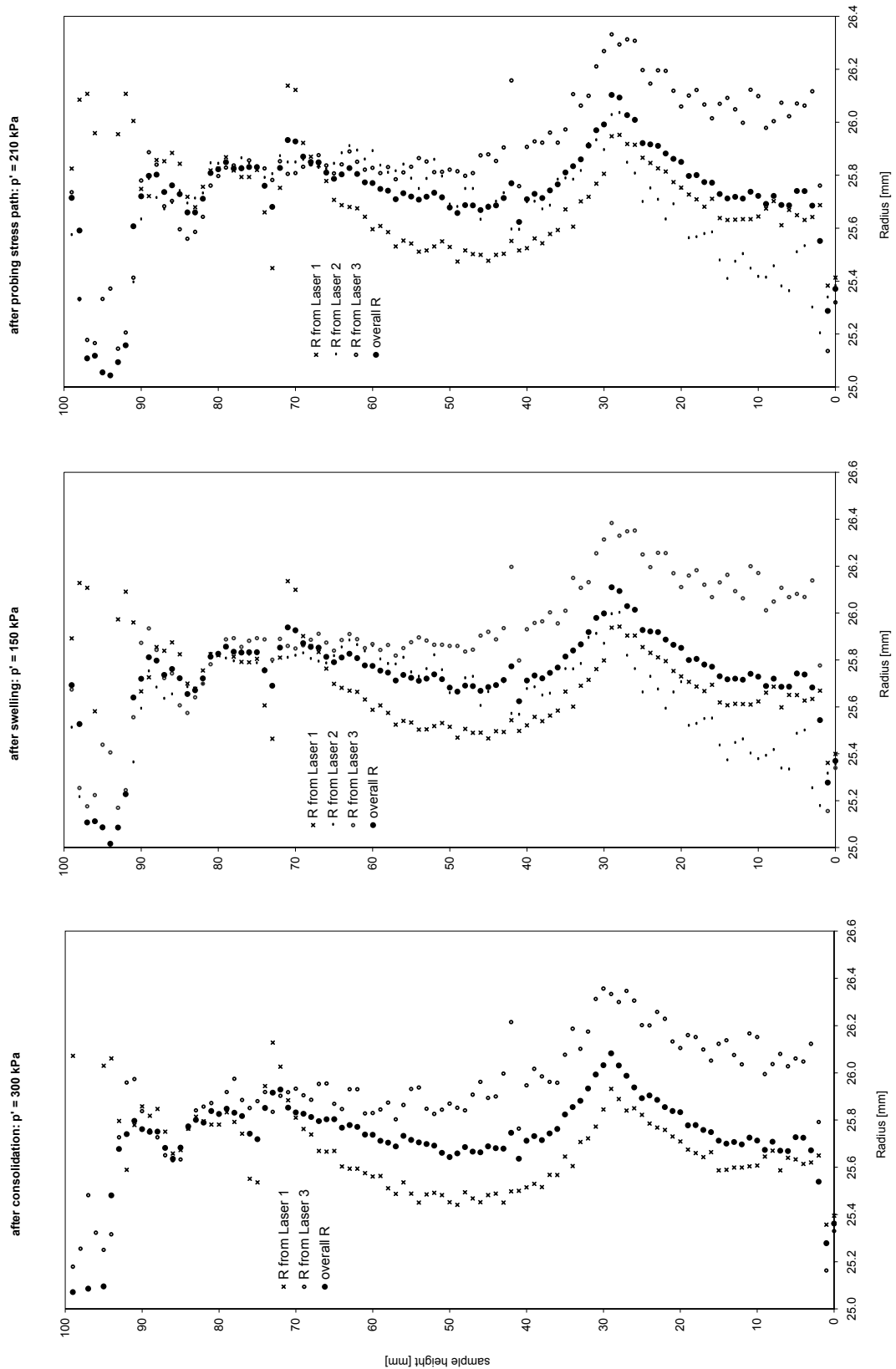
Fig. 10.51: Laser scan data of the triaxial stress path test S2aT1 on natural Kloten clay: comparison of radius determined from each laser together with the radius *R* determined from the circular slice approach.

Fig. 10.52:   Laser scan data of the triaxial stress path test S2aT1 on natural Kloten clay: between sample heights (from base) 20 – 30 mm.

Fig. 10.53: Laser scan data of the triaxial stress path test S2aT1 on natural Kloten clay: between sample heights (from base) 30 – 40 mm.

Fig. 10.54:   Laser scan data of the triaxial stress path test S2aT1 on natural Kloten clay: between sample heights (from base) 40 – 50 mm.

Fig. 10.55: Laser scan data of the triaxial stress path test S2aT1 on natural Kloten clay: between sample heights (from base) 50 – 60 mm.

Fig. 10.56: Laser scan data of the triaxial stress path test S2aT1 on natural Kloten clay: between sample heights (from base) 60 – 70 mm.

Fig. 10.57:   Laser scan data of the triaxial stress path test S2aT1 on natural Kloten clay: between sample heights (from base) 70 – 80 mm.

354

Triaxial Test   S2aT2

Test aim: Initial stiffness and stiffness degradation
Material number: 46862 Block sample of natural Kloten clay
Test apparatus: HIF B 24: Triax 2 (red)
File name: Serie4_Kloten_nat_cyl_rot.PRB
test start: 06.04.2004 20:52:26 test stop: 04.05.2004 11:17:02
Comments:

Measured sample data: **Determined sample data:** **Material parameter:**
Height H_0 106.67 [mm] Cross-sectional area: A 20.34 [cm^2] density ρ_s 2.77 [g/cm^3]
Diameter D 5.09 [cm] Volume: f(H_0, D) V_0 216.96 [cm^3] specific gravity of water ρ_w 1 [g/cm^3]
Weight m_f 441.06 [g] Water content w 26.71 [%]
  Volume: f(m_f, w, ρ_s, S_r=1) V_0 218.64 [cm^3]
  Void ratio: f(m_f, w, ρ_s, S_r=1) e_0 0.740 [-]

Test data:

test-time	dH	force	cell-pressure	PWP bottom	PWP top	dV backpr.	H_{act}	V_{act}	A_c	σ_a'	σ_r'	q	p'	ε_a	ε_r	ε_s	ε_v	e
[hours]	[mm]	[kN]	[kPa]	[kPa]	[kPa]	[ccm]	[mm]	[ccm]	[cm^2]	[kPa]	[kPa]	[kPa]	[kPa]	[%]	[%]	[%]	[%]	[-]
0.0	0.000	-0.001	54.816	49.628	48.460	0.000	106.70	218.64	20.33	5.3	5.8	-0.5	5.6	0.000	0.000	0.000	0.000	0.740
32.9	1.570	0.054	70.314	49.609	48.483	-1.832	105.13	216.80	20.46	47.7	21.3	26.4	30.1	1.493	-0.324	1.212	0.845	0.725
63.0	2.348	0.098	93.008	49.355	48.274	-3.280	104.35	215.36	20.47	92.1	44.2	47.9	60.2	2.250	-0.363	1.742	1.523	0.714
93.2	3.524	0.143	115.800	49.599	48.418	-5.119	103.18	213.52	20.53	136.5	66.8	69.7	90.0	3.416	-0.509	2.616	2.397	0.699
123.6	5.280	0.188	138.869	49.623	48.524	-7.474	101.42	211.16	20.65	180.8	89.8	91.0	120.1	5.206	-0.833	4.026	3.539	0.680
153.6	6.485	0.233	161.749	49.545	48.393	-9.146	100.22	209.49	20.73	225.2	112.8	112.4	150.2	6.471	-1.053	5.016	4.366	0.667
184.0	7.376	0.277	184.601	49.585	48.463	-10.663	99.32	207.97	20.76	269.0	135.6	133.4	180.0	7.426	-1.150	5.717	5.127	0.655
214.2	8.090	0.321	207.515	49.500	48.380	-11.670	98.61	206.97	20.81	312.8	158.6	154.2	210.0	8.204	-1.283	6.324	5.639	0.647
243.8	8.681	0.366	230.322	49.350	48.221	-12.492	98.02	206.14	20.85	357.0	181.5	175.5	240.0	8.856	-1.398	6.836	6.060	0.640
274.4	9.201	0.411	253.445	49.574	48.404	-13.337	97.50	205.30	20.88	401.3	204.5	196.9	270.1	9.437	-1.470	7.272	6.496	0.634
329.8	9.756	0.445	274.933	49.411	48.276	-13.976	96.94	204.66	20.93	438.7	226.1	212.6	297.0	10.064	-1.617	7.787	6.829	0.629
357.6	9.780	0.409	253.751	49.365	48.289	-14.132	96.92	204.50	20.92	400.4	204.9	195.5	270.1	10.091	-1.590	7.787	6.911	0.627
387.9	9.775	0.365	230.634	49.403	48.317	-14.253	96.93	204.38	20.91	356.4	181.8	174.6	240.0	10.085	-1.556	7.761	6.974	0.626
418.0	9.755	0.320	207.961	49.568	48.398	-14.268	96.95	204.37	20.90	312.1	159.0	153.1	210.0	10.062	-1.540	7.735	6.982	0.626
448.3	9.723	0.275	185.001	49.471	48.282	-14.217	96.98	204.42	20.90	267.7	136.1	131.6	180.0	10.026	-1.536	7.708	6.955	0.627
502.4	9.664	0.224	162.791	49.521	48.387	-13.972	97.04	204.66	20.91	220.9	113.8	107.1	149.5	9.959	-1.566	7.684	6.827	0.629
512.8	9.667	0.220	158.887	49.550	48.402	-13.867	97.03	204.77	20.92	215.1	109.9	105.1	145.0	9.963	-1.595	7.705	6.772	0.630
522.7	9.648	0.212	155.141	49.423	48.306	-13.721	97.05	204.92	20.94	207.5	106.3	101.3	140.0	9.941	-1.622	7.709	6.696	0.631
533.3	9.647	0.204	151.476	49.518	48.334	-13.595	97.05	205.04	20.95	199.9	102.6	97.4	135.0	9.940	-1.655	7.730	6.630	0.632
543.4	9.631	0.197	147.685	49.527	48.419	-13.598	97.07	205.04	20.94	192.8	98.7	94.1	130.1	9.922	-1.645	7.711	6.632	0.632
564.3	9.607	0.182	140.016	49.458	48.398	-13.490	97.09	205.15	20.95	178.0	91.1	86.9	120.0	9.895	-1.659	7.703	6.576	0.633
585.7	9.587	0.166	132.535	49.484	48.311	-13.248	97.11	205.39	20.97	162.8	83.6	79.2	110.0	9.872	-1.711	7.722	6.450	0.634
606.7	9.559	0.152	124.997	49.617	48.418	-13.023	97.14	205.61	20.99	148.4	76.0	72.4	100.1	9.840	-1.753	7.729	6.334	0.636
627.7	9.526	0.136	117.473	49.695	48.453	-12.884	97.17	205.75	21.00	133.2	68.4	64.8	90.0	9.803	-1.771	7.716	6.262	0.637
662.2	9.484	0.129	111.693	49.522	48.441	-12.600	97.22	206.04	21.02	124.1	62.7	61.4	83.2	9.756	-1.820	7.717	6.115	0.640

Fig. 10.58:   Triaxial test data of stress path test S2aT2 on natural Kloten clay.

Fig. 10.59: Triaxial test data of stress path test S2aT2 on natural Kloten clay.

Triaxial Test   S2aT3

Test aim: Initial stiffness and stiffness degradation
Material number: 46862   Block sample of natural Kloten clay
Test apparatus: HIF B 24: Triax 3 (yellow)
File name: Serie4_Kloten_nat_cyl_yellow.PRB
      test start: 06.04.2004   21:00:29   test stop: 04.05.2004   17:11:32
Comments:

Measured sample data: **Determined sample data:**   **Material parameter:**
Height H_0 112.47 [mm]   Cross-sectional area: A   20.34 [cm^2]   density ρ_s 2.77 [g/cm^3]
Diameter D   5.09 [cm]   Volume: f(H_0, D) V_0 228.76 [cm^3]   specific gravity of water ρ_w 1 [g/cm^3]
Weight m_f 424.05 [g]   Water content   w   25.93 [%]
                                            Volume: f(m_f, w, ρ_s, S_r=1) V_0 208.88 [cm^3]
                                            Void ratio: f(m_f, w, ρ_s, S_r=1) e_0 0.718 [-]

Test data:

test-time [hours]	dH [mm]	force [kN]	cell-pressure [kPa]	PWP bottom [kPa]	PWP top [kPa]	dV backpr. [ccm]	H_{act} [mm]	V_{act} [ccm]	A_c [cm^2]	σ_a' [kPa]	σ_r' [kPa]	q [kPa]	p' [kPa]	ε_a [%]	ε_r [%]	ε_s [%]	ε_v [%]	e [-]
0.0	0.000	0.005	54.831	50.925	53.325	0.000	112.50	208.88	20.33	5.2	2.7	2.5	3.5	0.000	0.000	0.000	0.000	0.718
35.5	1.671	0.059	72.162	50.662	52.902	-2.357	110.83	206.52	20.42	49.3	20.4	28.9	30.0	1.508	-0.183	1.127	1.141	0.699
65.4	2.411	0.103	94.666	50.366	52.600	-3.730	110.09	205.15	20.43	93.6	43.2	50.4	60.0	2.190	-0.186	1.584	1.818	0.688
96.2	3.787	0.149	117.638	50.671	52.936	-5.512	108.71	203.37	20.53	138.4	65.8	72.6	90.0	3.483	-0.386	2.580	2.711	0.673
126.5	5.492	0.195	140.573	50.877	53.165	-7.634	107.01	201.25	20.66	182.9	88.6	94.4	120.0	5.132	-0.670	3.868	3.793	0.655
157.2	6.628	0.239	163.222	50.482	52.815	-8.987	105.87	199.89	20.75	226.7	111.6	115.2	150.0	6.260	-0.882	4.762	4.496	0.644
188.0	7.485	0.283	186.472	50.505	52.826	-9.940	105.02	198.94	20.83	270.7	134.8	135.9	180.1	7.128	-1.065	5.462	4.997	0.636
218.3	8.166	0.330	209.224	50.677	52.975	-10.655	104.33	198.22	20.90	315.3	157.4	157.9	210.0	7.827	-1.226	6.035	5.375	0.631
243.1	8.731	0.375	232.048	50.539	52.917	-11.317	103.77	197.56	20.95	359.3	180.3	179.0	240.0	8.414	-1.343	6.504	5.728	0.625
273.6	9.223	0.420	255.350	50.830	53.149	-11.745	103.28	197.14	21.01	403.3	203.4	199.9	270.0	8.930	-1.486	6.944	5.958	0.622
324.0	9.677	0.445	274.577	50.461	52.835	-11.904	102.82	196.98	21.08	434.0	222.9	211.1	293.3	9.411	-1.684	7.397	6.043	0.620
348.4	9.700	0.414	256.152	50.284	52.654	-11.556	102.80	197.32	21.12	400.7	204.7	196.0	270.0	9.436	-1.790	7.484	5.856	0.623
378.5	9.693	0.370	233.401	50.433	52.777	-11.085	102.81	197.80	21.17	356.6	181.8	174.8	240.1	9.428	-1.912	7.560	5.604	0.627
408.9	9.677	0.325	210.936	50.702	53.047	-10.555	102.82	198.33	21.21	312.3	159.1	153.2	210.1	9.411	-2.045	7.637	5.322	0.631
439.1	9.649	0.281	187.752	50.594	52.963	-10.047	102.85	198.83	21.26	268.2	136.0	132.2	180.0	9.382	-2.164	7.697	5.053	0.636
496.4	9.595	0.224	162.764	50.476	52.861	-9.079	102.91	199.80	21.34	216.1	111.1	105.0	146.1	9.324	-2.390	7.809	4.544	0.644
500.5	9.600	0.235	160.829	50.658	53.076	-9.058	102.90	199.82	21.34	219.1	109.0	110.1	145.7	9.329	-2.398	7.819	4.533	0.644
508.9	9.604	0.246	158.644	50.575	52.916	-8.920	102.90	199.96	21.36	222.1	106.9	115.2	145.3	9.334	-2.436	7.847	4.461	0.645
518.0	9.607	0.257	155.888	50.369	52.803	-8.811	102.89	200.07	21.37	224.6	104.3	120.3	144.4	9.337	-2.466	7.869	4.404	0.646
525.9	9.618	0.268	153.966	50.865	53.238	-8.661	102.88	200.22	21.39	227.2	101.9	125.3	143.7	9.349	-2.511	7.907	4.326	0.647
534.5	9.627	0.279	151.532	50.513	52.962	-8.533	102.87	200.35	21.40	230.2	99.8	130.4	143.3	9.358	-2.549	7.938	4.259	0.648
543.2	9.637	0.290	149.066	50.337	52.705	-8.371	102.86	200.51	21.42	232.9	97.5	135.4	142.7	9.369	-2.597	7.977	4.175	0.649
550.4	9.655	0.300	147.165	50.694	53.073	-8.271	102.85	200.61	21.43	235.3	95.3	140.0	141.9	9.388	-2.633	8.014	4.123	0.650
559.2	9.672	0.311	144.653	50.516	52.863	-8.129	102.83	200.75	21.45	238.0	93.0	145.1	141.3	9.406	-2.678	8.056	4.049	0.651
567.3	9.698	0.322	142.166	50.406	52.789	-7.975	102.80	200.91	21.47	240.5	90.6	150.0	140.6	9.434	-2.732	8.110	3.970	0.653
576.2	9.748	0.334	139.801	50.623	53.001	-7.791	102.75	201.09	21.50	243.3	88.0	155.4	139.8	9.487	-2.806	8.195	3.875	0.654
584.7	9.809	0.345	137.589	50.468	52.858	-7.563	102.69	201.32	21.53	246.1	85.9	160.2	139.3	9.552	-2.898	8.300	3.757	0.656
592.8	9.935	0.356	135.315	50.523	52.885	-7.336	102.57	201.54	21.58	248.6	83.6	165.0	138.6	9.687	-3.023	8.473	3.640	0.658
600.9	10.448	0.367	133.066	50.638	53.058	-6.934	102.05	201.95	21.73	250.1	81.2	168.9	137.5	10.238	-3.402	9.093	3.434	0.661
603.5	13.890	0.368	132.391	50.665	53.096	-6.613	98.61	202.27	22.52	243.9	80.5	163.4	135.0	14.086	-5.408	12.996	3.269	0.664
604.1	19.019	0.370	132.213	50.502	52.853	-6.600	93.48	202.28	23.76	236.3	80.5	155.7	132.4	20.345	-8.541	19.258	3.263	0.664

Fig. 10.60:   Triaxial test data of stress path test S2aT3 on natural Kloten clay.

Fig. 10.61: Triaxial test data of stress path test S2aT3 on natural Kloten clay.

Triaxial Test S2aT4

Test aim: Initial stiffness and stiffness degradation
Material number: 46862 Block sample of natural Kloten clay
Test apparatus: HIL B 58: Triax 4 (blue)
File name: Serie4_Kloten_nat_cyl_blau_backpressure.PRB
 test start: 06.04.2004 21:04:46 test stop: 17.05.2004 16:45:09
Comments: Electricity supply stopped during reloading. This resulted in the kink in the reloading stress path in the q - p' plot just below the p' axis.

Measured sample data:

Height H_0	118.23	[mm]
Diameter D	5.67	[cm]
Weight m_f	609.06	[g]

Determined sample data:

Cross-sectional area:	A	25.27	[cm^2]
Volume: f(H_0, D)	V_0	298.74	[cm^3]
Water content	w	26.48	[%]
Volume: f(m_f, w, ρ_s, S_r=1)	V_0	301.36	[cm^3]
Void ratio: f(m_f, w, ρ_s, S_r=1)	e_0	0.733	[-]

Material parameter:

density	ρ_s	2.77	[g/cm^3]
specific gravity of water	ρ_w	1	[g/cm^3]

Test data:

test-time	dH	force	cell-pressure	PWP bottom	PWP top	dV backpr.	H_{act}	V_{act}	A_c	σ_a'	σ_r'	q	p'	ε_a	ε_r	ε_s	ε_v	e
[hours]	[mm]	[kN]	[kPa]	[kPa]	[kPa]	[ccm]	[mm]	[ccm]	[cm^2]	[kPa]	[kPa]	[kPa]	[kPa]	[%]	[%]	[%]	[%]	[-]
0.0	0.000	-0.018	54.230	49.945	47.873	0.000	118.10	301.36	25.25	-1.8	5.3	-7.1	2.9	0.000	0.000	0.000	0.000	0.733
27.5	1.352	0.032	74.675	49.986	47.995	-3.554	116.75	297.80	24.98	38.5	25.7	12.8	30.0	1.158	0.018	0.760	1.193	0.713
57.4	2.204	0.088	97.144	49.956	47.958	-5.255	115.90	296.10	24.85	83.6	48.2	35.4	60.0	1.902	-0.063	1.310	1.775	0.703
87.4	3.333	0.144	119.467	49.936	47.920	-7.075	114.77	294.28	24.72	128.8	70.5	58.3	90.0	2.904	-0.250	2.103	2.404	0.693
116.9	5.003	0.200	141.611	49.806	47.723	-9.546	113.10	291.81	24.55	174.3	92.8	81.5	120.0	4.424	-0.576	3.333	3.271	0.679
146.6	6.365	0.255	163.916	49.817	47.687	-11.739	111.74	289.62	24.39	219.7	115.2	104.6	150.0	5.697	-0.822	4.345	4.053	0.666
176.2	7.376	0.313	186.348	50.046	47.859	-13.262	110.72	288.09	24.28	266.3	137.4	128.9	180.4	6.662	-1.029	5.127	4.603	0.657
205.4	8.172	0.366	208.167	49.727	47.507	-14.637	109.93	286.72	24.18	310.9	159.6	151.4	210.0	7.434	-1.164	5.732	5.105	0.649
235.0	8.837	0.422	230.391	49.889	47.580	-15.795	109.26	285.56	24.09	356.8	181.7	175.2	240.0	8.088	-1.278	6.244	5.531	0.643
264.5	9.412	0.477	252.531	49.875	47.588	-16.753	108.69	284.60	24.02	402.4	203.8	198.6	270.0	8.660	-1.387	6.698	5.886	0.637
330.0	10.308	0.561	274.944	49.870	47.495	-17.791	107.79	283.57	23.95	460.5	226.3	234.2	304.3	9.563	-1.645	7.472	6.274	0.631
363.7	10.367	0.497	249.620	49.875	47.522	-17.641	107.73	283.72	23.97	408.3	200.9	207.4	270.0	9.623	-1.703	7.550	6.218	0.632
393.2	10.363	0.442	227.374	49.895	47.490	-17.431	107.74	283.83	23.98	363.0	178.7	184.3	240.1	9.619	-1.740	7.572	6.139	0.633
422.9	10.344	0.386	205.025	49.913	47.395	-17.529	107.76	283.83	23.98	317.4	156.4	161.0	210.0	9.599	-1.712	7.541	6.176	0.633
452.7	10.311	0.330	182.713	49.870	47.202	-17.681	107.79	283.68	23.96	271.9	134.2	137.7	180.1	9.566	-1.667	7.488	6.233	0.632
502.6	10.275	0.280	162.813	49.858	46.915	-17.675	107.83	283.68	23.96	231.3	114.4	116.9	153.4	9.529	-1.649	7.452	6.231	0.632
507.5	10.274	0.270	164.055	49.989	46.901	-17.659	107.83	283.70	23.96	228.3	115.6	112.7	153.2	9.528	-1.652	7.453	6.225	0.632
511.5	10.274	0.264	165.204	49.936	46.725	-17.680	107.83	283.68	23.96	227.1	116.9	110.2	153.6	9.528	-1.648	7.451	6.232	0.632
518.7	10.269	0.252	167.107	49.818	46.208	-17.675	107.83	283.68	23.96	224.3	119.1	105.2	154.2	9.523	-1.646	7.446	6.231	0.632
525.4	10.266	0.240	169.031	49.844	45.779	-17.681	107.83	283.68	23.96	221.4	121.2	100.2	154.6	9.520	-1.644	7.443	6.233	0.632
532.7	10.264	0.228	171.080	49.884	45.186	-17.725	107.84	283.63	23.96	218.7	123.5	95.2	155.3	9.518	-1.634	7.435	6.249	0.632
539.8	10.257	0.216	172.978	49.814	44.310	-17.717	107.84	283.64	23.96	216.1	125.9	90.2	156.0	9.511	-1.632	7.429	6.246	0.632
547.5	10.252	0.204	175.116	49.806	43.637	-17.687	107.85	283.67	23.96	213.5	128.4	85.1	156.8	9.506	-1.636	7.428	6.235	0.632
554.7	10.249	0.192	177.162	49.873	43.369	-17.784	107.85	283.57	23.95	210.7	130.5	80.2	157.3	9.503	-1.616	7.412	6.272	0.631
569.0	10.236	0.168	181.154	49.779	42.351	-17.786	107.86	283.57	23.95	205.2	135.1	70.1	158.5	9.490	-1.609	7.399	6.272	0.631
583.1	10.225	0.144	185.100	49.889	41.460	-17.754	107.88	283.60	23.95	199.5	139.4	60.1	159.5	9.479	-1.609	7.392	6.260	0.631
612.0	10.188	0.096	193.126	49.831	39.799	-17.671	107.91	283.69	23.96	188.4	148.3	40.1	161.7	9.441	-1.606	7.365	6.229	0.632
640.5	10.133	0.048	201.042	49.893	38.974	-17.563	107.97	283.85	23.97	176.6	156.6	20.0	163.3	9.385	-1.598	7.322	6.189	0.632
669.6	10.062	0.000	209.221	49.855	38.289	-17.504	108.04	283.85	23.97	165.1	165.1	0.0	165.1	9.313	-1.573	7.258	6.167	0.633
698.2	9.962	-0.048	217.201	49.960	38.065	-17.453	108.14	283.90	23.97	153.2	173.2	-20.0	166.5	9.212	-1.532	7.163	6.147	0.633
734.3	9.769	-0.104	228.178	49.948	37.857	-17.503	108.33	283.85	25.91	144.1	184.3	-40.1	170.9	9.018	-1.426	6.962	6.166	0.633
764.5	9.513	-0.155	236.635	49.806	37.732	-17.618	108.59	283.74	25.84	132.9	192.9	-60.0	172.9	8.761	-1.276	6.691	6.209	0.632
794.6	9.108	-0.206	244.978	49.860	37.753	-17.939	108.99	283.42	25.71	121.1	201.2	-80.1	174.5	8.357	-1.014	6.247	6.329	0.630
824.9	8.434	-0.256	253.413	49.942	37.909	-18.289	109.67	283.07	25.52	109.2	209.5	-100.3	176.1	7.691	-0.615	5.537	6.461	0.628
853.5	7.300	-0.303	261.415	49.232	38.182	-18.721	110.80	282.64	25.22	97.6	217.7	-120.1	177.7	6.588	0.018	4.380	6.624	0.626
878.5	5.088	-0.346	268.243	49.886	40.634	-19.259	113.01	282.10	24.68	82.8	223.0	-140.2	176.3	4.502	1.162	2.227	6.827	0.623
898.1	0.194	-0.378	273.753	49.934	42.302	-19.571	117.91	281.79	23.63	67.7	227.6	-160.0	174.3	0.165	3.390	-2.151	6.945	0.621
904.8	-3.397	-0.390	275.624	49.802	42.776	-19.413	121.50	281.94	22.95	59.4	229.3	-170.0	172.7	-2.796	4.841	-5.091	6.885	0.622
907.9	-9.526	-0.392	276.584	50.053	43.362	-19.200	127.63	282.16	21.86	50.6	229.9	-179.3	170.1	-7.464	7.134	-9.732	6.805	0.623
908.0	-12.914	-0.376	277.084	49.873	43.164	-19.181	131.01	282.18	21.30	54.0	230.6	-176.6	171.7	-9.857	8.327	-12.123	6.798	0.623
908.1	-20.212	-0.217	276.273	49.969	43.268	-19.253	138.31	282.10	20.17	122.1	229.7	-107.6	193.8	-14.613	10.719	-16.888	6.825	0.623

Fig. 10.62: Triaxial test data of stress path test S2aT4 on natural Kloten clay.

Fig. 10.63:   Triaxial test data of stress path test S2aT4 on natural Kloten clay.

Triaxial Test   S2bT1

Test aim: Initial stiffness and stiffness degradation
Material number: 46862   Block sample of natural Kloten clay
Test apparatus: HIF B 24: Triax 1 (green)
File name: S5_1_kons; S5_1_unl; S5_1_rel
  test start: 02.07.2004   15:24:07   test stop: 11.08.2004   08:27:42
Comments:

Measured sample data:

Height H_0	101.53	[mm]
Diameter D	5.08	[cm]
Weight m_f	418.37	[g]

Determined sample data:

Cross-sectional area:	A	20.29	[cm²]
Volume: $f(H_0, D)$	V_0	206.03	[cm³]
Water content	w	26	[%]
Volume: $f(m_f, w, \rho_s, S_r=1)$	V_0	206.20	[cm³]
Void ratio: $f(m_f, w, \rho_s, S_r=1)$	e_0	0.720	[-]

Material parameter:

density	ρ_s	2.77	[g/cm³]
specific gravity of water	ρ_w	1	[g/cm³]

Test data:

test-time [hours]	dH [mm]	force [kN]	cell-pressure [kPa]	PWP bottom [kPa]	PWP top [kPa]	dV backpr. [ccm]	H_{act} [mm]	V_{act} [ccm]	A_c [cm²]	σ_a' [kPa]	σ_r' [kPa]	q [kPa]	p' [kPa]	ε_a [%]	ε_r [%]	ε_s [%]	ε_v [%]	e [-]
0.0	0.000	0.009	205.040	200.182	199.516	0.000	101.53	206.20	20.29	9.6	5.2	4.4	6.7	0.000	0.000	0.000	0.000	0.720
23.2	0.742	0.043	223.058	200.352	199.725	-2.580	100.79	203.62	20.19	44.3	23.0	21.3	30.1	0.736	0.265	0.314	1.267	0.699
53.4	1.503	0.088	245.634	200.191	199.611	-4.207	100.03	201.99	20.18	89.3	45.7	43.6	60.3	1.503	0.290	0.808	2.083	0.685
83.0	2.267	0.132	268.254	200.081	199.501	-5.739	99.26	200.46	20.18	133.9	68.5	65.4	90.3	2.284	0.290	1.330	2.863	0.672
93.0	2.578	0.146	275.639	200.043	199.347	-6.379	98.95	199.82	20.18	148.3	75.9	72.4	100.1	2.605	0.294	1.541	3.192	0.667
112.8	3.421	0.176	290.831	200.047	199.437	-7.864	98.11	198.34	20.20	178.2	91.1	87.1	120.1	3.487	0.239	2.165	3.965	0.655
143.4	4.594	0.221	313.914	200.069	199.326	-9.914	96.94	196.29	20.23	223.4	114.2	109.2	150.6	4.739	0.156	3.056	5.051	0.637
173.2	5.461	0.265	336.366	200.032	199.382	-11.461	96.07	194.74	20.26	267.5	136.7	130.8	180.3	5.684	0.100	3.723	5.885	0.625
193.0	5.961	0.294	351.521	200.069	199.435	-12.299	95.57	193.90	20.27	296.8	151.8	145.0	200.1	6.237	0.053	4.123	6.343	0.618
203.0	6.185	0.309	359.222	200.081	199.480	-12.629	95.35	193.57	20.29	311.8	159.4	152.3	210.2	6.487	0.019	4.312	6.524	0.615
233.0	6.754	0.354	381.772	200.012	199.367	-13.747	94.78	192.45	20.29	356.5	182.1	174.5	240.2	7.126	0.008	4.745	7.143	0.606
243.0	6.924	0.369	389.349	200.014	199.342	-14.084	94.61	192.12	20.29	371.5	189.7	181.8	250.3	7.319	0.006	4.875	7.331	0.603
263.0	7.237	0.398	404.523	200.063	199.413	-14.660	94.29	191.54	20.30	400.7	204.8	196.1	270.1	7.675	-0.011	5.124	7.654	0.598
402.6	8.021	0.442	424.759	199.962	199.324	-16.469	93.51	189.73	20.27	443.1	225.1	218.0	297.8	8.578	0.051	5.684	8.680	0.583
430.0	8.023	0.401	404.405	200.313	199.707	-16.520	93.51	189.68	20.27	402.2	204.4	197.8	270.3	8.580	0.065	5.677	8.709	0.582
450.0	8.002	0.371	388.852	200.072	199.467	-16.631	93.53	189.57	20.25	372.3	189.1	183.2	250.1	8.556	0.109	5.631	8.773	0.581
460.2	7.979	0.356	381.143	199.963	199.236	-16.589	93.55	189.61	20.25	357.3	181.5	175.8	240.1	8.529	0.110	5.613	8.749	0.582
489.8	7.976	0.312	358.617	200.099	199.521	-16.726	93.55	189.47	20.24	313.0	158.8	154.2	210.2	8.526	0.151	5.583	8.828	0.581
499.8	7.958	0.297	351.051	199.968	199.271	-16.736	93.57	189.46	20.23	298.2	151.4	146.8	200.4	8.505	0.164	5.560	8.834	0.581
519.8	7.956	0.268	335.995	199.936	199.333	-16.667	93.57	189.53	20.24	268.4	136.4	132.4	180.5	8.502	0.146	5.571	8.794	0.581
593.2	7.901	0.220	312.436	200.005	199.370	-16.908	93.63	189.29	20.20	221.7	112.7	108.9	149.0	8.439	0.247	5.461	8.932	0.579
595.7	7.889	0.215	313.535	200.070	199.501	-16.951	93.64	189.25	20.19	220.2	113.7	106.5	149.2	8.425	0.266	5.439	8.957	0.579
598.2	7.880	0.211	313.908	200.031	199.376	-16.948	93.65	189.25	20.19	218.7	114.2	104.5	149.0	8.414	0.271	5.429	8.955	0.579
602.2	7.866	0.202	315.755	200.142	199.445	-16.959	93.66	189.24	20.19	216.0	116.0	100.1	149.3	8.398	0.282	5.411	8.962	0.579
607.2	7.878	0.192	317.250	199.855	199.226	-16.989	93.65	189.21	20.19	212.8	117.7	95.1	149.4	8.412	0.283	5.419	8.979	0.578
612.2	7.886	0.182	318.875	200.273	199.635	-17.015	93.64	189.19	20.19	209.1	118.9	90.2	149.0	8.421	0.286	5.423	8.994	0.578
617.2	7.875	0.173	320.554	200.055	199.411	-17.067	93.66	189.13	20.18	206.6	120.8	85.7	149.4	8.409	0.308	5.401	9.024	0.578
622.2	7.853	0.163	322.169	200.073	199.377	-17.070	93.68	189.13	20.17	203.2	122.4	80.8	149.4	8.383	0.321	5.375	9.026	0.578
632.7	7.844	0.142	326.044	200.098	199.458	-17.132	93.69	189.07	20.17	196.7	126.3	70.4	149.7	8.373	0.344	5.352	9.061	0.577
643.7	7.814	0.121	329.341	200.284	199.652	-17.160	93.72	189.04	20.16	189.4	129.4	60.0	149.4	8.338	0.370	5.312	9.077	0.577
653.7	7.786	0.101	332.751	200.043	199.370	-17.206	93.74	188.99	20.15	183.2	133.0	50.1	149.8	8.306	0.399	5.271	9.104	0.577
663.7	7.787	0.081	335.794	200.139	199.568	-17.244	93.74	188.96	20.14	176.2	135.9	40.2	149.3	8.307	0.410	5.265	9.126	0.576
683.7	7.706	0.041	342.717	200.061	199.472	-17.278	93.82	188.92	20.12	163.3	143.0	20.4	149.7	8.213	0.466	5.165	9.146	0.576
704.7	7.597	0.001	349.815	200.113	199.539	-17.482	93.93	188.72	20.08	150.5	150.0	0.5	150.2	8.088	0.588	5.000	9.264	0.574
719.7	7.401	-0.040	356.866	200.166	199.648	-17.733	94.13	188.47	20.01	137.0	157.0	-20.0	150.3	7.863	0.773	4.726	9.409	0.572
740.2	7.037	-0.080	363.635	200.108	199.393	-17.938	94.49	188.26	19.91	123.7	163.9	-40.2	150.5	7.447	1.041	4.271	9.528	0.571
760.2	6.386	-0.119	370.103	200.189	199.513	-18.360	95.14	187.84	19.73	109.9	170.3	-60.3	150.1	6.712	1.531	3.454	9.774	0.567
778.7	5.147	-0.156	376.491	200.099	199.493	-18.848	96.38	187.35	19.42	96.4	176.7	-80.3	149.9	5.340	2.360	1.987	10.060	0.563
795.2	2.436	-0.189	382.321	200.171	199.550	-19.316	99.09	186.88	18.84	82.2	182.5	-100.3	149.0	2.458	3.939	-0.987	10.336	0.559
805.7	-3.602	-0.209	385.504	200.035	199.416	-19.168	105.13	187.03	17.78	68.2	185.8	-117.6	146.6	-3.426	6.837	-6.842	10.249	0.560
807.7	-8.460	-0.211	386.256	199.936	199.339	-18.883	109.99	187.32	17.02	62.6	186.6	-124.0	145.3	-7.692	8.886	-11.052	10.081	0.563

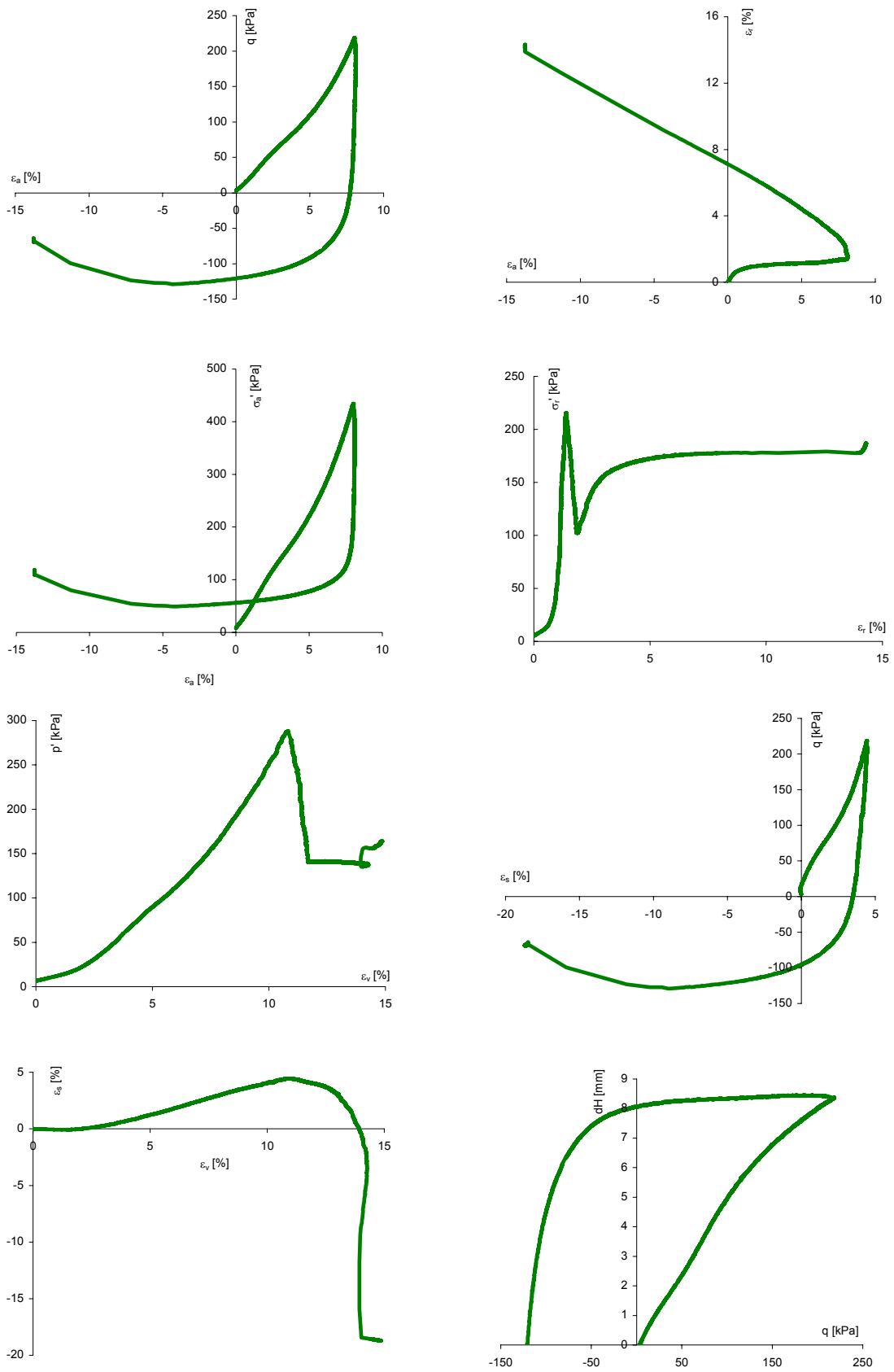

Fig. 10.64:   Triaxial test data of stress path test S2bT1 on natural Kloten clay.

Fig. 10.65:   Triaxial test data of stress path test S2bT1 on natural Kloten clay.

Test data:

test-time [hours]	dH LVDT 1 [mm]	dH LVDT 2 [mm]	ε_a LVDT 1 [%]	ε_a LVDT 2 [%]	ε_r LVDT 1 [%]	ε_r LVDT 2 [%]	ε_s LVDT 1 [%]	ε_s LVDT 2 [%]	V_{act} Laser [ccm]	dV Laser [ccm]	ε_v Laser [%]	ε_r LVDT 1 & Laser [%]	ε_r LVDT 2 & Laser [%]	ε_s LVDT 1 & Laser [%]	ε_s LVDT 2 & Laser [%]	e Laser [-]	V_{act} Cellpr. [ccm]	ε_v Cellpr. [%]
0.0	0.000	0.000	0.000	0.000	0.000	0.000	0.00	0.00	206.94	0.00	0.00	0.00	0.00	0.00	0.00	0.73	206.20	0.00
23.2	0.537	0.578	0.773	0.833	0.247	0.217	0.35	0.41	205.37	-1.57	0.76	-0.01	-0.04	0.52	0.58	0.71	200.26	2.97
43.6	0.852	0.961	1.232	1.392	0.303	0.223	0.62	0.78	204.70	-2.24	1.09	-0.07	-0.15	0.87	1.03	0.71	197.68	4.31
53.4	0.993	1.129	1.439	1.639	0.322	0.222	0.74	0.95	203.09	-3.85	1.90	0.23	0.13	0.81	1.01	0.69	196.62	4.87
83.4	1.484	1.696	2.166	2.483	0.349	0.190	1.21	1.53	202.41	-4.53	2.24	0.04	-0.12	1.42	1.74	0.69	193.82	6.39
93.0	1.697	1.922	2.485	2.823	0.354	0.185	1.42	1.76	201.71	-5.23	2.59	0.05	-0.11	1.62	1.96	0.68	192.79	6.95
112.8	2.250	2.489	3.321	3.687	0.322	0.139	2.00	2.37	200.77	-6.17	3.08	-0.12	-0.31	2.30	2.66	0.67	190.75	8.10
143.4	3.084	3.310	4.609	4.963	0.221	0.044	2.93	3.28	197.93	-9.01	4.55	-0.03	-0.21	3.09	3.45	0.65	187.59	9.92
173.2	3.683	3.919	5.554	5.931	0.166	-0.023	3.59	3.97	196.52	-10.42	5.30	-0.13	-0.32	3.79	4.16	0.64	185.47	11.17
193.0	4.012	4.267	6.080	6.491	0.132	-0.074	3.97	4.38	195.02	-11.92	6.11	0.02	-0.19	4.04	4.45	0.63	184.20	11.94
203.0	4.162	4.426	6.322	6.750	0.101	-0.113	4.15	4.57	195.02	-11.92	6.11	-0.10	-0.32	4.28	4.71	0.63	183.72	12.24
233.0	4.563	4.857	6.973	7.456	0.085	-0.156	4.59	5.07	193.91	-13.03	6.72	-0.13	-0.37	4.73	5.22	0.62	182.22	13.16
243.0	4.684	4.981	7.171	7.661	0.080	-0.165	4.73	5.22	193.39	-13.55	7.01	-0.08	-0.33	4.84	5.33	0.61	181.74	13.46
263.0	4.906	5.215	7.537	8.050	0.059	-0.198	4.99	5.50	192.88	-14.06	7.29	-0.12	-0.38	5.11	5.62	0.61	180.99	13.93
402.6	5.433	5.774	8.415	8.990	0.133	-0.155	5.52	6.10	192.15	-14.79	7.69	-0.36	-0.65	5.85	6.43	0.60	178.96	15.22
430.0	5.431	5.777	8.411	8.995	0.149	-0.143	5.51	6.09	192.00	-14.94	7.78	-0.32	-0.61	5.82	6.40	0.60	178.81	15.32
450.0	5.421	5.770	8.394	8.983	0.189	-0.105	5.47	6.06	192.66	-14.28	7.41	-0.49	-0.78	5.92	6.51	0.61	178.77	15.34
460.2	5.414	5.765	8.383	8.975	0.183	-0.113	5.47	6.06	191.39	-15.55	8.12	-0.13	-0.43	5.67	6.27	0.60	178.63	15.43
489.8	5.390	5.746	8.342	8.943	0.243	-0.058	5.40	6.00	191.52	-15.42	8.05	-0.15	-0.45	5.66	6.26	0.60	178.68	15.40
499.8	5.379	5.741	8.324	8.934	0.255	-0.050	5.38	5.99	192.04	-14.90	7.76	-0.28	-0.59	5.74	6.35	0.60	178.61	15.45
519.8	5.360	5.724	8.292	8.905	0.251	-0.056	5.36	5.97	192.08	-14.86	7.74	-0.28	-0.58	5.71	6.33	0.60	178.67	15.41
593.2	5.316	5.688	8.218	8.844	0.357	0.044	5.24	5.87	191.86	-15.08	7.86	-0.18	-0.49	5.60	6.22	0.60	178.96	15.22
595.7	5.315	5.683	8.217	8.836	0.370	0.061	5.23	5.85	192.13	-14.81	7.71	-0.25	-0.56	5.65	6.27	0.60	179.11	15.12
598.2	5.314	5.688	8.215	8.844	0.370	0.056	5.23	5.86	192.32	-14.62	7.60	-0.31	-0.62	5.68	6.31	0.60	179.09	15.14
602.2	5.312	5.689	8.212	8.846	0.375	0.058	5.22	5.86	192.74	-14.20	7.36	-0.42	-0.74	5.76	6.39	0.61	179.07	15.15
607.2	5.309	5.682	8.207	8.834	0.386	0.072	5.21	5.84	192.26	-14.68	7.63	-0.29	-0.60	5.66	6.29	0.60	179.11	15.12
612.2	5.305	5.681	8.200	8.833	0.397	0.081	5.20	5.83	192.18	-14.76	7.68	-0.26	-0.57	5.64	6.27	0.60	179.01	15.19
617.2	5.301	5.686	8.187	8.841	0.415	0.091	5.19	5.83	192.49	-14.45	7.50	-0.34	-0.67	5.69	6.34	0.60	179.11	15.12
622.2	5.297	5.679	8.187	8.829	0.420	0.098	5.18	5.82	193.09	-13.85	7.17	-0.51	-0.83	5.80	6.44	0.61	179.06	15.15
632.7	5.287	5.670	8.170	8.814	0.446	0.124	5.15	5.79	193.14	-13.80	7.15	-0.51	-0.83	5.79	6.43	0.61	179.07	15.15
643.7	5.274	5.659	8.148	8.795	0.465	0.141	5.12	5.77	192.12	-14.82	7.71	-0.22	-0.54	5.58	6.22	0.60	179.12	15.12
653.7	5.260	5.649	8.125	8.778	0.490	0.163	5.09	5.74	192.67	-14.27	7.40	-0.36	-0.69	5.66	6.31	0.61	179.07	15.15
663.7	5.244	5.634	8.098	8.753	0.514	0.186	5.06	5.71	192.76	-14.18	7.36	-0.37	-0.70	5.65	6.30	0.61	179.16	15.09
683.7	5.200	5.593	8.025	8.684	0.560	0.231	4.98	5.64	192.79	-14.15	7.34	-0.34	-0.67	5.58	6.24	0.61	179.14	15.11
704.7	5.131	5.530	7.910	8.578	0.677	0.343	4.82	5.49	193.45	-13.49	6.97	-0.47	-0.80	5.59	6.25	0.61	179.08	15.15
719.7	5.024	5.424	7.732	8.399	0.838	0.505	4.60	5.26	192.49	-14.45	7.51	-0.11	-0.45	5.23	5.90	0.61	179.03	15.18
740.2	4.827	5.239	7.406	8.090	1.061	0.719	4.23	4.91	191.77	-15.17	7.91	0.25	-0.09	4.77	5.45	0.60	178.85	15.29
760.2	4.427	4.847	6.751	7.439	1.512	1.167	3.49	4.18	192.16	-14.78	7.69	0.47	0.13	4.19	4.88	0.60	178.64	15.43
778.7	3.628	4.061	5.466	6.159	2.297	1.951	2.11	2.81	192.62	-14.32	7.44	0.98	0.64	2.99	3.68	0.61	178.26	15.68
795.2	1.812	2.229	2.657	3.289	3.839	3.523	-0.79	-0.16	192.38	-14.56	7.57	2.45	2.14	0.14	0.77	0.60	177.83	15.95
805.7	-2.403	-2.091	-3.319	-2.901	6.784	6.575	-6.74	-6.32	192.00	-14.94	7.78	5.55	5.34	-5.91	-5.49	0.60	178.11	15.77
807.7	-4.677	-4.774	-6.263	-6.385	8.172	8.233	-9.62	-9.74	191.33	-15.61	8.16	7.21	7.27	-8.98	-9.10	0.60	178.41	15.58

Fig. 10.66: Triaxial test data of stress path test S2bT1 on natural Kloten clay: comparison of strain determination with various measurement methods.

Fig. 10.67:   Triaxial test data of stress path test S2bT1 on natural Kloten clay: comparison of strain determination with various measurement methods.

Fig. 10.68:   Triaxial test data of stress path test S2bT1 on natural Kloten clay: comparison of strain determination with various measurement methods.
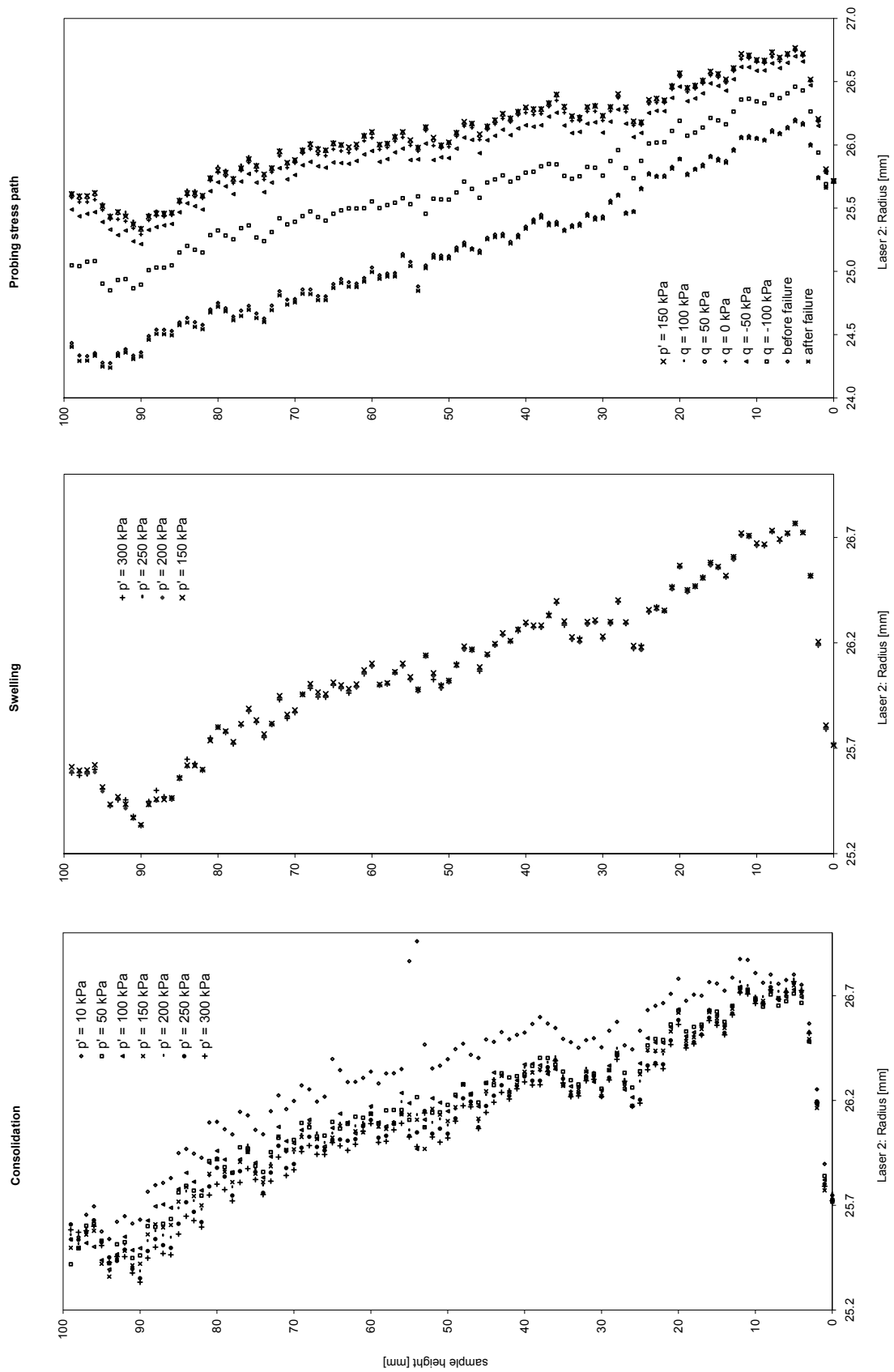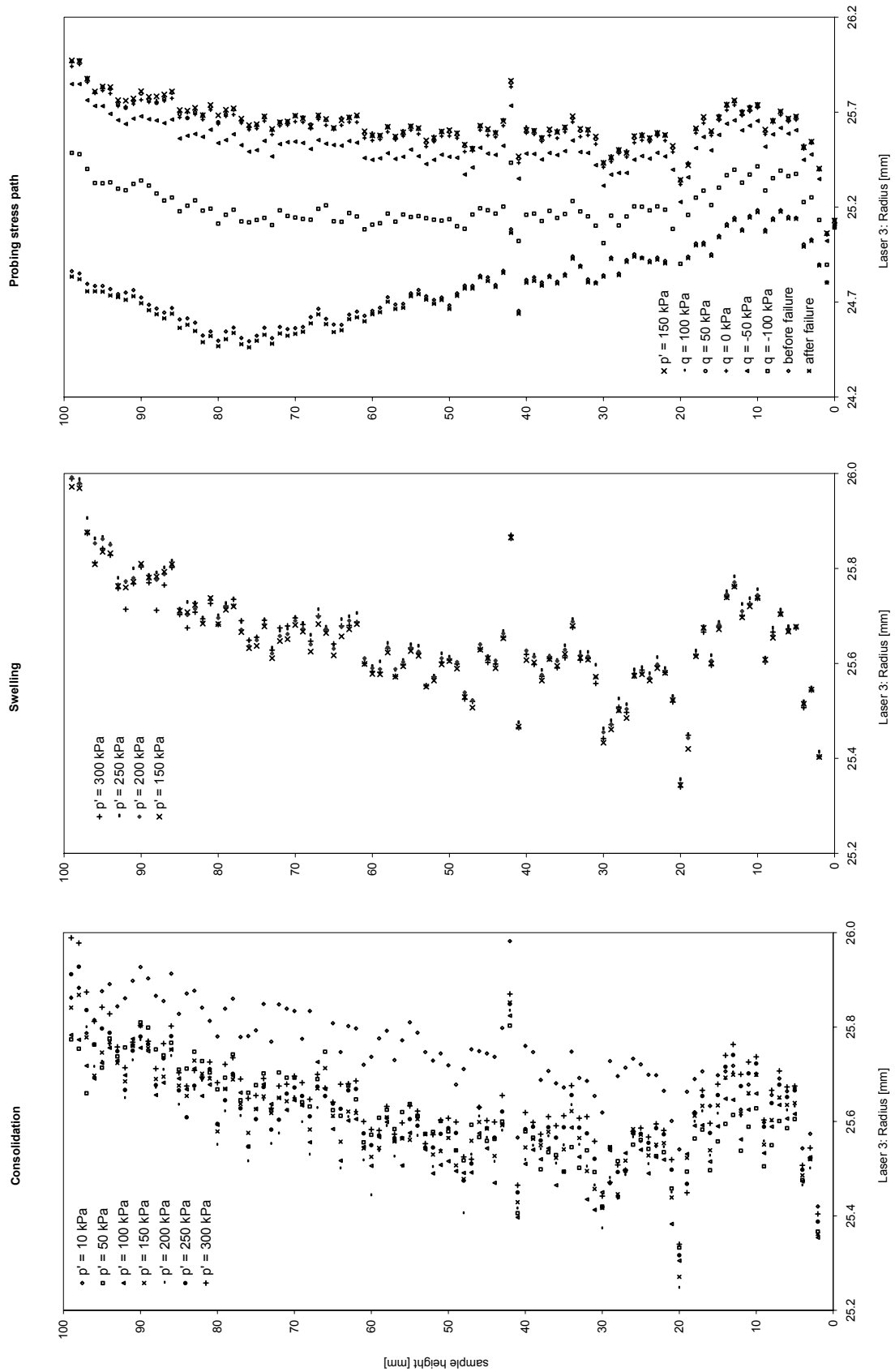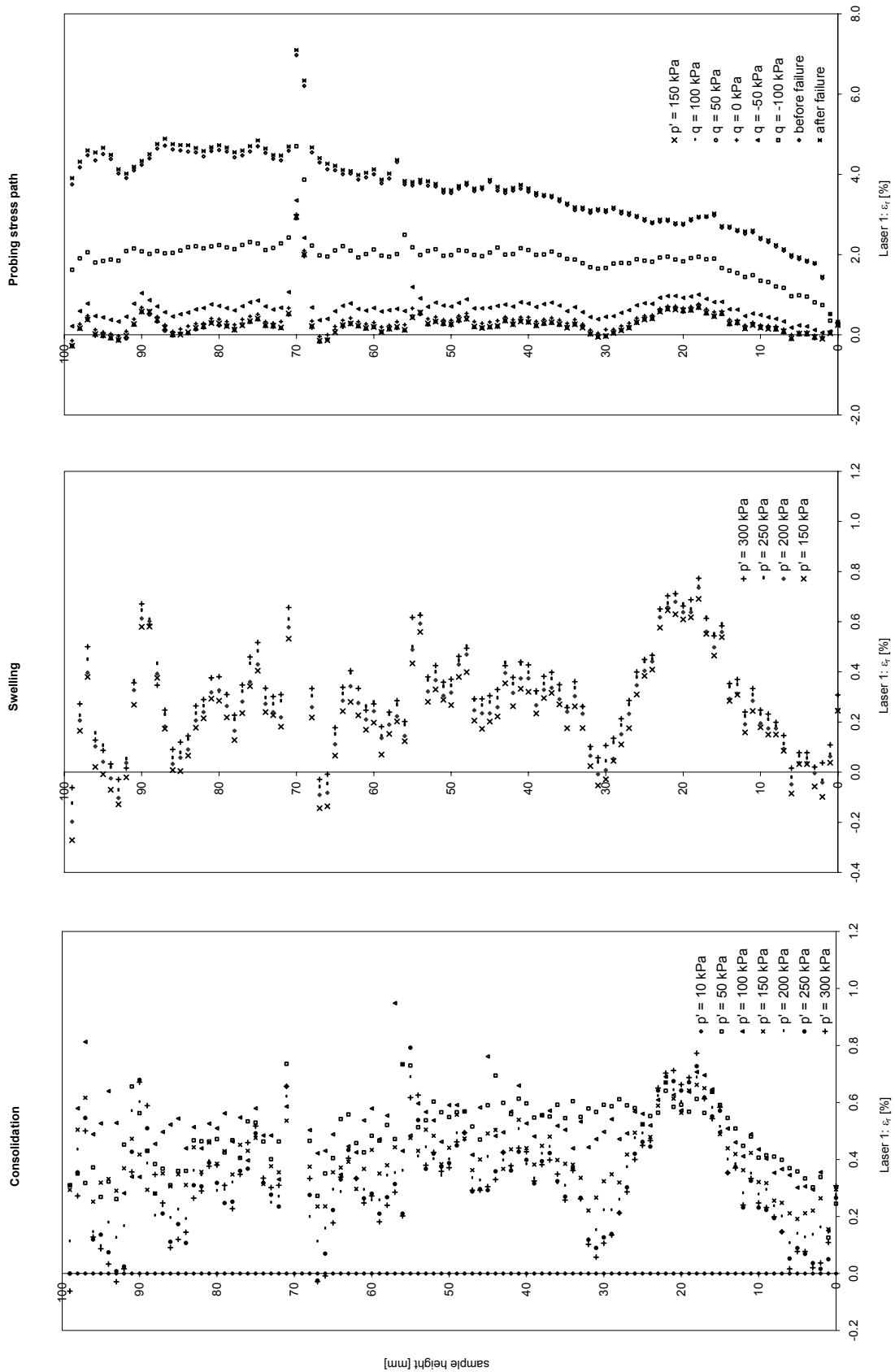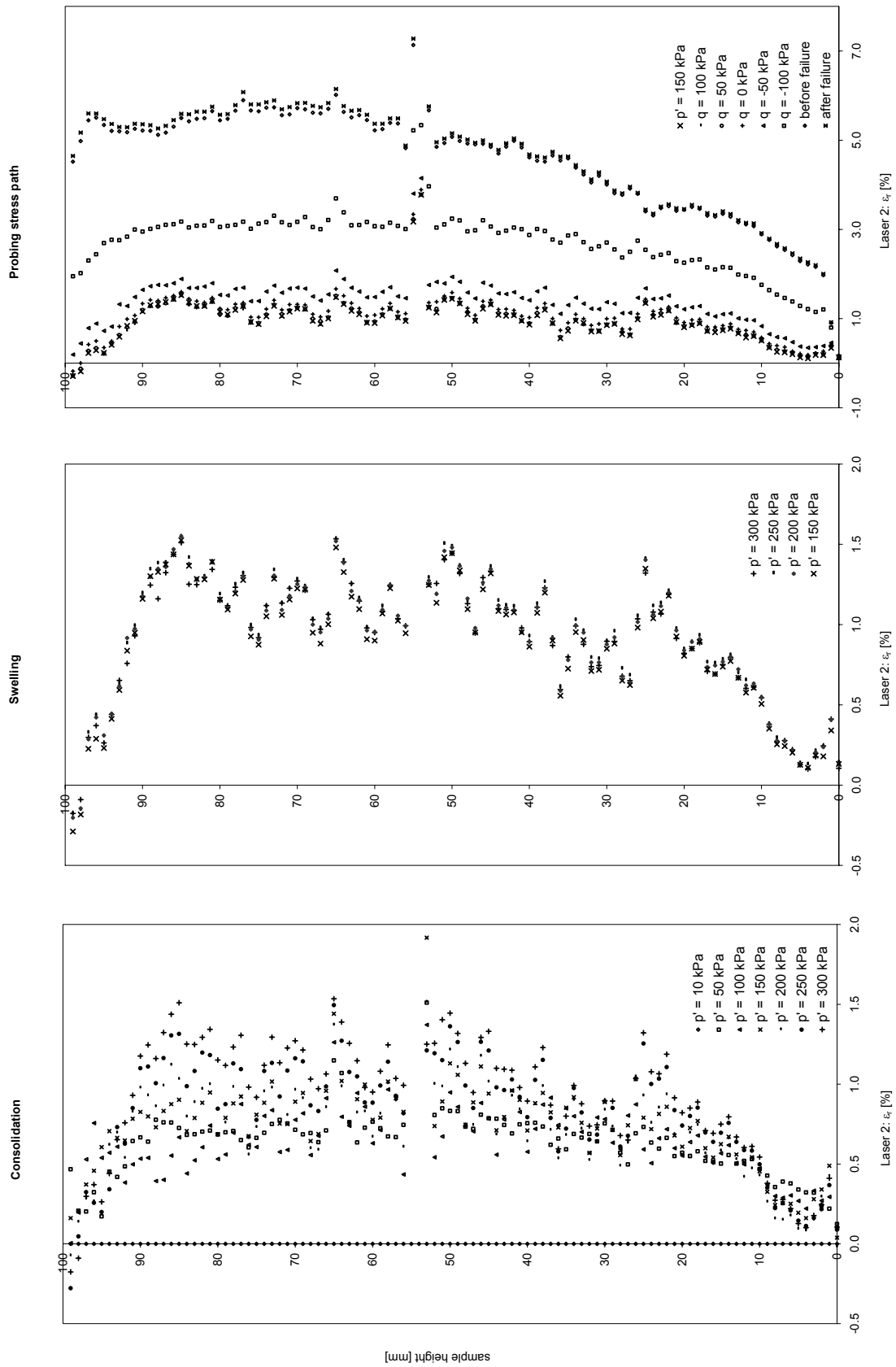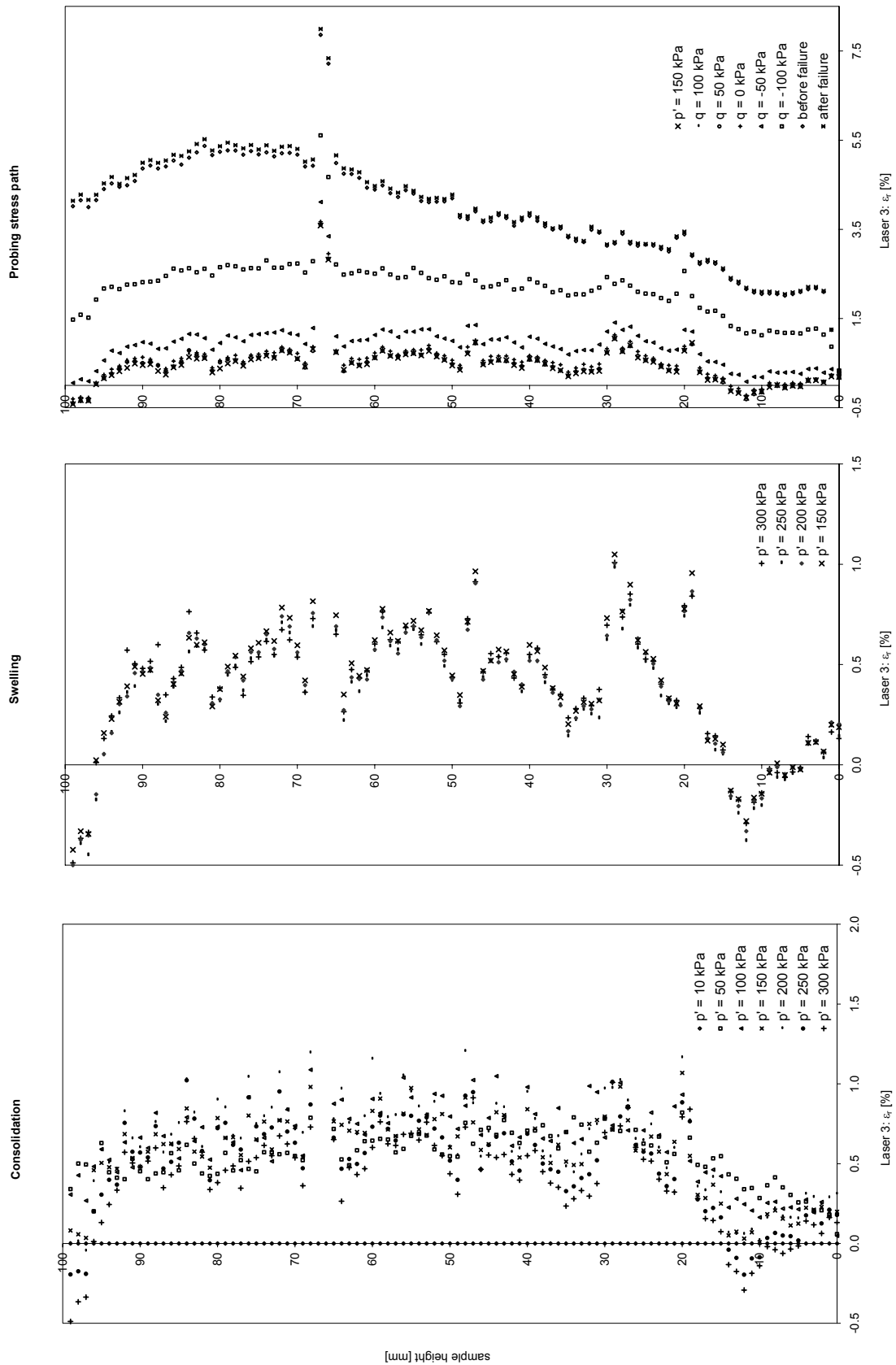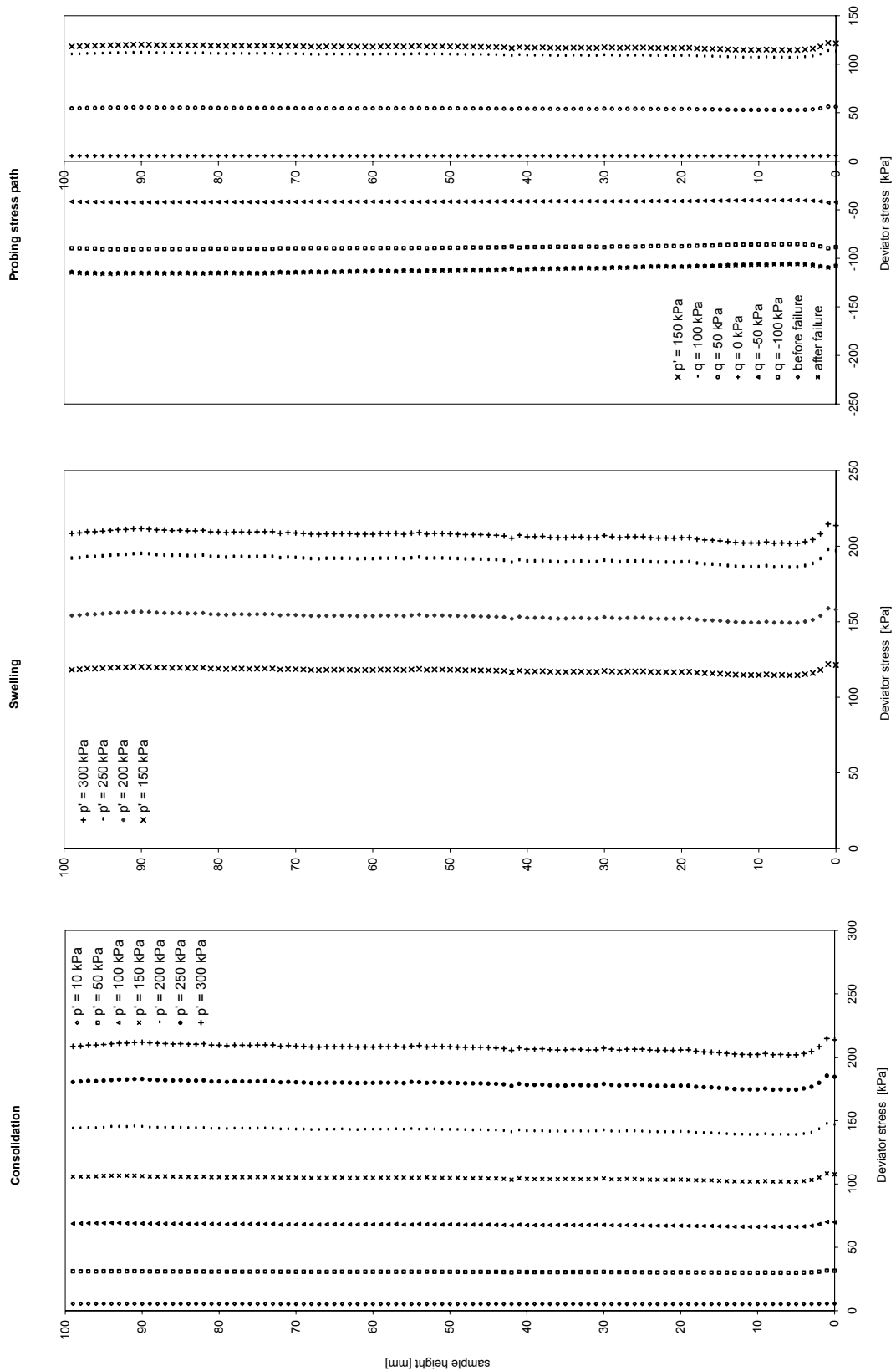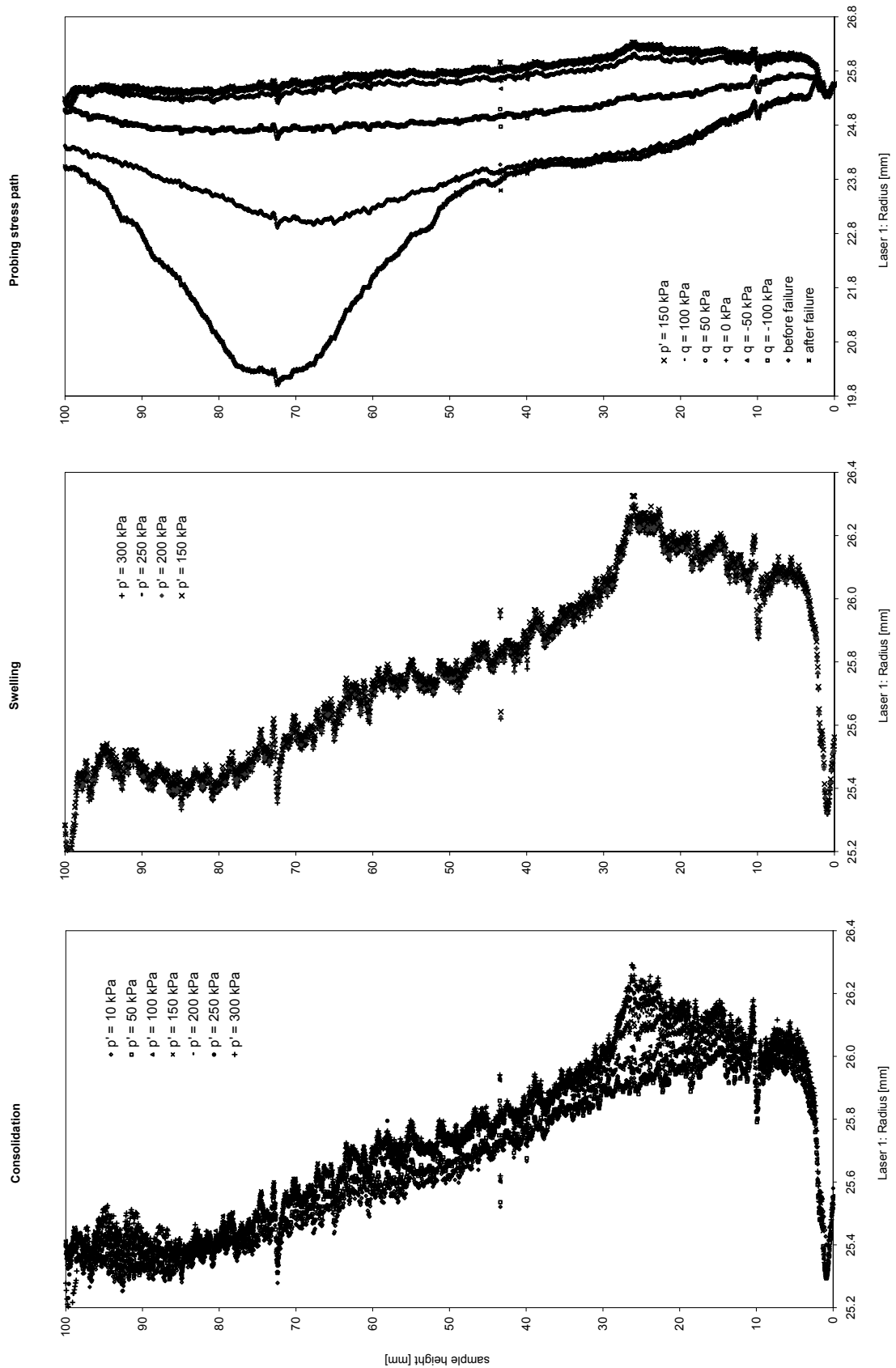
Fig. 10.69: Laser scan data of the triaxial stress path test S2bT1 on natural Kloten clay: radius from laser 1.
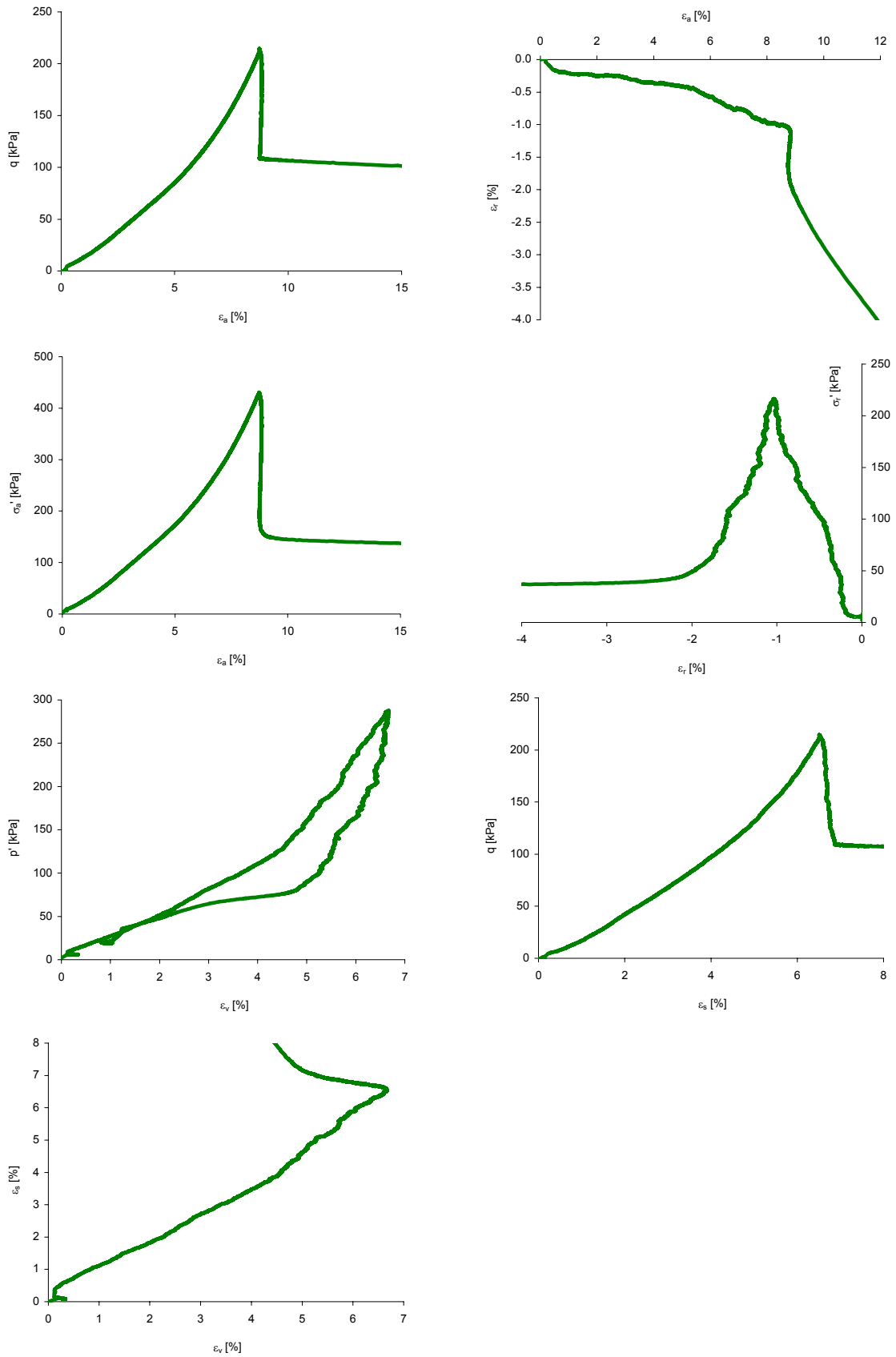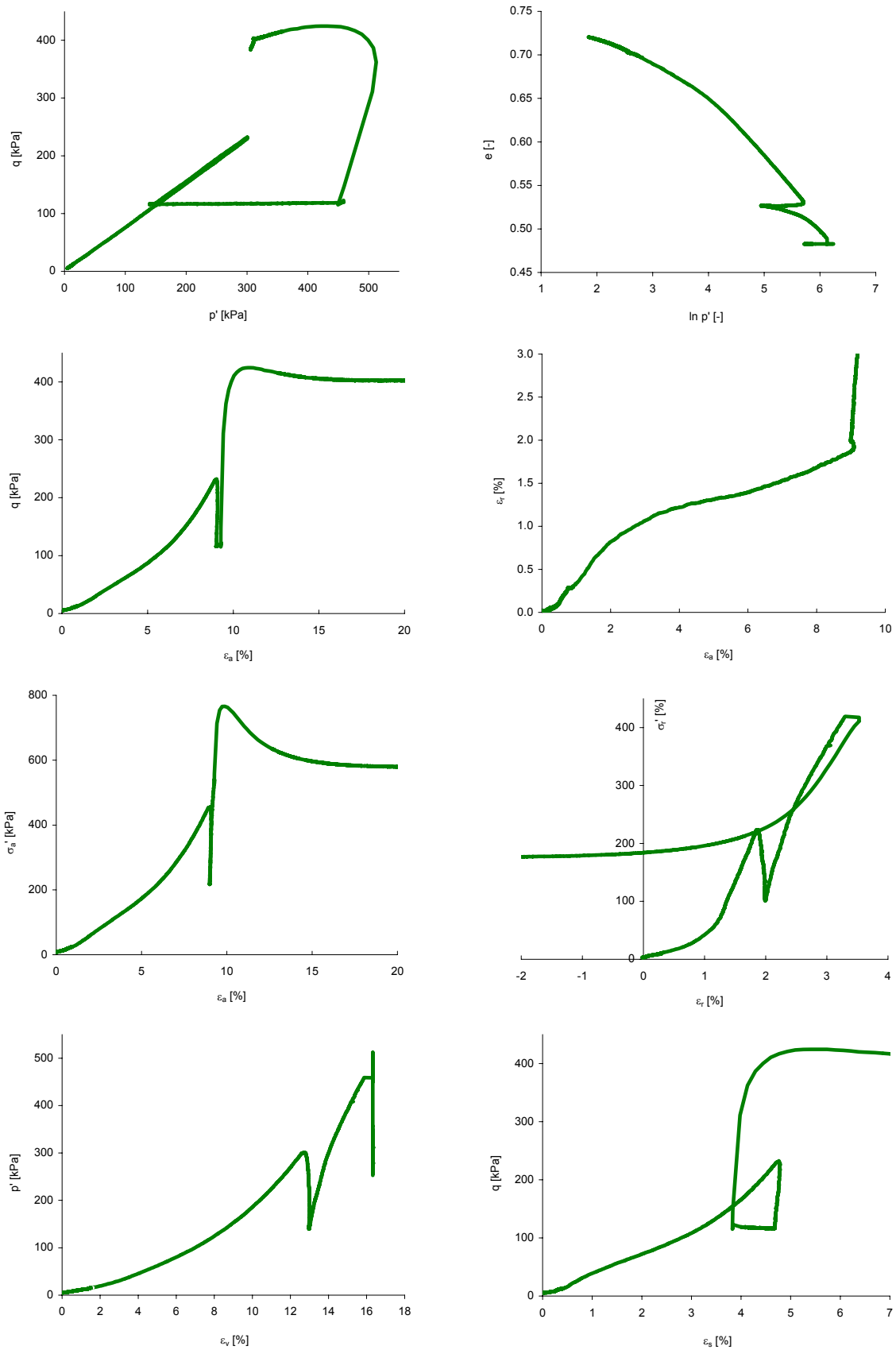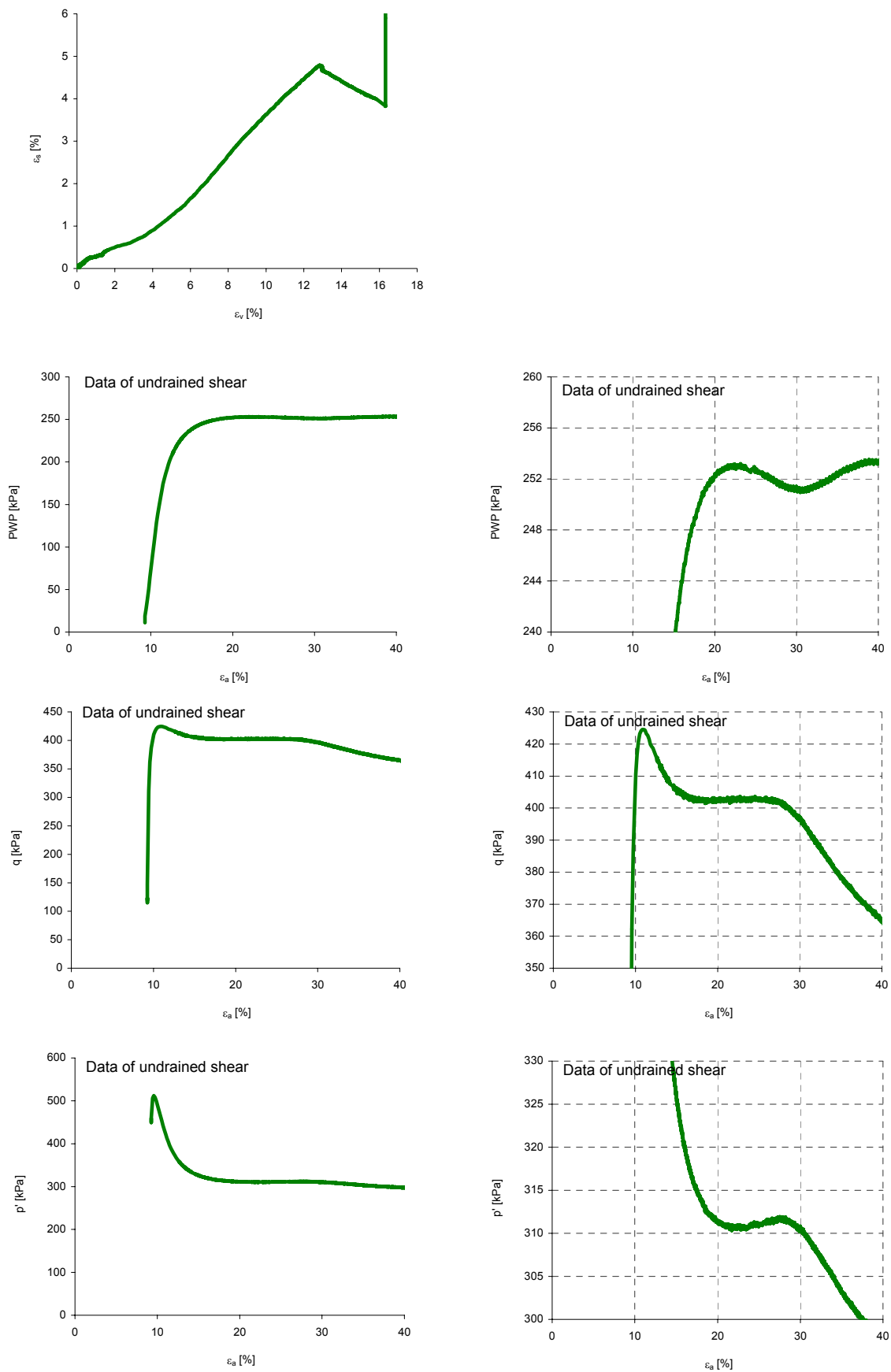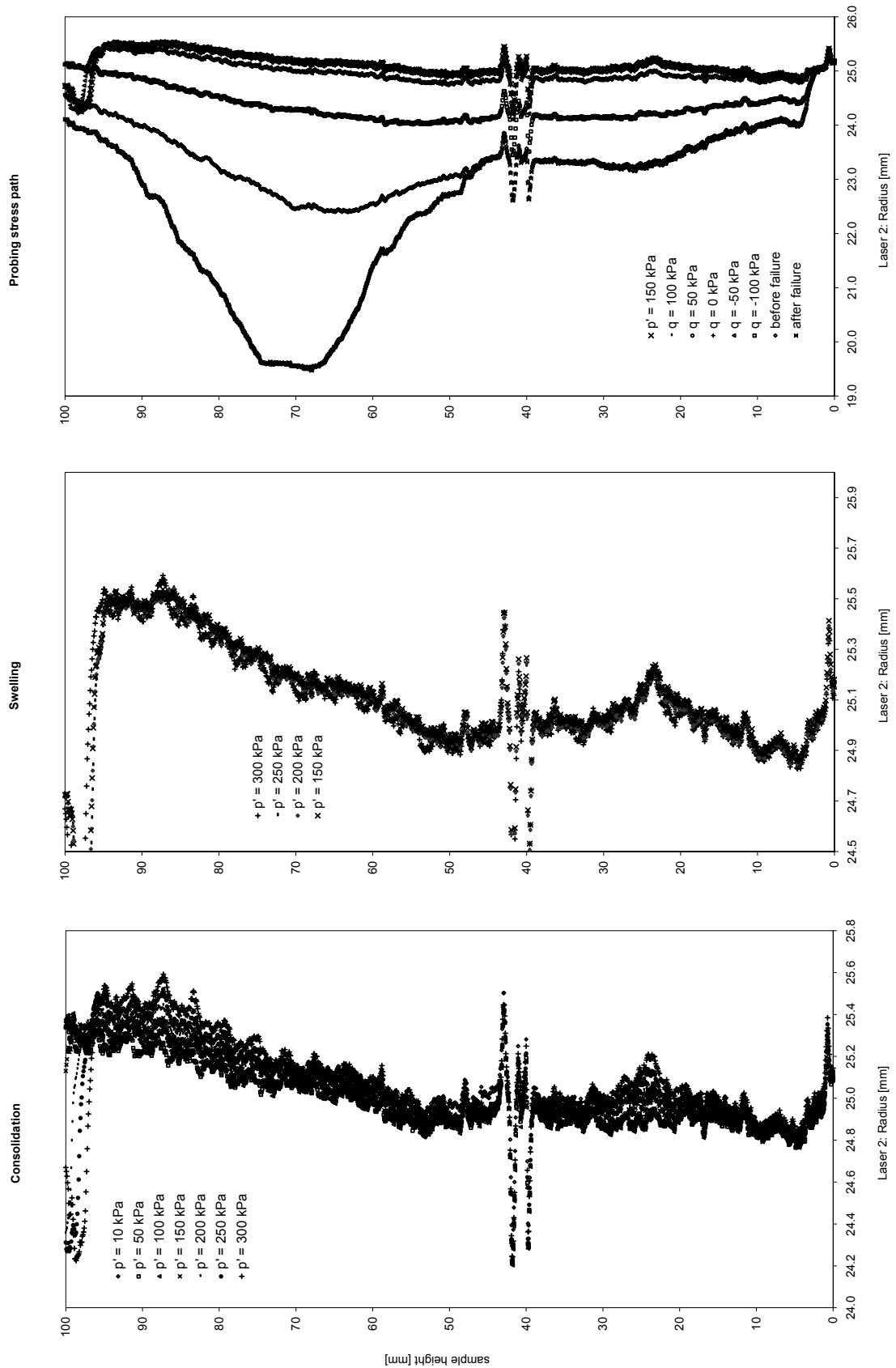
Fig. 10.70:   Laser scan data of the triaxial stress path test S2bT1 on natural Kloten clay:
radius from laser 2.
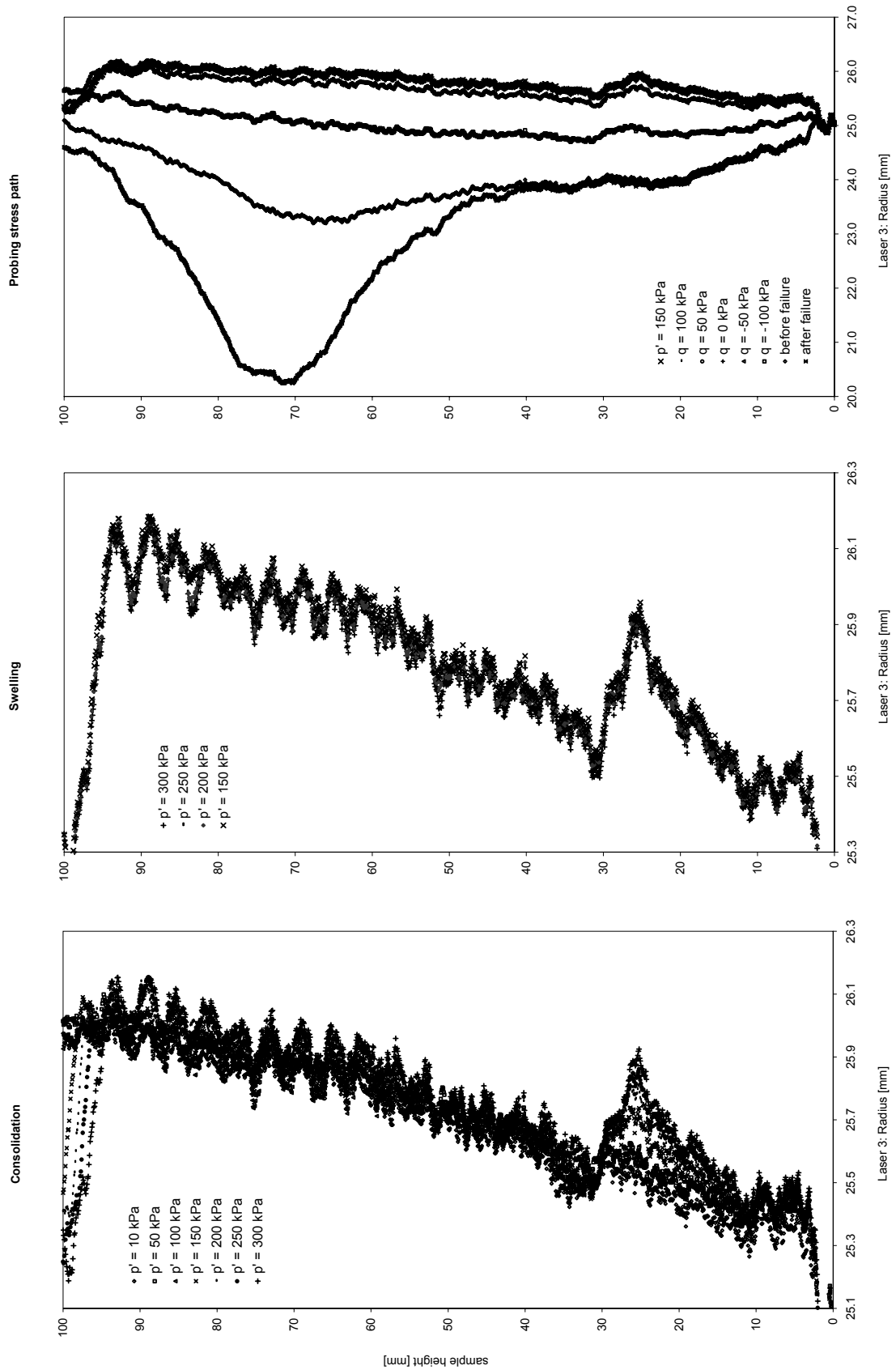
Fig. 10.71:   Laser scan data of the triaxial stress path test S2bT1 on natural Kloten clay: radius from laser 3.
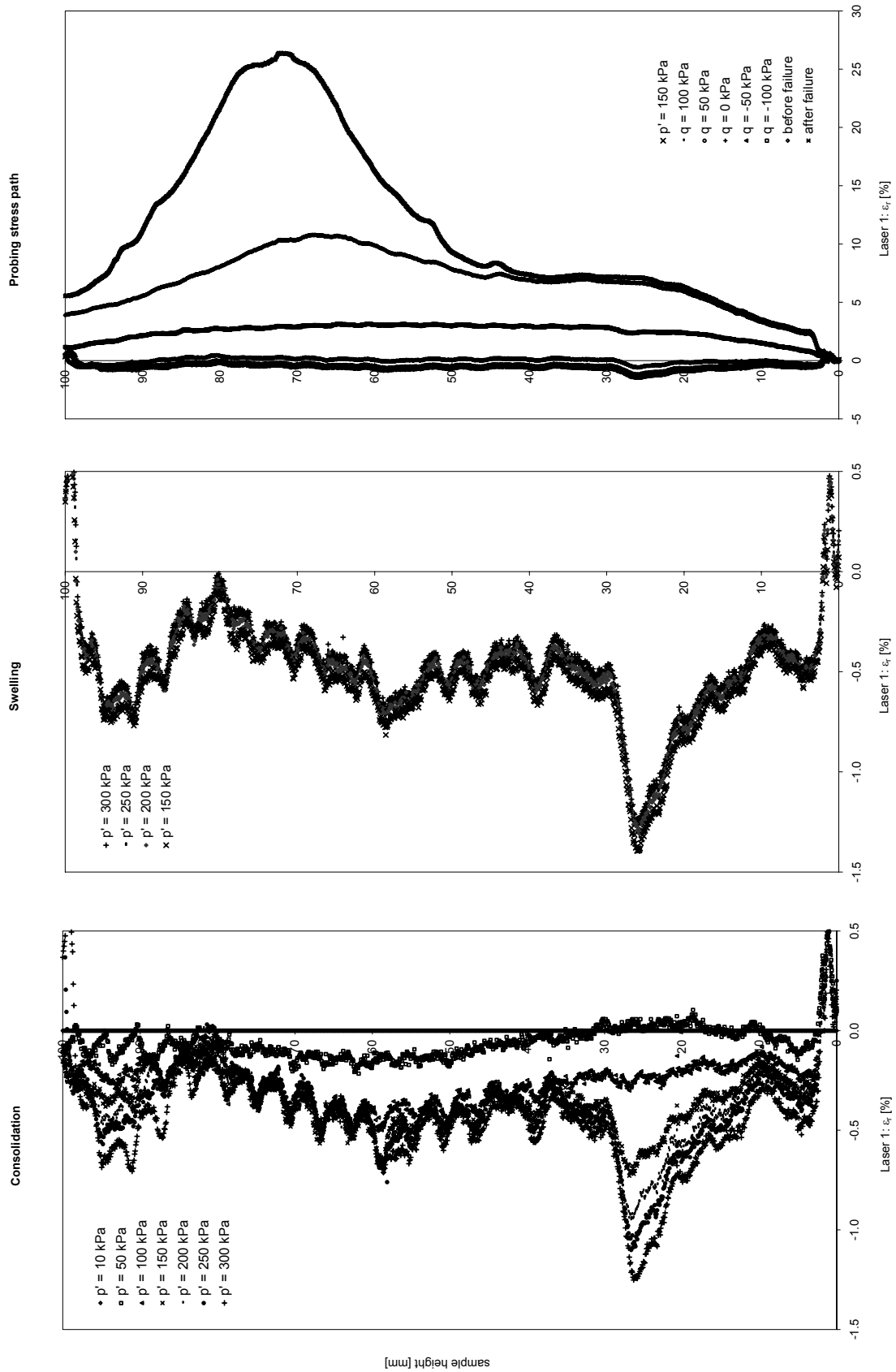
Fig. 10.72:   Laser scan data of the triaxial stress path test S2bT1 on natural Kloten clay: radial strain from laser 1.
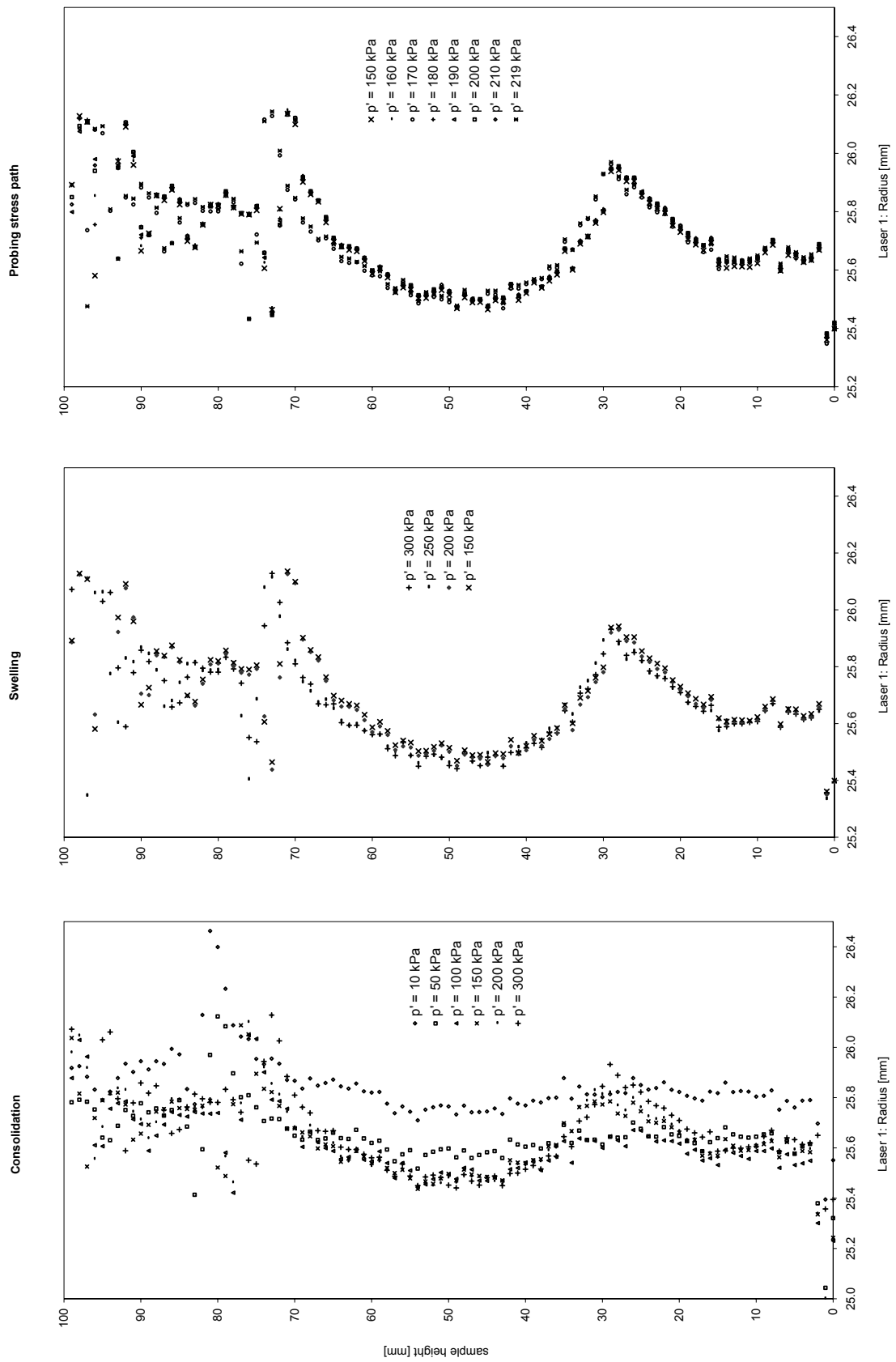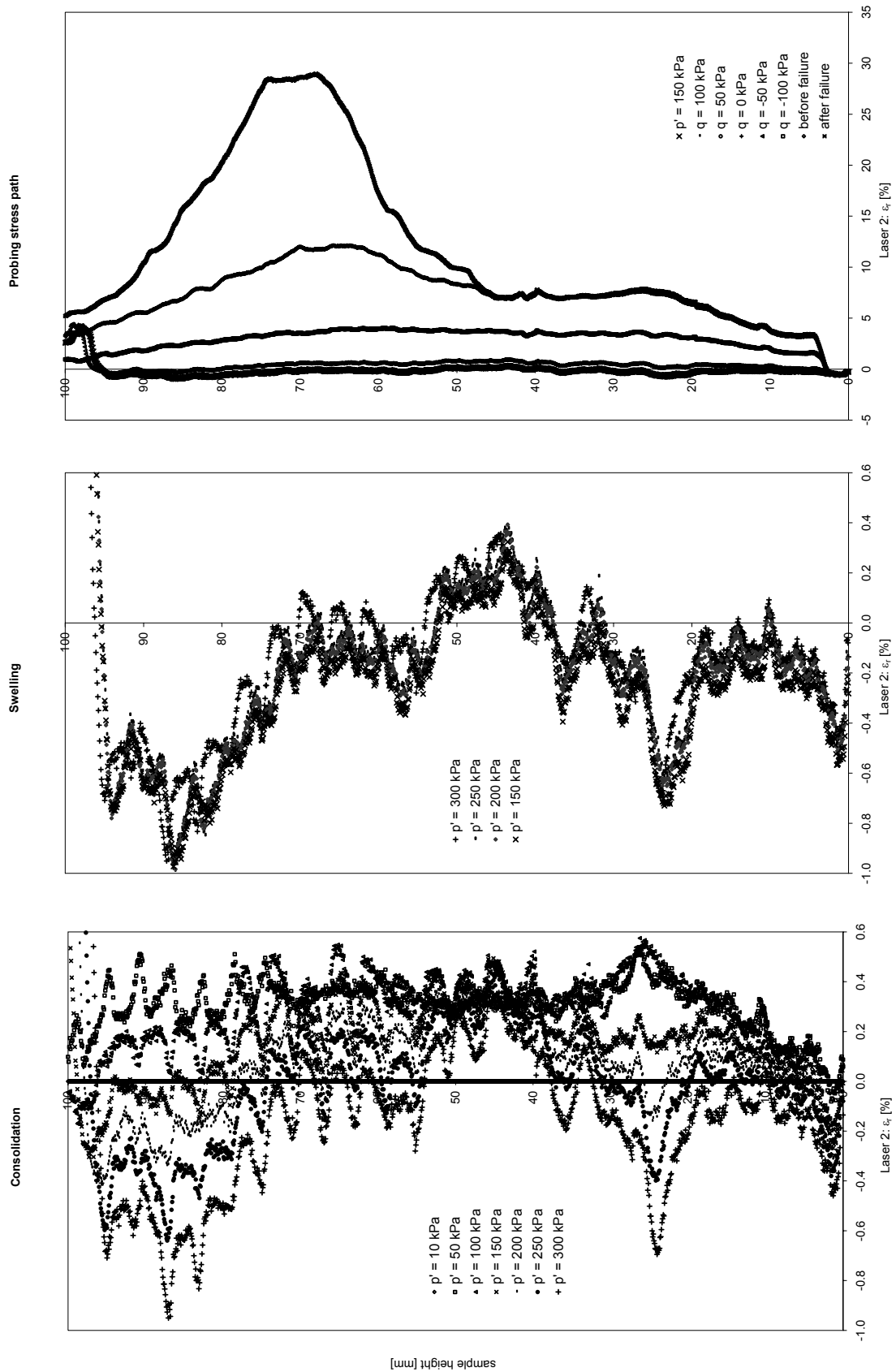
Fig. 10.73: Laser scan data of the triaxial stress path test S2bT1 on natural Kloten clay: radial strain from laser 2.
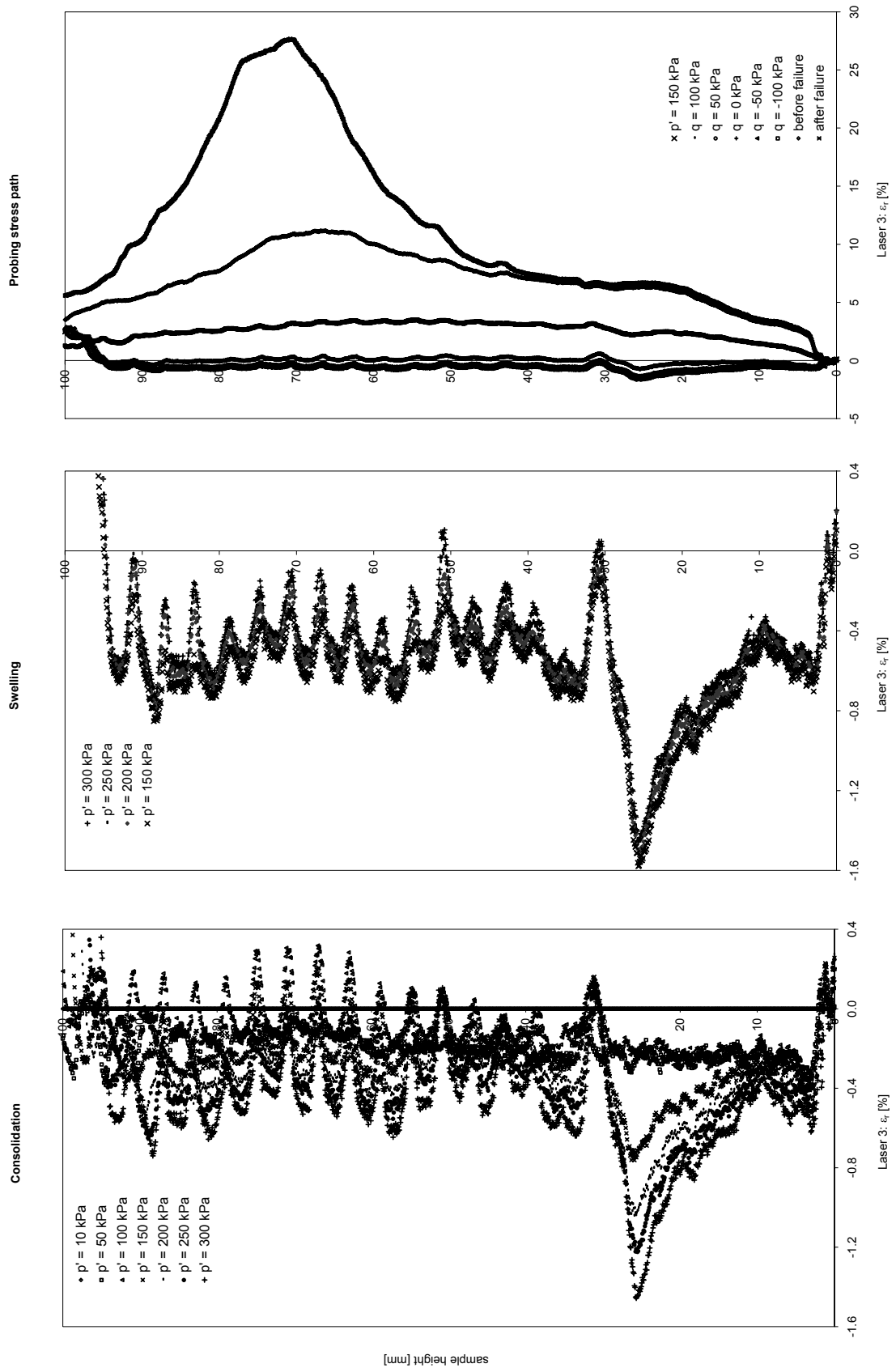
Fig. 10.74:   Laser scan data of the triaxial stress path test S2bT1 on natural Kloten clay: radial strain from laser 3.
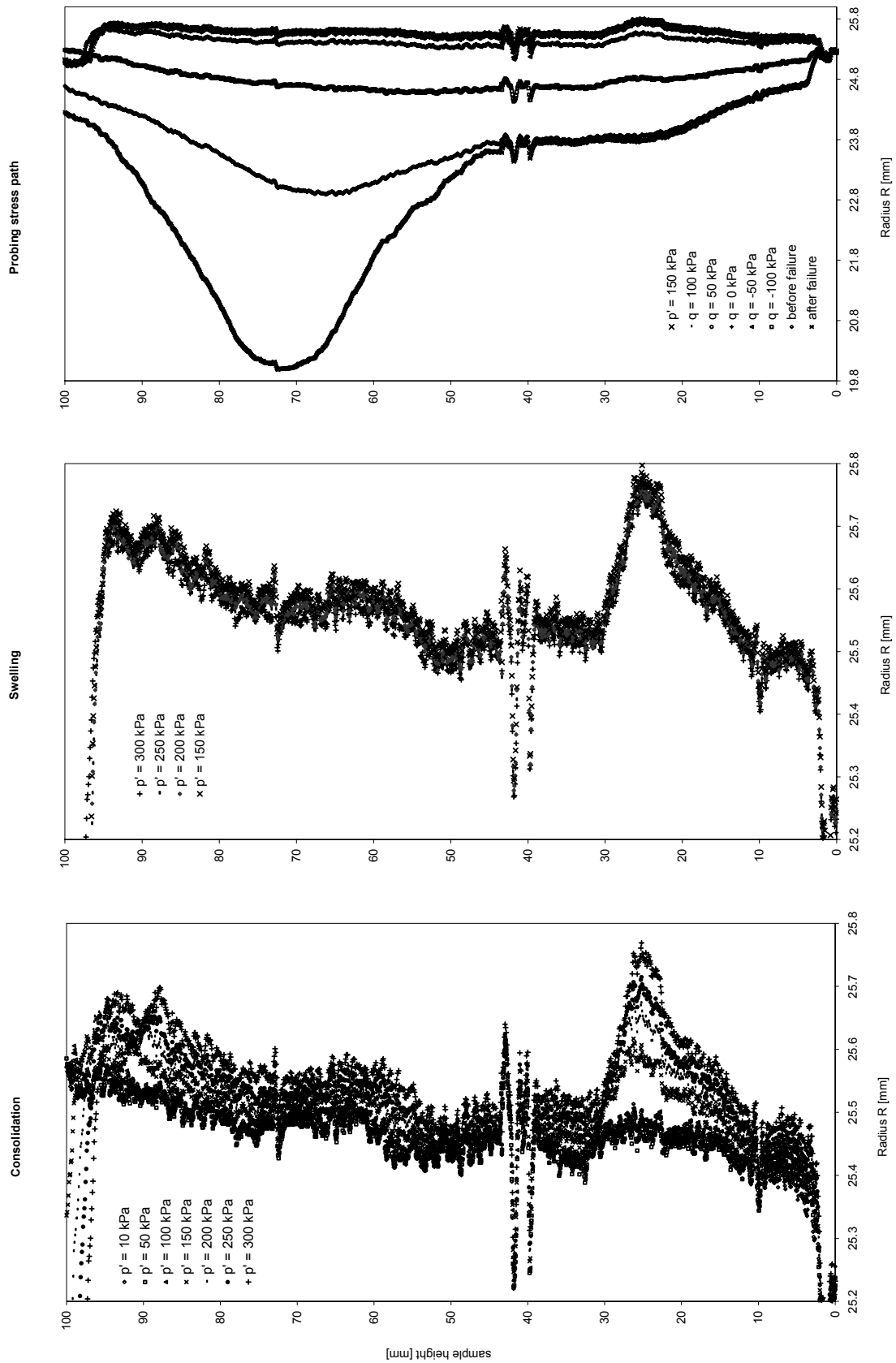
Fig. 10.75: Laser scan data of the triaxial stress path test S2bT1 on natural Kloten clay: radius determined with the circular slice approach.
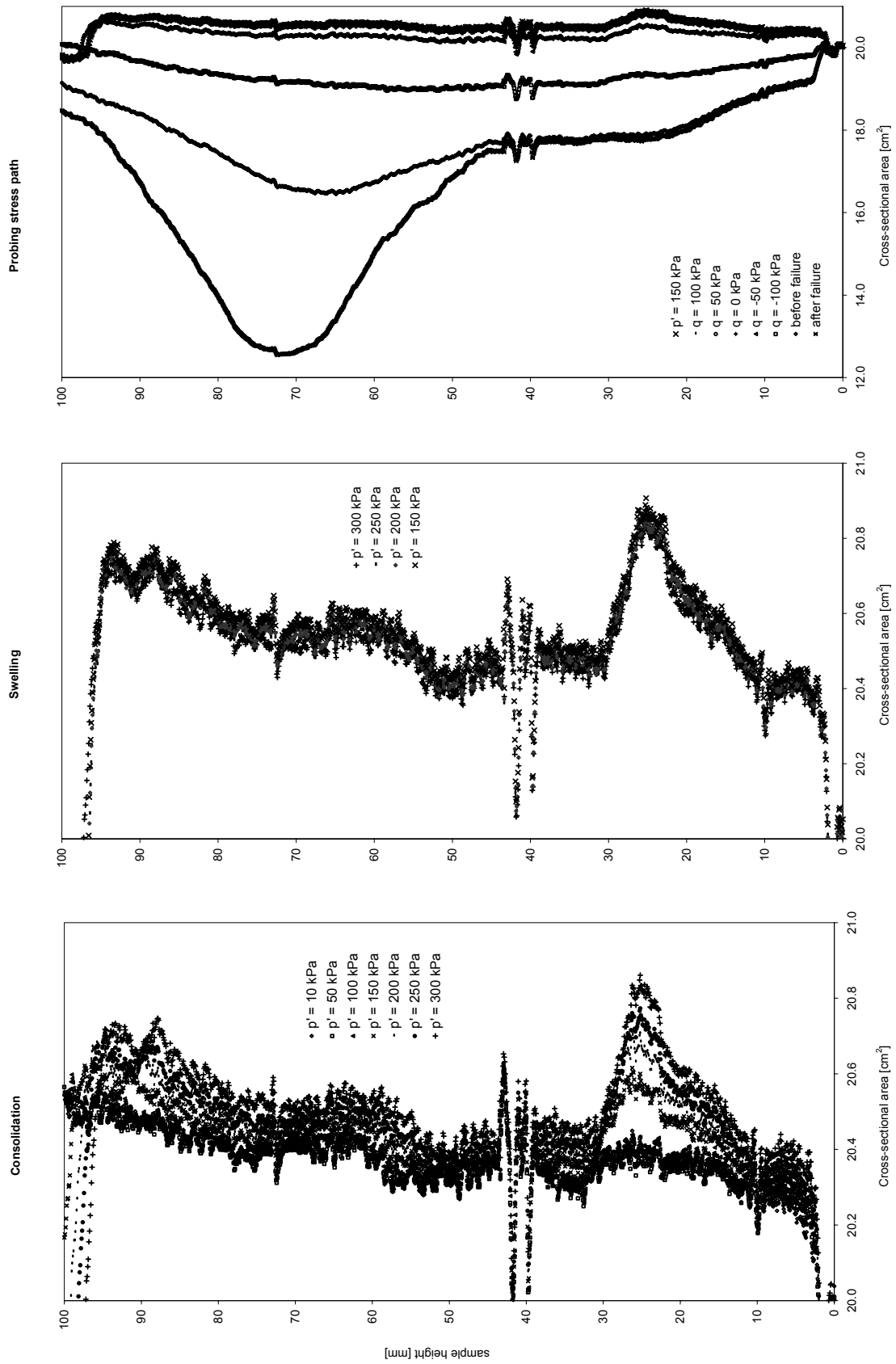
Fig. 10.76:   Laser scan data of the triaxial stress path test S2bT1 on natural Kloten clay:
cross-sectional area calculated from *R* (Fig. 10.75).
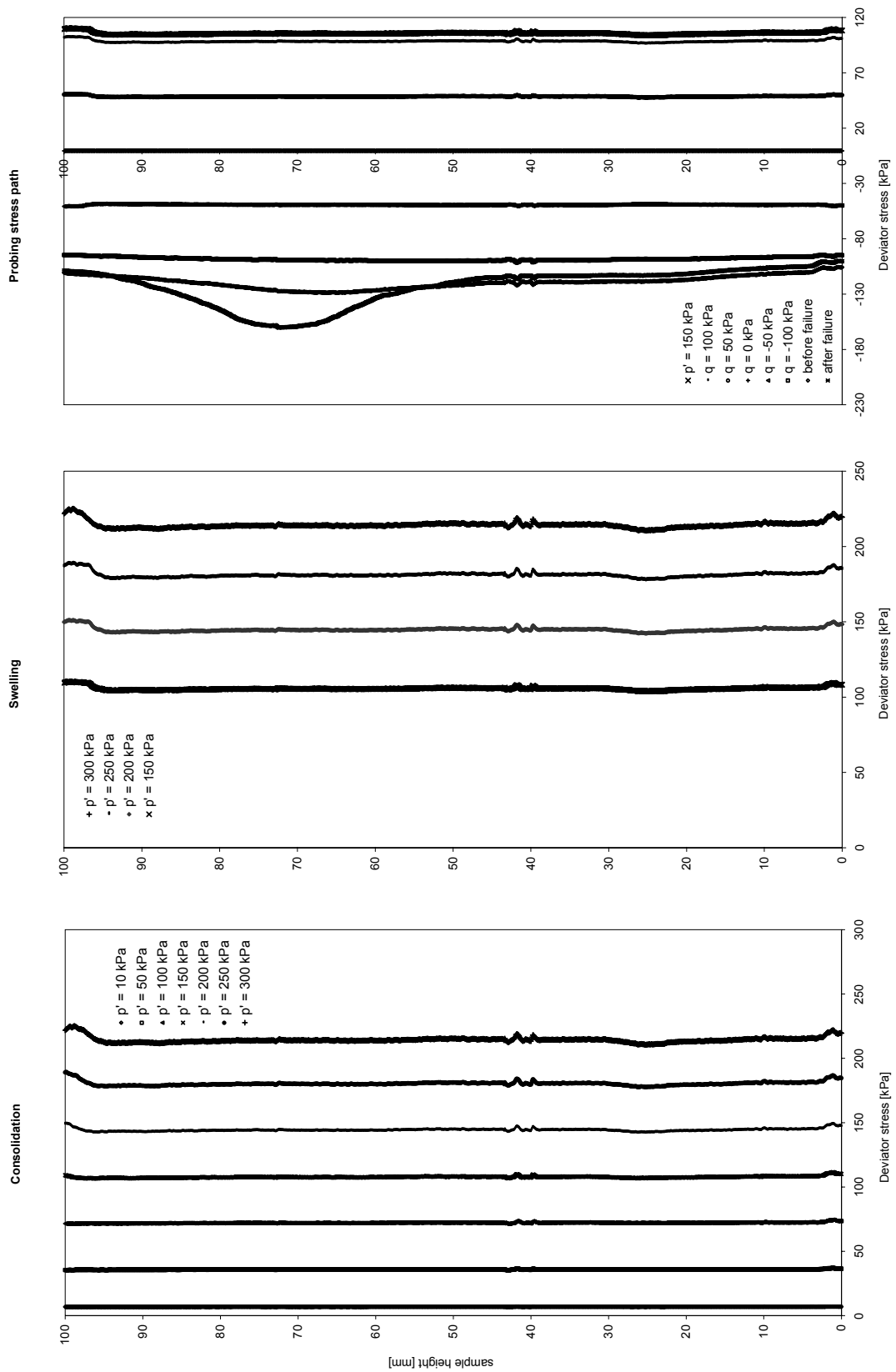
Fig. 10.77: Laser scan data of the triaxial stress path test S2bT1 on natural Kloten clay:
change of deviator stress.
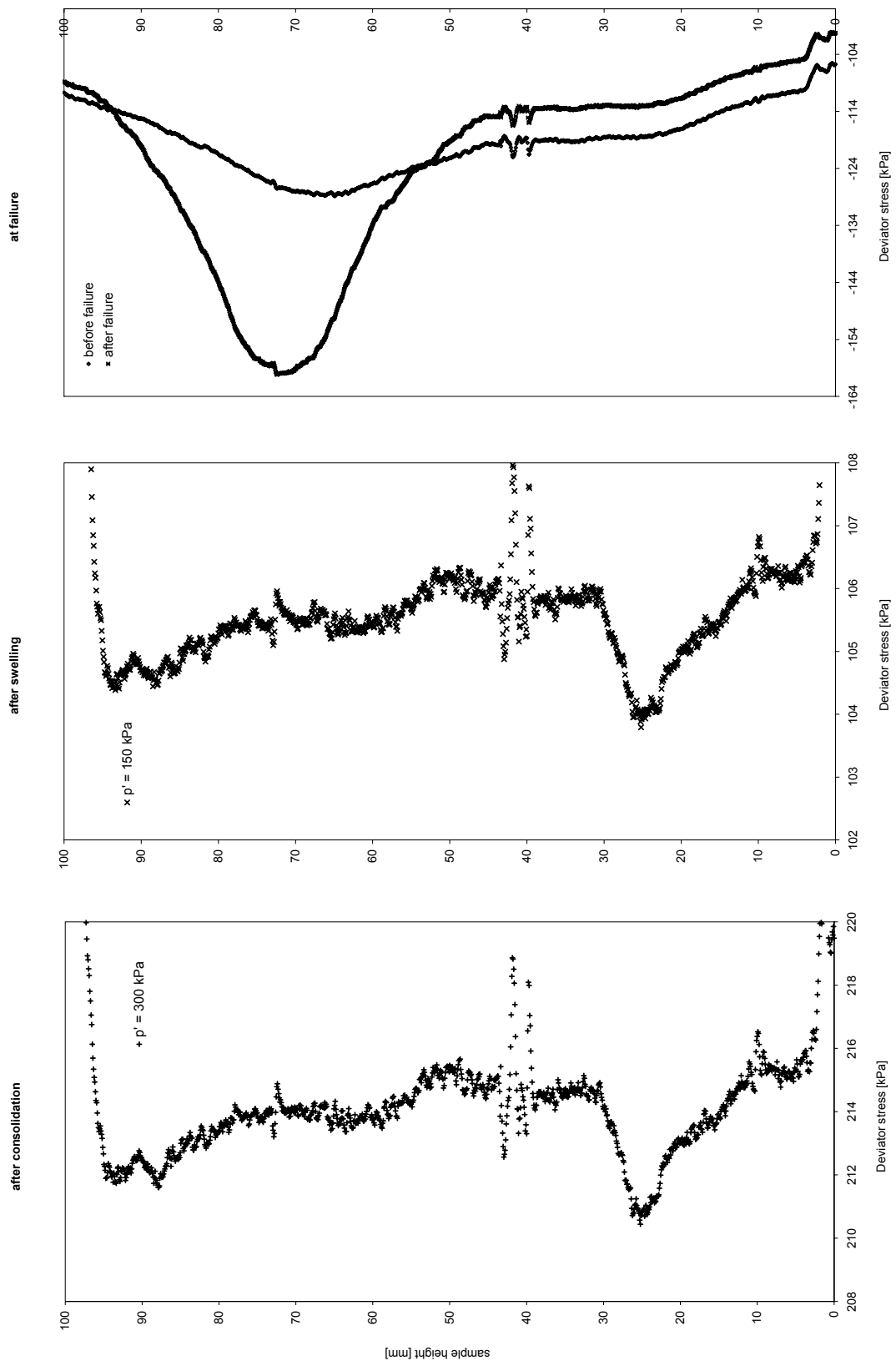
Fig. 10.78:   Laser scan data of the triaxial stress path test S2bT1 on natural Kloten clay:
Change of deviator stress (enlarged scale).
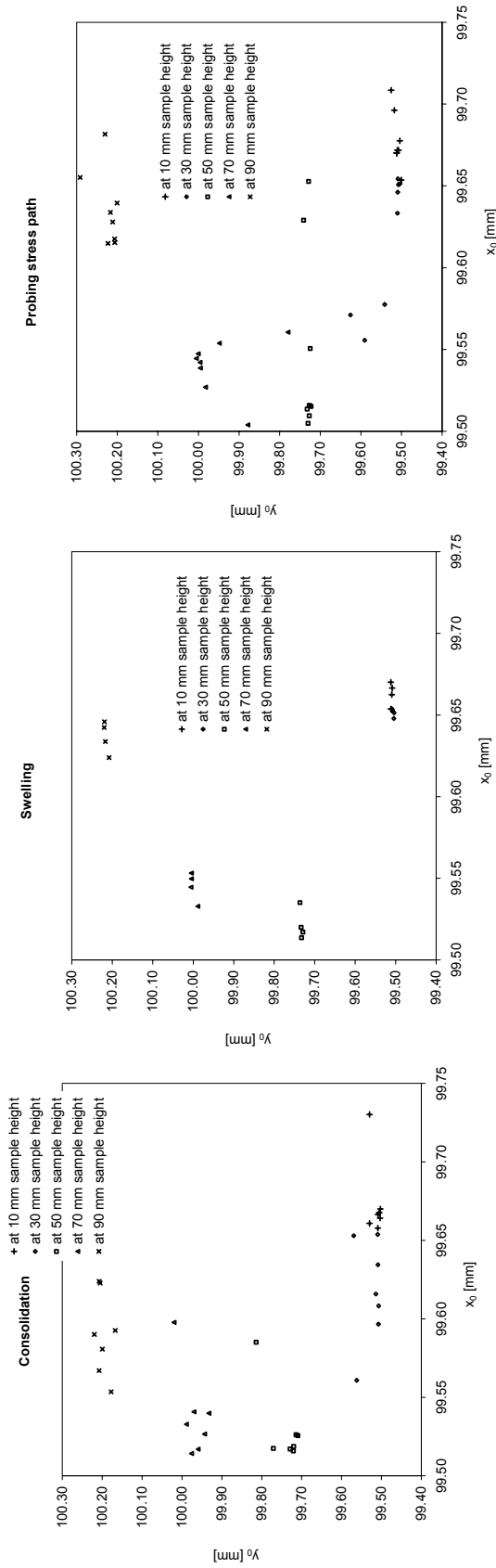
Fig. 10.79:   Laser scan data of centre of each disc for the triaxial stress path test S2bT1
on natural Kloten clay.
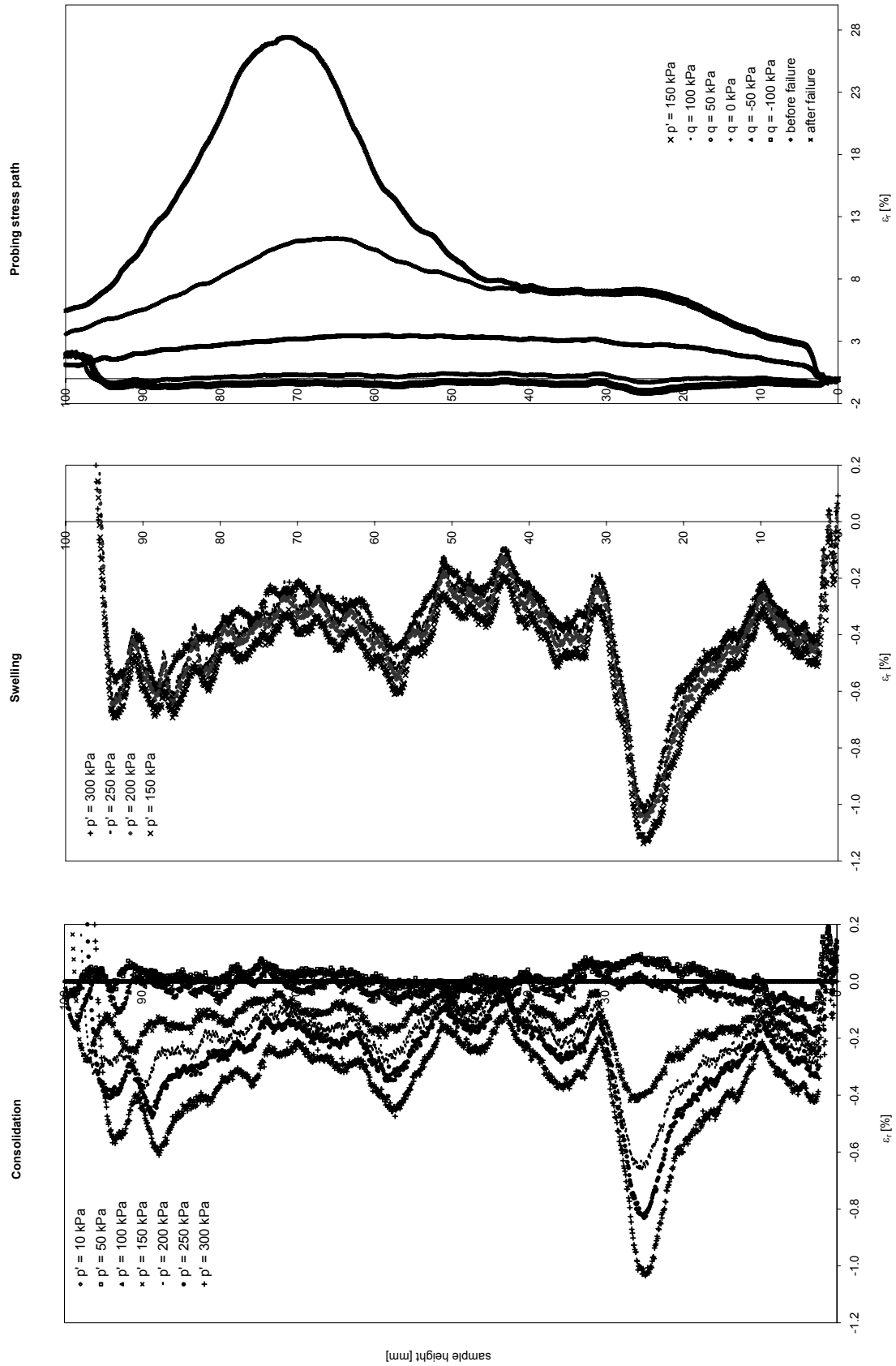
Fig. 10.80: Laser scan data of the triaxial stress path test S2bT1 on natural Kloten clay: radial strain calculated from *R* (Fig. 10.75).
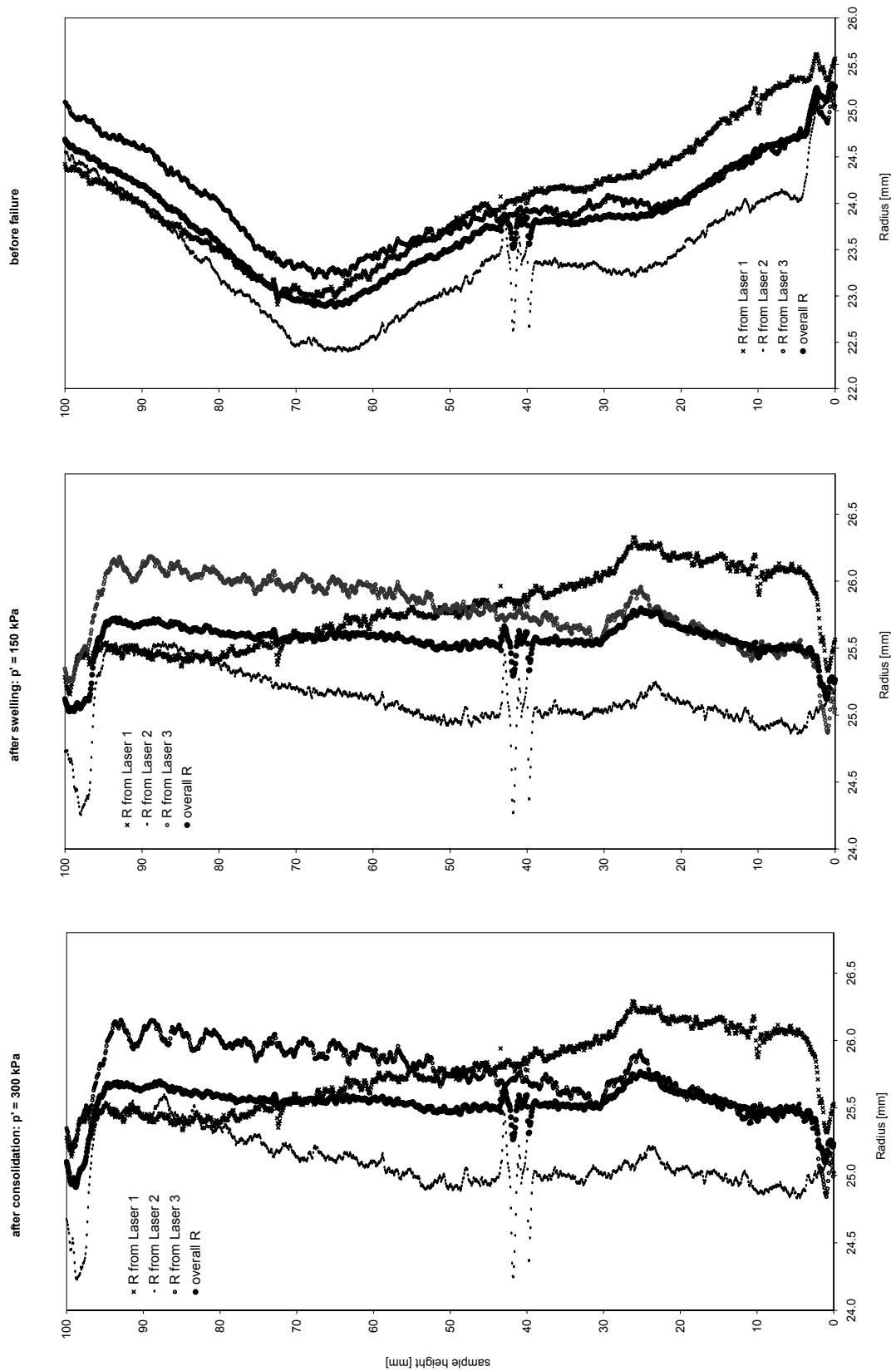
Fig. 10.81: Laser scan data of the triaxial stress path test S2bT1 on natural Kloten clay: comparison of radius determined from each laser together with the radius *R* determined from the circular slice approach.

Fig. 10.82:   Laser scan data of the triaxial stress path test S2bT1 on natural Kloten clay: between sample heights (from base) 50 – 51 mm.
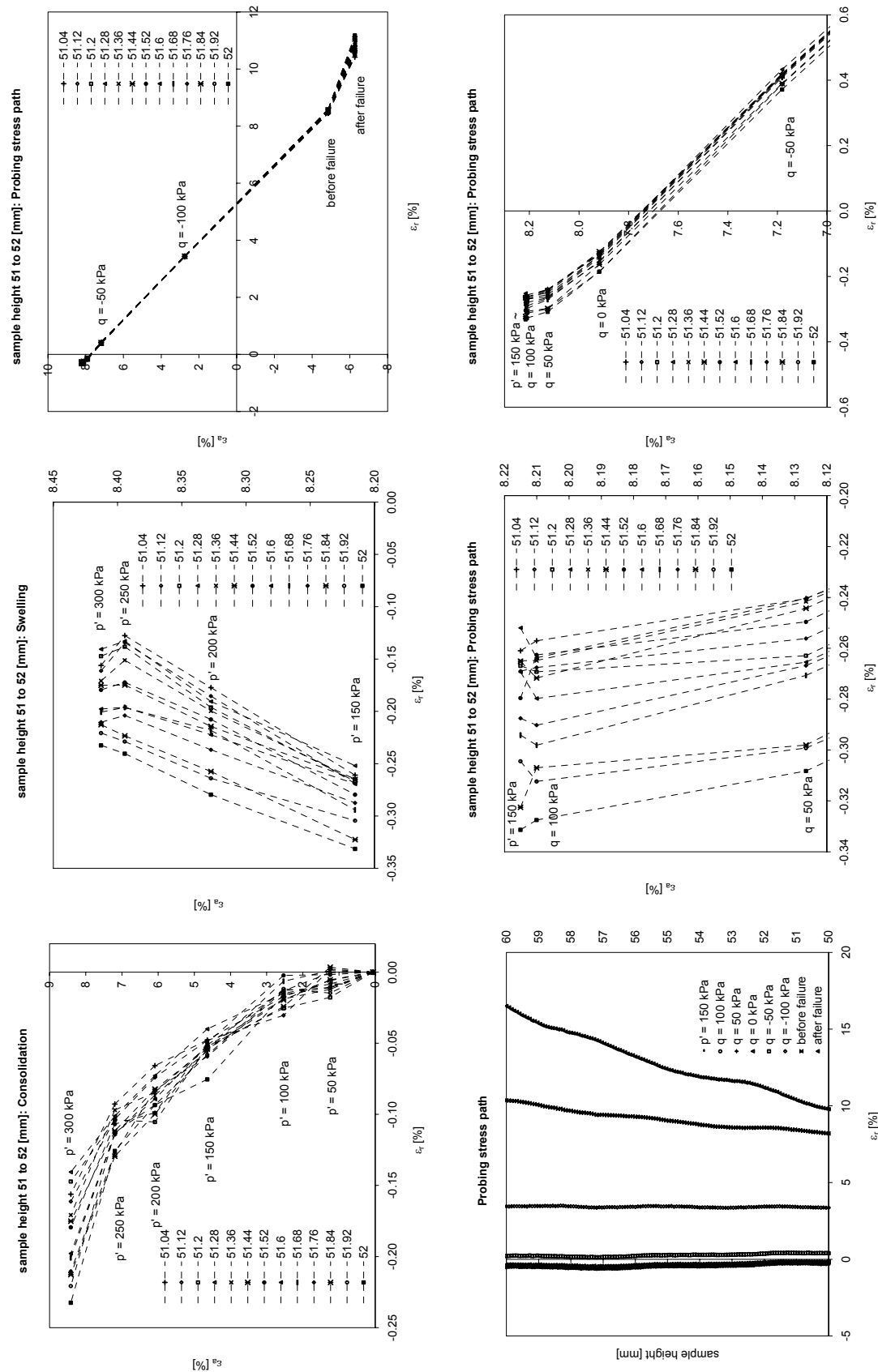
Fig. 10.83: Laser scan data of the triaxial stress path test S2bT1 on natural Kloten clay: between sample heights (from base) 51 – 52 mm.
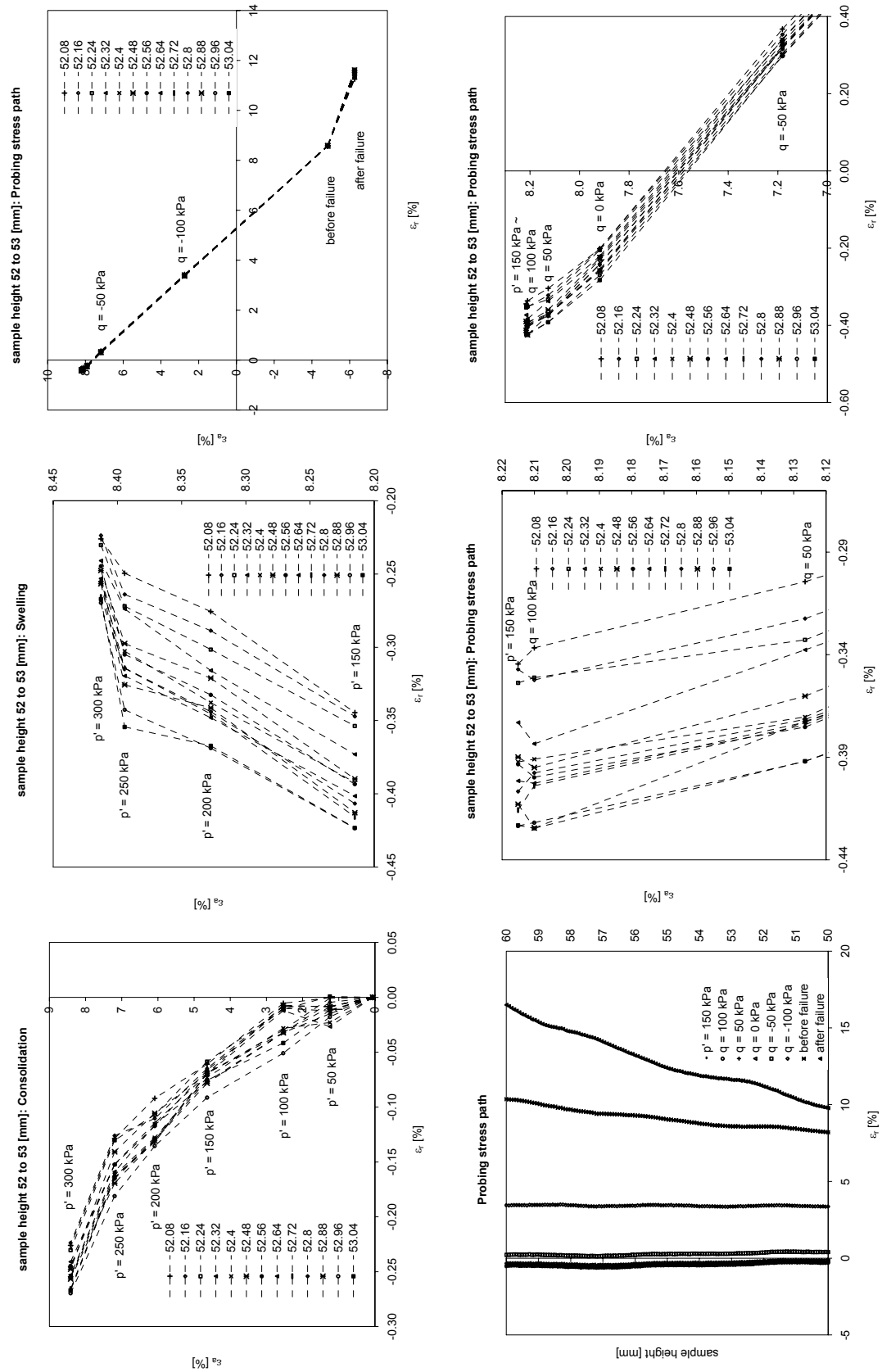
Fig. 10.84: Laser scan data of the triaxial stress path test S2bT1 on natural Kloten clay: between sample heights (from base) 52 – 53 mm.
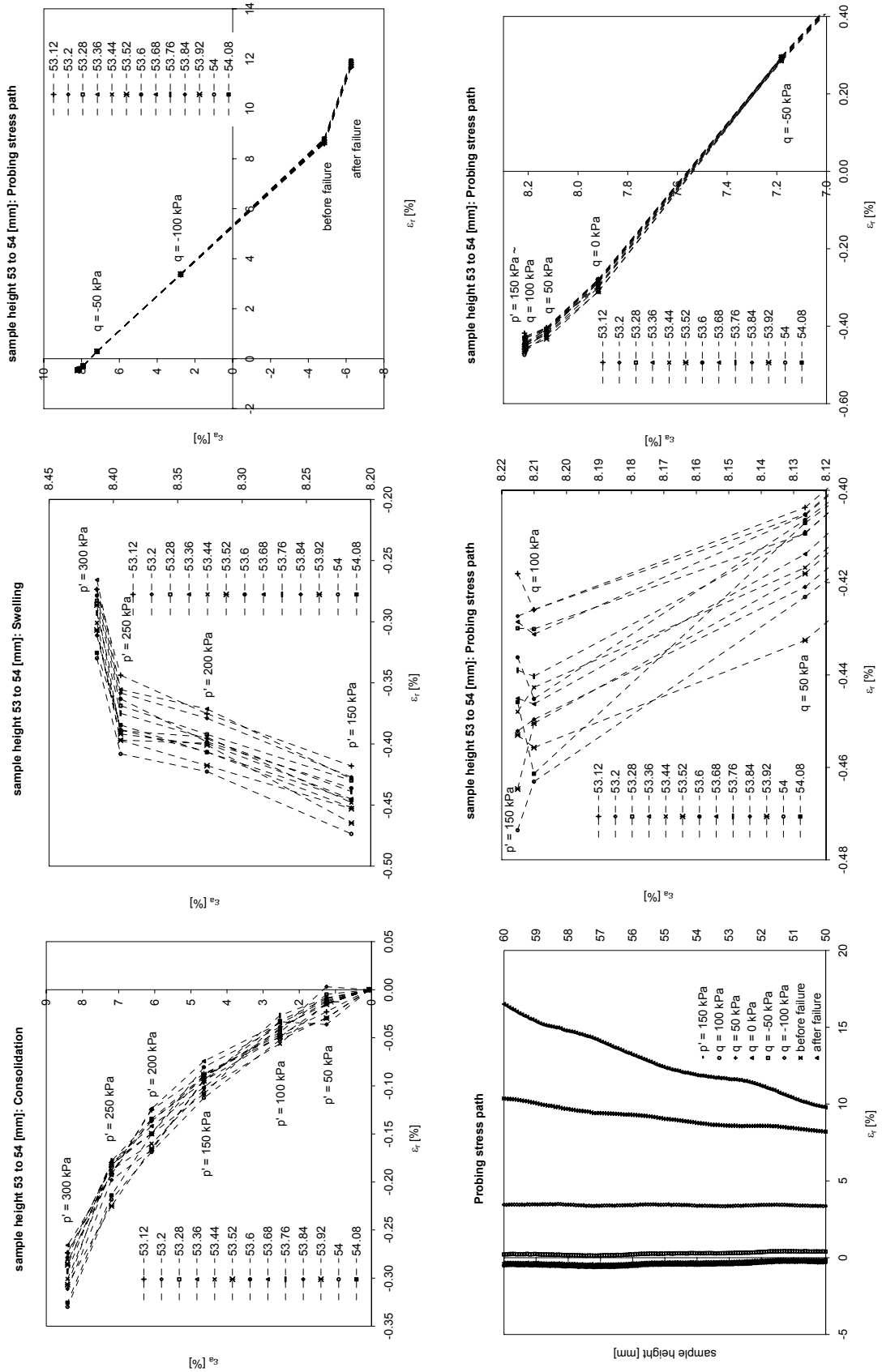
Fig. 10.85:   Laser scan data of the triaxial stress path test S2bT1 on natural Kloten clay: between sample heights (from base) 53 – 54 mm.

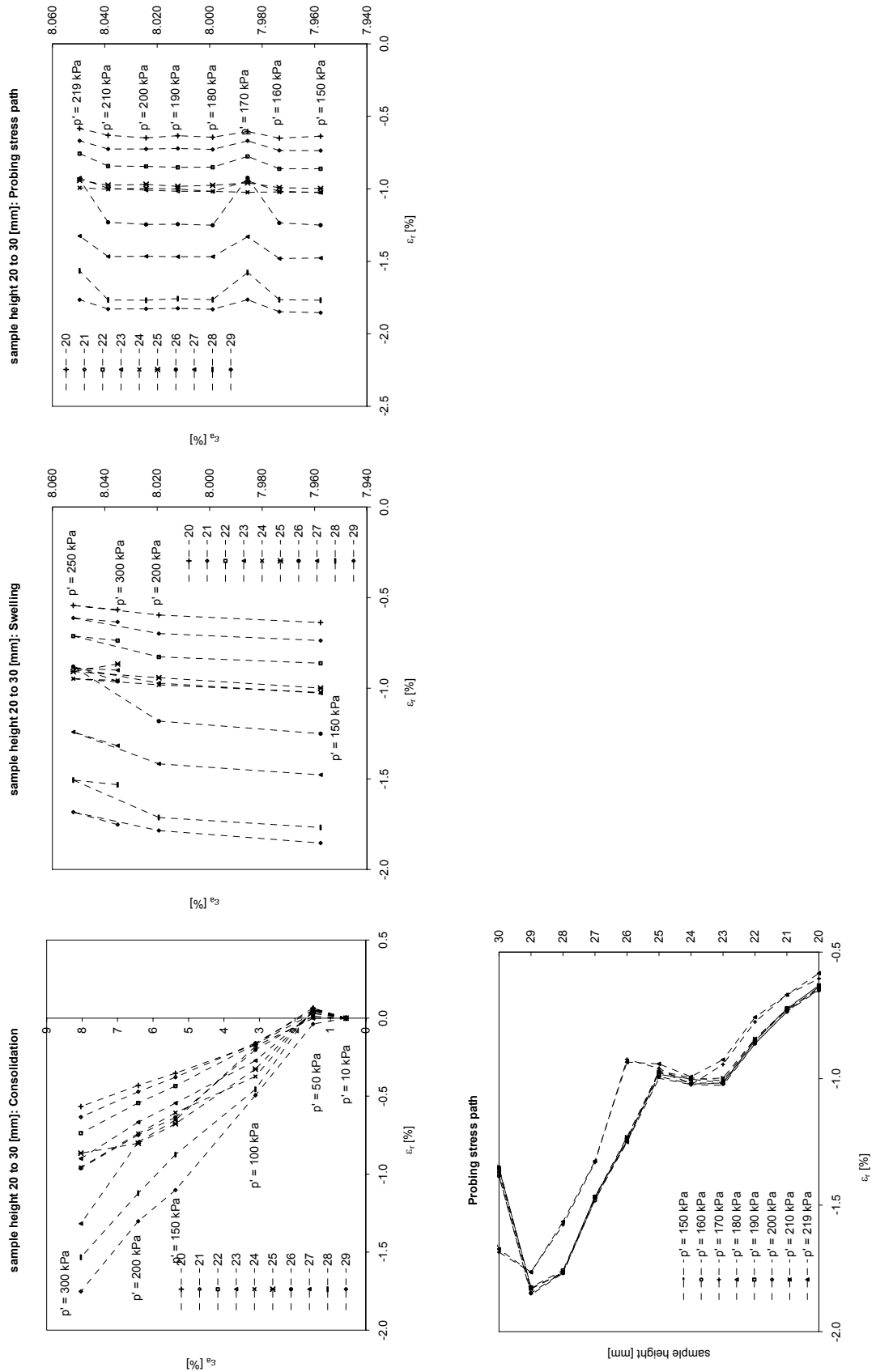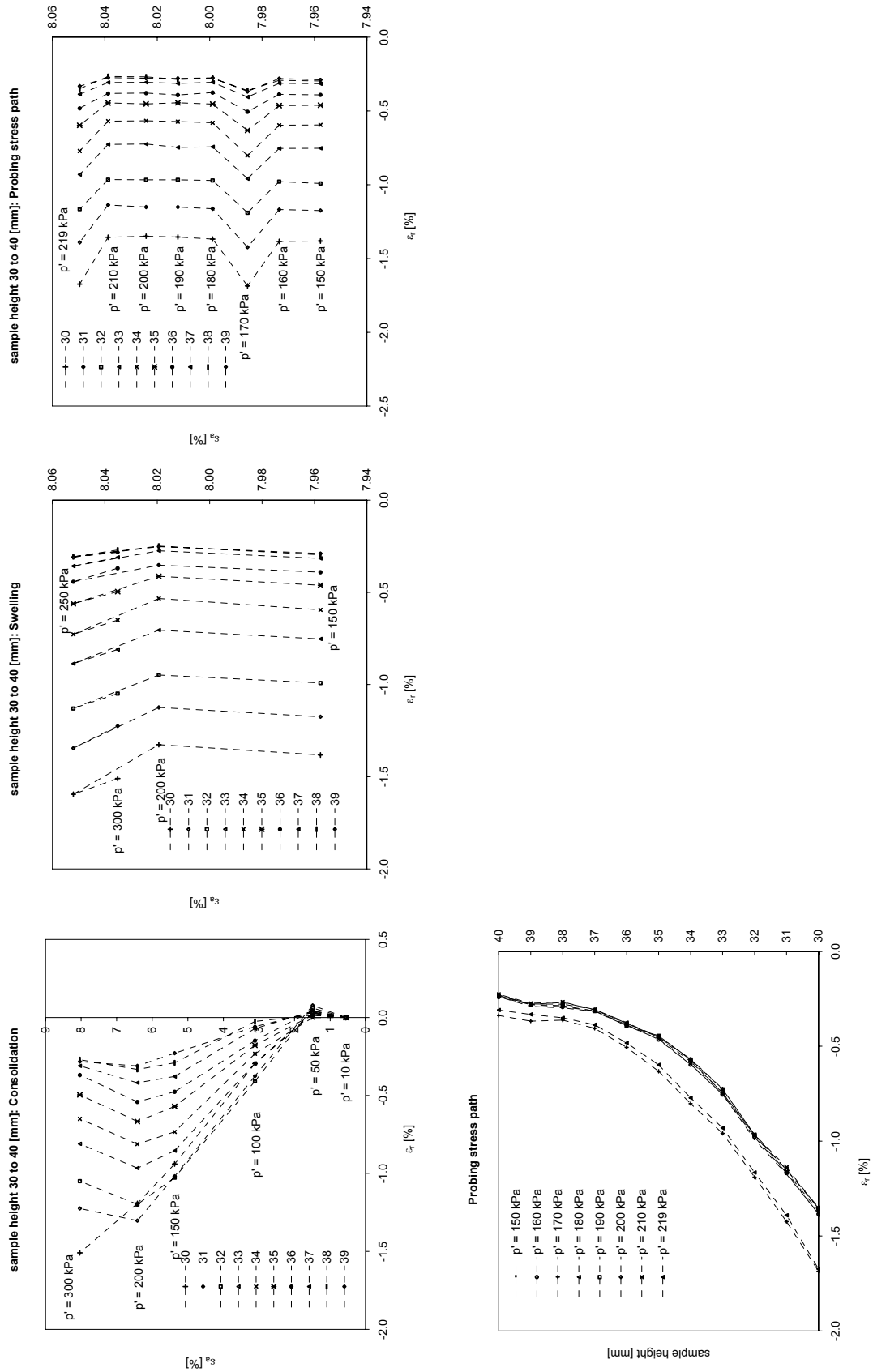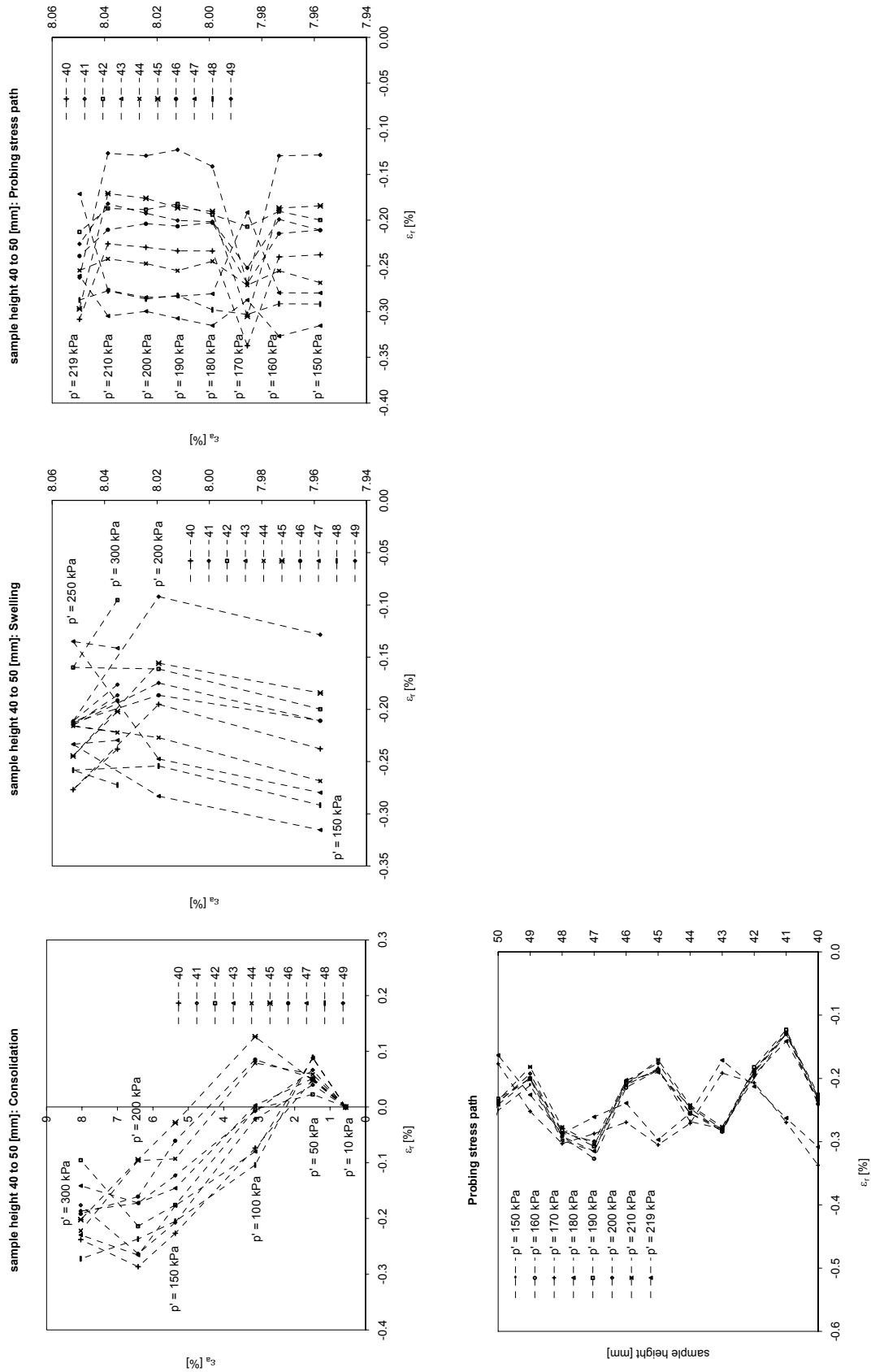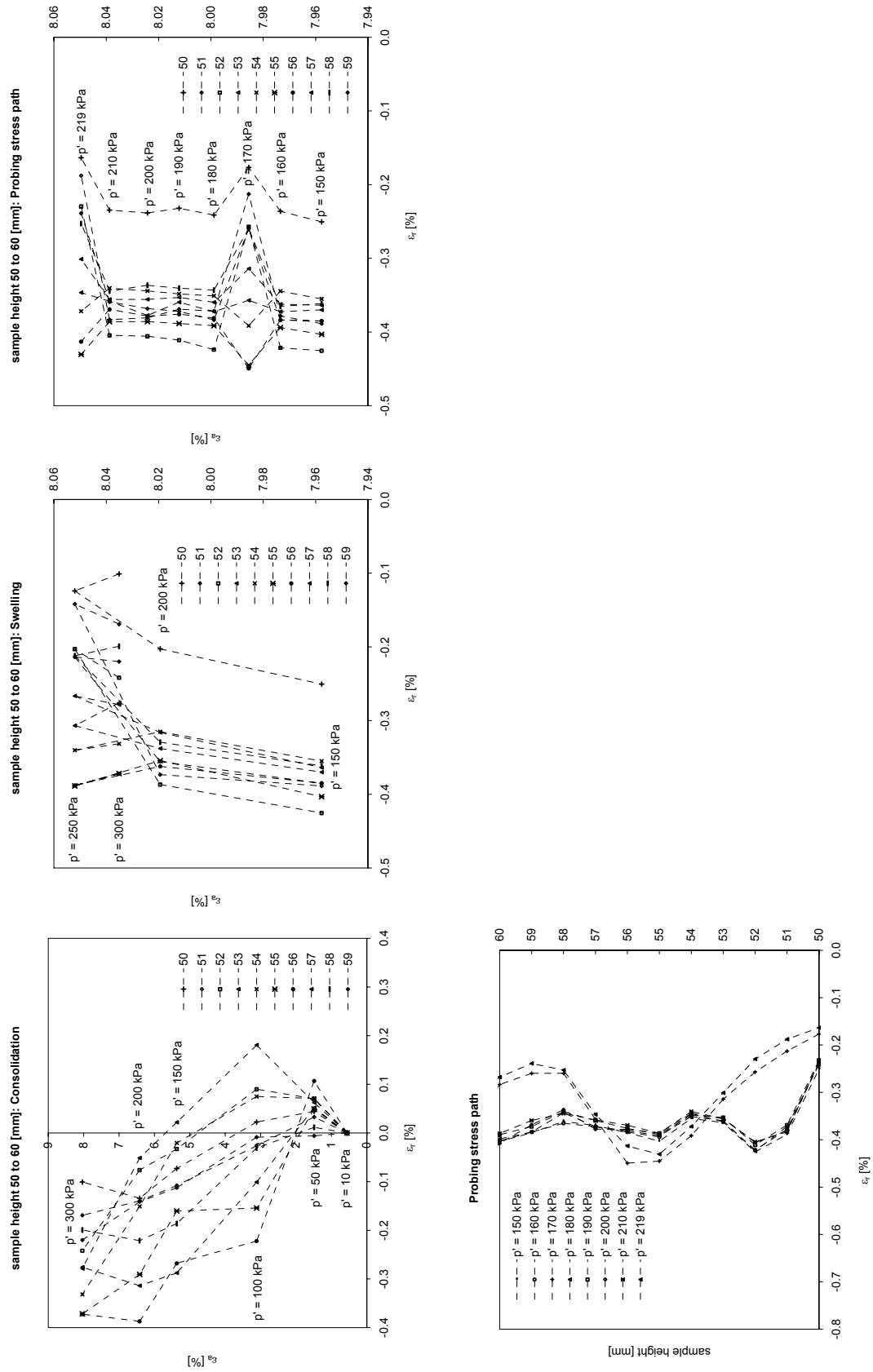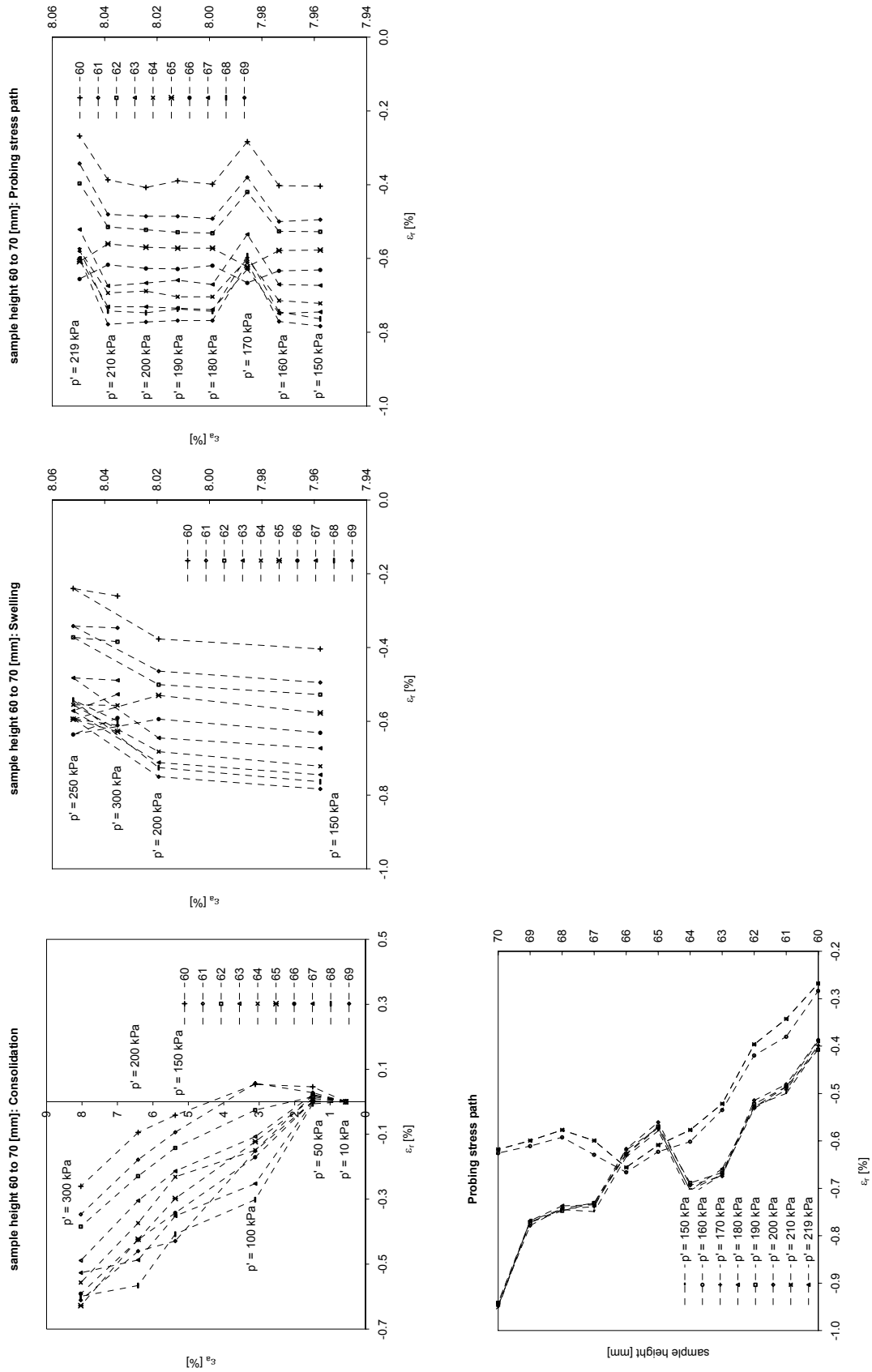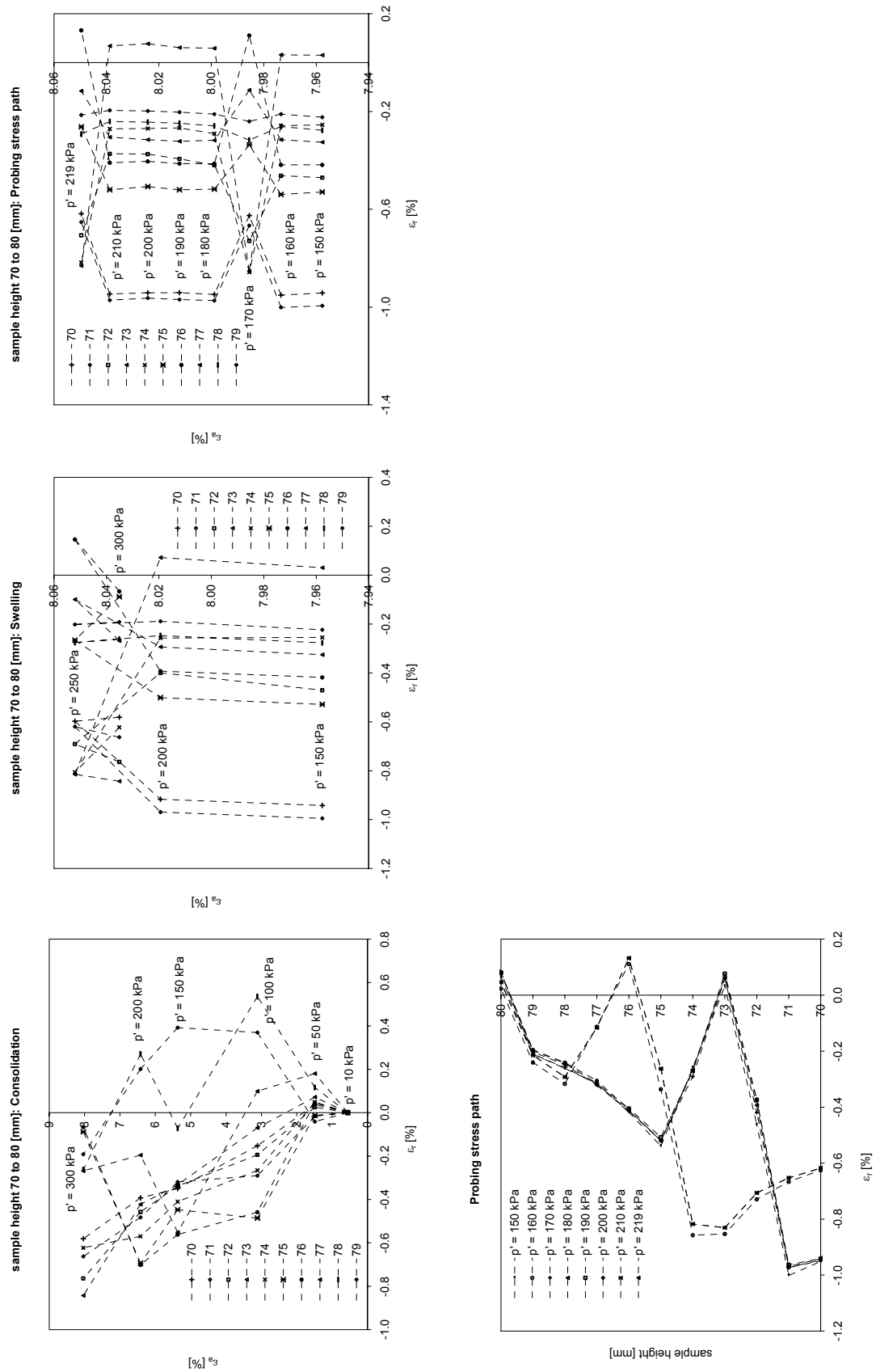Fig. 10.86: Laser scan data of the triaxial stress path test S2bT1 on natural Kloten clay: between sample heights (from base) 54 – 55 mm.

Triaxial Test   S2bT3

Test aim: Initial stiffness and stiffness degradation
Material number: 46862   Block sample of natural Kloten clay
Test apparatus: HIF B 24: Triax 3 (yellow)
File name: S5_3.PRB
     test start: 02.07.2004   15:25:13   test stop: 26.08.2004   09:33:25
Comments:

Measured sample data:

Height H_0	105.93 [mm]	
Diameter D	5.09 [cm]	
Weight m_f	436.79 [g]	

Determined sample data:

Cross-sectional area:	A	20.31	[cm^2]
Volume: f(H_0, D)	V_0	215.12	[cm^3]
Water content	w	25.91	[%]
Volume: f(m_f, w, ρ_s, S_r=1)	V_0	215.12	[cm^3]
Void ratio: f(m_f, w, ρ_s, S_r=1)	e_0	0.718	[-]

Material parameter:

density	ρ_s	2.77	[g/cm^3]
specific gravity of water	ρ_w	1	[g/cm^3]

Test data:

test-time	dH	force	cell-pressure	PWP bottom	PWP top	dV backpr.	H_{act}	V_{act}	A_c	σ_a'	σ_r'	q	p'	ε_a	ε_r	ε_s	ε_v	e
[hours]	[mm]	[kN]	[kPa]	[kPa]	[kPa]	[ccm]	[mm]	[ccm]	[cm^2]	[kPa]	[kPa]	[kPa]	[kPa]	[%]	[%]	[%]	[%]	[-]
0.0	0.000	-0.015	204.770	200.954	203.453	0.000	105.93	215.12	20.31	-4.8	2.6	-7.4	0.1	0.000	0.000	0.000	0.000	0.718
30.1	1.906	0.033	227.132	201.122	203.731	-4.092	104.02	211.03	20.29	41.0	24.7	16.3	30.1	1.832	0.053	1.186	1.939	0.685
60.1	2.539	0.078	249.890	201.198	203.810	-5.289	103.39	209.83	20.30	85.8	47.4	38.4	60.2	2.456	0.032	1.616	2.520	0.675
90.1	3.391	0.121	272.212	200.858	203.261	-6.654	102.54	208.47	20.33	129.7	70.2	59.5	90.0	3.307	-0.058	2.243	3.192	0.665
120.6	5.050	0.166	295.151	200.798	203.088	-8.943	100.88	206.18	20.44	174.4	93.2	81.2	120.3	5.006	-0.334	3.560	4.337	0.646
151.1	6.353	0.211	318.170	201.082	203.516	-10.727	99.58	204.39	20.53	218.7	115.9	102.8	150.1	6.380	-0.566	4.631	5.248	0.632
181.1	7.266	0.256	340.689	200.912	203.410	-11.951	98.66	203.17	20.59	262.8	138.5	124.3	180.0	7.364	-0.741	5.404	5.882	0.622
211.6	8.005	0.303	363.628	201.050	203.574	-12.847	97.93	202.27	20.66	308.0	161.3	146.7	210.2	8.175	-0.912	6.057	6.351	0.615
242.1	8.643	0.346	386.488	200.780	203.104	-13.597	97.29	201.52	20.71	351.6	184.5	167.0	240.2	8.884	-1.069	6.635	6.747	0.609
272.6	9.153	0.392	409.335	201.122	203.569	-14.318	96.78	200.80	20.75	395.9	207.0	188.9	270.0	9.458	-1.164	7.081	7.131	0.603
402.6	9.747	0.445	425.169	200.624	203.096	-15.249	96.18	199.87	20.78	437.4	223.3	214.1	294.7	10.134	-1.252	7.591	7.630	0.596
428.6	9.780	0.417	405.588	200.687	203.050	-14.855	96.15	200.27	20.83	403.9	203.7	200.2	270.5	10.172	-1.377	7.699	7.418	0.599
459.1	9.787	0.372	382.730	200.755	203.070	-14.297	96.14	200.82	20.89	358.9	180.8	178.1	240.2	10.180	-1.530	7.806	7.119	0.604
489.1	9.759	0.328	360.275	200.932	203.346	-13.929	96.17	201.19	20.92	314.9	158.1	156.8	210.4	10.148	-1.612	7.840	6.923	0.606
519.1	9.731	0.284	337.985	201.253	203.734	-13.476	96.20	201.64	20.96	271.0	135.5	135.5	180.7	10.115	-1.716	7.888	6.683	0.610
593.1	9.707	0.233	312.074	201.007	203.564	-12.740	96.22	202.38	21.03	220.6	109.8	110.8	146.7	10.088	-1.896	7.990	6.295	0.616
598.6	9.710	0.226	316.727	200.844	203.198	-12.698	96.22	202.42	21.04	222.1	114.7	107.4	150.5	10.091	-1.909	8.001	6.273	0.616
605.6	9.717	0.220	322.551	201.030	203.432	-12.668	96.21	202.45	21.04	224.9	120.3	104.5	155.2	10.099	-1.921	8.014	6.257	0.617
612.6	9.708	0.213	328.442	200.925	203.418	-12.592	96.22	202.53	21.05	227.5	126.3	101.2	160.0	10.089	-1.936	8.017	6.217	0.617
620.1	9.723	0.205	334.766	200.815	203.305	-12.500	96.21	202.62	21.06	230.0	132.7	97.3	165.2	10.106	-1.969	8.050	6.169	0.618
627.6	9.732	0.198	340.562	200.674	203.029	-12.463	96.20	202.66	21.07	232.7	138.7	94.0	170.0	10.117	-1.983	8.067	6.150	0.618
635.6	9.719	0.191	347.513	200.912	203.407	-12.348	96.21	202.77	21.08	236.0	145.4	90.6	175.6	10.102	-2.006	8.072	6.090	0.619
642.6	9.717	0.183	353.348	200.798	203.156	-12.273	96.21	202.85	21.08	238.2	151.4	86.8	180.3	10.099	-2.025	8.083	6.050	0.620
657.6	9.726	0.169	365.535	200.941	203.488	-12.211	96.20	202.91	21.09	244.3	163.3	80.1	190.0	10.110	-2.046	8.104	6.018	0.620
672.6	9.729	0.154	378.230	200.790	203.188	-12.120	96.20	203.00	21.10	249.2	176.2	73.0	200.6	10.113	-2.071	8.123	5.970	0.621
701.6	9.709	0.126	402.516	201.062	203.603	-12.090	96.22	203.03	21.10	259.9	200.2	59.7	220.1	10.090	-2.068	8.105	5.955	0.621
731.1	9.693	0.097	427.045	201.112	203.693	-11.924	96.24	203.20	21.11	270.6	224.6	45.9	240.0	10.072	-2.102	8.116	5.868	0.622
755.6	9.673	0.067	451.862	201.041	203.467	-11.830	96.26	203.29	21.12	281.3	249.6	31.7	260.2	10.049	-2.115	8.109	5.819	0.623
785.1	9.650	0.037	476.251	200.661	203.046	-11.584	96.28	203.54	21.14	291.9	274.4	17.5	280.2	10.023	-2.166	8.126	5.692	0.625
814.6	9.606	0.009	500.703	200.807	203.198	-11.436	96.32	203.68	21.15	303.0	298.7	4.3	300.1	9.973	-2.179	8.101	5.614	0.626
858.6	9.521	-0.034	537.308	200.761	203.236	-11.225	96.41	203.89	21.15	319.2	335.3	-16.1	330.0	9.876	-2.183	8.039	5.510	0.628
903.1	9.427	-0.079	574.696	200.958	203.357	-11.100	96.50	204.02	21.14	335.2	372.5	-37.4	360.1	9.769	-2.164	7.955	5.441	0.629
947.6	9.318	-0.122	611.374	200.851	203.287	-11.376	96.61	203.74	21.09	351.5	409.3	-57.8	390.0	9.645	-2.031	7.784	5.583	0.627
992.6	9.058	-0.166	648.997	200.887	203.485	-11.533	96.87	203.59	21.02	367.8	446.8	-79.0	420.5	9.350	-1.843	7.462	5.665	0.626
1037.1	8.925	-0.210	685.646	200.908	203.493	-11.558	97.01	203.56	20.99	383.4	483.4	-100.1	450.1	9.201	-1.761	7.308	5.678	0.626
1082.1	8.756	-0.255	722.975	200.862	203.374	-11.502	97.17	203.62	20.95	399.2	520.9	-121.7	480.3	9.011	-1.681	7.128	5.649	0.626
1126.1	8.604	-0.298	759.689	200.760	203.125	-11.827	97.33	203.29	20.89	415.1	557.7	-142.7	510.2	8.840	-1.511	6.901	5.817	0.623
1171.1	8.515	-0.342	797.009	200.755	203.201	-11.993	97.42	203.13	20.85	431.0	595.0	-164.0	540.4	8.741	-1.418	6.773	5.904	0.622
1215.6	8.422	-0.386	834.070	200.854	203.481	-12.432	97.52	202.69	20.79	446.2	631.9	-185.7	570.0	8.637	-1.252	6.593	6.134	0.618
1260.1	8.378	-0.430	871.291	200.780	203.307	-13.194	97.55	201.93	20.70	461.5	669.2	-207.7	600.0	8.588	-1.027	6.410	6.534	0.612
1308.1	8.276	-0.459	900.308	200.728	203.236	-13.387	97.65	201.73	20.66	476.1	698.3	-222.2	624.3	8.475	-0.920	6.263	6.636	0.611
1308.1	8.255	-0.404	900.490	224.124	221.120	-13.387	97.68	201.73	20.65	482.3	677.9	-195.6	612.7	8.451	-0.908	6.240	6.636	0.611
1308.2	8.250	-0.369	900.446	235.060	229.198	-13.387	97.68	201.73	20.65	489.7	668.3	-178.7	608.8	8.446	-0.905	6.234	6.636	0.611
1308.2	8.250	-0.337	900.429	245.255	237.352	-13.387	97.68	201.73	20.65	496.0	659.1	-163.2	604.7	8.446	-0.905	6.234	6.636	0.611
1308.2	8.245	-0.309	900.444	254.553	245.331	-13.387	97.69	201.73	20.65	500.9	650.5	-149.6	600.6	8.440	-0.902	6.228	6.636	0.611
1308.2	8.241	-0.259	900.537	271.429	260.593	-13.387	97.69	201.73	20.65	509.1	634.5	-125.4	592.7	8.436	-0.900	6.224	6.636	0.611
1308.3	8.318	-0.192	900.143	292.014	281.367	-13.387	97.61	201.73	20.67	520.6	613.5	-92.9	582.5	8.521	-0.943	6.310	6.636	0.611
1308.3	8.301	-0.115	900.349	319.592	307.988	-13.387	97.63	201.73	20.66	530.9	586.6	-55.7	568.0	8.503	-0.933	6.291	6.636	0.611
1308.3	8.363	-0.009	900.165	356.291	346.312	-13.387	97.57	201.73	20.68	544.5	548.9	-4.4	547.4	8.572	-0.968	6.360	6.636	0.611
1308.6	8.412	0.110	900.114	399.063	391.055	-13.387	97.52	201.73	20.69	558.2	505.1	53.2	522.8	8.626	-0.995	6.414	6.636	0.611
1308.8	8.458	0.210	900.180	436.063	429.915	-13.387	97.47	201.73	20.70	568.7	467.2	101.5	501.0	8.677	-1.021	6.465	6.636	0.611
1309.1	8.581	0.311	900.104	472.725	469.641	-13.387	97.35	201.73	20.72	579.0	428.9	150.1	478.9	8.815	-1.089	6.603	6.636	0.611
1309.4	8.673	0.418	900.122	512.502	510.912	-13.387	97.26	201.73	20.74	589.8	388.4	201.5	455.6	8.918	-1.141	6.706	6.636	0.611
1309.9	8.862	0.521	900.085	547.134	548.260	-13.387	97.07	201.73	20.78	603.1	352.4	250.7	435.9	9.130	-1.247	6.918	6.636	0.611
1310.7	9.129	0.626	900.108	580.078	582.088	-13.387	96.80	201.73	20.84	619.4	319.0	300.4	419.2	9.431	-1.397	7.219	6.636	0.611
1312.0	9.534	0.733	900.095	609.181	612.015	-13.387	96.40	201.73	20.93	639.7	289.5	350.2	406.2	9.890	-1.627	7.679	6.636	0.611
1315.2	10.646	0.857	900.038	642.764	645.987	-13.387	95.28	201.73	21.17	660.4	255.7	404.8	390.6	11.173	-2.269	8.961	6.636	0.611
1332.2	16.391	1.016	900.131	673.784	676.657	-13.387	89.54	201.73	22.53	675.8	224.9	450.9	375.2	18.306	-5.835	16.094	6.636	0.611
1347.6	21.497	1.099	900.055	670.349	673.225	-13.387	84.43	201.73	23.89	688.2	228.3	460.0	381.6	25.460	-9.412	23.249	6.636	0.611
1357.2	24.902	1.133	900.151	667.075	670.068	-13.387	81.03	201.73	24.90	686.6	231.6	455.1	383.3	30.733	-12.048	28.521	6.636	0.611

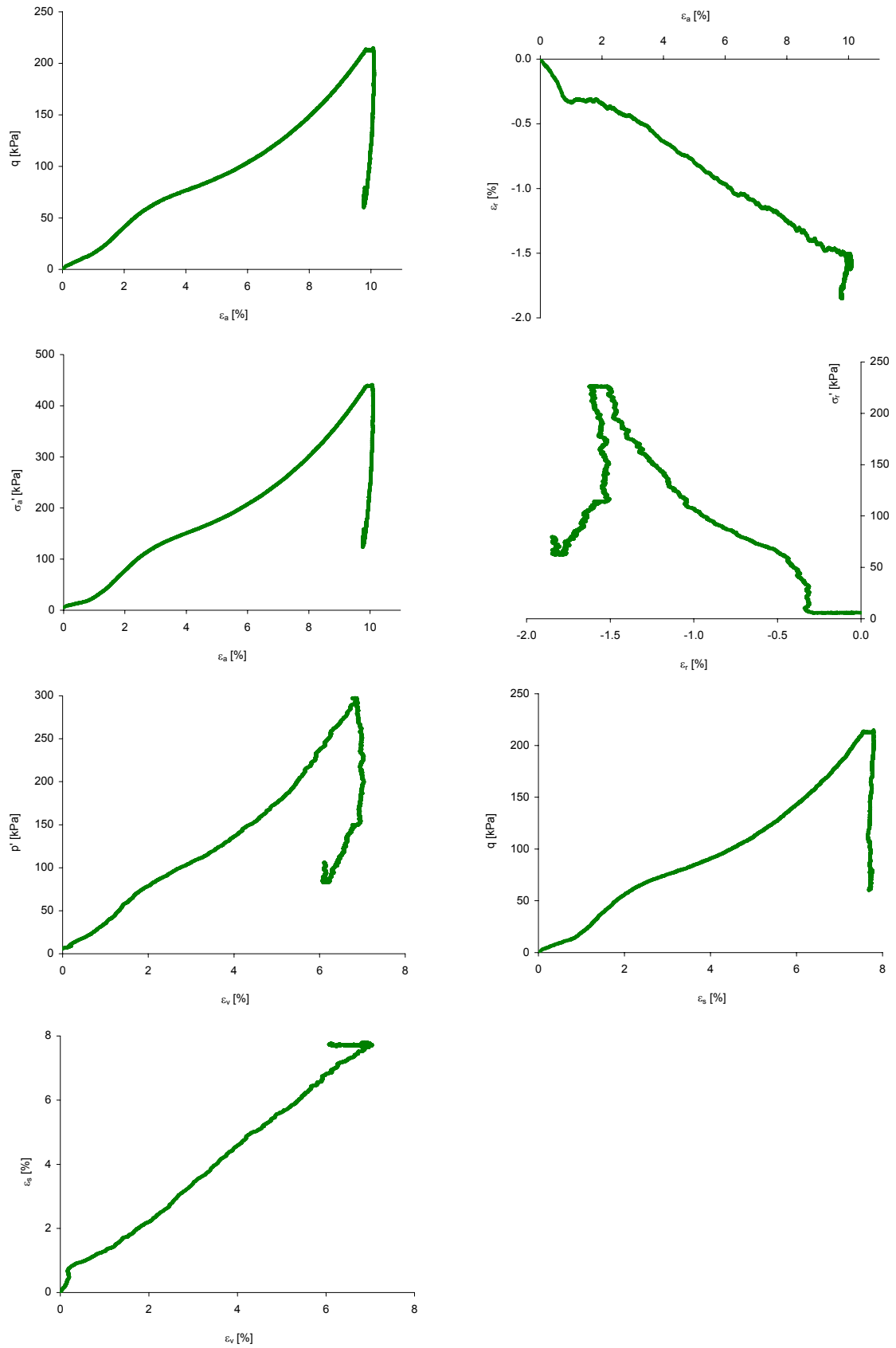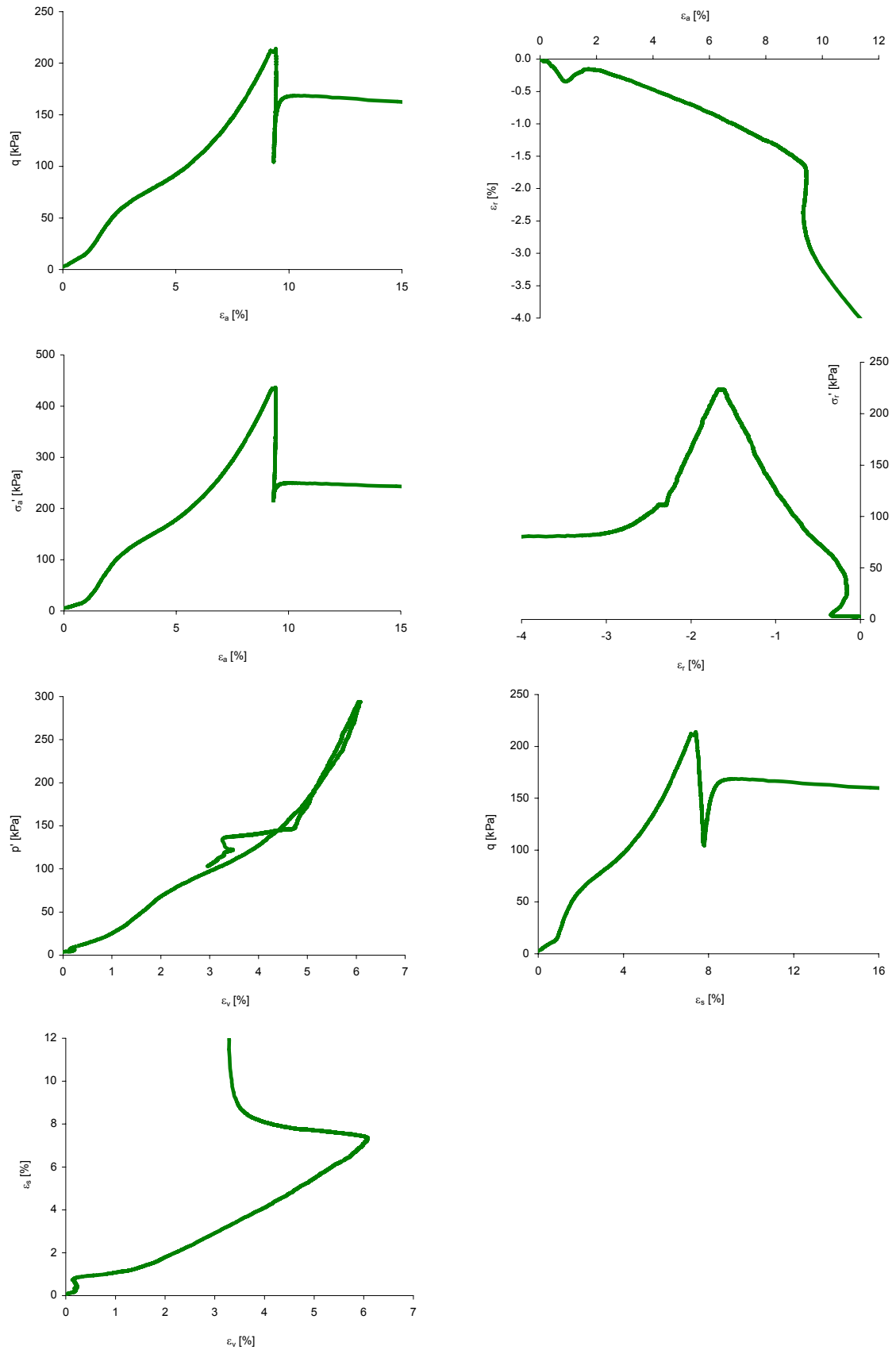Fig. 10.87:   Triaxial test data of stress path test S2bT3 on natural Kloten clay.

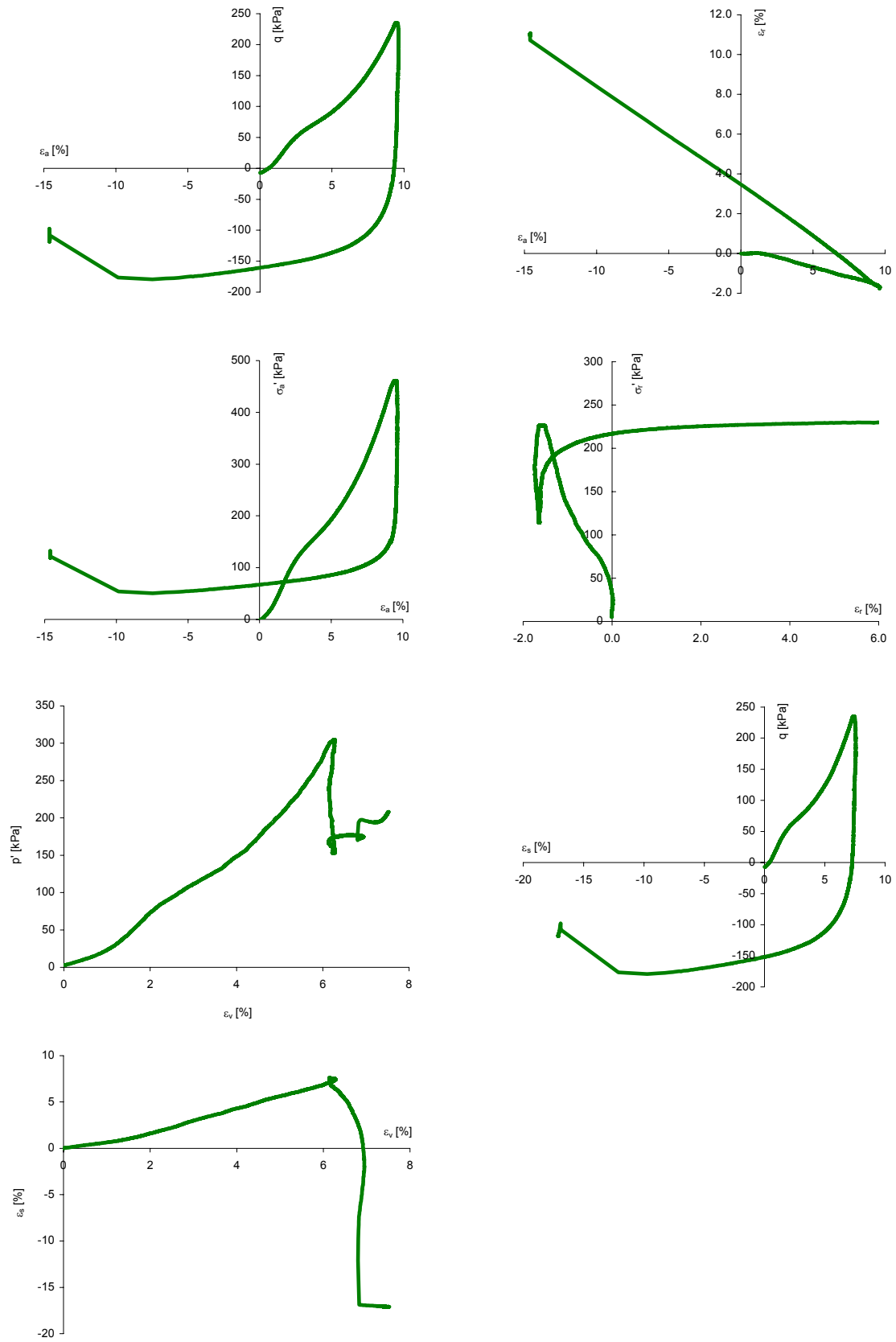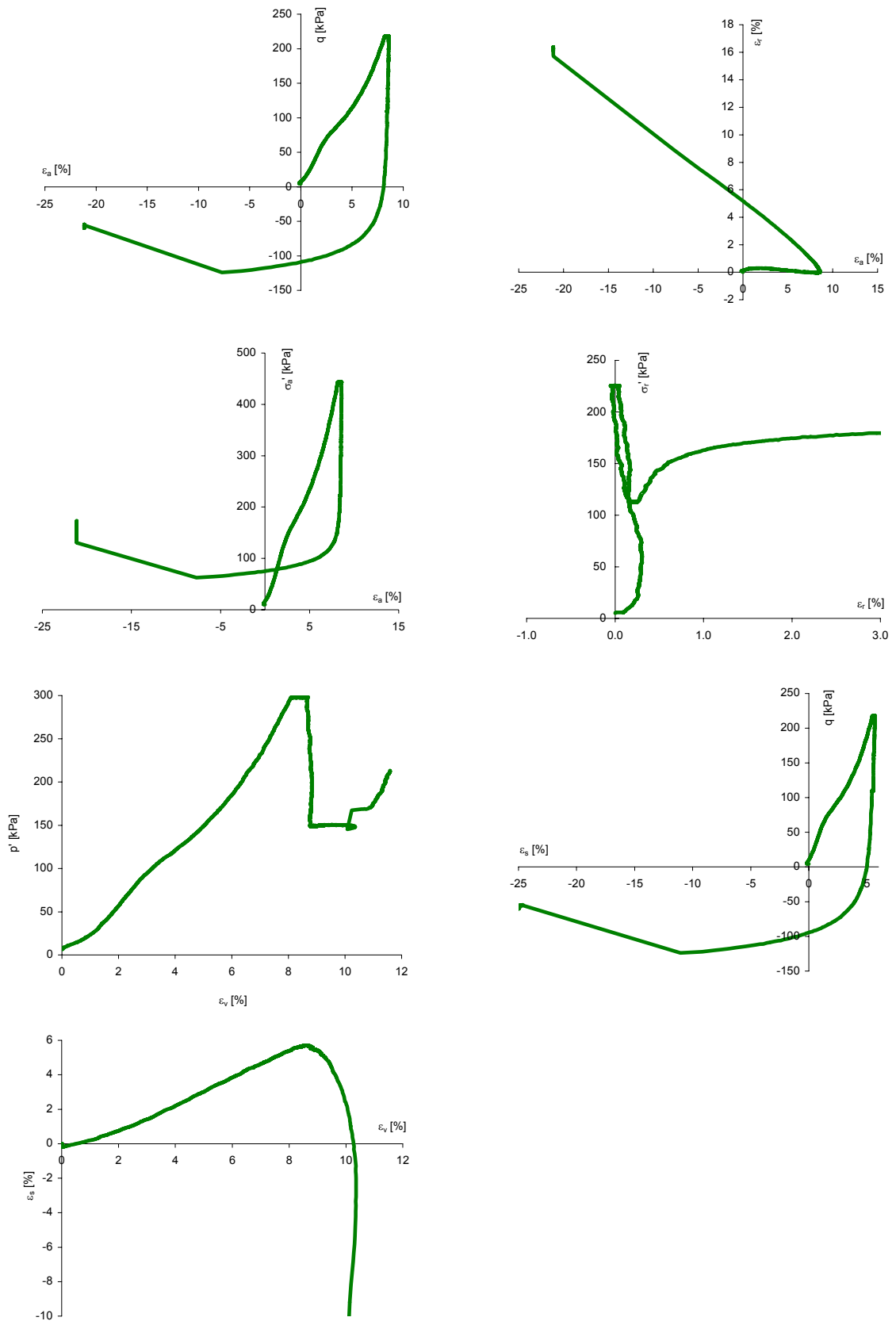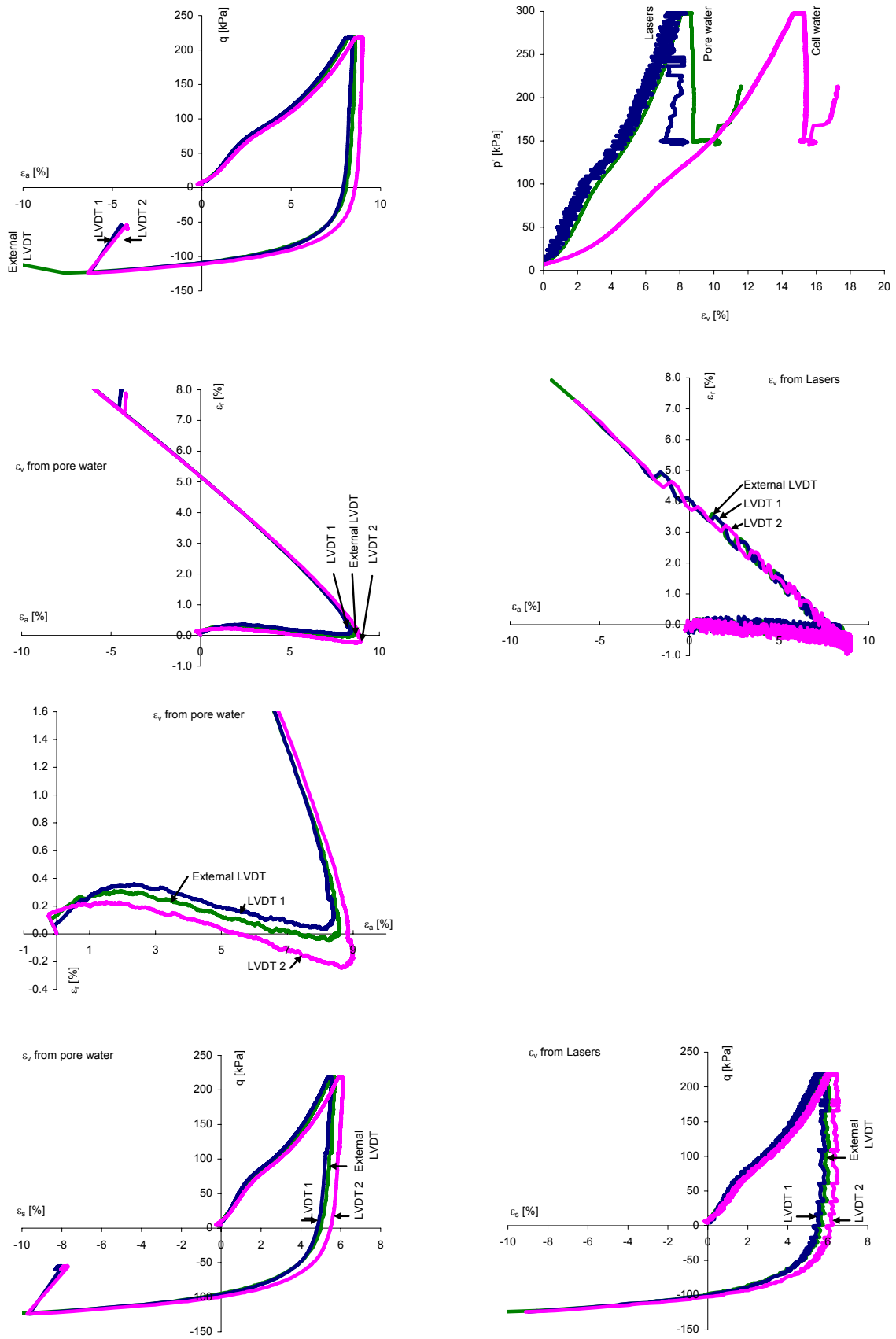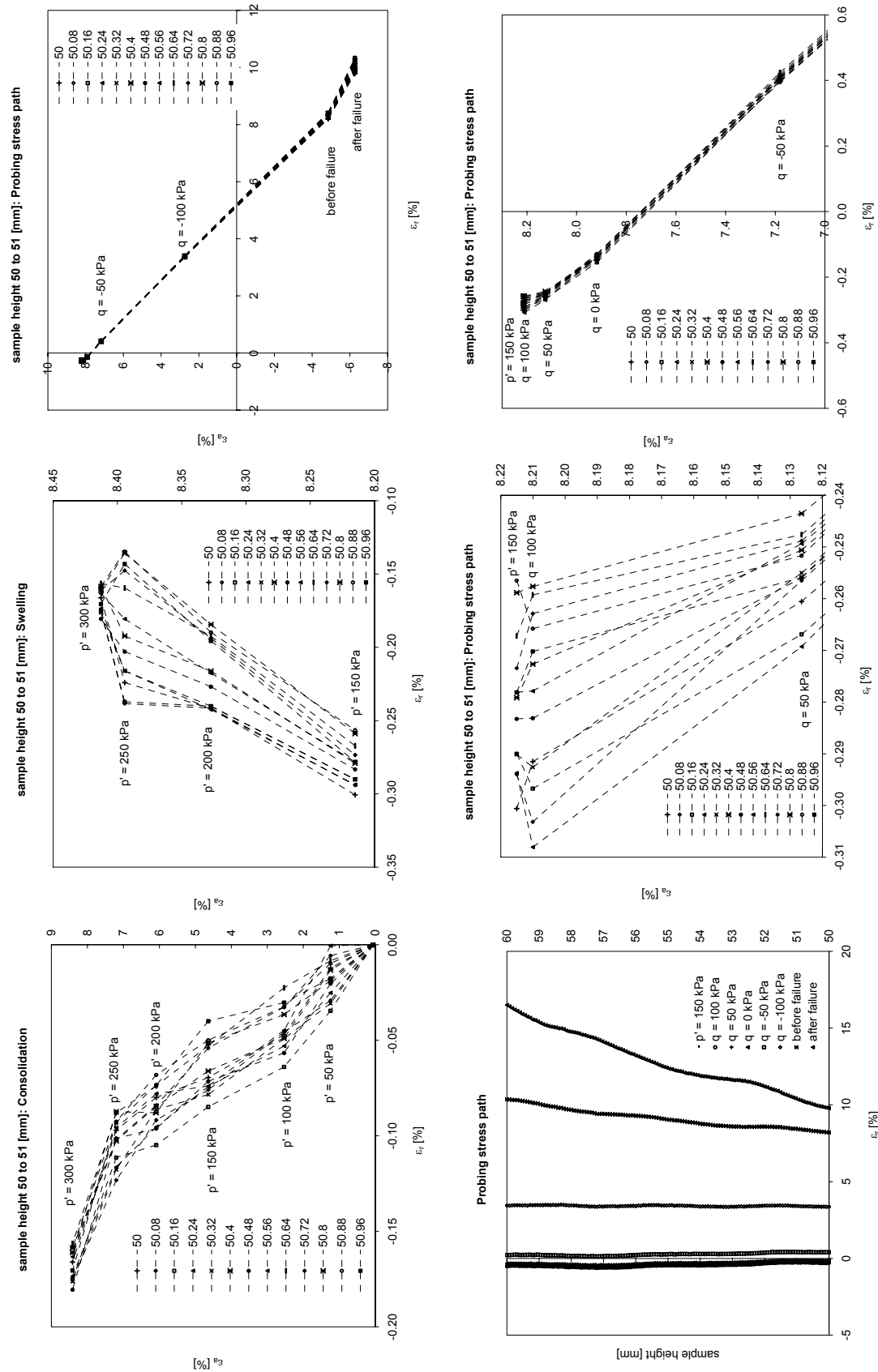Fig. 10.88:   Triaxial test data of stress path test S2bT3 on natural Kloten clay.

Fig. 10.89:   Triaxial test data of stress path test S2bT3 on natural Kloten clay.

Triaxial Test   S2bT4

Test aim: Initial stiffness and stiffness degradation
Material number: 46862   Block sample of natural Kloten clay
Test apparatus: HIL B 58: Triax 4 (blue)
File name: S6_2.PRB
   test start: 02.07.2004   15:58:19   test stop: 12.08.2004   20:22:44
Comments: Electricity supply stopped during unloading. This resulted in the kink in the unloading stress path in the q - p' plot just before reloading.

Measured sample data: **Determined sample data:**   **Material parameter:**

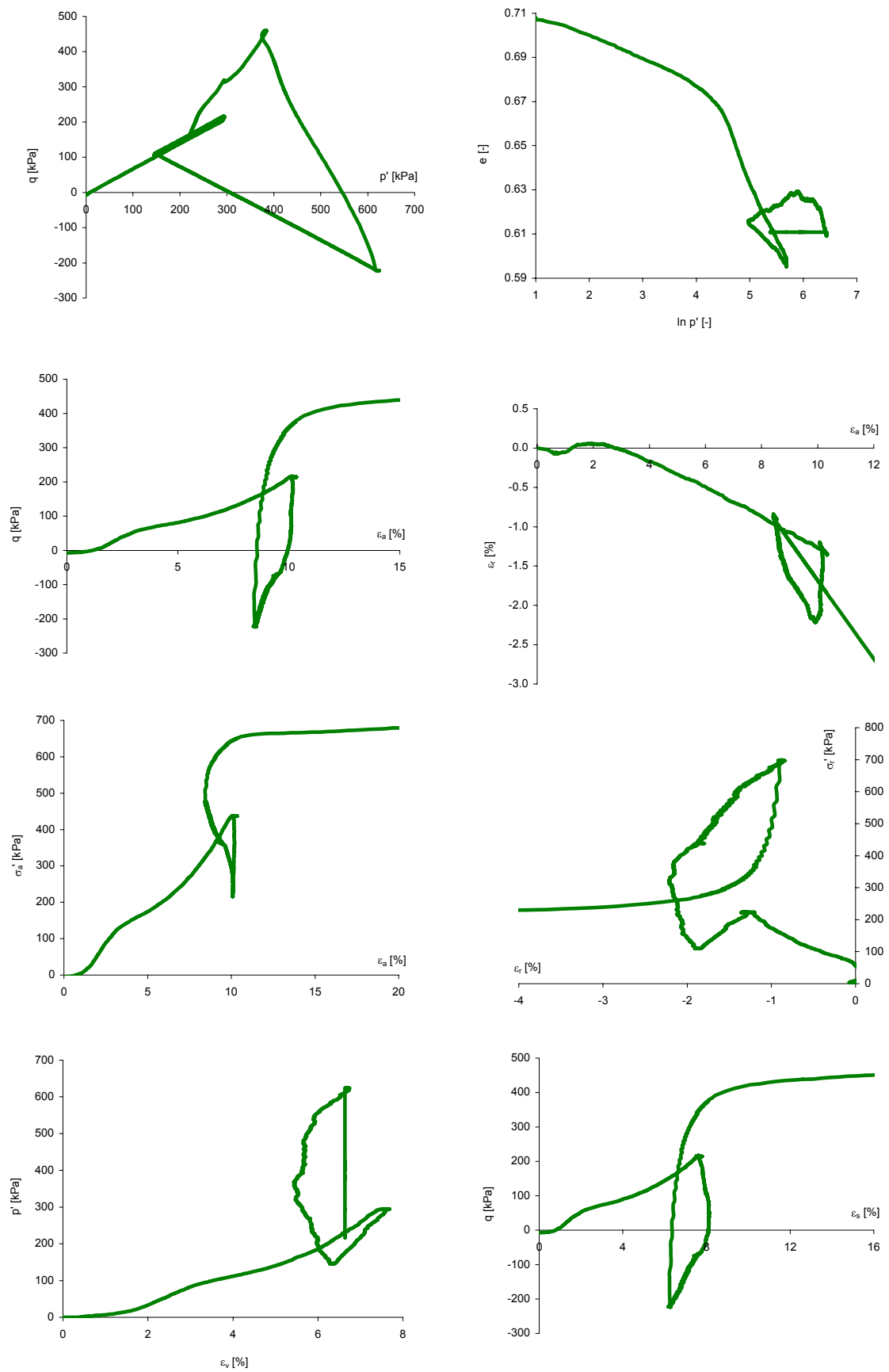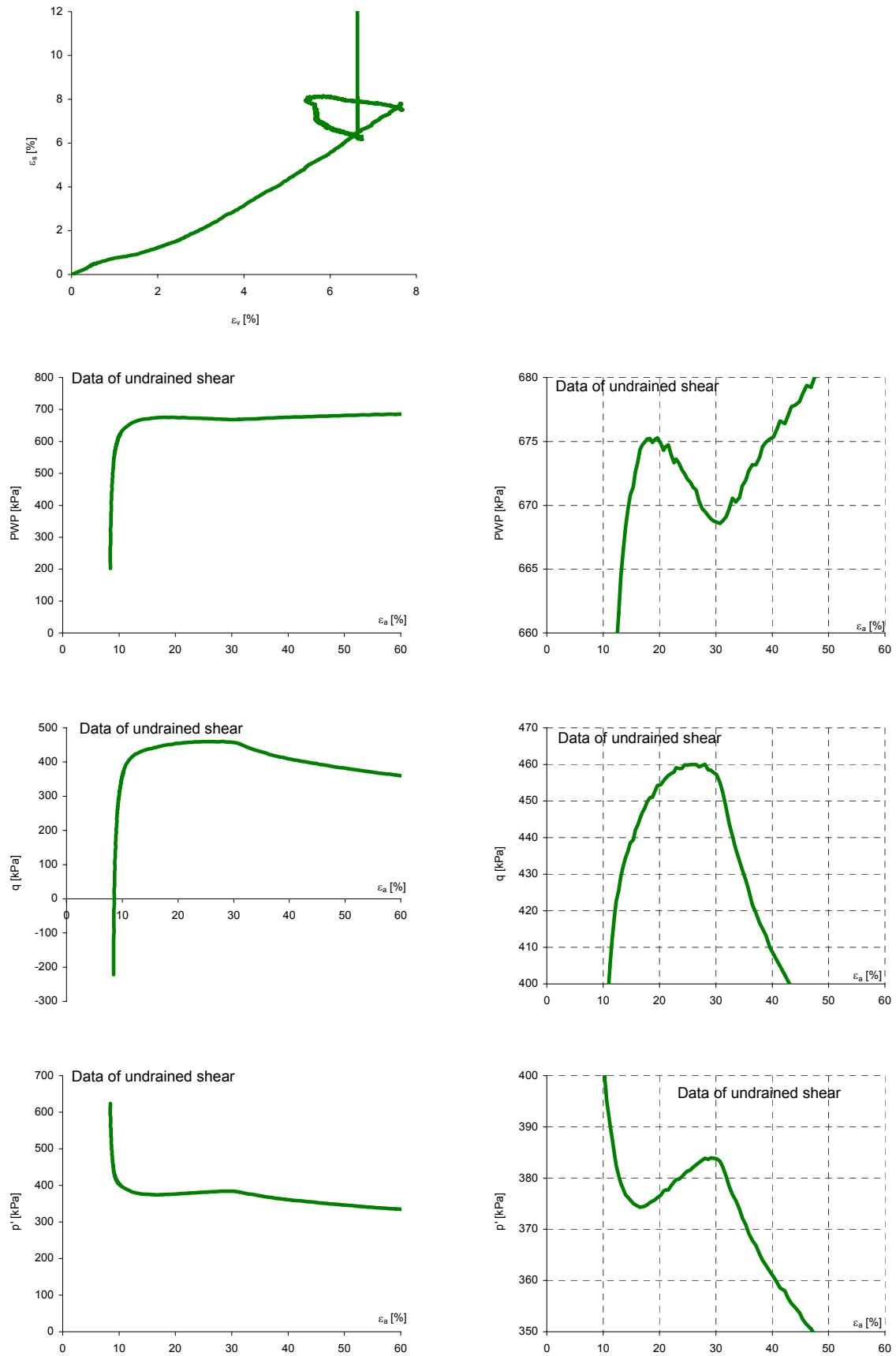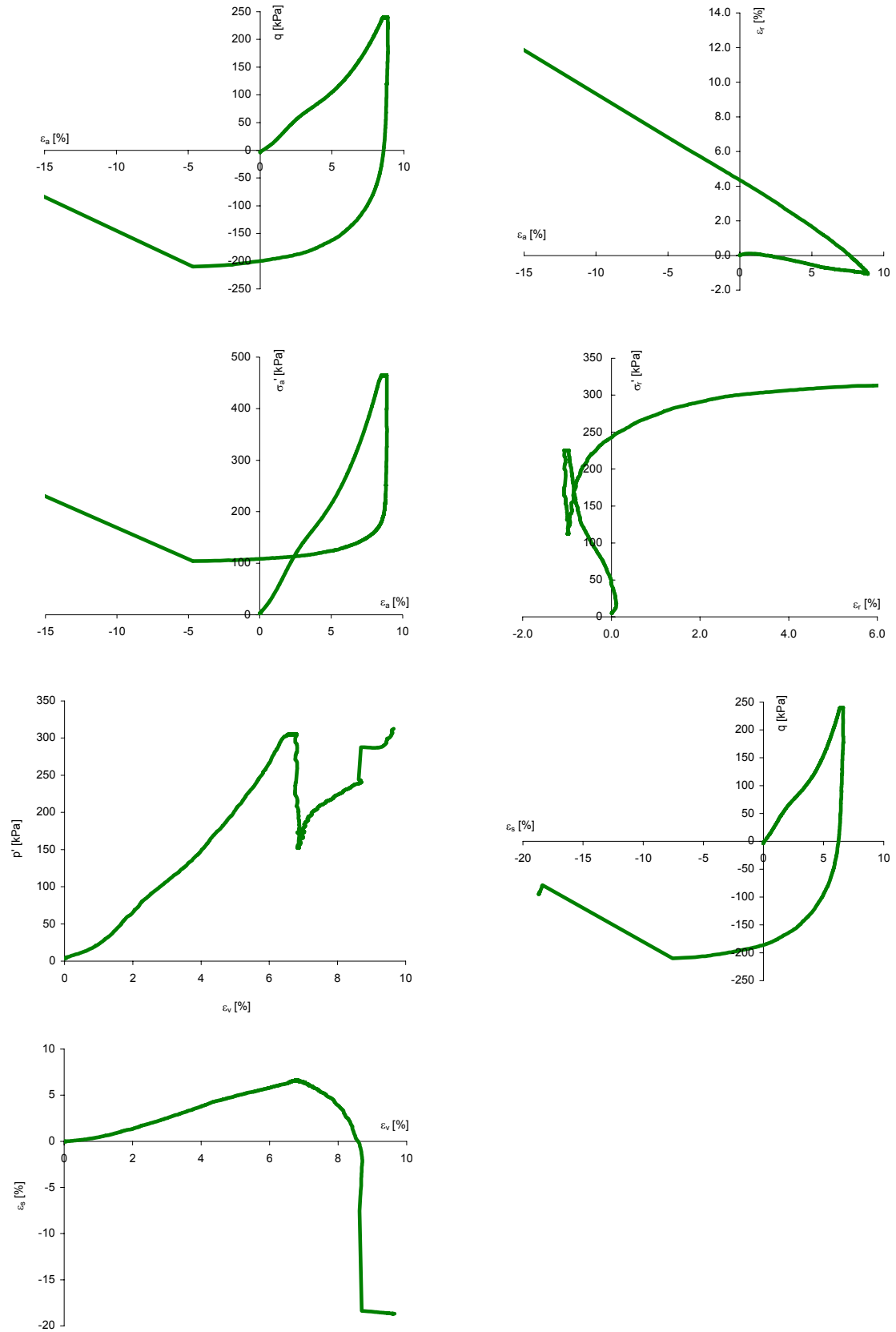|					
Height H_0	116.73 [mm]	Cross-sectional area:	A	24.83 [cm^2]	density ρ_s 2.77 [g/cm^3]
Diameter D	5.62 [cm]	Volume: f(H_0, D)	V_0	289.78 [cm^3]	specific gravity of water ρ_w 1 [g/cm^3]
Weight m_f	594.62 [g]	Water content	w	25.32 [%]	
		Volume: f(m_f, w, ρ_s, S_r=1)	V_0	291.43 [cm^3]	
		Void ratio: f(m_f, w, ρ_s, S_r=1)	e_0	0.701 [-]	

Test data:

test-time	dH	force	cell-pressure	PWP bottom	PWP top	dV backpr.	H_{act}	V_{act}	A_c	σ_a'	σ_r'	q	p'	ε_a	ε_r	ε_s	ε_v	e
[hours]	[mm]	[kN]	[kPa]	[kPa]	[kPa]	[ccm]	[mm]	[ccm]	[cm^2]	[kPa]	[kPa]	[kPa]	[kPa]	[%]	[%]	[%]	[%]	[-]
0.0	0.000	-0.009	204.877	200.124	200.539	0.000	116.73	291.43	24.83	0.9	4.5	-3.6	3.3	0.000	0.000	0.000	0.000	0.701
26.2	1.173	0.040	224.773	200.093	200.240	-3.445	115.55	287.99	24.56	40.9	24.6	16.3	30.0	1.015	0.090	0.616	1.196	0.681
55.7	2.139	0.095	247.099	200.014	199.959	-5.296	114.59	286.14	24.42	86.0	47.1	38.9	60.1	1.867	-0.008	1.250	1.851	0.670
85.7	3.217	0.151	269.841	199.864	199.872	-7.197	113.51	284.23	24.28	132.2	70.0	62.2	90.7	2.834	-0.151	1.990	2.532	0.659
114.2	4.540	0.205	291.463	199.834	199.858	-9.421	112.19	282.01	24.11	176.6	91.6	85.0	120.0	4.047	-0.353	2.933	3.341	0.646
143.7	5.737	0.261	313.843	200.024	199.982	-11.269	110.99	280.16	23.98	222.7	113.8	108.8	150.1	5.169	-0.573	3.828	4.022	0.636
173.2	6.648	0.317	336.215	200.082	200.125	-12.836	110.08	278.60	23.86	269.0	136.1	132.8	180.4	6.039	-0.716	4.504	4.607	0.626
202.7	7.383	0.372	358.643	199.890	199.944	-14.248	109.34	277.18	23.76	315.3	158.7	156.6	210.9	6.752	-0.806	5.039	5.140	0.618
231.2	7.982	0.425	380.222	199.785	199.847	-15.514	108.74	275.92	23.66	360.0	180.4	179.6	240.3	7.340	-0.859	5.466	5.623	0.611
260.2	8.505	0.481	402.234	200.078	200.093	-16.607	108.22	274.82	23.57	406.2	202.1	204.0	270.2	7.859	-0.908	5.845	6.043	0.604
404.2	9.519	0.561	424.986	199.814	199.843	-18.567	107.21	272.86	23.43	464.6	225.2	239.5	305.0	8.879	-1.037	6.611	6.804	0.593
438.2	9.522	0.496	399.423	200.035	200.029	-18.514	107.20	272.92	23.43	411.1	199.4	211.7	270.0	8.882	-1.049	6.621	6.784	0.593
449.7	9.517	0.445	331.149	154.797	153.983	9.693	107.21	301.12	25.87	348.8	176.8	172.0	234.1	8.877	-6.048	9.950	-3.219	0.758
478.7	9.515	0.390	331.308	176.694	176.259	9.625	107.21	301.06	25.86	305.6	154.8	150.8	205.1	8.875	-6.036	9.941	-3.197	0.758
508.2	9.487	0.335	331.450	199.138	198.953	9.433	107.24	300.86	25.84	262.0	132.4	129.6	175.6	8.847	-5.991	9.892	-3.135	0.756
617.2	9.443	0.279	312.408	200.015	199.910	9.474	107.28	300.91	25.85	220.4	112.4	107.9	148.4	8.802	-5.975	9.852	-3.148	0.757
626.7	9.436	0.254	318.657	199.742	199.443	9.560	107.29	300.99	25.85	217.3	119.1	98.2	151.8	8.795	-5.985	9.854	-3.176	0.757
635.2	9.432	0.233	324.423	200.050	199.930	9.351	107.29	300.78	25.84	214.6	124.4	90.2	154.5	8.791	-5.950	9.827	-3.109	0.756
642.7	9.426	0.214	329.410	199.765	199.557	9.363	107.30	300.79	25.84	212.6	129.7	82.8	157.4	8.785	-5.949	9.822	-3.113	0.756
659.2	9.409	0.173	340.469	200.139	200.024	9.209	107.32	300.64	25.82	207.4	140.4	67.0	162.7	8.768	-5.915	9.789	-3.063	0.755
674.7	9.387	0.133	350.587	199.658	199.376	9.279	107.34	300.71	25.83	202.6	151.1	51.5	168.2	8.745	-5.915	9.774	-3.086	0.756
706.7	9.314	0.053	372.102	199.814	199.495	9.125	107.41	300.56	25.81	193.0	172.4	20.5	179.3	8.671	-5.854	9.683	-3.036	0.755
739.2	9.177	-0.028	393.921	200.027	199.902	8.770	107.55	300.20	25.78	183.1	194.0	-10.9	190.3	8.533	-5.727	9.507	-2.921	0.753
771.2	8.925	-0.109	415.187	199.663	199.446	8.481	107.80	299.91	25.75	173.3	215.6	-42.3	201.5	8.279	-5.553	9.222	-2.828	0.751
803.7	8.458	-0.189	437.112	199.884	199.840	7.820	108.27	299.25	25.68	163.7	237.3	-73.6	212.7	7.812	-5.213	8.683	-2.613	0.747
837.2	7.595	-0.274	459.399	199.670	199.536	6.912	109.13	298.34	25.58	152.7	259.8	-107.1	224.1	6.960	-4.638	7.732	-2.317	0.742
870.7	6.045	-0.358	481.679	199.808	199.605	6.071	110.68	297.50	25.48	141.5	282.0	-140.5	235.1	5.462	-3.751	6.142	-2.041	0.737
904.2	1.810	-0.441	504.262	199.966	200.018	4.916	114.92	296.35	25.29	129.9	304.3	-174.4	246.1	1.575	-1.617	2.128	-1.659	0.730
910.2	-0.138	-0.457	508.075	199.641	199.515	4.902	116.86	296.33	25.24	127.5	308.5	-181.0	248.1	-0.118	-0.768	0.433	-1.654	0.730
915.2	-2.311	-0.470	511.548	199.832	199.715	4.942	119.04	296.37	25.20	125.3	311.8	-186.5	249.6	-1.941	0.137	-1.386	-1.668	0.730
918.2	-5.735	-0.477	513.617	199.661	199.576	5.061	122.46	296.49	25.14	124.2	314.0	-189.8	250.7	-4.683	1.488	-4.114	-1.707	0.731
918.7	-21.365	-0.176	513.860	199.954	199.864	4.902	138.09	296.33	24.79	243.0	314.0	-71.0	290.3	-15.472	6.909	-14.920	-1.654	0.730

Fig. 10.90:   Triaxial test data of stress path test S2bT4 on natural Kloten clay.

Fig. 10.91:   Triaxial test data of stress path test S2bT4 on natural Kloten clay.

Triaxial Test   S2cT1

Test aim: Initial stiffness and stiffness degradation
Material number: 46862   Block sample of natural Kloten clay
Test apparatus: HIF B 24: Triax 1 (green)
File name: S5_6_kons.PRB; S5_6_entl.PRB
    test start: 26.08.2004   12:28:40   test stop: 11.10.2004   10:26:28
Comments: The internal LVDT was defective after the unloading path, therefore the axial displacement analysis was done with measurement data from the external displacement measurement with the load frame.

Measured sample data:

Height H_0	110.80 [mm]
Diameter D	5.13 [cm]
Weight m_f	466.62 [g]

Determined sample data:

Cross-sectional area:	A	20.68 [cm²]
Volume: f(H_0, D)	V_0	229.10 [cm³]
Water content	w	26.5 [%]
Volume: f(m_f, w, ρ_s, S_r=1)	V_0	230.92 [cm³]
Void ratio: f(m_f, w, ρ_s, S_r=1)	e_0	0.734 [-]

Material parameter:

| density | ρ_s | 2.77 [g/cm³] |
| specific gravity of water | ρ_w | 1 [g/cm³] |

Test data:

test-time [hours]	dH [mm]	force [kN]	cell-pressure [kPa]	PWP bottom [kPa]	PWP top [kPa]	dV backpr. [ccm]	H_{act} [mm]	V_{act} [ccm]	A_c [cm²]	σ_a' [kPa]	σ_r' [kPa]	q [kPa]	p' [kPa]	ε_a [%]	ε_r [%]	ε_s [%]	ε_v [%]	e [-]
0.0	-0.003	0.010	205.052	200.151	199.535	0.000	110.80	230.92	20.68	10.0	5.2	4.8	6.8	-0.003	0.001	-0.003	0.000	0.734
24.0	1.047	0.044	223.164	200.130	199.503	-2.838	109.75	228.08	20.62	44.7	23.3	21.3	30.5	0.954	0.145	0.539	1.244	0.713
54.0	1.720	0.089	245.551	200.020	199.541	-4.388	109.08	226.53	20.60	89.0	45.8	43.2	60.2	1.577	0.180	0.931	1.937	0.701
84.0	2.440	0.133	268.269	200.337	199.785	-5.768	108.36	225.15	20.61	132.7	68.2	64.5	89.7	2.252	0.155	1.398	2.562	0.691
115.0	3.630	0.179	291.498	200.063	199.495	-7.858	107.17	223.06	20.64	178.4	91.7	86.7	120.6	3.387	0.068	2.213	3.523	0.675
145.0	4.834	0.223	313.942	200.066	199.413	-10.035	105.97	220.88	20.67	222.1	114.2	107.9	150.2	4.562	-0.009	3.047	4.543	0.659
176.0	5.739	0.269	337.402	200.127	199.550	-11.743	105.06	219.17	20.69	267.6	137.6	130.0	180.9	5.463	-0.052	3.677	5.358	0.646
206.0	6.425	0.314	359.828	200.050	199.477	-12.936	104.38	217.98	20.71	311.7	160.1	151.6	210.6	6.156	-0.111	4.178	5.935	0.637
237.0	7.016	0.359	383.417	200.244	199.693	-14.085	103.78	216.83	20.72	356.7	183.4	173.3	241.2	6.760	-0.132	4.595	6.496	0.628
267.0	7.482	0.404	405.733	200.008	199.361	-14.992	103.32	215.92	20.72	401.0	206.0	194.9	271.0	7.242	-0.132	4.927	6.943	0.621
331.0	8.037	0.441	425.124	200.020	199.498	-16.192	102.76	214.72	20.72	438.2	225.4	212.9	296.3	7.821	-0.140	5.307	7.541	0.612
357.0	8.053	0.403	405.197	200.122	199.536	-16.274	102.75	214.64	20.71	399.9	205.4	194.6	270.2	7.838	-0.128	5.310	7.582	0.612
387.0	8.055	0.358	382.698	200.197	199.651	-16.372	102.75	214.55	20.70	355.7	182.8	172.9	240.4	7.840	-0.104	5.296	7.631	0.611
418.0	8.037	0.312	359.593	200.116	199.586	-16.343	102.76	214.57	20.70	310.4	159.7	150.7	210.0	7.821	-0.102	5.282	7.617	0.611
448.0	8.019	0.268	336.836	200.023	199.454	-16.247	102.78	214.67	20.71	266.5	137.1	129.4	180.2	7.802	-0.117	5.279	7.568	0.612
522.0	7.956	0.220	312.399	200.192	199.683	-16.212	102.84	214.70	20.70	218.7	112.5	106.3	147.9	7.736	-0.093	5.219	7.551	0.612
526.0	7.960	0.224	314.102	200.027	199.380	-16.220	102.84	214.70	20.70	222.6	114.4	108.2	150.5	7.740	-0.093	5.222	7.555	0.612
536.0	7.977	0.242	321.202	200.285	199.637	-16.246	102.82	214.67	20.70	238.1	121.2	116.9	160.2	7.758	-0.095	5.235	7.568	0.612
541.0	7.986	0.251	324.811	200.203	199.693	-16.267	102.81	214.65	20.70	246.1	124.9	121.2	165.3	7.767	-0.095	5.241	7.578	0.612
547.0	7.997	0.261	328.822	200.151	199.583	-16.319	102.80	214.60	20.70	255.1	129.0	126.1	171.0	7.779	-0.087	5.244	7.604	0.612
552.0	8.009	0.270	332.504	200.169	199.541	-16.391	102.79	214.53	20.69	263.1	132.6	130.5	176.1	7.792	-0.075	5.245	7.641	0.611
557.0	8.016	0.279	335.876	199.997	199.429	-16.417	102.78	214.50	20.69	271.0	136.2	134.8	181.1	7.799	-0.073	5.248	7.654	0.611
567.0	8.030	0.296	343.124	200.356	199.846	-16.442	102.77	214.47	20.69	286.1	143.0	143.0	190.7	7.814	-0.074	5.258	7.666	0.611
577.0	8.061	0.314	350.175	200.034	199.477	-16.563	102.74	214.35	20.69	302.2	150.4	151.8	201.0	7.846	-0.060	5.270	7.727	0.610
597.0	8.089	0.350	364.104	200.214	199.644	-16.738	102.71	214.18	20.68	333.5	164.2	169.3	220.6	7.875	-0.030	5.271	7.815	0.608
617.0	8.131	0.385	378.185	200.034	199.472	-16.959	102.67	213.96	20.66	364.8	178.4	186.3	240.5	7.920	0.003	5.277	7.926	0.607
637.0	8.174	0.421	392.162	200.162	199.634	-17.061	102.63	213.86	20.66	396.0	192.3	203.8	260.2	7.965	0.006	5.306	7.978	0.606
657.0	8.239	0.456	406.288	200.037	199.501	-17.240	102.56	213.68	20.66	427.3	206.5	220.7	280.1	8.033	0.018	5.344	8.068	0.605
698.0	8.457	0.529	435.005	200.148	199.545	-17.933	102.34	212.98	20.63	491.5	235.2	256.4	320.6	8.263	0.078	5.457	8.420	0.599
738.0	8.896	0.600	462.949	199.960	199.467	-19.053	101.90	211.86	20.61	554.3	263.2	291.1	360.3	8.730	0.132	5.732	8.993	0.591
779.0	9.447	0.672	492.075	200.346	199.806	-20.308	101.35	210.61	20.60	618.2	292.0	326.2	400.7	9.321	0.161	6.107	9.642	0.582
819.0	9.914	0.743	519.698	200.020	199.405	-21.250	100.89	209.67	20.60	680.6	320.0	360.6	440.2	9.827	0.154	6.449	10.135	0.574
860.0	10.336	0.816	548.437	199.947	199.342	-22.172	100.46	208.74	20.60	745.0	348.8	396.2	480.8	10.288	0.167	6.748	10.622	0.568
900.0	10.709	0.887	576.624	200.258	199.696	-23.125	100.09	207.79	20.58	807.7	376.6	431.0	520.3	10.699	0.215	6.990	11.129	0.560
940.0	11.035	0.958	604.773	200.174	199.638	-23.978	99.77	206.94	20.56	870.8	404.9	465.9	560.2	11.061	0.263	7.199	11.587	0.554
957.0	11.179	0.988	616.641	200.027	199.416	-24.333	99.62	206.58	20.56	897.6	416.9	480.7	577.1	11.222	0.279	7.295	11.779	0.551

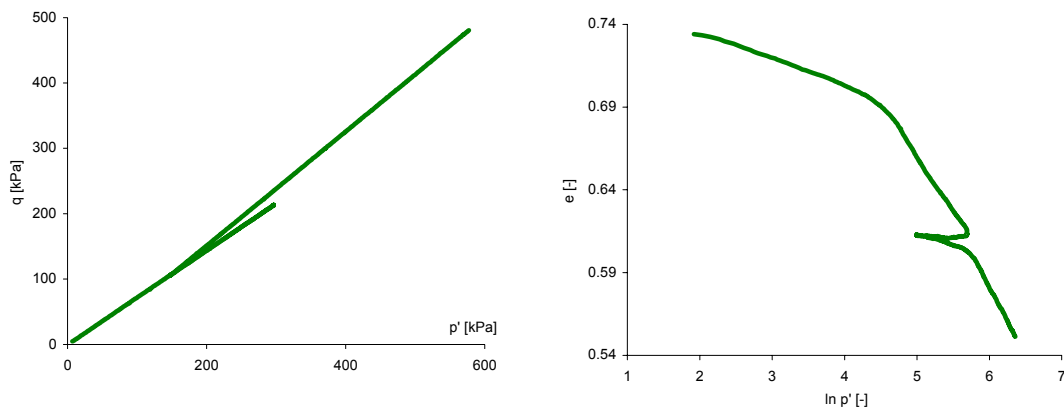

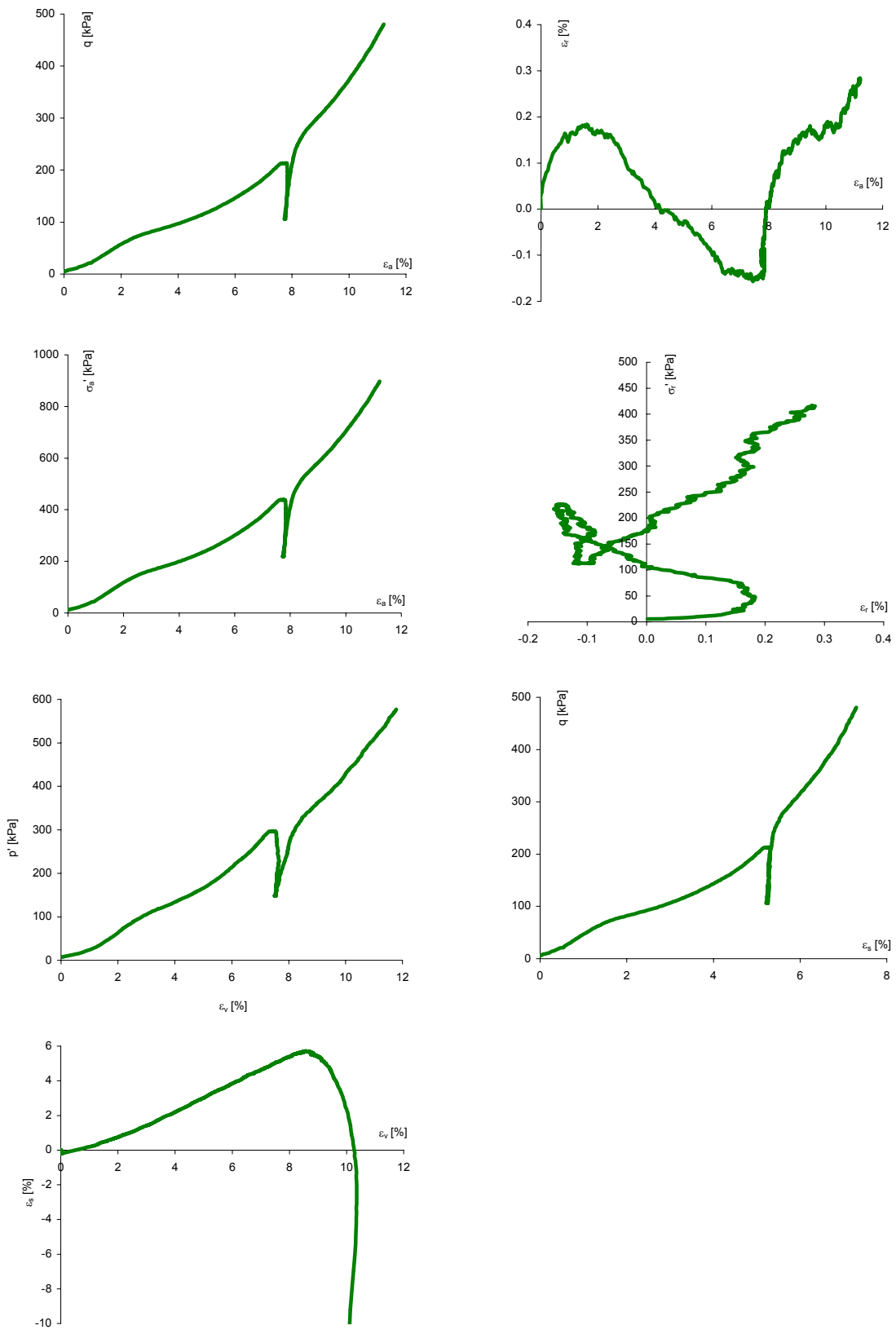Fig. 10.92:   Triaxial test data of stress path test S2cT1 on natural Kloten clay.

Fig. 10.93:   Triaxial test data of stress path test S2cT1 on natural Kloten clay.

Test data:

test-time	dH LVDT 1	dH LVDT 2	ε_1 LVDT 1	ε_1 LVDT 2	ε_3 LVDT 1	ε_3 LVDT 2	ε_s LVDT 1	ε_s LVDT 2	V_{act} Laser	dV Laser	ε_v Laser	ε_3 LVDT 1 & Laser	ε_3 LVDT 2 & Laser	ε_s LVDT 1 & Laser	ε_s LVDT 2 & Laser	e Laser	V_{act} Cellpr.	ε_v Cellpr.
[hours]	[mm]	[mm]	[%]	[%]	[%]	[%]	[%]	[%]	[ccm]	[ccm]	[%]	[%]	[%]	[%]	[%]	[-]	[ccm]	[%]
3.0									246.25	0.00	0.00					0.72	230.37	0.23
24.0									244.25	-2.00	0.88					0.70	227.57	1.47
54.0									243.50	-2.76	1.22					0.70	225.55	2.38
84.0									241.95	-4.30	1.92					0.68	223.57	3.29
115.0									238.54	-7.71	3.49					0.66	220.82	4.57
145.0									236.22	-10.03	4.59					0.64	217.80	6.02
176.0									235.86	-10.40	4.77					0.64	216.05	6.88
206.0									233.76	-12.49	5.78					0.62	214.41	7.70
237.0									232.63	-13.62	6.34					0.61	213.16	8.33
267.0									230.81	-15.45	7.25					0.60	211.99	8.93
331.0									229.14	-17.11	8.09					0.59	210.83	9.53
357.0									230.75	-15.50	7.28					0.60	210.57	9.66
387.0									229.39	-16.86	7.97					0.59	210.50	9.70
418.0									229.84	-16.41	7.74					0.59	210.44	9.73
448.0									230.80	-15.45	7.25					0.60	210.48	9.71
522.0									243.60	-2.66	1.18					0.70	185.28	24.63
526.0									243.33	-2.92	1.29					0.69	184.76	24.98
536.0									243.79	-2.46	1.09					0.70	183.84	25.61
541.0									245.33	-0.92	0.40					0.71	183.78	25.65
547.0									246.50	0.25	-0.11					0.72	183.02	26.17
552.0									245.26	-1.00	0.44					0.71	182.06	26.84
557.0									245.37	-0.88	0.39					0.71	181.44	27.27
567.0									245.20	-1.06	0.46					0.71	180.26	28.10
577.0									246.07	-0.18	0.08					0.71	179.18	28.87
597.0									246.12	-0.13	0.06					0.72	178.03	29.71
617.0									242.39	-3.86	1.72					0.69	175.62	31.48
637.0									242.68	-3.57	1.59					0.69	174.49	32.34
657.0									242.78	-3.47	1.54					0.69	173.32	33.23
698.0									242.07	-4.18	1.86					0.68	170.66	35.31
738.0									241.21	-5.05	2.26					0.68	169.03	36.61
779.0									241.03	-5.22	2.34					0.68	167.68	37.71
819.0									240.89	-5.36	2.40					0.68	166.62	38.59
860.0									240.51	-5.74	2.58					0.67	165.39	39.62
900.0									239.74	-6.52	2.93					0.67	164.60	40.29
940.0									239.94	-6.31	2.84					0.67	163.02	41.65
957.0									239.70	-6.55	2.95					0.67	162.27	42.30
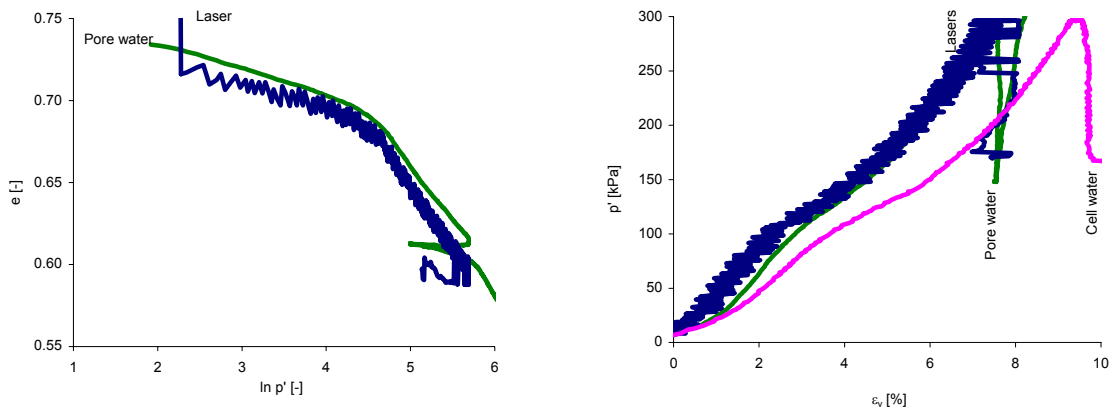
Fig. 10.94: Triaxial test data of stress path test S2cT1 on natural Kloten clay: comparison of strain determination with various measurement methods.
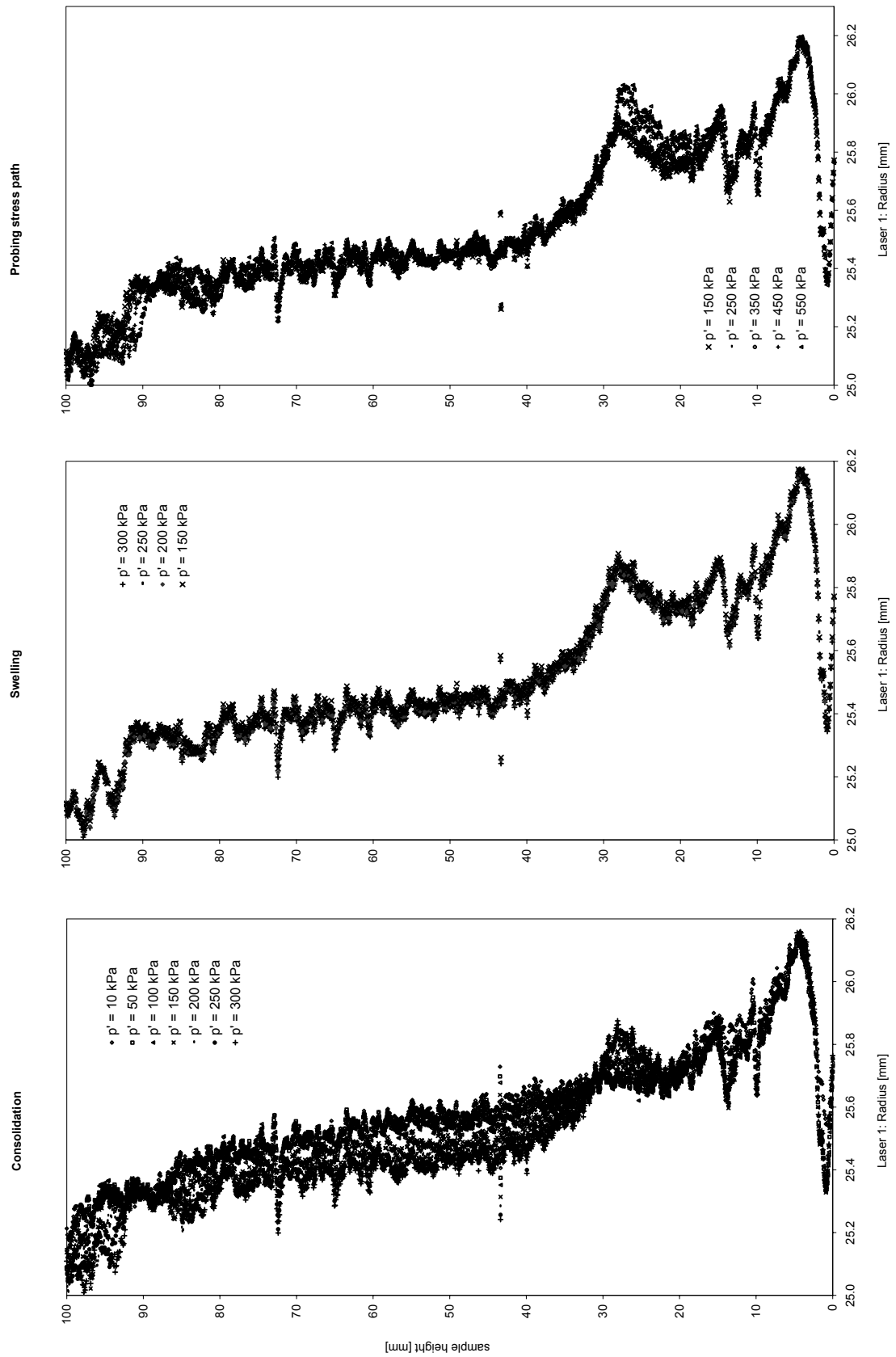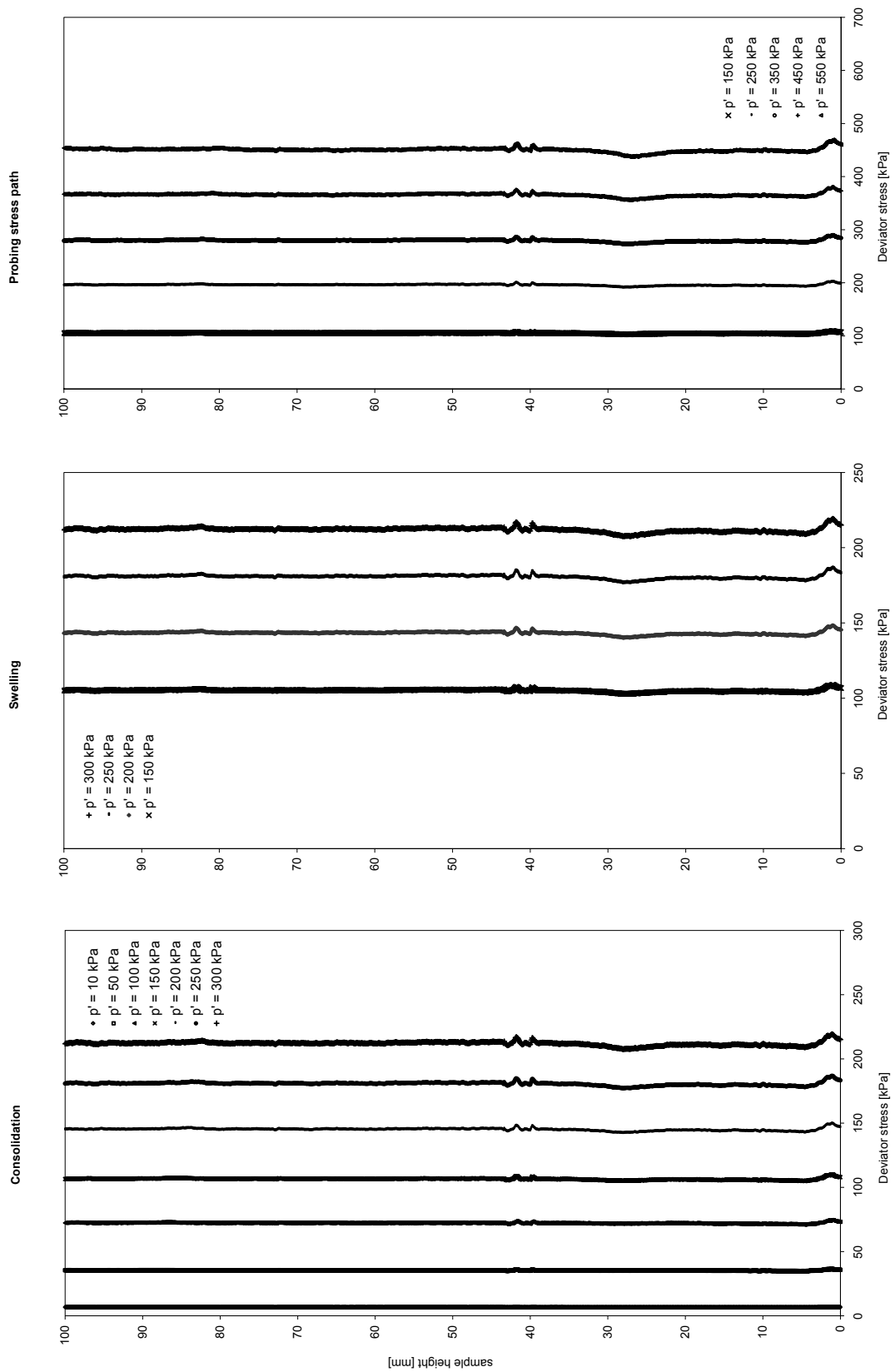
Fig. 10.95:   Laser scan data of the triaxial stress path test S2cT1 on natural Kloten clay: radius from laser 1.
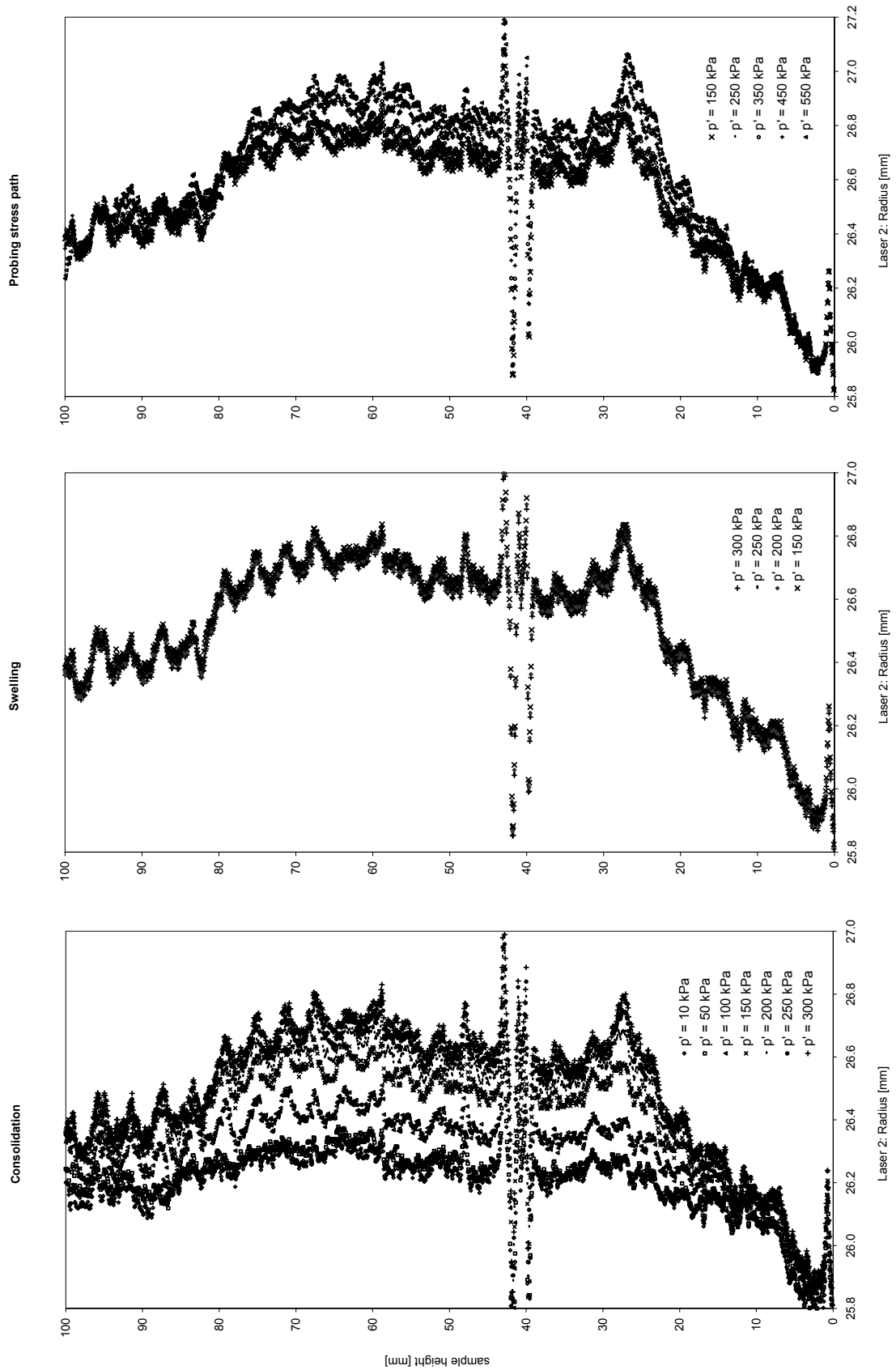
Fig. 10.96: Laser scan data of the triaxial stress path test S2cT1 on natural Kloten clay: radius from laser 2.
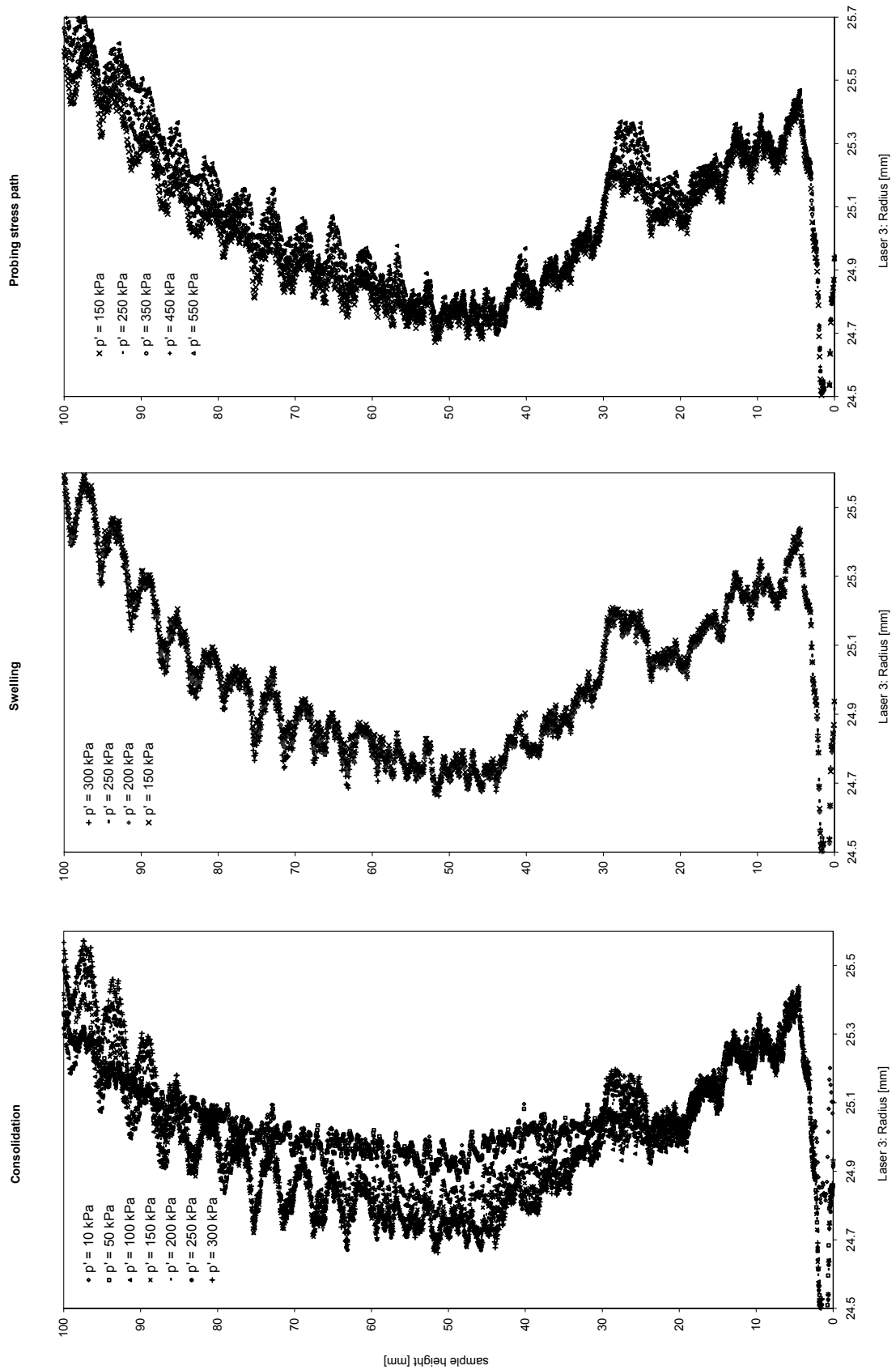
Fig. 10.97:   Laser scan data of the triaxial stress path test S2cT1 on natural Kloten clay:
radius from laser 3.
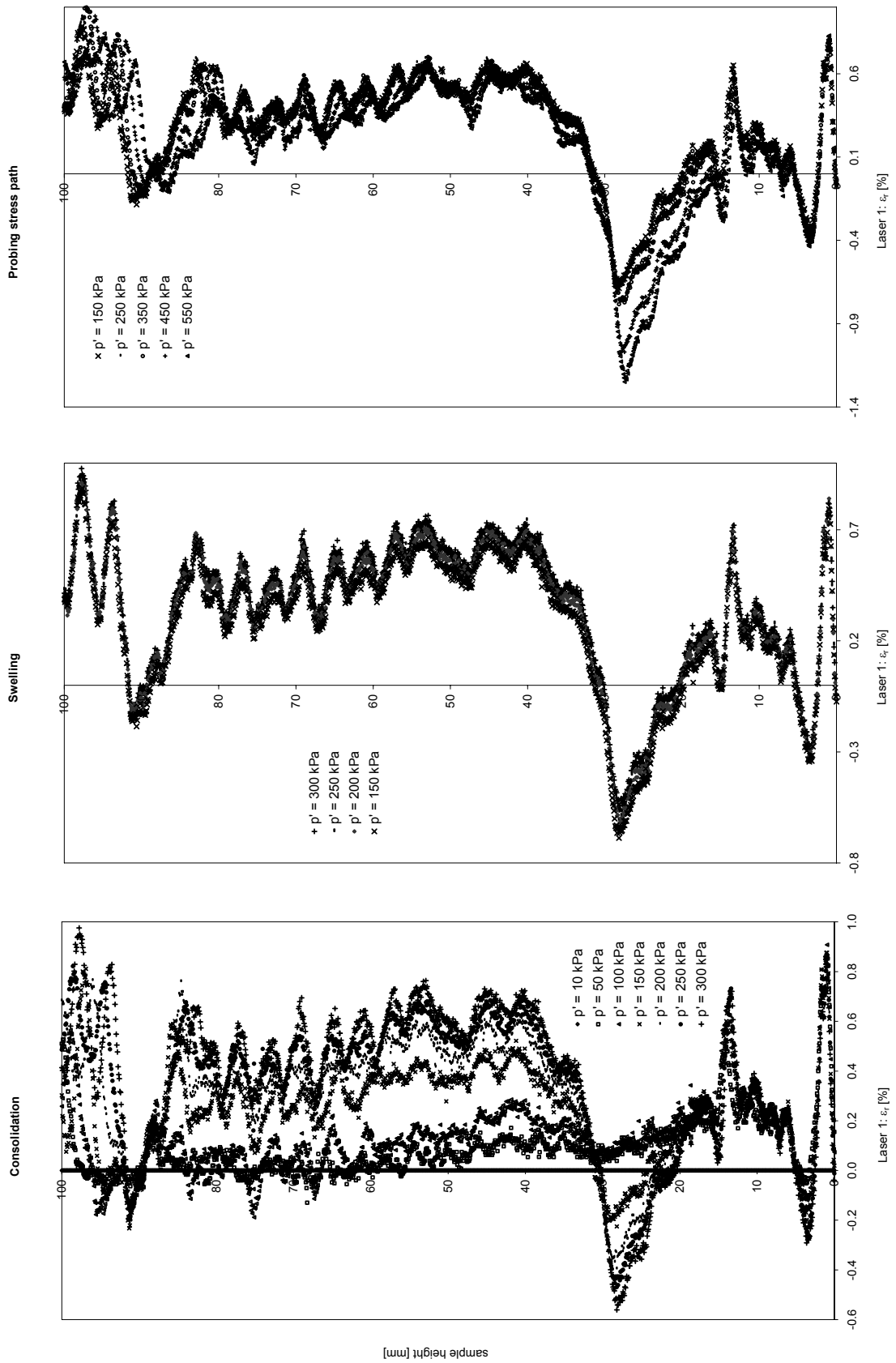
Fig. 10.98: Laser scan data of the triaxial stress path test S2cT1 on natural Kloten clay: radial strain from laser 1.
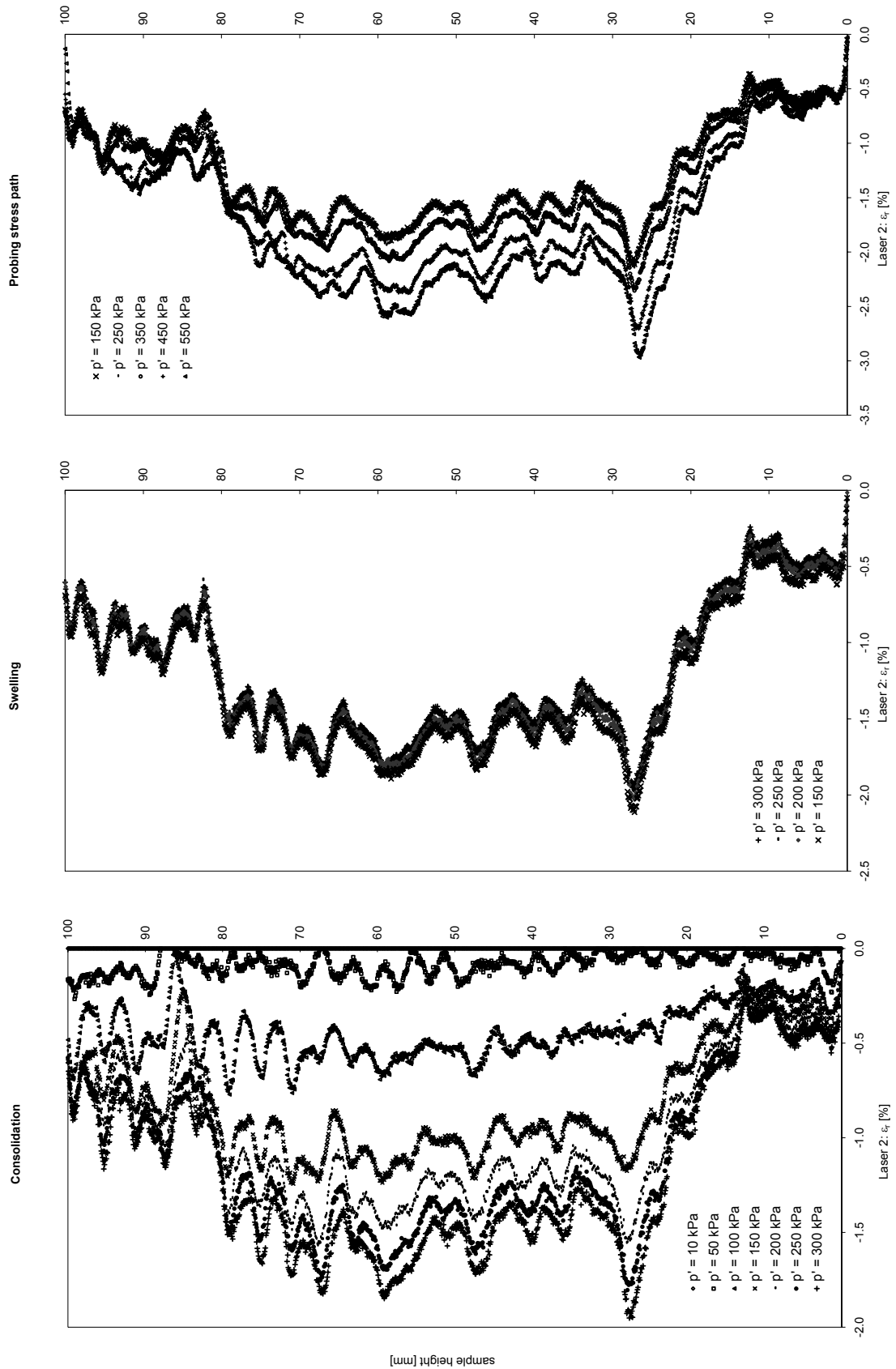
Fig. 10.99:   Laser scan data of the triaxial stress path test S2cT1 on natural Kloten clay: radial strain from laser 2.
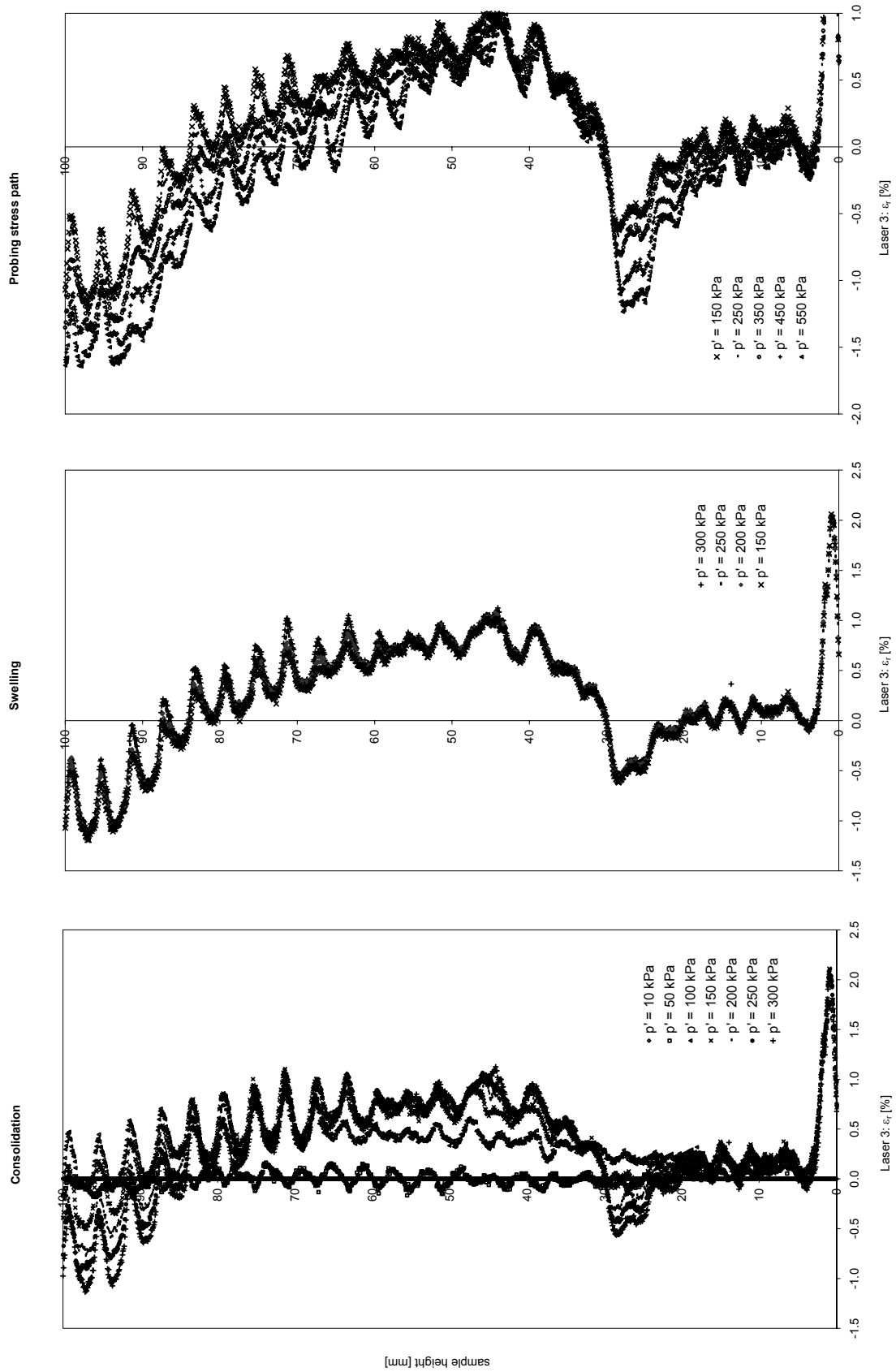
Fig. 10.100: Laser scan data of the triaxial stress path test S2cT1 on natural Kloten clay: radial strain from laser 3.
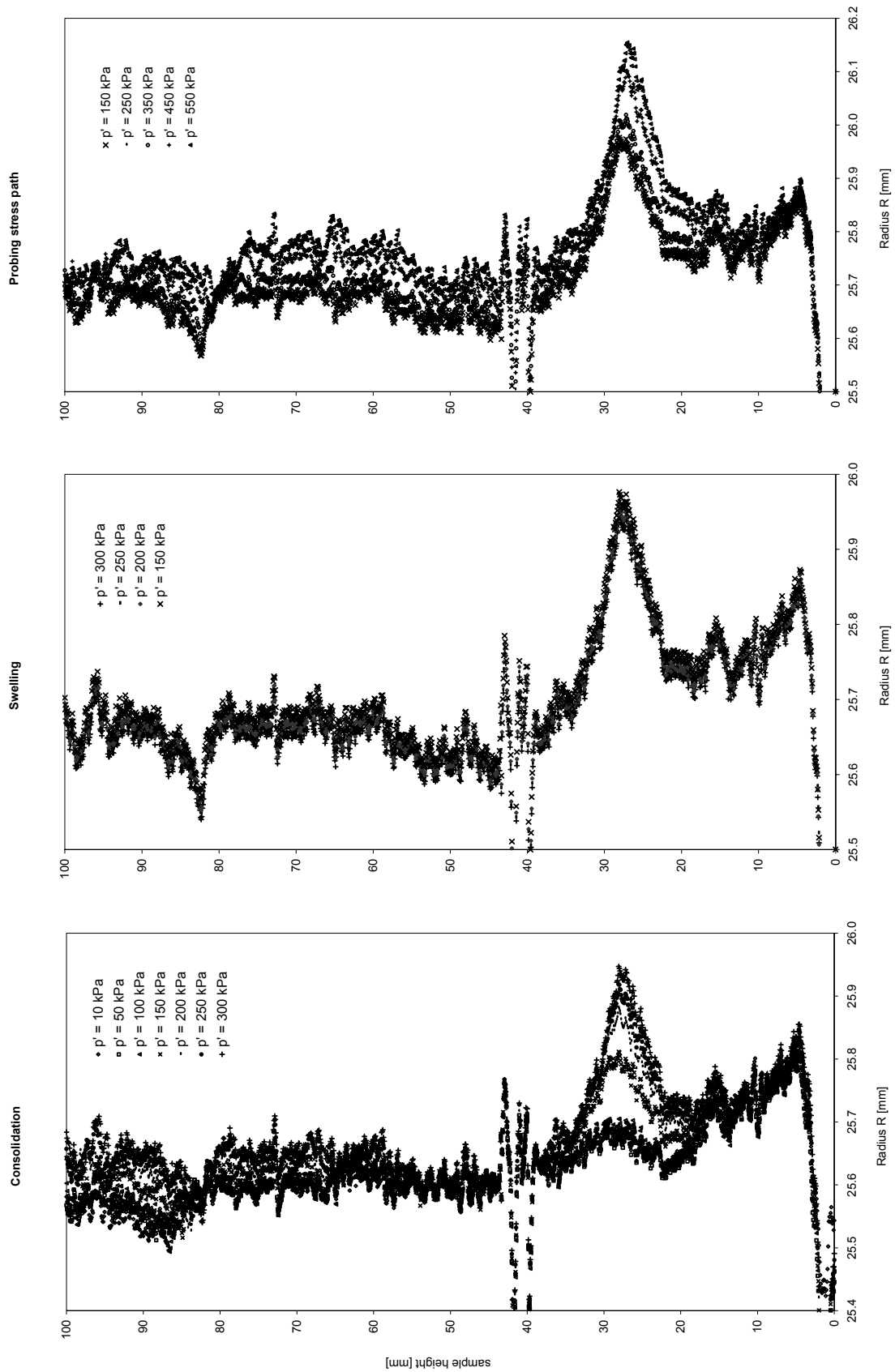
Fig. 10.101: Laser scan data of the triaxial stress path test S2cT1 on natural Kloten clay: radius determined with the circular slice approach.
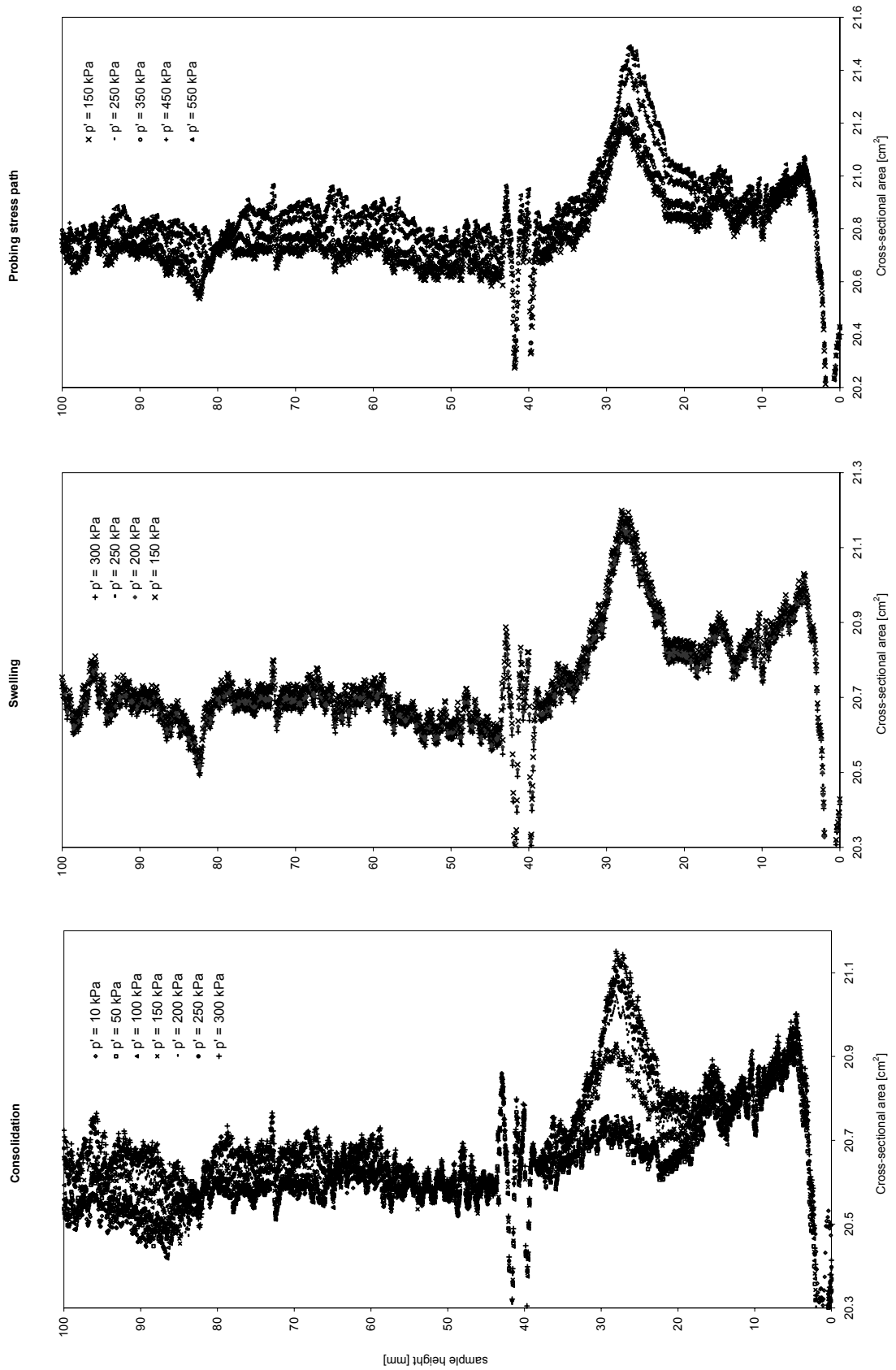
Fig. 10.102: Laser scan data of the triaxial stress path test S2cT1 on natural Kloten clay: cross-sectional area calculated from *R* (Fig. 10.101).

Fig. 10.103: Laser scan data of the triaxial stress path test S2cT1 on natural Kloten clay:
change of deviator stress.
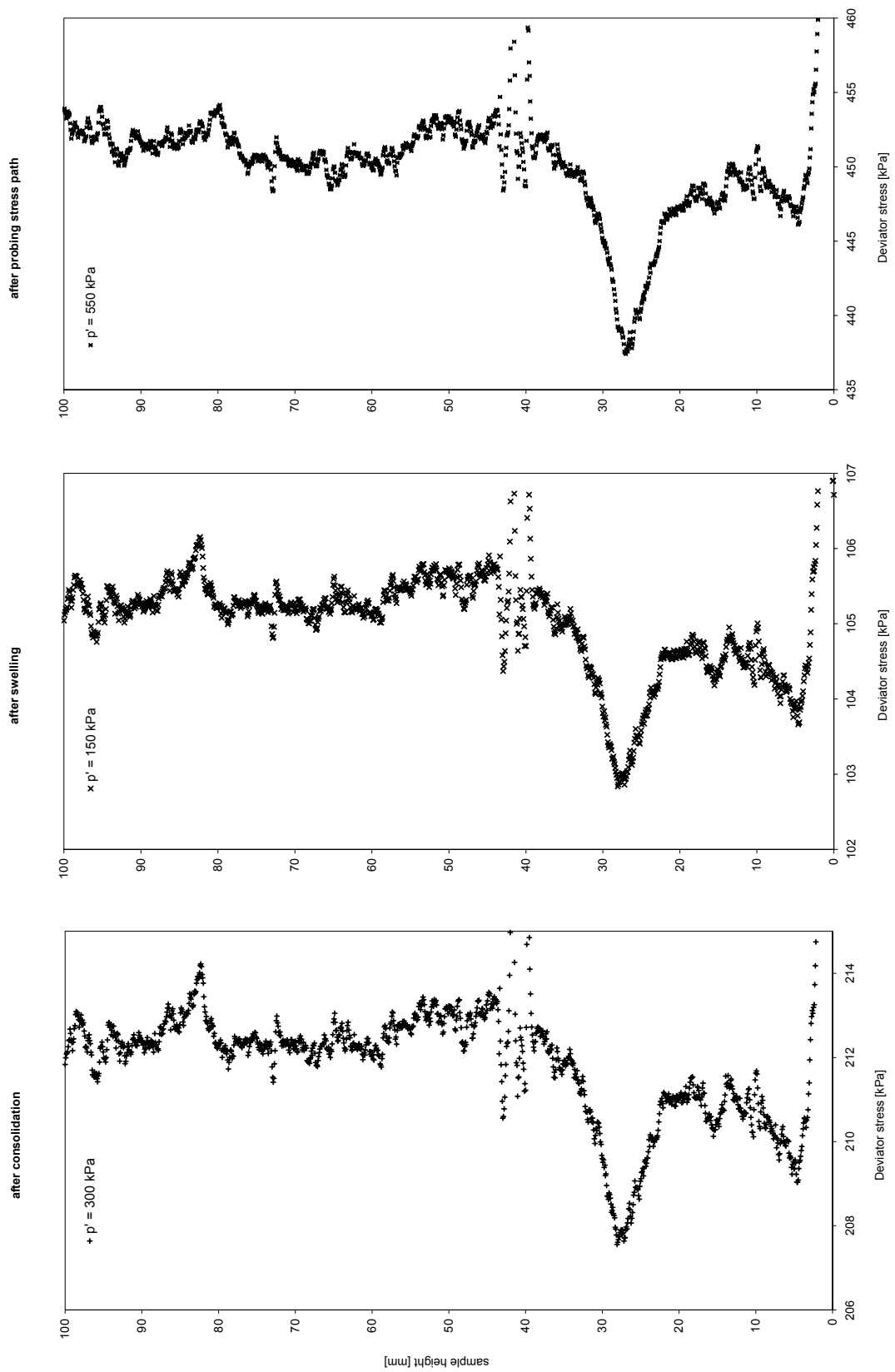
Fig. 10.104: Laser scan data of the triaxial stress path test S2cT1 on natural Kloten clay: change of deviator stress (enlarged scale).
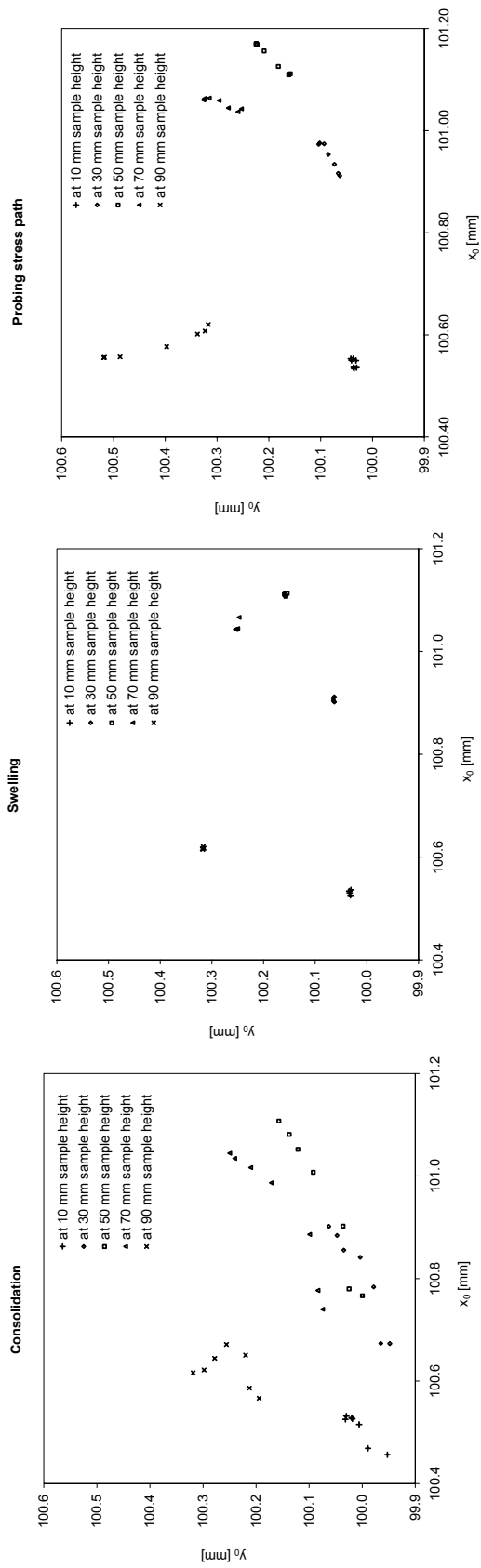
Fig. 10.105: Laser scan data of centre of each disc for the triaxial stress path test S2cT1 on natural Kloten clay.
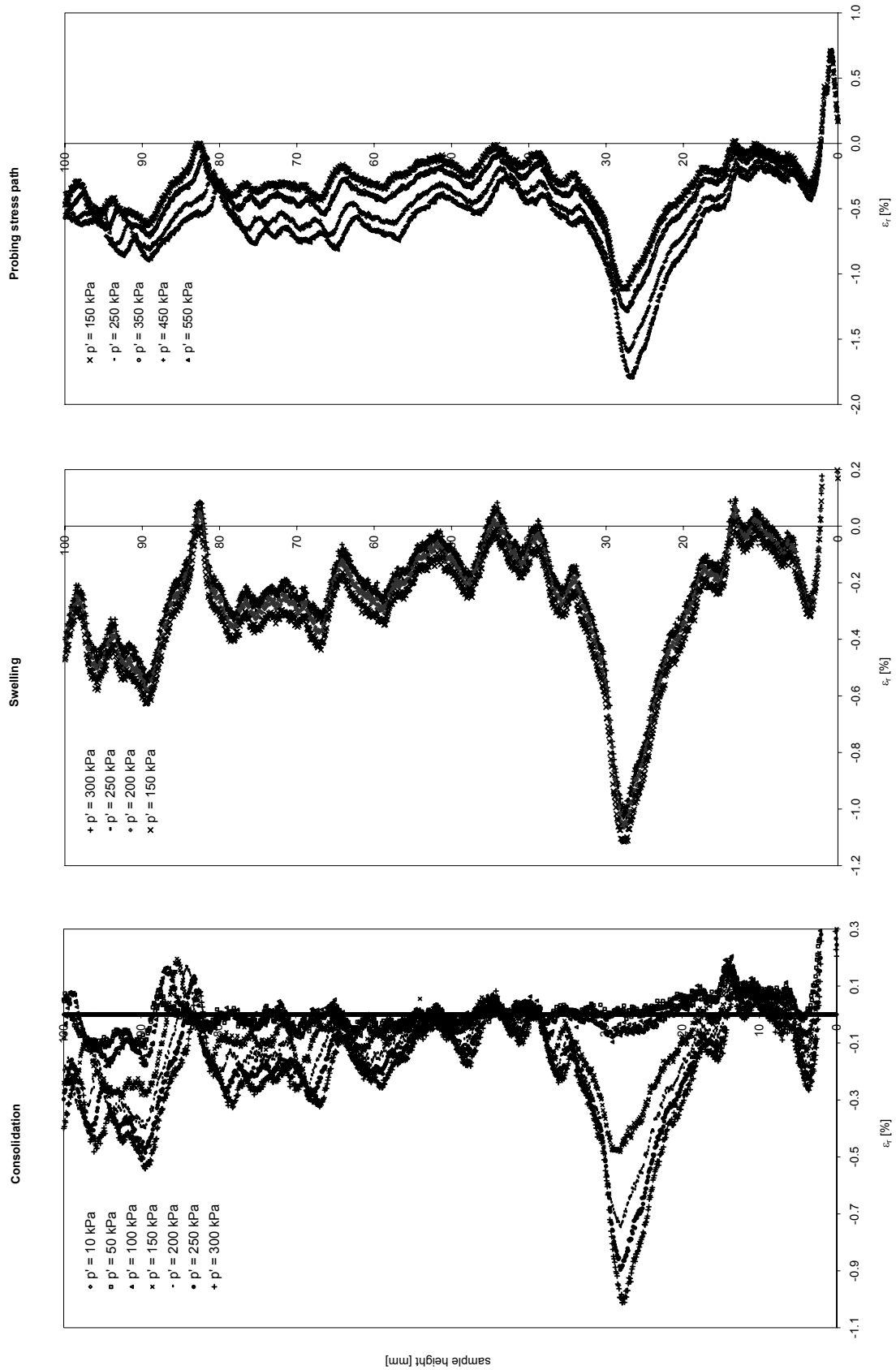
Fig. 10.106: Laser scan data of the triaxial stress path test S2cT1 on natural Kloten clay: radial strain calculated from *R* (Fig. 10.101).
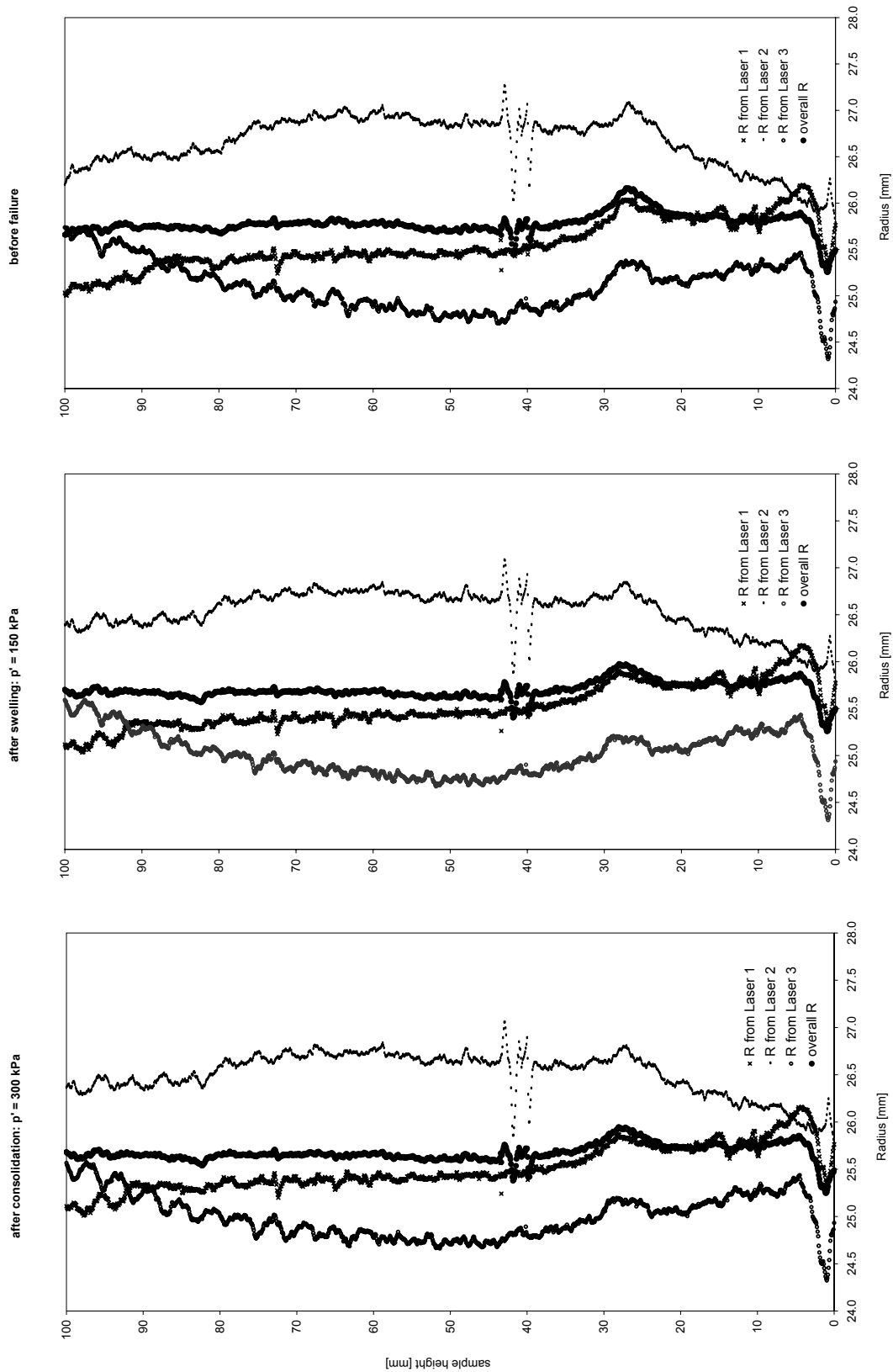
Fig. 10.107: Laser scan data of the triaxial stress path test S2cT1 on natural Kloten clay: comparison of radius determined from each laser together with the radius *R* determined from the circular slice approach.
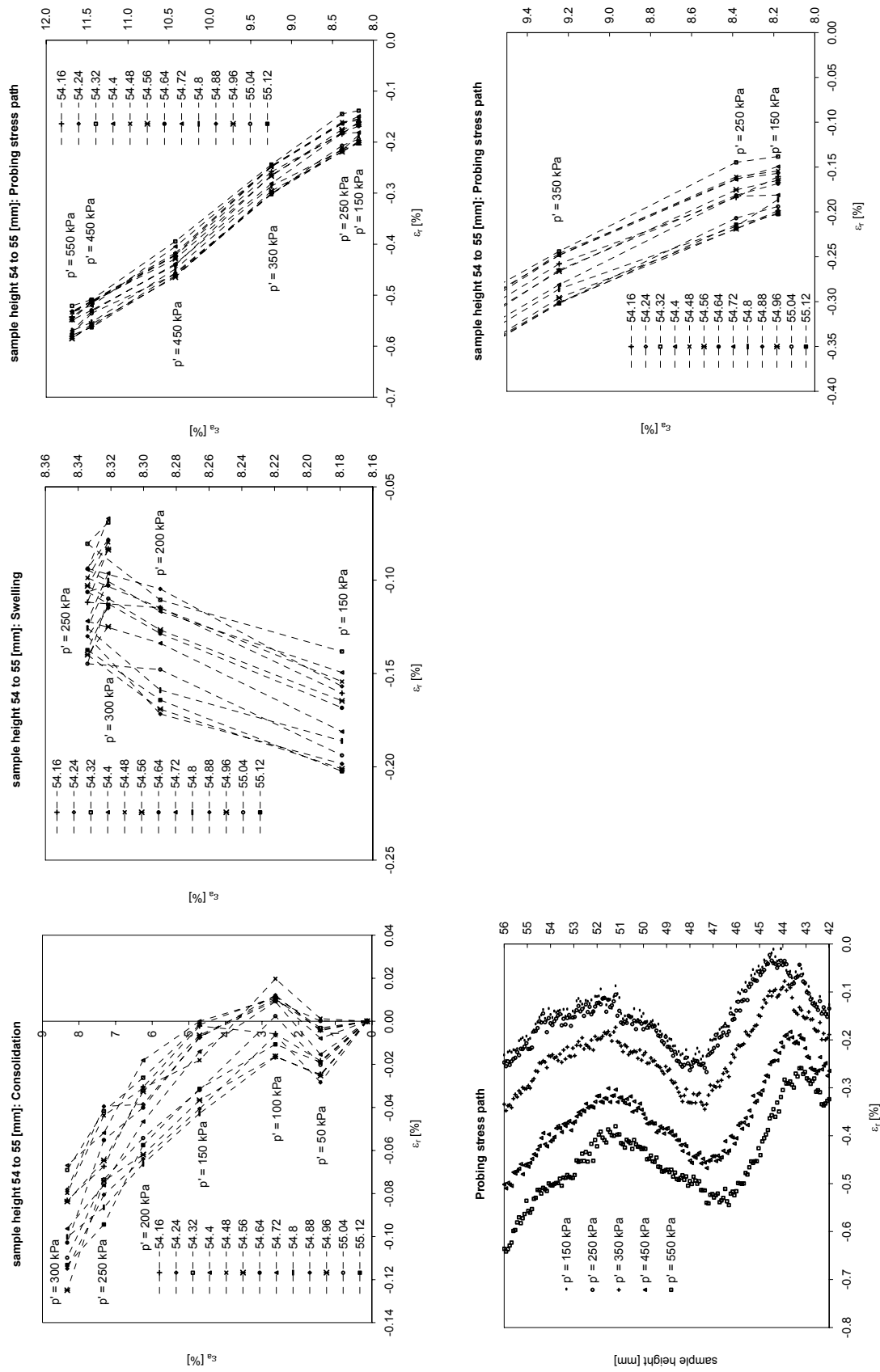
Fig. 10.108: Laser scan data of the triaxial stress path test S2cT1 on natural Kloten clay: between sample heights (from base) 54 – 55 mm.
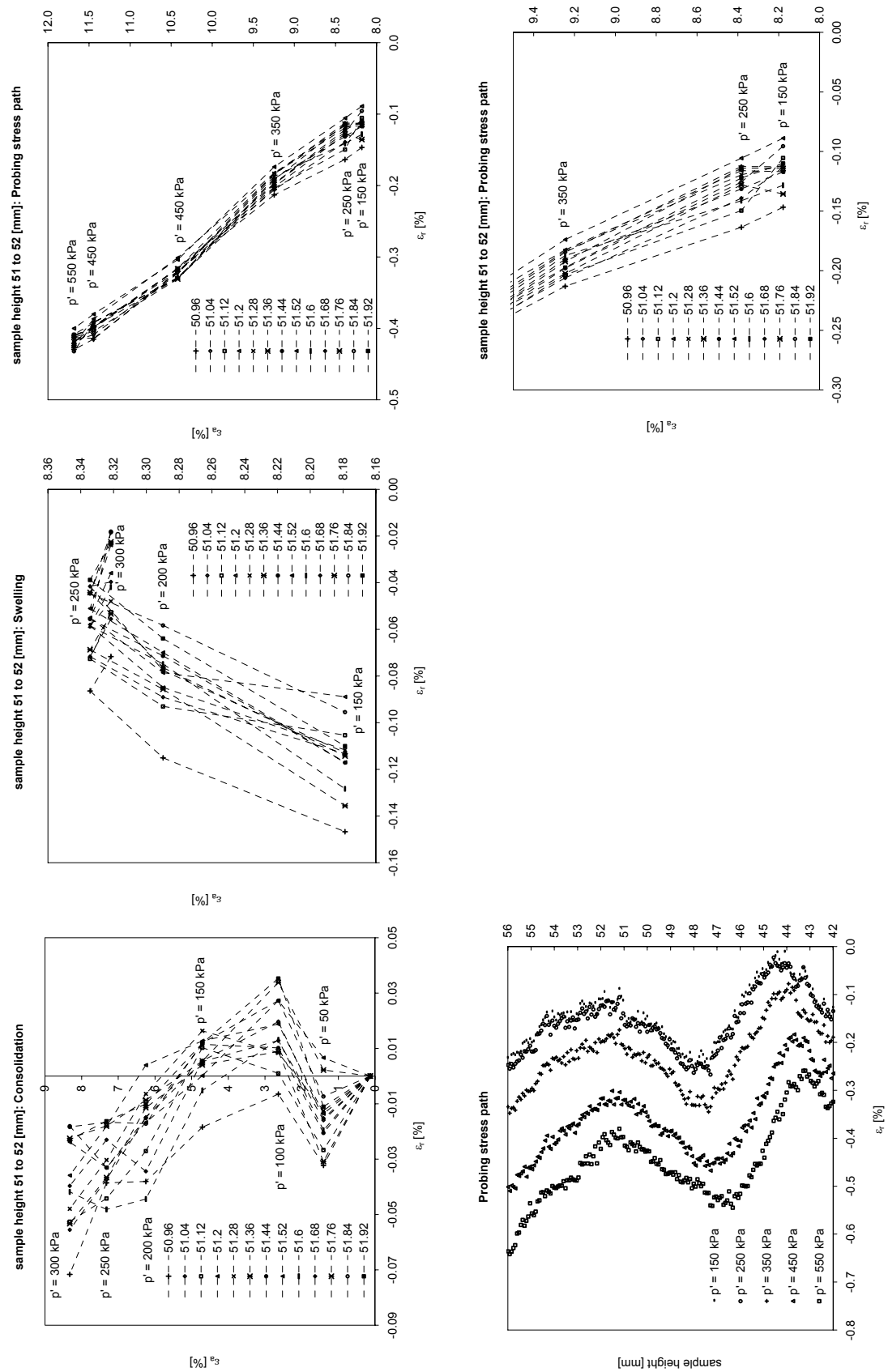
Fig. 10.109: Laser scan data of the triaxial stress path test S2cT1 on natural Kloten clay between sample heights (from base) 51 – 52 mm.
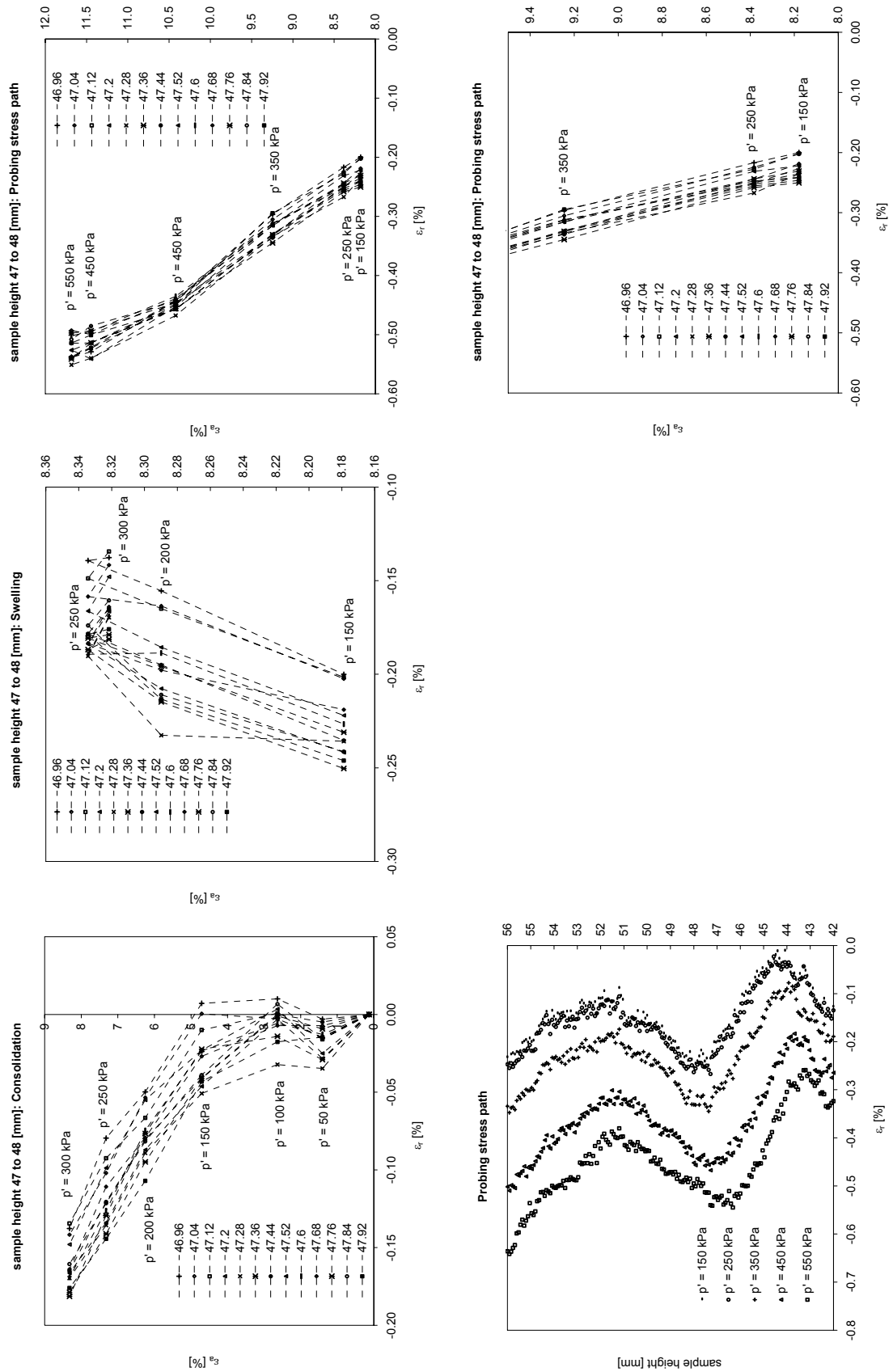
Fig. 10.110: Laser scan data of the triaxial stress path test S2cT1 on natural Kloten clay between sample heights (from base) 47 – 48 mm.

Triaxial Test   S2cT4

Test aim: Initial stiffness and stiffness degradation
Material number: 46862   Block sample of natural Kloten clay
Test apparatus: HIL B 58: Triax 4 (blue)
File name: S5_7_gesamt_stufen.PRB
   test start: 26.08.2004   12:19:18   test stop: 24.09.2004   10:19:56
Comments: The load was applied stepwise not continuously!!

Measured sample data:

Height H_0 121.10 [mm]
Diameter D   5.62 [cm]
Weight m_f 610.86 [g]

Determined sample data:

Cross-sectional area:	A	24.85	[cm^2]
Volume: f(H$_0$, D)	V_0	300.88	[cm^3]
Water content	w	26.22	[%]
Volume: f(m$_f$, w, ρ_s, S$_r$=1)	V_0	301.61	[cm^3]
Void ratio: f(m$_f$, w, ρ_s, S$_r$=1)	e_0	0.726	[-]

Material parameter:

density	ρ_s	2.77	[g/cm^3]
specific gravity of water	ρ_w	1	[g/cm^3]

Test data:

| test-time [hours]	dH [mm]	force [kN]	cell-pressure [kPa]	PWP bottom [kPa]	PWP top [kPa]	dV backpr. [ccm]	H_{act} [mm]	V_{act} [ccm]	A_c [cm^2]	σ_1' [kPa]	σ_3' [kPa]	q [kPa]	p' [kPa]	ε_1 [%]	ε_3 [%]	ε_s [%]	ε_v [%]	e [-]
35.9	0.006	0.067	227.013	200.037	202.359	-2.574	121.09	299.04	24.63	53.0	25.8	27.2	34.9	0.005	0.428	-0.282	0.861	0.712
59.9	0.006	0.111	245.038	199.905	202.232	-5.523	121.09	296.09	24.39	89.5	44.0	45.5	59.1	0.005	0.930	-0.617	1.865	0.695
83.9	-0.003	0.155	262.663	199.855	201.932	-7.682	121.10	293.93	24.21	125.8	61.8	64.0	83.1	-0.002	1.308	-0.874	2.614	0.682
107.9	-0.001	0.201	280.704	199.876	201.987	-9.841	121.10	291.77	24.03	163.4	79.8	83.6	107.7	-0.001	1.687	-1.125	3.373	0.670
131.9	0.011	0.247	298.752	200.139	202.467	-11.608	121.09	290.00	23.89	200.9	97.4	103.4	131.9	0.009	1.997	-1.325	4.003	0.660
155.9	0.018	0.292	316.861	199.886	202.286	-12.933	121.08	288.68	23.78	238.6	115.8	122.8	156.7	0.015	2.233	-1.478	4.480	0.652
179.8	0.012	0.336	334.894	200.233	202.594	-14.103	121.08	287.51	23.68	275.4	133.5	141.9	180.8	0.010	2.448	-1.625	4.905	0.646
203.8	0.006	0.381	352.832	199.878	202.185	-15.166	121.09	286.45	23.59	313.3	151.8	161.5	205.6	0.005	2.645	-1.760	5.294	0.639
227.8	0.003	0.426	370.499	199.860	201.996	-16.117	121.10	285.50	23.51	350.7	169.6	181.2	230.0	0.002	2.821	-1.879	5.645	0.634
251.8	0.000	0.470	388.504	199.731	201.859	-16.851	121.10	284.76	23.45	388.1	187.7	200.4	254.5	0.000	2.959	-1.973	5.918	0.630
275.8	0.006	0.517	406.885	200.127	202.486	-17.849	121.09	283.76	23.37	426.8	205.6	221.2	279.3	0.005	3.143	-2.092	6.290	0.624
323.8	0.014	0.561	424.699	199.968	202.397	-19.022	121.09	282.59	23.28	464.5	223.5	241.0	303.9	0.012	3.360	-2.232	6.731	0.617
347.8	0.010	0.516	406.686	199.796	202.061	-18.878	121.09	282.73	23.29	427.3	205.8	221.6	279.6	0.008	3.334	-2.217	6.677	0.618
371.8	0.007	0.472	388.751	199.948	202.414	-19.019	121.09	282.59	23.28	390.4	187.6	202.8	255.2	0.006	3.362	-2.238	6.730	0.617
395.8	0.007	0.425	370.576	199.889	202.173	-18.786	121.09	282.83	23.29	352.0	169.5	182.4	230.4	0.006	3.318	-2.208	6.642	0.619
431.8	0.001	0.360	353.951	200.089	202.541	-18.866	121.10	282.75	23.29	307.2	152.6	154.6	204.2	0.001	3.336	-2.223	6.673	0.618
443.8	0.014	0.337	334.880	200.040	202.597	-18.826	121.09	282.79	23.29	278.3	133.6	144.7	181.8	0.012	3.323	-2.208	6.657	0.619
455.8	0.017	0.314	325.879	200.171	202.760	-18.738	121.08	282.87	23.30	259.2	124.4	134.8	169.3	0.014	3.305	-2.194	6.624	0.619
467.8	0.021	0.291	316.846	200.027	202.666	-18.684	121.08	282.93	23.30	240.4	115.5	124.9	157.1	0.017	3.293	-2.184	6.604	0.619
503.8	0.020	0.281	312.457	199.989	202.672	-18.659	121.08	282.95	23.31	231.7	111.1	120.6	151.3	0.017	3.289	-2.182	6.595	0.619
515.8	0.023	0.299	322.089	200.096	202.811	-18.756	121.08	282.86	23.30	249.0	120.6	128.3	163.4	0.019	3.306	-2.191	6.631	0.619
527.8	0.022	0.317	331.734	200.085	202.821	-18.789	121.08	282.82	23.29	266.4	130.3	136.1	175.6	0.018	3.313	-2.196	6.643	0.618
539.8	0.024	0.335	341.335	200.044	202.802	-18.861	121.08	282.75	23.29	283.8	139.9	143.8	187.9	0.020	3.325	-2.204	6.670	0.618
551.8	0.024	0.353	350.954	200.000	202.783	-18.933	121.08	282.68	23.28	301.2	149.6	151.6	200.1	0.020	3.339	-2.213	6.698	0.618
563.8	0.018	0.371	360.591	199.896	202.661	-18.995	121.08	282.62	23.28	318.7	159.3	159.4	212.4	0.015	3.353	-2.226	6.721	0.618
575.8	0.020	0.389	370.161	199.924	202.687	-19.090	121.08	282.52	23.27	336.0	168.9	167.2	224.6	0.017	3.370	-2.236	6.757	0.617
587.8	0.023	0.408	379.723	200.008	202.827	-19.172	121.08	282.44	23.26	353.7	178.3	175.4	236.8	0.019	3.384	-2.244	6.788	0.617
599.8	0.021	0.425	389.346	199.921	202.724	-19.237	121.08	282.37	23.26	370.8	188.0	182.7	248.9	0.017	3.398	-2.254	6.813	0.616
611.8	0.026	0.443	398.990	200.082	202.972	-19.291	121.07	282.32	23.25	388.0	197.5	190.5	261.0	0.021	3.406	-2.256	6.833	0.616
623.8	0.021	0.461	408.517	199.821	202.679	-19.372	121.08	282.24	23.25	405.6	207.3	198.3	273.4	0.017	3.423	-2.271	6.864	0.615
635.8	0.025	0.480	418.130	199.954	202.867	-19.423	121.08	282.19	23.24	423.2	216.7	206.5	285.6	0.021	3.431	-2.274	6.883	0.615
647.8	0.020	0.498	427.765	200.076	202.956	-19.500	121.08	282.11	23.24	440.6	226.2	214.3	297.7	0.017	3.448	-2.288	6.912	0.615
659.8	0.023	0.515	437.421	199.898	202.843	-19.604	121.08	282.01	23.23	457.8	236.1	221.7	310.0	0.019	3.466	-2.298	6.952	0.614
671.8	0.022	0.533	446.999	200.005	202.942	-19.733	121.08	281.88	23.22	475.1	245.5	229.6	322.1	0.018	3.491	-2.315	7.000	0.613
683.8	0.026	0.552	456.628	200.110	203.090	-19.865	121.07	281.75	23.21	492.9	255.0	237.9	334.3	0.021	3.515	-2.329	7.051	0.613
693.8	0.022	0.569	466.255	199.889	202.837	-20.022	121.08	281.59	23.19	510.2	264.9	245.3	346.7	0.018	3.546	-2.352	7.111	0.612
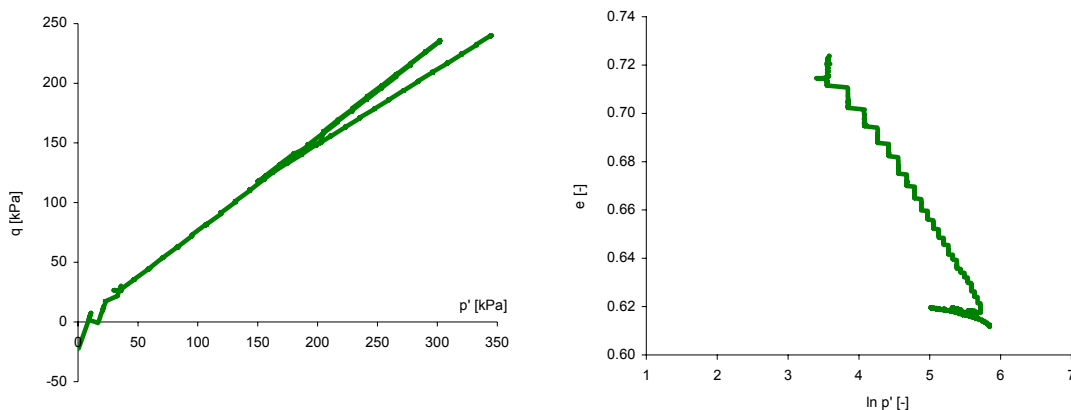
Fig. 10.111: Triaxial test data of stress path test S2cT4 on natural Kloten clay.

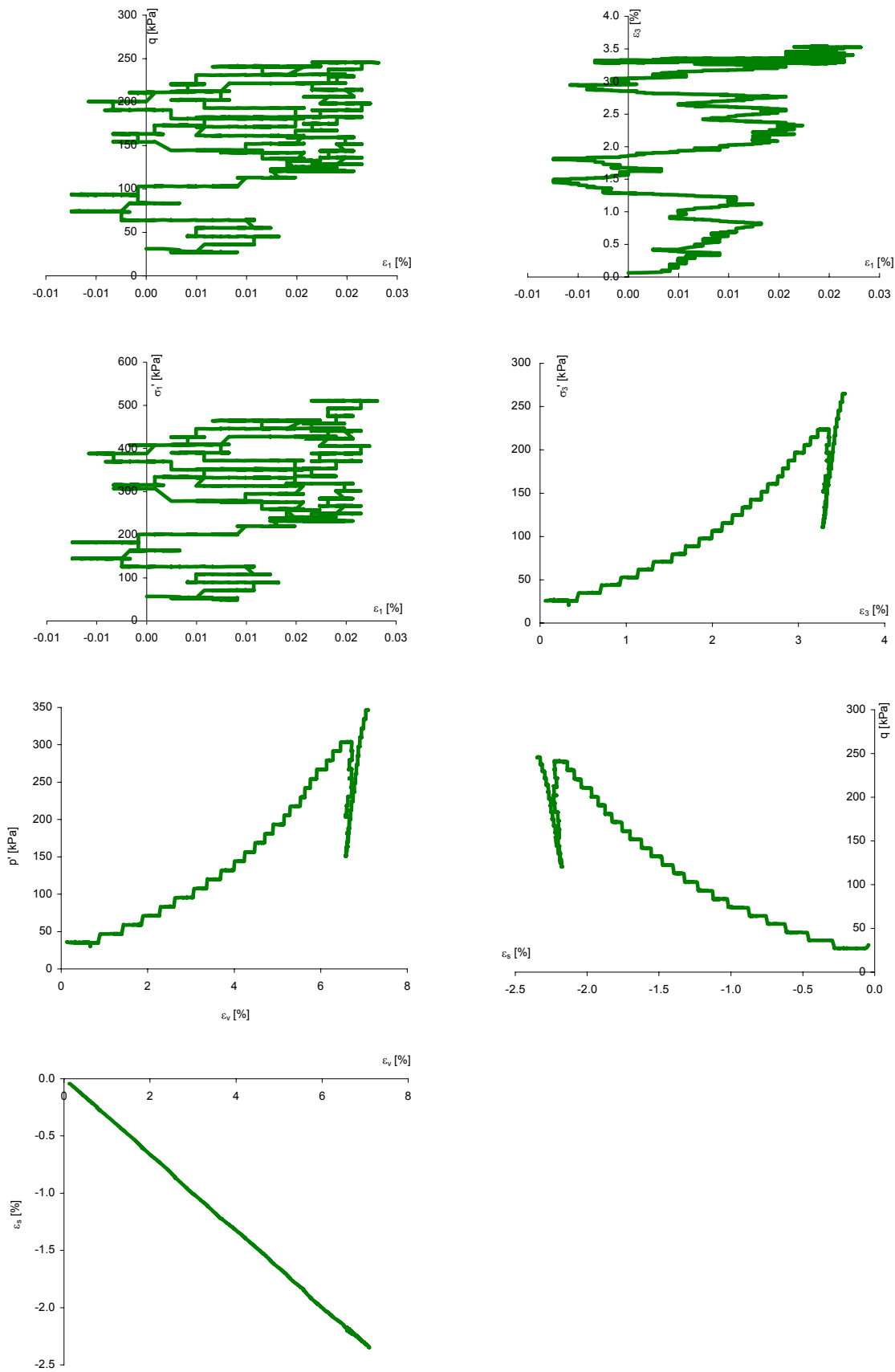Fig. 10.112: Triaxial test data of stress path test S2cT4 on natural Kloten clay.

Triaxial Test   S3T1

Test aim: Failure behaviour
Material number: 46810   Reconsituted Kloten clay sample
Test apparatus: HIF B 24: Triax 1 (green)
File name: S6d_T1_cons.PRB; S6d_T1_unl.PRB; S6d_T1_abs-2.PRB
    test start: 25.04.2005   16:01:13   test stop: 11.05.2005   09:04:48
Comments: Undrained sheared

Measured sample data:

Height H_0	106.40	[mm]
Diameter D	5.12	[cm]
Weight m_f	458.27	[g]

Determined sample data:

Cross-sectional area:	A	20.59	[cm^2]
Volume: f(H_0, D)	V_0	219.06	[cm^3]
Water content	w	21.21	[%]
Volume: f(m_f, w, ρ_s, S_r=1)	V_0	216.68	[cm^3]
Void ratio: f(m_f, w, ρ_s, S_r=1)	e_0	0.588	[-]

Material parameter:

density	ρ_s	2.77	[g/cm^3]
specific gravity of water	ρ_w	1	[g/cm^3]

Test data:

test-time	dH	force	cell-pressure	PWP bottom	PWP top	dV backpr.	H_{act}	V_{act}	A_c	σ_a'	σ_r'	q	p'	ε_a	ε_r	ε_s	ε_v	e
[hours]	[mm]	[kN]	[kPa]	[kPa]	[kPa]	[ccm]	[mm]	[ccm]	[cm^2]	[kPa]	[kPa]	[kPa]	[kPa]	[%]	[%]	[%]	[%]	[-]
0.0	0.000	0.031	205.281	200.298	201.024	0.000	106.40	216.68	20.58	19.7	4.6	15.1	9.6	0.000	0.000	0.000	0.000	0.588
7.0	0.653	0.061	220.926	200.377	201.102	-1.921	105.75	214.76	20.53	49.9	20.2	29.7	30.1	0.618	0.138	0.319	0.894	0.573
14.0	0.966	0.093	237.009	200.357	201.158	-2.712	105.43	213.97	20.51	81.6	36.3	45.3	51.4	0.916	0.176	0.494	1.267	0.568
17.0	1.070	0.106	243.849	200.258	201.022	-2.965	105.33	213.72	20.51	94.9	43.2	51.7	60.4	1.016	0.186	0.553	1.387	0.566
27.0	1.408	0.150	266.003	199.980	200.676	-3.648	104.99	213.03	20.51	138.8	65.7	73.1	90.1	1.341	0.186	0.770	1.712	0.561
31.0	1.563	0.168	275.043	200.276	200.978	-3.883	104.84	212.80	20.52	156.3	74.4	81.9	101.7	1.491	0.167	0.883	1.825	0.559
37.0	1.812	0.194	288.445	200.261	200.992	-4.318	104.59	212.36	20.52	182.3	87.8	94.5	119.3	1.733	0.150	1.055	2.033	0.556
47.0	2.307	0.240	311.372	200.221	201.030	-5.143	104.09	211.54	20.54	227.6	110.7	116.8	149.7	2.216	0.107	1.406	2.431	0.550
48.0	2.361	0.243	313.394	200.021	200.702	-5.217	104.04	211.46	20.55	231.3	113.0	118.3	152.5	2.269	0.099	1.447	2.467	0.549
57.0	2.905	0.283	333.876	200.360	201.171	-6.068	103.50	210.61	20.57	270.7	133.1	137.6	179.0	2.807	0.037	1.847	2.881	0.543
58.0	2.968	0.287	335.880	200.119	200.806	-6.202	103.43	210.48	20.57	274.9	135.4	139.5	181.9	2.870	0.039	1.887	2.947	0.542
64.0	3.306	0.314	349.513	199.965	200.647	-6.696	103.09	209.99	20.59	301.7	149.2	152.5	200.0	3.207	-0.009	2.144	3.189	0.538
68.0	3.517	0.332	358.345	200.035	200.728	-7.008	102.88	209.67	20.60	319.1	158.0	161.1	211.7	3.418	-0.038	2.304	3.342	0.536
77.0	3.963	0.372	378.671	200.331	201.013	-7.677	102.44	209.00	20.63	358.3	178.0	180.3	238.1	3.869	-0.098	2.644	3.673	0.531
81.0	4.145	0.390	387.622	200.122	200.816	-7.984	102.26	208.70	20.63	376.2	187.2	189.0	250.2	4.054	-0.114	2.778	3.826	0.529
88.0	4.434	0.420	403.586	200.146	200.951	-8.410	101.97	208.27	20.65	406.4	203.0	203.4	270.8	4.349	-0.155	3.002	4.038	0.526
89.0	4.473	0.425	405.733	200.259	200.954	-8.496	101.93	208.19	20.65	410.9	205.1	205.8	273.7	4.388	-0.154	3.028	4.081	0.525
90.0	4.509	0.429	407.858	199.983	200.673	-8.554	101.89	208.13	20.65	415.3	207.5	207.7	276.8	4.425	-0.158	3.055	4.110	0.525
91.0	4.548	0.434	410.049	200.145	200.862	-8.634	101.85	208.05	20.65	419.7	209.5	210.2	279.6	4.465	-0.158	3.082	4.150	0.524
123.0	4.937	0.441	425.298	200.294	201.080	-9.320	101.46	207.36	20.66	438.0	224.6	213.4	295.8	4.866	-0.186	3.368	4.495	0.519
148.0	4.966	0.403	405.978	200.124	200.838	-9.272	101.43	207.41	20.67	400.4	205.5	194.9	270.2	4.896	-0.213	3.406	4.471	0.520
168.0	4.956	0.374	390.912	200.400	201.099	-9.214	101.44	207.47	20.68	371.0	190.2	180.9	250.5	4.885	-0.222	3.405	4.441	0.520
178.0	4.960	0.359	383.231	200.142	200.832	-9.216	101.44	207.47	20.68	356.4	182.7	173.6	240.6	4.890	-0.224	3.409	4.442	0.520
208.0	4.942	0.315	360.777	200.400	201.202	-9.195	101.46	207.49	20.68	312.3	160.0	152.3	210.8	4.871	-0.220	3.394	4.431	0.520
219.0	4.934	0.298	352.228	200.227	200.906	-9.153	101.47	207.53	20.68	295.8	151.7	144.1	199.7	4.863	-0.226	3.393	4.411	0.520
239.0	4.917	0.269	337.057	200.388	201.070	-9.123	101.48	207.56	20.68	266.4	136.3	130.1	179.7	4.845	-0.225	3.380	4.395	0.521
328.0	4.882	0.220	312.579	200.278	200.964	-9.002	101.52	207.68	20.68	218.3	112.0	106.4	147.4	4.809	-0.237	3.364	4.335	0.522
328.0	4.857	0.148	312.315	192.522	193.600	-9.125	101.54	207.65	20.67	190.9	119.3	71.6	143.1	4.783	-0.193	3.318	4.396	0.521
328.1	4.822	0.100	312.743	185.774	186.682	-9.137	101.58	207.54	20.66	174.9	126.5	48.4	142.7	4.747	-0.172	3.280	4.402	0.521
328.8	4.595	0.000	312.682	177.243	177.318	-9.153	101.81	207.53	20.61	135.4	135.4	0.0	135.4	4.514	-0.052	3.043	4.410	0.520
339.2	0.817	-0.100	312.474	204.001	204.898	-9.104	105.58	207.58	19.88	57.7	108.0	-50.3	91.3	0.774	1.806	-0.688	4.386	0.521
346.3	-1.785	-0.117	312.427	198.129	199.350	-9.114	108.19	207.57	19.40	53.4	113.7	-60.3	93.6	-1.650	3.021	-3.114	4.391	0.521
353.8	-4.486	-0.133	312.518	187.192	188.211	-9.134	110.89	207.55	18.92	54.5	124.8	-70.3	101.4	-4.046	4.223	-5.513	4.401	0.521
360.0	-6.744	-0.142	312.628	178.383	181.065	-9.148	113.14	207.53	18.54	56.3	132.9	-76.6	107.4	-5.961	5.184	-7.430	4.408	0.520
361.2	-7.169	-0.142	312.733	176.941	179.637	-9.151	113.57	207.53	18.48	57.6	134.4	-76.9	108.8	-6.312	5.361	-7.782	4.409	0.520
373.8	-11.716	-0.125	312.535	175.450	176.505	-9.155	118.12	207.53	17.76	66.2	136.6	-70.4	113.1	-9.919	7.165	-11.390	4.412	0.520

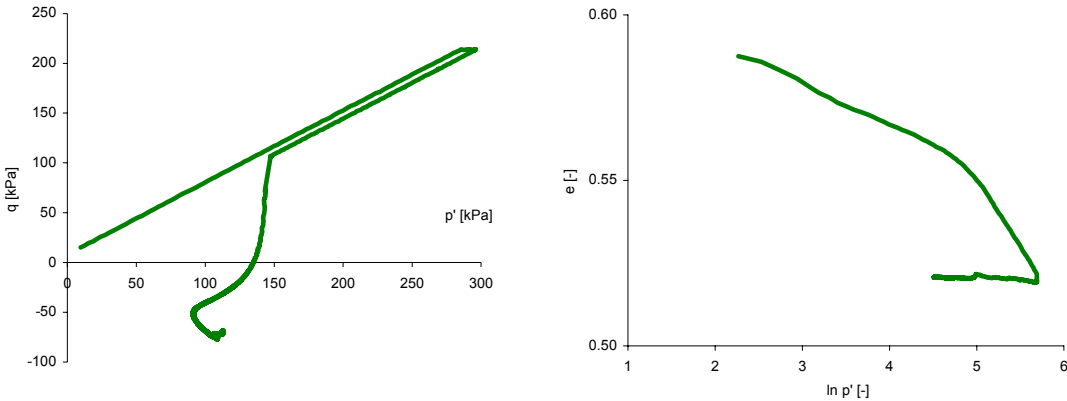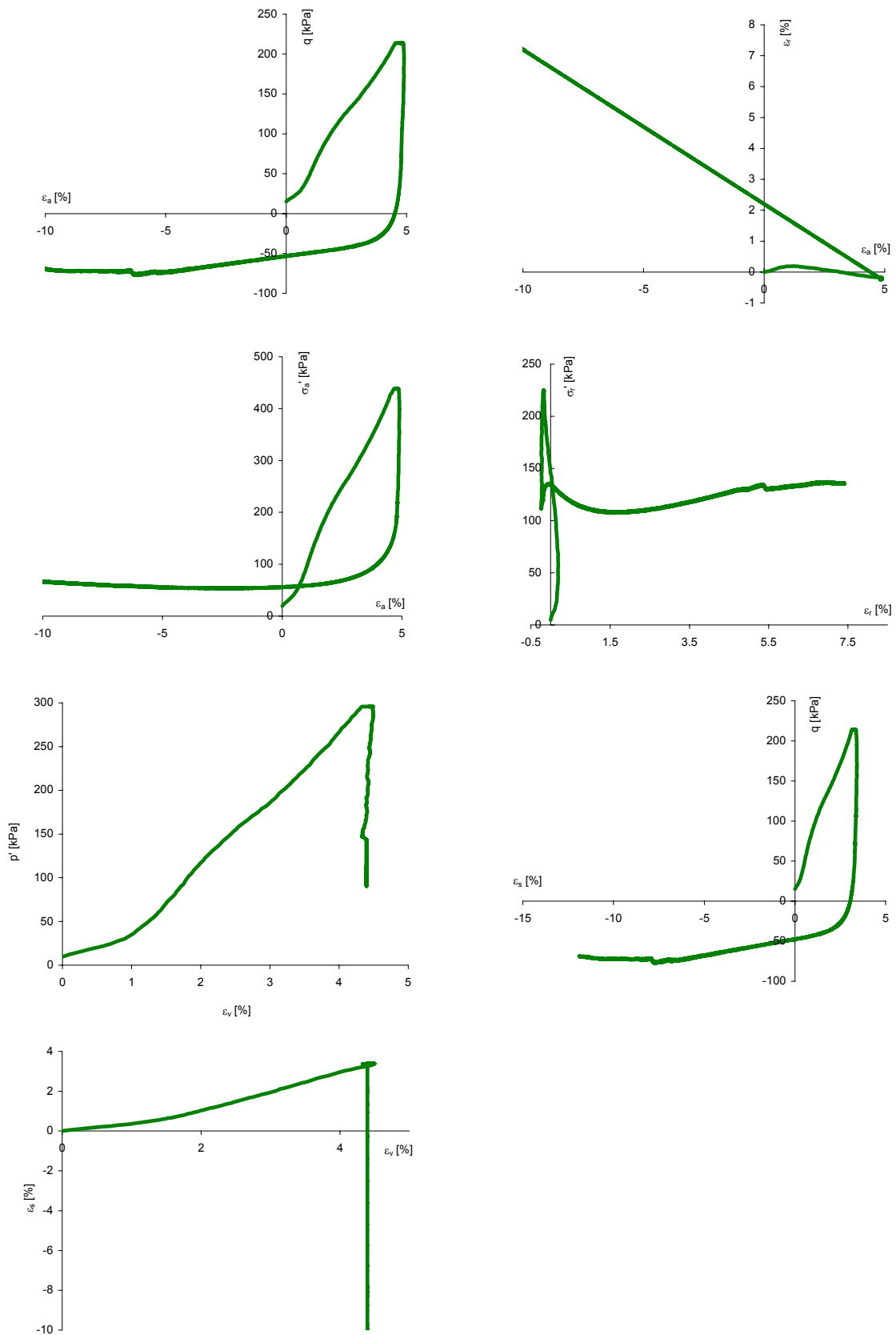Fig. 10.113: Triaxial test data of stress path test S3T1 on reconstituted Kloten clay.

Fig. 10.114: Triaxial test data of stress path test S3T1 on reconstituted Kloten clay.

Test data:

test-time [hours]	dH LVDT 1 [mm]	dH LVDT 2 [mm]	ε_a LVDT 1 [%]	ε_a LVDT 2 [%]	ε_r LVDT 1 [%]	ε_r LVDT 2 [%]	ε_s LVDT 1 [%]	ε_s LVDT 2 [%]	V_{act} Laser [ccm]	dV Laser [ccm]	ε_v Laser [%]	ε_r LVDT 1 & Laser [%]	ε_r LVDT 2 & Laser [%]	ε_s LVDT 1 & Laser [%]	ε_s LVDT 2 & Laser [%]	e Laser [-]	V_{act} Cellpr. [ccm]	ε_v Cellpr. [%]
0.0	0.000	0.000	0.000	0.000	0.000	0.000	0.000	0.00	220.28	0.00	0.00	0.00	0.00	0.00	0.00	0.61	216.68	0.00
7.0	0.306	0.448	0.439	0.644	0.228	0.125	0.14	0.35	219.14	-1.14	0.52	0.04	-0.06	0.27	0.47	0.61	212.56	1.94
14.0	0.465	0.647	0.669	0.933	0.299	0.167	0.25	0.51	218.72	-1.56	0.71	0.02	-0.11	0.43	0.70	0.60	210.83	2.78
17.0	0.519	0.706	0.747	1.019	0.320	0.184	0.28	0.56	219.90	-0.38	0.17	-0.29	-0.42	0.69	0.96	0.61	210.29	3.04
27.0	0.693	0.912	1.000	1.320	0.356	0.196	0.43	0.75	218.84	-1.44	0.66	-0.17	-0.33	0.78	1.10	0.60	209.14	3.60
31.0	0.767	0.992	1.108	1.438	0.358	0.194	0.50	0.83	218.69	-1.59	0.73	-0.19	-0.36	0.87	1.20	0.60	208.69	3.83
37.0	0.893	1.149	1.292	1.669	0.371	0.182	0.61	0.99	218.02	-2.26	1.04	-0.13	-0.32	0.95	1.32	0.60	208.13	4.11
47.0	1.182	1.477	1.718	2.155	0.357	0.138	0.91	1.35	216.88	-3.40	1.57	-0.07	-0.29	1.19	1.63	0.59	207.24	4.56
48.0	1.217	1.513	1.769	2.209	0.349	0.129	0.95	1.39	217.27	-3.01	1.39	-0.19	-0.41	1.31	1.75	0.59	206.99	4.68
57.0	1.554	1.888	2.270	2.772	0.305	0.055	1.31	1.81	216.69	-3.59	1.65	-0.31	-0.56	1.72	2.22	0.59	206.01	5.18
58.0	1.593	1.928	2.329	2.832	0.309	0.057	1.35	1.85	215.20	-5.08	2.36	0.02	-0.24	1.54	2.05	0.58	205.83	5.27
64.0	1.816	2.169	2.663	3.198	0.263	-0.005	1.60	2.13	215.99	-4.29	1.99	-0.34	-0.61	2.00	2.54	0.58	205.11	5.64
68.0	1.954	2.311	2.872	3.414	0.235	-0.036	1.76	2.30	214.45	-5.83	2.72	-0.08	-0.35	1.96	2.51	0.57	204.77	5.82
77.0	2.235	2.624	3.298	3.895	0.187	-0.111	2.07	2.67	214.54	-5.73	2.67	-0.31	-0.61	2.41	3.00	0.57	203.92	6.26
81.0	2.350	2.749	3.474	4.088	0.176	-0.131	2.20	2.81	213.61	-6.66	3.12	-0.18	-0.48	2.43	3.05	0.57	203.58	6.44
88.0	2.535	2.954	3.758	4.406	0.140	-0.184	2.41	3.06	213.76	-6.52	3.05	-0.35	-0.68	2.74	3.39	0.57	203.09	6.69
89.0	2.560	2.984	3.796	4.453	0.143	-0.186	2.44	3.09	212.76	-7.52	3.53	-0.13	-0.46	2.62	3.27	0.56	202.86	6.81
90.0	2.585	3.005	3.834	4.485	0.138	-0.188	2.46	3.12	213.60	-6.68	3.13	-0.35	-0.68	2.79	3.44	0.56	202.83	6.83
91.0	2.609	3.031	3.871	4.526	0.139	-0.188	2.49	3.14	212.68	-7.60	3.57	-0.15	-0.48	2.68	3.34	0.56	202.80	6.84
123.0	2.852	3.298	4.247	4.944	0.124	-0.225	2.75	3.45	212.31	-7.97	3.75	-0.25	-0.60	3.00	3.69	0.56	201.88	7.33
148.0	2.866	3.313	4.269	4.968	0.101	-0.249	2.78	3.48	211.80	-8.47	4.00	-0.13	-0.48	2.94	3.63	0.55	201.58	7.49
168.0	2.866	3.312	4.269	4.966	0.086	-0.263	2.79	3.49	212.05	-8.23	3.88	-0.19	-0.54	2.98	3.67	0.55	201.52	7.52
178.0	2.863	3.309	4.264	4.962	0.089	-0.260	2.78	3.48	211.97	-8.31	3.92	-0.17	-0.52	2.96	3.66	0.55	201.49	7.54
208.0	2.855	3.299	4.252	4.946	0.090	-0.257	2.77	3.47	212.44	-7.84	3.69	-0.28	-0.63	3.02	3.72	0.56	201.48	7.55
219.0	2.853	3.297	4.249	4.943	0.081	-0.266	2.78	3.47	212.66	-7.61	3.58	-0.33	-0.68	3.06	3.75	0.56	201.41	7.58
239.0	2.844	3.285	4.235	4.924	0.080	-0.264	2.77	3.46	213.22	-7.06	3.31	-0.46	-0.81	3.13	3.82	0.56	201.30	7.64
328.0	2.821	3.255	4.199	4.877	0.068	-0.271	2.75	3.43	212.42	-7.86	3.70	-0.25	-0.59	2.97	3.64	0.56	201.27	7.66
328.0	2.809	3.238	4.181	4.850	0.108	-0.227	2.72	3.38	213.02	-7.26	3.41	-0.39	-0.72	3.04	3.71	0.56	201.42	7.58
328.1	2.791	3.216	4.153	4.816	0.122	-0.209	2.69	3.35	212.16	-8.12	3.83	-0.16	-0.49	2.88	3.54	0.55	201.32	7.63
328.8	2.675	3.073	3.973	4.592	0.212	-0.097	2.51	3.13	212.19	-8.09	3.81	-0.08	-0.39	2.70	3.32	0.55	201.57	7.50
339.2	0.560	0.572	0.806	0.824	1.795	1.786	-0.66	-0.64	214.45	-5.83	2.72	0.96	0.95	-0.10	-0.08	0.57	205.82	5.28
346.3	-0.727	-1.264	-1.028	-1.774	2.712	3.085	-2.49	-3.24	216.86	-3.42	1.58	1.30	1.67	-1.55	-2.30	0.59	206.66	4.85
353.8	-1.883	-2.824	-2.620	-3.878	3.508	4.137	-4.09	-5.34	218.55	-1.73	0.79	1.71	2.33	-2.88	-4.14	0.60	207.10	4.63
360.0	-2.666	-3.699	-3.669	-5.019	4.033	4.708	-5.13	-6.48	218.16	-2.11	0.97	2.32	2.99	-3.99	-5.34	0.60	207.30	4.52
361.2	-2.819	-3.801	-3.871	-5.150	4.134	4.773	-5.34	-6.62	218.93	-1.35	0.62	2.24	2.88	-4.08	-5.36	0.60	207.35	4.50
373.8	-3.492	-4.814	-4.752	-6.435	4.574	5.416	-6.22	-7.90	212.92	-7.36	3.46	4.10	4.95	-5.90	-7.59	0.56	207.39	4.48
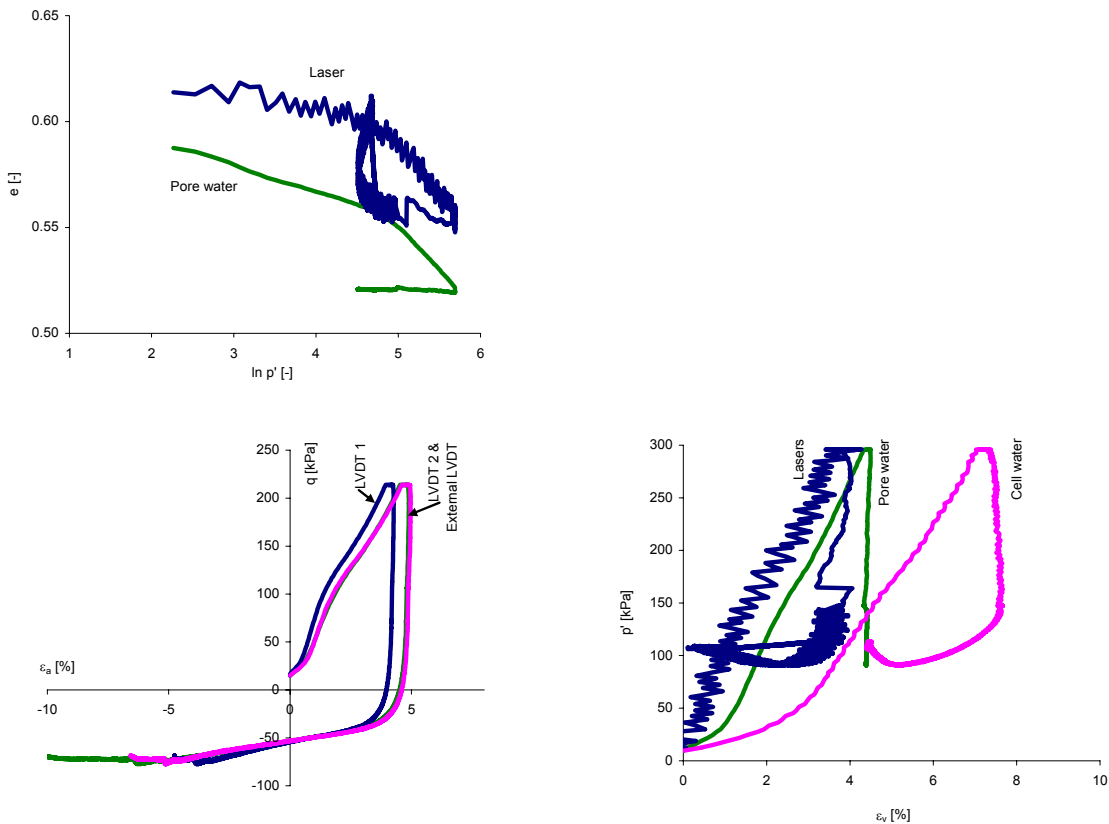
Fig. 10.115: Triaxial test data of stress path test S3T1 on reconstituted Kloten clay: comparison of strain determination with various measurement methods.
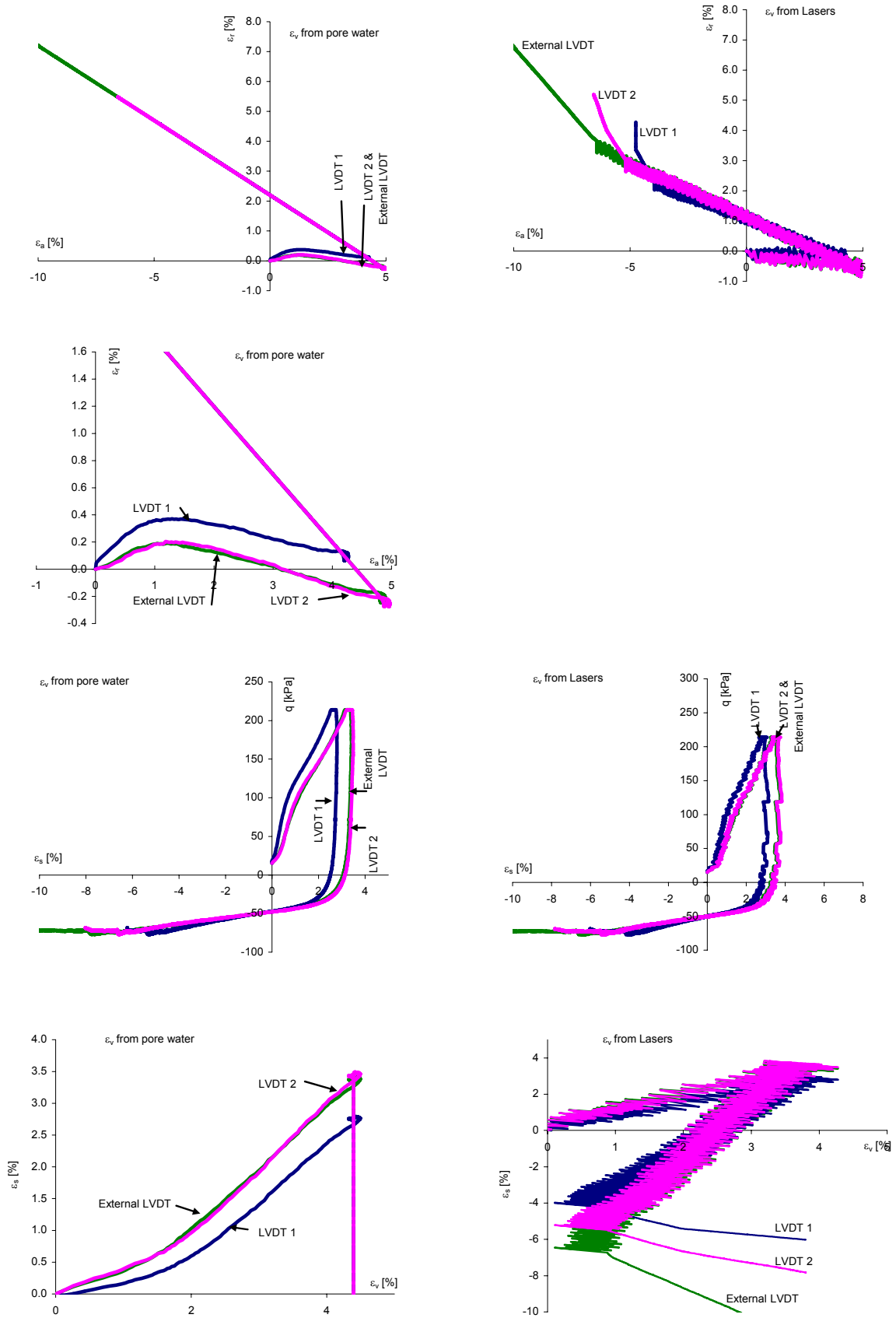
Fig. 10.116: Triaxial test data of stress path test S3T1 on reconstituted Kloten clay: comparison of strain determination with various measurement methods.
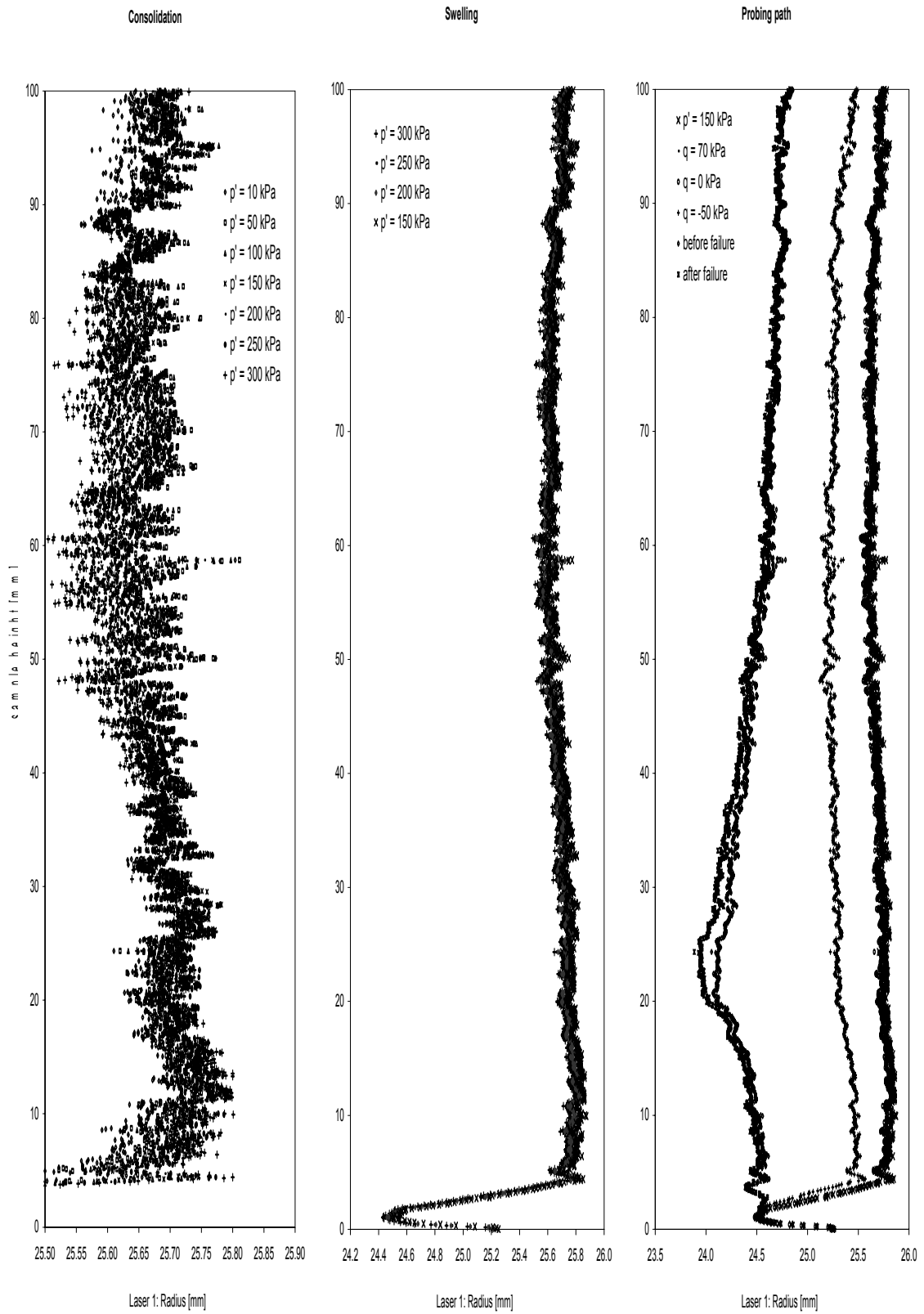
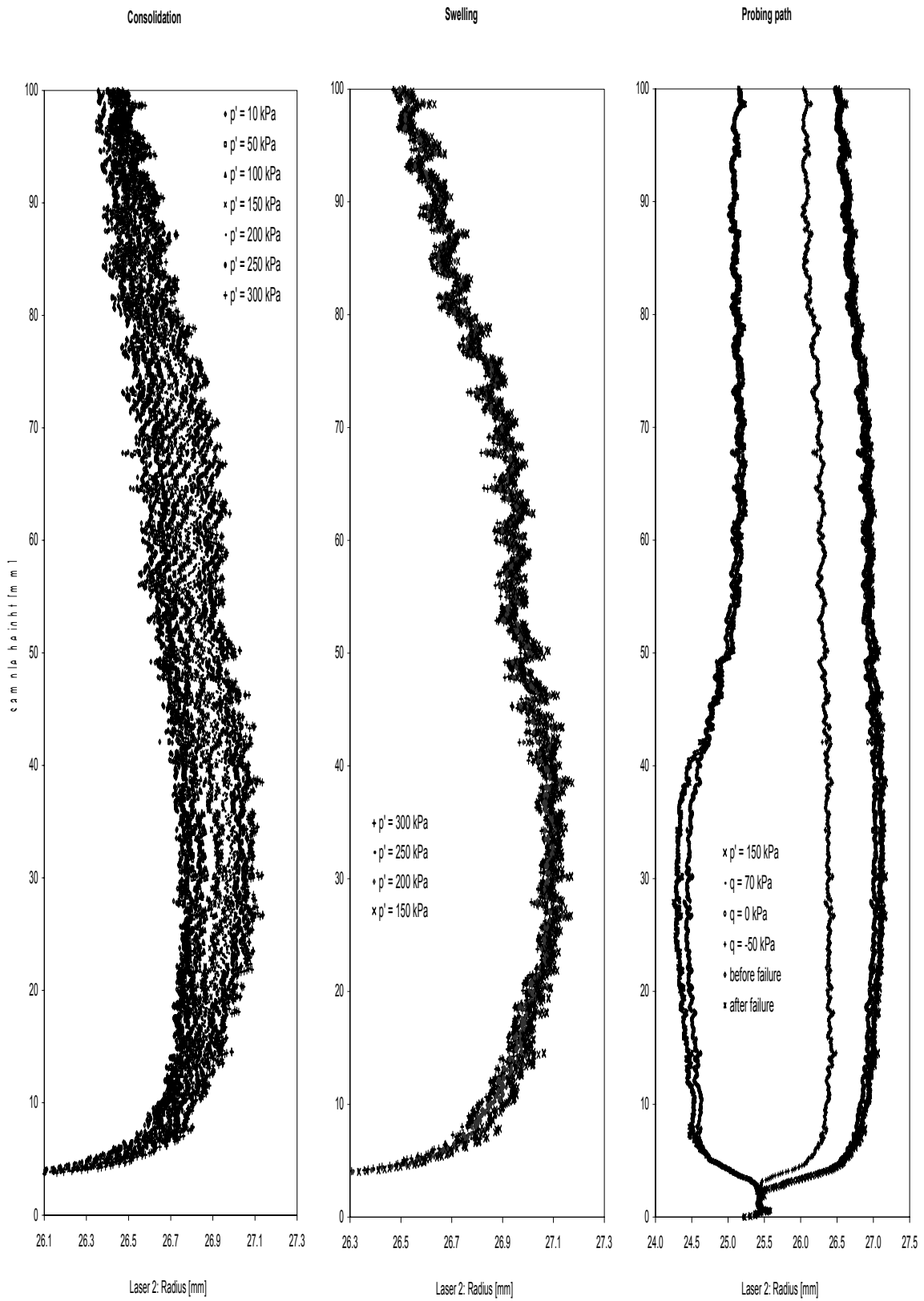Fig. 10.117: Laser scan data of triaxial stress path test S3T1 on reconstituted Kloten clay: radius from laser 1.

Consolidation

Swelling

Probing path

Legend (Consolidation):
- p' = 10 kPa
- p' = 50 kPa
- p' = 100 kPa
- p' = 150 kPa
- p' = 200 kPa
- p' = 250 kPa
- p' = 300 kPa

Legend (Swelling):
+ p' = 300 kPa
· p' = 250 kPa
· p' = 200 kPa
x p' = 150 kPa

Legend (Probing path):
x p' = 150 kPa
· q = 70 kPa
○ q = 0 kPa
+ q = -50 kPa
· before failure
x after failure

sample height [mm]

Laser 2: Radius [mm]

Fig. 10.118: Laser scan data of triaxial stress path test S3T1 on reconstituted Kloten clay: radius from laser 2.
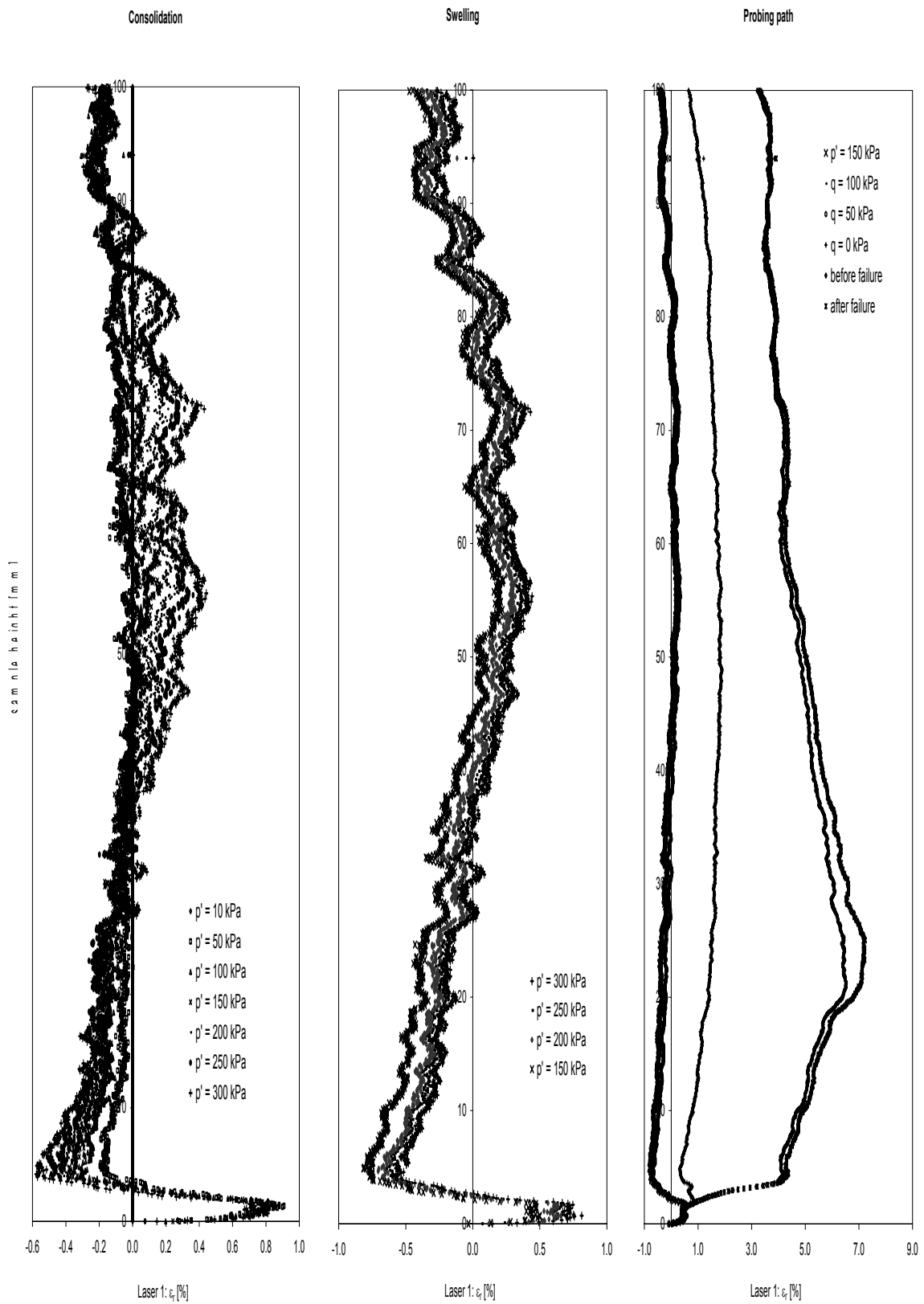
Fig. 10.119: Laser scan data of triaxial stress path test S3T1 on reconstituted Kloten clay: radial strain from laser 1.
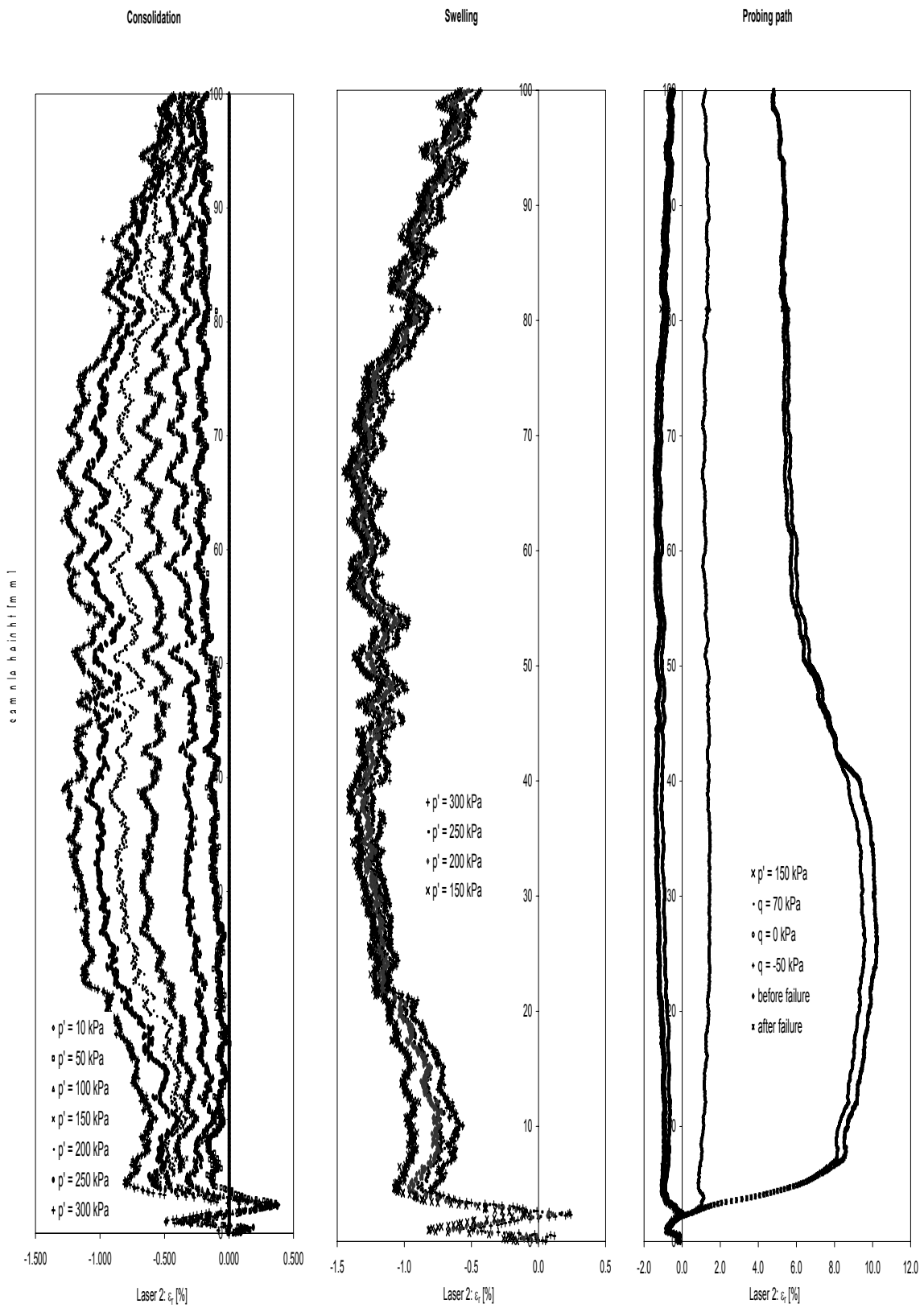
Fig. 10.120: Laser scan data of triaxial stress path test S3T1 on reconstituted Kloten clay: radial strain from laser 2.
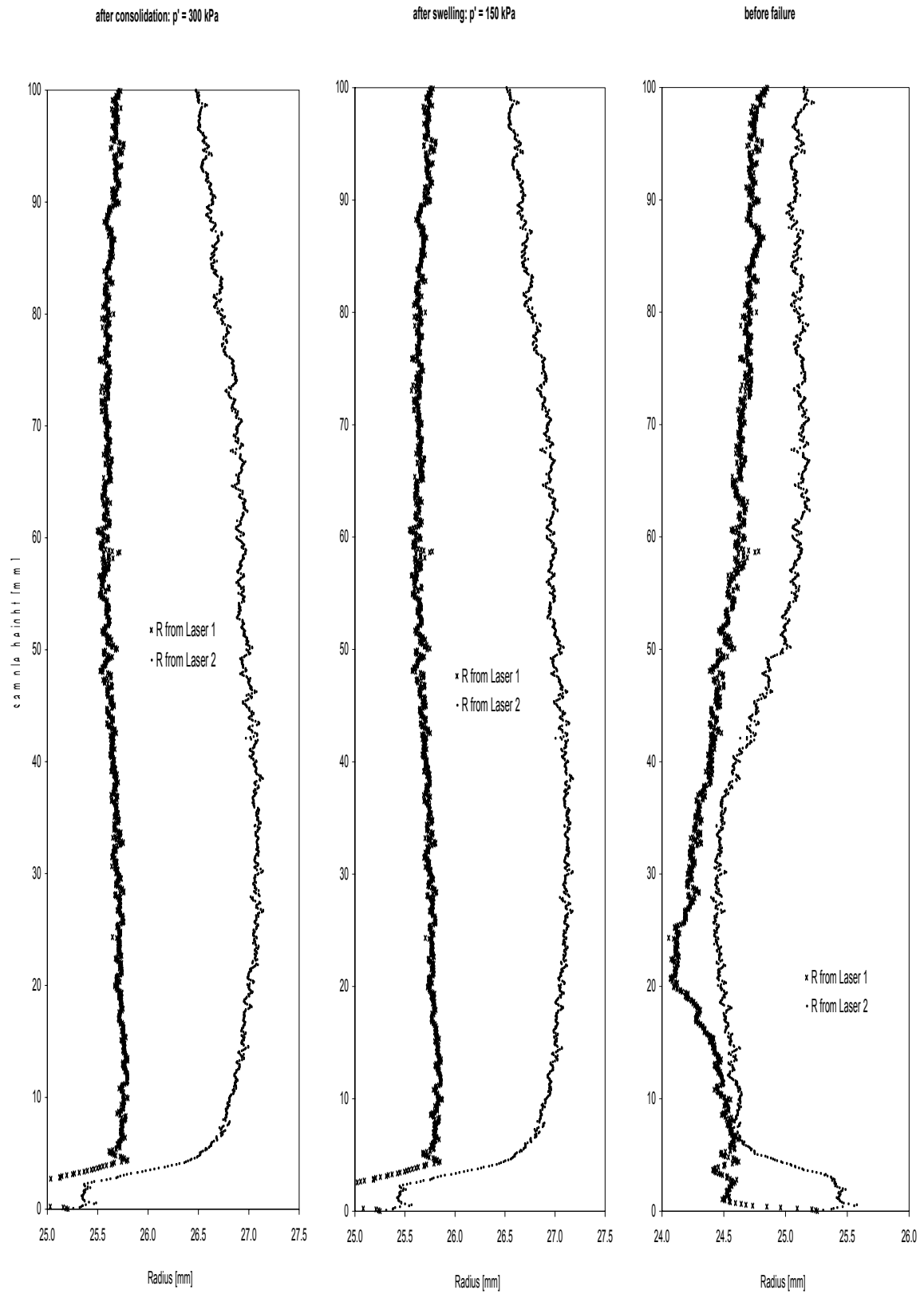
Fig. 10.121: Laser scan data of triaxial stress path test S3T1 on reconstituted Kloten clay: comparison of radius determined from laser 1 & 2.
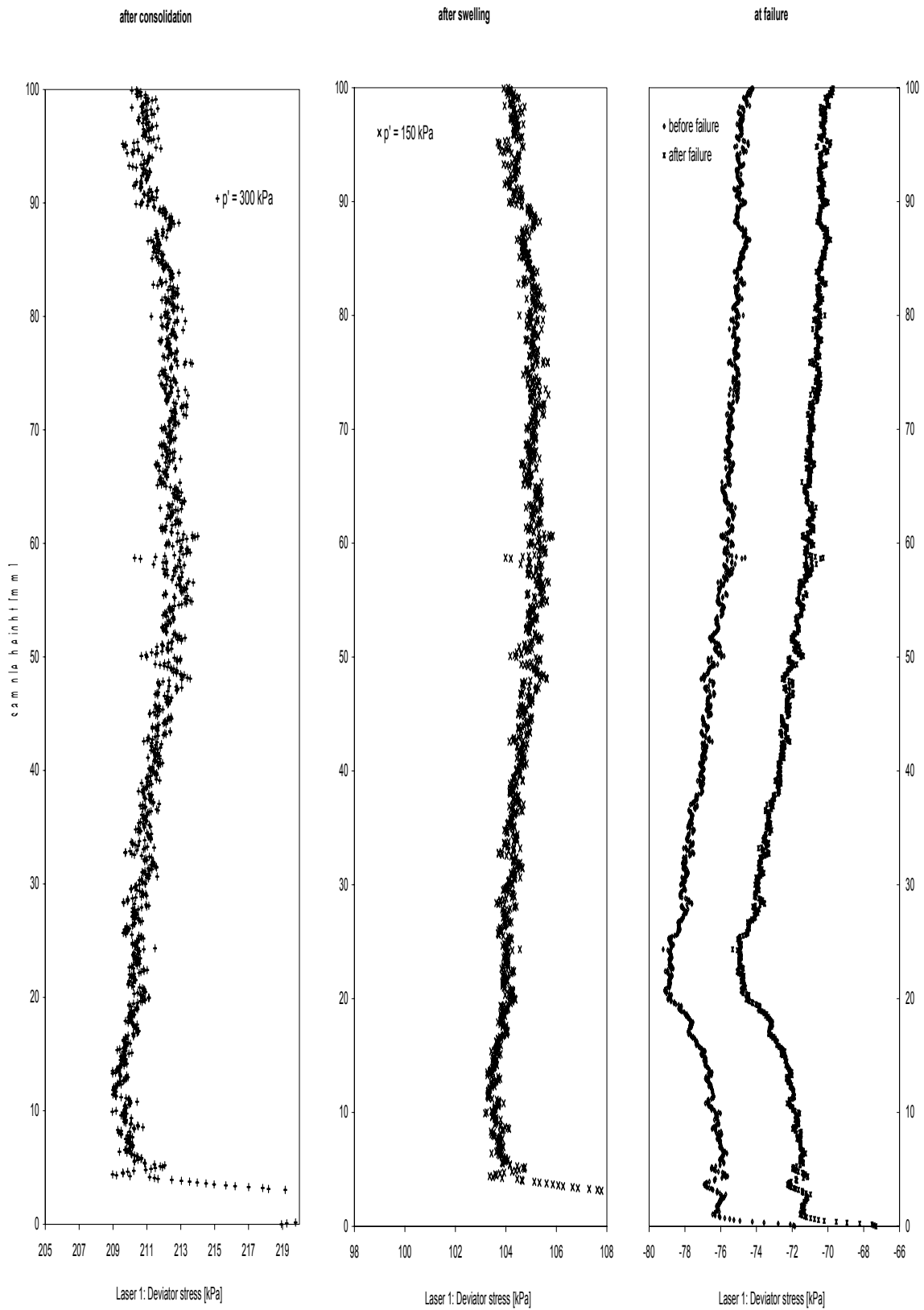
Fig. 10.122: Laser scan data of triaxial stress path test S3T1 on reconstituted Kloten clay: change in deviator stress from laser 1.
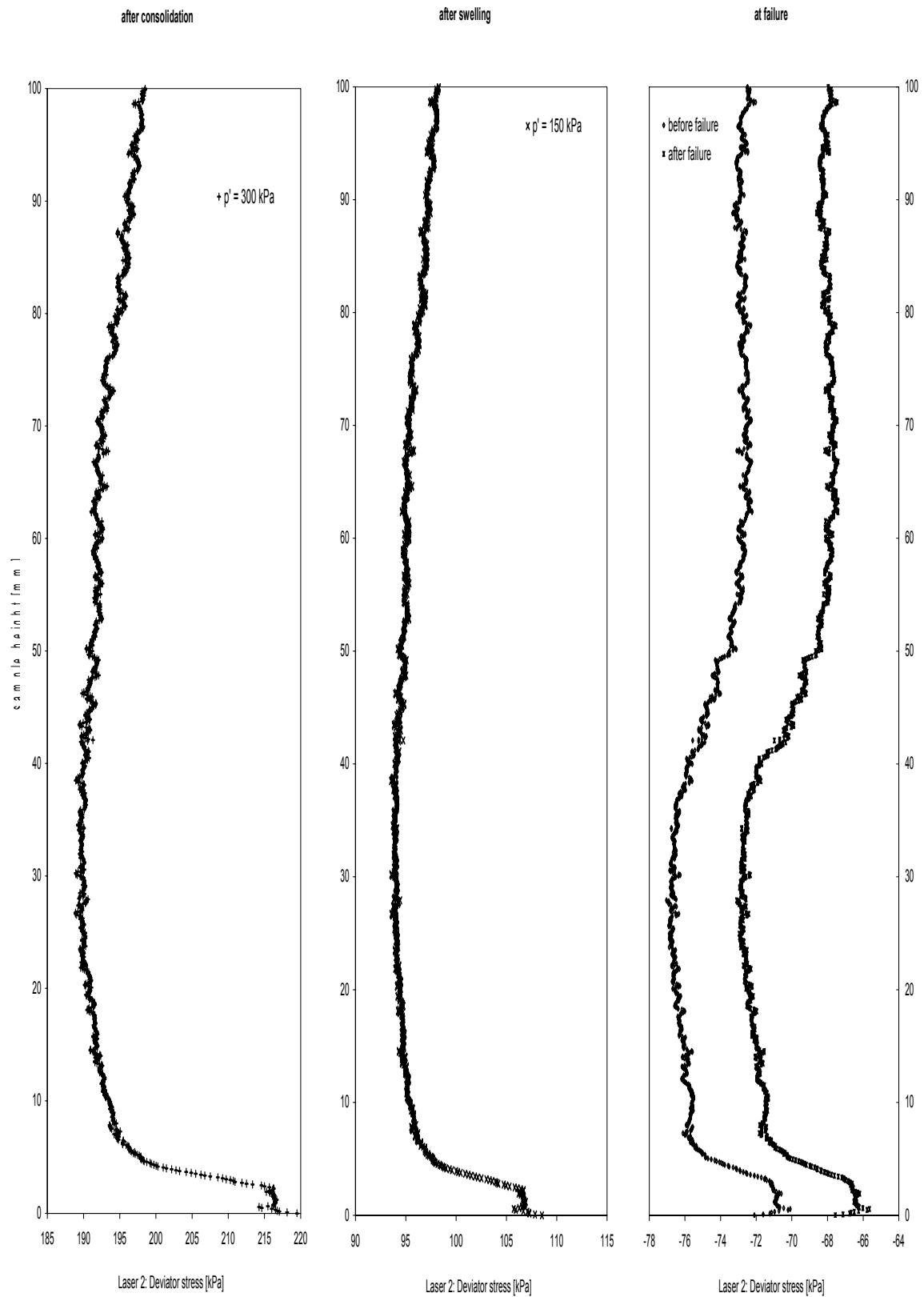
Fig. 10.123: Laser scan data of triaxial stress path test S3T1 on reconstituted Kloten clay: change in deviator stress from laser 2.

Test data:

material:	sample height: [mm]
S2bT4 Kloten 46862	116.6

Calculations:

load stage:	frequency:	≅t shearwave [≅s]	H_{act} [mm]	$H_{act} - 4$ [mm]	V_{act} [cm³]	weight: [g]	density: [g/cm³]	v_s [m/s]	G_{max}: [MPa]	p' [kPa]
before Consolidation	50 kHz	419.2	116.73	112.73	291.43	594.62	2.040	269	148	
after Consolidation	50 kHz	403.6	107.21	103.21	272.86	576.05	2.111	256	138	300
	20 kHz	414	107.21	103.21	272.86	576.05	2.111	249	131	300
	10 kHz	417	107.21	103.21	272.86	576.05	2.111	248	129	300
	5 kHz	426	107.21	103.21	272.86	576.05	2.111	242	124	300
after Swelling	20 kHz	484	107.28	103.28	272.71	575.9	2.112	213	96	150
	10 kHz	490	107.28	103.28	272.71	575.9	2.112	211	94	150
	5 kHz	464	107.28	103.28	272.71	575.9	2.112	223	105	150
after Shearing	20 kHz		138.09	134.09	268.14	571.33	2.131			245
	10 kHz	576	138.09	134.09	268.14	571.33	2.131	233	115	245
	5 kHz	582.4	138.09	134.09	268.14	571.33	2.131	230	113	245

Fig. 10.124: Bender element test data of stress path test S2T4 on natural Kloten clay.

421
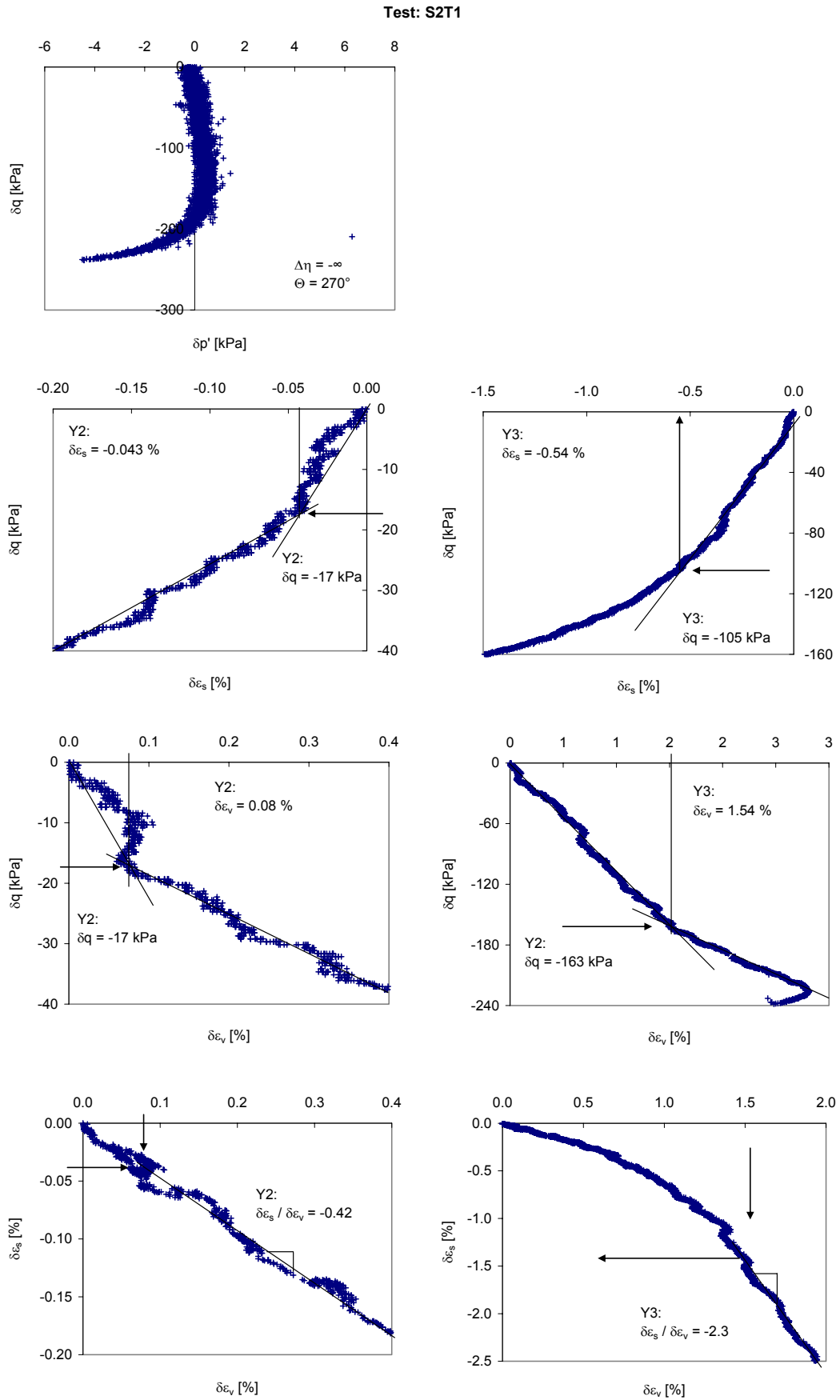
Fig. 10.125: Stiffness analysis of the probing path of test S2T1 on natural Kloten clay.
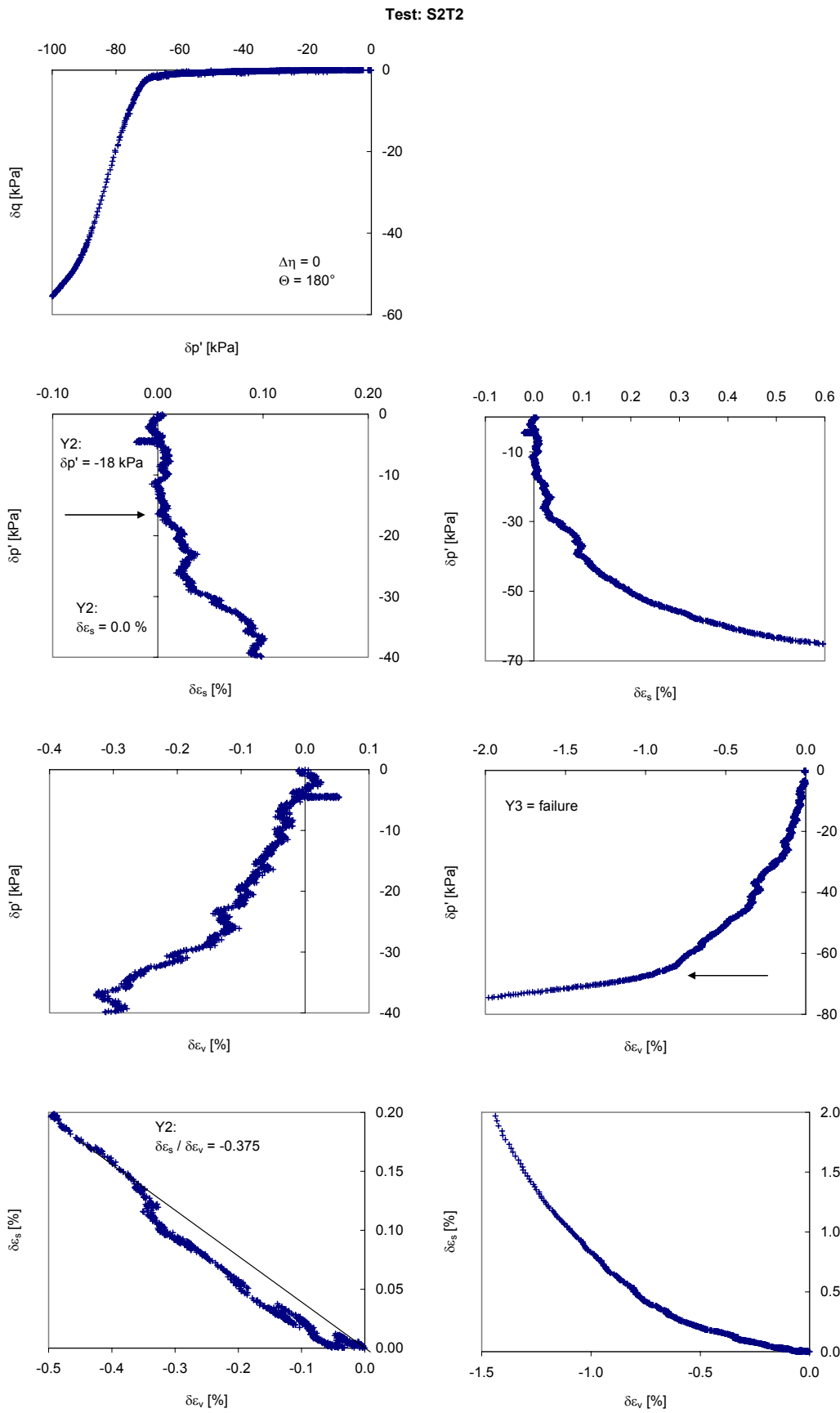
Test: S2T2
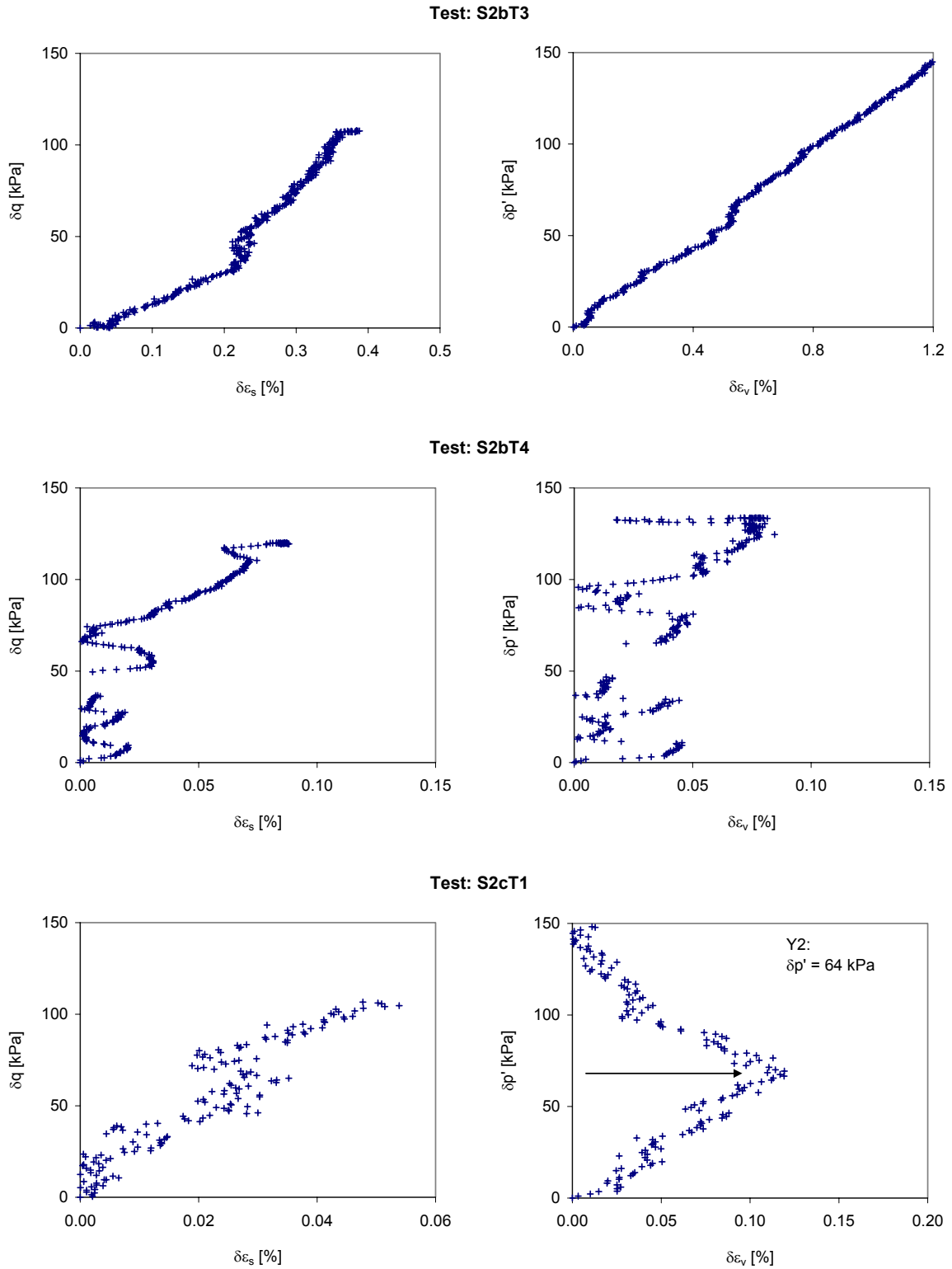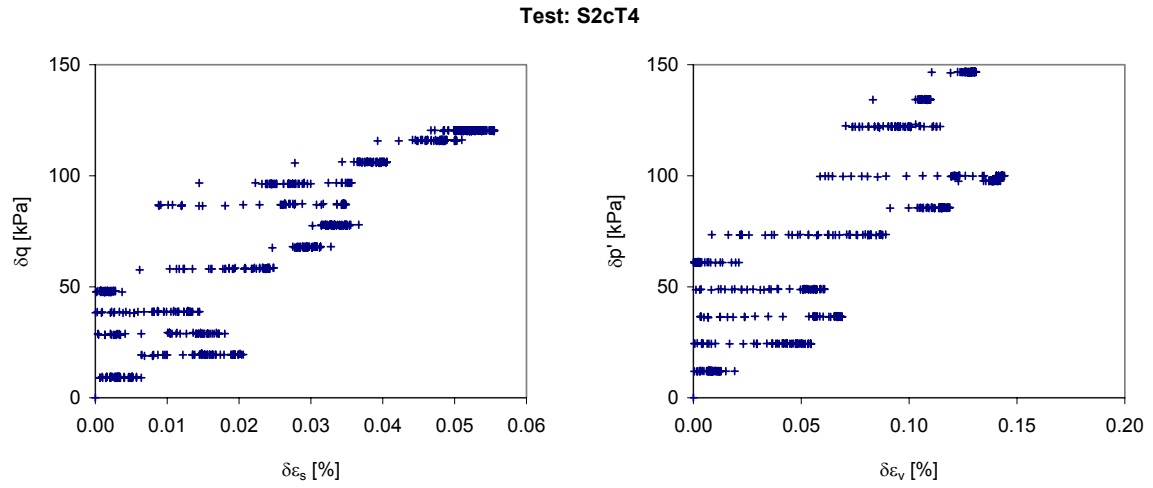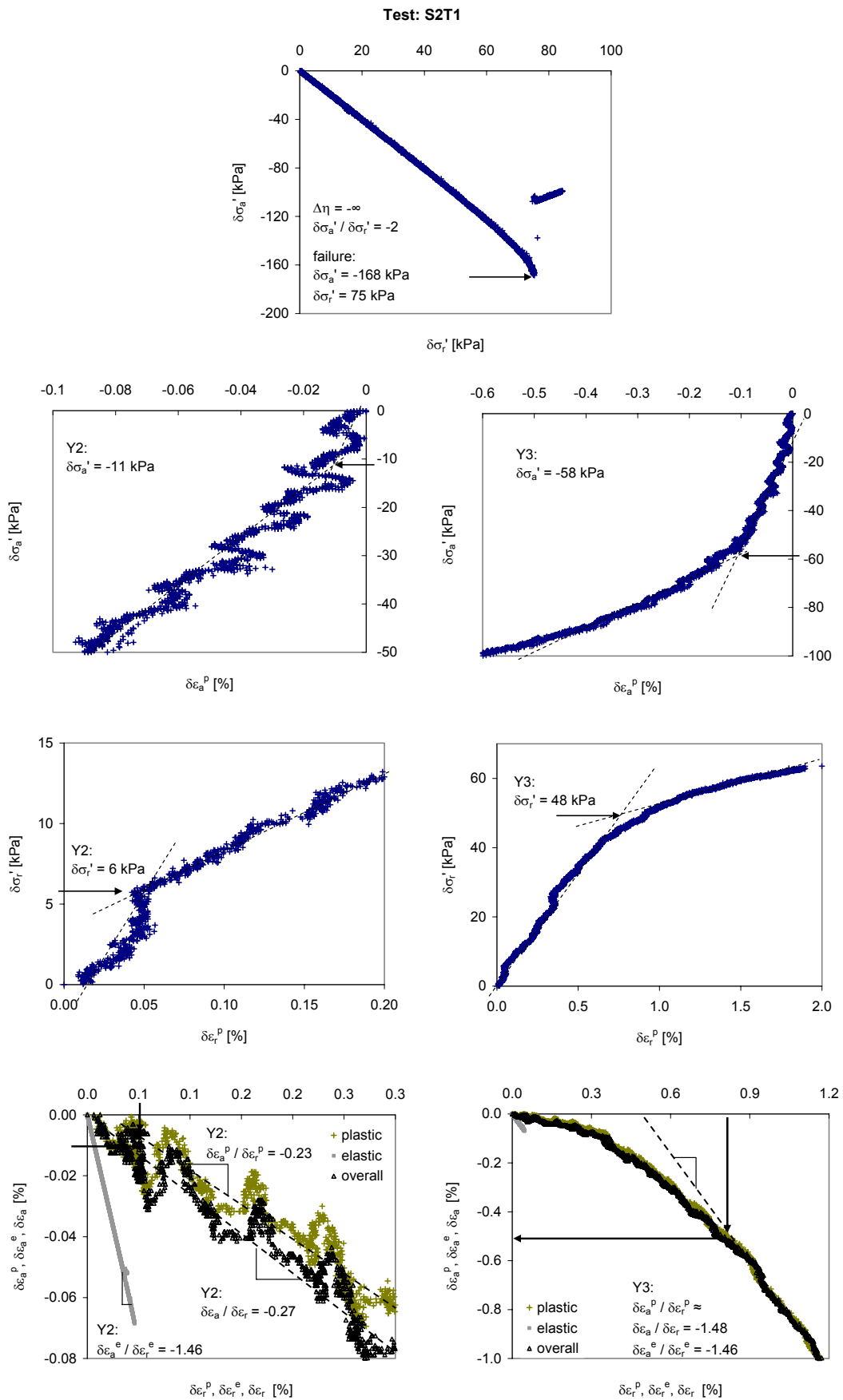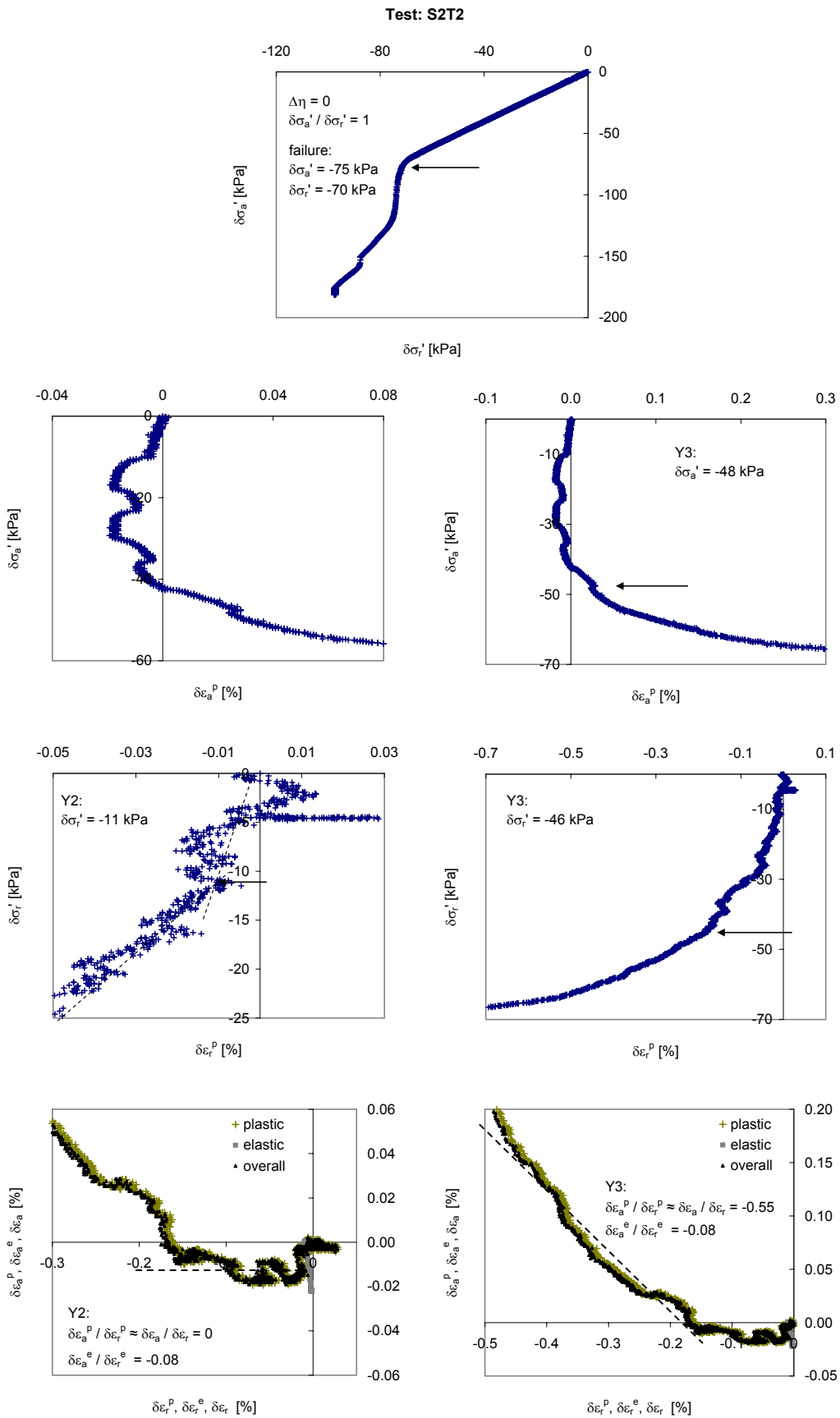

Fig. 10.126: Stiffness analysis of the probing path of test S2T2 on natural Kloten clay.
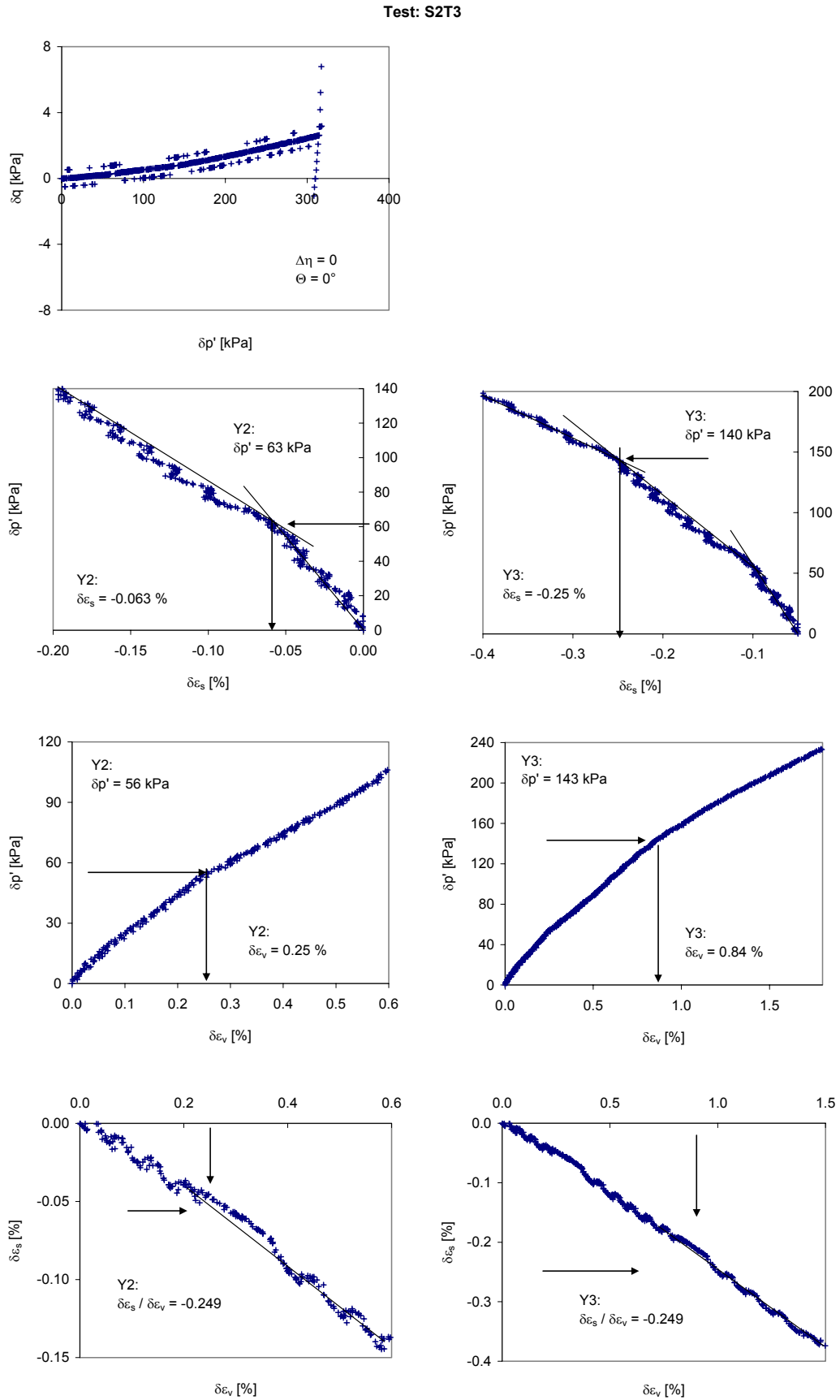
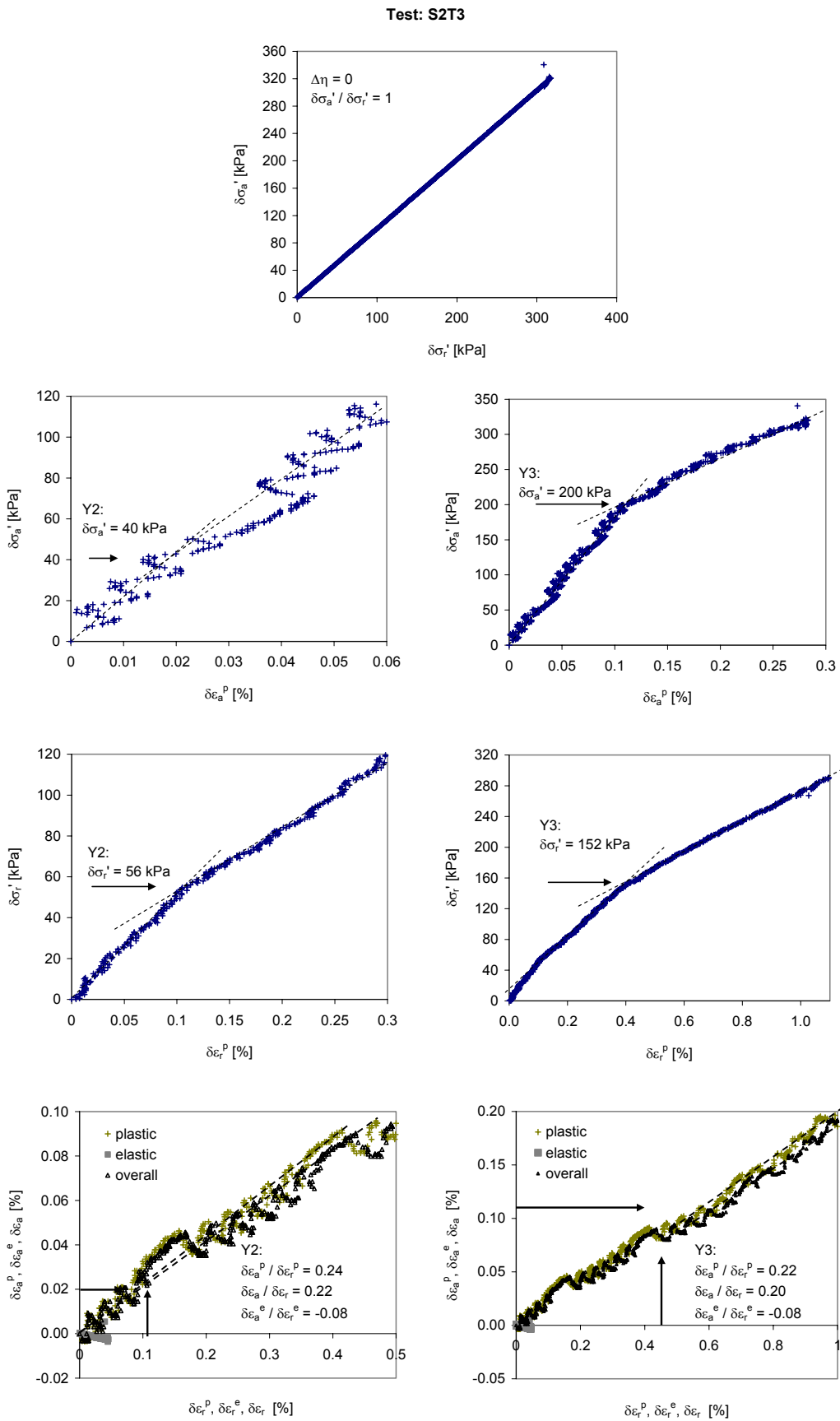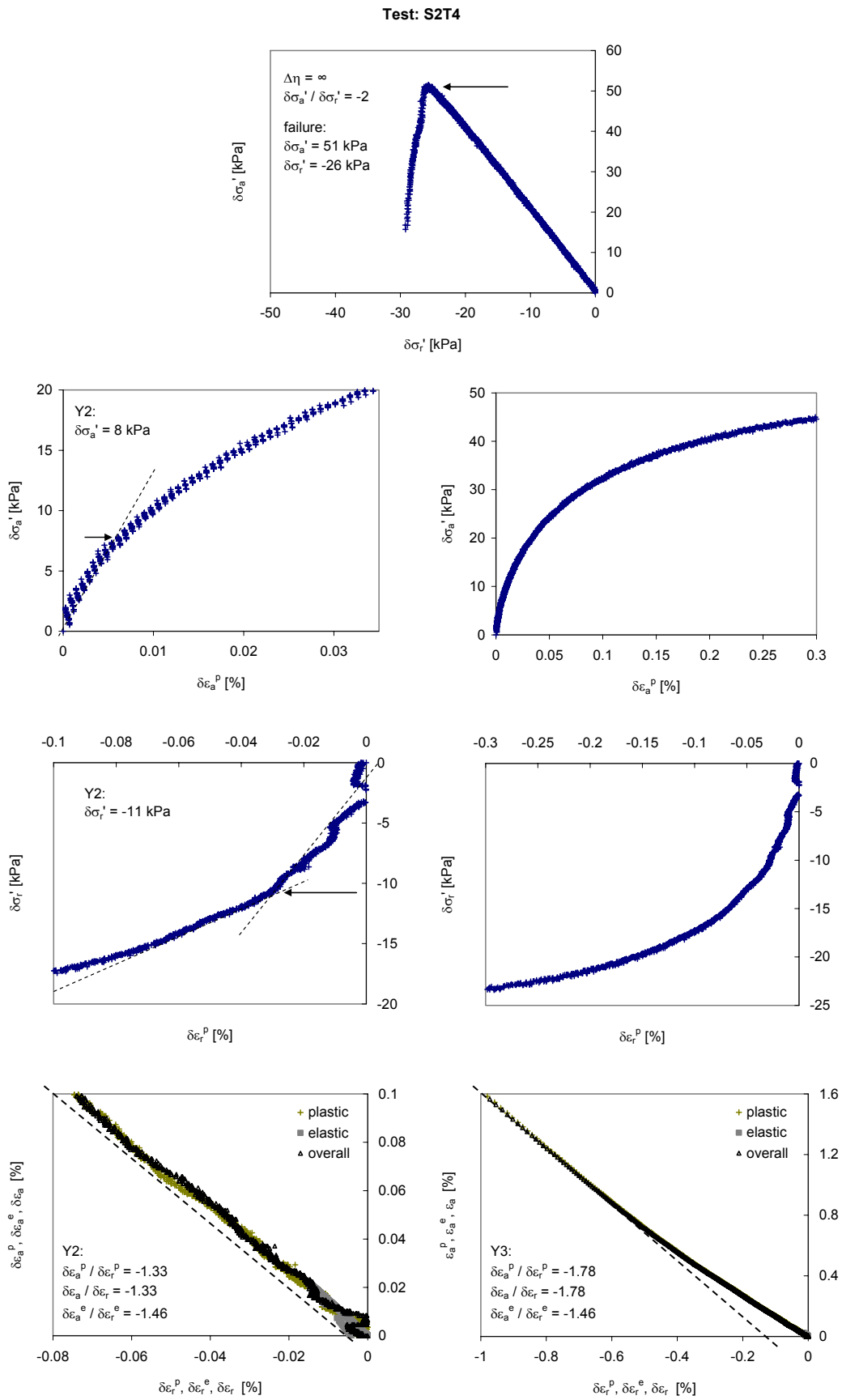Fig. 10.127: Stiffness analysis of the probing path of test S2T3 on natural Kloten clay.
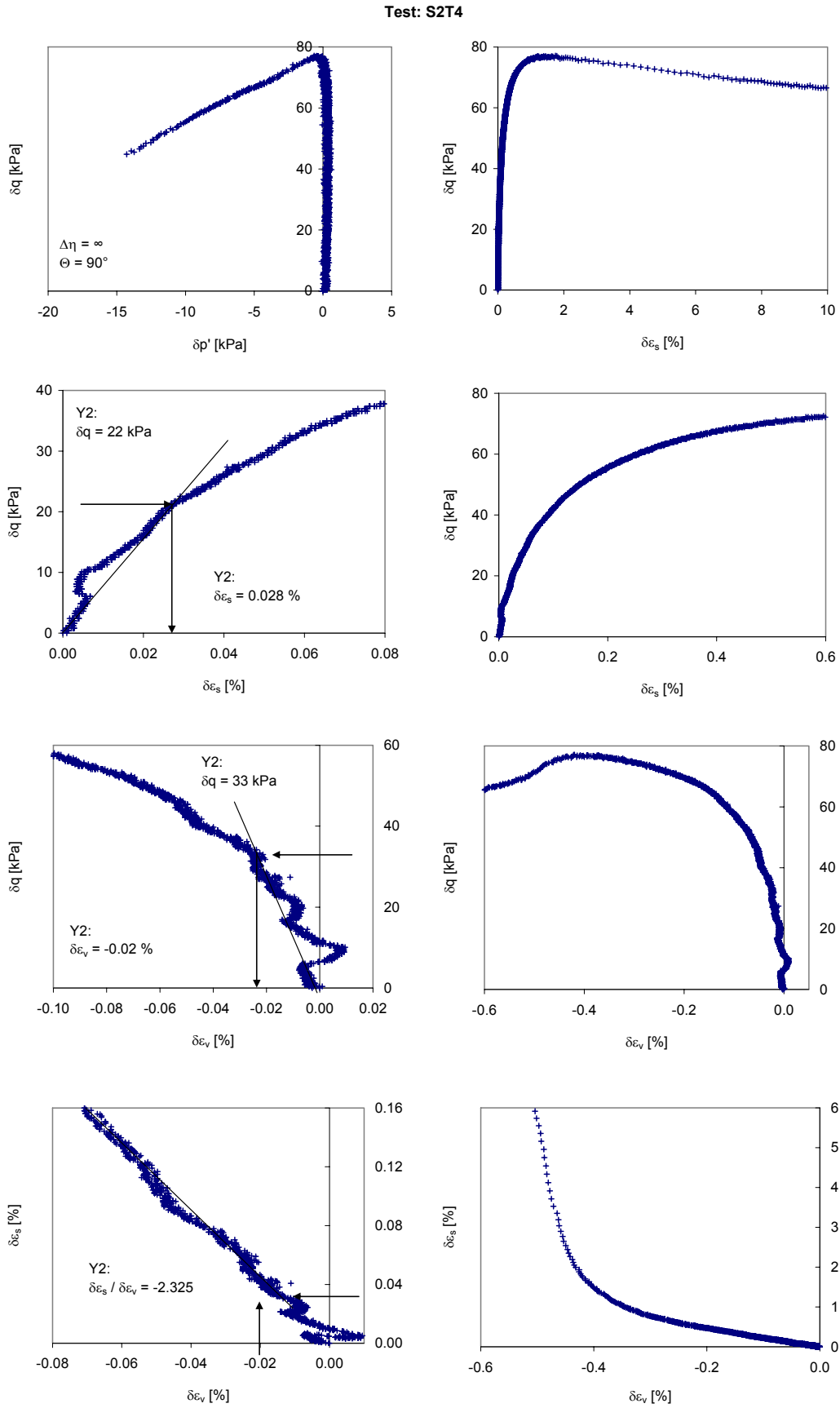
Test: S2T4

Fig. 10.128: Stiffness analysis of the probing path of test S2T4 on natural Kloten clay.
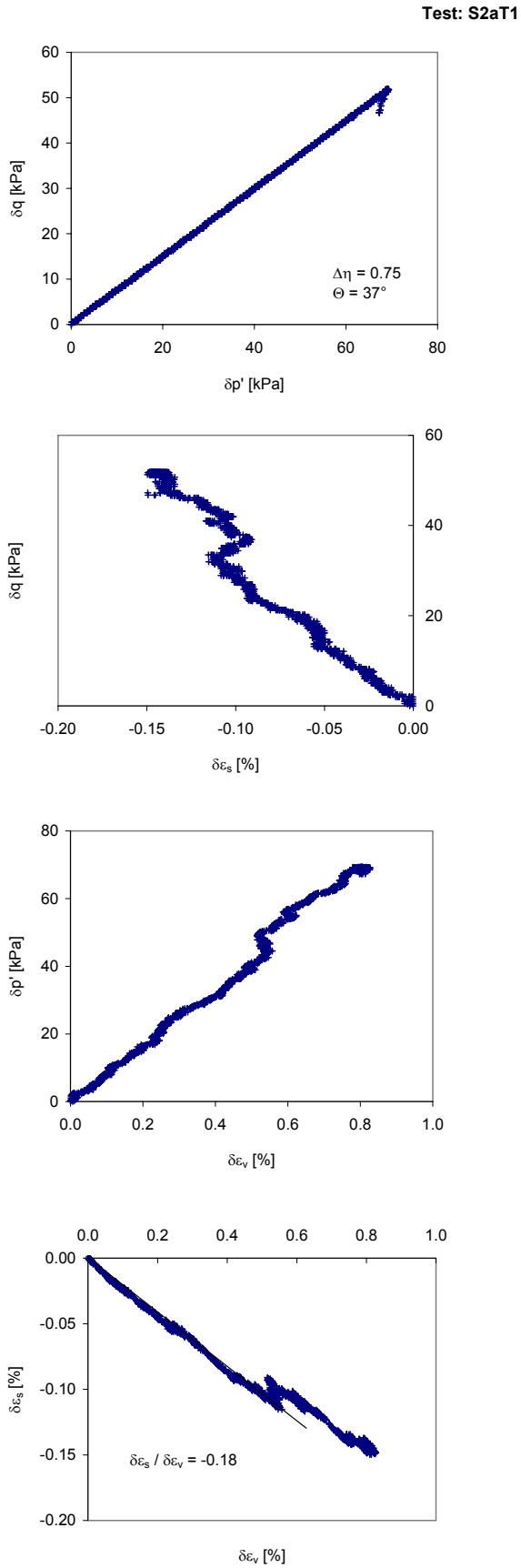
Test: S2aT1

Fig. 10.129: Stiffness analysis of the probing path of test S2aT1 on natural Kloten clay.
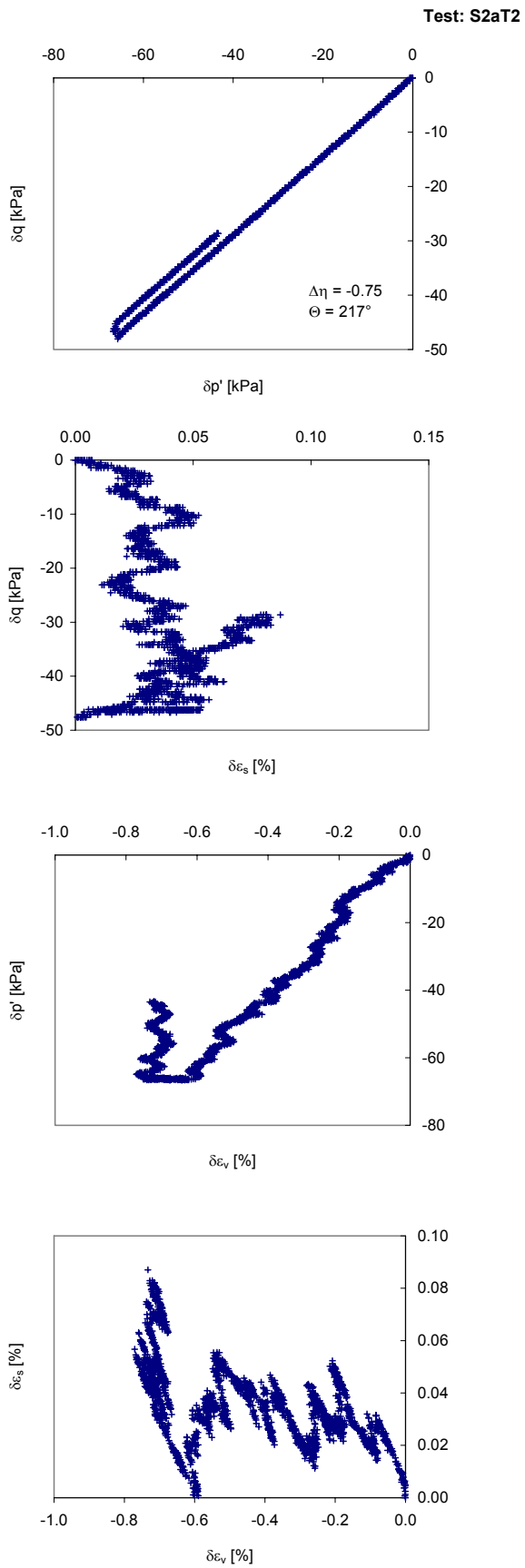
Test: S2aT2

Fig. 10.130: Stiffness analysis of the probing path of test S2aT2 on natural Kloten clay.
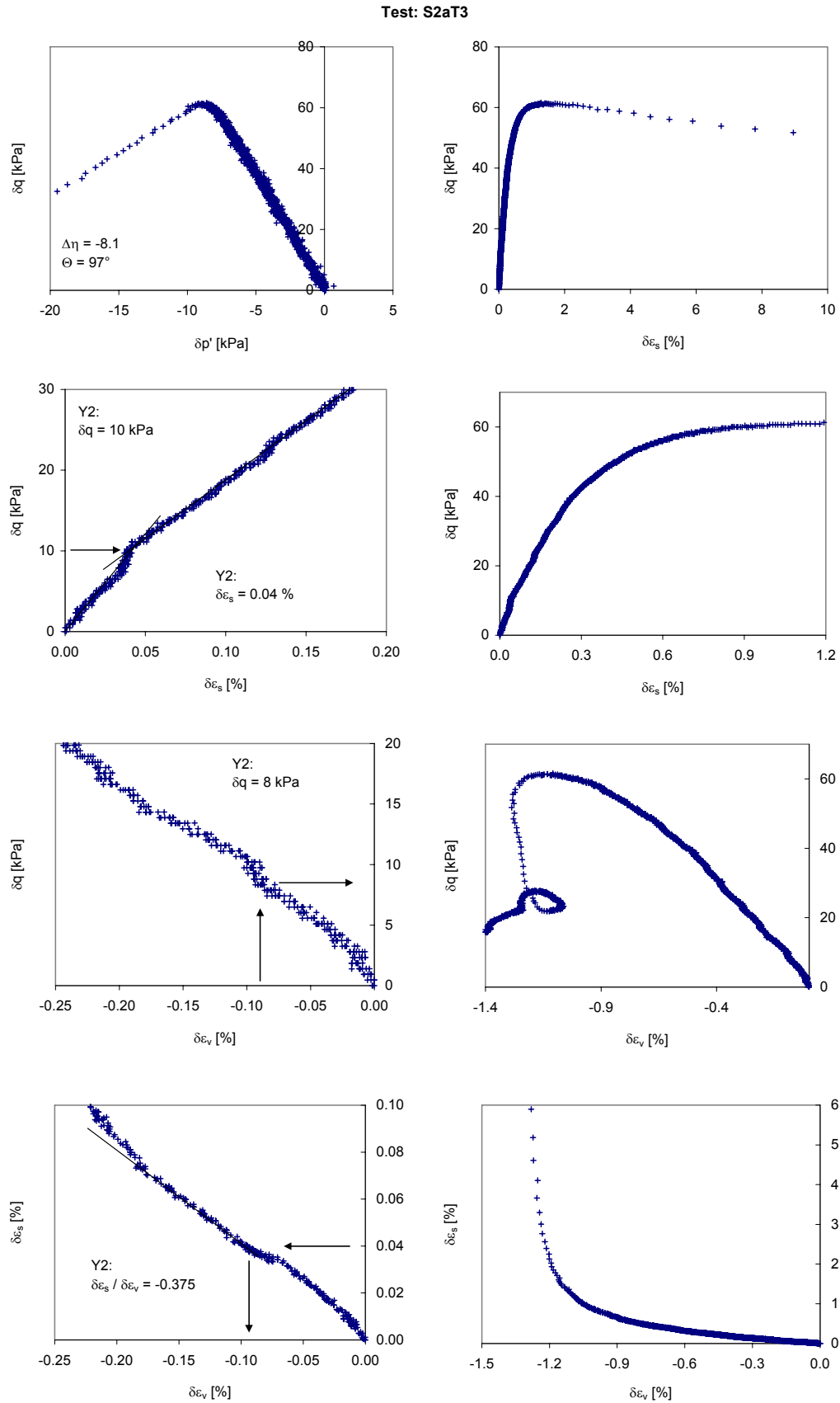
Test: S2aT3

Fig. 10.131: Stiffness analysis of the probing path of test S2aT3 on natural Kloten clay.

428
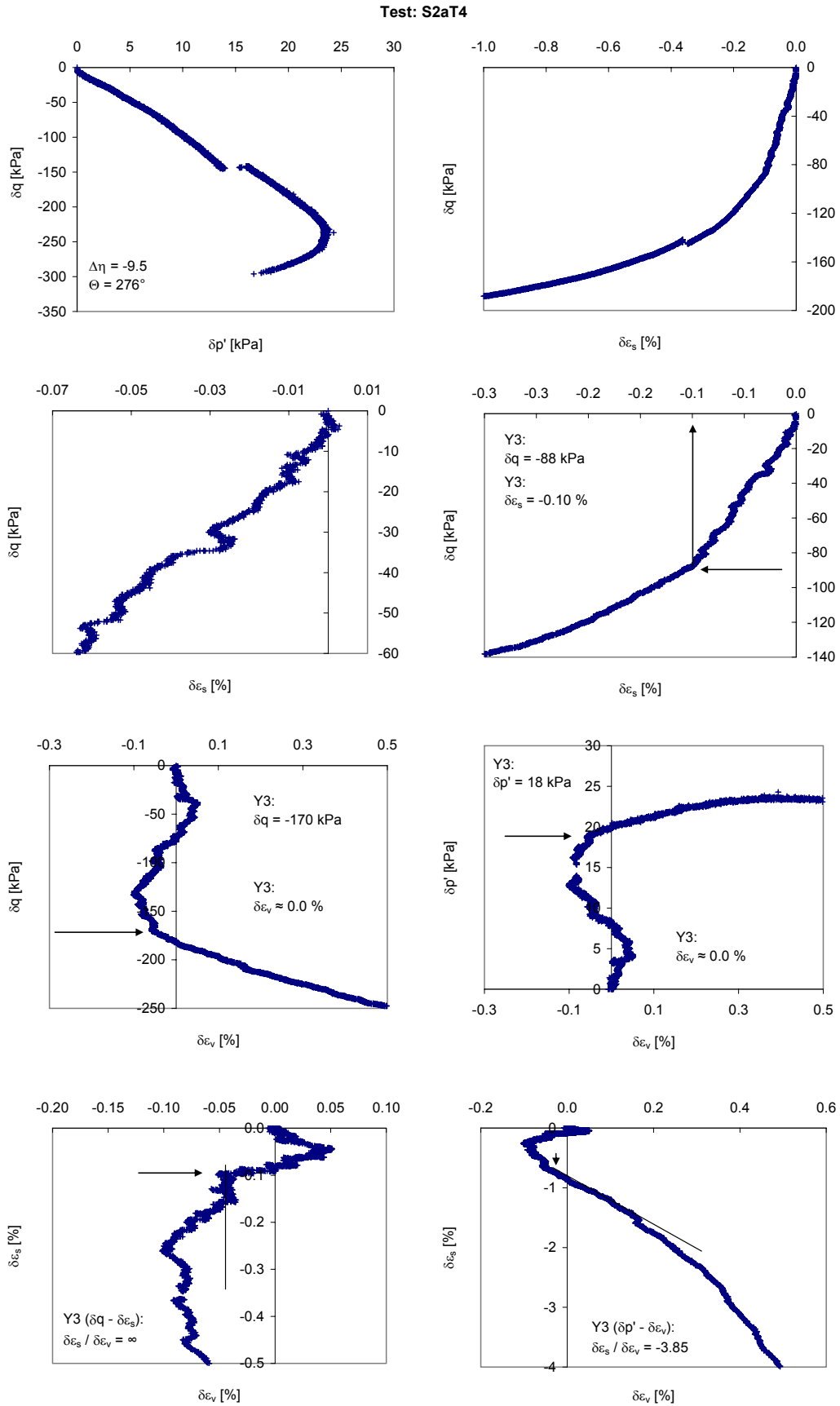
Test: S2aT4

Fig. 10.132: Stiffness analysis of the probing path of test S2aT4 on natural Kloten clay.
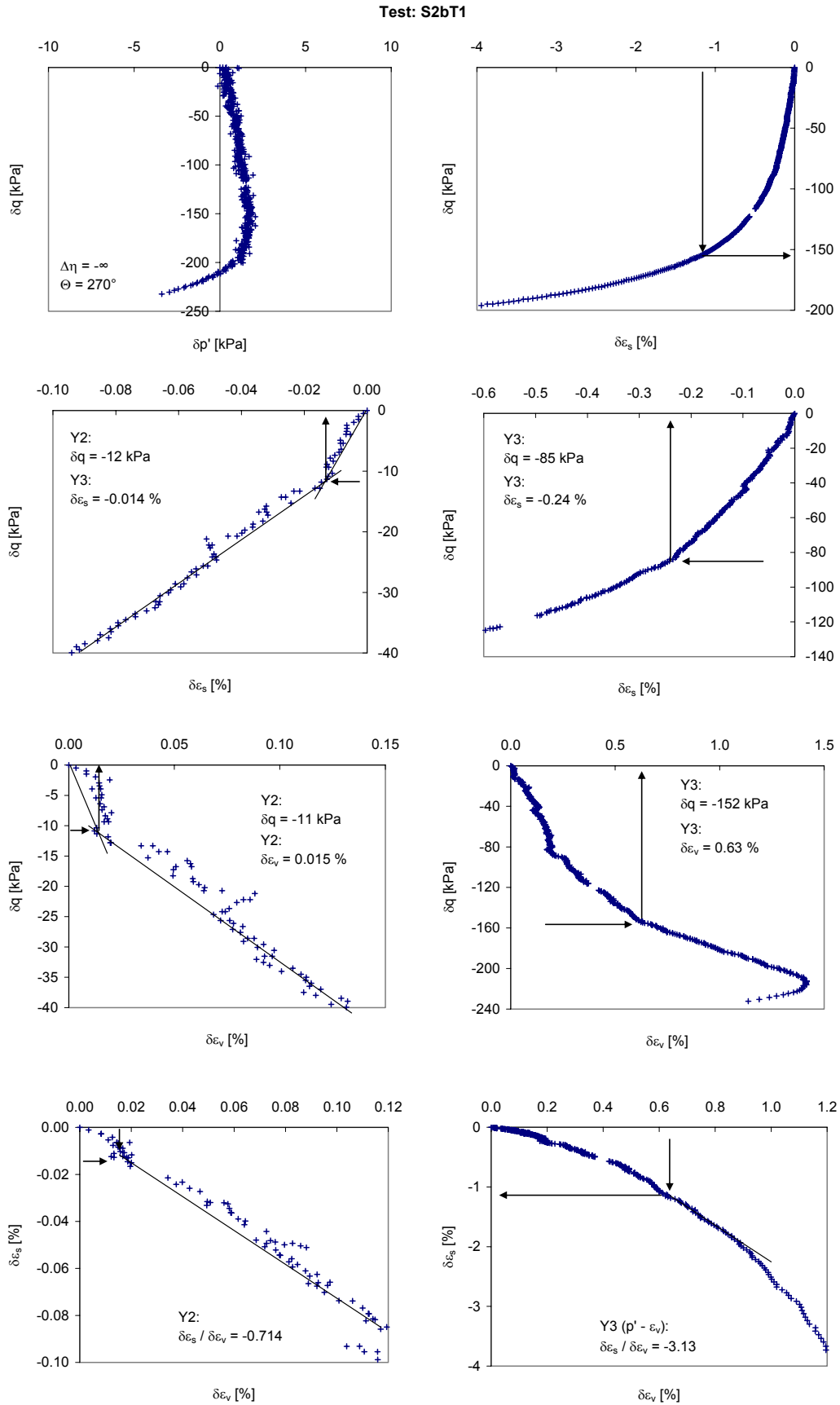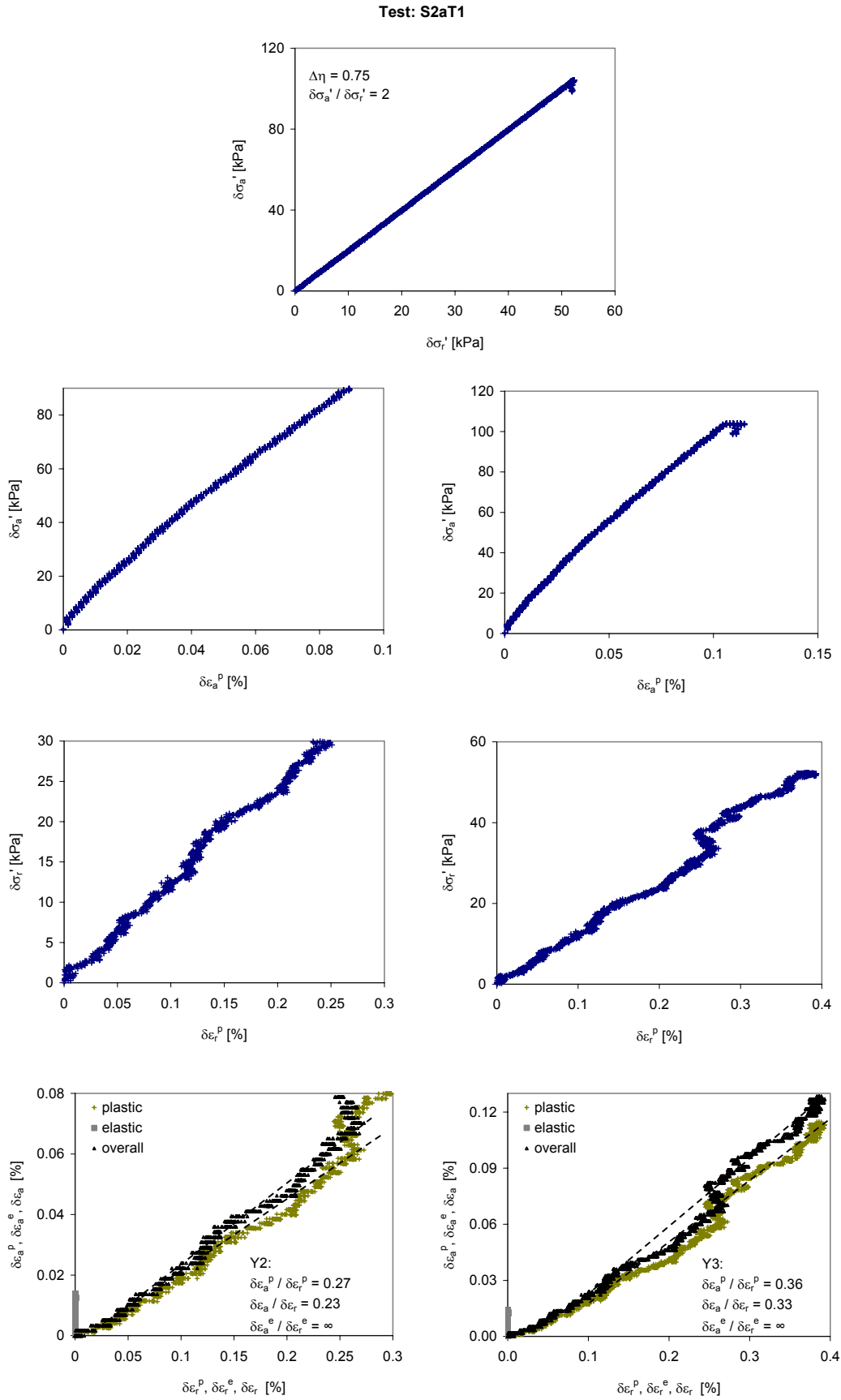
Fig. 10.133: Stiffness analysis of the probing path of test S2bT1 on natural Kloten clay.
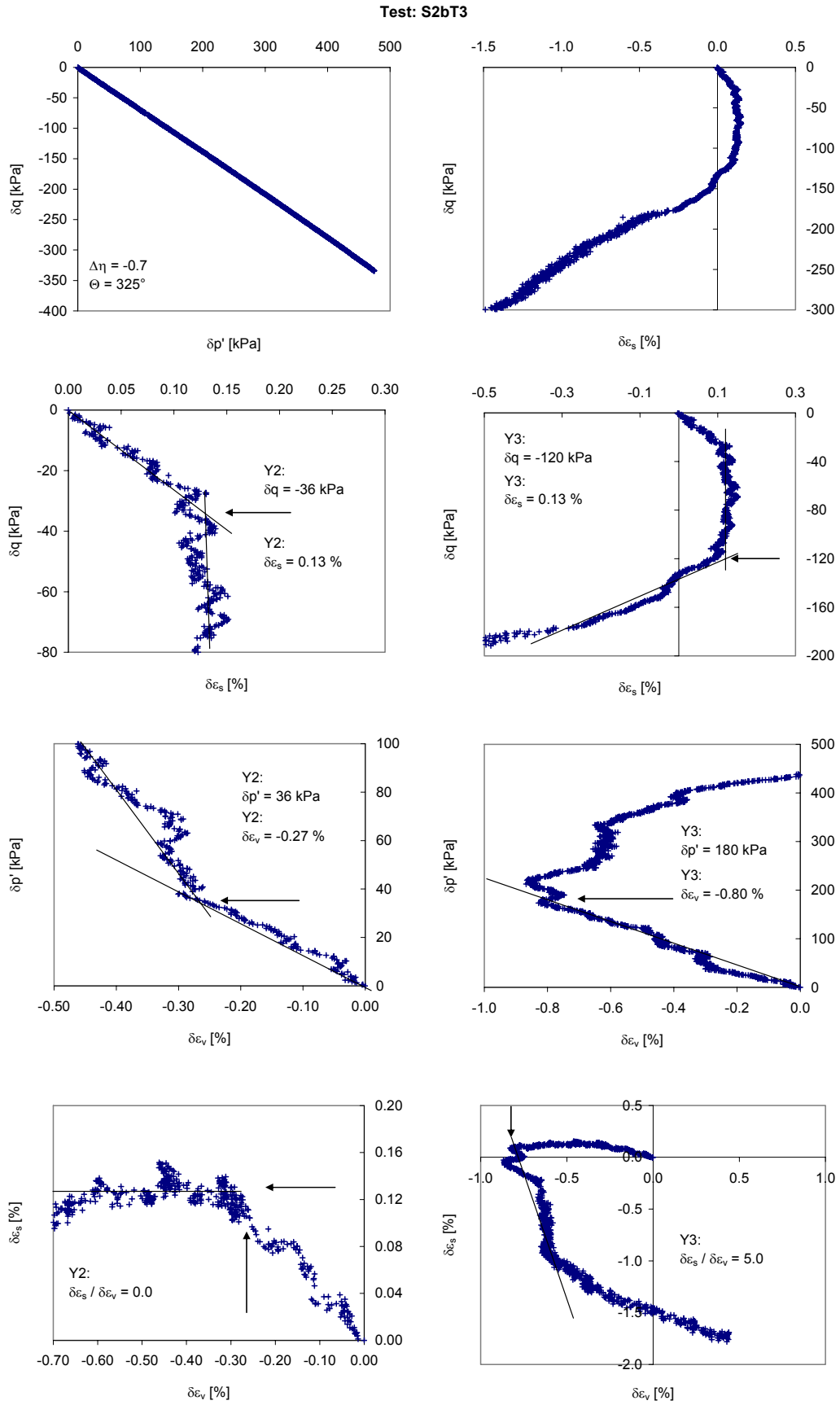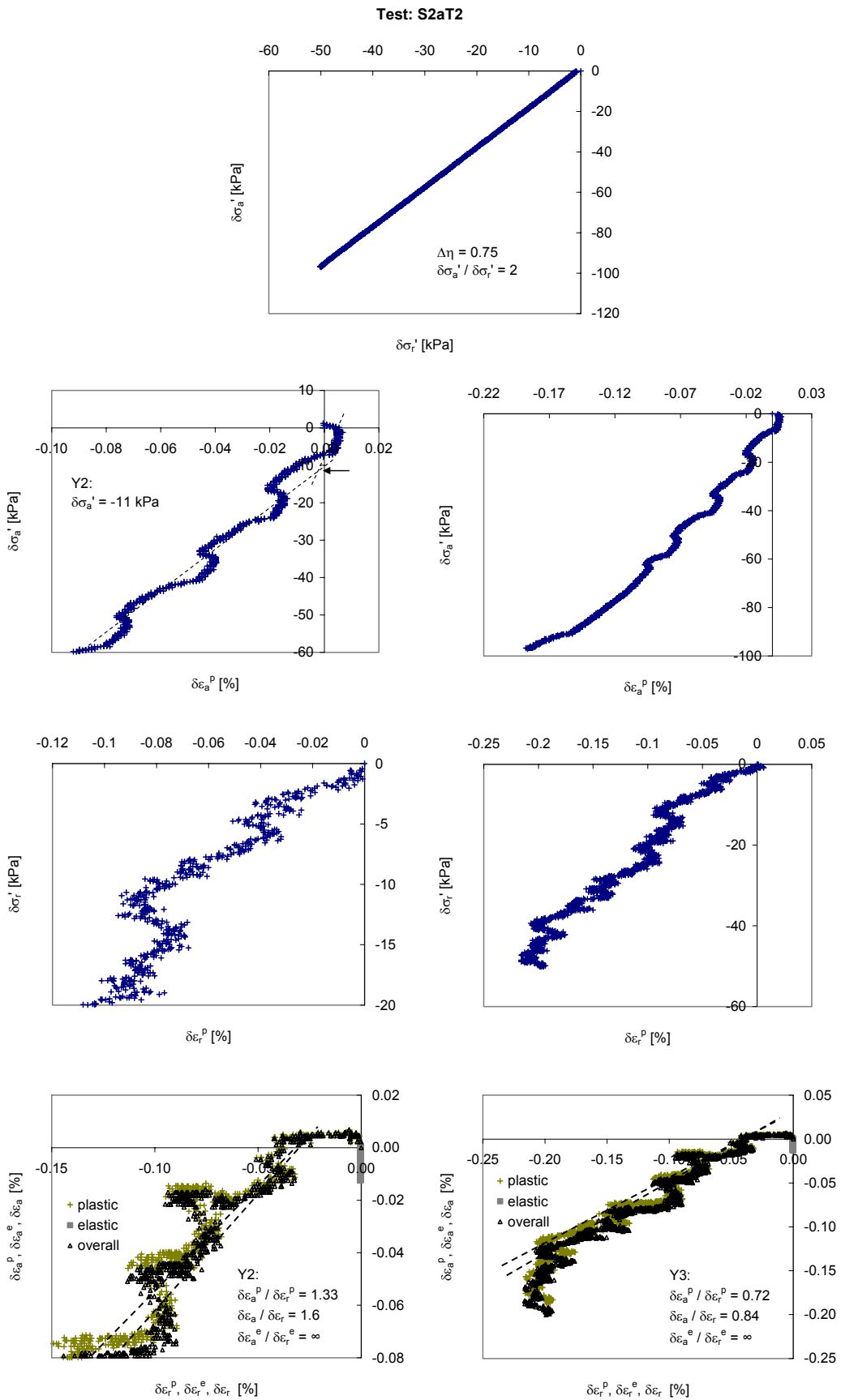
Fig. 10.134: Stiffness analysis of the probing path of test S2bT3 on natural Kloten clay.
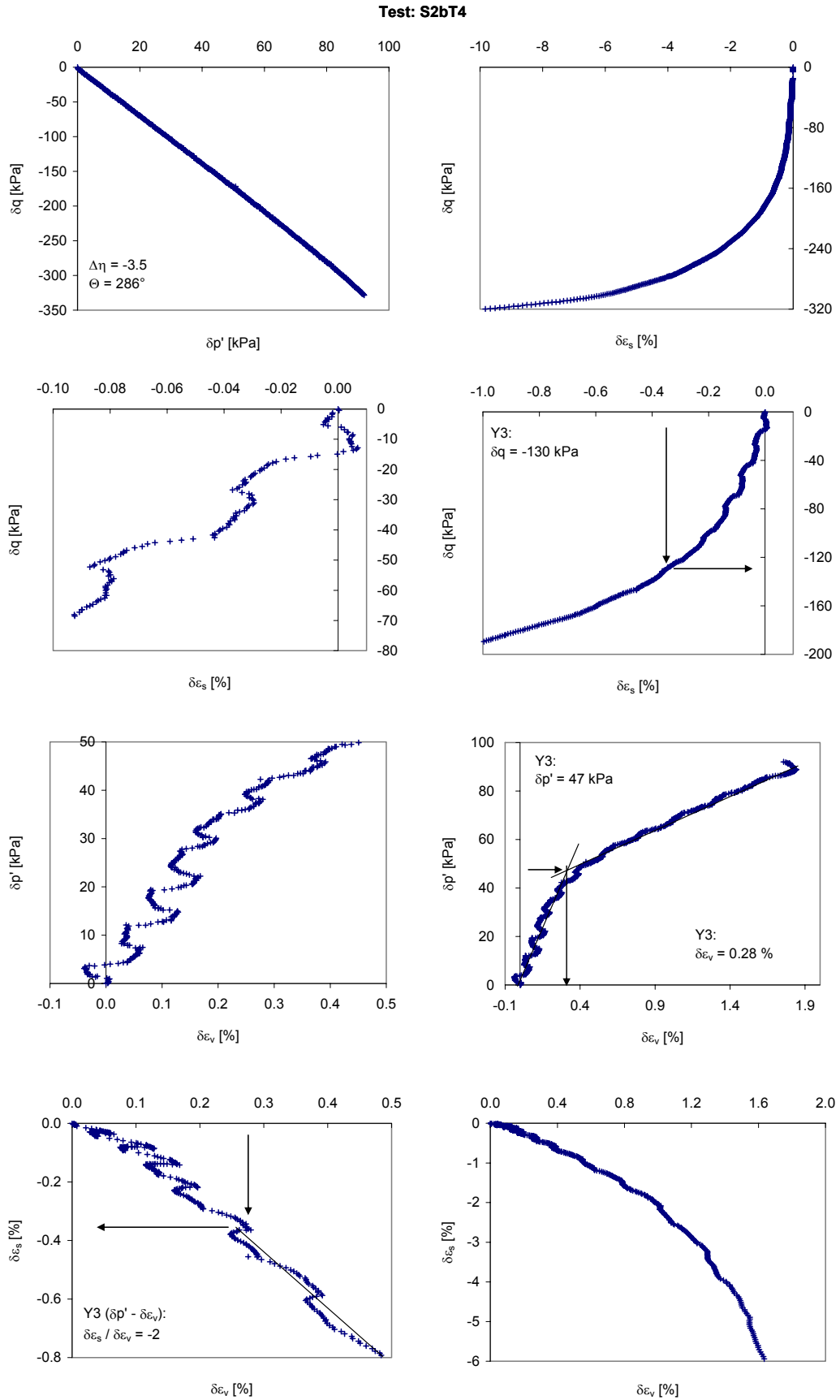
Fig. 10.135: Stiffness analysis of the probing path of test S2bT4 on natural Kloten clay.
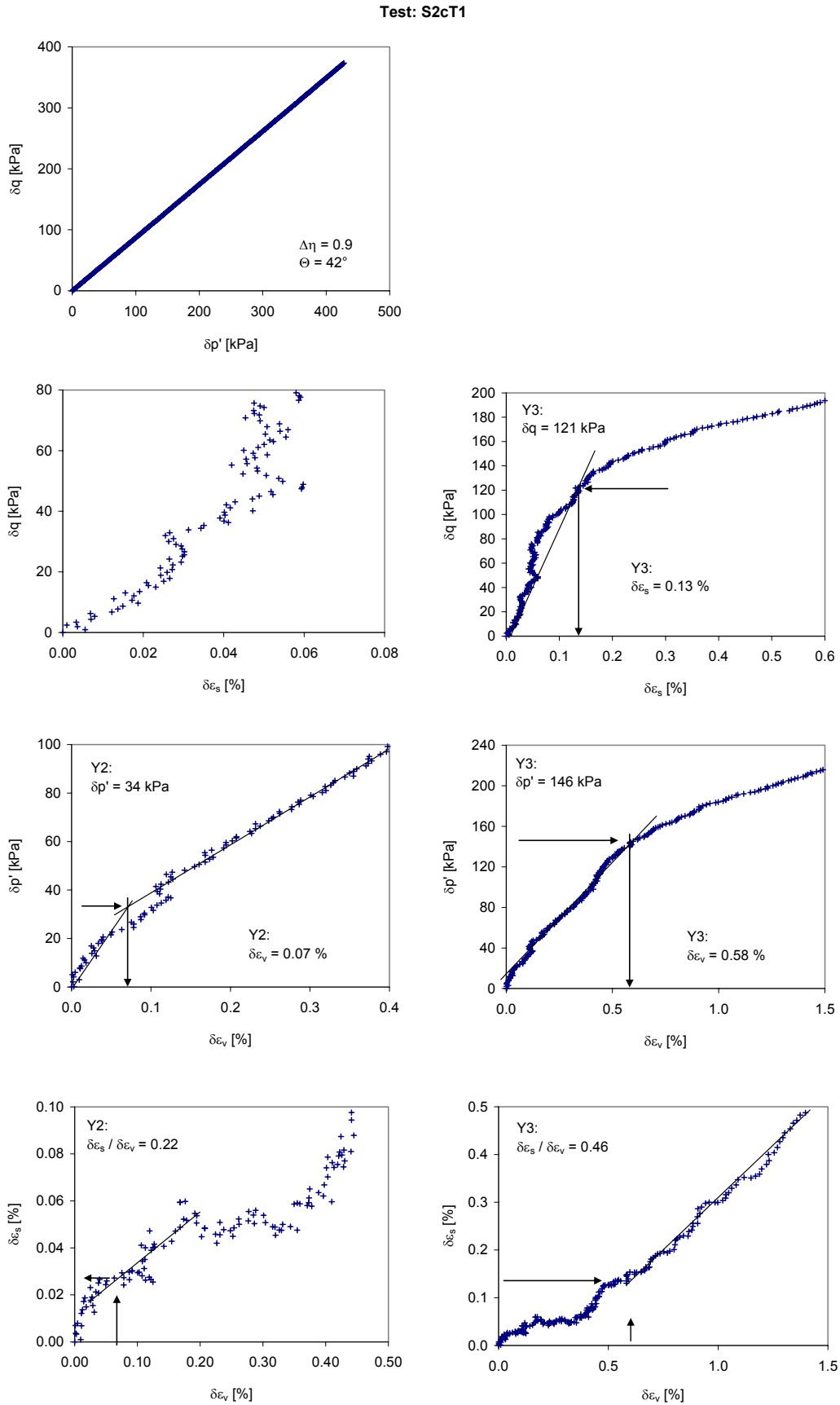
Test: S2cT1

Fig. 10.136: Stiffness analysis of the probing path of test S2cT1 on natural Kloten clay.
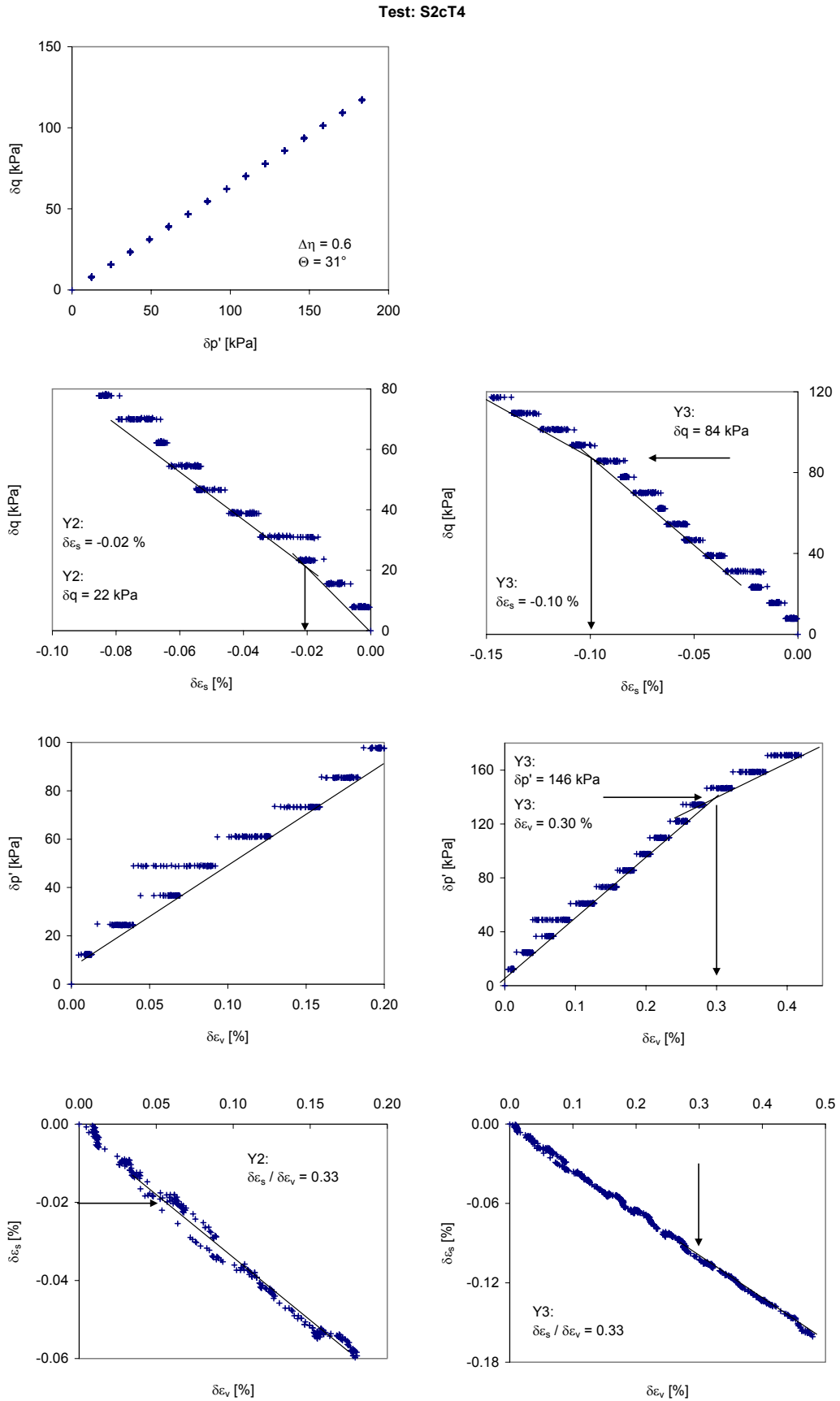
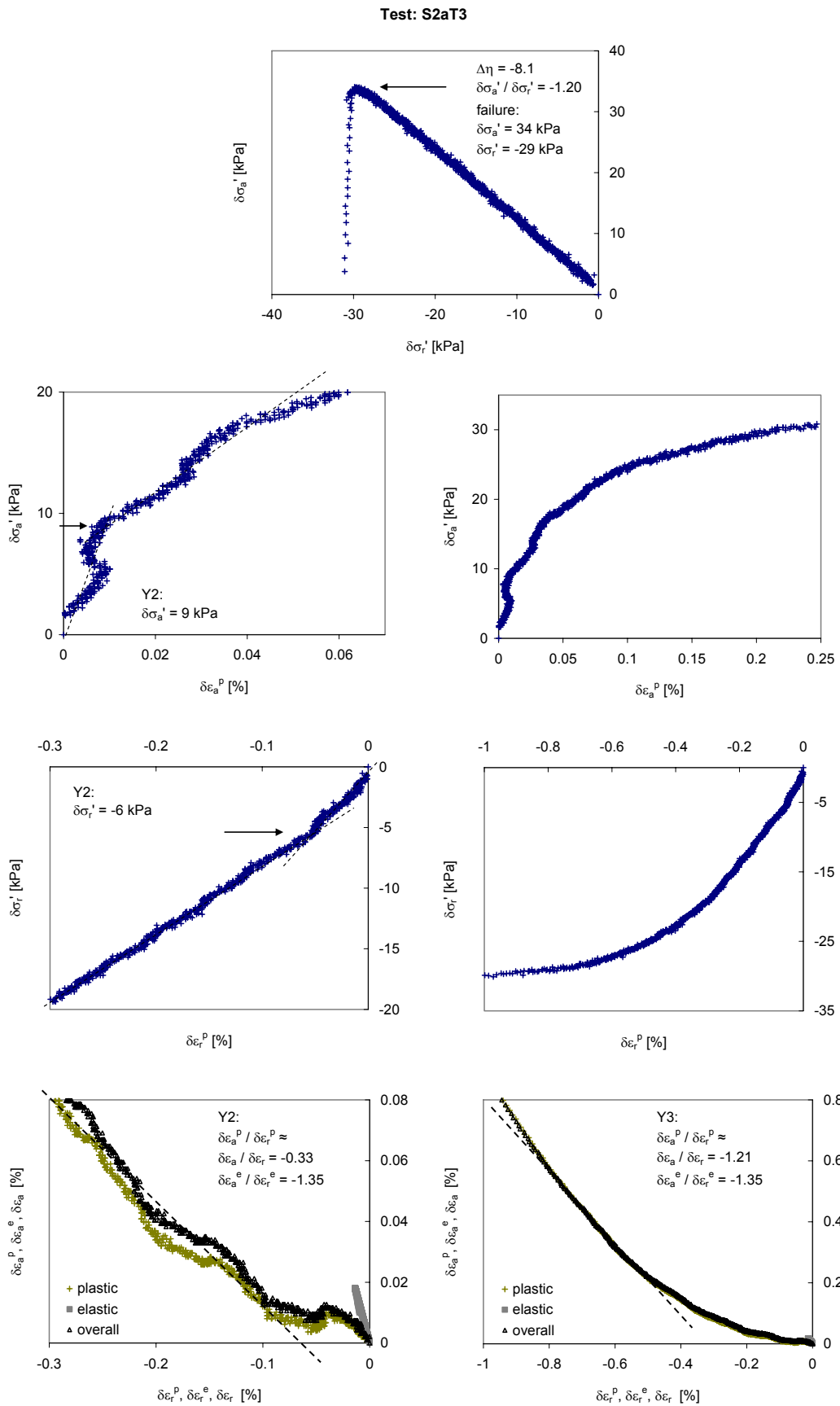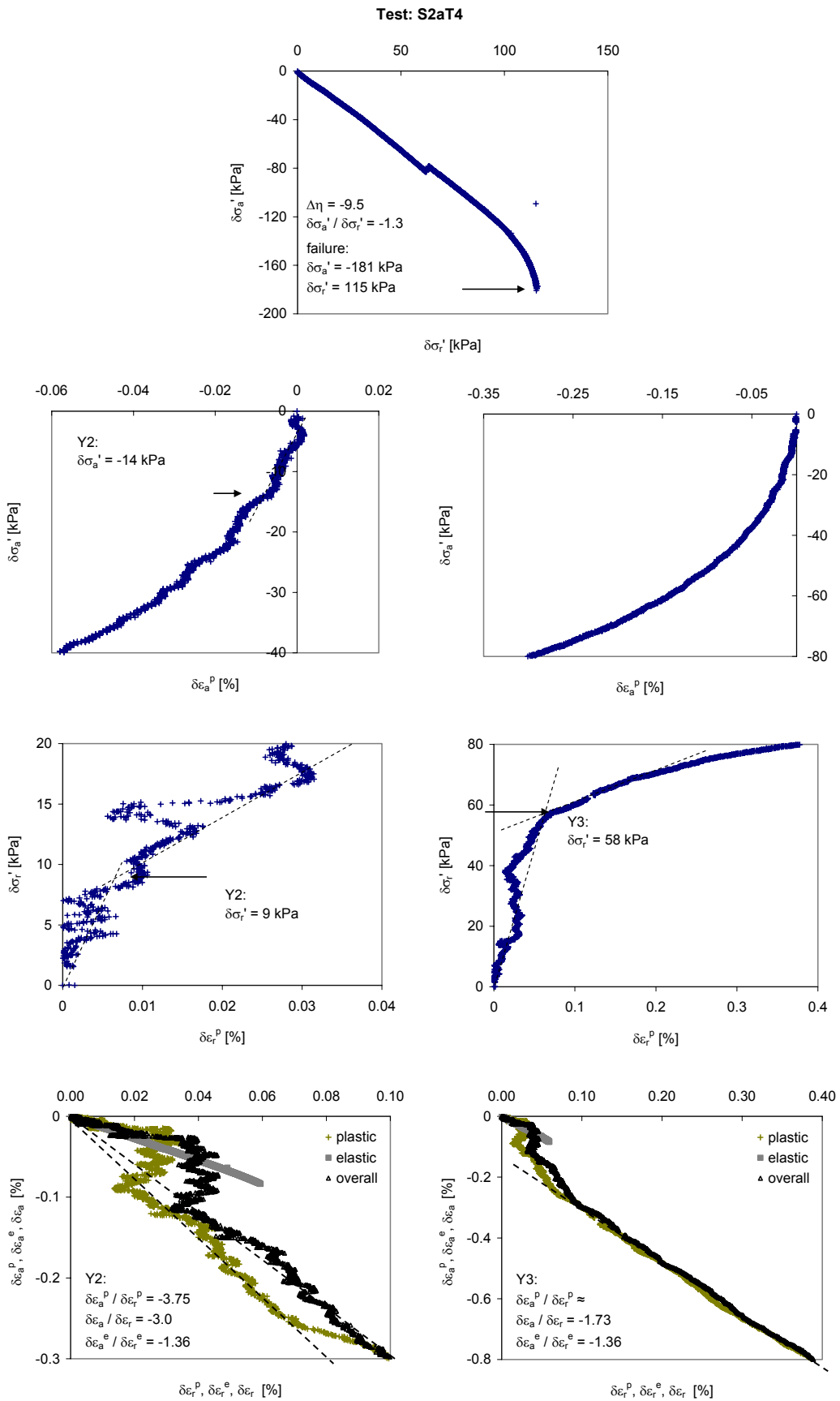Fig. 10.137: Stiffness analysis of the probing path of test S2cT4 on natural Kloten clay.

Test: S2T1

Test: S2T2

Test: S2T3
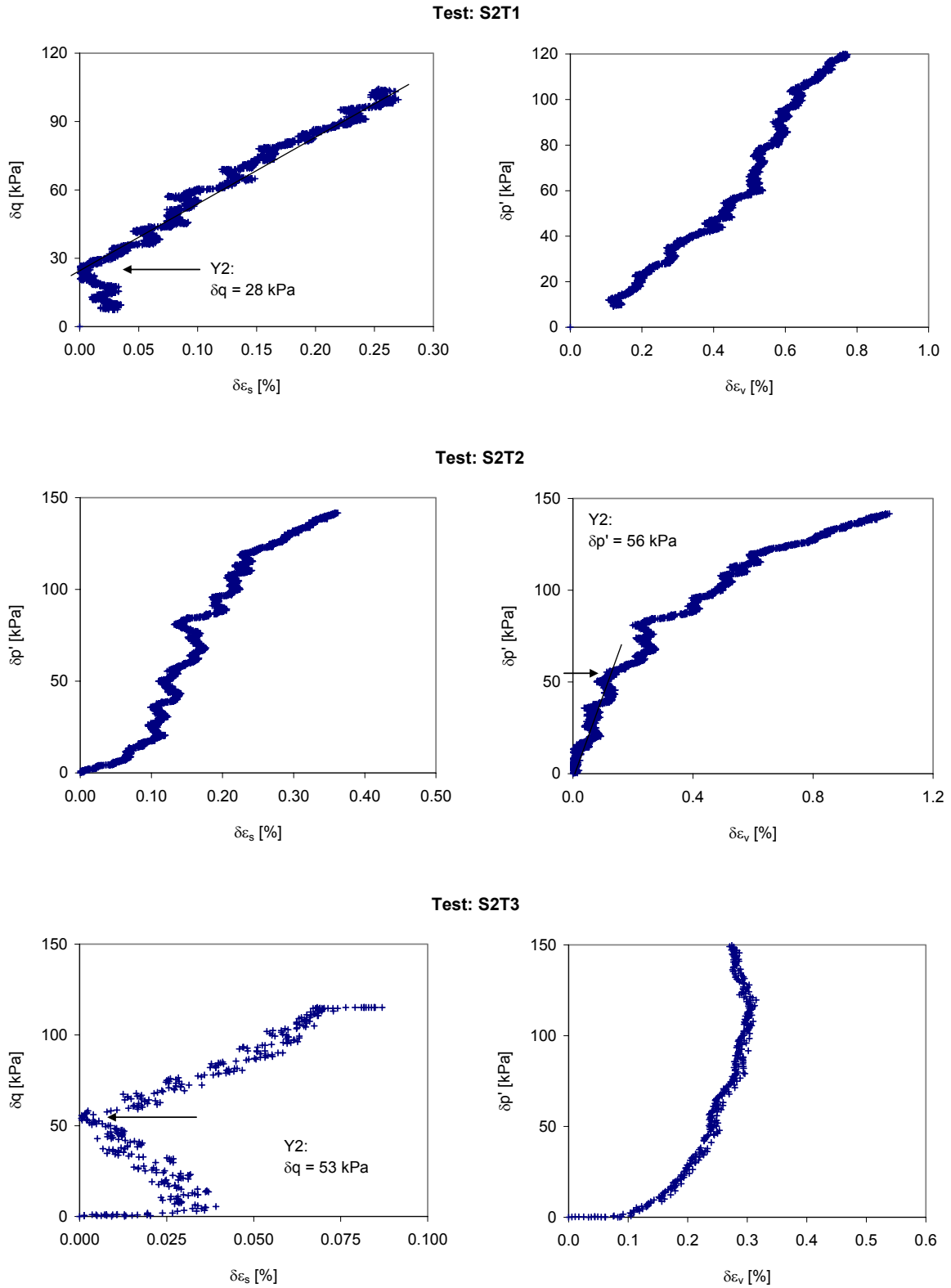
Fig. 10.138: Stiffness analysis of the swelling path of triaxial tests on natural Kloten clay.

Test: S2T4

Test: S2aT1

Test: S2aT2
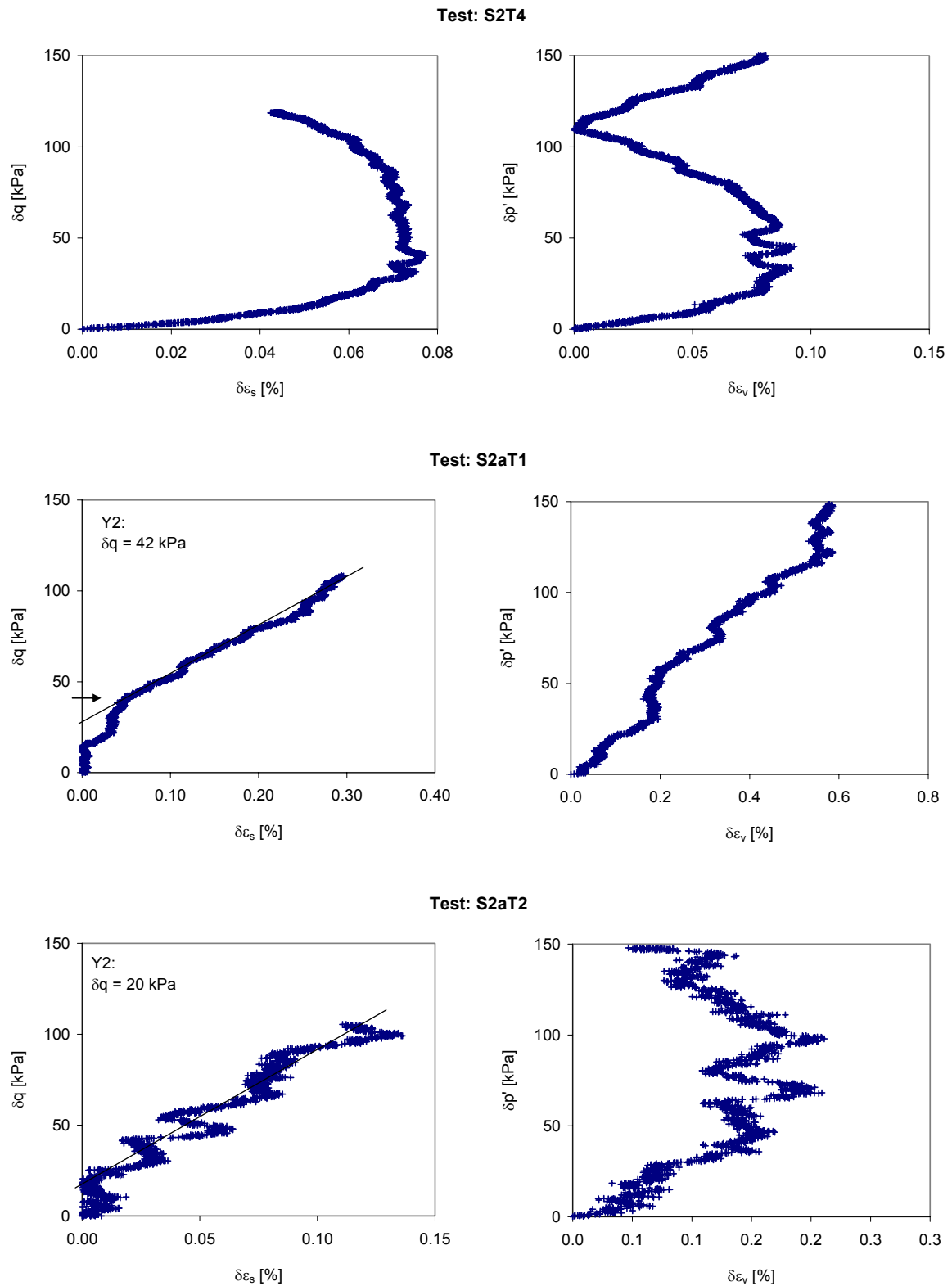
Fig. 10.139: Stiffness analysis of the swelling path of triaxial tests on natural Kloten clay.

Test: S2aT3

Test: S2aT4

Test: S2bT1
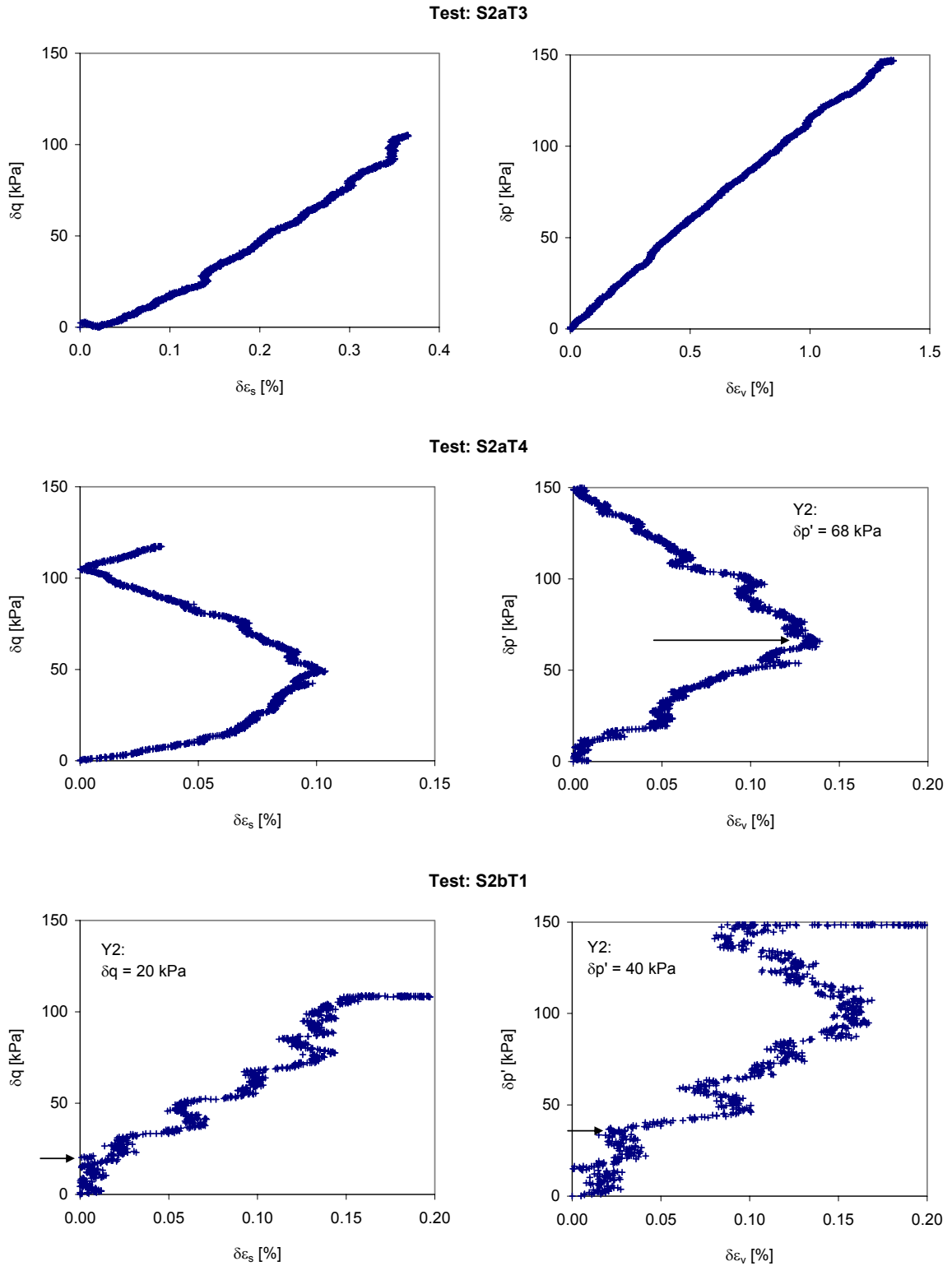
Fig. 10.140: Stiffness analysis of the swelling path of triaxial tests on natural Kloten clay.

Test: S2bT3

Test: S2bT4

Test: S2cT1

Fig. 10.141: Stiffness analysis of the swelling path of triaxial tests on natural Kloten clay.

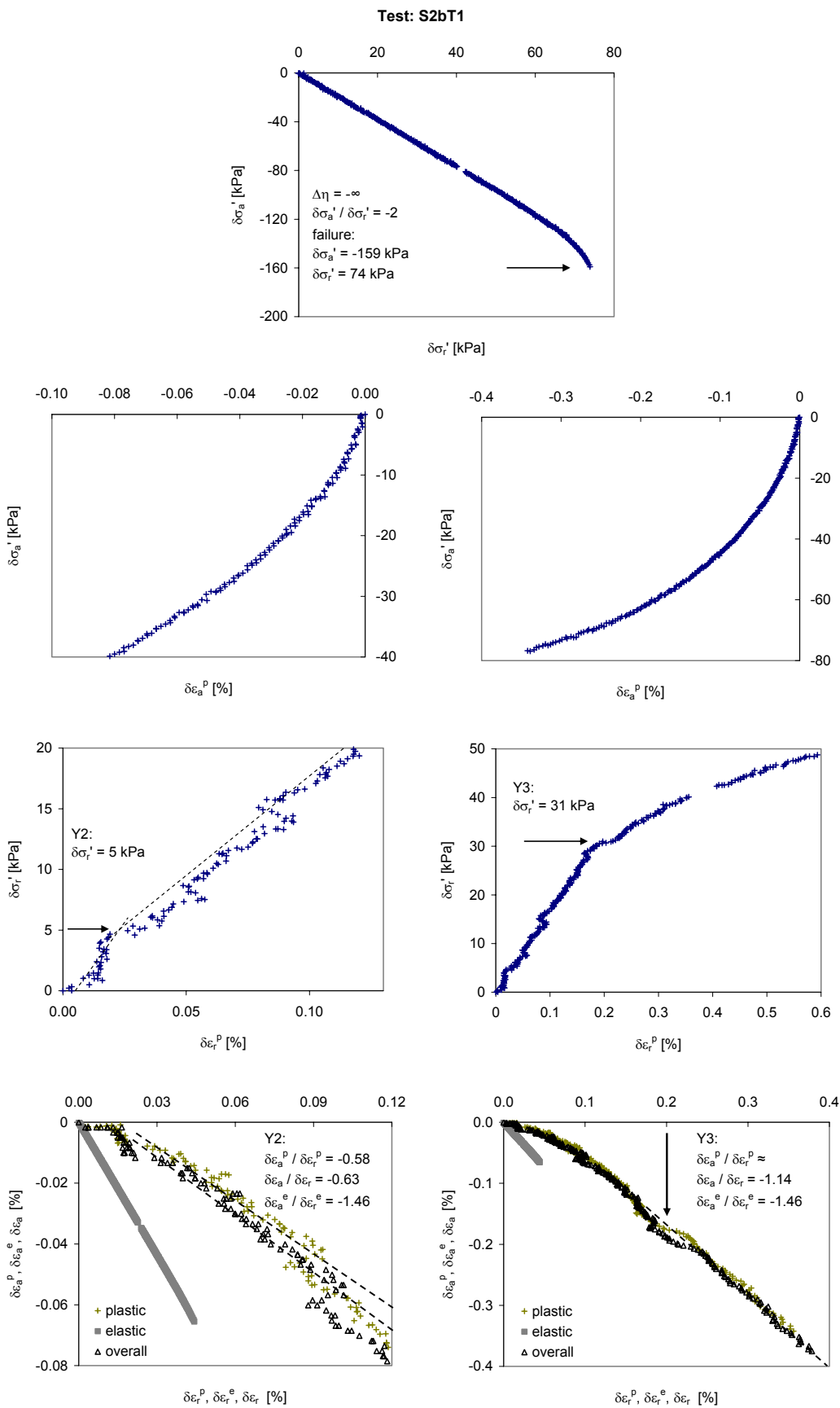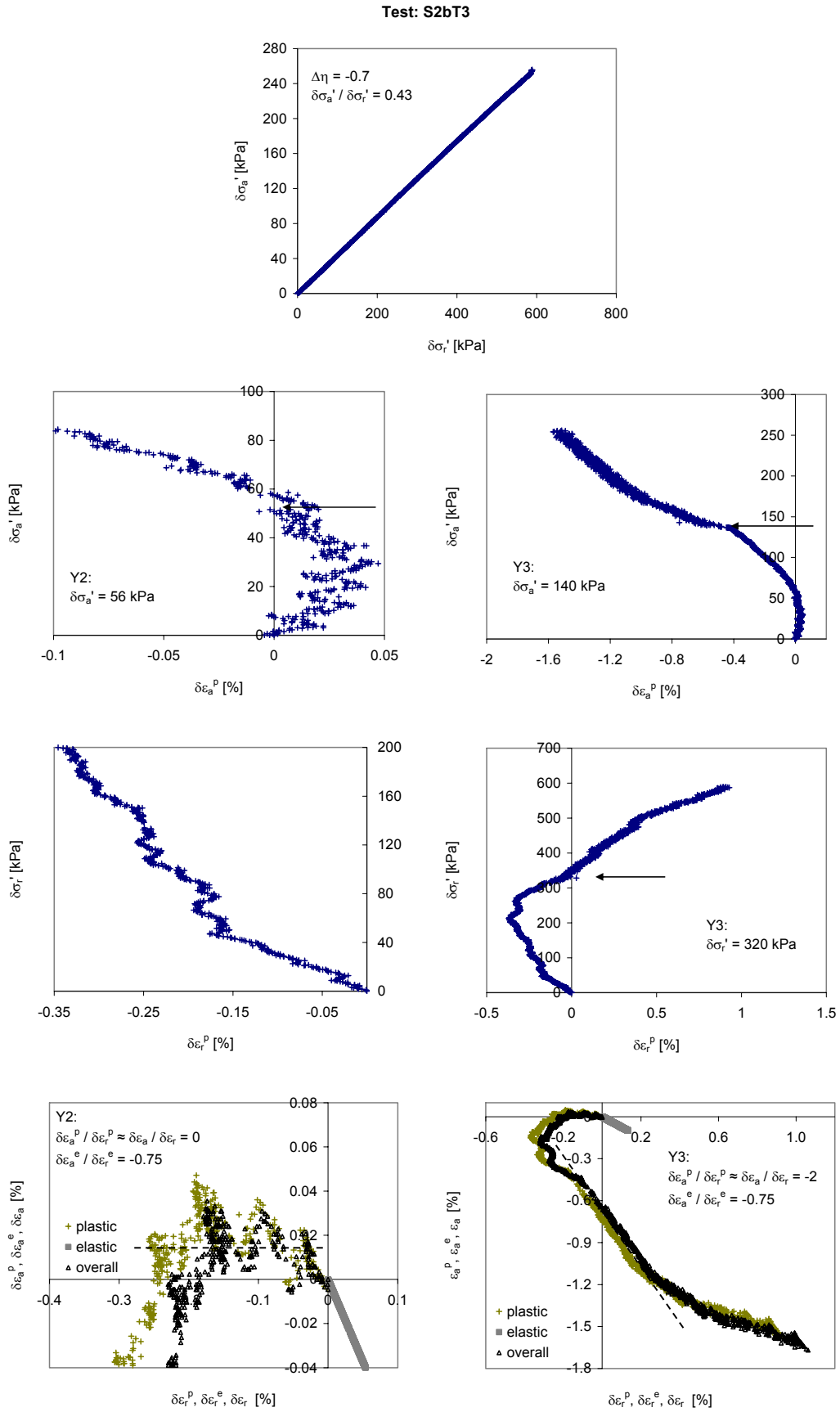Fig. 10.142: Stiffness analysis of the swelling path of triaxial tests on natural Kloten clay.

Fig. 10.143: Stiffness analysis of the probing path of test S2T1 on natural Kloten clay.

Fig. 10.144: Stiffness analysis of the probing path of test S2T2 on natural Kloten clay.

Test: S2T3

Fig. 10.145: Stiffness analysis of the probing path of test S2T3 on natural Kloten clay.

Test: S2T4

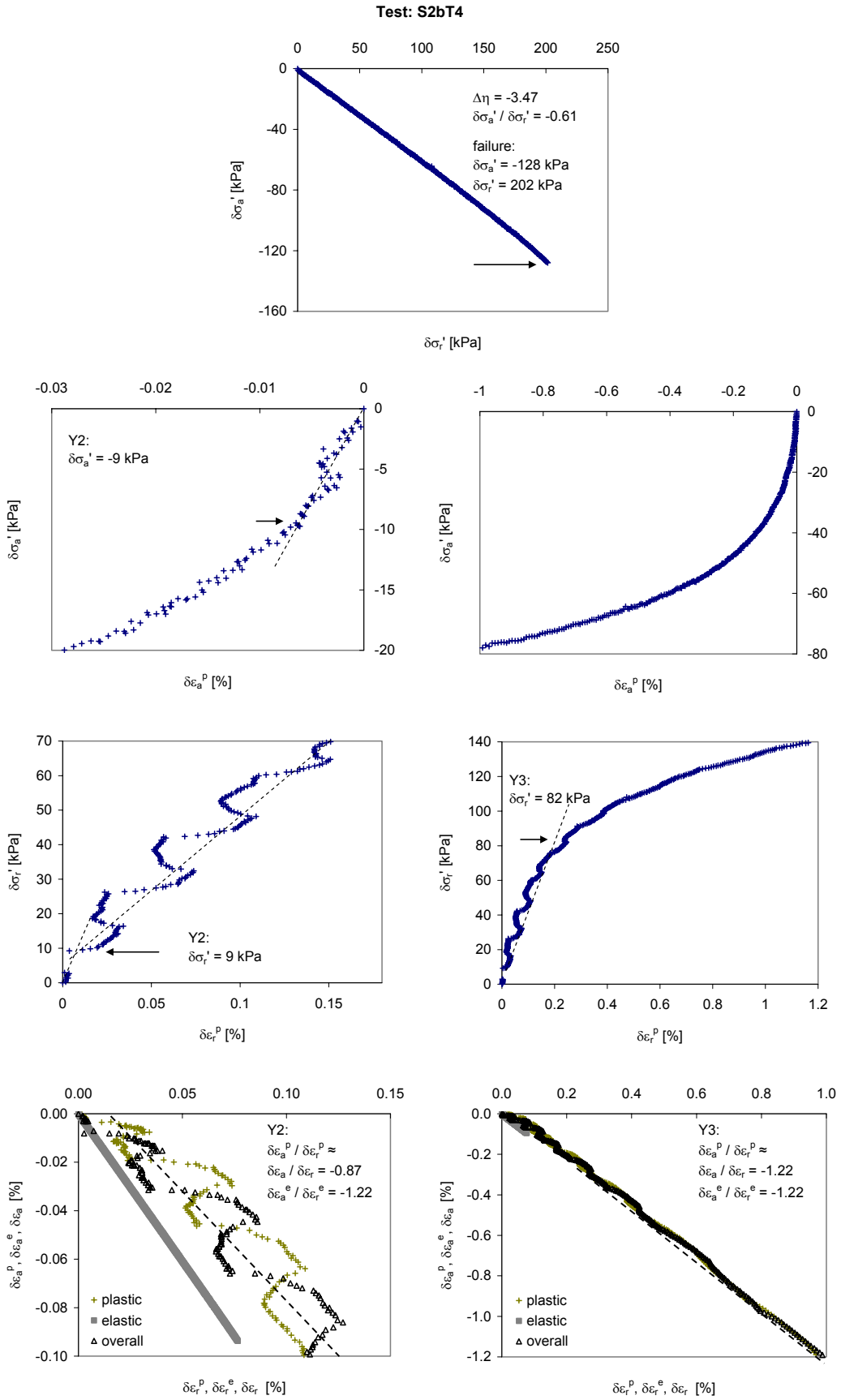Fig. 10.146: Stiffness analysis of the probing path of test S2T4 on natural Kloten clay.

443

Fig. 10.147: Stiffness analysis of the probing path of test S2aT1 on natural Kloten clay.

Fig. 10.148: Stiffness analysis of the probing path of test S2aT2 on natural Kloten clay.

Test: S2aT3

Fig. 10.149: Stiffness analysis of the probing path of test S2aT3 on natural Kloten clay.

Test: S2aT4

Fig. 10.150: Stiffness analysis of the probing path of test S2aT4 on natural Kloten clay.

447

Test: S2bT1

Fig. 10.151: Stiffness analysis of the probing path of test S2bT1 on natural Kloten clay.

Fig. 10.152: Stiffness analysis of the probing path of test S2bT3 on natural Kloten clay.

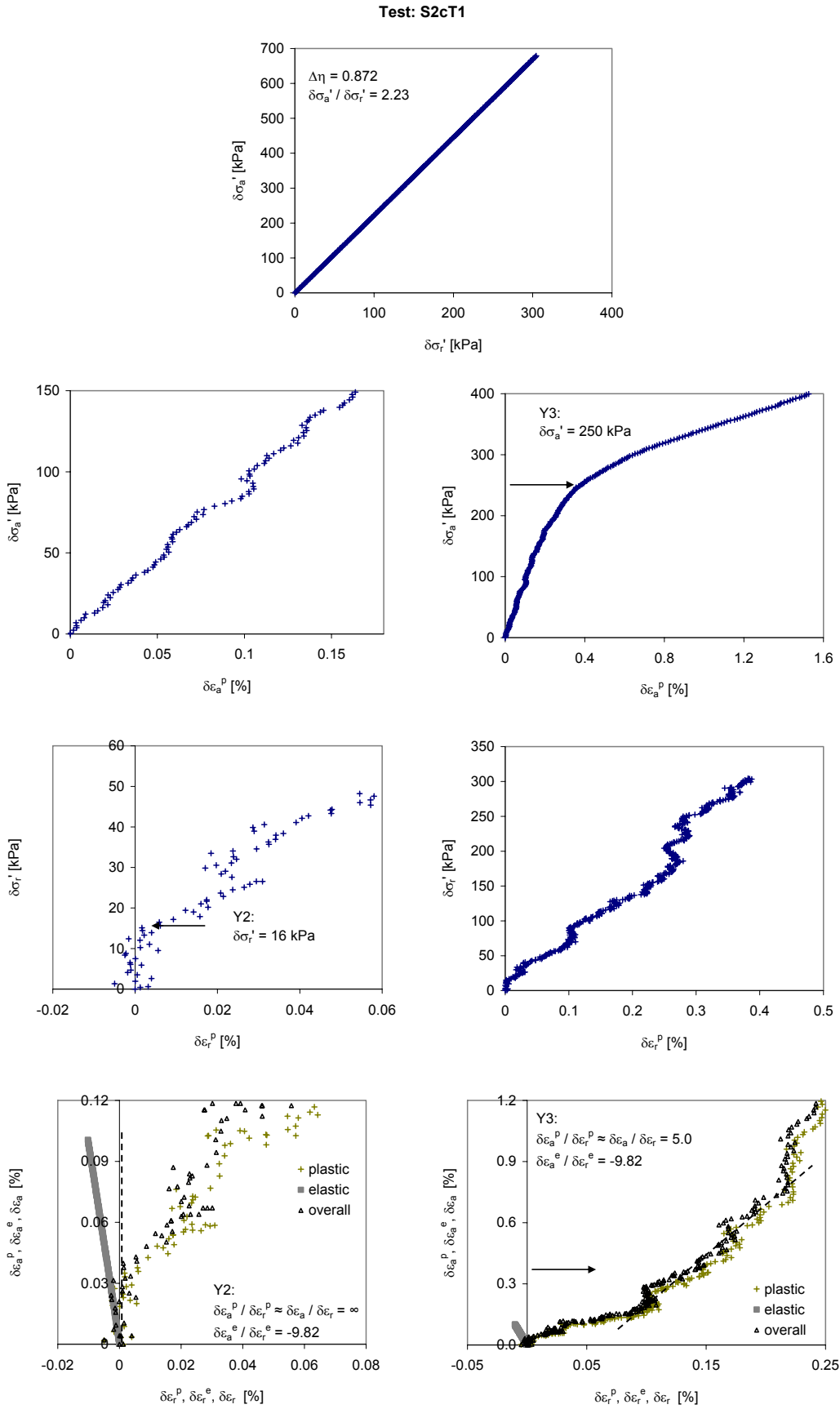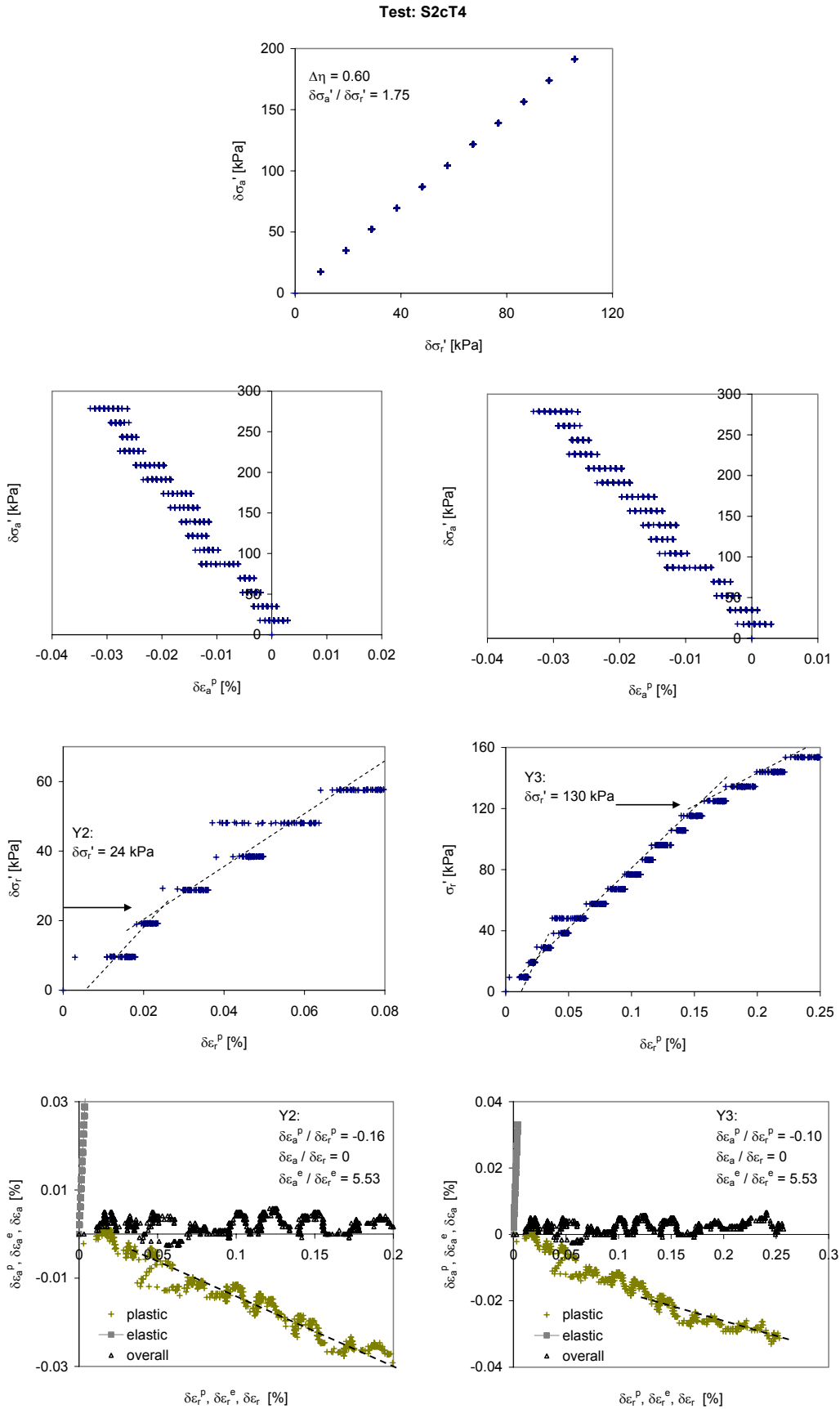Fig. 10.153: Stiffness analysis of the probing path of test S2bT4 on natural Kloten clay.

Test: S2cT1

Fig. 10.154: Stiffness analysis of the probing path of test S2cT1 on natural Kloten clay.

Fig. 10.155: Stiffness analysis of the probing path of test S2cT4 on natural Kloten clay.

Curriculum vitae

Sophie Messerklinger

Personal data:

Born on September 23, 1977 in Salzburg, citizen of Austria

Languages: German (native) and English

Professional education:

2003 – 2006	Dissertation, Institute for Geotechnical Engineering, ETH Zürich
2001	Diploma thesis, University of Glasgow (GB)
1996 – 2001	Bachelor and Master in Civil Engineering Science: Construction Engineering, Graz University of Technology
1996 – 2001	Bachelor and Master in Civil Engineering – Economics, Graz University of Technology
1991 – 1996	A-levels in civil engineering: structural engineering, Technical High School, Salzburg

Professional experience:

2002 – 2006	Teaching and research assistant, Institute for Geotechnical Engineering; Prof. Springman, ETH Zürich
2000	Practical training, construction company Hartl-Bau, Salzburg
1999	Practical training in surveying, Electrical Power company, Salzburg
1997 – 1998	Design training, consulting engineers Dr. Medicus, Salzburg
1995 – 1996	Practical training, construction company Ing. Franz Messerklinger GesmbH & CoKG, Ostermiething
1994	Architectural practice, Architect Kredwig, Freilassing (BRD)
1992 & 1993	Practical training, construction company Hutterer, Strasswalchen

Additional activities:

2004 – 2005	Secretary of the European Marie Curie Research Training Network "Advanced Modelling of Ground Improvement on Soft Soils – AMGISS"
2004	Master craftsman's certificate in construction engineering (Austrian Federal Economic Chamber)
1998 – 2001	Member of the Steel Structures Student Union at Graz University of Technology
1999 – 2001	Member of the Curriculum commission of the Bachelor and Master programmes: Civil Engineering Science and Civil Engineering Science - Economics at Graz University of Technology

Zurich, February 14, 2006 — Sophie Messerklinger